

# **SOLAR ASIA – 2011**

**PROCEEDINGS OF THE INTERNATIONAL CONFERENCE**

**ON**

## **SOLAR ENERGY MATERIALS, SOLAR CELLS AND SOLAR ENERGY APPLICATIONS**

**28-30 July 2011**

**INSTITUTE OF FUNDAMENTAL STUDIES, KANDY, SRI  
LANKA**

*Jointly Organized by*



**Institute of Fundamental Studies  
Kandy, Sri Lanka**



**National Science Foundation  
Colombo, Sri Lanka**

*Editors*

M.A.K.L. Dissanayake  
I.M. Dharmadasa  
R. Weerasooriya  
G.K.R. Senadeera  
J.M.S. Bandara

## PREFACE

Research on solar energy materials and solar cells is a fast growing interdisciplinary area of science and technology today. During the past two decades, physicists, chemists, material scientists, engineers and industry personnel have focused their attention to develop novel materials for highly efficient and low cost solar cells and PV devices. There are also significant developments in solar photovoltaic and solar thermal applications. Scientists and technologists in Asian countries continue to make notable contributions to these developments. The Solar-Asia 2011 international conference, jointly organized by the Institute of Fundamental Studies (IFS), Kandy, Sri Lanka and the National Science Foundation (NSF), Colombo, Sri Lanka and held at the Institute of Fundamental Studies, Kandy from 28<sup>th</sup> to 30<sup>th</sup> July 2011 provided a forum for researchers from Asia and other countries to present their research, to exposed to latest developments in their respective research areas and to network with experts in the field.

SOLAR ASIA – 2011 international conference covered research and R&D of solar energy materials, solar cell structures and solar energy applications. 90 research scientists representing 14 countries, including 60 from Sri Lanka, participated in the three-day conference. 58 research papers of high standard were presented. This includes 12 state of the art review lectures given by experts in respective fields. We wish to thank all the invited speakers for accepting our invitation to deliver invited lectures and all the authors and co-authors for sending their manuscripts in time despite their regular busy schedules. Without their cooperation, the printing of the Proceedings would not have been possible.

We are grateful to the Institute of Fundamental Studies (IFS) and the Director Professor C.B. Dissanayake for his active support and constant encouragement throughout the organization of this conference and for providing the necessary infrastructure facilities. We express our gratitude to the National Science Foundation (NSF), its Chairperson Professor Sirimali Fernando and its Director Dr. Sarath Abayawardana for their decision to be a co-organizer of this important international research conference and for providing funds for the printing of the Conference Proceedings.

The conference owes its success primarily to the dedication of the members of the Organizing Committee. We are grateful to the members of the International and Local Advisory Committees, who contributed in numerous ways to make this event a reality. Active support provided by the Secretary of the IFS, Mr. W.T. Waisundara and administrative staff, research staff, secretarial and technical staff, Ms. Sagarika Samarakkody and the accounts division, Dr. Kumari Tilakaratne and the Science Dissemination Unit is gratefully acknowledged. We acknowledge with gratitude the assistance provided by Ms. S. Sellam for formatting the manuscripts, Mr. Chathuranga Thotawattage, Ms. Nadeepa Rupasinghe and Ms. Shasheekala Jayaratne for their help in finalizing the proceedings volume.

M.A.K.L. Dissanayake  
I.M. Dharmadasa  
R. Weerasooriya  
G.K.R. Senadeera  
J.M.S. Bandara

*Editors*

*28 July 2011  
Kandy, Sri Lanka*

## CONTENTS

Preface	ii
Contents	iii
<b>Invited Lectures</b>	
<i>Solar Villages for Social Development and Poverty Reduction</i> I.M. Dharmadasa and L.Gunaratne	1
<i>Technology to Harvest Solar Energy: Single-Crystal CdTe-Based II-VI Materials for Multijunction Cells</i> C.H.Grein, S. Sivananthan and J. Garland	10
<i>Advances in CdTe, CuInGaSe<sub>2</sub> and GaAs/AlGaAs Thin Film PV Solar Cells</i> I.M. Dharmadasa	16
<i>Challenges and Opportunities in Polycrystalline Thin-Film Solar Cells</i> R.Dhere and S.Sivananthan	27
<i>Chemically Deposited Thin Films and Their Application in Solar Cells</i> C.D. Lokhande and S.S. Joshi	28
<i>II-VI Photovoltaic Devices and Applications</i> P. Wijewarnasuriya	35
<i>Electrodeposited Cuprous Oxide for Low Cost Solar Energy Applications</i> W. Siripala	36
<i>Key Factors for Improving the Efficiency of Dye-Sensitized Solid-State Solar Cells</i> A. Konno and E.V.A. Premalal	44
<i>Gel Polymer Electrolytes for Dye-Sensitized Solar Cells : A Review</i> O.A. Illeperuma	51
<i>Probing the Iodide Ions in Polymer Electrolytes by Impedance and Dielectric Spectroscopy</i> B-E. Mellander	60

<i>Plasmonics for Improved Photovoltaic Devices</i> A.K. Pal	61
<i>Exciton-Coupled Charge-Transfer Dynamics in a Porphyrin J-Aggregate/TiO<sub>2</sub> Complex</i> H. N. Ghosh	70
<i>Thin Film Polycrystalline Silicon Solar Cells</i> H.S. Reehal	71
<b>Thin Film Solar Cells</b>	
<i>Studies on Structural, Electrical and Dielectric Properties of Thermally Evaporated Cadmium Sulphide (CdS) Thin Films</i> S.Tewari and A.Bhattacharjee	82
<i>Fabrication of Solar Cells by Hydrothermally Synthesized Titania Nanotubes and CdS Quantum Dots</i> J. Akilavasanand J. Bandara	91
<i>Polymer Electrolyte Based CdS Quantum Dot Sensitized Solar Cells</i> K. Kumaraarachchi, M.A. Careem, G.K.R. Senadeera, T.M.W.J. Bandara and B.-E. Mellander	96
<i>Surface and Thin-Film Analysis of CdCl<sub>2</sub> Treated CdS/CdTe Layers for Solar Cells</i> K. Abuel-Rub, S-R. Hahn, S. Tari and M.A.K.L. Dissanayake	102
<i>Structural and Optical Characterization of In<sub>2</sub>S<sub>3</sub> Films Deposited By Silar Method</i> E. Turan, T. Taskopru, M. Zor, M. Kul and A.S. Aybek	103
<i>Fabrication of CuO/Cu<sub>2</sub>O Heterojunction and its Local Structural Characterization</i> R.P. Wijesunderaand M. Hidaka	105
<i>Sulphidation of Electrodeposited Nanocrystalline Cuprous Oxide Thin Films for Solar Energy Applications</i> K.M.D.C. Jayathilaka, W. Siripala and J.K.D.S. Jayanetti	112

<i>Study of Electrodeposited ZnS Thin Films Grown with ZnSO<sub>4</sub> and (NH<sub>4</sub>)<sub>2</sub>S<sub>2</sub>O<sub>3</sub> Precursors for use in Solar Cells</i>	120
A.R. Weerasinghe, O.K. Echendu, D.G. Diso and I.M. Dharmadasa	
<i>Photoluminescence and Magnetic Properties of Hexagonal YMnO<sub>3</sub> Nanofibers Prepared by Using Electrostatic Spinning</i>	126
H. Fan	
<i>Effect of Applied Voltage on ZnO Nanorods Synthesized Using Continuous Spray Pyrolysis (CoSP) Technique</i>	131
C. Dwivedi and V. Dutta	
<b>Dye Sensitized and other PEC Solar Cells</b>	
<i>Efficient Dye Sensitized Solar Cells Based on TiO<sub>2</sub> Nanotubes and Nanotube-Nanoparticle Composites</i>	136
E.V.A. Premalal, R.M.G. Rajapakse, K. Murakami and A. Konno	
<i>Chemically Modified CuSCN for all Solid-State, TiO<sub>2</sub>/N719/CuSCN, Dye-Sensitized Solar Cells</i>	142
E.V.A. Premalal, N. Dematage, G.R.R.A. Kumara, R.M.G. Rajapakse and A. Konno	
<i>Suppression of Recombination in Dye Sensitized Solar Cells Based on TiO<sub>2</sub> with Barrier Layer of Metal Oxides</i>	148
L.R.G. Wickramasinghe, V.P.S. Perera and G.K.R. Senadeera	
<i>The Improved Performance of Dye Sensitized Solar Cell by Pyrrolidinedithiocarbamate Modified TiO<sub>2</sub> Surface</i>	152
D.M.B.P. Ariyasinghe, H.M.N. Bandara, R.M.G. Rajapakse and M. Shimomura	
<i>Highly Transparent SnO<sub>2</sub>/CaCO<sub>3</sub> Composite Films for Dye-Sensitized Solar Cells with Superior Performance</i>	158
S.G. Anuradha, H.M.N. Bandara, W.A.P.N. Wickramaarachchi, G.R.A. Kumara and R.M.G. Rajapakse	
<i>Dye Sensitized Solar Cells with Polymethylmethacrylate (PMMA) Based Gel Polymer Electrolyte and Tetrapropylammonium Iodide Salt (Pr<sub>4</sub>N<sup>+</sup>I)</i>	163
H. Iqbal, K. Perera, V.A. Seneviratne, W.N.S. Rupasinghe, C.A. Thotawatthage, G.K.R. Senadeera and M.A.K.L. Dissanayake	

<i>Highly Efficient, Optically Semi-Transparent, ZnO-Based Dye-Sensitized Solar Cells with Indoline D-358 as the Dye</i>	169
K. Premaratne, R.M.G. Rajapakse, G.R.A. Kumara and M.L. Karunarathne	
<i>Mixed Cation Effect in Enhancing the Efficiency of Dye Sensitized Solar Cells Based on Polyacrylonitrile (PAN) and Nano-Porous TiO<sub>2</sub></i>	175
C.A. Thotawatthage, G.K.R. Senadeera, T.M.W.J. Bandara and M.A.K.L. Dissanayake	
<i>Efficient Quasi-Solid Poly (Acrylonitrile) (PAN) Based Polymeric Electrolyte for Dye Sensitized Solar Cells and its Characteristics</i>	180
P.D.N. Gunasekara, Y.P.Y.P. Ariyasinghe, T.R.C.K. Wijayarathna, C.A. Thotawatthage, M.A.K.L. Dissanayake and G.K.R. Senadeera	
<i>Quasi-Solid State Dye Sensitized Solar Cells with Poly(Vinylidene-Fluoride) (PVdF) Based Gel Polymer Electrolyte and Nano-Porous TiO<sub>2</sub> Electrode</i>	186
H.A.C.S. Perera, K. Perera, K. Vidanapathirana, V.A. Seneviratne, W.N.S. Rupasinghe, C.A. Thotawatthage, G.K.R. Senadeera and M.A.K.L. Dissanayake	
<i>Estimation of Ion Transport Parameters by Modeling Space Charge Relaxation in PEO Based Solid Polymer Electrolyte Intended for Photoelectrochemical Solar Cells</i>	193
T.M.W.J. Bandara, M.A.K.L. Dissanayake, P.S.L. Fernando, W.J.M.J.S.R. Jayasundara and B.-E. Mellander	
<i>Chitosan-Based Polymer Electrolyte for Dye-Sensitized Solar Cell</i>	200
M.H. Buraidah, L.P. Teo, S.N.F. Yusuf, M.M. Noor, M.A. Careem, S.R. Majid and A.K. Arof	
<i>Dye-Sensitized Solar Cell with Chlorophyll and Plasticized PVdF-HFP Based Electrolytes</i>	206
M.M. Noor, M.H. Buraidah, S.N.F. Yusuf, M.A. Careem, S.R. Majid and A.K. Arof	
<i>Synthesis and Characterization of N-Phthaloylchitosan Based Polymer Electrolytes for Dye-Sensitized Solar Cell</i>	213
S.N.F. Yusuf, M.M. Noor, M.H. Buraidah, M.A. Careem, R. Yahya, S.R. Majid and A.K. Arof	

<i>Quasi Solid-State Solar Cells Containing Novel Gel Polymer Electrolyte Based on Polyacrylonitrile and Tetrahexylammonium Iodide Salt</i>	221
T. Svensson, T.M.W.J. Bandara, E.Lundell, I. Svensson, M. Furlani, I. Albinsson and B.-E. Mellander	
<i>Nanocrystalline TiO<sub>2</sub> Photo-Sensitized with Natural Dyes</i>	229
P.W. Abeygunawardhana, S. Palamakubura, C.A. Thotawatthage , M.A.K.L. Dissanayakeand G.K.R. Senadeera	
<i>Utilization of Natural Pigment Extracted from Henna Leaf in Combination with Gelatine as a Sensitizer in Photoelectrochemical Solar Cells</i>	236
C.N. Nupearachchi , T.R.C.K. Wijayarathna and V.P.S. Perera	
<i>Comparison of Natural Pigments in Black Tea and Green Tea With DSSCs</i>	241
C.N. Nupearachchi , C.A. Thotawatthage , G.K.R. Senadeeraand V.P.S. Perera	
<i>Evaluation of Dyes from MelastromaMalabathricum: a Native Plant of Borneo, as Potential Natural Colour for Dye-Sensitized Solar Cells</i>	246
P. Ekanayake, R. Zain, M.Iskandar, K. Tennakoon,S. Yoshikawaand G.K.R. Senadeera	
<i>Fluorene-Based Organic Dyes for Dye-Sensitized Solar Cells</i>	252
K.R. Justin Thomas	
<i>Visible Light Responsive Nanocrystalline Titanium Dioxide for Dye Sensitized Solar Cells</i>	253
B. Kajitha, S. Sarathchandran, M. Senthilnanthananand P. Ravirajan	
<i>Enhancing the Performance of Hybrid TiO<sub>2</sub>/Polymer Multilayer Solar Cells by Modifying the TiO<sub>2</sub>/Polymer Interface By Single Wall Carbon Nanotube</i>	258
K. Balashangar, T. Jaseetharan, S. Sarathchandranand P. Ravirajan	
<i>Conversion Of Solar Energy To Electricity By Natural Dye-Sensitization</i>	264
C.I.F. Attanayake , B.A.J.K. Premachandra , A.A.P. De Alwis And G.K.R. Senadheera	

## **Silicon Solar Cells, Solar Panels and Other Solar Energy Applications**

<i>Effect of Thin Zinc Oxide Transparent Layers on Crystalline Silicon Solar Cells</i>	265
G.D.K. Mahanama and H.S. Reehal	
<i>Growth of Zinc Oxide Nanostructures on (100) Silicon Surface for Crystalline Solar Cell</i>	271
H. Dhasmana, C. Dwivedi and V. Dutta	
<i>Simulation and Characterization of Shunts in Silicon Solar Cells by Pspice and Lock-In Infrared Thermography</i>	277
P.Somasundaran, D.K. Nandi and R.Gupta	
<i>Solar PV Based Micro-Grid System for Emergency Situations</i>	284
W. T. Sion, Liyanage C. De Silva and M.Iskandar Petra	
<i>Wind Power Development: an Innovative Means of Reducing Global Warming Emissions</i>	291
O.I. Olusola and S.S. Oluyamo	
<i>Development of a 2.5kVA Pulse Width Modulated Controlled Automatic Inverter System</i>	297
O.I. Olusola and S.S. Oluyamo	
<i>State of the Art Solar Air Heater for Commercial Applications</i>	308
A.C.Dhanemozhi	
<i>Enhanced Heat Transfer in Solarwater Heater (With Parabolic Collector) Using Partially Reflective Glass</i>	312
T. Chandrasegaran	
<i>Structural Evolution of Indium Phosphide Films Prepared by Co-Evaporation Technique</i>	317
R.N. Gayen, S. Hussain, R. Bhar and A.K. Pal	
<i>Efficient way of using Solar System to the Households' Normal Applications</i>	324
J. Amalendran and A. Atputharajah	
<i>Synthesis of II–VI Semiconductor Nanoparticles by Continuous Spray Pyrolysis (CoSP) for Organic Solar Cell Applications</i>	331
N. Kumar and V. Dutta	



<i>Low-Cost Thermoelectric Power Generation Using Solar Energy</i> N.D. Subasinghe, N.B. Suriyaarachchi and T.B. Nimalsiri	336
Author Index	342

## **SOLAR VILLAGES FOR SOCIAL DEVELOPMENT AND POVERTY REDUCTION**

I. M. DHARMADASA<sup>1\*</sup> AND LALITH GUNARATNE<sup>2</sup>

<sup>1</sup>*Faculty of Arts Computing Engineering & Sciences, Sheffield Hallam University, Sheffield S1 1WB, United Kingdom.*

<sup>2</sup>*Energy Forum, 247 Polhengoda Road, Colombo 6, Sri Lanka.*

\*Corresponding Author, e-mail: *Dharme@shu.ac.uk*

### **ABSTRACT**

This presentation describes how solar power could assist in the social and economic development of developing and developed countries, using various applications at different power levels. The largest impact in developing countries, in the short-term will come from drip irrigation and community water pumping systems, combined with "solar village" concepts introduced recently for social development. Solar energy can be used as the first wave of actions to improve agriculture and enhance food production. In the second wave of actions, small industries could be established to benefit from an enhanced food production process. This will lead to an establishment of a healthy export business creating jobs and wealth for economic development. Other large scale solar power applications are also presented and relevant recommendations are made in order for developing countries to move towards energy independent and fully developed countries establishing a low-carbon economy in the future.

### **1. PROGRESS IN SOLAR ENERGY APPLICATIONS**

The conversion of light energy into electricity was invented by Edmund Becquerel in 1839, but the practical solar cells and their applications did not appear until 1950s. By the beginning of the 1960s, solar power was used in small power applications and to provide remote power requirements. The following list indicates how the solar power levels have grown to produce MW scale large power systems in numerous applications.

- Low power applications in calculators, wristwatches etc. (~mW and W range)
- Remote applications in satellites, tele communication stations etc.
- Applications in solar home systems (~50 W range)
- Applications in small drip irrigation systems (~100 W range)
- Powering computers in remote schools and road signage (500-1000 W range)
- Applications in large scale water pumping systems (~1000-5000 W range)
- Solar power applications on buildings (solar roofs) and solar farms (~3-1000 kW range)
- Large scale solar farms in deserts for electricity generation (larger MW range)

### **2. ENERGY SITUATION IN SRI LANKA**

Sri Lanka has a population of ~20 million people of whom, ~75% inhabit rural areas. The total installed capacity is ~3.0 GW and the summary of current energy production methods is given in the following Table.

About 85% of the country's households are now connected to the national grid. This still leaves about 800,000 households without access to electricity from the grid. A good fraction of these, the more affluent households use an automotive battery, which is periodically re-charged to power a few 12 V lamps and in some cases a DC powered TV and a radio. Solar energy businesses

Conventional production of energy	Approximate figures in MW
Large hydro power stations	1180
Thermal power stations	1682
Non conventional renewable energy	Approximate figures in MW
Mini-hydro	174
Bio-mass	12
Wind	30
Solar	8
Total power generation	~3044 MW = 3.0 GW

estimate that about 10% of the un-electrified homes can afford to purchase solar home systems if all other barriers were out of the way. The rest of the households will continue to live with kerosene lamps. This population has little chance of coming out of poverty as there are other added barriers to their development. This is the target community that requires assistance to move to a level where they can begin to participate in the economy of the nation. The solar village projects are designed to lift the living standards of these most vulnerable communities, establishing food security, clean environment and sustainable development.

### **3. SOLAR PV APPLICATIONS IN SRI LANKA**

Sri Lanka has a rich history in solar PV applications over the last three decades. Over 150,000 solar home systems already exist in a private sector driven market development initiative. The current rate of installation of solar home systems is about 1000 per month. These systems however, are used by the more affluent, off-grid population in rural areas. Most of the customers have paid cash between £200 (Rs. 35,000) and £300 (Rs. 55,000) for these systems. However, the micro-credit facilitations have been established for installing solar home systems in the country.

Solar PV also provides power for water pumping, drip irrigation and telecommunication systems around the country. There are 5000 solar powered drip irrigation systems currently operating in the dry zone. Therefore, the solar PV technology is a proven and well accepted alternative to the fuel based electricity generation in off-grid areas. In promoting solar PV, all these projects have to ensure that proper installation and customer service is part and parcel of the system. These can now be provided by the commercial vendors that operate in the country through Solar Industries Association (SIA). It is good news for the country to notice development of several companies during the past few decades in this sector, creating new jobs for younger generation.



Figure 1. A solar roof (25 kW) on a commercial building in Colombo and one of the two solar farms (500 kW each) installed in Sri Lanka for initial training and promotional purposes.

#### **4. BACKGROUND TO SOLAR VILLAGE PROJECT**

It is good news to see that the grid connected households is reaching ~85% of the population. The extension of the grid to provide 100% electrification will not be economically viable and therefore the solar home systems could serve the remote communities from the national grid. The next stage is to rapidly introduce solar roofs on well-to-do households and feed the national grid during the day time. For example, in April 2010, UK Government introduced solar tariff of 40.3p per kWh unit instead of present grid-electricity cost of 22p. This incentive created over 20,000 solar roofs of the size 2-3 kW round the country in 14 months. This is equivalent to ~ (40-60) MW clean power feeding to the national grid during the day time. This also accelerated formation of new companies, job creation and rapid reduction of cost of solar roofs due to a healthy competition in industry. Countries in the sun-belt could do extremely well with such positive policy making opening doors for sustainable development. It is pleasing to see the recent appearance of domestic solar roofs (2-3 kW each), commercial solar roofs (~25 kW each) and two solar farms (~500 kW each) in Sri Lanka to feed the national grid or local use of the produced clean energy.

The Higher Education-Link (HE-Link) programme funded by the DFID-UK, managed by the British Council and coordinated by the main author, continued during the 1990s. This programme held many rural schools based solar awareness creation activities over a period of 10 years in Sri Lanka. The idea of the solar village community project evolved from the discussions with communities living in the dry zone. The pilot project for Centres for Application of Renewable Energy Sources (CARES) or solar village committee has been formed in a north western province village called Kaduruwewa, centering around the village primary school. These stakeholders unanimously accepted that the CARES concept would help in dealing with some of the acute problems facing people in the surrounding areas. Lack of energy services and clean water supply were said to be the biggest barriers to the development of the area.



Figure 2. A child artist's impression of a CARES centre or solar village at initial design stage, and a photograph of the solar water pumping station in the pilot solar village established in July 2008.

## **5. THE "SOLAR VILLAGE" OR "CARES" CONCEPT**

This concept focuses on the rural communities who are off the national grid or cannot afford currently commercially available alternatives, and trapped in poverty due to various reasons. In such a typical community, lighting comes from kerosene lamps and cooking is done with firewood.

The project is developed so that rural communities will learn to help themselves in meeting their energy needs. The design of the project ensures that credible leaders in the community (led by the educationists) will create the CARES, which will enable target householders to gain access to energy services at an affordable price. The project also aims to begin with a small number of households and to grow the number with their own contributions. A CARES scholarship programme for village children will be established from the growing revolving fund to support the development of people in the area. In addition, various development projects and activities to improve the environment depending on the geography, climate and the livelihood of people will be introduced. The project can be modified according to the requirements of the community and the promoters will act as advisors to the project. One important aspect that is built into the project is regular monitoring, evaluation and wide publicity for encouraging its replication.

This is a project to assist people to help themselves and to catalyse the eradication of poverty through rural economic development. Currently, these marginalised rural households are condemned to a perpetuation of their poverty. Not having access to basic lighting, information, and entertainment denies them opportunities. Poor lighting makes it difficult for children to study at night, the effects of kerosene fumes and the kerosene lamp fire risks are detrimental for their health and safety, and overall the quality of life is very bleak.

Therefore, the project proposes to install solar powered water pumping systems in a number of selected clusters of villages. The customers are required to do a monthly payment for their water usage, and this creates a useful funding mechanism for them. This revolving credit fund would be administered by the CARES committee of the village in a transparent way so that these small communities will grow minimising corruption. These projects will merely plant the seeds to catalyse sustainable development of the villages through the efforts of the village community. The

main aim is to empower them for their own economic development keeping all good values within the society.

This particular project is more attractive to Sri Lanka, since it combines with already completed agro-wells within the dry zone of the country. Most of these 6 metre diameter agro-wells have been built for rural communities to develop themselves by growing food around the well by pumping water using diesel pumps. However, the bottle-neck of pumping water is due to the cost of diesel engine and fuel, and therefore a large fraction of these agro-wells are not fully used today. There are also thousands of clean water pumping systems built round the country, but the main difficulty again the expensive water pumping systems based on imported diesel with their ever increasing costs.

The first stage is to form a small community group close to an unused agro-well, any other water source or established water pumping infra structure. This eventually grows into a CARES or a solar village. After having several meetings to explain the procedures and with the agreement to take part in the project, installation of one solar powered water pumping system can be completed with available funds. In this process, local government, private companies or any other association could help through a competitive bidding process, and train a few people from the group to look after the system. Vegetable growing around the agro-well for example will bring regular and additional income to families involved. The required funds must be raised within the country rather than depending on aid from outside or external loans to the country.

In order to recover the cost of the system and accelerate the development process, a group of 5 people could produce bricks during the dry season. It is possible to produce 100,000 bricks within 4-5 months, and this could cover a good fraction of the cost of the whole system. One way of using this income would be to use half of the income to pay the initial capital and share the rest among the group participants. Continuation of this process within 3 years, will pay back the initial loan, and earn funds locally for a new system within the solar village. Since the new system is virtually earned by the community itself, the rest of the process will show a cascading effect for a rapid development of the country. This scheme will be attractive, since it creates employment opportunities in construction and related areas especially in conflict affected northern and eastern areas for rapid recovery. After a period of few years, the small community fully owns the whole system, but should contribute a small tariff to the country-wide CARES account for sustainable development. This will provide a continuous income to the CARES for various development activities within the community.

The above additional activities are also a good solution to a serious social problem one can find in the farming communities in Sri Lanka. After completion of the work in paddy fields, most of the men are free for about 4-5 months in a year, and waste their valuable time consuming illegal alcohol, smoking, gossiping in coffee shops and gambling. This has been a main cause for their ill health and poverty, and the additional activities in solar villages will gradually take them away from these detrimental social habits. These improvements have already been observed in the pilot solar village.

Since the water in the well is pumped out daily during the day time, using solar energy, it is important to educate the community on water management. In order to keep the soil wet, organized tree plantation round the well-area is essential. This will provide long term income through fruit production and timber required for buildings and carpentry. Organic farming methods and bee keeping projects encouraged within the solar village will produce healthy food while increased pollination double and treble the annual crops from this agriculture related activities. More importantly, while the power is generated with zero emission of CO<sub>2</sub> (by using

sunlight), the built-in tree plantation enhances the removal of CO<sub>2</sub> from the atmosphere through photo-synthesis.

The same project could be carried out using a small wind turbine which is another source of renewable energy. However, water pumping depends on the available wind and this could happen any time during the day without overlapping with the working hours of the day. In this respect, solar power is more suited for the project but storage tank could solve this problem to a certain level. To use the limited amount of water available in the dry zone, drip irrigation should be introduced widely to these communities for water management.

A large fraction of the country's electric power is generated using hydropower (~40%), another renewable energy source. In order to maintain this power source, the water management throughout the country is essential to avoid power cuts during droughts. The repairing programme of water reservoirs and tree plantation projects around the country are most important in retaining ground water and hence helping solar water pumping and drip-irrigation. These projects will also rapidly provide the right solution to the slow desertification of the Jaffna peninsula. The sand and palm trees are the main signs of desertification and the solar water pumping, drip irrigation systems and tree planting programmes will convert the country into a "green carpet" avoiding this extremely detrimental desertification process. Organised planting of 1.1 million trees in 11 minutes, involving school children in Sri Lanka last year is a good example for many other countries to exercise, as an effective contribution to the climate change.

## **6. WHAT HAPPENS IN THE PILOT SOLAR VILLAGE ?**



Figure 3. The official opening of the pilot solar village in July 2008, with the participation of Geography final year undergraduates from Sri Jayawardanapura University in Colombo.

The first solar power project under the solar village programme was completed at Kaduruwea village in the Kurunegala district. Here the water supply scheme to the village was provided by using solar pumps replacing a diesel pump. The villagers have formed a society to operate the scheme and they are now saving about Rs 100,000 per annum on diesel costs. This enables them to use their saved funds in various development projects to uplift their living standards.

The whole community is directed to work together, to grow more trees around the area, to keep bees for honey production, use organic agriculture methods, etc. to improve the quality of environment. In short "Solar Villages" use clean energy technologies as well as developing their living environment. By developing themselves, contributions are made for the economic development of the country via enhanced food production. As already mentioned in the above

section, there are many individual projects one can incorporate in this social development programme. The projects depend more on the nature of the society, climate and the geography. Another key feature of this solar village is that one of the local universities or an established school adopts this cluster of villages to guide the development of that society. For example, the pilot project is adopted by a team led by Prof. Krishan Deheragoda (previous Chairman of the Sri Lanka Sustainable Energy Authority) at the Dept. of Geography, University of Sri Jayawardanapura (USJ). The Geography special students carry out their final year survey in this village cluster feeding new ideas for development. Imagine the impact of fresh ideas from enthusiastic university dons and undergraduate students for rural communities and the use of younger generation to spread out these new ideas round the country for replicating these new projects. In fact, the solar village is a “social science laboratory” for training young graduates with social responsibilities.

The individual projects emanating from this programme are: Tree planting, honey production, brick making, vegetable & animal farming in dry areas, development of cottage businesses, scholarships and micro-finance schemes using saved funds within the community due to use of renewable energy sources. The development of the village temple, pre-school, the local school, library and the environment through Sramadana (voluntary work) activities are organised and encouraged. These individual projects can be selected to suit the community and keep the people away from detrimental habits mentioned above..

#### **7. MONITORING PROGRESS, GATHERING INFORMATION AND DISSEMINATING KNOWLEDGE**

The pilot projects will have a further benefit to the solar PV technology itself where the installed systems will serve as a demonstration in the area. This will also act as a showcase for the government to provide further support to the dissemination of solar PV technology and rapidly develop the poorest section of the community. To build up and maintain the momentum, identify problems and their solutions during implementation, conferences like “Solar Asia” and "Solar Africa" organized in different regions will stimulate the acceleration and replication of this project.

In the EU-solar energy conference held in Paris in 2003, Sri Lanka was identified and announced as the "Hot Spot of Solar Energy Applications". With these developments and recognitions, the country should move forward towards to become an energy independent "Renewable Energy Island". The Maldive islands are ideal examples to convert into renewable energy islands, and hence to convert into an attractive eco-tourist centre.



Figure 4. Dissemination of new knowledge through public lectures to young people in Sri Lanka and Maldives as the first step of replication of solar villages.



The next phase will be the replication of these projects in other parts of Sri Lanka and outside the country, based on the experience gathered with the pilot project. The South Asia Renewable Energy Programme (SAREP) will disseminate this knowledge worldwide through: newsletters: <http://apsl.org.uk/Newsletter/Forms/Public%20View.aspx> websites: <http://apsl.org.uk/dharme/default.aspx> and conferences: (<http://www.solarasia2011.ifs.ac.lk>) in order to spread this project.

Even though, the technology is proven, the unknown factors lay mostly in the administrative, social, financial and the technology/human interface areas. There will be a structured process of gathering information from these projects to learn about these areas. Taking new technologies from laboratories to the society needs considerable efforts through various dissemination programmes overcoming numerous barriers.

## **8. BENEFITS OF THE “SOLAR VILLAGE” PROJECTS**

- immediate benefit of electric power or clean water to the households; replacing kerosene use resulting in improved health, removal of kerosene lamp induced fire risks, reducing carbon dioxide emissions and extending the productive hours for work and study, access to information and entertainment via TV/radio etc.
- empowerment of the rural community to develop themselves and escape from their poverty traps. This project fulfills three Millenium Development Goals namely; clean water, clean environment and reducing poverty.
- capacity building so the community can manage their own projects minimizing corruption.
- development of the CARES revolving fund to support more renewable energy applications and solar water pumping systems for providing clean water for drinking and drip irrigation.
- revolving fund supporting CARES scholarship programme and the development of the school by purchasing library books for example.
- installed systems will act as a demonstration to the area and will help solar PV business development.
- CARES becoming a part of the wider local, regional and later an international project, contributing to reduction of poverty and creation of a cleaner environment.
- Sri Lanka will gain publicity and reputation through SAREP, on implementation of village power pilot projects well-suited to developing countries with renewable energy applications, while developing rapidly with untapped and freely available solar energy.

## **9. SOLAR VILLAGES AS SOCIAL SCIENCE LABORATORIES**

In Higher Education Institutes, it is a well established practice to build laboratories to teach subjects like physics, chemistry, engineering, agriculture, biology and medicine. In fact “solar village” is a “social science laboratory” suitable for all faculties in these institutes. Establishing a solar village attached to every university or well established secondary school, the opportunities are open for all subjects to contribute. This will not only produce young graduates in their chosen subjects with social responsibilities, but also contribute to develop the most vulnerable section of the society. These ideas have been openly discussed with 108-universities in Nigeria during a recent UK-Nigeria special delegation took place in March 2011. The event was organized by the UKTI, Training gateway, the National Commission of Universities-Nigeria and the British High Commission in Nigeria. The initiation of the conference series "Solar Africa" has been discussed in order to stimulate both solar energy research and applications in the Continent.



Figure 5. Part of the UK-Nigeria delegation took place in March 2011 in order to discuss development projects through Higher Education Institutes. IMD presented the capacity building in solar energy conversion and replication of solar villages in Nigeria via HE sector.

#### **10. REPLICATION PLANS OF “SOLAR VILLAGES”**

After a successful pilot project established in July 2008, in Sri Lanka, the work is progressing to replicate solar villages widely in Sri Lanka, neighboring countries (Bangladesh, India and Maldives) and in Nigeria. Nigeria will eventually provide the gateway to other countries in the African continent for this information and knowledge. Raising funding for these projects is an issue but the local governments should take the responsibility in planting seeds (solar powered water pumping systems) of the solar villages in right locations. By applying solar village concepts, the communities will rapidly grow with their own initiations. The teachers, university dons, political leaders and community & religious leaders have an important role to play in this project to develop the society in addition to their main stream duties.

*"Solar Energy is a clean and free natural resource, available to the mankind. The effective use of this un-tapped energy resource has huge potential to develop every corner of the globe, and establish a peaceful, safe and pleasant world for our future generations. It is our responsibility to start this onerous but honourable task"*

## TECHNOLOGY TO HARVEST SOLAR ENERGY: SINGLE-CRYSTAL CdTe-BASED II-VI MATERIALS FOR MULTI-JUNCTION CELLS

C.H. GREIN\*, S. SIVANANTHAN and J. GARLAND

*Episensors/Sivananthan Laboratories and EPIR Technologies, Inc.  
590 Territorial Drive, Bolingbrook, IL 60440, USA*

\*Corresponding Author, e-mail: [grein@uic.edu](mailto:grein@uic.edu)

### 1. INTRODUCTION

Solar energy is the only form of renewable energy that has the potential to largely replace fossil and nuclear fuels. However, because of its high cost, it makes up only 1% of the world's energy production. Even so, solar energy production has grown at a compound annual growth rate of 43% since 2000 [1]. Once the cost of solar energy is sufficiently reduced, it will have the great advantage of a much shorter deployment time than any other form of electric power generation, as shown in Figure 1 [2].

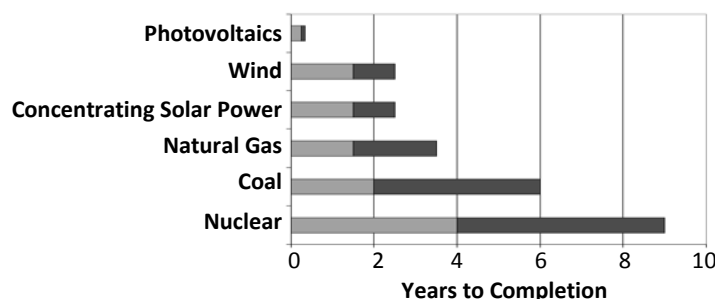


Figure 1. Deployment times of various power generation technologies (from Ref. 2).

In its simplest form, a photovoltaic solar cell consists of a semiconductor homojunction with bandgap  $E_g$  having electrical contacts at its front and back faces, as shown in Fig. 2. Almost all photons with sufficient energy,  $\hbar\omega > E_g$ , excite valence-band electrons across the gap, forming mobile electron-hole (e-h) pairs. Each electron and hole is rapidly thermalized, so that the energy  $\hbar\omega - E_g$  is immediately lost. If the electron and hole reach the external cell terminals, they contribute to the current. The open-circuit output voltage  $V_{oc}$  is equal to the difference between the electron and hole quasi-Fermi levels,  $E_{qe} - E_{qh}$ , which is greater than or approximately equal to  $E_g - 0.5$  eV for a good solar cell. For a single-junction (1J) cell, if  $E_g$  is too small the output power is reduced because  $V_{oc}$  becomes too small, and if  $E_g$  is too large the current becomes too small. A multijunction cell consists of a series of homojunctions stacked on top of one another with each junction having a larger bandgap than the one below it. Thus, the maximum thermalization energy loss from any photon is the difference between the bandgaps of successive junctions, so that in principle the fraction of energy lost to thermalization can be reduced almost to zero by using a sufficiently large number of junctions. However, to date practical concerns such as increased e-h recombination, the difficulty of obtaining current matching between all of the junctions and growth concerns have limited the practical number of junctions to three. For simplicity of wiring, multijunction cells should be monolithic, with each junction connected with the one below it by a low resistance tunnel junction.

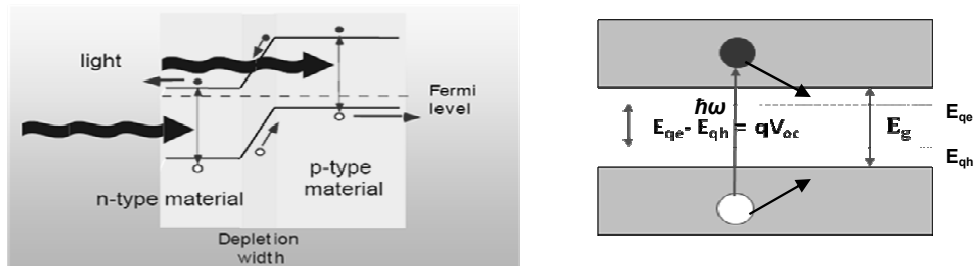


Figure 2. Schematic drawing of a simple single-junction solar cell, showing the homojunctions, photon absorption, e-h thermalization and the electron and hole quasi-Fermi levels.

Concentrated photovoltaics (CPV) combines high conversion efficiency with very low semiconductor materials usage, resulting in the possibility of expansion unlimited by material or land availability. CPV also has the lowest balance-of-system (BOS) costs. However, because of the cost of the high-precision tracking and optics components of the present high-concentration photovoltaic (HCPV) systems, CPV requires very high efficiency solar cells and is the most costly of the commercialized PV technologies. Thus it has not gained a large share of the PV market; of the primary solar PV technologies only CPV is not on a path to come close to the U.S. Department of Energy (DOE) Strategic America Initiative levelized cost of electricity (LCOE) target for 2015, as shown in Figure 3 [3,4]. The solar cells currently used in CPV and PV systems for space are predominantly monolithic three-junction (3J) cells utilizing single-crystal III-V semiconductor homojunctions grown on Ge substrates. These cells have demonstrated very high efficiencies under concentration, up to 41.6% in the lab [5] and 39% in manufactured form [6], although their efficiencies are limited by the low minority-carrier lifetimes  $\tau$  of non-lattice-matched III-V materials [7]. However, they are inherently very expensive, costing up to  $\$13/\text{cm}^2$  to manufacture. [8]. The high cost of these cells that has driven CPV to the use of extremely high solar concentrations  $X$  ( $X \geq 500$ ) and thus extremely precise, and hence expensive, tracking and optics systems.

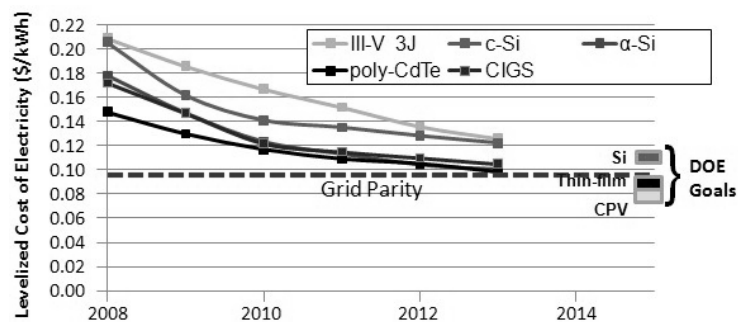


Figure 3. Levelized cost of electricity (LCOE) forecast for different solar PV technologies. (from Ref. 3 for all technologies except CPV, from Ref. 4 for CPV with III-V solar cells). The “grid parity” line represents the average U.S. retail cost of electricity.

To make CPV economically competitive, much-higher-efficiency and/or much-lower-cost solar cells must be developed. We propose the use of single-crystal CdTe-based II-VI materials grown via high-throughput molecular beam epitaxy (MBE) on Si substrates, as opposed to III-V materials grown on Ge substrates, to achieve higher efficiencies at an order of magnitude lower cost,  $\sim \$1/\text{cm}^2$ . The much lower cell costs will allow the use of lower optical concentrations,  $X \leq 200$  rather than  $X \geq 500$ , which will reduce the CPV system cost by at least 35%. Both (1) the ability to use CdTe-based materials grown by MBE on Si, which has a much smaller lattice constant, and (2) the theoretical prediction of higher solar-cell efficiencies using CdTe-based homojunction materials rather than III-V materials follow from a single little-known fundamental phenomenon: the fact that dislocations and other crystalline defects have a far smaller effect on the electronic properties of CdTe-based alloys than on III-V alloys such as GaInAs and GaInP, which are commonly used in III-V multijunction cells. That fact is the basis of the central thesis of this talk. It means that the requirement of lattice matching, which is very important for the epitaxial growth of III-V materials, can be dropped for the MBE growth of CdTe and CdZnTe on Si for regular (uninverted) solar cells and of HgCdTe on CdTe or on CdZnTe for inverted solar cells.

Because of its near ideal bandgap ( $E_g \approx 1.48$  eV) and high absorption coefficient, CdTe has emerged as a technologically important material for PV applications. Based purely on bandgap considerations, ideal 1J CdTe solar cells should be capable of reaching efficiencies  $\eta \approx 28\%$ . However, to date the record thin film CdTe AM1.5 solar cell efficiency is only 16.7%, with typical production panels having efficiencies only in the 8-12% range. [9] This large discrepancy between the maximum theoretical cell efficiencies and the best realized cell efficiencies is generally believed to be due to three primary technical challenges: a lack of ability to dope CdTe highly p-type, the low minority-carrier lifetimes ( $< 5$  ns) of polycrystalline CdTe and the difficulty in making a good ohmic contact to p-type polycrystalline CdTe. [10] The growth of single-crystal CdTe and CdZnTe thin films by MBE on Si substrates provides a possible pathway for overcoming all three technical challenges associated with thin film CdTe cells and has the potential to dramatically increase the efficiency of II-VI solar cells. Epitaxial CdTe and CdZnTe can be grown as high quality single crystals on Si substrates and can be doped p-type using various techniques during low temperature MBE growth, which allows for the growth and fabrication of CdTe-based multilayer structures and thus CdTe-based multijunction solar cells as equivalents to high-efficiency, but much-higher-cost, III-V multijunction cells [11].

## **2. INITIAL SOLAR CELL EXPERIMENTAL RESULTS**

We grew  $\sim 3$   $\mu\text{m}$  thick CdZnTe homojunctions on p-doped Si and on p-n Si homojunctions by MBE. The Zn content in each layer grown was determined from the lattice constant, which was measured by x-ray diffraction. Because of the large difference between the lattice constants of CdTe and ZnTe ( $>5.5\%$ ) and the linearity of the lattice constant of CdZnTe with Zn concentration  $x$ , this determination of  $x$  should be accurate despite the strain in the CdZnTe layers. For the Zn concentrations of the two CdZnTe epilayers used for the 1J solar cell fabrications,  $x = 0.278$  and  $x = 0.518$ , formulas from the literature [12,13,14] give  $1.616 \text{ eV} \leq E_g \leq 1.698 \text{ eV}$  and  $1.781 \text{ eV} \leq E_g \leq 1.869 \text{ eV}$ . From a comparison of the reflectance of CdTe, ZnTe and CdZnTe films of thickness  $\sim 3$   $\mu\text{m}$ , we found  $E_g \approx 1.66$  eV and  $E_g \approx 1.82$  eV for the two epilayers, in the middle of the ranges of values given by the literature formulas for  $E_g(x)$ .

Pieces of two layers grown on p-doped Si were used to form 1J solar cell structures, and pieces of two layers grown on the p-n Si homojunctions were used to form 2J structures. Both were mesa structures 4 mm in diameter. In both cases the Si solar cell surface was subjected to an RCA cleaning process prior to loading into the MBE growth chamber. The surface oxide generated during the RCA process was desorbed at a temperature  $T > 750^\circ\text{C}$  prior to epilayer

growth. The CdZnTe films were doped p-type in situ during MBE growth with a target p-doping level of  $\sim 10^{17} \text{ cm}^{-3}$ , but post-growth current-voltage (I-V) curves indicated that only  $\sim 10^{16} \text{ cm}^{-3}$  p-doping was achieved. The actual level of dopant incorporation and the possibility of activation annealing to acquire a higher doping level will be investigated. To form the p-n junction in the CdZnTe layers, a thin layer of indium was deposited on the CdZnTe surface and diffused into the layer at  $400^\circ\text{C}$  under a nitrogen ambient atmosphere. The Si substrates served as a p-side contact for the 1J cells and as a bottom junction in the 2J solar cells. A top contact was formed on the 2J pieces and the first 1J pieces by depositing a metal In grid directly on the n-type CdZnTe top surface. On subsequent 1J pieces a non-optimized e-beam evaporated thin indium tin oxide (ITO) film was deposited as a transparent conducting oxide (TCO) to lower the contacting resistance, followed by the deposition of In contact pads. The ITO film on the 1J cell also served as a partial antireflection coating (ARC), but  $J_{sc}$  was essentially unchanged by the deposition of the ITO because light absorption in the ITO essentially cancelled its benefit as a partial ARC. The cells were tested at room temperature on an Oriel solar simulator under AM1.5G illumination, and the light and dark I-V curves were measured.

Figure 4 shows the I-V response from the 1J cell with  $E_g \approx 1.82 \text{ V}$ , along with that from a 2J cell with the CdZnTe junction having  $E_g \approx 1.79 \text{ V}$ . For both of these cells, the measured  $J_{sc}$  ( $16 \text{ mA/cm}^2$ ) is  $\sim 27\%$  lower than the value  $J_{sc} \approx 22 \text{ mA/cm}^2$  calculated [22], [41] for an optimized cell, which is determined solely by the CdZnTe bandgap  $E_g \approx 1.8 \text{ V}$ . The low measured values of  $J_{sc}$  can be attributed partially to optical losses from surface reflection and optical absorption in any TCO coating present, and partly to too thick an n-doped layer at the top of the cell; secondary ion mass spectroscopy (SIMS) recently revealed our n-doped layers to be between  $0.5$  and  $1 \mu\text{m}$  thick. For the 1J cell, which has an ITO coating to reduce resistive losses and has no tunneling junction,  $FF = 0.77$ ,  $\sim 10\%$  below optimal, [22],[41] presumably largely because of a small series resistance. The efficiency of the 1J cell is  $16.4\%$ .

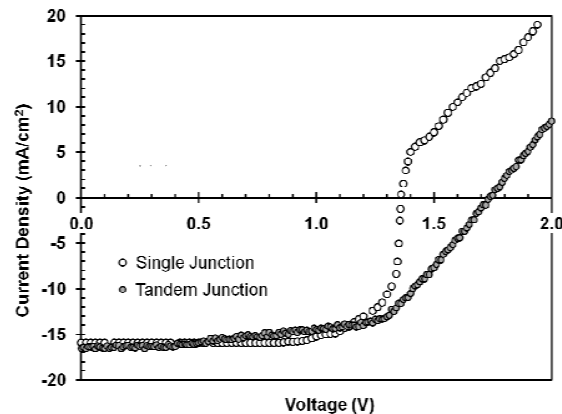


Figure 4. Current-voltage curves for 1J and 2J CdZnTe/Si cells, both with  $E_g \approx 1.8 \text{ eV}$ .

In the 2J structures the CdZnTe and Si junctions were connected by a wide-gap II-VI-based n<sup>++</sup>/p<sup>++</sup> tunneling junction grown on the Si. The bottom Si junctions were fabricated from (111) oriented p-doped ( $\sim 10^{17} \text{ cm}^{-3}$ ) Si by spin coating phosphorus on the surface and diffusing the phosphorus into the Si at  $\sim 1000^\circ\text{C}$  to form a p-n junction. The 2J values of  $J_{sc}$  were almost identical with those found for the 1J structures, again  $\sim 27\%$  lower than the value calculated for an optimized cell. As evident from the linear part of the I-V curve for the 2J cell, it had a large series resistance and a resultant small  $0.60$  fill factor  $FF$ . The large series resistance resulted at least partly from the lack of a TCO coating on the 2J cell to aid lateral conduction to its contacts and

possibly from its unoptimized tunnel junction. Largely because of the poor quality of the Si bottom junction and because of its small fill factor, the efficiency of the 2J cell,  $\eta = 16.8\%$ , is little more than that of the 1J cell.

### 3. CONCLUSION

The properties of wide-gap II-VI materials of intense interest in the search for an economical, nonpolluting renewable energy source. A new direction in CPV system technology, towards lower solar concentrations to lower tracking and optics costs, rather than towards higher solar concentrations, will be needed to gain the maximum advantage from the much lower projected cost of II-VI multijunction solar cells. The absence of a lattice matching requirement for CdTe-based multijunction solar cells also would mean that the restrictions on the choice of bandgaps for III-V multijunction solar cells would be removed for II-VI multijunction cells. That in turn would allow multijunction cells fabricated from II-VI materials to have even higher efficiencies than those fabricated from III-V materials.

Initial growths and fabrication of CdZnTe/Si 1J and 2J solar cells have been performed with very promising results. However, much work remains to be done to obtain high-efficiency II-VI multijunction solar cells: the TCO layer deposited must be optimized to reduce the series resistance so as to obtain higher fill factors  $FF$  and to reduce light absorption so as to increase  $J_{sc}$ , the contacts and tunneling junctions must be optimized to ensure low resistances and obtain higher fill factors, and high-quality ARCs must be developed and deposited to increase  $J_{sc}$ . However, there exists a clear path to the accomplishment of this work and to the attainment of efficiencies  $\eta$  in the range 22%-25% for 1J CdZnTe solar cells fabricated on Si substrates and an efficiency  $\eta \approx 40\%$  for 2J CdZnTe/Si solar cells.

### REFERENCES

1. "Lux Research Inc. – Solar State of the Market – Finding the Solar Market's Nadir" February, 2009.
2. U. S. DOE Solar Energy Technologies Program, August 2007.
3. Deutsche Bank publication "Solar Photovoltaic Industry: Looking through the Storm" January 21, 2009.
4. CPV Today CPV Summit in San Diego, February 3-4, 2009.
5. Wolfgang Guter, Jan Schöne, Simon P. Philipps, Marc Steiner, Gerald Siefer, Alexander Wekkeli, Elke Welser, Eduard
6. Oliva, Andreas W. Bett, and Frank Dimroth, *Appl. Phys. Lett.* **94**, 223504 (2009).
7. [www.emcore.com](http://www.emcore.com), [www.spectrolab.com](http://www.spectrolab.com).
8. [www.nrel.gov/docs/gen/fy04/36831.pdf#ovw](http://www.nrel.gov/docs/gen/fy04/36831.pdf#ovw). R.K. Ahrenkiel, Electrical and Optical Characterization of Semiconductors, DOE/National Association of State Universities and Land Grant Colleges (NASULGC) Biomass and Solar Energy Workshops, August 3-4, 2004.
9. "Lux Research Inc. Briefing: Sunovia Energy", September 2009.
10. X. Wu, J.C. Keane, R.G. Dhere, C. DeHart, A. Duda, T.A. Gessert, S. Asher, D.H. Levi and P. Sheldon, Conference Proceedings, 17th European Photovoltaic Solar Energy Conference, Munich, 22-26 October 2001; 995-1000.
11. J. Sites and J. Pan, Strategies to increase CdTe solar-cell voltage, *Thin Solid Films*, **515**, 6099 (2007).
12. T.J. Coutts, J.S. Ward, D.L. Young, K.A. Emery, T.A. Gessert and R. Noufi, *Prog. in Photovolt: Res. Appl.* **11**, 359
13. (2003).

14. D. J. Olego, J. P. Faurie, S. Sivananthan and P. M. Raccach, *Appl. Phys. Lett.* **47**, 1172 (1985).
15. S. M. Johnson, S. Sen, W. H. Konkel, and M. H. Kalisher, *J. Vac. Sci. Technol. B* **9**, 1897 (1991).
16. S. P. Tobin, J. P. Tower, P. W. Norton, D. Chandlerhorowitz, P. M. Amirtharaj, V. C. Lopes, W. M. Duncan, A. J. Syllaios, C. K. Ard, N. C. Giles, J. Lee, R. Balasubramanian, A. B. Bollong, T. W. Steiner, M. L. W. Thewalt, D. K. Bowen, B. K. Tanner, *J. Electron. Mater.* **24**, 697 (1995).



## **ADVANCES IN CdTe, CuInGaSe<sub>2</sub> AND GaAs/AlGaAs THIN FILM PV SOLAR CELLS**

I. M. DHARMADASA

*Electronic Materials & Sensors Group, Materials & Engineering Research Institute  
Faculty of Arts Computing Engineering and Sciences  
Sheffield Hallam University, Sheffield S1 1WB, United Kingdom.*

Corresponding Author, e-mail: *Dharme@shu.ac.uk*

### **ABSTRACT**

This paper summarises the latest developments in thin film solar cells based on CdTe, CuInGaSe<sub>2</sub> and GaAs/AlGaAs absorber materials. After proposing a new model for CdS/CdTe solar cells in 2002, similar observations were noted for CuInGaSe<sub>2</sub> based solar cells. It has been shown that the Fermi level pinning takes place at one of the four experimentally observed defect levels in p-CuInGaSe<sub>2</sub>/metal interfaces very similar to that of n-CdTe/metal contacts. These levels are at 0.77, 0.84, 0.93 and 1.03 eV with  $\pm 0.02$  eV error and are situated above the valence band maximum. As a result, discrete values of open circuit voltages are observed and the validity of the new model for CuInGaSe<sub>2</sub> solar cells were published in 2009. It is becoming clear that Fermi level pinning due to defect levels dominates the performance in all CdTe, CuInGaSe<sub>2</sub> and GaAs thin film devices and the future research should be directed towards resolving associated issues and hence improving the performance of PV solar cells. New designs based on graded bandgap multi-layer solar cells have been proposed for photovoltaic (PV) solar cell development. These new designs have been tested with well researched materials, GaAs/AlGaAs, and highest open circuit voltages of 1175 mV and fill factors of ~0.85 were produced for initial solar cell fabrications. The graded bandgap solar cells are capable of making use of surrounding heat radiation, via native defects using impurity PV effect. These devices produce  $V_{oc}$  values in excess of 750 mV in complete darkness. This work has also led to the identification of disadvantages of the use of tunnel-junctions within tandem cells.

### **1. INTRODUCTION**

The development of a low-cost thin film solar cell device attracted worldwide research interest during the past 3-4 decades in order to convert sunlight into electrical power. The two most successful systems are based on inorganic semiconducting compounds, CdTe and CuInGaSe<sub>2</sub> (CIGS) absorbers. At present, highest reported conversion efficiencies for lab-scale devices stand at 16.5% [1] and 20.3% [2] for CdTe and CIGS solar cells respectively. Both systems have been successfully scaled up to manufacture large area solar panels, in industrial scale, but further improvements in conversion efficiency is a crucial step for reduction of cost of solar technology. The lab-scale device efficiencies have stagnated especially for CdTe and further development is severely hindered by lack of deep understanding of solid state physics principles behind these important devices. This paper summarises the advances in scientific understanding of (a) CdTe (b) CIGS (c) GaAs and (d) graded bandgap multi-layer solar cells.

### **2. ADVANCES IN CdS/CdTe THIN FILM SOLAR CELLS**

Since late 1970s, CdS/CdTe solar cell attracted active research and this work was successful in achieving reasonable efficiencies using electrodeposited CdTe material [3]. The device was considered as a simple n-p hetero-junction between n-CdS window material and p-CdTe absorber material (see Figure 1a). Attempts were made to fabricate low resistance ohmic contacts to p-CdTe and the main issues on the reproducibility, yield, device stability and lifetime were found to be related to the CdTe/metal interface.

The author's comprehensive work on II-VI compounds and electrical contacts to these materials [4] revealed that there is a strong Fermi level pinning phenomenon at metal/II-VI compound interfaces as shown in Figure 1b. In the case of n-type CdTe, there exist five experimentally observed defect levels causing Fermi level pinning. Therefore depending on the pinning position, reproducibility of good devices and their stability and yield were unpredictable and caused issues during solar cell fabrication. The  $V_{oc}$  values observed for reasonably high efficiency (>10%) solar cells appeared in well separated discrete groups as shown in Figure 1c. These findings led to the proposed new model in 2002 for the CdS/CdTe system, as shown by the energy band diagram in Figure 1d [5-8].

According to the new model, in high efficiency devices, the CdTe material remains n-type after post-deposition heat treatment and the device is a combination of an n-n hetero-junction and a large Schottky barrier at the n-CdTe/metal interface (Figure 1d). The Fermi level pinning towards the conduction band ( $E_1$  &  $E_2$ ) produce low Schottky barriers, reduce internal electric field and therefore severely affect the reproducibility of high efficiency and yield of these devices, unless these defects are dealt with accordingly.

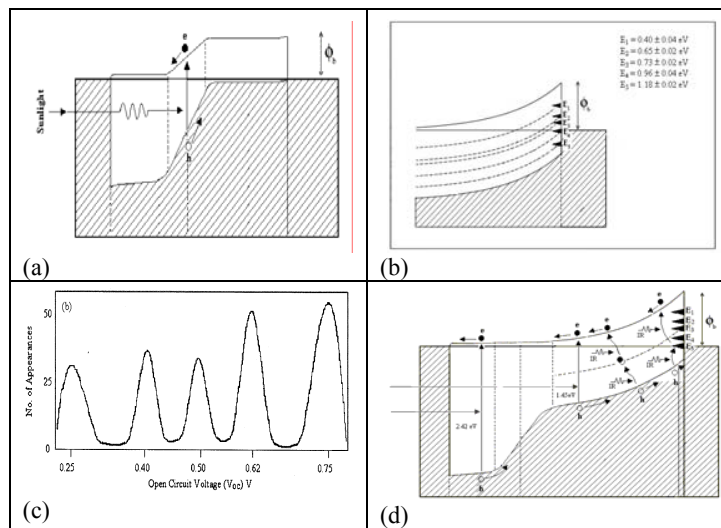


Figure 1. (a) The energy band diagram of CdS/CdTe solar cell as a simple p-n junction, visualised in the past, (b) Schottky barrier formation at n-CdTe/metal interface with an influence of five defect levels causing Fermi level pinning at ( $E_1$ - $E_5$ ), (c) observation of  $V_{oc}$  values for this solar cell in discrete groups and (d) the energy band diagram of high efficiency CdS/CdTe solar cells with latest understanding.

The experimental results supporting this new concept have been published recently in a series of four papers [5-8]. This new concept explains the negative results observed in the past when p-type dopants were used to improve the electrical conductivity of the CdTe layer [9]. Instead of the expected improvement of the devices, drastic deterioration of the device was observed when doped with p-dopants such as Na, Ag and Cu. According to new understanding, CdTe layer requires n-type doping in order to improve the electrical conductivity and develop the device. The first positive effects of n-type doping and making MIS structures at the n-CdTe/metal interface on device performance were reported in two of the recent publications [6,7], confirming the validity of the new ideas for CdTe solar cells. The incorporation of halogens (Cl, F, I), well

known n-type dopants in CdTe will produce high efficiencies according to the latest understanding of the CdTe solar cell.

### 3. LATEST UNDERSTANDING OF CIGS BASED SOLAR CELLS

Any type of PV solar cell consists of two electrical contacts to extract electrical power from the device. These are usually metal/semiconductor interfaces and form either low resistive ohmic contacts or a rectifying contact. Naturally, these two interfaces play a very important role in the function of PV activity of the device. Although, CIGS based lab-scale solar cells have achieved 20.3% efficiency to date [2], the published research reports on electrical contacts to CIGS material are scarce.

The author's group recently collaborated with Showa-Shell in Japan and conducted research on these p-CIGS/metal interfaces. The findings are reported in a recent publication [10] in 2008, and the summary is given in Figure 2b. The Fermi level pinning situation is identical to that of metal/n-CdTe interfaces (Figure 1b). The only difference is the electrical conductivity type of the semiconductor, but the Fermi level pinning at native defects of the material is very similar. Four pinning level positions ( $E_1$ - $E_4$ ) have been experimentally identified.

In the scientific literature, glass/Mo/CIGS/CdS/i-ZnO/Al:ZnO/metal-grid solar cell structure has been considered as (i) a hetero-junction between p-CIGS and n-CdS, (ii) hetero-junction between p-CIGS and n-type ordered defect compound (ODC) layer and (iii) a homo-junction within the CIGS material. The energy band diagram widely used to describe this device in the literature is shown in Figure 2a. There are two concerns arising from this energy band diagram; the position of the Fermi level within i-ZnO (this should be in the middle of the bandgap), and the distance across the device is not to scale and therefore this diagram provides a mis-leading impression in representing a genuine hetero-junction.

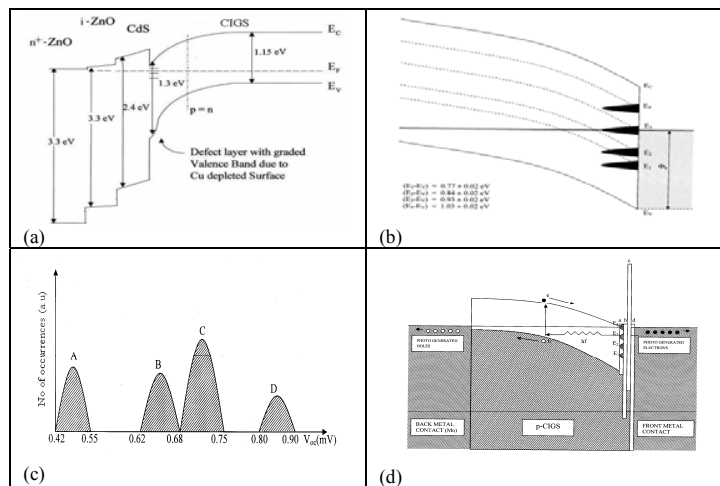


Figure 2. (a) the energy band diagram used in the literature to describe the photovoltaic activity of CIGS thin film solar cells, (b) the energy band diagram of the p-CIGS/metal interface with the observed Fermi level pinning positions, (c) observation of  $V_{oc}$  values for this solar cell in discrete groups and (d) the energy band diagram of the CIGS solar cell according to latest understanding

The Figure 2d shows an energy band diagram to describe the above structure using a p-type CIGS layer. For the construction of this energy band diagram the recently observed Fermi level pinning has been used. Since the Fermi level is pinned at one of the native defect levels, it is more appropriate to use the Fermi level as the reference energy level.

The band diagram shown in Figure 2a has been constructed following the Anderson's electron affinity rule using electron affinity values of semiconductors and the vacuum level as the reference level. Although this is valid for ideal systems, the Fermi level does not change the position in practical systems such as thin film solar cells due to its pinning at a defect level. Figure 2d shows both the vertical (Energy) and horizontal (Thickness) axes with an approximate scale and therefore the above concern with i-ZnO (layer c) has been removed; the Fermi level is situated in the middle of its bandgap. Furthermore, the four layers {(a) ODC layer, (b) n-CdS, (c) i-ZnO and (d) Al:ZnO} together forms a combined MIS structure with the i-ZnO layer acting as a blocking layer for photo-generated electrons returning back over the potential barrier. The Fermi level pinning at ( $E_1-E_4$ ) makes the situation more complicated producing discrete values of  $V_{oc}$  for this device. In order to produce most efficient devices, the Fermi level should be pinned at  $E_4$ . The detailed descriptions and the experimental evidence for this concept are given in our latest publication [11].

Figure 3 shows an additional p-n homo-junction within the CIGS layer. During growth of CIGS layer, some groups deposit a Cu-rich CIGS layer followed by In & Ga containing CIGS layers. The recent work shows that Cu-rich CIGS are p-type and In-rich CIGS are n-type in electrical conduction [12-14]. Therefore, there exists a p-n junction within a few  $\mu\text{m}$  thick CIGS layer, making this structure more attractive than the one shown in Figure 2d. This band diagram shows the validity of all three concepts currently considered for CIGS solar cells. The device can be considered as:

- (i) A hetero-junction between CIGS and CdS, or (ii) hetero-junction between the CIGS and ODC layer, or (iii) homo-junction within the CIGS layer.

The recent observations summarised in this paper introduce two more complications to this device structure.

- (i) Fermi level pinning at one of the four levels ( $E_1-E_4$ ) observed to date, and (ii) The front electrical contact acting as a compound MIS structure with i-ZnO serving as a blocking layer for preventing photo-generated electrons returning to the back contact (electron back diffusion barrier - ebdb - layer) and a plugging material for any pin-holes present.

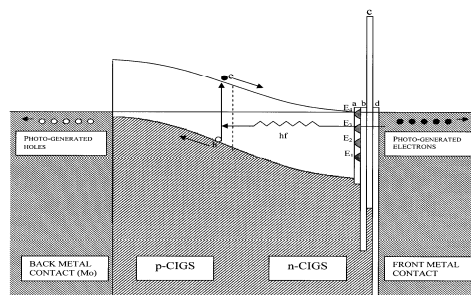


Figure 3. Energy band diagram for back metal contact/p-CIGS-n-CIGS/ODC layer(a)/n-CdS(b)/i-ZnO(c)/Al:ZnO(d)/front metal contact structure. The device is a combination of a p-n junction within CIGS layer and an MIS structure at the front contact.

Understanding these complexities and hence continuing relevant research will lead to further improvements of this solar cell based on CIGS material.

#### 4. EMERGING PATTERNS IN GAAS SOLAR CELLS

The recent work in author's group and the observations of published work in the literature reveal that the  $V_{oc}$  values observed for GaAs based solar cells also appear in at least 3 discrete groups. These results are shown in Figure 4, and the 3 groups appearing are clearer than those observed for CdTe (Figure 1c) and CIGS (figure 2b) thin film solar cells.

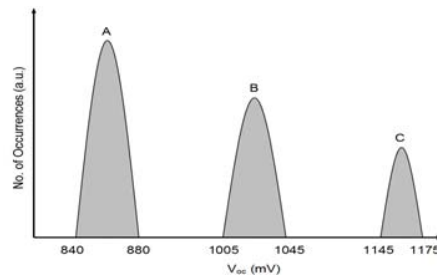


Figure 4. The appearance of  $V_{oc}$  values in 3 discrete groups for GaAs based thin film solar cells. These observations are identical to those observed for CdTe and CIGS solar cells.

Therefore, it seems very likely that Fermi level pinning phenomenon observed for both CdTe and CIGS solar cells also has drastic effects on GaAs solar cells. Dealing with these effects of defects therefore has paramount importance in R&D work on thin film solar cells.

#### 5. GRADED BANDGAP MULTI-LAYER SOLAR CELLS

In order to absorb a major part of the solar spectrum, the main feature of the energy band diagram shown in Figure 1d can be improved. This is namely the use of larger bandgap materials in front and smaller bandgap materials towards the back of the solar cells. This feature can be further improved using many layers (ideally an infinite number of layers) as shown in Figure 5(a) starting from an n-type window material [15].

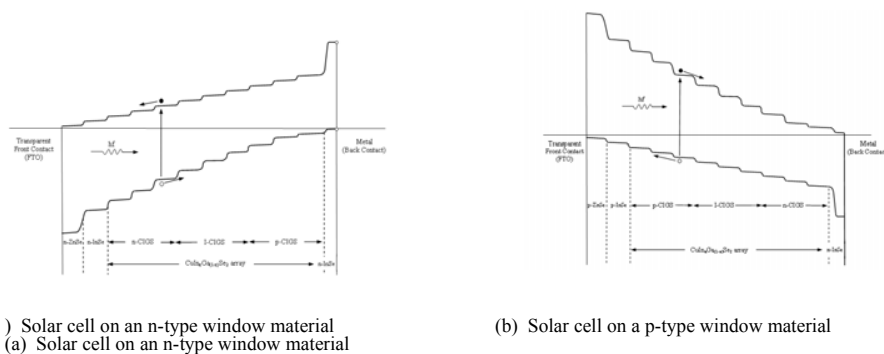


Figure 5. The energy band diagrams of graded bandgap solar cells based on (a) n-type and (b) p-type window materials [16].

The novel devices based on p-type window materials can also be used with an added advantage of larger potential barrier present for electron conduction through the device. This is shown in Figure 5(b) for comparison and larger bandgap of window material forms a high potential barrier height ( $\phi_b$ ), steep gradient and hence capable of producing effective charge carrier separation and larger open circuit voltage ( $V_{oc}$ ) values. In solar cell devices, the  $V_{oc}$  produced is a function of the potential barrier,  $\phi_b$ , present within the device.

Out of these two graded bandgap solar cell designs, the second structure (Figure 5b) has more advantages. It can absorb UV, visible and IR radiation from the solar spectrum, and combine both impact ionisation and impurity PV effect in one device in order to enhance charge carriers. Therefore the experimental testing was carried out only on this device design [17,18].

### 5.1 Summary of experimental results to date

The new design was experimentally tested using well researched and MOCVD grown GaAs/ $Al_xGa_{(1-x)}$ As system. The design shown in Figure 5(b) was selected for testing and the device structure was grown starting from n-type GaAs substrate as the small bandgap material. A 3  $\mu\text{m}$  thick layer of  $Al_xGa_{(1-x)}$ As alloy compound was grown using MOCVD technique and gradually increased the aluminium content in order to increase the energy bandgap. The electrical conductivity type of the thin layers was also gradually changed from n-type to p-type by variation of dopant concentrations. The n-type dopant used was silicon (Si) and the p-type doping was achieved by taking advantage of the naturally formed background carbon within the reactor. The devices were fabricated with 0.5 mm diameter,  $3\times 3$ ,  $5\times 5$ ,  $10\times 10$  mm<sup>2</sup> sizes by forming ohmic contacts to the front and the back of the solar cells [17,18].

The I-V characteristics of fully processed devices are shown in Figure 6(a). For clarity, only one I-V curve under dark conditions and two curves under AM1.5 conditions are shown in this Figure. The devices were measured in five different laboratories in order to test the accuracy of measurements. The I-V characteristics measured at NREL in US for comparison is also shown in Figure 5b. The details of other measurements are summarised in Table 1.

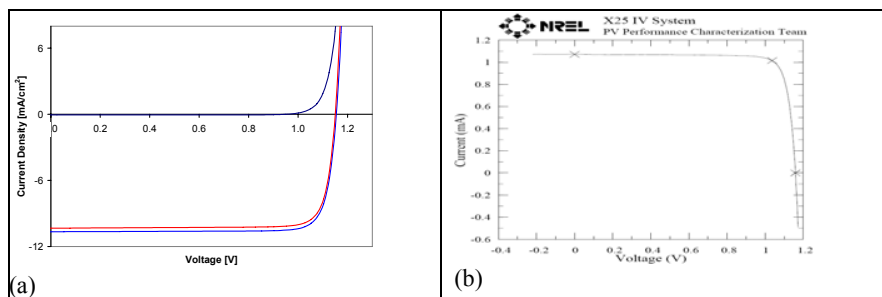


Figure 6. The I-V characteristics of graded bandgap multi-layer solar cells as measured in (a) Zürich Labs and (b) NREL in US for comparison.

Table 1. The summary of device parameters measured for first growth of graded bandgap multi-layer solar cells based on p-type window materials.

Device	$V_{oc}$ (mV)	FF	$J_{sc}$ (mA cm <sup>-2</sup> )	$R_s$ ( $\Omega$ cm <sup>-2</sup> )	$R_p$ ( $\Omega$ cm <sup>-2</sup> )	Place of Assessment
1	1170	0.87	----	----	----	SHU Labs
2	1160	0.86	----	----	----	I M Dharmadasa
3	1148	0.86	10.7	2.5	10,400	Zürich Labs
4	1141	0.86	10.3	4.0	5100	Ayodhya Tiwari
5	1169	0.85	11.5	---	---	SBU Labs
6	1149	0.86	10.0	---	---	Hari Reehal
7	1150	0.85	12.1	3.8	----	EPFL Labs Michael Grätzel
8	1159	0.85	12.3	---	----	NREL - USA
9	1156	0.85	11.9	---	----	Tim Gessert

The advantages of this structure were shown by this first experimental test using MOCVD grown GaAs/Al<sub>x</sub>Ga<sub>(1-x)</sub>As system. The summary of parameters observed for this first fabrication is:

$$V_{oc} \sim (1141-1170) \text{ mV}, \quad J_{sc} \sim (11 - 12) \text{ mAcm}^{-2}, \quad FF \sim (0.82 - 0.87), \quad \eta = (10-12)\%$$

The  $V_{oc}$  and FF have achieved the highest possible values, but the  $J_{sc}$  for the first growth was not as expected. In fact the  $V_{oc}$  achieved is the highest recorded to date for a single device. The expected band diagram for this cell is as in Figure 5b, but the EBIC and SIMS results [19] indicated that the structure of the experimentally produced devices was different (Figure 7). The doping concentrations at the two ends were high in the region of  $10^{18} \text{ cm}^{-3}$ , and hence the resultant energy bands were almost flat reducing the current collection. However, the middle part with the internal electric field acts as a solar cell with a reduced thickness (about 1.5  $\mu\text{m}$ ) creating features expected in the design and therefore produces excellent values for  $V_{oc}$  and FF. The loss in  $J_{sc}$  occurs due to collection of charge carriers created towards the blue-end and the IR-end.

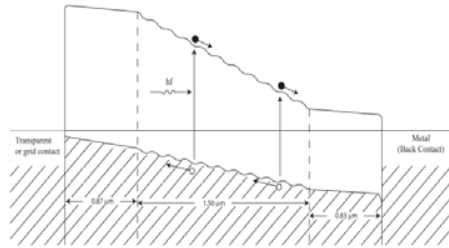


Figure 7. The band diagram of the device fabricated during first growth due to high doping concentrations at both ends of the structure, effectively reducing the thickness of the active region of the cell.

The second MOCVD growth reducing the n-type doping concentration (Si) at the rear of the device from  $\sim 10^{18}$  to  $\sim 10^{15} \text{ cm}^{-3}$  gave following overall improved device performance.

$$V_{oc} \sim (870-900) \text{ mV}, \quad J_{sc} \sim (22 - 26) \text{ mAcm}^{-2}, \quad FF \sim (0.82 - 0.87), \quad \eta = (16-20)\%$$

This improvement in the doping concentration at the rear of the device provides a better shape for the expected device (Figure 8). Therefore the device parameters have improved considerably. The reduction of the high carbon doping in the front from  $\sim 10^{18}$  to  $\sim 10^{15} \text{ cm}^{-3}$  is not possible from MOCVD method, due to presence of background carbon in the reactor. Therefore

this doping optimisation should be carried out using a growth technique like MBE in order to fulfill this requirement. The work is continuing to optimise the p-doping concentration of the front of the cell in order to achieve device structures as shown in figure 5b.

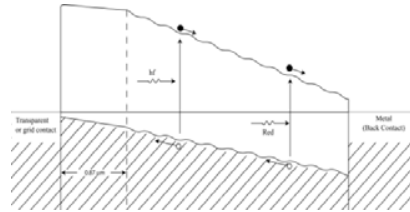


Figure 8. Energy band diagram of the improved device with lower Si doping at the rear of the solar cell. The reduction of the Si doping concentration from  $10^{18}$  to  $10^{15}$   $\text{cm}^{-3}$  extends the depletion region to the back ohmic contact.

### 5.2 Is impurity PV effect contributing to this cell?

The new device design is capable of absorbing all types of photons from sunlight. The most energetic blue-end photons are absorbed in the wide bandgap, front semiconducting material layer. As the light gradually travels through the device, the photons will be effectively absorbed in the order of UV, visible & IR, thereby minimizing the thermalisation effect. This in effect reduces the production of heat within the device and is an effective cooling mechanism for PV cells. All electrons and holes created by photons are instantaneously separated without any hindrance towards the two ohmic contacts due to the presence of an electric field throughout the device thickness. The IR photons are transmitted towards the back of the solar cell without absorption due to their low photon energies. In the vicinity of the interface (at  $\text{Al}_x\text{Ga}_{(1-x)}\text{As}/\text{GaAs}$  substrate), the density of native defects is high. Making use of these native defects, the IR radiation could produce e-h pairs using multi-absorption pathways as shown in Figure 9. Promoted electrons do not relax back, since the created holes are rapidly transferred to the ohmic contact at the front. Therefore this is an effective electron pumping mechanism created due to the shape of the energy band diagram, and makes effective use of native defects in the materials. When this process is taking place under illuminated conditions, the contributions to the detrimental recombination process is inhibited. This is another indirect advantage of this particular device structure and the experimental results to date have confirmed this effect.

The measurements of I-V curves under dark and illuminated conditions provide another useful parameter (ideality factor),  $n$  to observe this effect. Table 2 shows these experimental values and clearly demonstrated that the ideality factor  $n$  has reduced under illumination. This is a good indication of the dominance of the upward electron pumping process taking place and inhibiting the detrimental downward electron recombination process.

Table 2. The ideality factors for  $\text{Al}_x\text{Ga}_{(1-x)}\text{As}/\text{GaAs}$  based graded bandgap solar cells under dark and illuminated conditions.

Solar cell number	1	2	3	4	5
$n$ value under dark conditions	1.41	1.50	1.68	1.84	2.26
$n$ value under illuminated conditions	1.13	1.15	1.22	1.14	1.91



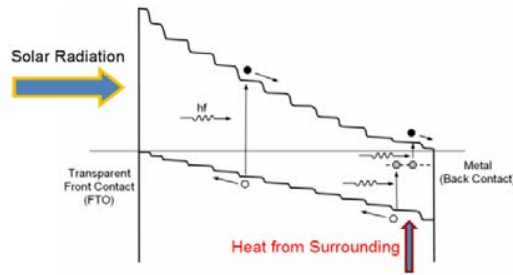


Figure 9. Schematic diagram showing the two energy inputs available to this device structure. When placed in complete darkness, the device still produces PV activity using heat energy from the surroundings due to impurity PV effect.

The impurity PV effect therefore effectively uses the naturally existing impurity levels, to this new device's advantage in converting IR photons present in the solar spectrum into useful charge carriers. The observation of large  $V_{oc}$  values in the range (600–900) mV in complete darkness shows the contribution from impurity PV activity using IR radiation from surroundings. The measurements of responsivity as a function of wavelength also show the collection of current in the IR region confirming the presence of impurity PV effect in these devices. These results are shown in Figure 10 with clear evidence of the contribution from IR radiation, via impurity PV effect.

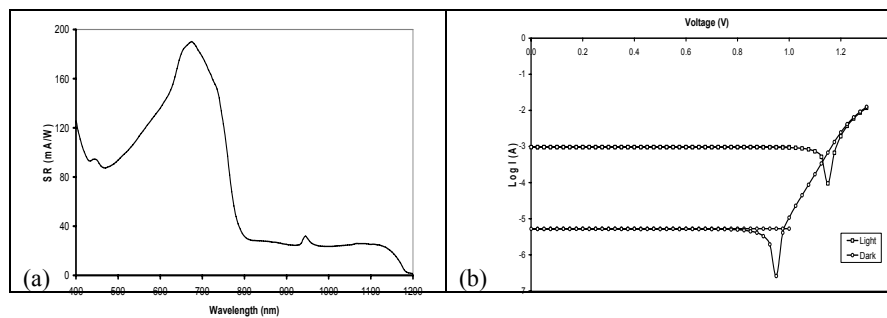


Figure 10. (a) Responsivity measurements showing collection in the IR region and (b) production of over 900 mV  $V_{oc}$  in the complete darkness proving the graded bandgap device is active in impurity PV effect and make use of IR radiation from surroundings to produce PV effect.

### 5.3 Is impact ionisation contributing to this cell?

The impact ionisation has also been incorporated into this device design. There are two ways to contribute to this effect; (i) the electrons produced in the front accelerate through the device thickness and create e-h pairs by breaking bonds at the rear of the device (via band-to-band excitations) and (ii) the electrons produced in the front accelerate and promote electrons from defect levels to the conduction band supporting the impurity PV effect. The second effect could have a substantial contribution to  $J_{sc}$  when the device is fully developed with doping optimisation. The experimental evidence for impact ionisation is positive even for early stage devices and the work is progressing.

## **6. CONCLUSIONS**

The latest results summarised in this communication lead to several important conclusions.

- (i) Thin film solar cell devices based on both CdTe and CIGS show Fermi level pinning at one of the several native defect levels observed within the structure. The latest observations indicate very similar behaviour also emerging for GaAs based solar cells.
- (ii) The construction of the energy band diagrams for practical thin film devices is more appropriate with respect to the pinned Fermi level rather than the vacuum level as used for ideal theoretical systems.
- (iii) Graded bandgap multi-layer solar cells have high potential for achieving greater conversion efficiencies. The devices formed starting from p-type window materials have better opportunity for achieving high performance parameters.
- (iv) Experimental results to date reveal that these devices are capable of producing charge carriers using IR radiation from both sunlight and the surroundings via impurity PV effect contributing to the production of useful electrical power.

## **7. ACKNOWLEDGEMENTS**

The author would like to acknowledge the contributions from a large number of researchers to this programme. In particular, the recent contributions from John Roberts, Geoff Hill, Sidath Kalyanaratne, Nishith Patel, Osama Elsherif, Drs. Mahanama, S Ito and P Liska are gratefully acknowledged.

## **REFERENCES**

1. X Wu, J C Keane, R G Dhere, C Dehart, D S Albin, A Duda, T A Gessert, S Asher, D H Levi and P Sheldon 2001 17<sup>th</sup> European Photovoltaic Solar Energy Conference; 22-26 October 2001, Munich, Germany, p995.
2. P Jackson, D Hariskos, E Lotter, S Paetel, R Wuerz, R Menner, W Wischmann and M Powalls, *Prog. of PV: Research & Appl.* (2011) doi: 10.1002/pip.1078.
3. B M Basol, (1984) *J. Appl. Phys.* 55 No. 2 p601.
4. I M Dharmadasa. Invited review paper. *Progress in Crystal Growth and Characterisation.* Vol. 36, No. 4. (1998) p249.
5. I M Dharmadasa, A P Samantilleke, J Young and N B Chaure, *Semicond. Sci. Technol.* 17 (2002) p1238.
6. N B Chaure, A P Samantilleke and I M Dharmadasa, *Solar Energy Materials & Solar Cells* 77 (2003) p303.
7. I M Dharmadasa, A P Samantilleke, J Young and N B Chaure, *Proc. of 3<sup>rd</sup> World PV Conference, Osaka-Japan, 11-18 May (2003)* p547.
8. I M Dharmadasa, J D Bunning, A P Samantilleke and T Shen. *Solar Energy Mat. & Solar Cells* 86 (2005) p373.
9. S Dennison (1994) *J. Mat. Chem.* 4 p41.
10. I M Dharmadasa, N B Chaure, A P Samantilleke, and A Hassan. *Solar Energy Materials & Solar Cells*, Vol.92, No.8 (2008) p923.
11. I M Dharmadasa, *Semicond. Sci. Technol.* 24 (2009) 055016 (10pp).
12. N B Chaure, A P Samantilleke, R P Burton, J Young and I M Dharmadasa, *Thin Solid Films* 472 (2005) p212.
13. I M Dharmadasa, R P Burton and M Simmonds, *Solar Energy Materials & Solar Cells* 90 (2006) p2191.

14. I M Dharmadasa, N B Chaure, G J Tolan and A P Samantilleke. *J. of The Elec.Chem. Soc.*, 154(6) (2007) p466.
15. I M Dharmadasa, *Solar Energy Materials & Solar Cells* 85 (2005) p293.
16. I M Dharmadasa, *Curr. Appl. Phys.* (2009), doi:10.1016/j.cap.2008.12.021.
17. I M Dharmadasa, J S Roberts and G Hill, *Solar Energy Materials & Solar Cells*, 88 (2005) p413.
18. I M Dharmadasa, G J Tolan, J S Roberts, G Hill, S Ito, P Liska and M Grätzel, *Proc. of 21<sup>st</sup> EU photovoltaic conference, Dresden Germany, June-2006*, p257.
19. I M Dharmadasa, "Advances in Thin Film Solar Cells", In Press, Pan Stanford Pub. Pte. Ltd., 2011.

## **CHALLENGES AND OPPORTUNITIES IN POLYCRYSTALLINE THIN-FILM SOLAR CELLS**

RAMESH DHERE\* and SIVA SIVANANTHAN

*Sivananthan Laboratories, Bollingbrook, Illinois, USA*

\*Corresponding Author, e-mail: *Ramesh.Dhere@nrel.gov*.

### **ABSTRACT**

Thin-film solar cells have come a long way in fulfilling their potential for terrestrial applications. There are three leading technologies in this area: CdTe, CuInGaSe<sub>2</sub> and a-Si. This presentation will focus on the polycrystalline contenders, namely CdTe and CIGS based, solar Cells. The cost of commercial CdTe modules has been reduced to \$0.75/W<sub>p</sub>, making this technology the undisputed leader on the production-cost front. Some potential exists for further cost reduction, but there is greater promise for performance gain. The highest efficiency of 16.7% reported to date for CdTe devices is much lower than the theoretical efficiency of 26%–28%. We will analyze the device parameters of CdTe solar cells and their correlation to materials, and device properties, to investigate the mechanisms affecting performance. Other issues such as materials availability, energy-payback time, and total cost for the systems need to be considered for large-scale deployment of this technology. We will consider these issues in order to determine the true potential of CdTe technology and the challenges that must be surmounted to realize the true potential. CIGS solar cells have achieved high performance, with the best cell efficiencies over 20%. There has been considerable activity on the industrial arena, with some companies reporting champion panel efficiencies of over 15%.

## **CHEMICALLY DEPOSITED THIN FILMS AND THEIR APPLICATION IN SOLAR CELLS**

C. D. LOKHANDE<sup>1\*</sup>, S. S. JOSHI<sup>2</sup>

<sup>1</sup>*Thin Film Physics Laboratory, Department of Physics, Shivaji University,  
Kolhapur- 416004 (M. S.) India.*

<sup>2</sup>*Rajaram Collage, Government of Maharashtra, Kolhapur, India*

\* Corresponding Author, e-mail: [l\\_chandrakant@yahoo.com](mailto:l_chandrakant@yahoo.com)

### **ABSTRACT**

Much attention has been paid to the preparation of nanostructured semiconductors and composite thin films by chemical solution processing. Currently, there is a great interest in the methods of creating nanostructured materials with high performance nano-devices for the solar cell, and dye-sensitized solar cells (DSSC), applications. The systematic study on the preparation of nanostructured metal chalcogenides, metal oxides and composites thin films by using chemical/electrochemical reactions from aqueous solutions for solar cell and dye-sensitized solar cells (DSSC) applications is explored.

This talk includes the different deposition methods such as chemical bath deposition (CBD), Successive ionic adsorption and reaction (SILAR), spray pyrolysis technique (SPT), electrodeposition (ED), etc. for the deposition of nanostructured metal chalcogenides, and metal oxide thin films from aqueous solutions. Such soft solution chemical methods allow bottom-up approach to tune morphology of nanocrystalline materials in thin film form with better control of particle size, shape, size distribution, particle composition, degree of particle agglomeration, etc.

Finally, the applications of thin films in solar cells, dye-sensitized solar cells (DSSC), and supercapacitive performance of various materials such as CdS, CdSe, CdTe, HgS, PbS, ZnO, etc are discussed.

### **1. INTRODUCTION**

In recent years, nanocrystalline thin film science has grown world-wide into a major research area. The importance of coatings and the synthesis of new materials for industry have resulted in a tremendous increase of innovative thin film processing technologies. Currently, this development goes hand-in-hand with the explosion of scientific and technological breakthroughs in microelectronics, optics and nanotechnology. A second major field comprises process technologies for films with thicknesses ranging from one to several microns. These films are essential for a multitude of production areas, such as thermal barrier coatings and wear protections, enhancing service life of tools and to protect materials against thermal and atmospheric influences. Presently, rapidly changing needs for thin film materials and devices are creating new opportunities for the development of new processes, materials, technologies and performance of thin films in various applications [1]. In basic research, special model systems are needed for quantitative investigations of the relevant and fundamental processes in thin film materials science. In particular, these model systems enable the investigation of nucleation and growth processes, solid state reactions, the thermal and mechanical stability of thin film systems and phase boundaries. Results of combined experimental and theoretical investigations are the prerequisites for the development of new thin film systems and the tailoring of their microstructure and performance. Thin film systems necessitate direct control of materials on the molecular and atomic scale, including surface modifications, deposition and structuring. Many of these techniques were improved during the last decade, resulting in remarkable advances in the fundamental understanding of the physics and chemistry of thin films, their microstructural evolution and their properties. This progress has led to the development of new materials, expanded applications and

new designs of devices and functional thin film systems. Some of the factors determine the physical, optical, electrical and other properties of a thin film are the following viz., rate of deposition, substrate temperature, environmental conditions, residual gas pressure in the system, purity of the material to be deposited, inclusion of foreign matter in the deposit, inhomogeneity of the film, structural and compositional variations of the film in localized or wider areas, etc. Huge variety of materials has been prepared in the form of thin films over a century because of their potential value and scientific curiosity in their properties [2–4]. The exceptional properties of nanocrystalline materials are determined by the three features of their nature: grain size spatially confined to less than 100 nm, significant number of grain boundaries, with a typical concentration of about  $10^{20}$  cm<sup>3</sup> and variations in composition between the grains and grain boundaries [5,6]. The methods involving the growth from chemical solution are called as chemical methods. Here, a fluid surface precursor undergoes a chemical change at a solid surface, leaving a solid layer. Chemical deposition method enables the growth of thin films from solutions, either aqueous or organic [7]. The solutions contain precursor molecules for a variety of elements in the thin film of interest. Chemical deposition methods are inexpensive and enable the synthesis of thin film materials with complex chemical compositions. For most applications, one would prefer films which have a special texture, low grain boundary density, and smooth surfaces. Chemical methods include electrodeposition, chemical bath deposition (CBD), successive ionic layer adsorption and reaction (SILAR), electroless deposition, anodization, spray pyrolysis, liquid phase epitaxy, etc.

In the present paper, the work carried out by our group in the recent years with various thin films using chemical deposition methods and their applications has been discussed. The chemical methods employed are chemical bath deposition (CBD), successive ionic layer adsorption and reaction (SILAR), spray pyrolysis and electrodeposition..

## **2. CHEMICAL METHODS FOR MICROSTRUCTURE THIN FILM DEPOSITION**

### *2.1. Chemical bath deposition method (CBD)*

Chemical bath deposition (CBD), which is also known as controlled precipitation or solution growth method, or simply chemical deposition, recently emerged as a method for the deposition of metal chalcogenide and metal oxide thin films. The CBD method requires simple equipments like hot plate with magnetic stirrer. The starting chemicals are commonly available and cheap. With CBD method, a large number of substrates can be coated in a single run with a proper jig design. Electrical conductivity of the substrate is not the necessary requirement. Any insoluble surface to which the solution has a free access will be a suitable substrate for deposition. The low temperature deposition avoids oxidation and corrosion of metallic substrates. Chemical deposition results in pin hole free and uniform deposits are easily obtained since the basic building blocks are ions instead of atoms. The preparative parameters are easily controllable and better orientations and desired grain structure can be obtained. The film formation takes place when ionic product exceeds solubility product [8, 9]. The experimental set up for the growth of the films using CBD method is shown in Fig. 1. In this method, the substrate may be stationary and solution is stirred with the help of magnetic stirrer. Water or paraffin bath with constant stirring is used to heat the chemical bath to the desired temperature. In some cases, stirring is continuous from room temperature, while in some cases, it is started after attaining the desired temperature. The representative example of the deposition of ZnO by the CBD method is based on the formation of solid phase from a solution, which involves two steps as the nucleation and particle growth. The film of certain thickness grows by heterogeneous reactions of precursor solution at the substrate surface. Preparative conditions used for deposition of TiO<sub>2</sub>, ZnO and CdO thin films are taken from references [10-13].

## 2.2. Successive ionic layer adsorption and reaction (SILAR) method

Successive ionic layer adsorption and reaction (SILAR) is relatively new and less investigated method for the deposition of metal chalcogenide thin films [14, 15]. It is based on the immersion of substrate into the separately placed anionic and cationic precursors and rinsing between every immersion in double distilled water to avoid homogeneous precipitation. Fig. 2 shows the schematic representation of SILAR method. A review by Pathan and Lokhande [16] reports the advantages of SILAR over CBD method. The preparative conditions of SILAR deposited  $\text{TiO}_2$ , ZnO and CdO thin films are used from references [17-20].

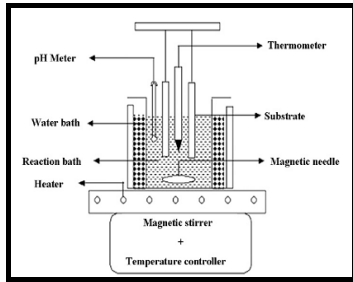


Fig.1. Schematic representation of chemical bath deposition method

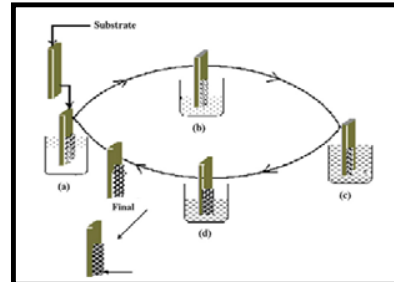


Fig.2. Schematic representation of SILAR method (a: cationic precursor, b and d: rinsing bath, c: anionic precursor)

## 2.3. Spray pyrolysis method

Spray pyrolysis is one of the most attractive and promising film Preparation methods. It is essentially the same film processing technique as the so-called pyrosol technique, in which a source solution is sprayed on the heated substrate to be deposited as a film. In other words, when a source solution is atomized, small droplets splash and vaporizes on the substrate and leaves a dry precipitate in which thermal decomposition occurs [21]. The schematic experimental set up of the spray pyrolysis method is shown in Fig. 3. The preparative conditions for spray deposited  $\text{TiO}_2$  and ZnO thin films are taken from references [22-25].

## 2.4. Electrodeposition method

Electrodeposition is based on the principle of electrolysis in which chemical reaction occurs at electrode–electrolyte interface due to the passage of electric current through an electrolyte. When electrolysis is carried out in the electrolyte, metal is deposited on the cathode and at the same time anode is dissolved in the solution. The amount of dissolution and deposition is determined by the quantity of electricity. Electrodeposition involves the movements of metallic ions in solution towards a cathode in an applied electric field. The ions accept electrons and deposited on the cathode as atoms or molecules [26, 27]. Fig. 4 shows the schematic of electrodeposition method. The preparative condition of electrodeposited  $\text{TiO}_2$  thin films are used from reference [28].

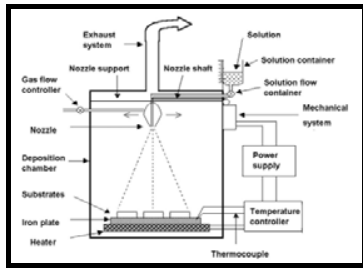


Fig.3. Schematic representation of spray pyrolysis method

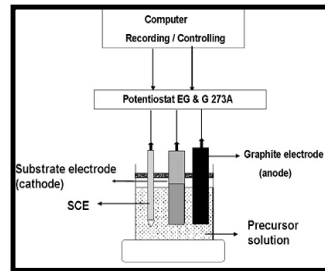
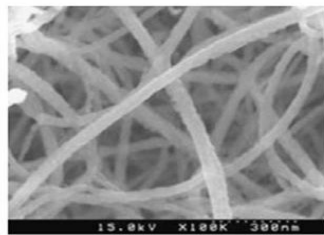


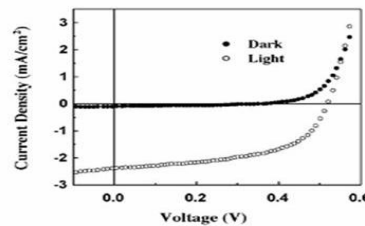
Fig.4. Schematic representation of electrodeposition method

### 3. MICROSTRUCTURE DEPENDENT SOLAR CELL APPLICATIONS

Dye sensitized solar cells (DSSC) operate on the principle of photo-electrochemical cells. The recombination of photo injected electrons in the conduction band of metal oxide ( $ZnO$ ,  $TiO_2$ , etc.) with the oxidized dye is one of the most important problems. To solve such problems compact barrier layers in addition with dye on metal oxide ( $ZnO$ ,  $TiO_2$ ) is used. The above discussion shows that the morphology of films and their device performance are closely related.



(B1)



(B2)

Fig.5. Microstructures and application CdO thin films by chemical bath deposition method B1: SEM image of CdO, and B2: application of CdO in DSSC.

The surface morphological characterization highlighted the importance of film preparation in maintaining a nanostructured phase. In this section, microstructure dependent applications of some of the nanocrystalline metal oxide ( $TiO_2$ ,  $ZnO$  and CdO thin films prepared by chemical methods have been exhibited in brief. Above metal oxides are chosen due to their proven potential applications in dye sensitized solar cells. Fig.5 (B1) shows the surface morphology of CdO thin film prepared by CBD method. Its application in solar cell device is shown in Fig. 5(B2). Fig.5(B1) shows the SEM picture of the CBD grown CdO film. The SEM shows the intertwined and randomly spaced CdO nanowires grown uniformly on the surface of the substrate. The average diameter of nanowires is  $\sim 30$  nm. There is no branching between two nanowires, even though it appears so. The film showed a high transparency in the visible region of solar spectrum, as well as low Ohmic resistance and therefore can be useful in DSSC's. The  $N_3$  dye is used to check DSSC performance. Fig.5 (B2) shows the I-V characteristics of DSSC formed with CdO intertwined nanowire network. After light exposure, (light intensity  $80\text{mW}/\text{cm}^2$ ) CdO electrode showed the photo conversion efficiency of  $\sim 1\%$ , and fill factor of 34% [12]. Thus, an easy transport through the nanowires network is retained in device-like environment and should result in faster carrier



extraction in the nanowire dye sensitized solar cell. High degree of networking and high surface area character of this unique surface morphology makes it potential candidate for dye sensitized solar cells.

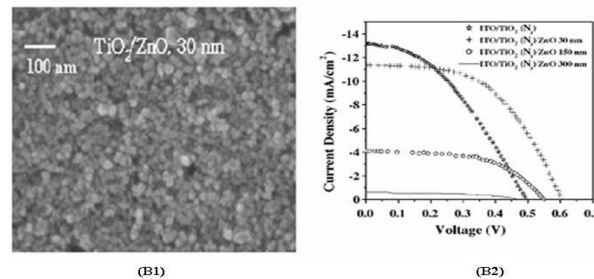


Fig.6. Microstructure and application of TiO<sub>2</sub>/ZnO film by SILAR deposition method

The SEM picture of SILAR coated ZnO layer on the ITO/TiO<sub>2</sub> is shown in Fig. 6(B1). It is seen that TiO<sub>2</sub> and ZnO coated TiO<sub>2</sub> films are smooth and have strong adhesion with the substrate. A close inspection of the image reveals that it is difficult to distinguish ZnO nanoparticles from TiO<sub>2</sub>. The thickness of ZnO layer is 30 nm. As discussed earlier, TiO<sub>2</sub> has the most extensively used oxide in DSSC. The use of additional blocking TiO<sub>2</sub> layer is essential for the p-type semiconductor cell to avoid short circuiting and loss of current through recombination at the conducting electrode. The compact nature of the SILAR deposited TiO<sub>2</sub> films is useful as blocking layer in DSSC. However, SILAR deposited ZnO layer with limited thickness also found to be useful in reducing recombination rate at electrode/electrolyte interface. Fig. 6(B2) shows the DSSC performance of TiO<sub>2</sub> and that of coated with ZnO for 30 and 300 nm thicknesses in tri-iodide electrolyte. It is seen that the DSSCs composed of TiO<sub>2</sub> has low open circuit voltage (*V*<sub>oc</sub>) i.e., 0.49V, which can be attributed to the significant charge recombination with either oxidized dye or tri-iodide electrolyte. However, after addition of 30nm ZnO layer thickness, *V*<sub>oc</sub> increased from 0.49 to 0.62 V, confirming its active role as an inherent energy barrier that leads to the decrease in recombination losses. However, short circuit current, *I*<sub>sc</sub> was decreased with increasing ZnO thickness due to its negative mass (0.2me). In the presence of 30nm ZnO film thickness on TiO<sub>2</sub> electrode, a photo conversion efficiency of 4.51% has been achieved [18,19]. Fig.7 (A1) shows the microstructure of TiO<sub>2</sub> thin films prepared by electrodeposition. A well covering, compact and non-porous TiO<sub>2</sub> coating surface was observed at the magnification of 20,000×. At high magnification, elongated grains of 100-200 nm sizes are well seen. However, careful observation of the SEM picture find seach grain made up with an aggregate of amorphous particles. Such morphology remained unchanged even after annealing above723K. In order to demonstrate the potential use of deposited TiO<sub>2</sub> coating in photoelectrochemical devices, I–V characteristic of TiO<sub>2</sub> thin film is studied in1M NaOH electrolyte.

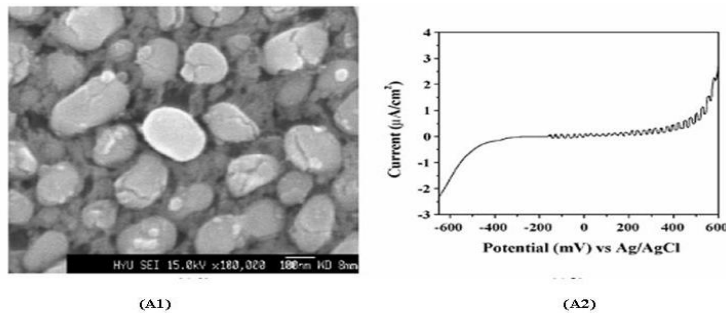


Fig.7. Microstructure and application of TiO<sub>2</sub> thin film by electrodeposition method (A1: SEM image of TiO<sub>2</sub> thin film, A2): application of TiO<sub>2</sub> in photoelectrochemical cell.

#### 4. CONCLUSIONS

In summarizing, nanocrystalline metal oxide thin films with different morphologies have been obtained with chemical methods. Such morphologies with large surface area are useful for applications in energy conversion devices. The deposition method, morphology of film and their applications are strongly related. Therefore, these simple and inexpensive chemical bath deposition, successive ionic layer adsorption and reaction, spray pyrolysis and electrodeposition methods may find huge potential in thin film technology and its applications.

#### REFERENCES

1. R.W.Siegel, E.H.Hu, M.C.Roco, WTEC Panel Report on R and D Status and Trend in Nanoparticles, Nanostructures Materials and Nanodevices, Workshop,(1997).
2. A.Goswami, Thin Film Fundamentals, New Age International Publishers, (1996).
3. K. L.Chopra, I. J. Kaur, Thin Films Device and Applications, Plenum Press, NY, (1983).
4. J.George, Preparation of Thin Films, Marcel Dekker, Inc., NY (1992).
5. I. Kosacki, H.U.Anderson, Ionics 6 (2000) 294.
6. S.C.Tjong, Nanocrystalline Materials Their Synthesis–Structure–property Relationships and Applications, Elsevier Ltd., (2006).
7. F. F. Lamge, Science 273 (1996) 903.
8. C. D. Lokhande, Mater. Chem.Phys.28(1991)1.
9. R. S. Mane, C. D.Lokhande, Mater.Chem.Phys .65(2000)1.
10. R. S.Mane, Y. H. Hwang, C. D. Lokhande, S. D. Sartale, S. H. Han, Appl.Surf.Sci. 246(2005)271.
11. V. R.Shinde, T. P.Gujar, C. D.Lokhande, R. S. Mane, S. H.Han, Mater .Sci., Eng.B 137(2007)119.
12. D. S. Dhawale, A. M. More, S. S. Latthe, K.Y. Rajpure, C. D. Lokhande, Appl. Surf. Sci., 254(2008)3269.
13. C. D. Lokhande, S. S. Kulkarni, Indian Patent No.604/MUM/2005.
14. M. Ristov,G. J. Sinadinovski, I.Grozdanov, Thin Solid Films 123(1985) 63.
15. Y. F. Nicolau, Appl. Surf. Sci. 23(1985)1061.
16. H. M. Pathan, C. D. Lokhande, Bull. Mater. Sci.27 (2004) 85.
17. S. S. Kale, R. S. Mane, H.Chung, M. Y. Yoon, C. D. Lokhande, S. H. Han, Appl. Surf. Sci.253(2006) 421.
18. S. J. Roh, R. S. Mane, S. K.Min,W. J. Lee, C. D. Lokhande, S. H. Han, Appl.Phys.Lett. 9(2006)253512.

19. R. S. Mane, H. M. Pathan, C. D. Lokhande, S. H. Han, *Solar Eng.* 80(2006)185.
20. V. R. Shinde, T. P. Gujar, C. D. Lokhande, R. S. Mane, S. H. Han, *Sens. Actuator B* 123 (2007)882.
21. P. S. Patil, *Mater. Chem. Phys.* 59( 1999) 185.
22. A. M. More, J. L. Gunjekar, C. D. Lokhande, R. S. Mane, S. H. Han, *Micron* 38(2007) 500.
23. V. R. Shinde, T. P. Gujar, C. D. Lokhande, R. S. Mane, S. H. Han, *Sens. Actuator B* 120 (2007) 551.
24. V. R. Shinde, S. B. Mahadik, T. P. Gujar, C. D. Lokhande, *Appl. Surf. Sci.* 252(2006) 7487.
25. T. P. Gujar, V. R. Shinde, C. D. Lokhande, W. Y. Kim, K. D. Jung, O. S. Joo, *Electrochem. Commun.*, 9(2007) 504.
26. R. K. Pandey, S. N. Sahu, S. Chandra, *Handbook of Semiconductor Electrodeposition*, Marcel Dekker, Inc., New York, (1996).
27. C. D. Lokhande, S. H. Pawar, *Phys. Stat. Sol. (a)* 111(1989)17.
28. C. D. Lokhande, S. K. Min, K. D. Jung, O. S. Joo, *J. Mater. Sci* 39(2004) 66.

## **II-VI PHOTOVOLTAIC DEVICES AND APPLICATIONS**

P. WIJEWARNASURIYA

*U.S. Army Research Laboratory, Sensors and Electronic Devices Directorate  
2800 Powder Mill Road, Adelphi MD 20783*

Corresponding Author, e-mail: *priyalal.wijewarnasuriya@us.army.mil*

### **ABSTRACT**

Cadmium telluride has been recognized as a promising photovoltaic material for thin-film solar cells because of its near optimum band gap of  $\sim 1.5$  eV and its high absorption coefficient. The energy gap is near optimum for a single junction solar cell and the high absorption coefficient allows films as thin as  $2 \mu\text{m}$  to absorb more than 98% of the above-band gap radiation, and cells with efficiencies near 17% have been produced. By alloying with HgTe,  $\text{Hg}_{1-x}\text{Cd}_x\text{Te}$  ( $0 \leq x \leq 1$ ) alloy can be obtained and has band gap energy falls between the end points of HgTe ( $E_g = -0.3$  eV) and CdTe ( $E_g = 1.5$  eV). Because of its band gap tunability with the Cd composition,  $\text{Hg}_{1-x}\text{Cd}_x\text{Te}$  alloy has evolved to become the most important/versatile material for detector applications over the entire infrared wavelength range. Hence, this multifunction II-VI materials system is of great importance to the IR community and as well as to the solar cell community. In this presentation, I will present status of HgCdTe II-VI materials system for IR detection and as well as for solar applications.

## **ELECTRODEPOSITED CUPROUS OXIDE FOR LOW COST SOLAR ENERGY APPLICATIONS**

WITHANA SIRIPALA

*Department of Physics, University of Kelaniya, Kelaniya, Sri Lanka.*

Corresponding Author, e-mail: [wps@kln.ac.lk](mailto:wps@kln.ac.lk)

### **ABSTRACT**

Cuprous oxide ( $\text{Cu}_2\text{O}$ ) is a candid semiconductor material for application in environmentally friendly low cost solar energy converting devices. Electrodeposition technique can be used to synthesize this material and has the ability to control both conductivity type (n- or p-type) and morphology of the films very easily. Aqueous acetate and hydrogen peroxide baths can be used for the electrodeposition of good quality n-type  $\text{Cu}_2\text{O}$  films. Control of the morphology of the films to obtain nanocrystalline and flower like structured films is also possible. A donor level is created in  $\text{Cu}_2\text{O}$  by the electrodeposition method and it results in the n-type conductivity. Using the electrodeposition technique homojunction and heterojunction  $\text{Cu}_2\text{O}$  based solar cell devices can be fabricated. Electrodeposited  $\text{Cu}_2\text{O}$  thin films demonstrate the possibility of developing environmentally benign low cost solar cell devices.

### **1. INTRODUCTION**

Development of environmentally friendly low cost solar energy converting devices is extremely important for wider applications of green energy technology. For this, investigation on the possible low cost solar energy converting materials is a vital task and a key issue to be addressed. It is very well known that transition metal oxides are extremely important for solar energy applications. Among various transition metal oxides, cuprous oxide ( $\text{Cu}_2\text{O}$ ) has attracted much attention because it is non toxic, inexpensive and can be prepared in large quantities due to abundance of the base material. This material shows a lot of promise not only for applications in thin film solar cells but also for many other applications [1-6].  $\text{Cu}_2\text{O}$  is a direct band gap (2 eV) semiconductor material and has a high absorption in the visible region of the solar spectrum. Indeed,  $\text{Cu}_2\text{O}$  is one of the earliest semiconductor material studied for possible applications in semiconductor devices including solar cells. However, the interest on  $\text{Cu}_2\text{O}$  was diminished in late fifties due to the advent of silicon. With the present growing demand for low cost solar energy devices, many alternative semiconductor materials are being investigated and  $\text{Cu}_2\text{O}$  is one of them.

$\text{Cu}_2\text{O}$  has been known generally as a p-type material due to the presence of Cu vacancies in the crystal lattice [7]. In early studies, for Schottky type or heterojunction type p-  $\text{Cu}_2\text{O}$  solar cells, many materials have been studied for making junctions with p-  $\text{Cu}_2\text{O}$ . However, it was found that the effective junction was always the Cu/  $\text{Cu}_2\text{O}$ , irrespective of the materials used to make junctions, due to photoreduction of  $\text{Cu}_2\text{O}$  to Cu at the interface [7]. As a result, the maximum reported efficiency of solar cells made with p-  $\text{Cu}_2\text{O}$  was limited to 2% [7]. It was realized that to overcome this problem n-type  $\text{Cu}_2\text{O}$  must be developed [7,8]. Band positioning of  $\text{Cu}_2\text{O}$  further encourages development of n-type  $\text{Cu}_2\text{O}$  because the low electron affinity of  $\text{Cu}_2\text{O}$  promises the possibility of developing efficient heterojunctions with suitable p-type materials. Also, n-type  $\text{Cu}_2\text{O}$  films has the added advantage in photocatalytic water splitting reaction over the p-type counterpart when considering the positioning of the respective redox potentials relative to the band edges. For the water splitting with solar energy using p-type  $\text{Cu}_2\text{O}$ , additional bias voltage is required because photogenerated holes lose energy when transferred to the back contact of the substrate. However, in n- $\text{Cu}_2\text{O}$ , light generated holes are transferred to the electrolyte without losing energy and hence without external bias water splitting is possible. As most of the earlier

research efforts were concentrated on thermally grown Cu<sub>2</sub>O, n-type doping of Cu<sub>2</sub>O was not realized. However, it has been reported recently that n-type Cu<sub>2</sub>O is possible to synthesize using the electrodeposition technique [9] or by dipping copper electrodes in Cu ions containing aqueous baths [10, 11] . Of course, electrodeposition of Cu<sub>2</sub>O has been known for a long time [12]. But parameters previously used for the electrodeposition hindered the growth of n-type films and resulted only the well established p-type conductivity.

## **2. ELECTRODEPOSITION OF CUPROUS OXIDE**

Cuprous oxide can be synthesized using various techniques such as thermal oxidation [13], chemical deposition [14], reactive magnetron sputtering [15], pulsed laser deposition [16], and electrodeposition [9,17,18]. Among these techniques, electrodeposition is attractive because not only it can produce n-type films compared with other techniques, but also it is simple, low cost and involves a low temperature process. Further, the technique of electrodeposition of Cu<sub>2</sub>O is important because it can deposit films on any conducting substrate and thereby device fabrication becomes simple, low cost and efficient.

Cu<sub>2</sub>O films can be electrodeposited on conducting substrates by reduction of aqueous solutions of Cu (II) in lactate [17, 18], acetate [19] or nitrate [20] baths under various bath conditions. Electrochemical process involved in the electrodeposition of cuprous oxide contains many steps. First will be the reduction of Cu (II) to Cu (I) via the reaction,



The next step will be the reaction with hydroxide ion,



and subsequently depositing Cu<sub>2</sub>O on the conducting substrates,



Another possible cathodic reaction is the following reaction which produces Cu.



It is important to note that reaction (2) is a crucial step which results in Cu<sub>2</sub>O. For instance, if the bath does not contain OH<sup>-</sup> ions then reaction (2) will not proceed. This may be the reason why in early studies only baths having high pH values (in the range of 9 to 12) were used for the electrodeposition of Cu<sub>2</sub>O and to overcome the problem of precipitation in baths at high pH values, complexing agents such as lactate, citrates were introduced. These baths produced good Cu<sub>2</sub>O films and the conductivity type was p-type. For baths of low pH values (acidic baths), reaction (4) will dominate and, in general, Cu deposition along with Cu<sub>2</sub>O was evident. However, in recent studies it was revealed that it is possible to electrodeposit Cu<sub>2</sub>O films without Cu deposition at low pH values [9, 19, 21]. For example, figure 1 shows the current voltage characteristics of a deposition bath containing 0.1 M sodium acetate and various Cu<sup>++</sup> ion concentrations in the bath at pH 6. In this bath complexing agents were not required and the pH values could be adjusted in the range of 5.5 to 7.5. The first cathodic peak corresponds to the formation of Cu<sub>2</sub>O following the reactions 1 to 3. The second cathodic peak corresponds to deposition of Cu. Therefore in a narrow potential domain of about 400 mV, Cu<sub>2</sub>O can be

electrodeposited. The most important result in this acetate bath is that good quality n-type Cu<sub>2</sub>O films can be electrodeposited.

The advantage of the of depositing Cu<sub>2</sub>O films using the electrodeposition technique is that, as the deposition follows many steps, it gives the opportunity to control the film quality by adjusting the parameters. Particularly the intermediate step of reaction ( 2) could control the stoichiometry of the film and thereby the conductivity of the films. Also, the selection of the proper deposition potential would eliminate unwanted impurities and at the same time elements useful for doping could be incorporated.

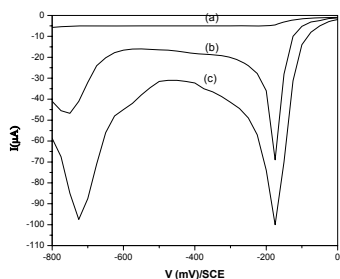


Figure 1. Current –voltage characteristics of a Ti electrode in a PEC containing 0.1 M sodium acetate and (a) 1mM, (b) 5 mM and (c) 16 mM cupric acetate.

The sensitivity of the pH of the deposition bath to the conductivity type of the film is demonstrated in figure 2, where current potential curves under chopped light illumination in a PEC containing 0.1 M sodium acetate were obtained for films prepared in baths of (a) pH 7.5 and (b) 6.0.

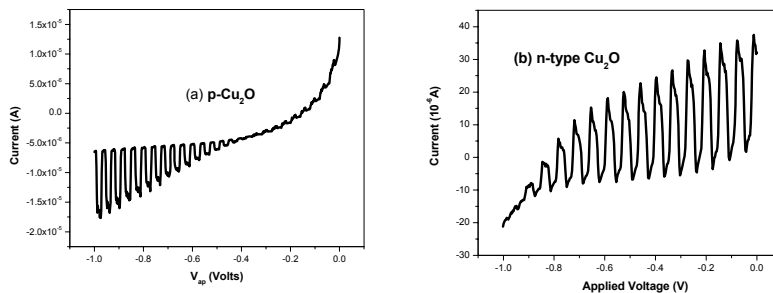


Figure 2. Chopped light current –voltage of Cu<sub>2</sub>O films, prepared in baths of (a) pH 7.5 (b) pH 6.0, in a PEC containing 0.1 M sodium acetate.

An alternative route to produce hydroxide ions for reaction (2) in a depositing bath of Cu<sub>2</sub>O will be the reduction of hydrogen peroxide according to the following reaction.



Indeed, it is known that hydrogen peroxide can be successfully used as an oxygen precursor, as given in reaction (5) , for electrodepositing zinc oxide thin films using a bath containing Zn(II) [22 ]. The important fact in this technique is that acidic baths can be used to produce Cu<sub>2</sub>O films because OH<sup>-</sup> ions can be produced on the substrate. In an aqueous bath containing Cu(II) and hydrogen peroxide, reaction of Cu(II) with H<sub>2</sub>O<sub>2</sub> is very complex . However, recently it was demonstrated that Cu<sub>2</sub>O films can be electrodeposited using a peroxide bath at pH 4 [20 ].

### **3. ELECTRICAL AND STRUCTURAL PROPERTIES AND MORPHOLOGY OF ELECTRODEPOSITED Cu<sub>2</sub>O FILMS.**

It is already discussed that conductivity type ( n-type or p-type) of electrodeposited films can be changed by adjusting the pH of the depositing bath. At high pH values Cu vacancies in the films are dominated and as a result, as thermally grown films, p-type films are produced due to the creation of an acceptor state in the band gap. However, the origin of the n-type conductivity of the Cu<sub>2</sub>O films is still not very well understood. There are many possibilities. Existence of oxygen vacancies and thereby creation of a donor level is a possibility. On the other hand, existence of Cu interstitials in the Cu<sub>2</sub>O lattice may also be another possibility. It has already been reported the existence of a donor level in electrodeposited n-type films, using photoluminescence studies. As shown in figure 3, an additional photoluminescence peak at 1.45 eV can be observed in n-type films at low temperatures [23]. This peak is assigned to a donor level located at 0. 38 eV below the conduction band of Cu<sub>2</sub>O and considered as responsible for the observed n-type conductivity. However, recent theoretical work of Scanion and Watson shows that neither copper vacancies nor oxygen vacancies could create a donor level within the band gap of Cu<sub>2</sub>O [24 ]. Nevertheless, existence of a donor level and n-type conductivity of native Cu<sub>2</sub>O films have already been established . Therefore further investigation using theoretical and experimental studies are needed to confirm the origin of the n-type conductivity in native Cu<sub>2</sub>O films.

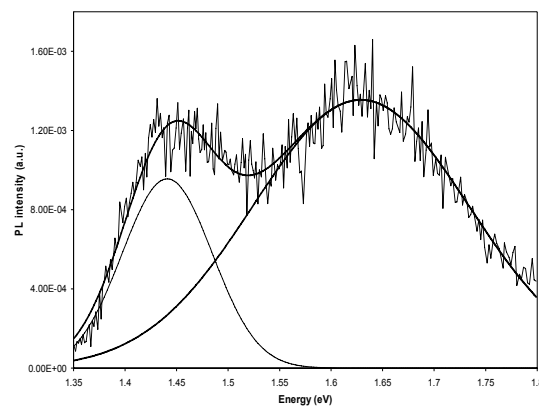


Figure 3. Photoluminescence spectrum of n-type Cu<sub>2</sub>O film at 140K [ Ref. 23 ]



It is well documented that deposition parameters, such as, pH, bath temperature, electrode potential, deposition current density and concentration of the constituent ions are very sensitive to the morphology, structure, optical and electrical properties of the resulting  $\text{Cu}_2\text{O}$  films. Particularly, deposition bath conditions can be controlled to obtain nano films and different polycrystalline films for applications in solar cell devices. Figure 4 shows different morphology of  $\text{Cu}_2\text{O}$  films which were obtained using various deposition baths. Figures 4 (a) and (b) confirm the control of the morphology of films by the bath temperature. Figures (c) and (d) demonstrate the possibility of controlling the growth habits of the films by adding anions to the solution. Adsorption of Ag ions on some crystal faces result in the change of the growth habits of the film yielding different film morphology. Figures (e) and (f) demonstrate when the growth of the  $\text{Cu}_2\text{O}$  film on the substrate is controlled by the reaction (5), only nano films are grown. This flower like morphology of the films may be very useful in photoelectrochemical cells, specifically, in water splitting reactions.

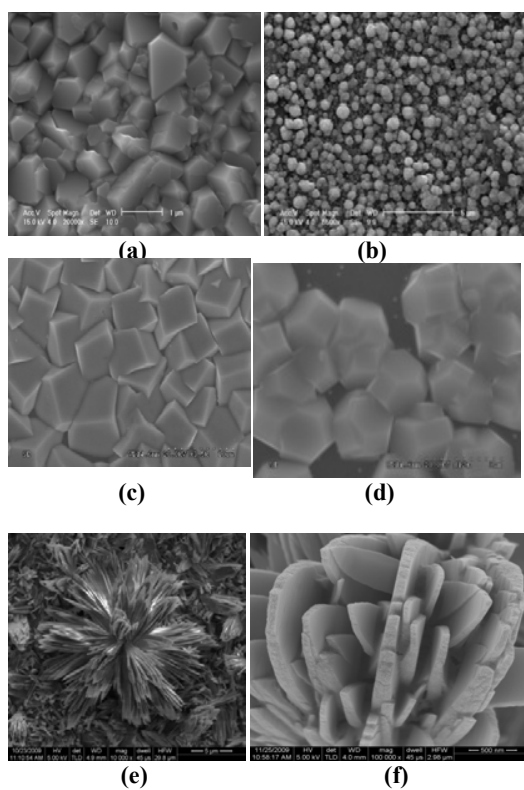


Figure 4. SEM pictures of  $\text{Cu}_2\text{O}$  films electrodeposited using various baths,  
 (a) 0.1 M sodium acetate + 0.02 M cupric acetate, deposited at 55 °C, - 300 mV vs SCE  
 (b) 0.1 M sodium acetate + 0.02 M cupric acetate, deposited at 20 °C, -200 mV vs SCE  
 (c) 0.1 M sodium acetate+ 0.01M cupric acetate, deposited at 60 °C, -50 mV vs SCE  
 (d) 0.1 M sodium acetate+ 0.01M cupric acetate + 0.4 mM  $\text{AgNO}_3$ , deposited at 60 °C, -50 mV vs SCE  
 (e) & (f) 0.1M  $\text{CuSO}_4$  + 40 mM  $\text{H}_2\text{O}_2$  at 70 °C, -100mV vs SCE

In the technique of electrodeposition, one of the important advantages is that deposition of unwanted elements, such as Cu and CuO, can be eliminated by proper control of the applied potential on the substrate. The first cathodic peak at -250 mV vs SCE in figure 1 corresponds to the deposition of

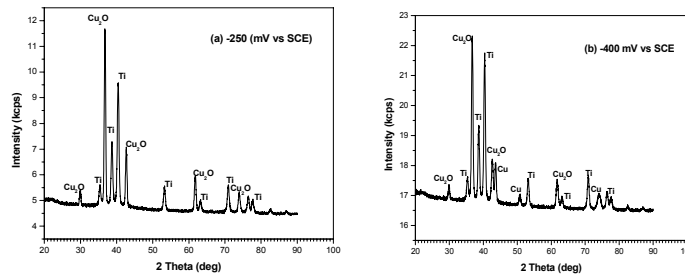


Figure 5. XRD spectra of electrodeposited Cu<sub>2</sub>O films obtained using a bath containing 0.1M sodium acetate and 0.02M cupric acetate at a deposition potential of (a) -250mV vs SCE and (b) -400 mV vs SCE .

the deposition of Cu<sub>2</sub>O on the substrate. If this potential domain is exceeded, the deposition will be Cu according to reaction (4). Figure 5 confirms this with the XRD spectra obtained for films deposited potentiostatically at (a) – 250 mV vs SCE and (b) -400 mV vs SCE. It is clearly shown in XRD spectra in figure 5 (b) that more cathodic potential, -400 mV vs SCE, produces Cu in addition to Cu<sub>2</sub>O. Thus, single phase Cu<sub>2</sub>O films can be electrodeposited onto conducting substrates by applying the correct potential on the substrate.

#### 4. LOW COST SOLAR CELL WITH ELECTRODEPOSITED CU<sub>2</sub>O FILMS

The homo junction of Cu<sub>2</sub>O will be an ideal structure to develop a thin film photovoltaic device. It has already been reported that homojunction of Cu<sub>2</sub>O can be fabricated by the electrodeposition technique [25,26,27]. As an example, figure 6 shows a p-n junction Cu<sub>2</sub>O solar cell fabricated on an ITO substrate.

However, the reported efficiency of homojunction Cu<sub>2</sub>O solar cells is still very low and further investigations are required [ 25,26]. Other possibility is the heterojunction solar cells with suitable low cost p-type semiconductors. For this, n- Cu<sub>2</sub>O /p-Cu<sub>x</sub>S and n-Cu<sub>2</sub>O/ p-CuO have already been tested. It is a common problem that was found in all the reported devices that the electrodeposited Cu<sub>2</sub>O films were having high resistivity. This seriously limits the short circuit current and the open circuit voltage of the devices. The resistivity of the films were of the order of 10<sup>5</sup> Ωcm and this value has to bring down by order of magnitudes to obtain efficient devices. This could be achieved by increasing the density of native point defects or by adding foreign impurities to Cu<sub>2</sub>O films. The technique of electrodeposition has the advantage that it could be used to electrodeposit Cu<sub>2</sub>O films in various baths and therefore addition of suitable impurities to the bath is possible. On the other hand, deposition parameters may be able to optimize to obtain high density of native point defects. Thus, the possibility of developing a low cost thin film solar cell devices using electrodeposition technique is promising.

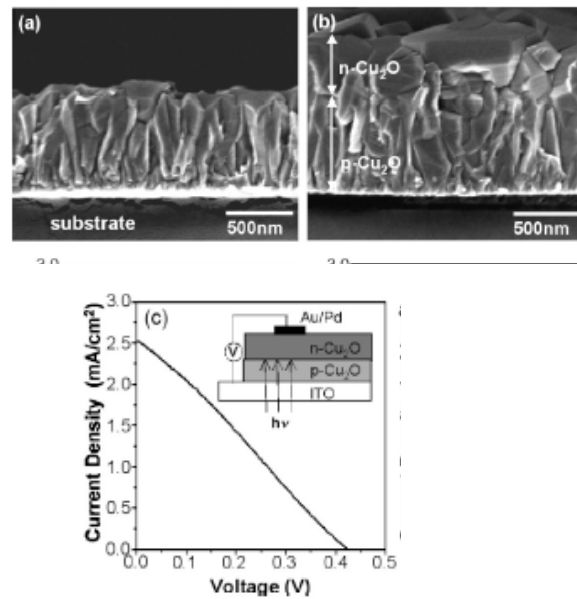


Figure 6. (a) p- Cu<sub>2</sub>O film grown on ITO substrate (b) n- Cu<sub>2</sub>O layer on p-Cu<sub>2</sub>O (c) IV characteristics of homojunction thin film solar cell [Ref. 25].

## 5. CONCLUSION

In conclusion, polycrystalline cuprous oxide thin films can be electrodeposited using aqueous baths to obtain good quality films with different morphology and conductivity types. Particularly, n-type films can be obtained for applications in low cost solar cell devices. Experimental observations lead to the conclusion that the n- type conductivity of the films is originated due to a donor level created by a native point defect. This point defect is yet to be identified. Preliminary investigations have revealed the possibility of developing Cu<sub>2</sub>O based homojunction and heterojunction thin film solar cell devices. These devices may be further improved by increasing the conductivity of electrodeposited Cu<sub>2</sub>O films and for this further study is required. With n- Cu<sub>2</sub>O films, photo splitting of water is possible without applying an external bias voltage. Low cost and non toxic semiconductor material Cu<sub>2</sub>O demonstrates the possibility for use in environmentally benign low cost energy applications.

## 6. ACKNOWLEDGMENT

Author gratefully acknowledges all research assistances and collaborators for their valuable contributions made to the work summarized here.

## REFERENCES

1. L.C.Olsen, F.W. Addis. W.Miller, Solar cells 7 (1982) 247.
2. J.H.Lee, B.X.Tang, L.M.Tao,Y.X.Xie, M.B.Zang,J.Org Chem. 71 (2006) 7488.
3. M.Hara, T.Konda, M.Komoda, S.Ikeda, K.Shinohara, A.Tanaka, J.N.Kondo, K.Domen, Chem. Communication (1998) 357.
4. X.Le,H.Gao,C.J.Murphy,L.Gou,Nanno Lett.4 (2004)1903.
5. Y Chang, J.J. Teo, H.C.Zeng,Langmuir 21 (2005) 1074.
6. J.T.Zang,J.F.Liu,Y.D.Li,Chemi. Mat. 18 (2006) 867.
7. L.C.Olsen, R.C. Bohara, M.W. Urie, Appl. Phys. Lett 34 (1979) 47.
8. R.P. Rai Solar cells 25 (1988) 265.
9. W.Siripala, J.R.P.Jayakody, Solar Energy Materials 14 (1986) 23.
10. U. Bertocci, J. Electrochem. Soc. 125 (1978) 1598
11. S.M.Wilhelm S.M. Y. Tanizawa, N. Hackerman, Corrosion Science 22 (1982) 791.
12. N.A. Economou, R.S. Toth, R.J. Komp, D.Trivich , Proc. EC Photovoltaic Solar Enrgy Conference (1977) 1180.
13. A.O.Musa, T. Akomolafe , M.J. Carter, Sol. Energy Materials and Solar cells 51 (1998) 305.
14. Yakup Hames , S. Eren San, Sol. Energy 77 (2004) 291.
15. A.A. Ogwu E. Bouquerel, O. Ademousu, S.Moh, E. Crossan, F. Placido, Acta Mater. 53 (2005) 5151.
16. M.I Vill, M.E. Overberg, C.R.Abernathy, D.P.Norton, A.F.Herbad,N. Theodoropoulou, J.D. Budai, Solid Sate Eelectron. 47 (2003) 2215.
17. A.E.Rakshani, Solid Stat. Electron. 29 (1987) 7.
18. J.A.Switzer, C.J. Hung, L.Y. Huang, E.R. Switzer,D.R. Kammler, T.D. Golden, E.W. Bohanan, J. Am. Chem. Soc. 120 (1998) 3530.
19. W.Siripala, J. Natn. Sci, Coun. Sri Lanka 23 (1) (1995) 49.
20. W.Siripala, .M.D.C. Jaythilleke, J.K.D.S. Jayanetti, J. Bionanoscience , 3(2009) 1.
21. W.Siripala, LDRD Perera,KTL de Silva, JKDS Jayanetti, IM Dharmadasa, Solar Energy Materials & Solar Cells 44 (1996) 251.
22. Th. Pauporte, D. Lincot, J. Eelectrochem. Soc. 148 (4) (2001)C310.
23. R. Garuthara, W.Siripala, J. Luminescence 121 (2006) 173.
24. D.O. Scanion, G.W. Watson , J. Phys. Chem. Lett. 1 (2010) 2582.
25. C. M. McShane, W.Siripala, Kyoung-Shin Choi, J.Phys. Chem. Lett. 1 (2010)2666.
26. K. Han and M. Tao, Solar Energy Materials and Solar cells 93 (2009) 153.
27. KMDC Jayathilleke,W.Siripala, JKDS Jayanetti, Sri Lanka J. Phys. 9 (2009)35.

## KEY FACTORS FOR IMPROVING THE EFFICIENCY OF DYE-SENSITIZED SOLID-STATE SOLAR CELLS

AKINORI KONNO\* AND E. V. A. PREMALAL

Department of Nano Materials, Graduate School of Science and Technology,  
Shizuoka University, 3-5-1 Johoku, Naka-ku, Hamamatsu 432-8011, Japan

\*Corresponding Author, e-mail: tsakonn@ipc.shizuoka.ac.jp

### 1. INTRODUCTION

Dye-sensitized photoelectrochemical cells (DS PECs) continue to receive much attention. The liquid electrolyte in the dye-sensitized solar cell (DSSC), leads to several technological problems such as: dye desorption, solvent evaporation and degradation, and seal imperfection, *etc.* Tennakone et al have developed a dye-sensitized solid-state cells (DSSSCs) using p-CuI as the hole-conductor (Figure. 1) [1]. Recently, it is found that incorporation of a small quantity of the molten salt 1-ethyl-3-methylimidazolium thiocyanate (EMISCN) to the CuI solution helps filling of the pores greatly improving the performance of the cell. This imidazolium salt acts as a CuI crystal growth inhibitor and being a molten salt the residue formed during evaporation of the solvent spreads over the crystallite grain boundaries [2]. We have also found that some other ammonium thiocyanates e.g. triethylammonium thiocyanate ( $\text{Et}_3\text{NHSCN}$ ) which are room temperature molten salts, are successfully applied to the formation of CuI film with fine particle for the development of efficient and stable DSSSC.

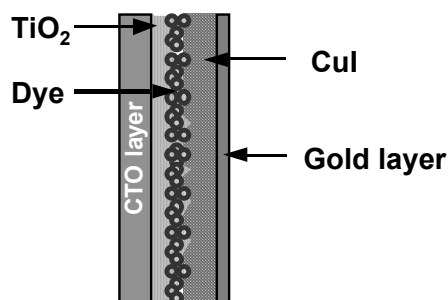


Figure 1. Schematic structure of  $\text{TiO}_2/\text{Dye}/\text{CuI}$  cell

Much effort has also been diverted towards development of alternative sensitizers, especially organic dyes. In general organic dyes possess higher molecular extinction coefficients compared to metal-complex sensitizers [3, 4]. An advantage of high molecular extinction coefficient happens to be the possibility of achieving a sufficient light absorption cross-section at a reduced film roughness factors. As devices free of encapsulated liquids, dye-sensitized solid-state solar cells (DSSSCs) where the electrolyte is replaced by a solid hole collector are extensively studied. Relatively high efficiency has been obtained using the N3 dye with CuI as a hole collector. It is important to examine how these new organic dyes (D) behave when adopted as sensitizers for the DSSSCs of the configuration  $\text{TiO}_2/\text{D}/\text{CuI}$ . Recently, 4.1 % of efficiency was reported for DSSSC using the indoline dye (D102) with organic hole conductor [5]. In this paper we present our observation on DSSSCs sensitized with metal-free organic dyes.

Another issue in order to improve the efficiency of DSSSCs, is filling the nano-sized pores in TiO<sub>2</sub> thin film electrode by hole collecting p-type semiconductor materials such as CuI. Nanocrystalline films required for DSSSCs, where the electrolyte is replaced by a solid hole-collector, have roughness factors smaller than that for conventional DSSC films and dyes with higher extinction coefficients are more useful. In this paper we present the improvement on DSSSC using screen-printed nanoporous titanium oxide thin film electrode.

## 2. EXPERIMENTAL

### 2.1. Fabrication of DSSSC sensitized by metal free organic dyes

The precursor for deposition of TiO<sub>2</sub> films was prepared by the procedure described below. Titanium isopropoxide (5 ml) mixed with few drops of glacial acetic acid is homogenized after addition of 20 ml of propan-2-ol. Water (5 ml) is quickly transferred and the mixture is ground to form a milky paste. Paste is mixed with 0.65g of TiO<sub>2</sub> (Nihon Aerosol, median particle size 30 nm), grounded again and spread on fluorine doped conducting tin oxide (FTO) glass plates (Nihon Sheet Glass) and heated to 150°C. Once the liquid component of paste evaporated, the powder not adhered to the surface was blown off, the process repeated several times and the film is sintered in air for 4 min at 500 °C. Above steps are repeated until the film grows to a thickness of ~ 6 μm. TiO<sub>2</sub> films were coated with a dye (indoline dyes or coumarine dyes: the structures are shown in Fig. 2) by soaking plates in a solution of the dye in tert-butanol / acetonitrile (1 / 1, 4 x 10<sup>-4</sup> M) for 3 h. The amount of the dye adsorbed was determined by extracting the dye into warm acetic anhydride. The heterojunction TiO<sub>2</sub>/Dye/CuI was formed by deposition of CuI from a solution of acetonitrile containing a trace amount triethylamine hydrothiocyanate (THT) which acts CuI crystal growth inhibitor. A gold or platinum plated conducting glass plate firmly clamped to CuI surface served as the back contact to the cell. I-V characteristics and photocurrent action spectra were recorded using a calibrated solar cell evaluation system.

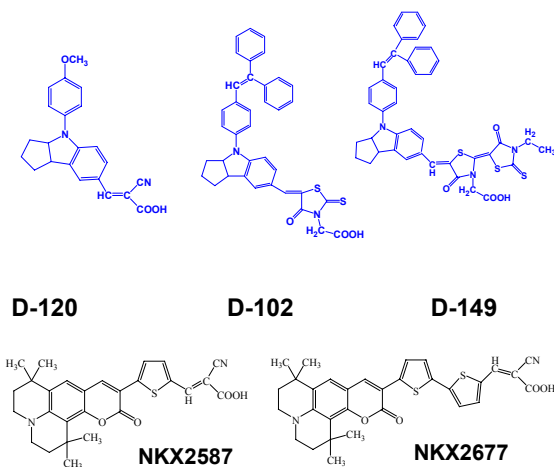


Figure 2. The Structure of the metal-free organic dyes.

### 2.2. Preparation of screen-printed TiO<sub>2</sub> films

TiO<sub>2</sub> films were prepared by screen-printing method using commercially available paste (18NR, Shokubai Kasei Co.) or P25 based paste followed by reported procedure [6] with the addition of various amount of polyethylene glycol (PEG: 0-5 wt% solution). Screen-printed TiO<sub>2</sub> films were coated with a dye by soaking plates in a solution of indoline dye (D-149) in tert-butanol / acetonitrile (1/1, 4 x 10<sup>-4</sup> M) for 3 h. The heterojunction TiO<sub>2</sub>/Dye/CuI was formed by deposition of CuI from a saturated solution of acetonitrile containing a trace amount triethylamine hydrothiocyanate (THT) which acts as CuI crystal growth inhibitor [7].

## 3. RESULTS AND DISCUSSION

### 3.1. DSSSCs sensitized by metal free organic dyes

The DSSSCs sensitized with indoline dyes afforded fairly good performances as shown in Fig. 3 and Table 1. The organic dyes having indoline or coumarine moiety sensitized DSSSC produce overall energy conversion efficiency of 3.6% or 2.0% respectively under standard AM 1.5 irradiation (100 mW cm<sup>-2</sup>). The indoline dye (D-149) sensitized DSSSC efficiency is higher than that of the cells of similar configuration sensitized with N3 dye (Table 1). It has been reported that

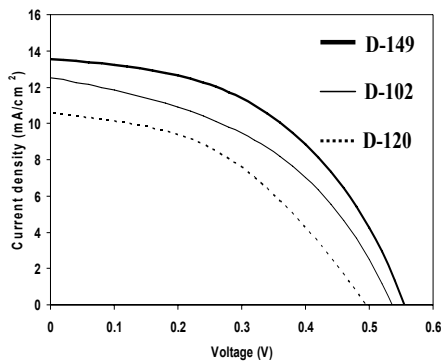


Figure 3. The I-V characteristics of TiO<sub>2</sub>/Indoline Dye/CuI cell.

Table 1. Solar cell performances of TiO<sub>2</sub>/Indoline Dye/CuI cell

Indoline dyes	Isc (mA/cm <sup>2</sup> )	Voc (mV)	FF	η (%)
D-149	13.6	556	0.48	3.6
D-102	12.5	536	0.44	2.9
D-120	10.6	493	0.44	2.3
NKX2587	8.56	520	0.45	2.0
NKX2677	7.08	510	0.43	1.6
N3	13.1	525	0.49	3.4

indoline dyes forms J aggregates that are not susceptible to concentration quenching. In this aspect indoline dyes have several major advantages in use as sensitizers for DSSSCs.

The second issue of this paper is the effect of surface treatment of nanocrystalline TiO<sub>2</sub> electrode with some metal oxides or acetates on the performance of DSSSCs. When the nanocrystalline TiO<sub>2</sub> electrode was dipped into magnesium acetate solution before or after the dyeing process, the open-circuit voltage (V<sub>oc</sub>) of the TiO<sub>2</sub>/Dye/CuI DSSSC was improved. The suppression of the charge recombination at the surface of nanocrystalline TiO<sub>2</sub> electrode by thin layer coating of magnesium acetate was suggested. The effect was depending on the kind of dyes.

### 3.2. DSSSCs using screen-printed TiO<sub>2</sub> film electrode

TiO<sub>2</sub> film made from 18NR paste has a uniform nanoporous structure and higher transparency than those from P25 based paste as shown in Figure 4 and Table 2. On the other hand, 18NR-TiO<sub>2</sub>/D-149 dye/CuI solar cell efficiency (1.14 %) was appreciably lower than the case of P25 based TiO<sub>2</sub> film (2.95 % for 2 wt% PEG, 3.75 % for 5wt% PEG). These results suggested the porosity of TiO<sub>2</sub> film is crucial factor for fabricating an efficient DSSSC. Filling the TiO<sub>2</sub> pore with CuI could be improved in the case of TiO<sub>2</sub> film with larger pore size which could be controlled by the addition of PEG to TiO<sub>2</sub> paste. The best performance (V<sub>oc</sub> = 0.62 V, J<sub>sc</sub> = 10.7 mAcm<sup>-2</sup>, FF = 0.56, Eff = 3.75 %) was achieved in the case of dual layerd TiO<sub>2</sub> film (2wt% PEG + 5wt% PEG).

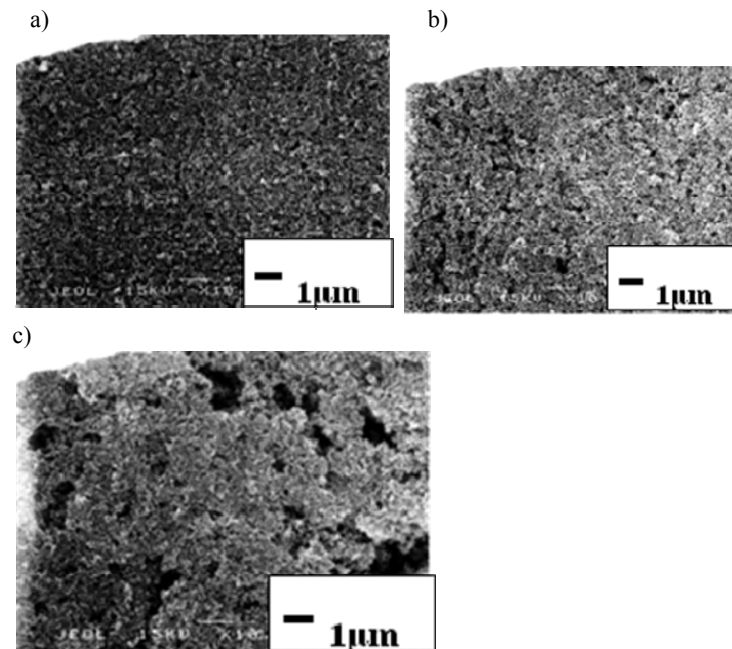
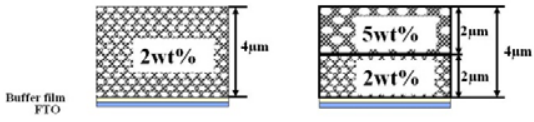


Figure 4. SEM photographs of screen-printed TiO<sub>2</sub> films. (a) 18NR, (b) 2 wt% PEG, (c) 3 wt% PEG.



Table 2. Optical properties of screen-printed TiO<sub>2</sub> films



	Thickness [µm]	Trans[%]	Ref[%]	Abs [%]
18NR	4	46.4	12.5	41.1
2wt%	4	32.1	12.4	55.5
2wt%+5wt%	4	31.5	13.0	55.3

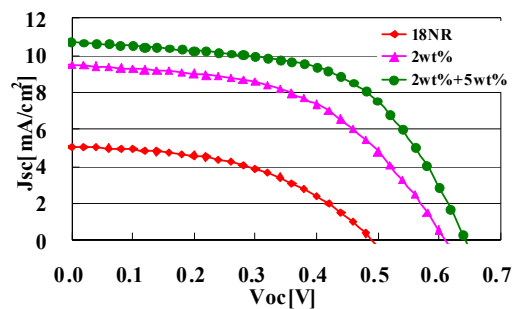


Figure 5. I-V characteristics of screen-printed TiO<sub>2</sub>/D-149 dye/CuI cell.

### 3.3. Improved conductivity of p-type material (CuSCN)

The major drawback of CuSCN as p-type semiconductor in this solar cell is its poor hole conductivity (10-2 S m<sup>-1</sup>) and consequent slower rate of reduction of oxidized dye molecules thus allowing the recombination of electrons injected to CB of TiO<sub>2</sub> with the oxidized dye molecules and/or with holes in CuSCN. In an attempt to increase p-type conductivity of CuSCN, Perera et al [8] have exposed solid CuSCN to halogen gases such as Cl<sub>2</sub> or to a solution of (SCN)<sub>2</sub> in CCl<sub>4</sub> and thereby doped the semiconductor with (SCN)<sub>2</sub> to create acceptor levels 2.6 eV below the band gap (3.6 eV) of CuSCN. This modification has enhanced the performance of the solar cell considerably with a magnitude of 1.64% from 0.75% without SCN doping and 2.39% after SCN doping. This is by far the best recorded efficiency. We reported a versatile procedure adopted for significantly enhancing the p-type conductivity of cuprous thiocyanate to result in significantly improved, controllable and tunable performance of the TiO<sub>2</sub>/N719 Dye/CuSCN all-solid state solar cell. We have made use of the following strategy to increase p-type conductivity of CuSCN by systematically introducing some triethylamine coordinated to copper ion sites into the CuSCN lattice and allowing to expose to thiocyanogen gas, which is being concomitantly generated in the reaction mixture, for doping. This was done by mixing CuSCN with sufficient amount of triethylammonium thiocyanate to have a paste and allowing it to dissolve in propylsulphide [(CH<sub>3</sub>CH<sub>2</sub>CH<sub>2</sub>)<sub>2</sub>S]. Table 3 depicts the conductivity values of the samples as a function of reaction time which clearly indicates significant and controllable enhancement of conductivity of the material providing another yet independent proof to the improvement of conductivity of CuSCN.

The TiO<sub>2</sub>/N719 Dye/CuSCN solar cells were fabricated by applying the CuSCN complex solution (mixture of CuSCN, THT and propylsulphide at different reaction times) on pre heated (~100 °C) dye-coated TiO<sub>2</sub> film using a glass dropper. Then cell parameters were measured by applying a thin layer of graphite film on the CuSCN and having Pt-sputtered FTO glass as a counter electrode. IV characteristics are given in figure 6. As the reaction time is increased, the p-type conductivity of CuSCN enhances and consequently the open

Table 3. Conductivity data for the samples prepared at different reaction times of CuSCN with triethyl ammonium thiocyanate in propyl sulphide.

Reaction time/ Days	Conductivity (S m <sup>-1</sup> )
1	0.064
3	0.103
5	0.399
10	0.509
15	0.716
20	1.009
30	1.101

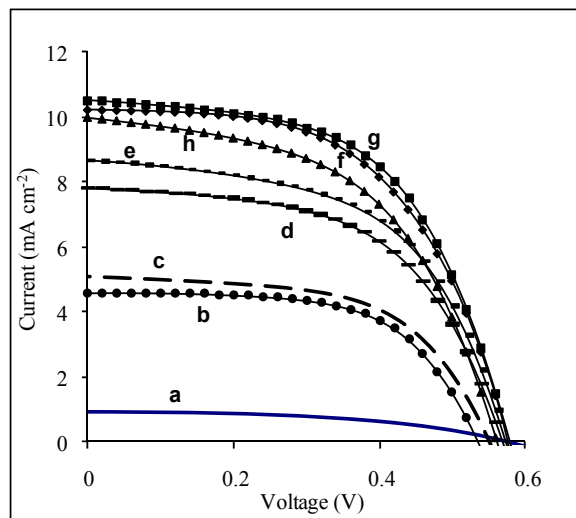


Figure 6. The I-V curves of the TiO<sub>2</sub>/N719/CuSCN cells prepared using (a) pure CuSCN (b) 1 day (c) 3 days (d) 5 days (e) 10 days (f) 15 days (g) 20 days and (h) 30 days of reacting CuSCN with triethylammonium thiocyanate in propyl sulphide. (Under a solar simulator at AM 1.5, 100 mW cm<sup>-2</sup>)

circuit voltage ( $V_{OC}$ ), short-circuit current density ( $J_{SC}$ ) and the overall conversion efficiency ( $\eta$ ) show progressive increase up to 20 days of reaction time. The fill factor (FF) also increases initially and then slightly decreases eventually plateauing at around 0.55 upto 20 days of reaction time. This is also in agreement with the progressive increase of the amount of holes in CuSCN as the reaction proceeds. The enhancement of conductivity causes the increase in FF while the recombination with TiO<sub>2</sub> CB electrons and CuSCN holes decreases the FF. The ways to suppress the latter would lead to further enhancement of efficiency. The way forward for this is to cover

TiO<sub>2</sub> surfaces completely with the dye and we are currently investigating into this aspect. The best result is obtained when CuSCN at the 20 days of reaction period is employed which is 3.39% (AM 1.5, 100 mW cm<sup>-2</sup>) as compared to the best reported 2.39% under the same conditions showing a 41.8% enhancement of the efficiency. According our results, the solar cell fabricated with pure CuSCN gives an efficiency of 0.25% and that with 20 days of reaction time 3.39% thus indicating more than a factor of ten efficiency was achieved [9].

#### 4. CONCLUSION

The DSSSCs sensitized with indoline dyes afforded fairly good performances. The organic dyes having indoline or coumarine moiety sensitized DSSSC produce overall energy conversion efficiency of 3.6% or 2.0% respectively. The indoline dye (D-149) sensitized DSSSC efficiency is higher than that of the cells of similar configuration sensitized with N3 dye. As the second issue, improvement was achieved by using the screen-printed TiO<sub>2</sub> electrode which have larger pore-size than conventional TiO<sub>2</sub> electrode (18NR-TiO<sub>2</sub>). Filling the TiO<sub>2</sub> pore with CuI could be improved in the case of TiO<sub>2</sub> film with larger pore size which could becontrolled by the addition of PEG to TiO<sub>2</sub> paste. 18NR-TiO<sub>2</sub>/D-149 dye/CuI solar cell efficiency (1.14 %) was appreciably lower than the case of P25 based TiO<sub>2</sub> film (2.95 % for 2 wt% PEG, 3.75 % for 5wt% PEG). These results suggested the porosity of TiO<sub>2</sub> film is crucial factor. Another improvement has achieved by using screen-printed TiO<sub>2</sub> electrode which have larger pore-size than conventional TiO<sub>2</sub> electrode. These results suggested that the porosity of TiO<sub>2</sub> film plays crucial role for achieving efficient DSSSCs. The third strategy for improvement of DSSSCs is increasing conductivity of p-type material (CuSCN). This is promising and open up a way to tailor-make CuSCN to possess right conductivity to efficiently compete with the oxidized dye molecules against recombination. Together with extraordinary stability of the polymeric form of CuSCN, fabrication of durable and stable all-solid state solar cell with considerable efficiency could be realized and we are now searching for faster synthetic routes to prepare CuSCN with custom-made p-type conductivity.

#### REFERENCES

1. K.Tennakone, et al, *Semicond. Sci. Technol.* **10** (1995), 1689; *Semicond. Sci. Technol.* **11** (1996), 1737; *J. Phys. D: Appl. Phys.* **31** (1998), 1492.
2. G. R. A. Kumara, A. Konno, K. Shiratsuchi, J. Tsukahara, K. Tennakone, *Chem. Mater.*, **14** (2002), 954.
3. T. Horiuchi, H. Miura, K. Sumioka and S. Uchida, *J. Am. Chem. Soc.* **126** (2004), 12218.
4. K. Hara, M. Kurashige, S. Ito, A. Shinpo, S. Suga, K.Sayama and H. Arakawa, *Chem. Commun.* (2003), 252.
5. L. Schmidt-Mende, U. Bach, R. Humphry-Baker, T. Horiuchi, H. Miura, S. Ito, S. Uchida, and M. Grätzel, *Adv. Mater.*, **17** (2005), 813.
6. S. Ito, M. Grätzel, et al., *Prog. Photovolt: Res. Appl.*, **15** (2007), 603.
7. G. R. A. Kumara, S. Kaneko, M. Okuya and K. Tennakone, *Langmuir* **18** (2002), 10493.
8. V.P.S. Perera, M.K.I. Senevirathna, P.K.D.D.P. Pitigala and K. Tennakone, *Sol. Energy Mater. Sol. Cells*, **86**, 443-450 (2005).
9. E.V.A. Premalal, G.R.R.A. Kumara, R.M.G Rajapakse, M. Shimomura, K. Murakami and A. Konno, *Chem. Commun.*, **46**, 3360 (2010).

**GEL POLYMER ELECTROLYTES FOR DYE-SENSITIZED SOLAR CELLS :  
A REVIEW**

O. A. ILEPERUMA

*Department of Chemistry, University of Peradeniya, Peradeniya, Sri Lanka*

Corresponding Author e-mail: *oliveri@pdn.ac.lk*

**1. INTRODUCTION**

Dye sensitized solar cells (DSCs) based on mesoporous TiO<sub>2</sub> have attracted attention owing to their ease of production from relatively impure materials as low cost alternatives to silicon photovoltaics. The use of a liquid electrolyte causes practical problems of leakages and its volatilization, desorption and photodegradation of the dye, corrosion of the platinum secondary electrode and ineffective sealing of cells for long term applications in solar panels. Some of the attempts to solve this problem include the use of polymer electrolytes [1-3], use of gelling agents [4] and the use of both organic [5] and inorganic [6] hole conductors. A common feature of all such alternatives is the notable reduction in efficiency of the resultant solar cells primarily due to the lower mobility of the iodide species through the solid or quasi-solid medium and imperfect wetting of pores with the electrolyte. The conversion efficiencies with the gel polymer electrolytes typically do not exceed 5%, but even at low efficiencies, these cells may become viable alternatives to the organic liquid containing Gratzel type cells due to improved stability and better sealing ability. The dyes are less liable to undergo photocorrosion and desorption and the corrosion effects on the Pt-electrode are lower. This review will cover only on the application of gel polymer electrolytes for Ru-dye sensitized TiO<sub>2</sub> systems in quasi-solid-state solar cells and will not cover the closely related areas of gelled electrolytes where the standard liquid electrolyte is gelled with gelling agents and conducting polymers used as hole conductors.

*1.1. General aspects of Polymer electrolytes*

A polymer electrolyte may be defined as a membrane that possesses transport properties similar to liquid ionic media. There are obvious advantages with such polymer electrolytes such as absence of internal shorting, leakage of electrolytes and non-combustible reaction products at the electrolyte surface existing in the liquid electrolytes. There are two basic types of polymer electrolytes; the “dry solid” type includes polyethylene oxide based lithium ion conductors which typically show conductivities in the range of 10<sup>-8</sup> S cm<sup>-1</sup> while the second category called the “gel” or “plasticized” polymer electrolytes have semi-solid character with much higher ionic conductivities of the order of 10<sup>-5</sup> – 10<sup>-3</sup> S cm<sup>-1</sup>. Gel polymer electrolytes or plasticized polymer electrolytes offer the advantages of the cohesive properties of a solid along with the diffusive nature of liquids. They offer good contacting properties and pore filling in the porous TiO<sub>2</sub> electrode and also show high conductivity in the film owing to free flow of ions through trapped electrolytes. A gel is formed between the polymer backbone and the plasticizer ensuring the non-volatile nature of the electrolyte. Tables 1 and 2 give the properties of some commonly employed polymer framework materials and plasticizers respectively [10].

Table 1. Some commonly used Polymer framework materials

Polymer framework	Repeat unit	Glass transition temperature/°C	Melting point/°C
Poly(ethylene oxide)	-{CH <sub>2</sub> CH <sub>2</sub> O} <sub>n</sub> -	-64	65
Poly(propylene oxide)	-{CH(-CH <sub>3</sub> )CH <sub>2</sub> O} <sub>n</sub> -	-60	-
Poly(acrylonitrile)	-{CH <sub>2</sub> -CH(-CN)} <sub>n</sub> -	125	317
Polymethylmethacrylate	-{CH <sub>2</sub> C(-CH <sub>3</sub> )(-COOCH <sub>3</sub> )} <sub>n</sub> -	105	-
Poly(vinyl chloride)	-{CH <sub>2</sub> CHCl} <sub>n</sub> -	85	-
Poly(vinylidene fluoride)	-{CH <sub>2</sub> CF <sub>2</sub> } <sub>n</sub> -	-40	171
Poly(vinylidene fluoride-hexafluoropropylene)	-(CH <sub>2</sub> CF <sub>2</sub> ) <sub>x</sub> {CF <sub>2</sub> CF(CF <sub>3</sub> )} <sub>y</sub>	-90	135

Table 2. Physical properties of some organic solvents commonly used as plasticizers

Plasticizer	M.P.(°C)	B.P.(°C)	Density (g cm <sup>-3</sup> )	Dielectric Constant	Mol. Wt.
Dimethyl carbonate	2.4	90	1.06	3.12	90.08
Diethyl carbonate	-43.0	126	0.975	2.82	118.13
γ-Butyllactone	-43.3	204	1.128	39.0	86.09
Propylene carbonate	-48.8	242	1.205	66.14	102.09
Ethylene carbonate	36.4	248	1.321	89.78	88.06

Composite electrolytes refer to polymer electrolytes with inert fillers such as Al<sub>2</sub>O<sub>3</sub>, TiO<sub>2</sub>, ZrO<sub>2</sub>, SiO<sub>2</sub> and Al<sub>2</sub>O<sub>3</sub>. These have the effect of enhancing ionic conductivity and improve the stability at the interface with electrodes. The purpose of this review is to evaluate several polymer hosts used as ion-conducting media in Dye sensitized solar cells (DSCs). For a general account on conducting polymer electrolytes for lithium batteries, an excellent review is available [7].

## 2. SOME COMMONLY USED GEL POLYMER ELECTROLYTES FOR Ru DYE SENSITIZED TiO<sub>2</sub> SOLAR CELLS

### 2.1 Poly(ethylene oxide) (PEO) based polymer electrolytes

Ionic conductivity of alkali metal salts in PEO and its use in lithium batteries prompted research activity in this area. PEO alone is amorphous in character and offers very low ionic conductivity from about 10<sup>-8</sup> – 10<sup>-6</sup> S cm<sup>-1</sup> in the temperature range of 40 -100°C. Batteries which function on lithium ion conductivity generally employ large relatively immobile anions. In the case of DSCs which function on the conductivity of anions (iodide/triiodide) exactly the opposite approach, viz. larger cations are used to enhance anionic conductivity.

Several approaches have been employed to enhance ionic conductivity of PEO based electrolytes as efficient conducting media for DSC applications. While PEO alone gave only a very low efficiency of about 0.6% for a Ru -N3 dye sensitized TiO<sub>2</sub> [8], use of plasticizers ethylene carbonate (EC) and propylene carbonate (PC) give efficiencies of 2.9 % and 3.6 % respectively for the PEO<sub>2000</sub> and PEO<sub>1500</sub> segments [9]. One striking feature here as well as with many other polymer electrolytes is the higher V<sub>OC</sub> values obtained compared to that of the wet cell. The polymer chains can block recombination sites and retard reactions of photogenerated electrons with triiodide ions thereby enhancing V<sub>OC</sub> values. However, their wet cell efficiency was quite low at 4.2% and hence there is scope for further improvement of this system. The ionic conductivity of the PEO with plasticizers depends on the plasticizer content and an abrupt increase

of ionic conductivity by two orders of magnitude was observed when the EC content was increased from 60% to 70% by weight [10].

Another approach to enhance ionic conductivity of PEO systems is by incorporating *co*-monomers or nanoparticle fillers. For example, poly(epichlorohydrin-*co*-ethylene oxide) with 9% NaI and 0.9% I<sub>2</sub> gave an ionic conductivity of  $1.7 \times 10^{-4} \text{ S cm}^{-1}$  and an efficiency of 2.6% at 10 mW cm<sup>-2</sup> [11]. Use of nano-fillers prevents crystal formation and consequently enhances the mobility of redox couples. For example, incorporation of TiO<sub>2</sub> into the PEO/LiI/I<sub>2</sub> system prevents crystal formation and yields an efficiency of 4.2% at 65.6 mW cm<sup>-2</sup> in a DSC. Another aspect of these systems is the interfacial contact between the polymer electrolyte and the photo-electrode surface. In order for the electrolyte to penetrate deeper into the pores of the semiconductor, radius of gyration of polymer chains should be adequately balanced by the pore diameter [12] and this leads to the other approach called the “oligomer approach” to prepare quasi-solid-state DSCs. Oligo-PEG along with KI/I<sub>2</sub> cross-linked with bifunctional glutaraldehyde results in solar cells of efficiency 3.64% at AM 1.5 irradiation and this high efficiency is attributed to enhanced interfacial contact and the deeper penetration of the electrolyte since the smaller coil size of the oligomer matches the average pore sizes in the TiO<sub>2</sub> structure.

Hybrid polymer compositions involving polyacrylic acid (PAA)-polyethylene glycol (PEG) have been fabricated and give solar cell efficiencies of 3.1% under AM1.5 irradiation [13]. While PAA is a superabsorbant of water it does not readily absorb organic liquids and hence it is modified with the amphiphilic PEG. This readily absorbs the liquid electrolyte and gives a highly stable gel polymer electrolyte and a solar cell efficiency of 3.2% at a light intensity of 100 mW cm<sup>-2</sup>. Lowering of efficiency can be attributed to the resistance losses arising from the thicker polymer membrane between the electrodes compared to a liquid film.

Use of PEO and polypropylene oxide (PPO) as framework materials to solidify room temperature ionic liquids in DSCs has been reported to give efficiencies of around 5% compared to a liquid electrolyte cell which gave only 5.3% efficiency. Lower conductivity and high viscosity have been used to explain the trend and the authors claim [14] that ionic conductivity has no relationship to solar cell efficiency with this particular system. This is ascribed to the fact that ionic conductivity arises due to both the cation and the anion and solar cell function depends only on the conductivity of the iodide anion. These results mean that anion diffusion and hence conductivity is governed by solvent diffusion rather than the amount of polyether added.

## 2.2 Polyacrylonitrile (PAN) based polymer electrolytes

Polyacrylonitrile (PAN) offers a homogeneous hybrid electrolyte film where the salts and the plasticizers are molecularly dispersed [10]. PAN host structure is inactive in ionic conduction but provides a matrix for structural stability. A typical polymer electrolyte composition of PAN (12%), ethylene carbonate (EC, 40%), propylene carbonate (PC, 40%) and LiClO<sub>4</sub> has a conductivity as high as  $2 \times 10^{-3} \text{ S cm}^{-1}$  at room temperature and this type of polymer electrolyte has been employed in lithium-manganese batteries [15]. The first report of the use of a solid polymer electrolyte in a DSC can be attributed to Se arson [16] who employed a polyacrylonitrile polymer with ethylene carbonate, propylene carbonate and acetonitrile as plasticizers. With NaI/I<sub>2</sub> redox couple, an ionic conductivity of  $4.5 \times 10^{-3} \text{ S cm}^{-1}$  and an energy efficiency of 4.4% at 30 mW cm<sup>-2</sup> were obtained. Lower efficiency compared to the liquid electrolyte is attributed to low IPCE values brought about by incomplete wetting of the TiO<sub>2</sub> film by the polymer electrolyte. It is also not clear whether this procedure gives a free standing film since gelation reportedly required 3 days for completing the setting process and the cell had to be sealed with epoxy.

Ileperuma and Dissanayake first reported the use of an acetonitrile free gel polymer electrolyte of PAN, along with EC and PC as plasticizers for the N3-dye sensitized TiO<sub>2</sub> solar cells with 2.99 % efficiency [2,3,17]. Here, these low molecular weight organic solvents decrease chain interactions in the polymer network and hence impart increased amorphous character to the resulting electrolyte. The ionic conductivities of such polymer electrolytes reach values in excess of 10<sup>-3</sup> S cm<sup>-1</sup> and approaching the conductivities in the liquid state. These quasi-solids keep a large percentage by mass of liquid electrolyte. The electrolyte compositions were selected based on the results developed for lithium batteries where the proportions of the plasticizers and the polymer have been optimized.

In the above report, an efficiency of 2.99% was obtained for a PAN based electrolyte where the PAN:PC:EC ratio was optimized for ionic conductivity, while the I<sup>-</sup>: I<sub>2</sub> molar ratio was maintained at a fixed value of 0.70 M: 0.05 M. The iodide salt used here was tetra-*n*-propyl ammonium iodide and this ratio was selected on the basis of the ratio of I<sup>-</sup>: I<sub>2</sub> generally employed in the organic liquid electrolytes used for wet DSCs. In polymer electrolytes, larger cations of a homologous series tend to interact stronger with the polymer matrix due to viscous forces thereby enhancing anionic conductivity [18]. Adsorbed cations have been shown to have an effect on the kinetics of the reduction of the oxidized dye by I<sup>-</sup> back electron transfer in DSCs [19]. Adsorption of cations on the TiO<sub>2</sub> particles controls the energy of the conduction band and affects the injection of electrons from photoexcited dye molecules. This is due to the screening effects of the different cations on the movement of the electron through the nanoparticle network. When a bulkier cation, viz. tetra-*n*-butylammonium is employed and the I<sup>-</sup>: I<sub>2</sub> is optimized, at a redox couple molar ratio of 1.5:0.05 M, a record high efficiency of 7.23% (J<sub>SC</sub> = 15.96 mA cm<sup>-2</sup>, V<sub>OC</sub> = 0.751 V, FF = 0.62) was achieved [20]. When the ionic liquid 1,2-dimethyl-3-propyl imidazolium iodide was used as the iodide source, a slightly higher efficiency of 7.49% was obtained. These high values were realized on high efficiency TiO<sub>2</sub> film electrodes fabricated by a unique spray technique employing two different kinds of nanoparticles of TiO<sub>2</sub> of sizes 6 and 25 nm and typically having solar cell efficiencies exceeding 10%. The solar cell characteristics obtained for these DSCs with the acetonitrile based liquid electrolyte were: J<sub>SC</sub> = 20.56 mA cm<sup>-2</sup>, V<sub>OC</sub> = 0.739 V, FF = 0.66 and η = 10.06 (%) [20]. From the above data, it is evident that the observed difference in solar cell performance is mainly due to a lowering of the short-circuit current density and the fill factor. This is the highest efficiency obtained for a quasi-solid electrolyte employing a gel polymer electrolyte. The high efficiency can be attributed to the high ionic conductivity of 4.4 × 10<sup>-3</sup> S cm<sup>-1</sup> of the polymer electrolyte.

Polyblend electrolytes containing alkali metal iodides show Arrhenius type conductivity-temperature behavior which can be attributed mechanistically to ionic transport involving intermolecular ion hopping. For ionic species such as tetra-*n*-butyl ammonium iodide where the cation is very large, such hopping is unlikely and the conductivity-temperature variation in general shows curvature. The temperature dependence of the conductivity of polymer electrolytes involving large cations and where the ion-transport is dominated by the mobility of solvent molecules, is best described by the Vogel-Tamman-Fulcher (VTF) equation [21],

$$\sigma = AT^{-1/2} \exp(-B/T-T_0)$$

Here, σ is the conductivity, A is a constant which is proportional to the number of carrier ions, B is a constant and T<sub>0</sub> is the temperature at which configurational entropy of the polymer becomes zero and is practically taken as the glass transition temperature (T<sub>g</sub>). The general applicability of this equation implies that ionic conductivity in the polymer is coupled to the flow behavior of the plasticizers in the polymer matrix. In the case of lithium ion batteries which work on Li ion conductivity, this is achieved by having large anions. Similarly where a high iodide ion

conductivity is desired, larger cations are preferable in order to obtain higher efficiencies in solar cells.

In general, high permittivity solvents such as PC and EC or their mixtures bring about high conductivities of the order of  $10^{-3}$  S  $\text{cm}^{-1}$  even at temperatures as low as  $-10^{\circ}\text{C}$ . The maximum ionic conductivity is observed for an electrolyte where the molar ratio of  $\Gamma^{-}/\text{I}_2 = 1.50:0.05$ . Lowering of ionic conductivity at higher concentrations of iodide may be due to increased viscosity of the resultant electrolytes and also due to a reduction of the segmental motion of the polymer chains. There is no evidence of any separation of salts at concentrations as high as 1.5 M. There were no liquids exuded from fabricated electrolytes after the photocurrent measurements were done indicating that the electrolyte is well encapsulated in the polymer matrix. As such, these polymer membranes will act as self sealants and will not have leakage problems normally encountered with organic liquid electrolytes.

The  $V_{\text{OC}}$  value, which is the difference between the Fermi level of  $\text{TiO}_2$  and the potential of the redox couple depends mainly on the molar ratio of the  $\Gamma^{-}/\text{I}_2$  couple. There are many reports [22] that the  $V_{\text{OC}}$  values increase when the liquid electrolyte is replaced by a quasi-solid electrolyte. A likely explanation is the reduction of the back electron transfer from the  $\text{TiO}_2$  film to the triiodide ion owing to the presence of a polymer film firmly attached to its surface and the slower diffusion of triiodide ions through the gel electrolyte. However, we observe only a marginal increase in the  $V_{\text{OC}}$  values with the PAN system, since at the higher iodide concentrations used by us, the dark reaction due to reduction of triiodide ion by conduction band electrons accumulated on  $\text{TiO}_2$  increases which results in a lowering of the  $V_{\text{OC}}$  values. These effects combined yield  $V_{\text{OC}}$  values comparable to those obtained for the liquid electrolyte cell.

It was found that optimal solar cell performance is obtained when the  $\Gamma^{-}/\text{I}_2$  ratio was 30:1 at concentrations of 1.50 M and 0.05 M respectively. This is quite surprising since the ratio of these two components generally used by other workers in this area of gel polymer electrolytes are 0.50 M and 0.05 M. However, in at least one related study of a wet cell, the highest efficiencies were observed at a fairly high iodide ion concentration of 1.5 M when 1,2-dimethyl-3-*n*-propylimidazolium iodide (DMHImI) was used which is attributed to the strong adsorption of the DMHIm cation on the  $\text{TiO}_2$  surface [23]. The quasi-solid electrolytes appear to require a higher concentration of the redox species in the electrolyte composition compared to the liquid electrolytes. Yanagida et al. found [26] relatively higher efficiencies for organic liquid free solidified pure ionic liquids using organic gelators where the high efficiencies are attributed to a Grotthus type of mechanism taking place through the polyiodide ions. Packing of polyiodide ions and the exchange of iodide through polyiodide chains is an attractive explanation to interpret these results where optimum efficiency is obtained at higher iodide concentrations.

The decrease of  $V_{\text{OC}}$  and the increase of  $J_{\text{SC}}$  with temperature for DSCs are now well established with optimum cell performances observed at ca.  $60^{\circ}\text{C}$  [24, 25]. Increase in the cell performance after a few minutes of illumination where  $J_{\text{SC}}$  increases substantially by about 30% was also observed [20] while the other parameters showed a slight decrease. This can be attributed to a heating effect which increased conductivity owing to a lowering of viscosity and the slow pore filling by the viscous electrolytes. Similar effects have been noted [26] for large area solar ( $625 \text{ cm}^2$ ) cells with poly(methyl methacrylate) gel polymer electrolytes where an initial decrease in the cell performance was observed followed up by an unexpected recovery when left for several hours in the dark. The optimum efficiency of these types of solar cells is at a temperature of ca.  $60^{\circ}\text{C}$  which represents a practical temperature reached on roof top solar panels. Thus, the gel polymer electrolytes have a critical advantage over cells employing organic liquid electrolyte for outdoor applications. This example is also unique since it is the first report of large area solar cells employing a polymer gel electrolyte even though its efficiency is only ca. 1%.



Gel polymer electrolytes based on poly(acrylonitrile-*co*-styrene)/NaI+I<sub>2</sub> along with plasticizers EC and PC have been fabricated giving an ionic conductivity of  $2.4 \times 10^{-4} \text{ S cm}^{-1}$  and a solar cell efficiency of 2.75%. Here, it was shown that ionic conductivity decreases after the NaI concentration reaches 0.5 M and this is explained on the basis of shrinkage of the polymer chains and a phase disengagement between polymer matrix and the liquid electrolyte [13].

Development of a polymer electrolyte consisting of poly(*n*-butyl acrylate), NaI and I<sub>2</sub> has been reported [28]. The maximum ionic conductivity observed was much lower than other comparable systems and the solar cell efficiencies are also considerably lower at 1.66% even under a low light intensity of  $10 \text{ W cm}^{-2}$ . Poor wetting ability and hence interfacial contact may be responsible for the observed trend.

Yanagida et al. [29] used a related polymer,  $\alpha$ -methacryloyl- $\omega$ -methoxyocta(oxyethylene) or 2-(2-methoxyethoxy)ethyl acrylate as base polymer and an ethylene glycol derivative as plasticizer which exhibited an ionic conductivity of  $2.67 \times 10^{-3} \text{ S cm}^{-1}$ . The energy conversion efficiency reported was 2.62% which is 86.4% of the value for the liquid electrolyte. Here the flexible structure of the polymer along with a high plasticizer content are considered important for obtaining high ionic conductivity. Gel polymer electrolytes prepared by incorporating the standard acetonitrile based liquid electrolyte into a matrix polymer such as PAN, PVDF and poly(methyl methacrylate) reportedly give high ionic conductivities of the order of  $10^{-3} \text{ S cm}^{-1}$  [30]. However these systems are sticky and soft due to the presence of liquid electrolyte and in order to overcome this problem, a polymer membrane based on acrylonitrile-methyl methacrylate *co*-polymer has been developed where the film was first prepared [31] and then soaked in the liquid electrolyte. An efficiency of 2.4% was obtained for this system and the relatively low value of efficiency is attributed to the lower  $J_{\text{SC}}$  value.

### *2.3 Poly(vinylidene fluoride) (PVDF) based polymer electrolytes*

Poly(vinylidene), PVDF, and its *co*-polymer, poly(vinylidene fluoride-*co*-hexafluoropropylene), PVDF-HFP, have been used in many studies of polymer gel polymer electrolytes. Wang et al. prepared a series of DSCs by adding 5 wt% PVDF-HFP to methoxypropionitrile based liquid electrolytes [32]. However, at such low levels of polymer concentrations, the physical form is rather like a glue instead of a free-standing film and sealing problems with the electrolytes still remain. This is a common problem associated with many so-called quasi-solid-state films which range from viscous liquids to glues to real free standing-solids. Increasing the polymer content, on the other hand, causes a decrease in the ionic conductivity and this is the dilemma faced by researchers working in this area. Various attempts have been made to alleviate this problem and one such approach is to chemically cross link the relatively non-polar PVDF polymer in a more polar polymer matrix such as polyethylene glycol methylmethacrylate in a cross linked reinforced network [33] The efficiency obtained for a  $11 \mu\text{m}$  film was 3.35% which decreased considerably for thicker films.

Another approach to enhance the efficiency of PVDF-HFP gel polymer electrolytes is to incorporate TiO<sub>2</sub> nanoparticles to form nanocomposite gel electrolytes [34]. Introduction of TiO<sub>2</sub> nanoparticles here increased the efficiency from 5.72% to 7.18% which reached the same level of efficiency as the liquid electrolyte (7.01%). The nanoparticles here are assumed to reduce the charge recombination at the interface of dyed electrode/electrolyte. This system shows excellent thermal stability and there was only 10% loss in efficiency after thermal soaking at 60°C for 1000 h. This is one instance where the efficiency in a quasi-solid state exceeded that of the liquid state. Gratzel et al. reported [35] a similarly constituted gel polymer electrolyte where fumed silica was employed as the nano-filler reaching the same efficiency as in the liquid state while Yanagida et al

reported an example where the gel polymer electrolyte efficiency exceeded that of the corresponding liquid electrolyte [38].

Recently, the use of an ultra-thin PVDF-HFP membrane deposited on Ru N-719/TiO<sub>2</sub> DSC which gives a DSC efficiency of 8.73% has been reported [39]. The efficiency of the corresponding liquid electrolyte DSC was 8.23% and this enhancement can be explained on the basis of the increased V<sub>OC</sub> value arising from the passivation of traps on the TiO<sub>2</sub> surface thereby retarding recombination reactions. In a related study, when 10% by weight of TiO<sub>2</sub> nano-filler was incorporated to the same membrane as in the previous example, an energy conversion efficiency of 10.40% compared to the value of 8.88% observed [40] in the absence of added TiO<sub>2</sub> was obtained. The increased efficiency can be attributed to scattering effects of the TiO<sub>2</sub> particles which enhances the absorption of longer wavelength light.

#### 2.4 Poly(acrylamide)(PAA) based polymer electrolytes

The advantage of this type of polymer is the presence of both amide and carbonyl groups in its structure which may promote the interaction of the sensitized dye and the polymer gel matrix. The carbonyl groups can also coordinate to alkali metal cations thereby enhancing iodide ion conductivity of the electrolyte and hence the DSC efficiencies. However, the reported [41] efficiencies for a variety of plasticizers is less than 3% at a light intensity of 60 mW cm<sup>-2</sup>. One drawback of this system is the high viscosity of the electrolytic medium which retards the movement of ions.

### 3. FUTURE OUTLOOK

While a considerable amount of research have been carried out on gel polymer electrolytes, it is difficult to critically assess the work since most reported efficiencies are not on optimized TiO<sub>2</sub> films. In some cases, efficiencies of the cells with liquid electrolyte reported are as low as ~3%. There is scope, however, to improve the efficiencies of these cells compared to those reported on wet cells and hence they offer excellent promise as future solar cell materials. Polymer electrolytes such as PAN offer self sealing films of exceptional stability and reaching efficiencies over 7%. The technology involves simple hot pressing and these may become competitive for practical applications in large area solar cells. While this review was aimed at Ru dye sensitized TiO<sub>2</sub> solar cells, the application of polymers to other more recently developed organic dyes is also promising. Recently the use of PAN based quasi-solid electrolyte based on plasticizers EC and PC yielding an efficiency of 5.3% for an indoline dye sensitized TiO<sub>2</sub> solar cell [42] has been reported.

### REFERENCES

1. A.F.Nogura, M.A. de Paoli, I. Montanari, R. Monkhouse, J. Nelson, J. Durrant, *J. Phys. Chem. B* 105 (2001) 7517.
2. M.A.K.L. Dissanayake, L.R.A.K. Bandara, R.S.P. Bokalawela, P.A.R.D. Jayathilaka,
3. O.A. Ileperuma, S. Somasunderam, *Mat. Res. Bull.* 37 (2002) 867.
4. O.A. Ileperuma, M.A.K.L. Dissanayake, S. Somasunderam, L.R.A.K. Bandara, *Sol. Energy Mater. Sol. Cells* 84 (2004) 117.
5. T. Kato, T. Kado, S. Tanaka, A. Okazaki, S. Hayase, *J. Electrochem. Soc.* 153 (2006) A626.
6. U. Bach, D. Lupo, P. Comte, J.E. Moser, F. Weissörtel, J. Salbeck, H. Sreizer, M. Grätzel, *Nature* 395 (1998) 583.
7. K. Tennakone, G.R.A. Kumara, A.R. Kumarasinghe, K.G.U. Wijayantha, P.M. Sirimanne, *Semicond. Sci. Technol.* 10 (1995) 1689.
8. A.M. Stephan, *European Polymer Journal*, 42 (2006) 21.

9. L.R.A.K. Bandara, M.A.K.L. Dissanayake, G.V.K. Ekanayake, O.A. Ileperuma, T.T.K. Weeraman, *Solid State Ionics: Science & Technology* eds. BVR. Chowdari et al. (World Scientific Publishing Co., Singapore) (1998) 493.
10. Y. Ren, Z. Zhang, S.Fang, M. Yang, S.Cai, *Sol energy Mater. Sol. Cells* 71 (2002) 253.
11. T.M.W.J.Bandara, M.A.K.L.Dissanayake, O.A.Ileperuma, K.Varaprathan, K.Vignarooban, B.E.Mellander, *J.Solid State Electrochem.* DOI 10.1007/s10008-007-0461-7.
12. M.S. Kang, J.K. Kim, J. Won, Y.S. Kang, *J. Photochem. Photobiol. A: Chem.* 183 (2006) 15.
13. Z. Lan, J. Wu, D. Wang, D.S. Hao, J. Lin, Y. Huang, *Solar Energy* 80 (2006) 1483.
14. 16. J. Xia, F. Li, C. Huang, J. Zhai, L. Jiang, *Sol Energy Mater. Sol. Cells* 90 (2006) 944]
17. K. Sun and S.H. Jin, *J. Mater. Chem.* 8 (1998) 2399.
15. F. Cao, G. Oskam, P.C. Searson, *J.Phys.Chem.* 99 (1995) 17071.
16. O.A. Ileperuma, M.A.K.L. Dissanayake, S. Somasunderam, *Electrochim.Acta* 47 (2002) 2801.
17. R. Komiya, L. Han, R. Yamanaka, A. Islam and T. Mitae, *J. Photochem. Photobiol. A: Chem.* 164 (2000) 123.
18. S. Ito et al., *Thin Solid Films* (2007), doi.10.1016/j.tsf2007.05.090.
19. O.A. Ileperuma, G.R.A. Kumara, K. Murakami, Manuscript in preparation.
20. K. Abraham, in: *Applications of Electroactive polymers: "Highly conductive Polymer electrolytes"*, B.
21. Scrossati (Ed.), Chapman & Hall (London) 1993, pp. 75-112.
22. S. Pelet, J.E. Moser and M. Grätzel, *J. Phys. Chem. B.* 104 (2000) 1791.
23. K. Hara, T. Nishikawa, M. Kurashige, H. Kawauchi, T. Kashima, K. Sayama, K. Aika and H. Arakawa, *Sol Energy Mater. Sol. Cells* 85 (2005) 21.
24. W. Kubo, K. Murakoshi, T. Kitamura, S. Yoshida, M. Haruki, K. Hanbusa, H. Shirai, Y. Wada, S.Yanagida, *J. Phys. Chem. B.* 105 (2001) 12809.
25. Y. Liu, A. Hagfeldt, Xu-Rui Xiao, Sten-Eric Lindquist, *Sol. Energy Mater. Sol. Cells* 55 (1998) 267.
26. P. Li, J. Wu, M. Huang, S. Hao, Z. Lan, Q. Li, S. Kang, *Electrochimca Acta* 53 (2007), 903.
27. M. Biancardo, K. West and F.C. Krebs, *Sol. Energy Mater. Sol. Cells* 90 (2006) 2575.
28. J.H. Kim, M.S. Kang, Y.J. Kim, J. Won, Y.S. Kang, *Solid State Ionics* 176(2005) 579
29. M. Matsumoto, Y. Wada, T. Kitamura, S. Shigaki, T. Inoue, M. Ikeda, S. Yanagida, *Bull.Chem. Soc. Jpn.*, 74 (2001) 387.
30. J.Y. Song, Y.Y. Yang, C.C. Wan *J. Power Sources* 77 (2001) A279.
31. D.W. Kim, Y.B. Jeong, S.H. Kim, D.Y. Lee, J.S. Song, *J. Power sources* 149 (2005) 112.
32. P. Wang, S.M. Zakeeruddin, R. Humphry Baker, J.E. Moser, M.K. Nazeeruddin, T. Sekiguchi, M. Grätzel, *Nature Materials* 2 (2003) 402.
33. T.C. Werli, C.C. Wan, Y.Y.Wang, *Sol. Energy Mater. Sol. Cells* 91 (2007) 1892.
34. Z. Huo, S. Dai, K.Wang, F. Kong, C.Zhang, X.Pan, X Fang, *Sol. Energy Mater. Sol. Cells* 91 (2007) 1959.
35. P. Wang, S.M. Zakeeruddin, P. Comte, I. Exnar, M.Grätzel, *J.Amer. Chem. Soc.* 125 (2003) 1166.]
36. H.Usui, H. Matsui, N. Tanabe, S.Yanagida, *J.Photochem.Photobiol. A.Chem.* 164 (2004) 97.
37. H. Yang, O.A. Ileperuma, M. Shimomura, K.Murakami, *17<sup>th</sup> International Photovoltaic Science and Engineering Conference*, Fukuoka, Japan December 3-7, 2007. Technical Digest pp. 1025-1026.

38. H. Yang, O.A. Ileperuma, M. Shimomura, K. Murakami, , *17<sup>th</sup> International Photovoltaic Science and Engineering Conference*, Fukuoka, Japan December 3-7, 2007. Technical Digest pp. 146-147.
39. J.Wu, Z. Lan, D. Wang, S. Hao, J. Lin, Y. Wei, S. Yin, T. Sato, Y. Huang, *J. Photochem. Photobiol. A: Chem.* 181 (2006) 333.]
40. O.A. Ileperuma, G.R.A. Kumara, K.Murakami, *Chem. Lett.* 37 (2008) 36.

## **PROBING THE IODIDE IONS IN POLYMER ELECTROLYTES BY IMPEDANCE AND DIELECTRIC SPECTROSCOPY**

B-E. MELLANDER

*Department of Applied Physics, Chalmers University of Technology, SE-412 96 Göteborg, Sweden*

Corresponding Author, e-mail: *f5xrk@chalmers.se*

### **ABSTRACT**

A common redox couple for TiO<sub>2</sub> based dye-sensitized solar cells is the I<sub>3</sub><sup>-</sup>/I<sup>-</sup> system, that is an iodide ion conducting electrolyte is needed for the device. The electrolyte is usually a liquid using a volatile, flammable and often toxic solvent. This type of electrolyte has the advantage of high conductivity but problems such as leakage and vaporization of the solvent are common and will drastically reduce the system lifetime and may also be harmful for the surroundings. There are many demands on the electrolyte, it should have a high ionic conductivity for the desired ion, have a negligible electronic conductivity and meet strict requirements regarding chemical and thermal stability. It should also be flexible enough to be in good contact with the other components of the system during expansion or contraction that occurs during operation and ageing. The quantum-dot-sensitized solar cell has a relatively low efficiency but an advantage of using quantum dots is that the absorption spectrum is dependent on the size of the dots and could thus be tuned to a specific application or to enlarge the range of absorbed energy. Also this type of solar cell may use an I<sub>3</sub><sup>-</sup>/I<sup>-</sup> electrolyte.

Polymer electrolytes may provide a stable, safe and efficient alternative to traditional liquid electrolytes. Electrolytes based on poly(ethylene oxide) are well known since a number of years. They have excellent mechanical properties but often suffer from a low ionic conductivity. In fact an undesired crystallization of the electrolytic mixture or of one of its components might compromise the durability and temporary or permanently reduce the performance in a practical device. Another alternative is gel polymer electrolytes using various host polymers and plasticizers mainly incorporating various iodides [1,2,3]. Still another alternative is using an ionic liquid based electrolyte where a polymer component offers mechanical stability is thus an attractive concept, the polymer can be a separate component or being the result of a polymerization of the ionic liquid itself. Ionic liquids are of practical interest because of their extremely low volatility, low flammability and low reactivity.

Impedance and dielectric spectroscopy provide a convenient method of probing the iodide ions in polymer electrolytes used for dye sensitized solar cells

### **REFERENCES**

1. Bandara T.M.W.J., Dissanayake M.A.K.L., Albinsson I., Mellander B.-E., *J. Power Sources* 195, 3730 (2010).
2. Ileperuma O.A., Kumara G.R.A., Murakami K., *Chemistry Letters* 37(1):36-37 (2008)
3. Tennakone K., Senadeera G.K.R., Perera V.P.S., Kottegoda I.R.M., Silva L.A.A.D., *J Chem. Mater.* 11:2474 (1999)

## **PLASMONICS FOR IMPROVED PHOTOVOLTAIC DEVICES**

A. K. PAL

*Department of Instrument Science, USIC Building, Jadavpur University,  
Calcutta-700 032, India*

Corresponding Author, e-mail: *msakp2002@yahoo.com*

### **ABSTRACT**

Several approaches have been adopted in the past for increasing the light absorption in photovoltaic solar cells. Introduction of a plasmonic layer of 1b metal nanoparticles (pure or embedded in a dielectric layer) has been recognized as a viable alternate approach for enhancing light absorption. The scattering from metal nanoparticles near their localized plasmon resonance seemed to be a promising way of increasing the light absorption in thin-film solar cells. Enhancements in photocurrent had been observed for a wide range of semiconductors and solar cell configurations. In this presentation, a review of the experimental and theoretical progress that has been made in recent years, the basic mechanisms, and an outlook on future prospects in this area is presented.

### **1. INTRODUCTION**

A number of methods [1-3] have been adopted in the past for increasing the light absorption in photovoltaic solar cells. But, acceptance of the above methods became debatable in context of optimizing cost and ease of their adaptation related to scalable technique demanded by the industries. The biggest problem for thin film solar cells is that they do not absorb as much light as the current generation bulk solar cells. Methods for trapping light on the surface, or in the solar cells are crucial in order to make thin film solar cells viable. A method being explored over the past few years [4-14] is to scatter light using metal nanoparticles excited at their surface plasmon resonance frequency. This method allows light to be absorbed directly without traversing through the relatively thick additional layer required in other types of thin-film solar cells. There have been quite a few pioneers working with plasmonic solar cells. One of the main focuses has been on improving the performance of the thin film solar cells through the use of metal nanoparticles distributed on the surface. In this system the increased Raman scattering provides more photons to become available to excite surface plasmons which cause electrons to be excited and travel through the thin film solar cells to create a current. Enhanced efficiencies for organic ultra thin film solar cells due to the presence of 5 nm diameter silver nanoparticles were also reported. Thus, plasmonic solar cells are recognized as a class of photovoltaic devices that would convert light into electricity by using plasmons. plasmonic solar cells are a type of thin-film solar cells which are typically 1-2 $\mu$ m thick. They can use substrates which are cheaper than silicon, such as glass, plastic or steel. They can use substrates which are cheaper than silicon, such as glass, plastic or steel.

Currently, there are three different generations of solar cells. The first generation (those in the market today) are made with crystalline semiconductor wafers, typically silicon. Current solar cells trap light by creating pyramids on the surface which have dimensions bigger than most thin film solar cells. Making the surface of the substrate rough (typically by growing SnO<sub>2</sub> or ZnO on surface) with dimensions on the order of the incoming wavelengths and depositing the solar cells on top has been explored. This increases the photocurrent, but the thin film solar cells then have poor material quality.

The second generation solar cells are based on thin film technologies such as those presented here. These solar cells focus on lowering the amount of material used as well as increasing the energy production. Because thin-film solar cells are only a few microns thick, standard methods of increasing the light absorption, which use surface textures that are typically around 10 microns in size, cannot be used. Plasma etch techniques, which can be used to etch submicron-sized features, can damage the silicon, thereby reducing the cell efficiency. Another alternative to direct texturing of Si is the texturing of the substrate. However, this also results in increased recombination losses through increased surface area. Though in practice, it has been experimentally proven to be very difficult to reduce recombination losses beyond a certain limit. Theoretically energy conversion efficiency of above 24% even for 1  $\mu\text{m}$  cells can be achieved. This highlights the need to incorporate better light-trapping mechanisms that do not increase recombination losses in thin-film solar cells to extract the full potential of the cells.

Third generation solar cells are currently being researched. They focus on reducing the cost of the second generation solar cells. To achieve this, a new method for achieving light trapping in thin-film solar cells by the use of metallic nanostructures supporting surface plasmons, has been evolved. This involves excitations of the conduction electrons at the interface between a metal and a dielectric. By proper engineering of these metallodielectric structures, light can be concentrated and 'folded' into a thin semiconductor layer, thereby increasing the absorption. Both localized surface plasmons excited in metal nanoparticles and surface plasmon polaritons (SPPs) propagating at the metal/semiconductor interface are of interest. Although there is now considerable experimental evidence that light scattered from metal nanoparticle arrays increases the photocurrent spectral response of thin-film solar cells, many of the underlying physical mechanisms and their interplay have not been studied systematically. The full potential of the particle scattering concept, taking into account integration with optimized anti-reflection coatings, is being studied by several research groups. In recent years, it has been indicated [25-22] that both shape and size of metal nano particles are key factors determining the incoupling efficiency. Moreover, the plasmon energy can be efficiently collected and transferred to an underlying waveguide as part of a solar cell. The cells performance would indicate an enhanced yield of power generation.

## **2. SURFACE PLASMON RESONANCE**

When light strikes a metal sample, it can initiate electrical disturbances in the surface, either as localized excitations called surface plasmons or as moving waves called surface plasmon polaritons. The plasmons can be considered as a sort of proxy for the light, except at a shorter wavelength. A flurry of experimental and theoretical activities over the past few decades [15-26] was devoted towards the understanding of the size and shape effects, broadening, effect of surrounding matrix, etc., on the surface plasmon band of gold, silver and its nanocomposites. The surface plasmon resonance largely depend on the particle size, shape, and of course the metallic material and its surrounding environment.

Although metal doping in another exhotic dielectric medium, diamond like carbon (DLC) films, prepared by chemical/physical vapour deposition techniques had been the issue of obtaining a new class of materials [15-26] but the difficulty of dispersing the metal particles homogeneously in the DLC matrix by the techniques used by the researchers was found to be difficult. Since DLC is a large band gap material, metal inclusion in nanocrystalline form should also reveal interesting optical properties like surface plasmon resonance in these classes of composite materials which have not been explored yet systematically.

A number of theoretical models were proposed [27-35] and several experiments were carried out to understand the effect of particle size on the surface plasmon effect and to justify the observed peak shift (either blue-shift or red-shift) and its broadening with decreasing size. Critical dependence of various intrinsic properties of metal particles on size, intercrystalline distance and their integrated effect on the plasma band shape and position were dealt with by Kreibig et al [27,31]. The observed blue-shift was attributed to several phenomena viz. contraction of lattice induced by surface stress [32], effect of surface potential [33], changes of optical interband transitions between the discrete energy levels, changes of electron band structure etc. Effects of deviation from perfect spherical shape and irregular size distribution were found to produce large inhomogeneous broadening [34].

Maxwell-Garnett (M-G) and Bruggeman obtained the effective dielectric constant of a composite system by considering the interaction of external electric field with metal particles acting as interacting dipoles with an effective polarizability given by Drude relation while the dielectric constant of the composite material was obtained through Clausius-Mossotti relation [35]. In the Maxwell-Garnett approach, the metal inclusion in the host material ( $f_m$ ) is very small and particle dimension ( $d$ ) and inter-particle separations are very small compared to the wavelength of light ( $\lambda$ ). The effective dielectric constant is then given by,

$$\frac{\epsilon_c - \epsilon_o}{\epsilon_c + \kappa\epsilon_o} = f_m \frac{\epsilon_m - \epsilon_o}{\epsilon_m + \kappa\epsilon_o} \quad (6)$$

where  $\epsilon_c$ ,  $\epsilon_m$ ,  $\epsilon_o$  are the dielectric constants of the composite, the metal and the host matrix respectively.  $\kappa$  is the screening parameter determined by the shape as well as the orientation of the nanoparticles with respect to the external electric field. For spherical particle  $\kappa=2$ .  $\epsilon_c$  and  $\epsilon_m$  are complex in nature and is related to the refractive index  $n$  and extinction coefficient  $k$  given by,

$$\epsilon = \epsilon' + i\epsilon''$$

$$\epsilon' = n^2 - k^2 \text{ and } \epsilon'' = 2nk$$

where  $\epsilon'$  and  $\epsilon''$  are the real and imaginary part of the dielectric constant respectively. The Bruggeman geometry consists of a random mixture of two dissimilar materials. The effective dielectric constant is obtained through,

$$f_m \frac{\epsilon_m - \epsilon_c}{\epsilon_m + \kappa\epsilon_c} + (1 - f_m) \frac{\epsilon_o - \epsilon_c}{\epsilon_o + \kappa\epsilon_c} = 0 \quad (7)$$

The above two relations are widely used to obtain the effective dielectric constant and in turn, the extinction coefficient of a composite system. But both the above relations suffer a serious drawback as they do not take into account the size and shape distribution of the nanocrystallites. To take into account the size as well as the shape effect simultaneously, a size dependent depolarization factor was introduced into the Maxwell-Garnett theory and the modified theory (dynamical Maxwell-Garnett theory) was used to evaluate the optical properties of the gold nanocomposite material [36,37]. The depolarization factor played a crucial role in determining the optical absorption features.

Recently, Gao et al. [30] introduced a shape distribution into the Maxwell-Garnett and Bruggeman type of geometry and calculated the effective dielectric constant of a two- component system. The particles having a kind of shape distribution were assumed to be ellipsoidal and the distribution function that was introduced into the theory to correctly describe the depolarization coefficient is given by,

$$P(L) = \frac{A}{\sqrt{L(1-L)}} \quad (8)$$



where  $A (=1/\pi)$  and  $L$  ( $0 < L < 1$ ) are the normalization constant and equivalent depolarization factor respectively. The two extreme values of  $L$  i.e.  $L \rightarrow 0$  and  $L \rightarrow 1$  determine a needle-like (prolate) and plate-like (oblate) shape of the particles. The depolarization factor depends critically on the axial ratio of the ellipsoidal particles.

Introducing the shape distribution as in equation (8), Gao et al. [30] obtained the dielectric constant in the limit of Maxwell-Garnett approximation as:

$$\frac{\varepsilon_c}{\varepsilon_o} = \frac{1 + f_m(\sqrt{\varepsilon_m/\varepsilon_o} - 1)}{1 + f_m(\sqrt{\varepsilon_o/\varepsilon_m} - 1)} \quad (9)$$

The shape distribution incorporated into the Bruggeman type of geometry relates the composite dielectric constant with that of the individual components as,

$$\frac{1}{\sqrt{\varepsilon_c}} = \frac{f_m}{\sqrt{\varepsilon_m}} + \frac{1-f_m}{\sqrt{\varepsilon_o}} \quad (10)$$

They also formulated a differential effective medium approximation, considering a shape distribution of small particles distributed in a previously homogeneous matrix and is given by,

$$\frac{\varepsilon_c}{\varepsilon_o} = \frac{1 + f_m + (1 - f_m)\sqrt{\frac{\varepsilon_m}{\varepsilon_o}}}{1 - f_m + (1 + f_m)\sqrt{\frac{\varepsilon_m}{\varepsilon_o}}} \quad (11)$$

### 3. CURRENT STATUS

#### 3.1. Silicon solar cells

Silicon is the favorite semiconductor used in photovoltaic cells. Still, one would like to reduce the amount of Si needed for large-area devices. Furthermore, silicon is a poor light emitter and absorber, and therefore solar cell efficiencies have generally been poor. The efficiency of thin-film Si cells is even poorer than for wafer-thick Si cells. How to make the cells cheap (using thin films) but also increasingly absorptive is an important goal. In conventional thick Si solar cells, light trapping was typically achieved using a pyramidal surface texture that causes scattering of light into the solar cell over a large angular range, thereby increasing the effective path length in the cell. Such large-scale geometries are not suitable for thin-film cells, for geometrical reasons (as the surface roughness would exceed the film thickness) and because the greater surface area would increase minority carrier recombination in the surface and junction regions.

Solar-cell design and materials-synthesis considerations are strongly dictated by the opposing requirements for optical absorption thickness and carrier collection length. Plasmonic structures can offer at least three ways of reducing the physical thickness of the photovoltaic absorber layers while keeping their optical thickness constant. First, metallic nanoparticles can be used as sub-wavelength scattering elements to couple and trap freely propagating plane waves from the sun into an absorbing semiconductor thin film, by folding the light into a thin absorber layer. Second, metallic nanoparticles can be used as sub-wavelength antennas in which the plasmonic near-field is coupled to the semiconductor, increasing its effective absorption cross-section. Third, a corrugated metallic film on the back surface of a thin photovoltaic absorber layer can couple sunlight into SPP modes supported at the metal/semiconductor interface [4].

For wafers, the enhancement was by a factor of 7 for light with a wavelength of 1200 nm. Silicon normally absorbs light only weakly in this part of the spectrum, so the enhancement is significant. Across all wavelengths, the photocurrent enhancement for the 1.25-micron film and the wafer samples was, respectively, 33% and 19%. Pillai et al. [6] observed that optimizing the nanoparticle size should bring additional improvements [5,6]. In this article, suitability of localized surface plasmons on silver nanoparticles for enhancing the absorbance of silicon solar cells has been investigated. It was found that surface plasmons can increase the spectral response of thin-film cells over almost the entire solar spectrum. At wavelengths close to the band gap of Si, a significant enhancement of the absorption for both thin-film and wafer-based structures was observed. They reported a sevenfold enhancement for wafer-based cells at ~1200 nm and up to 16-fold enhancement at ~1050 nm for 1.25  $\mu\text{m}$  thin silicon-on-insulator (SOI) cells, and also compared the results with a theoretical dipole-waveguide model. They also reported a close to 12-fold enhancement in the electroluminescence from ultrathin SOI light-emitting diodes and investigate the effect of varying the particle size on that enhancement.

Pillai et al. [5,6] have also investigated the effect of surface plasmons on silver nanoparticles as a means of improving the efficiency of thin-film and wafer-based solar cells. The results suggest that surface plasmons offer a promising way to improve the efficiency of thin-film solar cell structures, avoiding the problem of increased recombination which occurs when silicon is textured directly. This method also has the scope of further reducing the thickness of Si to below 1.5  $\mu\text{m}$  with good light trapping provided by the metal nanoparticles. The results show that for front surface application, smaller metal particles provide maximum overall enhancement in the visible as well as the near-IR for solar cell applications, but that larger metal particles would be more beneficial for light emission from both thin and thick Si LEDs.

An engineered enhancement in short-circuit current density and energy conversion efficiency in amorphous silicon *p-i-n* solar cells was achieved via improved transmission of electromagnetic radiation arising from forward scattering by surface plasmon polariton modes in Au nanoparticles deposited above the amorphous silicon film by Derkacs et al. [7]. The total Mie extinction is a sum of contributions from absorption and from scattering associated with each supported surface plasmon polariton mode of the particle. For small particles supporting only dipolar modes, the total extinction cross section consists of a large absorption cross section and a smaller scattering cross section. For larger particles, with diameters of ~100 nm or larger, the opposite is true: although the total extinction cross section remains dominated by dipolar contributions, the scattering cross section is much larger than the absorption cross section. For a Au nanoparticle density of  $\sim 3.7 \times 10^8 \text{ cm}^{-2}$ , an 8.1% increase in short-circuit current density and an 8.3% increase in energy conversion efficiency are observed. Finite-element electromagnetic simulations confirm the expected increase in transmission of electromagnetic radiation at visible wavelengths, and suggest that substantially larger improvements should be attainable for higher nanoparticle densities.

Si *pn* junction diodes were fabricated by Schaadt et al. [8] by diffusion of boron at 900 °C for 30 min into an *n*-type Si (001) wafer with resistivity  $\sim 10^{-2}$  Ohm-cm. Based on the diffusion conditions employed, the boron depth profile was computed analytically and yielded a *pn* junction depth of 80 nm, with the boron concentration at the wafer surface estimated to be  $\sim 1.1 \times 10^{20} \text{ cm}^{-3}$ . Ohmic contacts to the *p*-type surface were formed by optical lithography followed by thermal evaporation of ~150 nm Al. A large-area Ohmic contact to the *n*-type underside of the wafer was formed by a second thermal evaporation of ~150 nm Al. Au nanoparticles were deposited by placing a drop of Au colloidal solution containing Au particles of uniform size onto the surfaces of fabricated devices that had been subjected to a prior exposure to a poly-L-lysine solution to facilitate immobilization of the Au nanoparticles on the device surface.

### 3.2. Compound semiconductor solar cells

Konda et al [10] have engineered a device consisting of *n*-CdSe/*p*-Si (001) junction diode with spherical Au nanoparticles deposited on CdSe semiconductor surface, It is noted that a significant enhancement in the photocurrent was observed in Au/CdSe/ *p*-Si compared to CdSe/ *p*-Si using white light. These results clearly show that while the white light is the highest source of absorption for the generation of the photocurrent due to wide spectrum of absorption wavelengths available from the Au nanoparticles and clusters due to plasmon resonance, the light with a certain band of wavelengths is less effective. The enhancement in absorption within the semiconductor results in an increased photocurrent response in junction diode that corresponds closely to the nanoparticle plasmon resonance.

Konda et al. [10] reported on the significant enhancement of photocurrent in *pn* heterojunction diode, consisting of *n*-CdSe/ *p*-Si substrates, *in situ* deposited with Au nanoparticles on the surface by the pulsed-laser deposition technique. This is attributed to the large enhancement in electromagnetic field that occurs in the vicinity of the metal surface, causing surface plasmons. The large enhancement in Raman and photoluminescence intensity was observed due to surface plasmon resonance. Their results suggest that the photo-detectors and optoelectronic devices, such as high-performance thin-film solar cells, optical communication, and sensing devices, including bio- and molecular sensors, can be fabricated with improved functionality.

Surface plasmon enhanced antireflection coatings for GaAs solar cells [11] have been designed theoretically. The reflectance of double-layer antireflection coatings (ARCs) with different suspensions of Ag particles is calculated as a function of the wavelength according to the optical interference matrix and the Mie theory. The mean dielectric concept was adopted in the simulations. A significant reduction of reflectance in the spectral region from 300 to 400 nm was found to be beneficial for the design of ARCs. A new SiO<sub>2</sub>/Ag-ZnS double-layer coating with better antireflection ability can be achieved if the particle volume fraction in ZnS is 1%–2%. The performance of the modified ARC system is simulated by calculating the system reflection from the standard optical theorem and the Mie theory with different structural parameters, including the complex refractive indices of the medium and the volume fraction of the metal particles. When the particle volume fraction in a ZnS medium is 1%–2%, and the diameter of particles is larger than 100 nm, the calculated enhancement of the antireflection is significant in the near-UV region for GaAs solar cells. The nanoparticles also have the potential to increase the near band absorption for extra-thin GaAs cells. The simulation contributes to the design and the fabrication of high-quality antireflection coatings of GaAs solar cells.

### 3.3. Organic Solar Cells

Improved optical absorption and photocurrent for polythiophene–fullerene bulk heterojunction photovoltaic devices is demonstrated by Yoon et al. [13] using a unique self-assembled monolayer of Ag nanoparticles formed from a colloidal solution. With the presence of suitable nanoparticle organic capping groups that inhibit its propensity to agglomerate, the particle-to-particle spacing can be tailored. Transmission electron microscopy reveals the self-assembled Ag nanospheres are highly uniform with an average diameter of ~4nm and controllable particle-to-particle spacing. The localized surface plasmon resonance peak is ~465 nm with a narrow full width at half maximum (95 nm). In the spectral range of 350–650 nm, where the organic bulk heterojunction photoactive film absorbs, an enhanced optical absorption is observed due to the increased electric field in the photoactive layer by excited localized surface plasmons within the Ag nano-spheres. Under the short-circuit condition, the induced photo-current efficiency (IPCE) measurement demonstrates that the maximum IPCE increased to ~51.6% at 500 nm for the experimental devices with the self-assembled layer of Ag nanoparticles, while the IPCE of the

reference devices without the plasmon-active Ag nanoparticles is ~45.7% at 480 nm. For the experimental devices under air mass 1.5 global filtered illuminations with incident intensity of 100mW/cm<sup>2</sup>, the increased short-circuit current density is observed due to the enhancement of the photo-generation of excitons near the Plasmon resonance of the Ag nanoparticles.

Morpha et al. [38] included plasmon-active silver nanoparticle layers in solution-processed bulk-heterojunction solar cells. Nanoparticle layers were fabricated using vapor-phase deposition on indium tin oxide electrode. Owing to the increase in optical electrical field inside the photoactive layer, the inclusion of such particle films lead to increased optical absorption and consequently increased photoconversion at solar-conversion relevant wavelengths. The resulting solar energy conversion efficiency for a bulk heterojunction photovoltaic device of poly(3-hexylthiophene)/(6,6)-phenyl C<sub>61</sub> butyric acid methyl ester was found to increase from 1.3% ±0.2% to 2.2% ±0.1% for devices employing thin plasmon-active layers. Based on six measurements, the improvement factor of 1.7 was demonstrated to be statistically significant.

Rand et al. [39] investigated the optical properties of silver nanoparticles used in tandem ultrathin-film organic photovoltaic cells. Experimental results indicate that the enhancement of an incident optical field persists into an organic dielectric for distances of up to 10 nm from the center of an array of approximately 5-nm-diameter nanoparticles. Furthermore, this enhancement exists far from the resonant particle surface-plasmon excitation energy. They proposed a model to explain this long-range enhancement and investigated the role that cluster spacing, shape, and an embedding dielectric medium with a complex dielectric constant play in determining plasmon enhancement. This effect is shown to increase the efficiency of tandem organic solar cells, and the implications for further solar cell efficiency improvements are discussed.

An interesting possibility to improve the conversion and cost efficiencies of photovoltaic dye sensitized solar cells is to exploit the large optical cross sections of localized (nanoparticle) surface plasmon resonances (LSPRs). Hagglund et al [40] have investigated this prospect for dye sensitized solar cells. Photoconductivity measurements were performed on flat TiO<sub>2</sub> films, sensitized by a combination of dye molecules and arrays of nanofabricated elliptical gold disks. An enhanced dye charge carrier generation rate was found and shown to derive from the LSPR contribution by means of the polarization dependent resonance frequency in the anisotropic, aligned gold disks.

#### *3.4. Possibilities in CIGS cells*

Copper-indium-gallium-diselenide based solar cells have attained a very useful efficiency values now-a-days. The generally accepted cell structure is shown below:

ZnO-low resistive-Sputtered  
ZnO-high resistive-Sputtered  
CBD-CdS  
CIGS-high resistive-Coevaporation  
CIGS low resistive-Coevaporation  
Mo- sputtered  
Glass

The different layers for the best cell (efficiency ~17%) have the parameters as shown below:

### **BEST CELL PARAMETERS**

Mo-R.F. Sputtering (0.8 $\mu$ m, 0.2-0.3  $\Omega/\square$  )  
CIGS-Evaporation (3 $\mu$ m,  $T_s > 450^\circ\text{C}$ )  
CdS-CBD (20-30nm)  
ZnO-R.F. Sputtering (300nm,  $10^3 \Omega\text{-cm}$ )  
ZnO: Al (2%)- R.F. Sputtering (200nm, 20  $\Omega/\square$  )  
Cu: In: Ga: Se =23.4: 19.7: 6.99: 49.91  
 $\eta \sim 17\%$

Thus, the problem would be simpler for CIGS cells to introduce a plasmonic layer using a ZnO:Ag layer constituting the window layers for improving the efficiency further. One has to play with the size, shape and the effective dielectric constant of the plasmonic layer (i.e. metal loading) to make the plasmonic layer compatible with the above cell structure.

### **REFERENCES**

1. J. Muller, B. Rech, J. Springer, M. Vanecek, *Solar Energy* 77 (2004) 917
2. P. Campbell and M. A. Green, *J. Appl. Phys.*, 62 (1987) 243
3. P. Campbell and M. A. Green *Solar Energy Materials and Solar Cells*, 65 (2001) 369
4. H. A. Atwater and A. Polman, *Nature Mater.* 9 (2010) 206
5. S. Pillai, M.A. Green, *Sol. Energy Mater. Sol. Cells* (2010),  
doi:10.1016/j.solmat.2010.02.046
6. S. Pillai, K. R. Catchpole, T. Trupke, and M. A. Green *J. Appl. Phys.* **101** (2007) 093105
7. D. Derkacs, S. H. Lim, P. Matheu, W. Mar, and E. T. Yub, *Appl. Phys. Lett.* **89** (2006) 093103
8. K. R. Catchpole and A. Polman, *Appl. Phys. Lett.* 93 (2008) 191113
9. D. M. Schaadt, B. Feng, and E. T. Yub, *Appl. Phys. Lett.* 86 (2005) 063106
10. R. B. Konda, R. Mundle, H. Mustafa, O. Bamiduro, and A. K. Pradhan, U. N. P. Roy, Y. Cui, and A. Burger, *Appl. Phys. Lett.* 91 (2007) 191111
11. W. Yanshuo, C. Nuofu, Z. Xingwang, Y. Xiaoli, B. Yiming, C. Min, W. Yu, C. Xiaofeng, and H. Tianmao, *J. Semicond.* 30, (2009) 072005
12. S. Kim, S. Na, Jang Jo, D. Kim, and Y. Nah, *Appl. Phys. Lett.* **93** (2008) 073307
13. W. Yoon, K. Jung, J. Liu, T. Duraisamy, Rao Revur, F. L. Teixeira, S. Sengupta, P. R. Berger, *Solar En. Mater. & Solar Cells* 94 (2010) 128–132
14. W.L. Barnes, A. Dereux, T.W. Ebbesen, *Surface plasmon sub-wavelength optics*, *Nature* 424 (2003) 824–830.
15. R. Paul, S. Hussain and A K Pal, *Applied Surface Science* 255 (2009) 8076–8
16. R. Paul, S. Hussain, S. Majumder, S. Varma and A K Pal, *Mater. Sc. & Engg. B*, 164 (2009) 156
17. R. Paul, R.N. Gayen, S. Hussain, V. Khanna, R. Bhar, and A.K. Pal, *Euro. Phys. J. Appl. Phys.*, 47 (2009) 10502
18. S. Hussain, S. Datta, R. K. Roy and A. K. Pal, *J. Nanoscience & Nanotechnology*, 7 (2007) 1
19. R. K. Roy, S. Bandyopadhyay and A.K.Pal., *Euro.Phys. J. B*, 39 (2004) 491
20. S. Hussain and A. K. Pal, *Mater.Lett.* 62 (2008) 1874
21. R. Gayen, S.N. Das, S. Dalui, R. Bhar and A.K.Pal, *J. Cryst. Growth.* 310 (2008) 4073
22. S. Hussain, R K Roy and A K Pal, *J. Phys. D. Appl. Phys.*, 38 (2005) 908

23. K.I. Schiffmann, M. Fryda, G. Goerigk, R. Laure, P. Hinze, A. Bulack, *Thin Solid Films*, **347** (1999) 60.
24. K.K. Chan, S.R.P. Silva, G.A.J. Amaratunga, *Thin Solid Films*, **212** (1992) 232 .
25. I. Gerhards, C. Ronning, H. Hofsass, M. Seibt, H. Gibhard, *J. Appl. Phys.*, **93** (2003) 1203.
26. S. P. Lau, Y. J. Li, B.K.Tay, Z. Sun, G. Y. Chen, X.Z. Ding, *Diamond Relat. Mater.* **10** (2001) 1727.
27. U. Kreibig and M.Vollmer, *Optical Properties of Metal Clusters* (Springer-Verlag, Berlin, 1995).
28. Maxwell-J.C.Garnett, *Philos. Trans. R. Soc. Lon. A*, **203** (1904) 385.
29. D.A.G.Bruggeman, *Ann. Phys. Lpz.* **24** (1935) 636.
30. L.Gao, Jones, T.K. Wan, K.W. Yu and Z.Y. Li, *J. Phys. Condensed Mater*, **12** (1991) 6825
31. U Kreibig, *J. Physique* **38**,C2-97, 1977; *Growth and Properties of Metal Clusters* Editor J.Bourdon (Elsevier, Amsterdam 1980) p.37.
32. W. Cai, Y.Zhang, J. Jia, and L. Zhang, *Appl. Phys. Lett.*, **73** (1998) 2709
33. H. Hovel, S. Fritz, A. Hilger, U. Kreibig, *Phys. Rev. B* **48** (1993) 18178
34. R. Gaans, *Ann Physik*, **37** (1912) 881
35. C.Kittel, *Introduction to Solid State Physics* (India: Wiley Easdtarn Limited) 1993.
36. P.B.Johnson and R.W.Christy, *Phys. Rev. B*, **6** (1972) 4370
37. C.A.J. Foss, G.L.Hornyak, J.A.Stokert, and C. Martin, *J. Phys. Chem.* **98** (1994) 2963
38. A. J. Morfa, K. L. Rowlen, T. H. Reilly III, M. J. Romero, and J. van de Lagemaat, *Appl. Phys. Lett.* **92** (2008) 013504
39. B. P. Rand, P. Peumans, S. R. Forrest, *J. Appl. Phys.*, **96** (2004) 7519
40. C. Hägglund, M. Zäch, and B. Kasemo *Appl. Phys. Lett.* **92** (2008) 013113

**EXCITON-COUPLED CHARGE-TRANSFER DYNAMICS IN A PORPHYRIN  
J-AGGREGATE/TiO<sub>2</sub> COMPLEX**

HIRENDRA N. GHOSH

Radiation & Photochemistry Division, Bhabha Atomic Research Centre,  
Mumbai – 400085, India

Corresponding Author, e-mail: [hngosh@barc.gov.in](mailto:hngosh@barc.gov.in)

**ABSTRACT**

5,10,15-trisphenyl-20-(3,4-dihydroxybenzene) porphyrin (TPPcat) found to couple strongly with TiO<sub>2</sub> nanoparticles with formation of 5-membered ring. Photoexcited TPP-cat molecule found to sensitize TiO<sub>2</sub> nanoparticles, and it inject electron in the conduction which has tremendous application in dye-sensitized solar cell [1]. However the main drawback using porphyrin molecule as sensitizer is due to formation of aggregation on nanoparticle surface. Interestingly TPP-cat form both **J**- and **H**-aggregates depending upon the concentration and pH of the solution. Photoexcited aggregates found to exhibit exciton dynamics in ultrafast time scale [2]. In the present we talk discuss exciton coupled charge transfer (CT) dynamics in porphyrin-**J**-aggregates sensitized TiO<sub>2</sub> nanoparticle as studied by femtosecond time resolved transient absorption spectroscopy. Interestingly, **J**-aggregates TPPcat exhibit CT complex formation on TiO<sub>2</sub> NP surface. The catechol mediated strong CT coupling between **J**-aggregate and TiO<sub>2</sub> NP facilitates interfacial exciton dissociation in favour of pulse width limited (<80fs) electron injection into the conduction band of TiO<sub>2</sub> nanoparticle. Here, the electron transfer (<80 fs) process dominates over intrinsic exciton relaxation process (**J**-aggregates; ~200fs) on account of exciton coupled CT interaction between **J**-aggregate and TiO<sub>2</sub>. The parent hole on **J**-aggregates is delocalized through excitonic coherence of **J**-aggregate. As a result, the hole immobilized in **J**-aggregates is spatially less accessible to electron injected in TiO<sub>2</sub> and thus leads to slower back electron transfer (BET) process in comparison to monomer/TiO<sub>2</sub> system. **J**-aggregate-porphyrin shows exciton spectral and temporal property for better charge separation in strongly coupled composite system [3].

**REFERENCES**

1. G. Ramakrishna, S. Verma, D. A. Jose, D. K. Kumar, A. Das, D. K. Palit, H. N. Ghosh,
2. *J. Phys. Chem. B* **2006**, 110, 9012.
3. S. Verma, A. Ghosh, A. Das, and H. N. Ghosh, *J. Phys. Chem. B*, **2010**, 114, 8327.
4. S. Verma, A. Ghosh, A. Das, and H. N. Ghosh, *Chem. Eur. J.*, *Chem. Eur. J.* **2011**, 17, 3458.

## **THIN FILM POLYCRYSTALLINE SILICON SOLAR CELLS**

H. S. REEHAL

*Department of Engineering and Design, London South Bank University  
103 Borough Road, London SE1 0AA, UK*

Corresponding Author, e-mail: [reehalhs@lsbu.ac.uk](mailto:reehalhs@lsbu.ac.uk)

### **ABSTRACT**

This paper focuses on the area of thin film polycrystalline silicon solar cells. The field has attracted significant attention in recent years due to the potential of reaching high single junction efficiencies at low costs and the inherent advantages of Si photovoltaic technology. The progress made and challenges in the field are discussed. Some new developments in the area of light trapping are outlined.

### **1. INTRODUCTION**

Photovoltaics (PV) is currently dominated by wafer-based crystalline silicon technology. Although the cost has reduced significantly in recent years, it is still a limiting factor for the deployment of PV on a truly global scale. Thin film approaches point the way to lower costs by virtue of using less active material on low cost substrates and integrated manufacturing. Amongst the several material systems, thin film silicon has been studied for many years in its various forms. Effort has mostly focussed on amorphous hydrogenated silicon (a-Si:H) and microcrystalline silicon ( $\mu\text{c-Si:H}$ ) which is a mixture of a-Si:H and Si nanocrystallites [1]. These materials lie at the heart of current thin film Si PV manufacturing. The light induced degradation problems in a-Si are well known and microcrystalline Si was introduced to improve stability and cell performance. This has led to the so called “micromorph” technology which is a tandem a-Si and microcrystalline Si structure. Despite the successes of this and other a-Si based multijunction approaches [2], photo-induced degradation is still an issue and stabilised efficiencies of small area micromorph cells are around 12% [3].

Fully crystalline forms of thin Si (without any amorphous content) offer the promise of stable device operation as well as the other attributes of crystalline Si. These include its non-toxicity, high abundance in the earth’s crust and, importantly, high efficiency potential despite its indirect band gap and poor optical absorption properties. Single junction efficiencies exceeding 15% have been suggested for many years as being possible in  $\mu\text{m}$  scale thicknesses by using effective light trapping [4]. Conventional, fully crystalline, thin forms consist of thin film polycrystalline Si (with grain sizes  $\geq 1 \mu\text{m}$ ) and monocrystalline silicon produced either epitaxially [5] or by a variety of etching or lift-off processes. Lift-off approaches generally yield fairly thick layers ( $>10\text{-}20 \mu\text{m}$ ) and have been studied for many years [4]. Ultra-thin ( $\sim 1 \mu\text{m}$ ) monocrystalline layers have also recently been demonstrated using lift-off [6].

This paper will focus on progress in thin film polycrystalline Si (TF poly-Si) on glass solar cell technology which has attracted significant attention over the past decade due to its low cost, high efficiency potential but which is highly challenging because of the temperature constraints of glass. Growth on some higher temperature substrates will be also be discussed briefly. Monocrystalline Si planar forms produced by epitaxy or by lift-off from wafers will not be discussed except in the above context. Microcrystalline Si technology with nm scale grains will also not be discussed. Finally, some new developments in light trapping will be outlined.



## **2. THIN FILM POLYCRYSTALLINE SILICON GROWTH**

Several approaches have been studied for the preparation of TF poly-Si over the past decade. The successful ones fall into two broad categories. The first is crystallisation of as-deposited amorphous layers using a variety of techniques such as solid phase crystallisation (SPC) and zone melting crystallisation. The second uses a two step process of forming a thin crystalline Si seed layer with large grains which is then epitaxially thickened. Temperatures have to be generally kept below  $\sim 600$  °C for glass substrates although excursions up to  $\sim 900$  °C are needed to remove defects, improve crystallinity and optimise dopant activation. This means the use of borosilicate or aluminosilicate substrates rather than the cheaper soda-lime glass.

### *2.1 Crystallisation of Amorphous Silicon*

In terms of device performance, solid phase crystallisation (SPC) of a-Si:H has been the most successful TF poly-Si formation technique so far. The process consists of thermally annealing the deposited films at  $\sim 600$  °C for a time period of up to several tens of hours. Film thicknesses are typically in the range 1-3  $\mu\text{m}$ . The average grain size of device grade SPC films is in the region of 1  $\mu\text{m}$  with a high density of intra-grain defects as well as grain boundaries. Sanyo reported a 9.2% efficient cell in 1996 [7]. Subsequently the process has been developed by several groups, most notably CSG Solar using their novel point contact crystalline silicon on glass device technology [8,9].

In the CSG Solar technology, amorphous Si layers ( $\sim 2$   $\mu\text{m}$  thick) with an  $n^+pp^+$  structure are deposited by PECVD onto textured and silicon nitride coated glass sheets. The coated sheets are heated to 600 °C for about 24 hours to achieve SPC. This is followed by a short defect anneal at  $\sim 900$  °C using rapid thermal annealing (RTA). Hydrogen plasma defect passivation is then carried out followed by contact patterning. An efficiency of 10.4% was realised in 2007 in a 94  $\text{cm}^2$  minimodule using a Si thickness of 2.2  $\mu\text{m}$  with an open circuit voltage (Voc) of 492 mV/cell. CSG Solar have successfully demonstrated batch processing to mitigate the slow nature of SPC but the complex nature of the contacting process has limited commercialisation. In recent years electron beam (e-beam) evaporation has been investigated as a higher deposition rate (up to  $\sim 1$   $\mu\text{m}/\text{min}$ ) alternative to PECVD for amorphous Si growth prior to SPC. Much of the work has been done by Aberle and his group [10,11]. Using this technique, Sontheimer et.al. [12] have recently achieved an efficiency of 7.8% in minimodules fabricated on planar SiN-coated glass confirming the electronic quality of e-beam deposited layers. These authors have also reported faster SPC on aluminium doped ZnO (ZnO:Al) coated substrates (which offer the potential of simpler device fabrication) due to a significant reduction in the activation energy of steady state nucleation from 5.0 eV on SiN to 2.9 eV on ZnO:Al. The SPC of a-Si on large grained poly-Si seed layers prepared by aluminium induced crystallisation (AIC) described below has also been reported [11,13]. The presence of the crystalline seed layer leads to the transfer of its structure to the SPC layer. However, the performance of these cells has been limited with Voc values below 450 mV. Various other aspects of SPC technology have been studied. Examples include the influence on crystallisation of the annealing temperature [14] and the RTA process [15].

Alternative techniques for a-Si crystallisation have been studied for many years. They include zone-melting crystallization processes using light sources and electron beams. An earlier review has been given by Bergmann [16]. Generally the processes require high temperature substrates such as ceramics. An example of recent work using e-beam zone-melting crystallization is the report by Amkreutz et.al.[17]. They achieved grain sizes of up to  $\sim 1 \times 10^3$   $\text{nm}^2$  in 8-13  $\mu\text{m}$  thick Si films. The films were deposited by LPCVD at 670 °C on SiC coated high temperature glass substrates (Corning Eagle XG). Solar cells formed using a-Si hetero-emitters yielded efficiencies up to 4.7 %. A Voc of up to 545 mV was achieved showing the high electronic quality

of the absorber layers. Improved light trapping is expected to lead to higher efficiencies. The use of high irradiance (several tens of  $J/cm^2$ ) Xe flash lamp annealing has also been reported for the crystallisation of a-Si films several  $\mu m$  thick on quartz glass substrates. The work is at an early stage with a reported solar cell efficiency of 1.37% in a  $2 \times 2 \text{ mm}^2$  crystallised device[18]. Laser crystallisation has been studied for the formation of seed layers on glass and is described below.

## 2.2 *Seed Layer Approaches*

The concept is based on first forming a thin layer of Si (the seed layer) with good crystalline quality and large grains. This is then epitaxially thickened to form the solar cell absorber layer with the crystalline structure of the underlying seed. The main techniques investigated for seed layer formation are aluminium induced crystallisation (AIC) and laser crystallisation.

### 2.2.1 *Seed Layer Formation by Aluminium Induced Crystallisation and Layer Exchange*

AIC is based on the layer exchange of thin ( $< 500 \text{ nm}$ ), adjacent a-Si or  $\mu c$ -Si and Al films when they are heated to below the eutectic temperature of Al ( $577 \text{ }^\circ\text{C}$ ) [19]. The subject has been studied extensively [20,21,22] and only the salient points are described below.

The starting layer sequence of substrate/Al/a-Si is the one most commonly employed. Both evaporated and sputtered Al layers have been successfully used. E-beam evaporation, sputtering and PECVD have been the techniques most widely used for Si deposition. The use of hot wire CVD (HWCVD) has also been reported. Upon annealing, Si atoms diffuse into the Al film through a thin permeable membrane at the Al/Si interface (usually Al oxide formed by atmospheric exposure). This is followed by nucleation of Si grains at the interface and grain growth within the Al layer until adjacent Si grains impinge. The Al is displaced towards the substrate leading to layer exchange and the transition of the a-Si into poly-Si which becomes  $p^+$  doped by the Al to its solid solubility limit in Si of  $\sim 18 \text{ cm}^{-3}$ . The poly-Si film thickness is defined by the thickness of the starting Al layer. The final layer sequence is substrate/poly-Si/Al+Si where the Al and Si phases segregate in the top Al rich layer. The poly-Si films generally exhibit a preferential (100) orientation of about 60-70% with average grain sizes in the region of  $\sim 10 \mu m$ , although grains exceeding  $50 \mu m$  have been observed. The permeable membrane at the interface plays a critical role in controlling these parameters. Schneider et. al. [23] have contributed to the theoretical understanding of the process. A property of the AIC process is that Si islands form on top of the poly-Si layer [20]. For subsequent epitaxial thickening of the seed layers, the Al and the Si islands have to be removed to leave a smooth surface. This is a critical factor for epitaxial thickening, especially at low temperatures. Various approaches to this have been implemented including wet chemical etching followed by mechanical abrasion, chemical-mechanical polishing and selective wet etching of Al combined with reactive ion etching of the remaining Si islands. The scale-up potential of some of these approaches is an issue.

The reverse of the structure described above (R-AIC), with the starting layer sequence of substrate/a-Si/Al, has also been studied [21,24]. This yields the final layer sequence of substrate/Al+Si/poly-Si after layer exchange with the Al rich, Al+Si mixed phase left underneath the poly-Si surface. Therefore, this geometry requires no Al etching step to expose the poly-Si layer and the Si islands form underneath the poly Si layer to leave a relatively smooth surface. In addition, the bottom Al+Si layer offers the possibility of forming a low resistance solar cell back contact. A cross section of the R-AIC process is shown in Figure 1 (a). Figure 1 (b) and (c) show an electron backscatter diffraction (EBSD) map and the corresponding inverse pole figure, respectively, confirming large grains with a preferred (100) orientation. Although Si island formation is avoided in this scheme, the as-formed poly-Si surface can still exhibit significant

roughness and requires further treatment for successful absorber layer deposition. Excimer laser crystallisation has been shown to improve surface morphology [25].

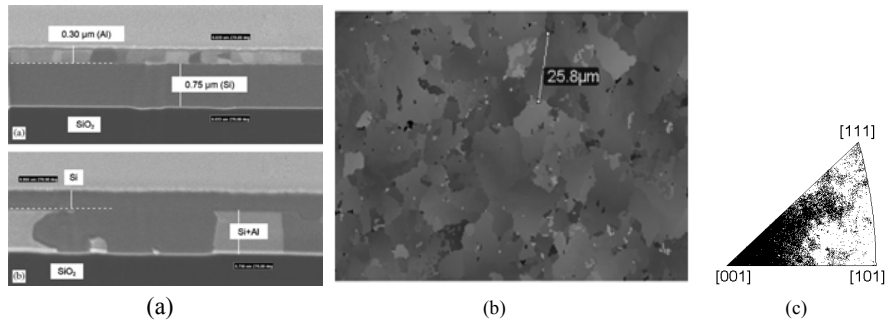


Figure 1: (a) Focussed ion beam images showing the layer exchange process for the R-AIC geometry : top-before annealing, bottom -after annealing (b) EBSD map of poly-Si grains after AIC (c) inverse pole figure showing preferred (100) orientation. The poly-Si layer is  $\sim 0.3\mu\text{m}$  thick. After [24]

Key issues with the AIC approach that impact device performance include the mixed grain orientation, intra-grain defects and surface roughness of the crystallised layers.

### 2.2.2 Seed Layer Formation By Laser Crystallisation

Laser crystallisation of thin amorphous Si layers on glass has been an active field of study for many years driven by the TFT market, with pulsed excimer lasers being the dominant technology. The utility of this technique to crystalline Si solar cells has been studied. The fact that excimer lasers operate in the UV and VUV (wavelengths between 351-157 nm) restricts the Si layer thickness that can be crystallised to below  $\sim 100$  nm. This is acceptable for seed layer formation but the grains are generally up to  $\sim 1$   $\mu\text{m}$  in size at best and possess a mixed orientation [26,27]. Pulsed copper vapour lasers operating at 511 or 578 nm enable the crystallisation of thicker layers. For example, via sequential lateral solidification using a copper vapour laser, Bergmann et. al. obtained Si crystallites of several tens of  $\mu\text{m}$  in length in 400 nm thick films on glass [28]. More recently, Falk and collaborators [29] have shown that large grained poly-Si seed layers on glass substrates can be produced by scanning the line focussed beam of a cw diode laser operating at 806 nm, or of a green pulsed laser emitting at 515nm. Grains exceeding  $100\mu\text{m}$  in size were formed in 400 nm thick amorphous Si starting layers by the cw laser, whereas the green laser yielded grains with sizes in the 10  $\mu\text{m}$  range in 60 nm thick layers. Both approaches led to mixed orientation grains as evidenced by EBSD analysis. New approaches are being studied including multiple-exposure mixed-phase solidification (MPS) using a scanning laser beam. Promising results have been obtained with large grain size ( $\sim 5\mu\text{m}$ ), nearly 100% (100) oriented, low intra-grain defect density poly-Si films being formed on quartz substrates [30].

### 2.2.3 Absorber Growth on Seed Layers and Device Results

Direct epitaxial growth has been widely reported for growing absorber layers on seed layers using a number of low to medium temperature techniques. In recent years interest has also increased in solid phase epitaxy of a-Si films deposited on the crystallised seed layers. To date, most of the work on solar cells on seed layers has used simple structures without any complex light trapping schemes thereby leading to modest short circuit currents ( $J_{sc}$ ).

The first successful epitaxial growth of Si on AIC seed layers used ion-assisted deposition (IAD) under non-UHV conditions [31]. The technique is based on e-beam evaporation and

subsequent creation of Si ions which are accelerated towards the substrate by a low voltage (typically 20V) to increase surface adatom mobilities. To obtain several  $\mu\text{m}$  thick smooth poly-Si films requires temperatures in the vicinity of 600 °C or above. Seed layers with a preferred (100) orientation were found to be advantageous for the epitaxial thickening. However, the development of solar cell structures using these layers has been challenging with typical as-grown devices having Vocs in the region of 100 mV. A high density of intra-grain defects and impurities have been identified as the key factors limiting performance. Post deposition treatments such as rapid thermal defect annealing at  $\sim 1000$  °C and remote plasma hydrogenation lead to a significant improvement in performance. However, performance has remained poor with best Voc values of  $\sim 420$  mV and efficiencies of  $\sim 2$  % in small area cells with  $\sim 2\mu\text{m}$  thick absorber layers [10].

Plasma deposition techniques such as electron cyclotron resonance CVD (ECRCVD) can also be used to provide low energy ion bombardment of the growth surface to increase adatom surface mobilities and reduce epitaxial growth temperatures to below 600 °C. Epitaxial thickening of AIC seed layers by ECRCVD has been reported by several authors including Gall et. al. [21] and Ekanayake et. al.[32]. The best quality epitaxial layers below 600 °C are obtained on (100) oriented Si wafers. Typically, epitaxy breaks down above a thickness of  $\sim 2.5$   $\mu\text{m}$  on (100) Si and at much lower thicknesses for other orientations. This has consequences for the epitaxial thickening of AIC seed layers with their mixed grain orientation. At best, epitaxial thickening of  $\sim 70$ -80% of the surface has been reported [21]. Like the IAD deposited absorber case, the performance of solar cells fabricated from ECR thickened seed layers has been limited. Best reported efficiencies in small area ( $4\times 4$   $\text{mm}^2$ ) cells on glass, with inter-digitated contacts and a 2  $\mu\text{m}$  thick absorber layer, are in the region of 1% with a Voc of 397 mV. This was achieved after post-deposition defect annealing using RTA at 900 °C and hydrogen plasma passivation [33]. Reference cells grown on  $\text{p}^+$  (100) Si wafers exhibited an efficiency exceeding 4.2 % without light trapping, with a Voc of 458 mV before defect annealing or passivation. Analysis of the layers using Seeco etching has shown that they exhibit a very high density ( $\geq 10^9$   $\text{cm}^{-2}$ ) of extended defects and growth regions of different structural quality which limits device performance [34]. Interestingly, in a recent study of cells prepared on AIC seed layers with the reverse structure (R-AIC) formed on a Ag/ITO back contact, Jaeger et al have reported cell efficiencies exceeding 5% using 2  $\mu\text{m}$  thick non-epitaxial absorber layers grown by PECVD at 180°C [35].

Epitaxial thickening of AIC seed layers on glass using high rate e-beam evaporation under non-UHV conditions has been systematically studied by the group at Helmholtz –Zentrum, Berlin [36]. As for the ECRCVD films, the layer structural quality depends strongly on the orientation of the underlying substrate, with (100) orientation producing the best results and pointing to the importance of a high preferential (100) orientation of the seed layers. Layers grown at 600 °C on Si (100) substrates exhibited no extended defects whereas defects are present on other orientations. Films grown on seed layers do exhibit defects and it has been suggested that these originate from imperfections at the seed layer surface. The defect densities are lower than in ECRCVD films. This translates to superior performance in solar cells. The best poly-Si cell on glass was reported to have an efficiency of 3.2% using an absorber thickness of 2.2  $\mu\text{m}$ . The Voc was 407 mV after RTA defect annealing and hydrogen plasma passivation. A 1.8  $\mu\text{m}$  thick reference cell grown on a  $\text{p}^+$  (100) Si wafer at 650 °C without any light trapping exhibited an efficiency of 5.86 %, with a Voc of 570 mV. The same group has also reported TF poly-Si cells grown on AIC seed layers formed on ZnO:Al coated glass. This allows for a simpler contacting scheme and light trapping. Initial solar cells using 2  $\mu\text{m}$  thick, e-beam evaporated epitaxial absorbers achieved a Voc of 389 mV and an efficiency of 2% [37].

Device fabrication on laser crystallised seed layers on glass has been investigated by a number of authors. Andra et. al. have studied layered laser crystallisation (LLC) whereby the laser

crystallised seed layer is epitaxially thickened by simultaneous deposition of a-Si using e-beam evaporation and repeated pulses of an excimer laser. A promising Voc of 517 mV was achieved with an efficiency of 4.2% using a 2  $\mu\text{m}$  thick absorber layer, without an antireflective coating (ARC) or light trapping [38]. However the approach is difficult to scale up. Schneider et. al. have reported solid phase epitaxial (SPE) thickening of e-beam deposited a-Si on cw laser crystallised seed layers [39]. The CSG Solar contacting technology was used and an efficiency of 4.9% reported in a minimodule (12 series connected cells) with further scope for improvement. Cell results based on excimer laser crystallised seed layers with grain size up to 1100 nm have recently been reported [27]. SPE of amorphous films on the seed layers gave higher Voc values (up to 443 mV) compared to e-beam deposited epitaxial absorber layers. Laser based approaches are still being developed and new routes to achieving epitaxy on seed layers via melting or in the solid state are being investigated [29].

More significant progress in terms of device performance using the AIC seed layer approach has been made using higher temperature substrates and thermal CVD at  $\sim 1100$   $^{\circ}\text{C}$  for epitaxial thickening. The group at IMEC have used alumina and transparent glass ceramic substrates and achieved a record efficiency of 8.5% on alumina using a heterojunction emitter and an inter-digitated contacting scheme [40]. A 2-3  $\mu\text{m}$  thick absorber layer was grown on a 250 nm thick seed layer followed by remote plasma hydrogen defect passivation and plasma texturing. The textured surface improved light trapping, and together with an ITO ARC, led to a Jsc of 21.6  $\text{mA}/\text{cm}^2$ , a Voc of 523 mV and a fill factor (FF) of 75.8%, giving an efficiency of 8.54%. An efficiency of 6.4% was reached on the glass ceramic. Detailed analysis has shown that the Voc of the cells is almost independent of the grain size and that a high density ( $\sim 10^9$   $\text{cm}^{-2}$ ) of defects present in the AIC seed layer, or at the seed layer-epitaxial layer interface, limits cell performance [41]. The use of laser mixed phase solidification for seed layer formation has been reported to lead to a drastic reduction in intra-grain defect density compared to AIC-based samples. A cell efficiency of 5.4% has been realised in early work on glass ceramic substrates with a thermal CVD grown absorber [42].

The use of monocrystalline seed layers has been reported by IMEC and demonstrates the potential of the seed layer approach. The seed layers were created by transferring 300 nm thick, (100) oriented monocrystalline Si layers onto glass ceramic substrates using anodic bonding and implant-induced separation. Seed layer size is limited by the size of the starting Si wafer so that wafer scale cells are, in principle, possible. Epitaxial thickening of the wafers by thermal CVD followed by plasma texturing led to an efficiency of 10.8% in a 1  $\text{cm}^2$  inter-digitated device with an absorber thickness of  $\sim 6$   $\mu\text{m}$ . Voc values in excess of 600 mV have been recorded illustrating the good layer quality (defect density reduced to  $\sim 10^5$   $\text{cm}^{-2}$ ) [6,43]. The Jsc values are still relatively low due to the absence of advanced light trapping schemes. The use of monocrystalline Si seed layers has also been investigated by Branz and co-workers using a heterojunction cell structure with an a-Si emitter [44]. They used HWCVD at 730  $^{\circ}\text{C}$  to epitaxially thicken 450 nm thick monocrystalline Si (100) layers, oxide bonded to Corning EAGLE XG display glass. The best device had a Voc of 460 mV and an efficiency of 4.8% using an absorber thickness of 2.5  $\mu\text{m}$  and without any RTA, defect passivation or light trapping. Reference wafer based devices reached an efficiency of 6.7% with a Voc of 570 mV. High dislocation densities are a limiting factor due to the lower growth temperature used compared to thermal CVD.

### **3. DEVELOPMENTS IN LIGHT TRAPPING**

Effective light trapping is critical to realise the high efficiency potential of TF poly-Si solar cells. Conventional methods of light trapping in bulk Si solar cells use textures on the scale of several microns and cannot be used for thin film poly-Si cells. The use of textured back reflectors

is also difficult as they tend to impede epitaxial overgrowth. Front surface isotropic plasma texturing has been successfully used by the IMEC group in the cells reported above but  $\sim 1\mu\text{m}$  of Si is still removed and plasma damage can be an issue. Increased surface recombination due to increased surface area can also be an issue for subwavelength surface structures formed by plasma etching and other techniques.

New approaches to light trapping in planar thin film cells include the use of photonic crystals as back reflectors. A combined grating and one-dimensional photonic crystal as a distributed Bragg reflector has been shown to enhance the efficiency in  $5\mu\text{m}$  thick monocrystalline Si cells fabricated using a layer transfer technique. The measured short circuit current density was increased by 19% compared to a theoretical prediction of 28% [45]. An issue with the photonic crystal approach is the cost effective scale-up and application to practical devices.

The use of plasmonic structures for light trapping in thin film PV devices is attracting considerable attention. These structures can improve absorption in a number of ways[46]. Of particular relevance to thin film Si cells is the ability of metal nanoparticles to scatter light efficiently over a wide angular range into the cells due to the excitation of localised surface plasmons (LSPs). Excited LSPs can decay radiatively resulting in scattering, or nonradiatively which gives rise to absorption. Absorption dominates for small particles  $<50\text{ nm}$  in size, whereas larger particles up to  $\sim 100\text{nm}$  are more efficient scatterers. For thin film poly-Si solar cells, low absorption losses across the visible and near infra-red (NIR) region and large scattering cross sections are required, particularly in the NIR where transmission losses are more significant. Silver has been studied widely as a nanoparticle as its resonance wavelength is in the visible and can be tuned towards NIR wavelengths. Au nanoparticles have been suggested for poly-Si cells [47]. A review of the field has recently been given by Pillai and Green [48].

Arrays of metal particles can be applied to the front or rear of thin film solar cells. Many designs have used Ag nanoparticles deposited by self assembly (annealing of nm scale thick films) on the front, illuminated surface of fully fabricated solar cells. This approach has led to an increase in photocurrent of up to a factor of 16, at a wavelength of  $1050\text{ nm}$ , in  $1.25\mu\text{m}$  thick silicon-on-insulator solar cells[49]. However, these designs frequently suffer from absorption losses in the nanoparticles in the blue end of the spectrum [50]. Locating the nanoparticles at the rear of the cell offers the advantage of short wavelength light being absorbed in the cell before reaching the particles while the long wavelength light reaching the rear of the cell can be scattered back and trapped. This approach is the focus of much current activity for a-Si solar cells [51]. It has also recently been applied to functional thin film poly-Si cells on glass prepared by SPC of e-beam evaporated Si films [52]. The total cell thickness was of the order of  $2\mu\text{m}$  and a superstrate structure with inter-digitated contacts was used. Random arrays of Ag nanoparticles were formed using self assembly by annealing a  $16\text{ nm}$  thick Ag film at  $\sim 250\text{ }^\circ\text{C}$  on the rear surface of the cell, separated from the Si surface by a thin dielectric spacer layer. The average diameter of the particles was  $\sim 120\text{ nm}$ . LSPs excited in the nanoparticles were shown to increase light absorption in the Si films and enhance the spectral response and efficiency. The short circuit current and efficiency increased by 13% and 10%, respectively, compared to control samples without surface plasmons. Subsequent work on the same devices by Pillai et al [53] have compared the effect of the dielectric spacer thickness on photocurrent enhancement for front or rear applied Ag nanoparticles. The most effective light trapping was achieved for rear located particles when deposited directly on the Si. One of the key issues with plasmonic solar cells is the large area fabrication of nanoparticle arrays having the desired size, shape and distribution. Self assembly provides poor control over all these parameters whilst particle distribution is a major limitation of using colloidal suspensions. Electron beam lithography is limited to small area research devices

[47]. Alternatives with scale-up potential such as nano-imprint lithography are being actively explored [51].

Finally, it should be mentioned that new cell geometries based on crystalline Si nanowires or micropillars with radial junctions are attracting considerable interest as they provide new opportunities for enhanced light trapping and potentially increased performance. The high efficiency potential of Si nanowire cells (~15%) has been shown theoretically [54]. The growth of crystalline Si wires from the gas phase has been demonstrated using the catalytic vapour-liquid-solid (VLS) method. Efficiencies up to 7.9% have been achieved in wire arrays using an active volume of Si equivalent to a 4  $\mu\text{m}$  thick wafer [55]. The wires were grown at high temperatures using Cu catalyst particles and had lengths of  $\sim 50\mu\text{m}$ . Lower temperature ( $<600\text{ }^\circ\text{C}$ ) growth of shorter crystalline Si nanowires from the gas phase using the VLS method has also been demonstrated on Si and a number of low cost substrates such as glass and metal foils [56,57,58,59]. The wires show promising absorption characteristics but work on solar cells using this bottom up approach is at an early stage. PV action has been demonstrated but efficiencies are at the 3-4% level on Si [56] and  $<1\%$  on glass [57,59]. Top down approaches where the nanowires or pillars are formed by etching of Si have shown higher performance. For example, Wang et. al. have reported  $\sim 4.9\%$  conversion efficiency in wire cells of 1.65  $\mu\text{m}$  diameter formed by reactive ion etching of  $\sim 2\text{ }\mu\text{m}$  thick p-epilayers grown on  $\text{p}^+\text{Si}$  (100) substrates [60]. Key challenges for Si nanowire cells include high levels of recombination due to the vastly increased surface area and efficient contacts for carrier extraction.

#### **4. CONCLUSIONS**

The approaches to and performance of experimental thin film poly-Si solar cells have been discussed. The use of glass substrates restricts processing temperatures to below  $\sim 600\text{ }^\circ\text{C}$ , with brief excursions to higher temperatures being possible for defect annealing. Solid phase crystallisation of amorphous Si films at  $\sim 600\text{ }^\circ\text{C}$  leads to grain sizes of the order of 1  $\mu\text{m}$  and has been demonstrated on the commercial scale with efficiencies up to  $\sim 10\%$  being achieved in minimodules. Larger grain sizes should lead to better performance and techniques for producing large grain size material have been developed. These are based on the use of thin seed layers followed by epitaxial thickening. However, this has not so far translated into higher efficiency devices due to material quality issues and the fairly simple cell designs which have been used without optimised contact structures or light trapping.

Aluminium induced crystallisation (AIC) and laser crystallisation have been the main techniques used for seed layer production. Grain sizes exceeding 50  $\mu\text{m}$  have been achieved by AIC but the performance of solar cells on AIC seed layers on glass has been limited so far with efficiencies below a few %. This is due not only to the temperature constraints of using glass, but also the quality of the seed layers. In addition to the mixed orientation of the grains (which impacts epitaxial growth quality and uniformity), studies have shown that AIC seed layers contain high densities of intra-grain defects which propagate into the absorber layer to compromise performance and negate any advantages of the larger grain size. Seed layer roughness and surface defects are also important issues, particularly at low epitaxial growth temperatures. Seed layers produced by laser crystallisation on glass have lower intra-grain defects but mixed grain orientation is still an issue. However, efficiencies approaching 5% have been achieved using these layers with e-beam deposited, solid phase epitaxy absorbers.

The use of higher epitaxial growth temperatures on high temperature substrates such as alumina leads to a significant increase in performance with an efficiency of 8.5% being achieved using AIC seed layers. However, seed layer quality (in particular, electrically active intra-grain

defects) still limits performance. The results of using monocrystalline Si seed layers have led to efficiencies of ~11% being achieved in non-optimised devices deposited by thermal CVD. This shows the high efficiency potential of the seed layer approach. To realise this on low temperature substrates such as glass remains highly challenging despite significant effort over the past decade. Further work is required to form fully oriented, low defect density seed layers and combine them with a deposition technique capable of providing high quality absorber layers. Mixed phase solidification shows promise as a new, potentially scaleable, route to high quality seed layer formation. If layer quality can be sufficiently improved and combined with advanced light trapping schemes in optimised cell designs, it should be possible to reach the goal of a 15% efficient thin film poly-Si solar cell technology.

## 5. ACKNOWLEDGEMENTS

The author acknowledges funding from the UK's EPSRC. He would also like to thank his past and current students including GDK Mahanama, G Ekanayake, T Quinn, J Ball and SB Ahmed.

## REFERENCES

1. AV Shah, J Meier, E Vallat-Sauvain, N Wyrsh, U Kroll, C Droz, U Graf, *Solar Energy Materials & Solar Cells* 78 (2003) 469–491
2. J Yang, B Yan, S Guha, *Thin Solid Films* 487 (2005) 162–169
3. J Bailat, L Fesquet, J Orhan, et. al., 25th European Photovoltaic Solar Energy Conf., Valencia, Sept. 2010, p 2720-2723
4. R B Bergmann, T J Rinke, *Prog. Photovolt: Res. Appl.* 8 (2000) 451-464
5. P Rosenits, F Kopp, S Reber, *Thin Solid Films* 519 (2011) 3288-3290
6. I Gordon, F Dross, V Depauw, A Masolin, Y Qui, J Vaes, D Van Gestel, J Poortmans, *Solar Energy Materials & Solar Cells* 95 (2011) S2-S7
7. T Matsuyama, N Terada, T Baba, T Sawada, S Tsuge, K Wakisaka, S Tsuda, *J Non-Crystalline Solids* 198-200 (1996) 940-944
8. M A Green, P A Basore, N Chang, D Clugston, R Egan, R Evans, D Hogg, S Jarnason, M Keevers, P Lasswell, J O Sullivan, U Schubert, A Turner, S R Wenham, T Young, *Solar Energy* 77 (2004) 857–863
9. M J Keevers, T L Young, U Schubert, M A Green, 22nd European Photovoltaic Solar Energy Conference, Milan, Sept. 2007, p 1783-1790
10. A G Aberle, *J Crystal Growth* 287 (2006) 386-390
11. O Kunz, Z Ouyang, S Varlamov, A G Aberle, *Progress in Photovoltaics: Research and Applications* 17 (2009) 567-573
12. T Sontheimer, C Becker, F Ruske, C Klimm, U Bloeck, S Gall, O Kunz, T Young, R Egan, J Hupkes, B Rech, 35th IEEE PVSC, Honolulu, June 2010, p 000614-000619
13. S He, J Wong, D Inn, B Hoex, A G Aberle, A B Sproul *Thin Solid Films* 518 (2010) 4351-4355
14. Y Tao, S Varlamov, J Wong, O Kunz, R Egan, 35th IEEE PVSC, Honolulu, June 2010, p 000620-000625
15. B Rau, T Weber, B Gorka, P Dogan, F Fenske, K Y Lee, S Gall, B Rech *Materials Sci. Eng. B* 159-160 (2009) 329-332
16. R B Bergmann, *Appl. Phys. A* 69 (1999) 187-194
17. D Amkreutz, J Muller, M Schmidt, T Hanel, T F Schulze, *Prog. Photovolt: Res. Appl.* (2011) DOI: 10.1002/pip.1098
18. K Ohdaira, T Nishikawa, S Ishii, et. al. 25th European Photovoltaic Solar Energy Conf., Valencia, 2010, p 3546-3548



19. O Nast, S R Wenham, *J Appl Phys* 88 (2000) 124-132
20. P I Widenborg, A G Aberle, *J Crystal Growth* 242 (2002) 270-282
21. S Gall, J Schneider, J Klein, K Hubner, M Muske, B Rau, E Conrad, I Seiber, K Petter, K Lips, M Stoger-Pollach, P Schattschneider, W Fuhs, *Thin Solid Films* 511-512(2006) 7-14
22. S Gall, C Becker, K Y Lee, T Sontheimer, B Rech, *J Crystal Growth* 312 (2010) 1277-1281
23. J Schneider, A Sarikov, J Klein, M Muske, I Sieber, T Quinn, H S Reehal, S Gall, W Fuhs, *J Crystal Growth* 287 (2006) 423-427
24. G Ekanayake, T Quinn, H S Reehal, *J Crystal Growth* 293 (2006) 351-358
25. T Quinn, H S Reehal, 24th European Photovoltaic Solar Energy Conference, Hamburg, Sept. 2009, p 2517-2520
26. S Summers, H S Reehal, G J Hirst, *J. Mat. Sci.: Materials in Electronics* 11 (2000) 557-563
27. M Weizman, C Klimm, M Nittel, M Kastner, C Hernandez, N H Nickel, T Sontheimer, B Rech, 25th European Photovoltaic Solar Energy Conf., Valencia, Sept. 2010, p 2828-2831
28. R B Bergmann, J Kohler, R Dassow, C Zaczek, J H Werner, *phys. stat. sol. (a)* 166 (1998) 587-602
29. G Andra, J Bergmann, A Gawlik, I Hoger, T Schmidt, F Falk, B Burghardt, G Eberhardt, 25th European Photovoltaic Solar Energy Conf., Valencia, Sept. 2010, p 3538-3542
30. J S Im, M Chahal, P C Van derWilt, U J Chung, G S Ganot, A M Chitu, N Kobayashi, K Ohmori, A B Limanov, *J Crystal Growth* 312 (2010) 2775-2778
31. N P Harder, T Puzzer, P I Widenborg, S Oelting, A G Aberle, *Crystal Growth & Design*, 3 (2003) 767-771
32. G Ekanayake, T Quinn, H S Reehal, B Rau, S Gall, *J. Crystal Growth* 299 (2007) 309-315
33. B Rau, E Conrad, S Gall, 21st European Photovoltaic Solar Energy Conf., Dresden, Sept 2006, p 1418-1421
34. B Rau, K Petter, I Sieber, M S Pollach, D Eyidi, P Schattschneider, S Gall, K Lips, W Fuhs *J Crystal Growth* 287 (2006) 433-437
35. C Jaeger, T Matsui, M Takeuchi, M Karasawa, M Kondo, M Stutzmann, *Japanese J Appl. Phys.* 49 (2010) 112301
36. S Gall, C Becker, E Conrad, P Dogan, F Fenske, B Gorka, K Y Lee, B Rau, F Ruske, B Rech, *Solar Energy Materials & Solar Cells* 93 (2009) 1004-1008
37. K Y Lee, P Dogan, F Ruske, B Gorka, S Gall, B rech, J Hupkes, 23rd European Photovoltaic Solar Energy Conf., Valencia, Sept 2008, p 2261-2264
38. G Andra, J Plentz, A gawlik, E Ose, F Falk, K Lauer, 22nd European Photovoltaic Solar Energy Conf., Milan, 2007, p1967-1970
39. J Schneider, J Dore, S Christianson, F Falk, N Lichtenstein, B Valk, R Lewandowska, A Slaoui, X Maeder, J Labar, G Safran, M Werner, V Naumann, C Hagendorf, 25th European Photovoltaic Solar Energy Conf., Valencia, Sept. 2010, p 3573-3576
40. Y Qiu, O Kunz, S Venkatachalam, D Van Gestel, R Egan, I Gordon, J Poortmans, 25th European Photovoltaic Solar Energy Conf., Valencia, Sept. 2010, p 3633-3637
41. I Gordan, L Carnel, D Van Gestel, G Beaucarne, J Poortmans, *Thin Solid Films* 516 (2008) 6984-6988
42. D Van Gestel, M Chahal, P C van der Wilt, Y Qiu, I Gordon, J S Im, J Poortmans, 35th IEEE PVSC, Honolulu, June 2010, p 000279-000282
43. I Gordan, Y Qiu, D Van Gestel, J Poortmans, 25th European Photovoltaic Solar Energy Conf., Valencia, Sept. 2010, p 3651-3653

44. D L Young, K Alberi, C Teplin, I Martin, P Stradins, M Shub, C Beall, E Iwaniczko, H Guthrey, M J Romero, T Chuang, E Mozdy, H M Branz, 35th IEEE PVSC, Honolulu, June 2010, p 000626-000630
45. L Zeng, P Bermel, Y Yi, B A Alamariu, K A Broderick, J Liu, C Hong, X Duan, J Joannopoulos, L C Kimerling, Appl. Phys. Lett. **93**, (2008) 221105
46. H A Atwater, A Polman, Nature Materials 9 (2010) 205-213
47. T Temple, D M Bagnall, J Appl. Phys. 109 (2011) 084343
48. S Pillai, M A Green, Solar Energy Materials & Solar Cells 94 (2010) 1481-1486
49. S Pillai, K R Catchpole, T TRupke, M A Green, J Appl. Phys, 101 (2007) 093105
50. T Temple, G D K Mahanama, H S Reehal, D Bagnall, Solar Energy Materials and Solar Cells 93 (2009) 1978-1985
51. V E Ferry, M A Verschuuren, H B T Li, E Verhagen, R J Walters, R E Schropp, H A Atwater, A Polman, 35th IEEE PVSC, Honolulu, June 2010, 000760-000765
52. Z Ouyang, F Beck, O Kunz, P Campbell, K R Catchpole, S Varlamov, S Pillai, M A Green, 24th European Photovoltaic Solar Energy Conference, Hamburg, Sept. 2009, p 2608-2610
53. S Pillai, F J Beck, K R Catchpole, Z Ouyang, M A Green, J Appl. Phys. 109 (2011) 073105
54. M D Kelzenberg, M C Putnam, D B Turner-Evans, N S Lewis, H A Atwater, 34th IEEE PVSC, Philadelphia, 2009 p 001948 - 001953
55. M C Putnam, S W Boettcher, M D Kelzenberg, D B Turner-Evans, J M Spurgeon, E L Warren, R M Briggs, N S Lewis, H A Atwater, Energy Environ. Sci. 3 (2010) 1037-1041
56. C Y Kuo, C Gau, B T Dai, Solar Energy Materials and Solar Cells 95 (2011) 154-157
57. G Andra, M Pietsch, V Sivakov, Th Stelzner, A Gawlik, S Christianson, F Falk, 23rd European Photovoltaic Solar Energy Conf., Valencia, Sept. 2008, p163-167
58. L Tsakalacos, J Balch, J Fronheiser, B A Korevaar, O Sulima, J Rand, 23rd European Photovoltaic Solar Energy Conf., Valencia, Sept. 2008, p11-16
59. L Yu, B O'Donnell, P-J Alet, P Roca i Cabarrocas, Solar Energy Materials and Solar Cells 94 (2010) 1855-1859
60. K Wang, O Gunawan, N Moumen, G Tulevski, H Mohammed, B Fallah, E Tutuc, S Guha, 35th IEEE PVSC, Honolulu, June 2010, p 000913-000917

## **STUDIES ON STRUCTURAL, ELECTRICAL AND DIELECTRIC PROPERTIES OF THERMALLY EVAPORATED CADMIUM SULPHIDE (CdS) THIN FILMS**

S.TEWARI<sup>1,\*</sup> AND A.BHATTACHARJEE<sup>2</sup>

<sup>1</sup>*Department of Physics, Karimganj College, Karimganj 788710, ASSAM, India*

<sup>2</sup>*Department of Physics, National Institute of Technology, Silchar, Assam 788010, India*

\*Corresponding Author, e-mail: [ayonbh@gmail.com](mailto:ayonbh@gmail.com)

### **ABSTRACT**

Thin films of Cadmium Sulphide (CdS) are prepared by thermal evaporation technique at different substrate temperatures at a vacuum of  $2 \times 10^{-5}$  mbar. Sandwich structures of CdS in Silver (Ag) electrodes (Ag/CdS/Ag) prepared by depositing Ag on the substrate before and after the deposition of CdS. Investigations on the structural, electrical and di-electric properties of the film as a function of frequency, and temperature are carried out in the frequency range  $10$ - $10^5$  Hz and temperature range of  $25$  -  $200$  °C. The structural studies showed formation of polycrystalline CdS films with largest peak along (002) orientation. The crystallite size was found to be increased from  $167.6$  nm to  $282.2$  nm on increasing the substrate temperature of deposition from  $25$ °C to  $300$  °C. The dielectric properties such as dielectric constant and dielectric loss are strongly dependent on temperature, frequency and indicate a distributed relaxation behaviour. The investigation reveals that the a.c conductivity of the CdS film is thermally activated, arising from localised states. The a.c. conduction behavior in CdS thin films is found to be in very good agreement with the correlated barrier-hopping (CBH) model.

**Key words:** cadmium sulfide, thin films, thermal evaporation, electrical properties, a.c. conductivity.

### **1. INTRODUCTION**

In recent times, there has been a tremendous development in the field of II–VI semiconductors for their multitude of use in photo electronic devices. One of the most intensively studied among them is Cadmium sulphide (CdS), because of its multiple advantages such as intermediate energy band gap, reasonable conversion efficiency, stability, low cost and of also due to its range of prominent applications in optoelectronic, piezo-electric and other thin film devices such as solar cells, photosensors, optical wave-guides and non-linear integrated optical devices etc.[1-5]. Further, thin films of CdS can easily be grown by a number of chemical and physical deposition techniques, such as spray pyrolysis, electro deposition, thermal evaporation, pulsed laser deposition(PLD), sputtering etc.[1-10]. Each of these methods has advantages and disadvantages depending on the process parameters of deposition and final application of the films.

The performance and efficiency of the thin film based devices are strongly determined the structural, electrical and di-electric properties of the component thin films. Hence, the study of these properties is of utmost importance for using the material in thin film devices. Thus studies on these physical properties of the thin films are very important.

Although CdS is an extensively studied material and a large number of reports are available on its structural, optical and electrical studies [1-20], still there exists is a lacuna on the frequency dependent studies, as there is rarely any report on the a.c. conductivity studies of CdS thin films particularly as a function of substrate temperature of deposition.

In this study we report the investigations carried out on CdS thin films of thickness 1500 Å, deposited at substrate temperatures 25, 100, 200 and 300 °C by thermal evaporation method technique. The results of structural, electrical (d.c. and a.c. conductivity) and dielectric studies (dielectric loss, dielectric constant etc.) of the CdS film are reported in detail. The observations are carried out as a function of frequency in the range 10-10<sup>5</sup> Hz, and temperature in the range of 25-200 °C.

## 2. EXPERIMENTAL

CdS films of thickness 1500 Å were prepared by the thermal evaporation technique at different substrate temperatures in a vacuum ~ 2x10<sup>-5</sup> mbar using HINDHIVAC 12'' Vacuum Coating Unit (Model: 12A4DM). A boat of molybdenum was used as the evaporation source and the substrates were properly cleaned microscopic glass plates at a distance of 20 cm directly above the source, held at temperatures 25 (room temperature), 100, 200 and 300 °C for different depositions. Deposition rate and film thickness were measured and controlled in situ by using HINDHIVAC digital thickness monitor (Model: DTM 101). The deposition rate was kept at ~ 2 Å/s. Using masks Ag/CdS/Ag sandwich structures of area 4.16 x10<sup>-6</sup> m<sup>2</sup> were obtained for all the films deposited at different substrate temperatures.

X-ray diffraction (XRD) scans of the films were performed using a PANalytical X'pert Pro X-ray diffractometer applying the step scanning mode in the scanning angle range 20-80° with a step of 0.01° (2θ) and a counting time of 0.3 s for each step using Cu-K<sub>α</sub> radiation with wavelength λ = 1.54060 Å. The X-ray source settings were 30 mA and 40 kV. The a.c. measurements of impedance, capacitance, Loss factor and phase angle carried out as function of frequency (10 Hz to 100 kHz) and temperature in the range 25-200 °C using HIOKI-LCR (Model: 3522-50 Hioki, Japan) hi-ester, maintaining a vacuum of 10<sup>-2</sup> mbar in an indigenously built unit for electrical characterisation (Fig.1).

## 3. RESULTS AND DISCUSSIONS

### 3.1 Structural studies

The XRD data were analyzed using the X'pert High Score software. Qualitative phase analysis of each diffraction pattern was then carried out using the ICDD diffraction database and the search-match tool. The XRD pattern of the CdS films deposited at different substrate temperatures RT (25°C), 100, 200 and 300°C is shown in Fig.2. It shows the formation of polycrystalline CdS films with highest intensity peak along the hexagonal (002) plane, other peaks corresponding to the planes (101), (103), (105), (112) were found to be present with lower intensities. The XRD patterns clearly indicate that in all cases the peak intensity was found to increase with the substrate temperature of deposition. This suggests improvement in crystallinity and increase in thickness with substrate temperature.

The crystallite size D is calculated using the Debye-Scherrer formula [19]

$$D = \frac{k\lambda}{\beta \cos \theta} \dots\dots\dots (1)$$

Where, k is a constant and in our case k = 0.9, λ is wavelength of the incident x-ray (λ = 1.5418 Å), β is the corrected FWHM (Full width at half maximum) for instrumental broadening of the maximum intensity peak and θ is the angle at which the maximum peak occurs.

The grain size thus calculated for the strongest peak corresponding to the plane (002) is found to be in between 167.6 nm to 282.2 nm, as listed in Table 1. The crystallite size was found to increase with the substrate temperature of deposition which is the same behaviour reported in

literature for spray-pyrolysed CdS [23] thin films and also on other materials [24]. This is because increasing the substrate temperature decreases the density of nucleation centres and, under these circumstances, a smaller number of centres start to grow, resulting in larger grains.

### 3.2 Electrical and dielectric properties

#### i. D.C. conductivity

The d.c. conductivity is expressed by the relation

$$\sigma = \sigma_0 \exp\left[-\frac{E}{kT}\right] \dots\dots\dots (2)$$

where,  $\sigma_0$  is pre exponential factor,  $k$  is Boltzmann's constant and  $E$  is the thermal activation energy.

In the present studies d.c. conductivity of the CdS films is found to increase with temperature, which indicates thermally activated conduction in the CdS film. The variation of d.c. conductivity ( $\ln\sigma_{dc}$ ) with inverse temperature ( $1000/T$ ) is shown in Fig.3 The plot is linear, confirming that the process of conduction in the film is a thermally activated one in the experimental temperature range (25 °C to 200 °C). The thermal activation energies calculated from these graphs are as shown in table 2. The d.c. conductivity studies show two different regions with different activation energies. This shows that the CdS films have two impurity levels responsible for conduction – one shallow level and another deep level. At lower temperature range (25 to 100 °C) the thermal activation energy does not vary significantly. However, the change is more pronounced at higher temperature range (125 -200 °C).

The results indicate that films have grain boundary-limited conduction corresponding to activation energy ( $E_1$ ) in the low temperature range and conduction via deep impurity level corresponding to activation energy ( $E_2$ ) in the high temperature range. At lower temperatures up to 100 °C, the rate of increase in the conductivity of these films with temperature is less, which may be due to decrease in the carrier mobility.

#### ii. Dielectric properties

The relative dielectric constant ( $\epsilon_r$ ) of the sandwich film is determined from the relation

$$\epsilon_r = \frac{Cd}{\epsilon_0 A}$$

Where,  $C$ = Capacitance,  $\epsilon_0 = 8.85 \times 10^{-12} \text{ Fm}^{-1}$ ,  $A$  is the area of the sandwich structure =  $4.16 \times 10^{-6} \text{ m}^2$  and  $d$  is the film thickness = 1500 Å in our case.

The dielectric constant ( $\epsilon_r$ ) of the CdS film is found to increase with increasing frequency and temperature as shown in Fig.4. This behaviour is attributed to the fact that at lower frequencies the dielectric constant depends on different types polarizations such as atomic, interfacial and electronic polarization but at higher frequencies the electronic polarization becomes dominant.

Also, the variation of the dielectric loss  $\tan\delta$  with frequency for the CdS thin film in the frequency range and temperature range (25 °C to 200 °C) for CdS films is shown in the Fig.5. The dielectric loss  $\tan\delta$  is found to increase with temperature but decrease with frequency. This is related to the fact that at higher temperatures the loss is dominated by thermally activated hopping of electrons whereas the effect dies out at low temperatures, resulting in a decrease or no

significant change at low temperatures [25]. This type of behaviour suggests a distribution of relaxation times in the CdS thin film system. The complex microstructure of films involving defects that may be present in the film such as cracks, micro voids, imperfections, defect centres, etc., at sufficiently high concentration give rise to defect states, both shallow and deep states. These states may be of acceptor type ( $D^0/D^+$ ) or donor type ( $D^-/D^0$ ), or with three charge states as  $D^+$ ,  $D^-$  and  $D^0$  [26]. These defects immensely affect the transport properties of the materials by acting as traps and recombination centres for carriers and also, some  $D^+/D^-$  centres in close proximity give rise to polar behaviour, which are responsible for the distributed dielectric relaxation. On subjecting the films to an electric field of varying frequency, the electrons hop between localized sites. The charge carriers moving between these sites hop from a donor to an acceptor state.

*iii. A.C. conductivity*

The a.c. conductivity is determined using the relation  $\sigma_{a.c.} = C \omega \tan \delta$  .....(3)

Where C is the capacitance,  $\omega$  is the angular frequency and  $\tan \delta$  is the loss tangent.

The dependence of  $\sigma_{a.c.}$  on temperature is given by the relation

$$\sigma_{a.c.} = \sigma_0 \exp(-E_{ac}/kT) \dots\dots\dots(4)$$

where  $\sigma_0$  is pre exponential factor, k is Boltzmann's constant and  $E_{ac}$  is the thermal activation energy.

Fig.6(a) shows the variation of a.c. conductivity with frequency at room temperature for CdS films grown at different constant substrate temperatures and Fig.6(b) gives the variation of a.c. conductivity with frequency at different temperatures (in the temperature range 25 °C to 200 °C) for CdS films grown at room temperature. It is evident from the figure that the a.c. conductivity increases with the increase in frequency and temperature. Two distinctly different regions are observed in the variation of a.c. conductivity with frequency, in the first region (10Hz - 22 kHz) the almost there is no change, whereas, in the second region (> 22 kHz) the change is more pronounced. This type of behaviour has been reported extensively for various other materials [27–29]. This is a feature of localized conduction where the a.c. conductivity increases with frequency. Contrary to this, in case of free band conduction the a.c. conductivity decreases with frequency [30]. This increase in a.c. conductivity with temperature also, evidences in support of thermally activated conduction processes, which we obtained in case of d.c. conductivity in section 3.2(i)

This type of variation of a.c. conductivity is ascribed to relaxations caused by the motion of electrons or atoms, which may involve hopping or tunneling between equilibrium sites, where there is an increase of carrier with increased temperature, which may be due to the release of trapped carriers with increase in thermal energy.

The a.c. conductivity is found to obey the universal relation

$$\sigma_{ac}(\omega) = A\omega^s \dots\dots\dots(5)$$

where A is a constant independent of frequency but weakly dependent on temperature.

The exponent s plays an important role in determining the nature of conduction.

This behaviour of temperature and frequency dependence of the a.c. conductivity has been interpreted by various theoretical models to explain mechanisms responsible for A.C. conduction.

The CBH model has been extensively applied to some chalcogenide semiconductors to explain the temperature-dependent properties. This model has been extensively applied to some chalcogenide semiconductors to explain the temperature-dependent properties.

In the correlated barrier hopping (CBH) model proposed by Pike [30] model, the electrons

in charged defect states hop over the Coulombic barrier whose height,  $W$ , is given as

$$W = W_m - (ne^2 / \pi\epsilon\epsilon_0 r) \text{-----(6)}$$

where  $W_m$  is the maximum barrier height,  $\epsilon$  the bulk dielectric constant,  $\epsilon_0$  the permittivity of free space,  $r$  the distance between hopping sites and  $n$  the number of electrons involved in a hop ( $n = 1$  and  $n = 2$  for the single polaron and bipolaron processes, respectively). In this model the ac conductivity is given by

$$\sigma(\omega) = \frac{\pi^3 \epsilon\epsilon_0 N N_p \omega (R_w^6)}{6} \text{-----(7)}$$

Where  $R_w$  is the inter-site separation, the frequency index is given by

$$s = 1 - \frac{6kT}{W_m + (kT \ln(\omega\tau_0))} \text{-----(9)}$$

It predicts that  $s$  should be less than 1, decreasing with increasing temperature. In the present study it is evident from the  $s$  versus  $T$  plot (Fig. 7) that  $s$  gradually decreases with temperature. The value of  $s$  is found to be in the range from 0.33 to 0.76 in the entire frequency range. It is observed that  $s$  increases with increasing frequency and decreases with the increase of temperature. This is quite in accordance with the correlated barrier hopping (CBH) model; hence the CBH model is the most suitable model for describing the conduction mechanism in the CdS thin film.

The QMT model ascribes a.c. conductivity due to a relaxation process arising from electronic or atomic tunnelling between equilibrium sites. It predicts the frequency exponent  $s$  to be frequency-dependent but independent of temperature.

The SPTM model explains a.c. conductivity in terms of trapped carriers at structural defects, i.e. small polarons, tunnelling between states lying close to the Fermi level. It predicts that  $s$  will increase with increasing temperature and that the tunnelling distance, and hence the a.c. conductivity, will decrease at high frequencies.

#### 4. CONCLUSIONS

Structural studies with XRD study revealed that the CdS thin film material is of crystalline nature having most intense peak along (002) plane orientation. The crystallite size was found to be between 167.6 nm to 282.2 nm, which increases with the temperature of deposition. The a.c conductivity of the film increases with temperature and frequency confirming thermally activated conduction from localised states. Also, the a.c. conduction is found to increase with the substrate temperature of deposition. The dielectric properties such as dielectric constant and dielectric loss are strongly dependent on temperature and frequency and indicate a distributed relaxation. The nature of the a.c. conduction parameter  $s$  is found to increase with frequency but decrease with temperature as per the theoretical prediction of the CBH model.

The Cole-Cole plots for each temperature were found to be single semicircular arcs with their centers lying below the real axis at certain angle and having non zero intersection with the real axis, a feature of multi relaxation behavior. The area under the impedance plots are found to decrease with increasing temperature of deposition, indicating that better conducting films are produced at higher temperatures.

## REFERENCES

1. Nair P. K., Nair M. T. S., Fernandez A., and Ocampo M. (1989), *J. Phys. D. Appl. Phys.* 22, 829.
2. Touskova J., Kindl D., and Tousek J. (1994), *phys. stat. sol. (a)* 142, 539.
3. Alivisatos A. P. (1996), *Science* 271, 933
4. Klein D. L., Roth R., Lim A. K. L. and Alivisatos (1997), A. P., *Nature (London)* 389, 699.
5. Sahay P. P., Nath R. K., and Tewari S. (2007), *Cryst. Res. Technol.* 42, No. 3, 275 – 280 / DOI 10.1002/crat.200610812.
6. Hasse M. A., Qiu J., DePuydt J. M., and Cheng H. (1991), *Appl. Phys. Lett.* 59, 1272.
7. Su B. and Choy K. L. (2000), *Thin Solid Films* 359, 160.
8. Byung-Sik Moon, Jae-Hyeong Lee, and Hakkee Jung (2006), *Thin Solid Films*, 511-512, 299.
9. Senthil K., Mangalaraj D., Narayandass Sa. K., and Adachi Sadao (2000), *Mat. Sci. Eng. B* 78, 53.
10. Oliva A. I., Solis-Canto O., Castro-Rodriguez R., and Quintana P. (2001), *Thin Solid Films* 391, 28.
11. Hoffmann Ph., Horn K., Bradshaw A. M., Johnson R. L., Fuchs D., and Cardona M. (1993), *Phys. Rev. B* 47, 1639.
12. Nishino J., Chatani S., Uotani Y., and Nosaka Y. (1999), *J. Electroanal. Chem.* 473, 217.
13. Bhattacharya R. and Saha S. (2008), *Pramana J. Phys.* 71, 187.
14. Maleki M., Ghamsari M. S., Mirdamadi S. and Ghasemzadeh R. (2007), *Semiconductor Physics, Quantum Electronics & Optoelectronics* 10, 30 .
15. Tiwari S. and Tiwari S. (2006), *Cryst. Res. Technol.* 41, 78.
16. El-Barry A.M.A., Atyia H.E. (2005), *Physica B* 368:1.
17. Elliott S.R. (1987) *Adv Phys* 36:135.
18. Padmssuvarna R., Raghavendra Rao K., Subbarangaiah K (2002), *Bull. Mater. Sci.* 25:647
19. Tewari S., Bhattacharjee A., Sahay P. P. (2009), *J. Mater. Sci.*, DOI 10.1007/s10853-008-3088-x
20. Sahay P. P., Tewari S., Nath R. K., Jha S. (2008), *Shamsuddin M., J. Mater. Sci.* 43:4534–4540 DOI 10.1007/s10853-008-2642-x
21. Sahay P. P., Jha S., and Shamsuddin M. (2002), *J. Mat. Sci. Lett.* 21, 923.
22. SHARMA B.L. (ed.), (1984) “Metal-semiconductor Schottky barrier junctions and their applications” (Plenum Press, New York).
23. Battisha I.K., Affy H.H., Abd El-Fattah G., Badr. Y., (2002), *Fizika*, A11, 31.
24. Ma Y.Y. and Bube R.H., (1977), *J. Electrochem. Sci.*, 124, 1430.
25. Pollak M. (1971), *Philos Mag* 23:519 .
26. Prabakar K, Narayandass SK, Mangalaraj D (2002) *Cryst Res Technol* 37:1094.
27. Mardare D, Rusu GI (2004) *J. Optoelectron. Adv. Mater.* 6:333.
28. Gaffar M.A., Abousehly A.M., Abu El-Fadl A, Mostafa M.M. (2006) *Cryst Res Technol* 41:1120.
29. Bhatangar V.K., Bhatia K.L. (1990) *J Non-Cryst Solids* 119:214.
30. Anwar M., Hogarth C.A. (1990) *J Mater Sci* 25:3906. doi: 10.1007/BF00582458.
31. Ghosh A. (1990) *Phys Rev B* 42:5665.
32. Pollak M., Pike G.E. (1972) *Phys Rev Lett* 28:1449.
33. Leclerc H.X. (1979) *J Phys* 40:27 .
34. Elliott S.R. (1977) *Philos Mag B* 36:1291.



35. Elliot S.R. (1978) Philos Mag B 36:129 .
36. Shimakawa K. (1982) Philos Mag B 46:123.
37. Pollak M., Pike G.E. (1972) Phys Rev Lett 28:1449.

Table:1 Variation of crystallite size with temperature of deposition

Substrate temperature of deposition <sup>0</sup> C	Crystallite size (nm)
300	167.6
373	182.4
473	258.3
573	282.2

Table:2 Thermal activation energies for CdS films deposited at different substrate temperatures.

Substrate temperature of deposition ( <sup>0</sup> C)	Activation energies (eV)	
	E <sub>1</sub> ( 25 – 100 <sup>0</sup> C )	E <sub>2</sub> ( 125 -200 <sup>0</sup> C )
Room temperature (25 <sup>0</sup> C)	0.29	0.126
100	0.27	0.182
<b>200</b>	<b>0.26</b>	<b>0.171</b>
<b>300</b>	<b>0.267</b>	<b>0.1173</b>

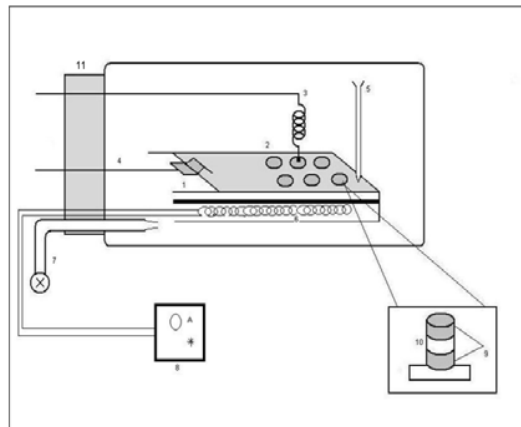


Fig.1 Schematic representation of inductively built unit for electrical characterisation

1. Substrate 2.Silver electrode 3.Upper Electrode contact 4. Lower Electrode contact 5. Thermocouple 6.Heater
- 7.Evacuating pump 8.Temperature controller 9. Silver electrodes 10.Sample film 11.Sealed Cap

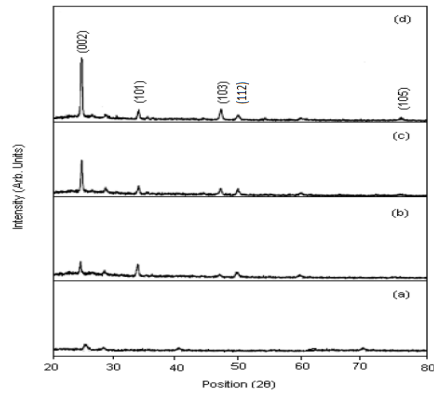


Fig.2 The XRD pattern of the CdS films of thickness 1500 Å deposited at different substrate temperatures RT (25<sup>0</sup>C), 100, 200 and 300<sup>0</sup>C.

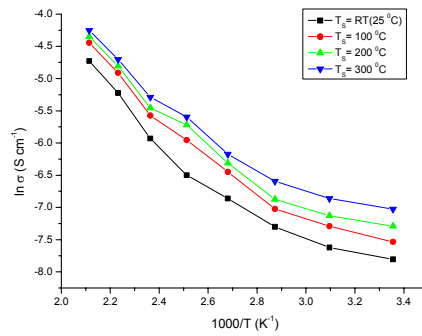


Fig.3 Variation of d.c. conductivity ( $\ln \sigma_{dc}$ ) with inverse temperature ( $1000/T$ ) for films

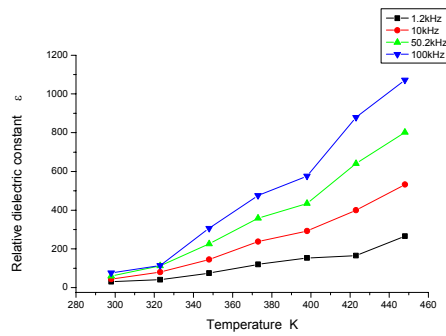


Fig.4 Variation of relative dielectric constant with temperature

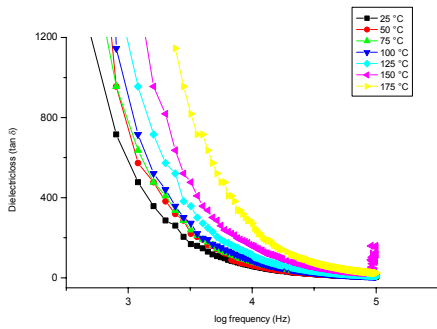


Fig.5 Variation of dielectric loss with frequency at different constant temperatures

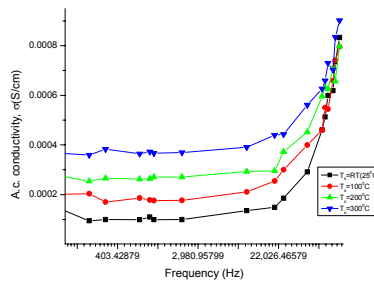


Fig.6(a) Variation of a.c. conductivity with frequency  $\sigma_{ac}$  at room temperature (25<sup>0</sup>C) for CdS films deposited at different constant temperatures

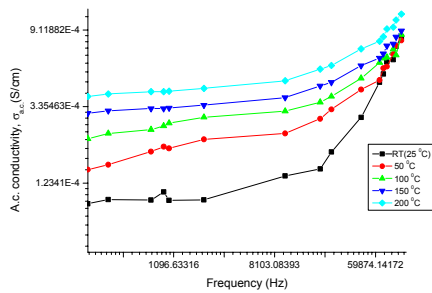


Fig.6(b) Variation of a.c. conductivity with frequency  $\sigma_{ac}$  versus frequency at different constant temperatures

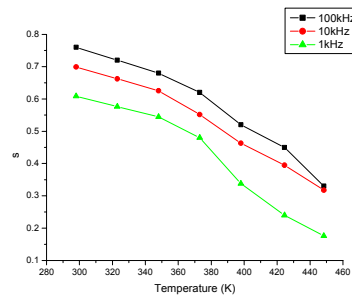


Fig.7 Variation of frequency index s with temperature

## **FABRICATION OF SOLAR CELLS BY HYDROTHERMALLY SYNTHESIZED TITANIA NANOTUBES AND CdS QUANTUM DOTS**

J. AKILAVASAN , J. BANDARA \*

*Institute of Fundamental Studies, Hanthana Road, Kandy, CP 20000, Sri Lanka.*

\*Corresponding Author, e-mail: [jayasundera@yahoo.com](mailto:jayasundera@yahoo.com)

### **ABSTRACT**

Hydrothermally synthesized titania nanotubes have been electrophoretically deposited onto a transparent conducting glass (F: SnO<sub>2</sub>). The electrode was sensitized with CdS quantum dots which were anchored on TiO<sub>2</sub> by Chemical Bath Deposition method. SEM analysis showed the formation of TiO<sub>2</sub> nanotubes with length of ~ 250 nm and diameter of ~ 10 nm. The cell performances were investigated with both iodide and polysulfide based electrolytes under AM 1.5 G irradiation. Solar cell showed better results, with polysulfide electrolyte compared to iodide electrolyte with overall efficiency of 0.16%, *J<sub>sc</sub>* of 1.02 mA/cm<sup>2</sup> and *V<sub>oc</sub>* of 520 mV.

Keywords: Hydrothermal; nanotubes; CdS Quantum Dot.

### **1. INTRODUCTION**

Quality of human life is largely depending on availability of energy sources. Recent critical moment of fossil fuel led development of alternative energy sources. Solar energy has been widely accepted best alternative energy source among many. However, the conventional devices used for harvesting solar energy are based on silicon and they involved with very expensive fabrication process. Therefore, in 1991, Michael Gratzel introduced a new type of solar cell called Dye Sensitized Solar Cells (DSSCs) which is a best alternative for conventional silicon based solar cells with economically viable cost [1]. However, the conversion efficiency of the DSSC must be improved a lot. Efficiency of a DSSC mainly depends on short circuit current density (*J<sub>sc</sub>*) and the open circuit voltage (*V<sub>oc</sub>*). *J<sub>sc</sub>* can be improved by introducing 1D nanostructures such as nanotubes and nanorods as they provide straight electron pathways reducing charge recombination [2]. In the DSSC configuration, dye molecules absorb light energy mainly in the visible region of the solar spectrum yet solar spectrum has wide band of infrared radiation energy. Inorganic semiconductor quantum dots (QDs) such as CdS, CdSe, InP having short band gap energy can be utilized as light absorbers instead of dye molecules [3-7]. Further, their band gap energies can be tuned by varying the particle size of the QD so that they could absorb light energy in the infrared region of the solar spectrum as well [8-11].

### **2. EXPERIMENTAL**

In this study titania nanotubes have been synthesized via hydrothermal method and it was electrophoretically deposited onto a conducting glass electrode as given in the literature with some modifications [12-21]. For the preparation of nanotubes, 2 g of titania nanoparticles (Degussa P25) were well dispersed in 10 M NaOH aqueous solution by stirring for half an hour followed by transferring into a Teflon lined autoclave and the chamber was kept at 150 °C for 48 hour. The resulted precipitate was washed with distilled water and 0.1 M HCl until pH reaches 8.5. Then, the precipitate was ultra-sonicated for 10 minutes for making TiO<sub>2</sub> nanotube suspension. Finally, titania nanotubes based working electrode was prepared by electrophoretic deposition method.

Conducting substrate (FTO from Solaronix, Sheet resistance 8 Ohm/cm<sup>2</sup>) was used as anode while Pt was used as counter electrode. The electrolyte for electrophoretic deposition was prepared by mixing titania nanotube suspension and methanol at 2:1 volume ratio followed by sonication for five minutes. Electrodeposition was carried out for 10 minutes at pH 8.5. After deposited, the substrate was kept at 130 °C for 10 minutes and sintered at 450 °C for 30 minutes. For the deposition of CdS by Chemical Bath Deposition (CBD) method, the electrode was immersed into the bath of 0.1 M Cd<sup>2+</sup> in ethanol for one minutes followed by washing in ethanol and successively immersed into bath of 0.1 M S<sup>2-</sup> in methanol for one minutes followed by washing in methanol. Successive immersion into Cd and S bath is called one cycle. The immersion procedure was repeated for six consecutive cycles. Finally, the electrode was heated under nitrogen at 300 °C for 15 minutes. The solar cell performance was measured at AM 1.5 G irradiation for effective area of 1 cm<sup>2</sup> with both polysulfide and iodide/triiodide based electrolytes. Polysulfide electrolyte was prepared as found in the literature with small modification [22].

### 3. RESULTS AND DISCUSSION

The I-V curves and the performance of the CdS QD sensitized solar cell with both polysulfide and iodine/triiodine electrolytes are shown in figure 1(a), (b) respectively and in Table 1. The tabulated readings are for six CBD cycles. As given in the table 1, the polysulfide based electrolyte showed  $J_{sc}$  of 1.02 mA/cm<sup>2</sup> and the  $V_{oc}$  of 502 mV with the overall efficiency of 0.16 % while, the iodide based electrolyte showed the  $J_{sc}$  of 0.16 mA/cm<sup>2</sup> and  $V_{oc}$  of 866 mV as given in the table 1. As shown in Figure 1, the polysulfide based electrolyte showed good and stable short circuit current density compared to iodide based electrolyte. However, iodide based electrolyte showed better open circuit voltage of ~ 860 mV due to high favourable redox potential compared to polysulfide electrolyte. However, iodide based electrolyte solar cells are found to be unstable which could be due to corrosive nature of metal chalcogen based semiconductors towards iodine.

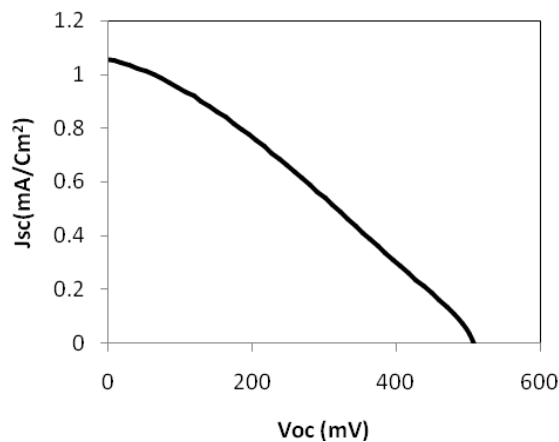


Figure 1(a): IV curve of the polysulfide based electrode

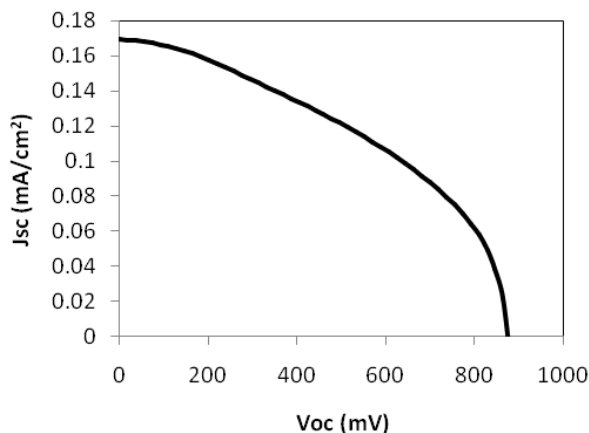


Figure 1(b): IV curve of the Iodide based electrode

Table 1: Cells parameters with both polysulfide and iodide/triiodide electrolytes

	Jsc (mA/cm <sup>2</sup> )	Voc(mV)	Fill Factor (FF) %	Efficiency (η) %
Polysulfide	1.02	502	32	0.16
Iodide/triiodide	0.16	866	44	0.06

Figure 2(a) shows the SEM image of the pristine titania nanotubes deposited onto a conducting substrate. SEM image reveals the formation of TiO<sub>2</sub> nanotubes with length of ~ 250 nm and diameter of ~ 10 nm. It can be clearly seen that the nanotubes have been deposited in random manner on FTO glass via electroporetic deposition method.

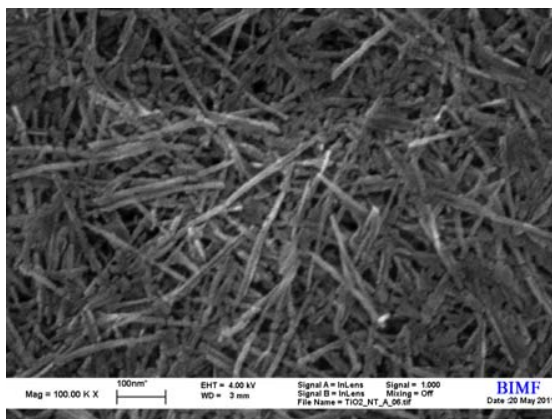


Figure 2(a) The SEM image of the titania nanotubes synthesized via hydrothermal method

Sensitization of CdS can be done in different ways such as chemical bath Deposition method, linking the CdS to titania nanotubes through linker molecules as provided in the literature [ 23-25]. However, in this study we followed CBD method for its simplicity. Figure 2(b) shows the CdS deposited titania nanotubes.

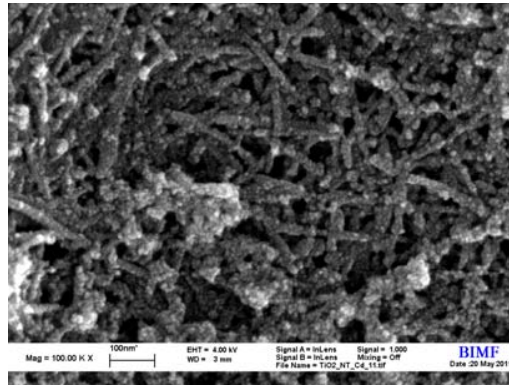


Figure 2(a) The SEM image of the titania nanotubes synthesized via hydrothermal method

As shown in figure 2(b), it can be clearly seen that CdS quantum dots have been deposited on titania nanotubes. By comparing the SEM images of the pristine and CdS deposited TiO<sub>2</sub> nanotubes, it was estimated the thickness of CdS layer as ~5 nm. Also, formation of large CdS aggregates/clusters was observed in few areas. The light absorption is increased when the number of CBD cycles increased, however the adsorption of CdS became saturated after six cycles. Depending on the bath concentration and the immersion time the saturation point could be varied [26]. After optimum point, it was observed some excess CdS aggregates were formed on the surface. We observed this after six CBD cycles in over study. In CBD method, each immersion process makes ions to penetrate into the nanotubes network. However, increasing number of cycles can causes two different kinds of CdS formations, ie formation of new similar CdS particles or formation of bigger CdS Particles by depositing onto already formed CdS particles [26].

The solar cell performances presented in this investigation for CdS and TiO<sub>2</sub> nanotube are relatively poor compared to the reported values which could be due to following facts: As shown in SEM image, TiO<sub>2</sub> nanotubes are randomly orientated and tightly packed. This random nature of the deposited nanotubes can reduce the cell performance when used in QDSSC due to higher charge recombination rates. Also, formation of aggregates/clusters of CdS may lead to poor solar cell performance. Therefore, methods should be developed to deposit nanotubes in a well aligned manner and defined CdS quantum dots on TiO<sub>2</sub> nanotubes.

#### 4. CONCLUSION

Quantum dot sensitized solar cells based on polysulfide electrolyte are very stable compared to iodide based electrolyte. The nanotubes synthesized must be defect free and a method should be developed to deposit titania nanotubes in an ordered manner. The deposited nanotubes seemed to be densely packed which may block the CdS reaching inner nanotubes.

## REFERENCES

1. B.O' Ragan, M. Gratzel, *Nature*, **1991**,353, 737-740
2. Elena Galoppini, Jonathan Rochford Hanhong Chen, Gaurav Saraf, Yicheng Lu, Anders Hagfeldt and Gerrit Boschloo, *J.Phys.Chem.B*, **2006**, 110(33), 16159-16161
3. Chengkun Xu, Paul H.Shin, Liangliang Cao, Jiamin Wu, and Di Gao *Chem.mater*, **2009**, 22(1),143-148
4. Elena Galoppini, Jonathan Rochford Hanhong Chen, Gaurav Saraf, Yicheng Lu, Anders Hagfeldt and Gerrit Boschloo, *J.Phys.Chem.B*, **2006**, 110(33), 16159-16161
5. G. Larramona, C.Chone, A. Jacob, D.Sakakura, B.Delatouche, D.Pere, X. Cieren, M.Nagino, R.Bayon, *Chem.mater*, **2006**, 18, 1688
6. K.Prabakar, T. Takahashi, T.Nakashima, Y.Kubota, A.Fujishima, J. Vac, *Sci.Technol.A*, **2006**, 24, 1613
7. K. Prabakar, T. Takahashi, T. Nazuka, K.Takashashi, Y. Kuboto, T. Nakashhima, A. Fujishima, J. Vac, *Sci. Technol.A*, **2007**, 25, 1188
8. K. Prabakar, S. Minkyu, S.Inyoung, K. Heeje, *J.Phys.D: Appl.Phys*, **2010**, 43, 012002
9. Anusorn Kongkand, Kevin Tvrdy, kensuke Takechi, masaru Kuno, Prashant V.Kamat, *J.Am.Chem.Soc*, **2008**, 130, 4007-4015
10. Prashant V. Kamat, *J.Phys.Chem.C*, **2008**, 112, 18737-18753
11. Jin Ho Bang, Prashant V. Kamat, *Adv.Funct.Mater*, **2010**, 20, 1970-1976
12. Gil-Sung Kim,hyung-kee Seo,V.P.Godble, Young-soon Kim, O-Bong Yang,Hyung-Shik Shin, *Electrochemistry Communication*,8,(**2006**),961-966
13. Jun-Nan Nian and Hsisheng Teng, *J.Phys. Chem.B*, 110,(**2006**),4193-4198
14. Gil-Sung Kim, Vijay P.Godbole, Hyung-Kee Seo,Young-Soon Kim, Hyung-Shik Shin, *Electrochemistry Communication*,8(**2006**), 471-474
15. LI Zhenhua,LIU Zhongqing, YAN Qingzhi,WANG Yichao,and GE Changchun, *Rare Metals*, 27(2), (**2008**),187
16. Tomoko Kasuga, Masayoshi Hiramatsu, Akihiko Hoson,Toru, and Koichi Niihara, *Langmuir*, 14,(1998), 3160-3163
17. Meili Wang, Gongbao Song, Jian Li, landing Miao, and Baoshu Zhang, *J.University of science and technology Beijing*,15(5),(**2008**),644
18. Yury V.Kolen'ko, Kirill A.Kovnir, Anton I.Gavrilov,Alexei V. Garshev, Johannes Frantii, Oleg I. Lebedev, Bulat R.Churagulov, Gustaaf Van Tendeloo and Masahiro Yoshimura, *J.Phys.Chem.B* 110,(**2006**),4030-4038
19. Xiaoming Sun and Yadong Li, *Chem.Eur.J*9(**2003**),2229-2238
20. Gil-Sung Kim, Young-Soon Kim, Hyung-Kee Seo and Hyung-Shik Shin, *Korean J.Chem.Eng*, 23(6), (**2006**),1037-1045
21. Li Zhao, Jiaguo Yu, JiaJie Fan, Pengcheng Zhai,Shiming Wang, *Electrochemistry communication*,11,(**2009**),2052-2055
22. Yuh-Lang Lee, Chi-Hsiu Chang, *Journal of Power Sources*, (**2008**), 185, 584-588
23. Prashant V.Kamat, *Journal of Phy. Chem. C*, (**2008**),112, 18737-18753
24. I.Robel, V.Subramanian, M.Kuno, Prashant V.Kamat, *Journal of Am.Chem.Soc.*,(**2006**), 128, 2385
25. A. Kongkanand, K.Tvrdy, K.Takechi, M. K.Kuno, Prashant V. Kamat, *Journal of Am.Chem.Soc.*, (**2008**), 130, 4007
26. David R. Baker, Prashant V.Kamat, *Adv.Funct. Mater.*, (**2009**), 19, 805-811



## POLYMER ELECTROLYTE BASED CdS QUANTUM DOT SENSITIZED SOLAR CELLS

K. KUMARAARACHCHI<sup>1</sup>, M.A. CAREEM<sup>1\*</sup>, G.K.R. SENADEERA<sup>2</sup>, T.M.W.J. BANDARA<sup>3</sup>,  
B.E. MELLANDER<sup>4</sup>

<sup>1</sup>Department of Physics, University of Peradeniya, Peradeniya, Sri Lanka

<sup>2</sup>Institute of Fundamental Studies, Kandy, Sri Lanka and Department of Physics,  
Open University of Sri Lanka, Polgolla, Sri Lanka

<sup>3</sup>Department of Physical Sciences, Rajarata University, Mihintale, Sri Lanka

<sup>4</sup>Applied Physics, Chalmers University of Technology, Gothenburg, Sweden

\*Corresponding Author, e-mail: mac@pdn.ac.lk

### ABSTRACT

Cadmium sulfide (CdS) quantum dots (QDs) are sequentially assembled on to a nanocrystalline TiO<sub>2</sub> films to prepare a TiO<sub>2</sub>/CdS photo-electrode by chemical bath deposition technique for QD-sensitized solar cell (QDSSC) applications. QDSSCs were fabricated with the above TiO<sub>2</sub>/CdS electrodes and gel type polymeric electrolytes based on either polyacrylonitrile (PAN), or poly(vinylidene fluoride) (PVdF) having sulfide (S<sup>2-</sup>/S<sub>x</sub><sup>2-</sup>), iodide (I<sup>-</sup>/I<sub>3</sub><sup>-</sup>) or ferric (Fe<sup>2+</sup>/Fe<sup>3+</sup>) redox couples. Among the gel electrolytes tested, the system having a composition of 19.6% PVdF: 15.7 % EC: 15.7% PC: 47% Na<sub>2</sub>S.8H<sub>2</sub>O: 2% S (by weight ratio) with the room temperature conductivity of 1.75 S m<sup>-1</sup> showed the optimum cell performance. The devices comprising with above electrolyte delivered an overall power conversion efficiency of 0.5-0.8 % with a short circuit current density of 2.6-2.8 mA cm<sup>-2</sup> and 390-410 mV open circuit voltage under the irradiance of 100 mW cm<sup>-1</sup> (AM 1.5). The fill factor of these devices were in the range of 0.43 - 0.73.

**Keywords:** Quantum dots, sensitized solar cells, CdS, solar cells, polymer electrolytes

### 1. INTRODUCTION

Dye sensitized solar cells (DSSCs) are potentially a low cost alternative to silicon solar cells to transfer the light energy of sun into electricity. Device with efficiencies of up to 11% have been reached in liquid electrolyte based ruthenium dye sensitized solar cells [1]. In these cells the dye is responsible for the light absorption and subsequent electron transfer reaction which are the main factors determining the light to electricity conversion efficiency. Some ruthenium complexes i.e. N3, N719 and black dye, etc., have produced good conversion efficiencies [2]. Beside these dye sensitized solar cells, narrow band gap semiconducting quantum dot sensitized solar cells (QDSSCs) have attracted attention as promising third-generation photovoltaic devices (3-8). In the form of quantum dots (QDs), the semiconductor sensitizers have very useful and often tunable optical properties: band gaps and their strong photo-response in the visible region. Even though it has been reported efficiencies up to 1.84 % for CdS QDSSCs with either iodine based or polysulfide based liquid electrolytes, the efficiencies are far unsatisfactory in many of the studies [5-7]. However due to the usage of liquid electrolytes in these cells, there exists many drawbacks especially towards instability and cell degradation due to the formation of gases, electrolyte leakage and side reactions [5, 9]. In order to overcome such problems, in this study we have explored the possibility of the use of several redox couples in a jellified electrolyte comprising either polyvinylene fluoride (PVdF) or polyacrylonitrile (PAN) in TiO<sub>2</sub>/CdS QDSSCs and here we report the preliminary results in this context.

## **2. EXPERIMENTAL**

### *2.1 Preparation of TiO<sub>2</sub>/CdS electrodes*

Dense, less porous (compact), films of TiO<sub>2</sub> were coated on fluorine doped conducting tin oxide (FTO) glasses (sheet resistance ~10 Ω/ square) by the following method. An ethanolic solution of titaniumtetra-isopropoxide Ti[OCH(CH<sub>3</sub>)<sub>3</sub>]<sub>4</sub> containing few drops of HNO<sub>3</sub> (pH 2) and 5 ml of acetic acid was spin coated on pre-cleaned FTO at 3000 rpm for 1 min. The films were then sintered at 500 °C for 30 minutes and cooled down to room temperature. The above procedure was then repeated to obtain ~100 nm thick compact layer of TiO<sub>2</sub>. Another paste of TiO<sub>2</sub> was produced by grinding 200 mg of TiO<sub>2</sub> (Degussa P-25) with 11 drops of Glacial acetic acid, one drop of Triton X-100 and about 2.00 ml of ethanol. This paste was spread on the previously prepared compact TiO<sub>2</sub> layer using the “doctor blade” technique and sintered again at 450 °C for 45 minutes and allowed to cool down to room temperature. This procedure results in a mesoporous TiO<sub>2</sub> layer with an average thickness of ~ 6 μm.

CdS quantum dots were deposited on to the mesoporous TiO<sub>2</sub> layer using the sequential chemical bath deposition (CBD) method as in reference 7. The TiO<sub>2</sub> electrode was first dipped in an ethanolic solution of 0.5 M Cd(NO<sub>3</sub>)<sub>2</sub> for 5 minutes and rinsed with ethanol and then dipped for another 5 minutes in a methanolic solution of 0.5 M Na<sub>2</sub>S and then rinsed again with methanol. This two step dipping process is considered as one CBD cycle. This procedure was repeated four times, i.e. 4 CBD cycles. After the deposition the samples were annealed at 400 °C for 10 min under N<sub>2</sub> atmosphere.

### *2.2 Fabrication of solar cells and characterization*

CdS QDSSCs were fabricated by sandwiching the above CdS adsorbed TiO<sub>2</sub> electrode with a Pt coated FTO glass incorporating a selected polymer electrolyte. The current-voltage (*I-V*) characteristics of the cells under the illumination of 100 mW cm<sup>-2</sup> (AM 1.5) simulated sunlight were recorded using a setup comprising a Keithly 2000 multimeter coupled with a Potentiostat/Galvanostat via computer controlled software. Xenon 500 lamp was used with AM 1.5 filters to obtain the simulated sunlight with above intensity. The active cell area was 0.25 cm<sup>2</sup>.

### *2.3 Preparation of gel type polymer electrolytes with various redox couples*

Appropriate amounts of the chemicals were dissolved in a selected solvent or plasticizer at a suitable temperature and the polymer was added to obtain gel type polymer electrolytes. After cooling down to room temperature the electrolytes were pressed between two clean glass plates to obtain thin flexible films. Poly(vinylidene fluoride) (PVdF) or Polyacrylonitrile (PAN) was used as the host polymer. The conductivities of different compositions of each electrolyte system were measured using the complex impedance technique to determine the composition with highest ionic conductivity. The performance of the QDSSC with the highest conductivity electrolyte of each system was investigated and the composition of the electrolyte was varied slightly until the optimum photoresponse was obtained. The compositions that showed optimum photo responses for the various electrolyte-redox couple systems tested and how the electrolyte systems were prepared are given below.

#### *2.3.1 PVdF based polymer electrolyte with polysulfide redox couple*

0.30 g of Na<sub>2</sub>S:xH<sub>2</sub>O was added to a mixture of 0.10 g of propylene carbonate (PC), 0.10 g of the plasticizer ethylene carbonate (EC), and 0.0125 g of S and the solution was stirred at 50 °C for 30 minutes. The resulted mixture was then allowed to cool down to 25 °C and 0.125 g of PVdF was added to it. The mixture was stirred well at 50 °C for about 30 minutes until the entire polymer has been dissolved. Then the mixture was allowed to cool to room temperature.

### 2.3.2 PVdF based polymer electrolyte with $Fe^{2+}/Fe^{3+}$ redox couple

PVdF (0.35 g),  $FeSO_4 \cdot 7 H_2O$  (0.02 g) and  $Fe_2(SO_4)_3 \cdot xH_2O$  (0.04 g) were added to 0.5 g of ethylene glycol and stirred for 5 minutes at 80 °C to get a homogenous viscous slurry. The resulting slurry was then cast on to a glass plate and pressed by another glass plate to get a thin polymer electrolyte.

### 2.3.3 PAN based polymer electrolyte with polysulfide redox couple.

0.20 g of solid EC was mixed with 0.2 g of PC and 0.05 g of PAN, 0.2 g of  $Na_2S \cdot xH_2O$  and 0.06 g of S were added to the mixture and stirred well for 5 minutes at 80 °C. The resulting slurry was then cast on to a glass plate and pressed with and another glass plate to obtain a thin film of polymer electrolyte.

### 2.3.4 PAN based polymer electrolyte with iodide redox couple.

The gel electrolyte system that was reported to have optimum photoresponse in reference 10 was used to test its performance in the QDSSC. This electrolyte was prepared by mixing 0.05 g of PAN, 0.03 g of  $MgI_2$ , 0.004g  $I_2$ , 0.2g PC and 0.2 g of EC in a glass bottle and magnetically stirred at 80 °C for 5 minutes. Thin films of polymer electrolyte were then obtained by the above mentioned method.

## 3. RESULTS AND DISCUSSION

Though it is difficult and challenging to see the sensitizing quantum dots on metal oxide surfaces, it is important to get the information on the size of semiconductor particles and their distribution over the host material ( $TiO_2$ ). Such information is also crucial for designing better deposited QD layers for improved photo responses of QDSSCs. Keeping this in mind we have performed scanning electron microscopic studies on both bare  $TiO_2$  and the CdS coated  $TiO_2$  layers. Figure 1 shows the SEM images of the bare  $TiO_2$  and the CdS coated  $TiO_2$  films used in our QDSSCs, obtained with a field emission scanning electron microscope (FE-SEM, JEOL, JSM6700F).

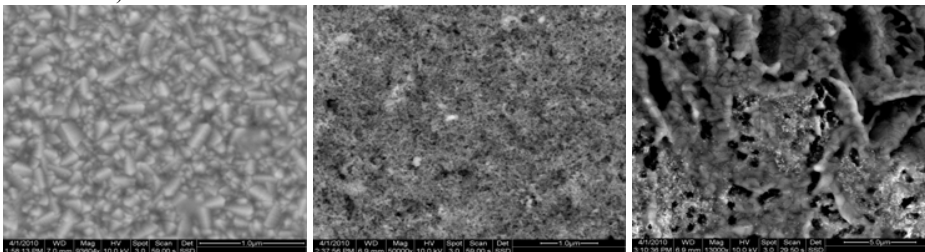


Fig 1: SEM images of (a) Compact and (b) Porous  $TiO_2$  (c)  $TiO_2/CdS$  films fabricated in aforementioned methods.

While the Figure 1(a) shows well-connected crack free but highly dense particle distribution in the thin  $TiO_2$  compact layer, Figure 1 (b) shows the porous structure of second thicker  $TiO_2$  layer suitable for the deposition of CdS. After depositing CdS, the bare surface of  $TiO_2$  particles appear to be covered by some smaller dots (CdS) which are more clearly seen at the edges of  $TiO_2$  clusters and many aggregated dots cover up almost the entire surface of  $TiO_2$  particles (Figure 1(c)).

Figure 2 shows the UV-Visible absorbance spectra obtained using a Cary 500 Spectrophotometer, of bare  $TiO_2$  (a) and the  $TiO_2$  porous layer incorporated with CdS quantum dots.

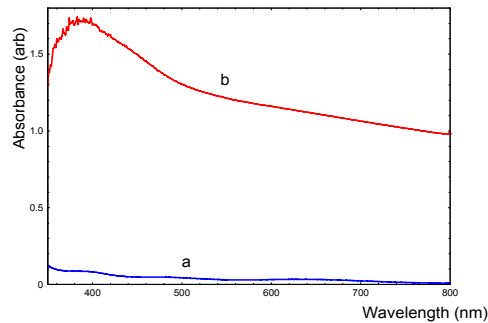


Fig 2: UV-VIS absorbance of (a) bare TiO<sub>2</sub> and (b) TiO<sub>2</sub> with CdS quantum dots incorporated by sequential chemical bath deposition

In order to obtain the best photo responses from the QD sensitized solar cells with polysulfide based electrolytes, the effect of the concentration of the sulfide in redox couple concentration, was investigated by varying the amount of Na<sub>2</sub>S:xH<sub>2</sub>O in the electrolyte. The conductivity values obtained from the complex impedance data and the corresponding photoresponses of the devices fabricated with different compositions in the electrolytes are shown in the Table 1. As can be seen from the table, the overall conductivity of the electrolyte increases with the amount of the Na<sub>2</sub>S.xH<sub>2</sub>O up to a certain value (0.39 g) reaching a maximum conductivity ~ 2.91 S m<sup>-1</sup> at room temperature. Further increment of the amount of the Na<sub>2</sub>S:xH<sub>2</sub>O in the electrolytes produces decrease in the overall conductivity of the polymer electrolytes. However, the photoresponse of the cells comprising the polymer electrolytes with highest conductivity does not correspond to the highest photoresponse. The highest photoresponse was obtained with the electrolyte having a lower conductivity of 1.75 S m<sup>-1</sup>. One of the possible reasons for this could be that the increase in the concentration of the cation in the electrolyte hinders the redox reactions in the electrolyte. On the other hand, there are several other governing factors such as viscosity, than the conductivity of the electrolyte, which really affect the penetration of the electrolyte into the mesopores of the QDs sensitized electrode.

Table 1: Variation of conductivity and photoresponse with varying amounts of Na<sub>2</sub>S: x H<sub>2</sub>O (Amount of EC = 0.1 g, PC = 0.1 g, PVdF = 0.125 g, S = 0.0125 g)

Amount of Na <sub>2</sub> S:xH <sub>2</sub> O (g)	Conductivity (S m <sup>-1</sup> )	J <sub>sc</sub> (mA cm <sup>-2</sup> )	V <sub>oc</sub> (mV)	FF (%)	Efficiency (%)
0.03	0.19				
0.06	0.28	0.32	430	35	0.05
0.09	0.45	1.00	350	46	0.16
0.30	1.75	2.60	410	73	0.78
0.36	1.70				
0.39	2.91	2.16	480	45	0.47
0.42	2.80				
0.45	2.22				
0.51	1.86				
0.60	1.76				

Figure 5 shows the typical photocurrent density –voltage ( $J$ - $V$ ) characteristics obtained from the QDSSCs fabricated by sandwiching with different polymer-redox couple electrolytes. The compositions of the electrolytes used in the cells are given under the experimental section 2.3. Typical solar cells parameters such as, the open circuit voltage ( $V_{oc}$ ), short circuit current density ( $J_{sc}$ ), fill factor (FF), and the efficiency ( $\eta$ ) obtained from the  $J$ - $V$  curves are shown in Table 1. The phot response curve shown for PVdF-sulphide electrolyte in Fig.5 and the corresponding parameter values given in Table 1 correspond to the best results obtained for this system. Generally the PVdF-sulphide electrolyte system showed the best cell performance with a short circuit current density 2.6-2.8 mA cm<sup>-2</sup>, open circuit voltage 390-410 mV, fill factor 0.43-0.73 and an overall power conversion efficiency of 0.5 – 0.8 %.

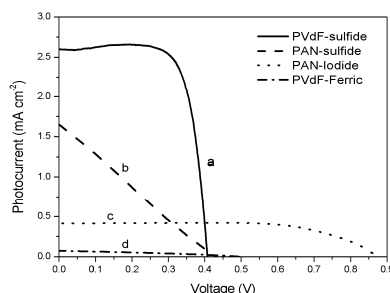


Figure 5. Photocurrent - voltage curves for solar cells fabricated with different polymer-redox couple electrolytes. (a) PVdF with Na<sub>2</sub>S/S (b) PAN with Na<sub>2</sub>S/S (c) PAN with MgI<sub>2</sub>/I<sub>2</sub> (d) PVdF with Fe<sup>2+</sup>/Fe<sup>3+</sup>

Table 2. Performance characteristics of solar cells with different electrolytes.

Electrolyte in the cell	$J_{sc}$ (mA cm <sup>-2</sup> )	$V_{oc}$ (mV)	FF%	Eff. %
(a) PVdF with Na <sub>2</sub> S/S	2.60	410	73	0.78
(b) PAN with Na <sub>2</sub> S/S	1.66	450	21	0.16
(c) PAN with MgI <sub>2</sub> /I <sub>2</sub>	0.40	880	69	0.24
(d) PVdF with Fe <sup>2+</sup> /Fe <sup>3+</sup>	0.08	495	33	0.01

It is clearly seen that the devices containing PVdF based polysulfide electrolyte exhibit better photoresponses than the devices with polymeric electrolytes with other than polysulfide redox couple. The PVdF-sulfide electrolyte system gives the best performance with a maximum efficiency of 0.78 %. It is also clearly seen from this study that the photo currents of the cells prepared with the polymer electrolytes based on both iodide and ferric redox couples are very poor compared to those of the devices with polysulfide based electrolyte. One of the reasons for these differences could be ascribed to the stability of the devices due to the reactivity of the redox couples with the S in the CdS QDs. Effect of the TiO<sub>2</sub> mesoporous film thickness on the cell performance was also studied by changing the film thickness with the same CdS sensitizer and it was observed that film thickness cannot be changed much due to the formations of aggregates of CdS crystallites thus reducing the direct contact areas between the bare TiO<sub>2</sub> surface and polysulfide electrolyte resulting in increase in shunt resistances at TiO<sub>2</sub>/CdS electrolyte interface. The photocurrent gradually increased with an increase in the film thickness to around ~ 6 μm, at which the best overall efficiency was obtained (Table1). Homogenous deposition of the CdS layer throughout the TiO<sub>2</sub> film would ensure the relatively thicker film to work better than the thinner

ones. However it becomes increasingly difficult to grow a homogenous layer of CdS sensitizer on the TiO<sub>2</sub> surface through mesoporous TiO<sub>2</sub> film thus reaching an optimum point as ~ 6 μm under our experimental conditions. However, the compact TiO<sub>2</sub> under layer was found to be critical in enhancing the performances of the devices by boosting both the photo-voltages and the fill factors possibly by reducing the recombination of the electrons from the QDs with S<sup>2-</sup>.

#### 4. CONCLUSION

On the basis of our preliminary results and the results reported recently it is certain that nanoscale semiconducting QDs can be used as a promising photocurrent generators for the next generation of solid state solar cells. Quasi solid state CdS QDSSC were fabricated with a maximum efficiency 0.78 % using PVdF-sulfide based electrolyte to overcome drawbacks of the wet type QDSSCs. However, the efficiencies of the fabricated quasi solid state QDSSC are low due to poor conductivity of the gel electrolytes compared to liquid type electrolytes. To further improve the photovoltaic performances, it is necessary to pay attention to the interfacial engineering between QDs and polymeric electrolytes which could yield higher  $V_{oc}$  and FF values.

#### 5. ACKNOWLEDGEMENTS

The authors wish to acknowledge financial support from the International Programmes in the Physical Sciences (IPPS), Uppsala University, Sweden and thank the University of Peradeniya, Sri Lanka for providing a Gate Mudaliyar A.G. Thilakarathne research fellowship to Kumudu Kumaraarachchi.

#### REFERENCES

1. Yasuo Chiba, Ashraful Islam, Yuki Watanabe, Ryoichi Komiya, Naoki Koide and Liyuan Han, "Dye-Sensitized Solar Cells with Conversion Efficiency of 11.1%", *Japanese Journal of Applied Physics*, 45 (25) (2006) pp. L638–L640
2. Michael Gratzel, "Recent Advances in Sensitized Mesoscopic Solar Cells", *Acc. Chem. Res.*, 42(11) (2009) 1788-1798
3. Yuh-Lang Lee and Yi-Siou Lo, "Highly Efficient Quantum-Dot-Sensitized Solar Cell Based on Co-Sensitization of CdS/CdSe", *Adv. Funct. Mater.* 19 (2009) 604–609
4. Prashant V. Kamat, "Quantum Dot Solar Cells. Semiconductor Nanocrystals as Light Harvesters", *J. Phys. Chem. C* 112 (2008) 18737–18753
5. Yuh-Lang Lee, Chi-Hsiu Chang, "Efficient polysulfide electrolyte for CdS quantum-dot sensitized solar cells", *Journal of Power Sources*, 185 (2008) 584–588.
6. Sheng-Qiang Fan, Duckhyun Kim, Jeum-Jong Kim, Dong Woon Jung, Sang Ook Kang, Jaejung Ko, "Highly efficient CdSe quantum-dot-sensitized TiO<sub>2</sub> photoelectrodes for solar cell applications", *Electrochemistry Communications*, 11 (2009) 1337–1339
7. Chi-Hsiu Chang and Yuh-Lang Lee, "Chemical bath deposition of CdS quantum dots onto mesoscopic TiO<sub>2</sub> films for application in quantum-dot-sensitized solar cells", *Applied Physics Letters*, 91(2007) 053503
8. Quanxin Zhang, Yiduo Zhang, Shuqing Huang, Xiaoming Huang, Yanhong Luo, Qingbo Meng, Dongmei Li, "Application of carbon counter electrode on CdS quantum dot sensitized solar cells", *Electrochemistry Communications*, 12 (2010) pp 327 – 330.
9. S. Biswas, M.F. Hossain, T. Takahashi, "Fabrication of Gratzel Solar Cell with CdS/TiO<sub>2</sub> bilayered photoelectrode", *Thin Solid Films*, 517(2008) pp 1284 -1288.
10. T.M.W.J. Bandara, M. A. K. L. Dissanayake, I. Albinsson, B. -E. Mellander, "Dye-sensitized, nano-porous TiO<sub>2</sub> solar cell with poly(acrylonitrile): MgI<sub>2</sub> plasticized electrolyte", *J. Power Sources*, 195, 11 (2010) 3730-3734.

## SURFACE AND THIN-FILM ANALYSIS OF CdCl<sub>2</sub> TREATED CdS/CdTe LAYERS FOR SOLAR CELLS

K. ABUEL-RUB<sup>A,B</sup>, S-R. HAHN<sup>A,\*</sup>, S. TARI<sup>A</sup>, M.A.K. L. DISSANAYAKE<sup>C</sup>

<sup>a</sup> Department of Physics, University of Illinois at Chicago, 845 W. Taylor St. Chicago, IL 60607, USA

<sup>b</sup> Department of Physics, Jordan University of Science & Technology, Irbid, Jordan

<sup>c</sup> Department of Physics, University of Peradeniya, Peradeniya, Sri Lanka

\* Corresponding Author. e-mail: srhahn@uic.edu

### ABSTRACT

Scanning electron microscopy (SEM) and x-ray photoelectron spectroscopy (XPS) were used to investigate the morphological and the chemical surface properties of CdS/CdTe thin film solar cells. CdS was deposited on indium tin oxides (ITO) substrate by chemical bath deposition (CBD). CdTe was deposited on CdS by the physical vapor deposition (PVD). Post anneal with and without supersaturated CdCl<sub>2</sub> solution was conducted on CdS/CdTe solar cells. Grain sizes and surface oxidations were investigated as a function of the annealing temperature. It was found that annealing the supersaturated CdCl<sub>2</sub> samples increased the grain sizes as well as roughness of the films and reduced the surface oxidation. SEM monographs show supersaturated CdCl<sub>2</sub> samples exhibited recrystallization and a progressive increase in grain sizes upon annealing. The grain sizes of the supersaturated CdCl<sub>2</sub> samples increased up to about 3-4 μm when annealed at 410 °C. XPS spectra for the Cd 3d, the Te 3d and the S 2p core-levels were recorded and analyzed for three cases: a) as grown structures b) CdCl<sub>2</sub> supersaturated structures annealed at different temperatures and c) structures annealed at different temperatures without CdCl<sub>2</sub> treatment. Te 3d related oxide peaks were observed in the XPS spectra of the as grown samples. The XPS spectra clearly indicates that annealing the CdCl<sub>2</sub> supersaturated samples removes TeO<sub>3</sub> peaks, while annealing the structures without CdCl<sub>2</sub> treatment enhances the TeO<sub>3</sub> peaks (see Fig 1).

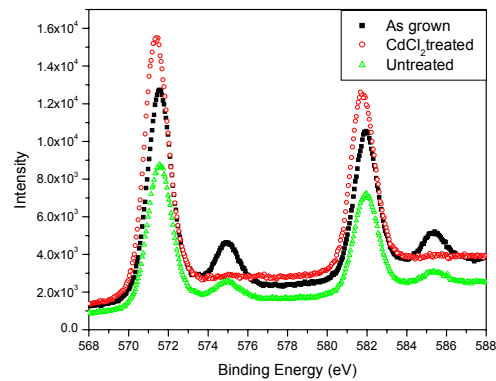


**Figure 1.** XPS spectra of the Te 3d core-level for the as grown and the untreated and the CdCl<sub>2</sub> treated CdTe film annealed at 420 °C.

## STRUCTURAL AND OPTICAL CHARACTERIZATION OF $\text{In}_2\text{S}_3$ FILMS DEPOSITED BY SILAR METHOD

E. TURAN<sup>1</sup>, T. TASKOPRU<sup>1,2\*</sup>, M. ZOR<sup>1</sup>, M. KUL<sup>1</sup>, A. S. AYBEK<sup>1</sup>

<sup>1</sup> Department of Physics, Anadolu University, Eskişehir 26470, Turkey

<sup>2</sup> Department of Physics, ÇankırıKaratekin University, Çankırı 18100, Turkey

\*Corresponding Author, e- mail: [ttaskopru@anadolu.edu.tr](mailto:ttaskopru@anadolu.edu.tr)

### ABSTRACT

Indium sulphide ( $\text{In}_2\text{S}_3$ ) is a compound semiconductor comprising of group III–VI elements which are being currently investigated due to its unique catalytic, optical, electronic, gas sensing properties, optoelectronic and photovoltaic potential applications [1-4]. The production of  $\text{In}_2\text{S}_3$  films by using suitable techniques still remains a future challenge and researchers always search alternative low cost deposition techniques. Successive ionic layer adsorption and reaction (SILAR) is a solution method to deposit a variety of compound materials and has some advantages, such as low cost, low deposition temperature, highly feasible for large area deposition and good control over deposition process along with film thickness.

The aim of the present work is to apply the SILAR method for preparing  $\text{In}_2\text{S}_3$  films and to investigate the structural and optical properties of the samples.

For the deposition of  $\text{In}_2\text{S}_3$  films, 0.01 M  $\text{InCl}_3$  solution (pH=8) is used as cationic precursor and 0.01 M  $\text{Na}_2\text{S}\cdot 5\text{H}_2\text{O}$  solution (pH=12) is used as anionic precursor. As rinsing agent, double deionized water is used as well as for preparing solutions. The deposition was carried out for 40, 50, 60, 80, 100 and 200 SILAR cycles at room temperature. All of the as-deposited films were annealed at 400°C for one hour in air.

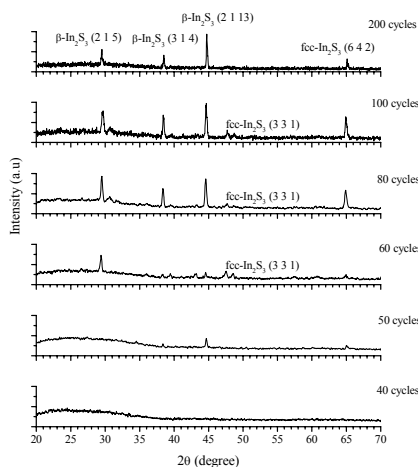


Fig. 1. X-ray diffraction patterns for  $\text{In}_2\text{S}_3$  films with different SILAR growth cycles.

X-ray diffractions of the films, as shown in Fig. 1, indicate the formation of  $\text{In}_2\text{S}_3$  films deposited at different SILAR cycles. The results show a mixture of tetragonal  $\beta\text{-In}_2\text{S}_3$  and face-centred cubic  $\beta\text{-In}_2\text{S}_3$  phases. Further increasing the SILAR cycle number 200, it can easily be



seen that the crystallinity has improved with the preferred orientation along with the [2 1 13] direction and tetragonal  $\beta$ - $\text{In}_2\text{S}_3$  phase dominates the structure as well.

FESEM images of  $\text{In}_2\text{S}_3$  films deposited at 50 and 200 SILAR cycles is shown in Fig. 2. The results show that at lower SILAR cycles, the samples consist of tetragonal  $\beta$ - $\text{In}_2\text{S}_3$  and fcc $\beta$ - $\text{In}_2\text{S}_3$  structures over the surface. Increasing the SILAR cycles, we observe that the tetragonal  $\beta$ - $\text{In}_2\text{S}_3$  structure dominates in the full image with mainly nanoflakes.

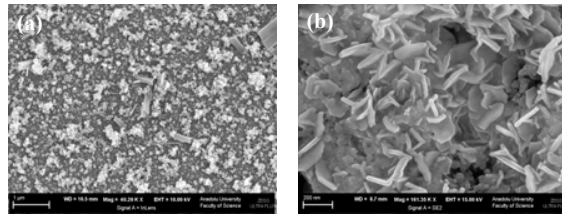


Fig. 2. FESEM images of  $\text{In}_2\text{S}_3$  films.

The optical properties of  $\text{In}_2\text{S}_3$  films have been studied by using optical absorbance and transmittance measurements as a function of wavelength between 190 and 3300 nm. The studies on the optical properties show that the direct band gap value decreases from 2.92 eV to 2.37 eV. The red shift is observed in the absorption edge as the number of SILAR cycles increases.

Comparing the FESEM results with X-ray results, it could be said that the crystallinity improves by increasing the SILAR cycles and tetragonal  $\beta$ - $\text{In}_2\text{S}_3$  phase dominates at higher SILAR cycles that is seen clearly in Fig 2.b. The SILAR method gives the possibility for a controllable deposition of  $\text{In}_2\text{S}_3$  films of preferred phase and is also favourable for practical applications considering large-scale synthesis, fabrication cost and facile preparation process.

## REFERENCES

1. G.X. Cao, Y.B. Zhao, Z.S. Wu, *J. Alloys Compd.* 472 (2009) 325–327.
2. P.U. Sastry, D.P. Dutta, *J. Alloys Compd.* 487 (2009) 351–353.
3. H. Zhu, X.L. Wang, W. Yang, F. Yang, X.R. Yang, *Mater. Res. Bull.* 44 (2009) 2033–2039.
4. S. Lazzez, K.B. Mahmoud, *J. Alloys Compd.* 476 (2009) 769–773.

## FABRICATION OF CuO/Cu<sub>2</sub>O HETEROJUNCTION AND ITS LOCAL STRUCTURAL CHARACTERIZATION

R. P. WIJESUNDERA<sup>1,2\*</sup> AND M. HIDAKA<sup>2</sup>

<sup>1</sup> Department of Physics, University of Kelaniya, Kelaniya, Sri Lanka

<sup>2</sup> Department of Physics, Graduate School of Science, Kyushu University, 33, Fukuoka 812-8581, Japan

\*Corresponding Author, e-mail: palitha@kln.ac.lk

### ABSTRACT

Cuprous oxide (Cu<sub>2</sub>O) thin films on Ti substrate were potentiostatically electrodeposited at -200 mV in an acetate bath. For the growth of p-type cupric oxide (CuO) thin films, Cu<sub>2</sub>O thin films were annealed at 500 °C for 30 min in air. In order to fabricate CuO/Cu<sub>2</sub>O heterojunction, thin film of Cu<sub>2</sub>O was potentiostatically electrodeposited on Ti/CuO electrode. Deposits were characterized by using X-ray diffraction (XRD) and scanning electron micrographs (SEM). Results revealed that well covered n-type polycrystalline Cu<sub>2</sub>O thin film can be electrodeposited on Ti/CuO electrode at -550 mV Vs the SCE in an acetate bath. The CuO/Cu<sub>2</sub>O heterojunction gave the open circuit voltage ( $V_{oc}$ ) of 210 mV and short circuit current ( $I_{sc}$ ) of 310  $\mu\text{A}/\text{cm}^2$ . Layer by layer structural properties of the electrodeposited Ti/CuO/Cu<sub>2</sub>O thin film heterojunction have been studied by means of the XRD and the X-ray absorption spectra (XAS) with different grazing angles of the incident X-ray beam. Results reveal that Cu<sub>2</sub>O and CuO are high quality semiconducting thin films but amorphous structure is formed between CuO and Cu<sub>2</sub>O while Cu<sub>2</sub>O deposition on CuO. It can be expected that amorphous structure formed in the middle of the CuO/Cu<sub>2</sub>O heterojunction attributes better lattice matching between CuO and Cu<sub>2</sub>O interface.

### 1. INTRODUCTION

Solar energy is considered as the most promising alternative energy source to replace environmentally distractive fossil fuel. However, it is a challenging task to develop solar energy converting devices using low cost techniques and environmentally friendly materials. Cuprous oxide (Cu<sub>2</sub>O) and cupric oxide (CuO) are possible candidates for photovoltaic applications because of their reasonable electrical and optical properties [1, 2]. Among the various Cu<sub>2</sub>O deposition techniques [3–7], electrodeposition [8–11] is an attractive one because of its simplicity, low cost, low-temperature process and possibility of making large area thin films. Although fabrication of Cu<sub>2</sub>O and CuO based heterojunctions with other materials have been reported [11–16], investigations of CuO/Cu<sub>2</sub>O heterojunction are very limited in the literature because of inability to grow n-type Cu<sub>2</sub>O (or CuO). Both Cu<sub>2</sub>O and CuO have been considered as nonstoichiometric p-type semiconductors till Siripala *et al* introduced n-type Cu<sub>2</sub>O in 1986. They have reported that electrodeposited Cu<sub>2</sub>O films in slightly acidic aqueous baths behave as n-type conductivity [17], whereas all the other methods yield p-type material. In the present investigation, the photoactive p-CuO/n-Cu<sub>2</sub>O heterojunction has been fabricated using the potentiostatical electrodeposition technique, and layer by layer structural information of the electrodeposited CuO/Cu<sub>2</sub>O heterojunction have been studied by means of the X-ray diffraction (XRD) and the X-ray absorption spectra (XAS) with different grazing angles of the incident X-ray beam using the synchrotron radiation.

### 2. EXPERIMENTAL

Cu<sub>2</sub>O thin films on Ti substrate were potentiostatically electrodeposited at -200 mV Vs saturated calomel electrode (SCE) in a three electrode electrochemical cell containing 0.1 M sodium acetate and 0.01 M cupric acetate aqueous bath. Cupric acetate are used as Cu<sup>2+</sup> source while sodium acetate are added to the solution making complexes releasing copper ions slowly

into the medium allowing a uniform growth of  $\text{Cu}_2\text{O}$  thin films. The counter electrode was a platinum plate and reference electrode was SCE. Temperature, pH and stirring speed of the baths were maintained at values of  $55\text{ }^\circ\text{C}$ , 6.6 (normal pH of the bath) and 300 rev./min respectively.  $\text{Ti}/\text{Cu}_2\text{O}$  thin films were annealed at  $500\text{ }^\circ\text{C}$  for 30 min in air for the growth of p-type  $\text{CuO}$  thin films. In order to fabricate  $\text{CuO}/\text{Cu}_2\text{O}$  heterojunction, thin films of  $\text{Cu}_2\text{O}$  were potentiostatically electrodeposited on  $\text{Ti}/\text{CuO}$  electrodes at different deposition potentials Vs SCE while maintaining the same electrolytic conditions, which used to deposit  $\text{Cu}_2\text{O}$  on the Ti substrate. Deposition period was varied from 240 min to 120 min in order to obtain sufficient thickness of the films. For the completion of the device, very thin gold (Au) grid ( $1\times 8\text{ mm}^2$ ) was deposited on the  $\text{Cu}_2\text{O}$  thin film in order to complete front contact to the  $\text{CuO}/\text{Cu}_2\text{O}$  heterojunction. The bulk structure, the surface morphology and the optoelectronic properties of the  $\text{Cu}_2\text{O}/\text{CuO}$  heterojunction were determined by the XRD measurements using a Rigaku (Model RADA, CN2155D5) X-ray diffractometer, the SEMs using a JEOL (Model JSM-6060) scanning electron microscope and dark and light current–voltage characteristics, respectively. In order to study the layer by layer structural deformation localized around Cu ions in the electrodeposited  $\text{CuO}/\text{Cu}_2\text{O}$  heterojunction, grazing angle measurements of XRD and XAS near the Cu–K edge were obtained using synchrotron radiations at the Pohang Light Source (2.5 GeV) of the Pohang Accelerator Laboratory (Korea).

### 3. RESULTS AND DISCUSSION

Bulk structures of the electrodeposited films on  $\text{Ti}/\text{CuO}$  were studied by the XRD patterns. Fig. 1 shows the XRD patterns of the films deposited on  $\text{Ti}/\text{CuO}$  electrodes at the deposition potentials of -250, -400, -550 and -700 mV Vs SCE. XRD patterns evidence the formation of  $\text{Cu}_2\text{O}$  for all deposition potentials on  $\text{Ti}/\text{CuO}$  electrodes while Cu deposition starts in addition to the  $\text{Cu}_2\text{O}$  when the film deposited at -700 mV Vs SCE. Single phase  $\text{Cu}_2\text{O}$  are possible at the deposition potentials less than -700 mV Vs SCE. XRD patterns further show that peak intensities corresponding atomic reflection of  $\text{Cu}_2\text{O}$  increase with deposition potential. It indicates that amount of  $\text{Cu}_2\text{O}$  deposit is increased by increasing deposition potential. This is further studied by using SEMs.

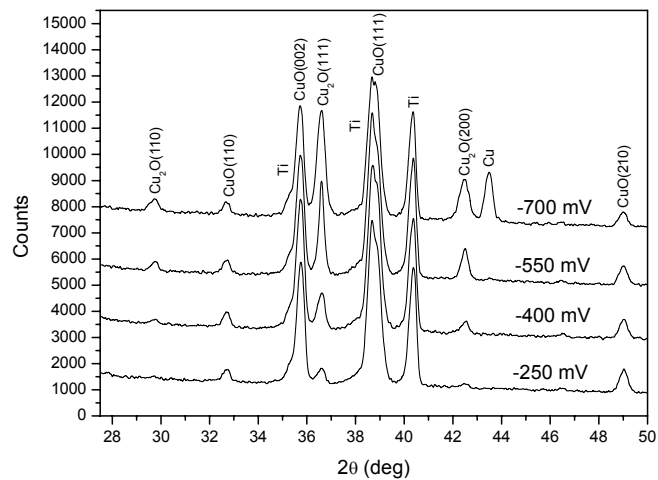


Figure 1. XRD pattern of thin films electrodeposited at -250, -400, -550 and -700 mV Vs SCE on the  $\text{Ti}/\text{CuO}$  electrode

The surface morphology of the films prepared on the Ti/CuO electrode at the different deposition potentials was studied using the SEMs in order to identify the Cu<sub>2</sub>O thin film deposition conditions on Ti/CuO electrode. Figs. 2(a) to (b) show the SEMs of Cu<sub>2</sub>O films deposited on the Ti/CuO at -250 and -550 mV Vs SCE. Fig. 2(a) shows the cubic shape Cu<sub>2</sub>O grains on the CuO film and Figs. 2(b) shows that the amount of Cu<sub>2</sub>O increases with increasing the deposition potential. The SEMs reveal that the well covered Cu<sub>2</sub>O layer can be deposited on Ti/CuO electrode under the potentiostatical condition of -550 mV Vs SCE. Grain size of the Cu<sub>2</sub>O deposited on Ti substrate is in the range of ~ 1-2 μm as shown in Fig. 2(a) while it is lower to 1 μm when Cu<sub>2</sub>O deposited on CuO at the deposition potential of -550 mV Vs SCE.

XRD and SEM reveal that well-covered single phase polycrystalline Cu<sub>2</sub>O thin film on the Ti/CuO electrode can be possible at the deposition potential of -550 mV Vs SCE in an acetate bath. Structural matching of two semiconductors is very essential for fabricating a heterojunction. In general, the cubic-like Cu<sub>2</sub>O grains and the monoclinic-like CuO grains are not match with each other to make the CuO/Cu<sub>2</sub>O heterojunction. However, the electrodeposition technique produces the good matching of the Cu<sub>2</sub>O grains to the monoclinic-like CuO grains. The shape of the grains can be easily changed when the electrodeposition technique is used to grow a semiconductor. The electrodeposition is a very good tool to fabricate the heterojunctions as it does not depend on the grain shape of the material. Further, the SEMs of the Cu<sub>2</sub>O/CuO heterojunction suggested that the Cu<sub>2</sub>O polycrystalline grains are grown from the surfaces of the CuO polycrystalline grains and make the good contacts between two thin film layers.

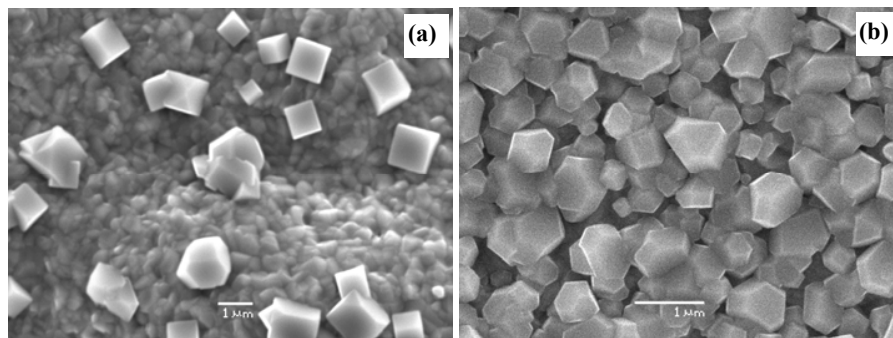


Figure 2. SEMs of Cu<sub>2</sub>O thin films electrodeposited at (a) -250 mV and (b) -550 mV Vs SCE on the Ti/CuO

Photoactivity of the CuO/Cu<sub>2</sub>O heterojunction was tested using dark and light current-voltage measurements under the white light illumination of 90 mWcm<sup>-2</sup>. The electrical contacts to the Cu<sub>2</sub>O surface (front contacts) is made using mechanically pressed transparent ITO plate to the Au grid, where the Ti substrate serves as back electrical contact to the CuO surface. Ti/CuO/Cu<sub>2</sub>O/Au heterojunction gave the open circuit voltage ( $V_{oc}$ ) of 210 mV, short circuit current ( $J_{sc}$ ) of 310 μA cm<sup>2</sup>. This initial stage performance of the p-CuO/n-Cu<sub>2</sub>O heterojunction is encouraging and can be enhanced photoactive properties by depositing very thin Cu<sub>2</sub>O window layer leading to minimize the high resistance of the electrodeposited Cu<sub>2</sub>O and choosing better ohmic contact to the Cu<sub>2</sub>O. Best ohmic contact to the n-type Cu<sub>2</sub>O may be Al but not the Au. This will be subject for future investigations.

CuO/Cu<sub>2</sub>O heterojunction was further investigated by means of XRD and XAS at the Cu-K edge with grazing angle measurements. Layer by layer structural information of the CuO/Cu<sub>2</sub>O

heterojunction can be studied with grazing angle measurements. Fig. 3 (a) shows the grazing angle ( $\phi$ ) dependency of the X-ray diffraction patterns of the CuO/Cu<sub>2</sub>O heterojunction. The Ti peak of highest intensity at  $2\theta = 40.23$  degree is indexed by (0,1,1) and (1,1,1) reflections of hexagonal structure and were not observed below  $\phi \sim 2.0$  degree. On the other hand, the reflections of Cu<sub>2</sub>O and CuO structures are observed in all the grazing angles, though the reflections of Cu<sub>2</sub>O structure shows the different grazing angle dependence to those of the CuO ones. Fig. 3(b) shows grazing angle dependency of (1,1,1) reflection of Cu<sub>2</sub>O, (1,1,-1) reflection of CuO, (1,1,1) reflection of Ti, and intensity ratio of Cu<sub>2</sub>O(1,1,1) and CuO(1,1,-1) reflections. With increasing the grazing angle, CuO layer can be observed gradually, as Ti-reflections. The bulk structural information of Cu<sub>2</sub>O layer can be obtained for the grazing angles around 2.5 degree since it produces highest intensity of (1,1,1) reflection of Cu<sub>2</sub>O. It reveals that it is possible to obtain optimum structural information within the Cu<sub>2</sub>O/CuO junction region in addition to the Cu<sub>2</sub>O, CuO, and Ti for the grazing angles slightly greater than 2.5 degree. Further it is found that the intensity ratio of the (1,1,1) reflection and (1,1,-1) reflection is approximately constant above  $\phi = 5.0$  degree, in contrast to the intensity of the Ti-reflection. It shows that the bulk structural information of the device (Cu<sub>2</sub>O and CuO) can be studied at the grazing angle of 5 degree or greater.

In order to study the structural deformation localized around Cu ions in the CuO/Cu<sub>2</sub>O heterojunction, measurements of XAS at the Cu-K edge for the bi-layer thin film structure were carried out. The XAS were measured near the Cu-K edge for the electrodeposited bi-layer thin films, by using synchrotron radiation at the Pohang Light Source (2.5 GeV). Double crystal monochromators of Si (1,1,1) gave an energy resolution  $\Delta E$  to be less than about 0.2 eV in the respective measurements for the XAS near the Cu-K edge. The incident X-ray photons ( $I_0$ ) were detected with an ionic chamber set in front of the thin film, and the X-ray fluorescence photons ( $I_F$ ) emitted from the specimen surface were simultaneously detected with an X-ray

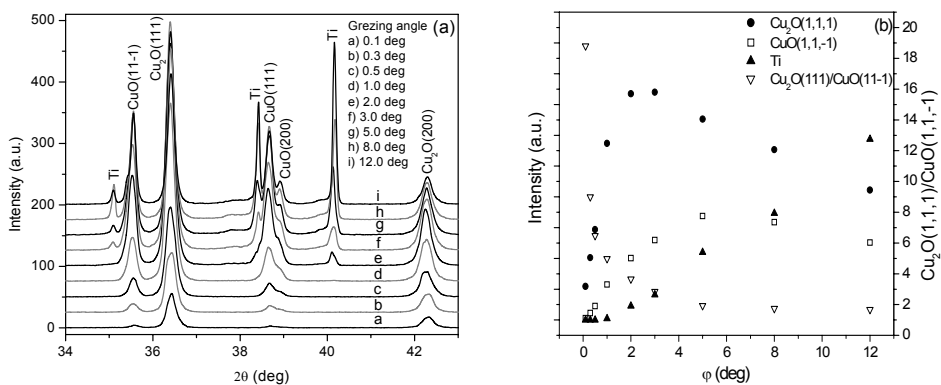


Figure 3. Grazing angle dependency of the (a) X-ray diffraction patterns for the electrodeposited Ti/CuO/Cu<sub>2</sub>O heterojunction and (b) (1,1,1) reflection of the Cu<sub>2</sub>O, (1,1,-1) reflection of the CuO structure, (1,1,1) reflection of Ti and intensity ratio of Cu<sub>2</sub>O (1,1,1) and CuO (1,1,-1) reflections

fluorescence detector (Canberra Planar Silicon detector; PD3000). During measurements of the XAS, the surface of the thin films was always set with a respective grazing angle from 0.3 to 10.0 degrees to the incident X-ray beam, of which a size was about 5 mm in horizontal and 0.2 mm in vertical to the electron orbit of the accelerator. The structural deformation localized around

Cu ions of the CuO/Cu<sub>2</sub>O heterojunction can be investigated from Extended X-ray Absorption Fine Structure (EXAFS). Fig. 4 shows the expanded partial XAS at Cu-K edge of Ti/CuO/Cu<sub>2</sub>O heterojunction at  $\phi = 0.3$  to 10.0 degree. The electrodeposited CuO/Cu<sub>2</sub>O thin film heterojunction includes Cu ions sited at different structures of Cu<sub>2</sub>O and CuO. The spectra result from a convoluted XAS induced by interference between the X-ray photoelectron waves emitted by X-ray absorbing Cu ions and the backscattering waves of its surrounding ions for both structures. The grazing angle dependency of the XAS suggests that the incident X-ray beam penetrate the thin films of Cu<sub>2</sub>O and CuO grains by the different path distance. It can be considered that the XAS measurements obtained at low grazing angles (0.3 and 0.5 degree) should be mainly the XAS of Cu<sub>2</sub>O thin film, which is the front layer of the heterojunction. Therefore, the XAS

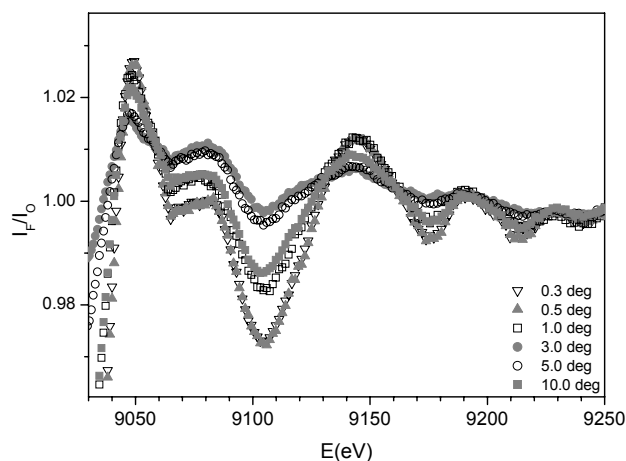


Figure 4. Oscillating amplitudes  $I_F/I_0$  of the X-ray absorption spectra of the Ti/CuO/Cu<sub>2</sub>O heterojunction at  $\phi = 0.3$  to 10.0 degrees

at  $\phi = 0.5$  and 3.0 degree are compared with the observed XAS of the electrodeposited thin films of Cu<sub>2</sub>O and CuO. Fig. 5 (a) shows the comparison of the expanded partial XAS at grazing angles of 0.3 and 3.0 degree and of the electrodeposited Cu<sub>2</sub>O and CuO thin films, in addition to the calculated one of (0.5Cu<sub>2</sub>O + 0.5CuO). However, XAS (local structure around Cu ions) at low grazing angles are not similar with Cu<sub>2</sub>O. It shows that the XAS obtained at even low grazing angles are the convoluted spectra induced by the Cu<sub>2</sub>O and CuO structures. The convolution effect of the XAS can be studied by fitting the observed XAS at  $\phi = 0.5$  degree from a simple mathematical convolution of Cu<sub>2</sub>O-XAS and CuO-XAS. Fig. 5(a) shows that the observed XAS at  $\phi = 0.5$  degree is very similar to the calculated one of 0.5(Cu<sub>2</sub>O-XAS) + 0.5(CuO-XAS). However, XAS at low grazing angles can be analyzed by a simple mathematical convolution of Cu<sub>2</sub>O and CuO structures but not for the grazing angles higher than 0.5 degree. This reveals that the complex XAS results from the convoluted spectra induced from unknown structure in addition to the Cu<sub>2</sub>O and CuO structures. The XAS modulation due to the unknown structure depends on the grazing angles, and the maximum XAS modulation appears at the grazing angle of 3.0 degree. This suggests that there exists very complex structure in the junction region.

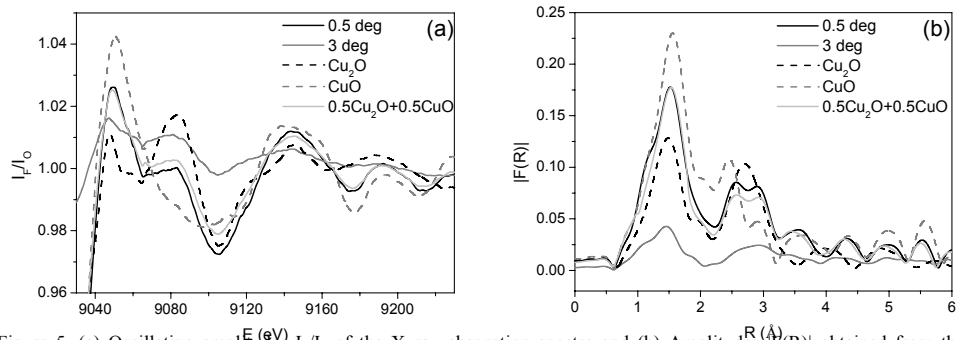


Figure 5. (a) Oscillating amplitudes  $I_F/I_0$  of the X-ray absorption spectra and (b) Amplitudes  $|F(R)|$  obtained from the Fourier transformation of the EXAFS spectra of the Ti/CuO/Cu<sub>2</sub>O heterojunction at grazing angles of 0.5 and 3.0 degrees and of the electrodeposited Cu<sub>2</sub>O and CuO thin films, in addition to the calculated one of (0.5Cu<sub>2</sub>O + 0.5CuO)

XAS of CuO/Cu<sub>2</sub>O heterojunction with different grazing angles can be further compared by studying corresponding Fourier transformations of the oscillating EXAFS spectra. Fig. 5(b) shows the observed  $|F(R)|$  for the bi-layer thin film of Ti/CuO/Cu<sub>2</sub>O heterojunction at  $\phi = 0.5$  and  $3.0$  degrees and for the electrodeposited Cu<sub>2</sub>O and CuO thin films with calculated one of (0.5Cu<sub>2</sub>O + 0.5CuO). It is further confirmed that the  $|F(R)|$  obtained at  $\phi = 0.5$  and  $3.0$  degrees are not similar with that of Cu<sub>2</sub>O structure and CuO one, but more complex. Comparison between the  $|F(R)|$  of the bi-layer thin film obtained at  $\phi = 0.5$  degree and the calculated one of (0.5Cu<sub>2</sub>O + 0.5CuO) suggests that the  $|F(R)|$  of the bi-layer thin film is also convoluted by those of the Cu<sub>2</sub>O and CuO structures. As in Fig. 5(b) peak amplitudes are very small for the  $|F(R)|$  at  $\phi = 3.0$  degree compared to the others. It implies that structure in the junction region is diluted one (the surrounding ions around the Cu absorbing ion do not well arranged). Results reveal that the formation of amorphous structure in the interface of CuO/Cu<sub>2</sub>O heterojunction. It can be expected that amorphous structure formed in the middle of the CuO/Cu<sub>2</sub>O heterojunction attributes better lattice matching between CuO and Cu<sub>2</sub>O interface. Further, it can be considered that formation of the smooth energy band lineup at the interface of CuO/Cu<sub>2</sub>O heterojunction without spikes at the conduction and valance bands. Band lineup between two semiconductors is a crucial parameter leading to better photoactive properties.

#### 4. CONCLUSION

In the present investigation, fabrication of photoactive CuO/Cu<sub>2</sub>O heterojunction and its layer by layer structural properties have been studied. In conclusion, our study reveals that it is possible to electrodeposite Cu<sub>2</sub>O on Ti/CuO at the deposition potential of -550 mV Vs SCE in an acetate bath. The SEMs and the photoelectric properties of the CuO/Cu<sub>2</sub>O heterojunction suggested that the Cu<sub>2</sub>O grains are grown from the surfaces of the CuO polycrystalline grains and make better contacts with the CuO grains. It reveals that p-CuO/n-Cu<sub>2</sub>O heterojunction solar cell can be fabricated using electrodeposition technique. XRD and the XAS, using the synchrotron radiation, reveal that Cu<sub>2</sub>O and CuO are high quality semiconducting thin films but amorphous structure is formed between CuO and Cu<sub>2</sub>O while Cu<sub>2</sub>O deposition on CuO.

## 5. ACKNOWLEDGEMENT

Dr. K. Koga, Advanced Instrument Centre, Kyushu Sangyo University, Japan, and Dr. J. Y. Choi and Dr. N. E. Sung, Beamline managers, Pohang Accelerator Laboratory, Korea are gratefully acknowledged for providing their facilities to obtain SEMs, XRD and XAS.

## REFERENCES

1. Rakhshani A E, *Solid-State Electron.* 29 (1986) 7–17
2. Siripala W., Perera L. D. R. D., De Silva K. T. L., Jayanetti J. K. D. S. and Dharmadasa I. M., *Sol. Energy Mater. Sol. Cells* 44 (1996) 251–260
3. Musa A. O., Akomolafe T. and Carter M. J., *Sol. Energy Mater. Sol. Cells* 51 (1998) 305–316
4. Hames Y. and Eren San S., *Sol. Energy* 77 (2004) 291–294
5. Ogwu A. A., Bouquerel E., Ademosu O., Moh S., Crossan E. and Placido F. , *Acta Mater.* 53 (2005) 5151–5159
6. Ivill M., Overberg M. E., Abernathy C. R., Norton D. P., Hebard A. F., Theodoropoulou N. and Budai J. D., *Solid-State Electron.* 47 (2003) 2215–2220
7. Santra K., Sarkar C. K., Mukherjee M. K. and Ghosh B., *Thin Solid Films* 213 (1992) 226–229
8. Wijesundera R. P., Perera L. D. R. D., Jayasuriya K. D., Siripala W., De Silva K. T. L., Samantilleka A. P. and Darmadasa I. M., *Sol. Energy Mater. Sol. Cells* 61 (2000) 277–286
9. Mahalingam T., Chitra J. S. P., Chu J. P. and Sebastian P. J., *Mater. Lett.* 58 (2004)1802–1807
10. Tang Y., Chen Z., Jia Z., Zhang L. and Li J., *Mater. Lett.* 59 (2005) 434–438
11. Wijesundera R. P., Hidaka M., Koga K., Sakai M. and Siripala W., *Thin Solid Films* 500 (2006) 241–246
12. Akimoto K., Ishizuka S., Yanagita M., Nawa Y., Paul Goutam K. and Sakurai T., *Sol. Energy* 80 (2006) 715–722
13. Herion J., Niekisch E. A. and Scharl G., *Sol. Energy Mater.* 4 (1980) 101–112
14. Papadimitriou L., Economou N. A. and Trivich D. 1981 *Sol. Cells* 3 73–80
15. Sears W. M., Fortin E. and Webb J. B., *Thin Solid Film* 103 (1983) 303–309
16. Tanaka H., Shimakawa T., Miyata T., Sato H. and Minami T., *Thin Solid Films* 469 (2004) 80–85
17. Siripala W. and Jayakody J. R. P., *Sol. Energy Mater.* 14 (1986) 23–27



## **SULPHIDATION OF ELECTRODEPOSITED NANOCRYSTALLINE CUPROUS OXIDE THIN FILMS FOR SOLAR ENERGY APPLICATIONS**

K.M.D.C. JAYATHILAKA<sup>1</sup>, W. SIRIPALA<sup>1</sup> and J.K.D.S. JAYANETTI\*<sup>2</sup>

<sup>1</sup>*Department of Physics, University of Kelaniya, Kelaniya.*

<sup>2</sup>*Department of Physics, University of Colombo, Colombo*

\*Corresponding Author, e-mail: [sumedhajayanetti@gmail.com](mailto:sumedhajayanetti@gmail.com)

### **ABSTRACT**

Investigations of the development of environmentally friendly low cost solar cells with cheaper semiconductor materials are extremely important for development of solar energy technology. Cuprous Oxide is non toxic, inexpensive and its component elements are readily available. This semiconducting material is attractive because its 2.0 eV band gap energy is suitable for solar cell and sensor applications. Cu<sub>2</sub>O thin films are prepared by several deposition methods and among them electrodeposition is attractive because of its simplicity, and associated low cost and low temperature of the fabrication process. Electrodeposition technique was used to synthesize the material and it was found that electrodeposition has the ability to control both conductivity type (n- or p-type) and morphology of the films.

Grain size of polycrystalline semiconductor thin films in solar cells can be optimized to enhance the efficiency of solar cells. In this paper, we report results on an investigation carried out on electrodeposited cuprous oxide (Cu<sub>2</sub>O) thin films using Ti substrates to obtain n-type thin films of small crystallites and sulphidation of them to produce a thin film solar cell. For the electrodeposition of Cu<sub>2</sub>O films, pH of an aqueous acetate bath was optimized to obtain Cu<sub>2</sub>O films of grain size about 100 nm, that were then used as templates to grow thicker n-type nanocrystalline Cu<sub>2</sub>O films. XRD and SEM analysis revealed that the films were of single phase and the substrates were well covered by the films. The AFM images were used to study the surface morphology and surface roughness of the films. The XRD, SEM and AFM analysis showed that the grain size decreased with increasing pH value of the bath. A Schottky Junction of Cu<sub>2</sub>O/Cu<sub>x</sub>S was formed by partially sulphiding the Cu<sub>2</sub>O films using an aqueous sodium sulphide solution. The EDX spectrum of the sulphided film confirmed that due to the sulphidation of the film S is incorporated into the film. It was observed that photovoltaic properties and diode characteristics of Nano-Cu<sub>2</sub>O/Cu<sub>x</sub>S structures is better than micro Cu<sub>2</sub>O/Cu<sub>x</sub>S solar cells. Resulting Ti/nanoCu<sub>2</sub>O/Cu<sub>x</sub>S/Au solar cell structure produced an energy conversion efficiency of 0.54 % , V<sub>oc</sub> = 610 mV and I<sub>sc</sub> = 3.4 mAcm<sup>-2</sup>, under AM 1.5 illumination. This is a significant improvement compared to the use of microcrystalline thin film Cu<sub>2</sub>O in the solar cell structure where the efficiency of the cell was limited to 0.11%.

Keywords: cuprous oxide, electrodeposition, nanocrystalline, spectral response, sulphidation

### **1. INTRODUCTION**

Cuprous oxide (Cu<sub>2</sub>O) is an attractive material for solar energy applications because it is a cheaper, non toxic material with a direct band gap of 2.0 eV. It has been well established that Cu<sub>2</sub>O is generally a p-type semiconductor material due to the Cu ion vacancies that exist in the crystal lattice [1-6]. Among the various methods available for growing Cu<sub>2</sub>O films, electrodeposition is attractive because it provides a low cost method for growing thin films for solar energy applications. Moreover, electrodeposition technique was studied to synthesize the material and it was found that electrodeposition has the ability to control both conductivity type (n- or p-type) and morphology of the films [7-9].

However, Cu<sub>2</sub>O has not been commonly used because of its low energy conversion efficiency which results from the fact that light generated charge carriers in micron sized Cu<sub>2</sub>O grains are not efficiently transferred to the surface and lost due to the recombination. For randomly generated charge carriers, the average diffusion time from the bulk to the surface is given by

$\tau = r^2/\pi^2 D$  where  $r$  is the grain radius and  $D$  is the diffusion coefficient of the carriers. If the grain radius is reduced from micron to nano size, the opportunities for recombination can be dramatically reduced and also nano particles increase the effective surface area of films by orders of magnitudes. Therefore, such structures will be very beneficial for improving the efficiency of solar cell devices. However, the resulting higher number of grain boundaries will affect negatively to the efficiency of the solar cell. This drawback in nanocrystalline films may be overcome if the grain boundary problem is over compensated by the improvements made due to the increase in the area of the active junction. Thus the preparation of nanocrystalline  $\text{Cu}_2\text{O}$  thin films is a key to improve the performance of solar cells [10-12].

In general, the resistance of electrodeposited  $\text{Cu}_2\text{O}$  films is higher than that of the  $\text{Cu}_2\text{O}$  films prepared using other techniques [7,13]. It has been reported earlier that sulphidation of electrodeposited p-type  $\text{Cu}_2\text{O}$  films could be used to improve the output characteristics of solar cells made with electrodeposited  $\text{Cu}_2\text{O}$  films by increasing the surface conductivity of the films [14,15]. In particular, Briskman [15] used sulphided p-type  $\text{Cu}_2\text{O}$  films deposited on Cu substrates using a lactate bath to obtain a solar cell of efficiency of 0.06%,  $V_{oc} = 380$  mV and  $J_{sc} = 600 \mu\text{A}/\text{cm}^2$ . Wijesundara *et al.* [16] sulphided n-type  $\text{Cu}_2\text{O}$  films deposited on ITO substrates using an acetate bath to make a heterojunction of n- $\text{Cu}_2\text{O}/\text{Cu}_x\text{S}$  and obtained  $V_{oc}$  of 255 mV and  $J_{sc}$  of 1.6  $\text{mA}/\text{cm}^2$ . In all of the reported work on sulphidation of electrodeposited  $\text{Cu}_2\text{O}$  films, microcrystalline films deposited on various substrates have been investigated. To our knowledge, electrodeposition of n-type nanocrystalline  $\text{Cu}_2\text{O}$  films and sulphidation of them for solar energy applications have not been reported earlier.

In this work, electrodeposition of  $\text{Cu}_2\text{O}$  thin films on Ti substrate was investigated using acetate baths [17] of different pH values in order to control the grain size of the polycrystalline films. We report the electrodeposition of nanocrystalline n-type  $\text{Cu}_2\text{O}$  thin films on Ti substrates and sulphidation of the films to obtain  $\text{Cu}_2\text{O}/\text{Cu}_x\text{S}$  Schottky structures for solar cell applications. The partial sulphidation of the cuprous oxide forms a thin degenerating nano crystalline semiconductor layer of copper sulphide ( $\text{Cu}_x\text{S}$ ) which forms a Schottky junction with  $\text{Cu}_2\text{O}$  facilitating the collection of the photogenerated carriers and thereby improving the output characteristics of the cells.

Morphology of the resulted films and device was investigated with Scanning Electron Microscopy (SEM) and Atomic Force Microscopy (AFM) while structural characterization was performed with X-ray Diffraction (XRD). Element composition of the films was investigated by Energy Dispersive X-ray spectroscopy (EDX). Conduction type of the films was studied with photocurrent spectral response measurements and capacitance – voltage measurements. All the solar cell structures were studied by IV, open circuit voltage, short circuit current and spectral response measurements. We observed that, for the first time to our knowledge, nano  $\text{Cu}_2\text{O}/\text{Cu}_x\text{S}/\text{Au}$  solar cell structure produced the highest open circuit voltage and the short circuit current density ( $V_{oc} = 610$  mV and  $J_{sc} = 3.4 \text{ mA}/\text{cm}^2$ , under AM 1.5 illumination) reported for the electrodeposited  $\text{Cu}_2\text{O}$  based thin film solar cells.

## 2. EXPERIMENTAL

$\text{Cu}_2\text{O}$  thin films were deposited on Ti substrates by the electrodeposition method. Prior to the film deposition, substrates were cleaned with detergent, diluted  $\text{HNO}_3$  and finally with distilled water. Electrodeposition of  $\text{Cu}_2\text{O}$  thin films on Ti substrates was accomplished in a three-electrode electrochemical cell containing aqueous solutions of 0.1M sodium acetate and 0.01 M cupric acetate (17). The temperature of the electrolyte was maintained at 60 °C and the electrolyte was continuously stirred using a magnetic stirrer. The counter electrode was a platinum plate and, a saturated calomel electrode (SCE) was used as the reference electrode. Electrodeposition was

carried out under a potentiostatic condition of -200 mV vs. SCE. pH of the electrolyte was adjusted by adding a dilute sodium hydroxide solution to the bath.

All Cu<sub>2</sub>O films were investigated in a three electrode photo electrochemical cell containing a 0.1M sodium acetate solution. The contact area of the film with the electrolyte was 4 mm<sup>2</sup>. Spectral responses of the electrodes were measured using a phase sensitive detection method to monitor the photocurrent signal produced by a chopped monochromatic light beam. The chopping frequency was 63 Hz. A monochromator (Sciencetech - 9010), a potentiostat (Hukoto Donko HAB-151), a lock-in amplifier (Stanford Research- SR 830 DSP), and a chopper (Stanford-SR 540) were used with a computer for the spectral response measurements.

X-ray diffraction measurements were obtained using a SHIMADZU (XD-D1) X-ray diffractometer. The surface morphology of the films and devices was determined by a scanning electron microscope (Philips XL40) and an atomic force microscope analysis (Burleigh, Vista-100). Element composition of the films was investigated by Energy Dispersive X-ray spectroscopy.

In order to grow n-type nanocrystalline Cu<sub>2</sub>O films, first films were deposited on Ti substrates using an acetate bath of pH 7.5 for 30 min. duration. The resulted films were p-type and therefore a brief annealing in air for 5 min duration was performed at 200 °C to make them n-type. These films were then used as templates for depositing thicker n-Cu<sub>2</sub>O films using an acetate bath of pH 6.2 for a duration of 30 min. For comparison, n-type films were also deposited on Ti substrates using the acetate bath of pH 6.2 for 60 min. duration without using the templates. Cu<sub>2</sub>O films were sulphided through a reaction at 200 °C with a thin layer of an aqueous solution of 0.01 M Na<sub>2</sub>S formed on the surface of the films. These thin layers of solution were formed on the films using a liquid droplet maker. After sulphidation, films were thoroughly rinsed with distilled water and then dried in air. Additional sulphidation on the already sulphided films were carried out by exposing them to ammonium sulfide gas at room temperature for about two seconds. A gold grid of thickness 100 nm was evaporated onto the sulphided Cu<sub>2</sub>O film using a thermal evaporator to make the front ohmic contact, to fabricate the Ti/Cu<sub>2</sub>O/Cu<sub>x</sub>S/Au thin film solar cell structure shown in Fig. 1.

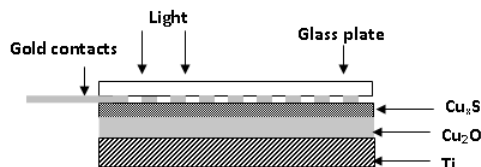


Figure 1. Ti/nanoCu<sub>2</sub>O/Cu<sub>x</sub>S/Metal Schottkey solar cell structure with electrical contacts

### 3. RESULTLS AND DISCUSSION

We observed that the morphology of the electrodeposited Cu<sub>2</sub>O thin films was strongly dependent on the pH value of the deposition bath. For example, Fig. 2 shows the SEM pictures of the films deposited in acetate baths containing 0.1M sodium acetate and 0.01M cupric acetate at pH values (a) 6.2 (b) 6.9 and (c) 7.5 respectively. Similar results of the dependence of morphology of the Cu<sub>2</sub>O films on the pH of the deposition bath have been reported earlier [18-21].

It is important to note here that at the high pH value of 7.5, the size of the crystal grains became smaller in size to about 100 nm.

Simultaneous AFM and XRD measurements showed that at smaller grain sizes, the surface roughness had increased without affecting the stoichiometry of the  $\text{Cu}_2\text{O}$  films. However, we observed that if the deposition time in this bath is increased to obtain thicker films, the grain size of the films is increased. The photocurrent spectral responses of the films prepared at pH (a) 6.2 (b) 6.9 (c) 7.5 are shown in Fig. 3. The films prepared at pH value 6.2 produced an n-type

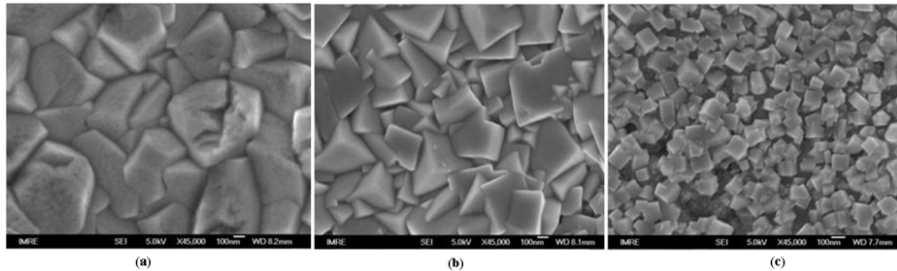


Figure 2. SEM pictures of thin films prepared in acetate baths of pH (a) 6.2, (b) 6.9 and (c) 7.5 on Ti substrate at 60°C

photosignal, Fig. 3(a), while the film prepared at pH of 6.9 and 7.5 produced p-type signals, Fig. 3 (b) and (c). It is well known that  $\text{Cu}_2\text{O}$  films electrodeposited using basic baths produced p-type films while films deposited in near neutral or acidic baths produced n-type films[13, 22-24].

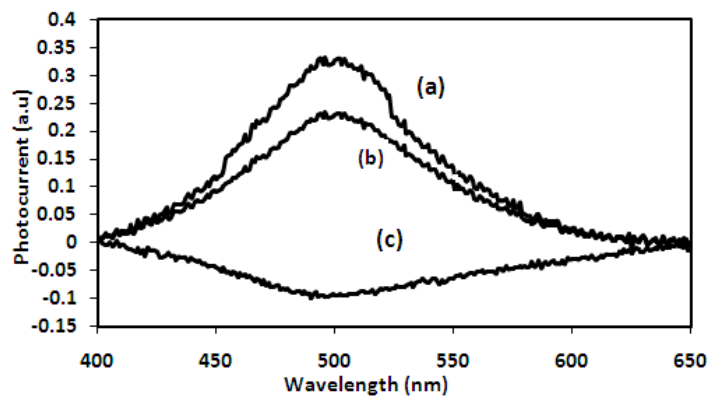


Figure 3. The photocurrent spectral responses of the films prepared at pH (a) 6.2 (b) 6.9 (c) 7.5

We observed that if the film prepared at pH 7.5 producing p-type signal is heat treated in air at 200 °C for 5 min., it is transformed to n-type. We did not investigate this transformation of the films in detail and it will be a subject for future work. In order to obtain thicker n-type  $\text{Cu}_2\text{O}$  films of small crystal size, the films deposited using the acetate bath of pH 7.5 followed by the annealing in air at 200 °C for 5 min. was employed as templates. The acetate bath used to obtain thicker n-type  $\text{Cu}_2\text{O}$  films using these templates was a solution containing 0.1M sodium acetate and 0.01M

cupric acetate at pH 6.2. Fig. 4(a) shows the SEM picture of an n-Cu<sub>2</sub>O film prepared using the 100 nm Cu<sub>2</sub>O template and it is evident in Fig. 4 (a) that the size of the crystals in the resulting film is about 100 nm. It is important to note here that if only the Ti substrate, without the templates, was used for the deposition in the acetate bath at pH 6.2, as shown in Fig 2 (a), the crystal size is about 1µm. Thus, in order to obtain a thicker n-type Cu<sub>2</sub>O film with a nanocrystalline structure, use of the nanocrystalline template was essential. Otherwise, although the film obtained in the bath is n-type, the resulting crystal size of the film will be of the order of 1µm. Fig.4(b) shows the SEM picture of the film shown in Fig 4(a) after the sulphidation. Film in Fig. 4(b) was obtained by heating the Cu<sub>2</sub>O film shown in Fig. 4 (a) at 200 °C with a thin layer of 0.01M aqueous solution of sodium sulphide on the surface of the film, followed by a brief exposure to ammonium sulphide vapor. It is clear in Fig.4 (b) that surface is covered by a film due to the sulphidation. XRD spectrum of the sulphided Cu<sub>2</sub>O film is shown in Fig. 5(a). It is evident that only Cu<sub>2</sub>O peaks are present in the XRD spectrum and peaks due to Cu<sub>x</sub>S are absent. However, as shown in SEM picture of the sulphided film in Fig. 4(b), Cu<sub>2</sub>O film is covered with another film.

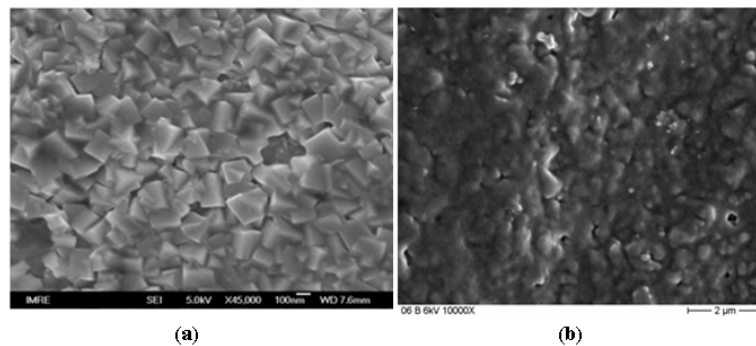


Figure 4(a) SEM picture of an n-Cu<sub>2</sub>O film prepared using the 100 nm Cu<sub>2</sub>O template (b) SEM picture of sulphided nanocrystalline Cu<sub>2</sub>O sample

The EDX spectrum of the sulphided film is shown in Fig. 5(a) and it confirms that the sulphidation of the film has incorporated sulfur into the film. The possible explanation of not observing any Cu<sub>x</sub>S peaks in XRD spectrum in Fig. 5(b) indicates that the Cu<sub>x</sub>S layer formed by the sulphidation is amorphous. Thus, the Cu<sub>2</sub>O layer is partially sulphided due to the sulphidation but the resulting Cu<sub>x</sub>S film is amorphous.

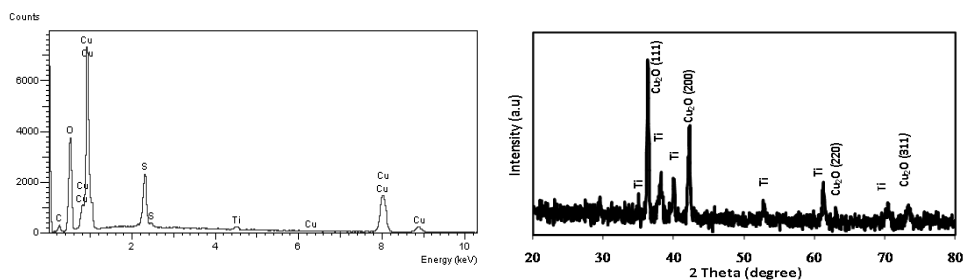


Figure5.(a) EDX spectrum (b) X-ray diffraction (XRD) spectrum obtained for the sulphided Cu<sub>2</sub>O film

By comparing the spectral response shown in Fig. 6 (a) with (b), it is clearly seen that the remarkable improvement of the solar cell performance is resulted due to the presence of the nano crystalline layer of  $\text{Cu}_2\text{O}$ .

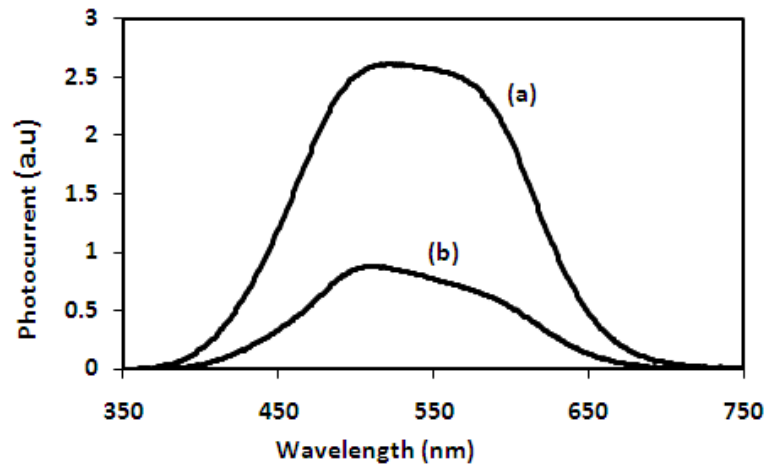


Figure.6 (a) and (b) The spectral responses of the solar cell made with sulphided nanostructured  $\text{Cu}_2\text{O}$  film and microstructured  $\text{Cu}_2\text{O}$  film.

It is clear in Fig.6 that mainly the carrier generation is limited to the  $\text{Cu}_2\text{O}$  layer, because only the contribution from the photons having energy larger than the band gap energy of  $\text{Cu}_2\text{O}$  ( 2.0 eV) is present. In the solar cell structure that we have studied here, as shown in Fig. 1, the light is incident through the  $\text{Cu}_x\text{S}$  layer. Therefore, short wavelengths are absorbed by the  $\text{Cu}_x\text{S}$  layer without making a contribution to the photocurrent. Accordingly, we can conclude the formation of  $\text{Cu}_2\text{O}/\text{Cu}_x\text{S}$  Schottkey junction.

Current – voltage characteristics of the solar cell device of  $\text{Ti}/\text{Cu}_2\text{O}/\text{Cu}_x\text{S}/\text{Au}$  is shown in Fig. 7. The solar cell structure produced by the sulphidation of nanocrystalline  $\text{Cu}_2\text{O}$  film

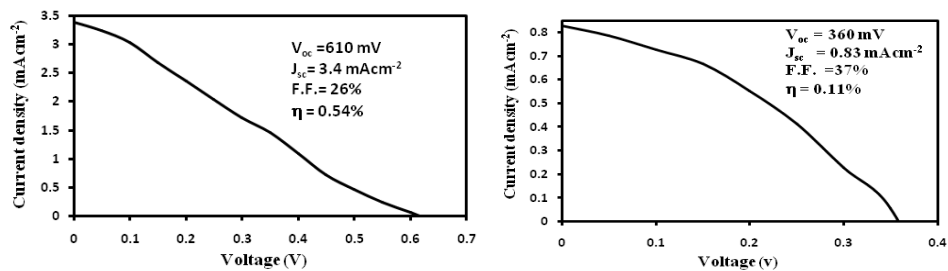


Figure 7. Current- voltage characteristics of  $\text{Ti}/\text{n-Cu}_2\text{O}/\text{p-Cu}_x\text{S}/\text{Au}$  solar cell made with (a) nano and (b) micro,  $\text{Cu}_2\text{O}$  films

results in an energy conversion efficiency = 0.54% ,  $V_{oc}$  = 610 mV and  $J_{sc}$  = 3.4 mA/cm<sup>2</sup> , at AM 1.5 illumination. The efficiency of the solar cell is limited by the poor fill factor of 26%. However, the efficiency value we report here, to our knowledge, is the highest reported efficiency value for a thin film solar cell made with electrodeposited Cu<sub>2</sub>O films. For comparison, Fig. 7 (b) shows the current voltage characteristics of a solar cell made with a sulphided Cu<sub>2</sub>O film where the microcrystalline Cu<sub>2</sub>O film was obtained without using the 100 nm template. All the conditions used to prepare the solar cell device in Fig. 7(b) are same as for Fig. 7(a), except the nanocrystalline template was not used for the deposition of the Cu<sub>2</sub>O film in Fig. 7(b). It is clearly shown in Fig. 7(b) that the efficiency of the solar cell has reduced to 0.11% in the absence of the nanocrystalline film. Therefore, the presence of the nanocrystalline film is responsible for the enhancement of the output characteristics of the solar cell made by sulphidation of n-Cu<sub>2</sub>O films. The improved efficiency is attributed to the increase in the active contact area between Cu<sub>x</sub>S layer with n-Cu<sub>2</sub>O, where the roughness of the surface of the Cu<sub>2</sub>O film is increased by the nanostructure of the film.

#### 4. CONCLUSIONS

In conclusion, in this investigation we have demonstrated that polycrystalline n-type cuprous oxide thin films having small crystals of the size of 100 nm could be electrodeposited. An acetate bath of pH 7.5 was used to obtain crystal size of 100 nm and the resulted films were used as templates to grow thicker n-type nanocrystalline films in a bath of pH 6.2. A thin film solar cell was made by sulphidation of the nanocrystalline films and the resulted solar cell produced an efficiency of 0.54%, the highest efficiency reported for the electrodeposited Cu<sub>2</sub>O based thin film solar cells. For this solar cell, an open circuit voltage,  $V_{oc}$  = 610 mV and a short circuit current,  $J_{sc}$  = 3.4 mA/cm<sup>2</sup>, were obtained at 1.5 AM illumination. This in turn is a significant enhancement compared to the solar cell structures based on microcrystalline Cu<sub>2</sub>O films that resulted in an efficiency of only 0.11%. The observed enhancement of the efficiency of the n-Cu<sub>2</sub>O/Cu<sub>x</sub>S Schottkey junction solar cell device is attributed to the increase in the active junction area of the cell due to the nanocrystalline nature of the Cu<sub>2</sub>O film.

#### 5. ACKNOWLEDGEMENTS

National Science Foundation (NSF) is gratefully acknowledged for the financial assistance through the research grant NSF/ RG/2005/W&E/02. Dr. S. Dharmathilleke of IMRE, Singapore is acknowledged for the SEM measurements. Help given in making some of the AFM measurements by Dr. V. Kapaklis of the Department of Materials Physics, Uppsala University, Sweden is also acknowledged.

#### REFERENCES

1. L.C.Olsen, F.W. Addis. W.Miller, Solar cells 7 (1982) 247.
2. J.H.Lee, B.X.Tang, L.M.Tao, Y.X.Xie, M.B.Zang, J. Org Chem. 71 (2006) 7488.
3. M.Hara, T.Konda, M.Komoda, S.Ikeda, K.Shinohara, A.Tanaka, J.N.Kondo, K.Domen, Chem. Communication (1998) 357.
4. X.Le, H.Gao, C.J.Murphy, L.Gou, Nanno Lett. 4 (2004) 1903.
5. Y Chang, J.J. Teo, H.C.Zeng, Langmuir 21 (2005) 1074.
6. J.T.Zang, J.F.Liu, Y.D.Li, Chemi. Mat. 18 (2006) 867.
7. L.C.Olsen, F.W. Addis and W Miller , Solar cells 7 (1982) 247.
8. R.P. Rai Solar cells 25 (1988) 265.
9. W.Siripala, J.R.P.Jayakody, Solar Energy Materials 14 (1986) 23.
10. W.Siripala, A. Ivanovskaya, T.F.Jaramillo, S.H.Baek, E.W. McFarland, Solar Energy Mat. Solar Cells 77 (2003) 229.

11. Yiwen Tang, Zhigang chen, Zhijie Jia, Lisha Zang, Jialin Li, *materials letters* 59 (2005) 434
12. T.Mahalingam, J.S.P. Chitra, J.P. Chu, S. Velumani, P.J.Sebastian, *Solar Energy Mater. Solar Cells* 88 (2005) 209.
13. K.Han, M. Tao, *Solar Energy Materials & Solar cells* 93 (2009) 153.
14. N.A. Economou, R.S. Toth, R.J.Komp, D. Trivich, *Proc. European Community Photovoltaic conference, 1977*, p. 1180.
15. R.N. Briskman, *Solar Cells* 27 (1992) 361.
16. R.P wijesundara, L.D.R.D.Perera, K.D Jayasuriya, W.Siripala, K.T.L De Silva, A.P. Samanthilleke, I.M Dharmadasa *Energy Mat. Solar Cells* 61 (2000) 277.
17. (a) W.Siripala, *J. Natn. Sci, Coun. Sri Lanka* 23 (1) (1995) 49. (b) W.Siripala, L.D.R.D. Perera, K.T.L. De Silva, J.K.D.S. Jayanetti, I.M.Dharmadasa, *Solar Energy Materials and Solar Cells* 44 (1996) 251
18. M.J. Siegfried, Kyoung-Shin Choi, *Adv. Mater.* 2004 , 16 (2004) 1743.
19. L.C. Wang, N.R. de Tacconi, C.R.Chenshamarakshan, K.Rajeshwar, and M. Tao *Thin Solid Films* , 515, 3090 (2007).
20. A.E. Rakhshani, A.A. Al-Jassar, J. Varghese, *Thin Solid Films* 148 , 191 (1987).
21. Y. Zhou, J.A. Switzer, *Script. Mater.* 38, 1731 (1988).
22. W. Siripala, J.R.P. Jayakody , *Solar Energy Mater.* 14 (1986) 23
23. L.Wang, M.Tao, *Eelectrochem. Solid Sate Lett.* 10 , H248 (2007).
24. C.M.McShane, Kyoung-Shin Choi, *J. Am. Chem. Soc.* , 131 (7) (2009), 2561



## STUDY OF ELECTRODEPOSITED ZnS THIN FILMS GROWN WITH ZnSO<sub>4</sub> AND (NH<sub>4</sub>)<sub>2</sub>S<sub>2</sub>O<sub>3</sub> PRECURSORS FOR USE IN SOLAR CELLS

A. R. WEERASINGHE\*, O. K. ECHENDU, D. G. DISO AND I. M. DHARMADASA

*Electronic Materials & Sensors Group, Materials & Engineering Research Institute  
Sheffield Hallam University, Sheffield S1 1WB, United Kingdom*

\*Corresponding Author, e-mail: [a.weerasinghe@shu.ac.uk](mailto:a.weerasinghe@shu.ac.uk)

### ABSTRACT

Electrodeposited thin films of zinc sulphide (ZnS) are researched and developed for thin film solar cells. The sulphur source, ammonium thiosulphate [(NH<sub>4</sub>)<sub>2</sub>S<sub>2</sub>O<sub>3</sub>] is used for the first time to prepare the aqueous electrolytes with zinc sulphate (ZnSO<sub>4</sub>) as the source of zinc ions. The deposited thin films of ZnS were characterised using optical absorption for bandgap estimation, X-ray diffraction (XRD) for identification of phases and structure, Scanning Electron Microscopy (SEM) for surface morphology, Energy Dispersive X-ray (EDX) for composition and photoelectrochemical (PEC) cell to determine the electrical conduction type. The optical absorption shows the bandgaps in the range (3.70 - 3.90) eV. XRD shows the ZnS layers are amorphous and SEM reveals their grain sizes to be ~30 nm. EDX qualitatively shows the presence of Zn and S in these layers. By using PEC cell, both *n*-type and *p*-type electrical conductivity have been detected in ZnS layers under various zinc ion concentrations and growth voltages. Initial CdTe based solar cells using ZnS as the window layer produced PV active devices with efficiency of ~2%. The glass/FTO/ZnS/CdTe/Au structures produced device parameters; V<sub>oc</sub> ~ 510 mV, J<sub>sc</sub> ~ 12 mAcm<sup>-2</sup> and FF ~ 0.40 indicating the possibility of further improvements. These results will be presented in this paper, and the work is continuing.

Keywords: electrodeposition, thin films, CdTe solar cells, zinc sulphide, II-VI semiconductors.

### 1. INTRODUCTION

The high production cost of solar energy materials, constitutes serious drawback for the full scale commercialisation of photovoltaic solar cells. Experiments are being conducted to develop low-cost materials with optimum characteristics required for solar energy conversion. ZnS is a binary compound from the II - VI family of semiconductors with a wide bandgap of approximately 3.70 eV [1]. Zinc sulphide (ZnS) has direct optical bandgap and is non-toxic for use as a material in optoelectronic devices such as solar cells, LEDs and laser diodes [2]. This material has previously been prepared by various methods including chemical bath deposition [3, 4], vapour deposition [5], sputtering [6], electron beam evaporation [7] and photochemical deposition [8]. All these methods produce high quality thin films but they require expensive equipments and/or expensive growth processes compared to electrodeposition.

Electrodeposition (ED) reduces the production cost, improves features like scalability, possibility of fine control of film thickness, particles size and surface morphology in order to achieve an optimal material for large area PV application. However, physical conditions have to be well established for uniform growth of thin films with desired properties [9, 10].

Cadmium sulphide (CdS) is the industry choice as the window layer in cadmium telluride (CdTe) based solar cells. The substitution of CdS in this device by ZnS has not been thoroughly investigated in the past. This paper presents the results of characterisation by selected methods of ED-ZnS layers deposited from an aqueous solution, and the initial device parameters.

## 2. EXPERIMENTAL METHOD

ZnS layers were electrodeposited on glass/FTO substrates with sheet resistance of  $15\Omega/\square$  provided by Pilkington Group Ltd. Substrates were treated for 10 minutes with detergent solution in an ultrasonic bath, then rinsed with deionised water, methanol, acetone, nitric acid and acetic acid in turn and rinsing with deionised water. Two electrolytes were prepared, one with 0.30M  $\text{ZnSO}_4$  and 0.03M  $(\text{NH}_4)_2\text{S}_2\text{O}_3$  and another with 0.15M  $\text{ZnSO}_4$  and 0.30M  $(\text{NH}_4)_2\text{S}_2\text{O}_3$ .  $\text{ZnSO}_4$  and  $(\text{NH}_4)_2\text{S}_2\text{O}_3$  provided  $\text{Zn}^{2+}$  and  $\text{S}^{2-}$  ions respectively. The pH values of the baths were ultimately adjusted to  $3.50 \pm 0.04$  using  $\text{H}_2\text{SO}_4$  or  $\text{NH}_4\text{OH}$  and temperatures were  $\sim 30^\circ\text{C}$  and stirring rates were low and constant. All the chemicals used were of high purity of 5Ns (99.999%).

A voltammogram was recorded for each bath using a carbon anode and the glass/FTO as the cathode. The experimental range for deposition of ZnS was narrowed down by conducting a voltammogram using an ACM-GillAC computerised potentiometer and by varying the applied potential in forward and reverse direction from 100 mV to -1800 mV at a moderated rate of  $\sim 3 \text{ mVs}^{-1}$  at  $30^\circ\text{C}$  temperature. The ZnS layers were grown on glass/FTO substrates using two-electrode method. Glass/FTO substrates were vertically mounted in the electrolyte. Resulting layers were dried using a flow of nitrogen gas, and annealed at various temperatures to improve the material quality. Both as-grown and annealed layers were characterised using optical absorption, XRD, SEM, PEC and EDX to investigate their properties and optimise the conditions of ZnS layers.

ED-ZnS layers in these ranges were characterised and optimised for the growth voltage. The energy bandgap of the thin film semiconductor was calculated using a Carry 50 UV-VIS spectrophotometer. The optical absorption measurement results were analysed using Stern relationship

$$\frac{\alpha}{\nu} = \frac{A}{\nu} \left( \frac{1}{\nu} \right)^n \quad (1)$$

[1] as in equation 1:  $\nu$  is the frequency of light,  $h$  is the Planck's constant and  $n$  has the value of either 1 or 4. The value of  $n = 1$  is for direct transitions and  $n = 4$  is for indirect transitions.

XRD was carried out using a Philips PW 3710 X-ray diffractometer using  $\text{CuK}_\alpha$  radiation ( $\lambda = 1.5416 \text{ \AA}$ ) in the range of  $2\theta = (10 - 70)^\circ$  for the structural analysis of deposited films. The X-ray generator tension and current were 40 kV and 40 mA respectively.

A NOVA NANO SEM 200 Field Emission Gun with accelerating voltage of 20 kV and a spot size of 3.0 was used to study the surface morphology of the thin film layers. The same equipment provided EDX spectra for analysis of the material layers.

Photoelectrochemical (PEC) measurements were conducted to determine the type of electrical conductivity of ZnS layers. A solid/liquid junction was formed by immersing glass/FTO/ZnS in a suitable electrolyte and the resulting voltage was measured with respect to a carbon electrode. The PEC signal was determined by the difference between voltages observed under illuminated and dark conditions. The magnitude of the PEC signal depends on the doping condition of the solid layer and hence, the width of the depletion region formed. The sign of the PEC signal determines the electrical conduction type of semiconducting layers.

### 3. RESULTS AND DISCUSSION

Voltammogram was used to deduce the approximate cathodic growth potentials. For the higher  $Zn^{+2}$  bath, this is in the range (1100 - 1600 mV) (Figure 1a) and for the lower  $Zn^{+2}$  bath this is in the range (1300-1600) mV, (Figure 1b) respectively.

The optimum bandgaps of the layers from the higher  $Zn^{+2}$  bath are in the range (3.70-3.80) eV as shown in Figure 2(a) with an indication of additional absorption edge, which may be due to possible presence of ZnO or Zn(OH)<sub>2</sub>. In the lower  $Zn^{+2}$  bath ZnS layers have bandgaps in the range (3.75- 3.90) eV as shown in Figure 2(b). Within these growth regions ZnS layers have good adhesions to glass/FTO substrates with very uniform light brown colour. Upon annealing at 350°C for 20 minutes, the best observed in this research, the layers became colourless.

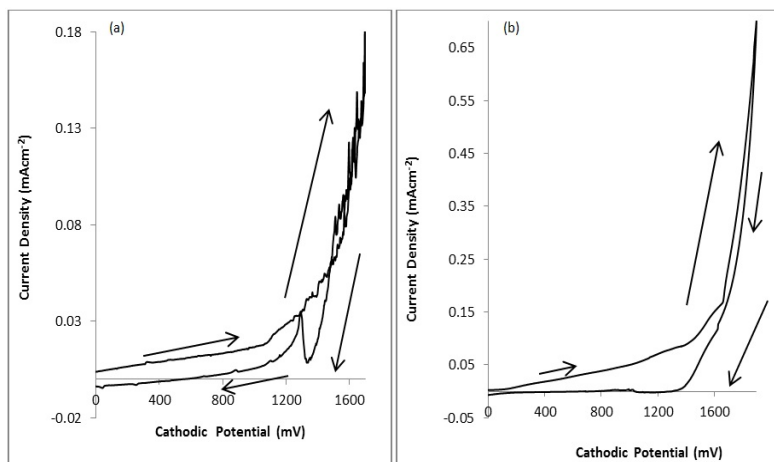


Figure 1: Voltammogram of ZnS bath containing an aqueous solution of (a) 0.30M ZnSO<sub>4</sub> + 0.03M (NH<sub>4</sub>)<sub>2</sub>S<sub>2</sub>O<sub>3</sub> and (b) 0.15M ZnSO<sub>4</sub>+ 0.30M (NH<sub>4</sub>)<sub>2</sub>S<sub>2</sub>O<sub>3</sub>, both pH ~3.50 and temperature ~ 30°C

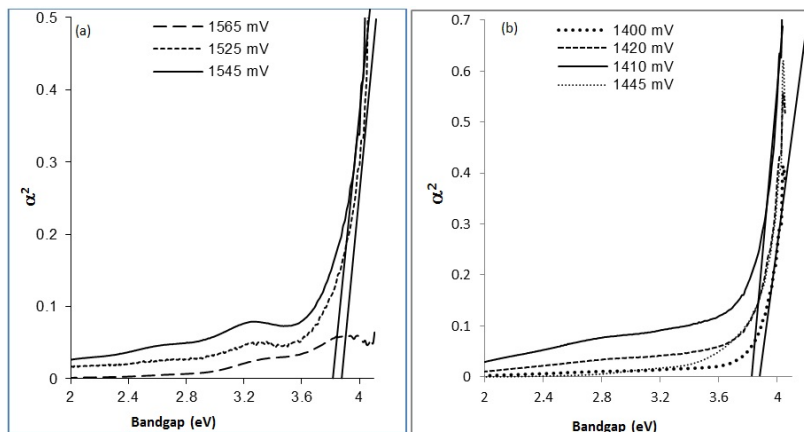


Figure 2: Optical absorption spectra of ZnS layers from: (a) 0.30M ZnSO<sub>4</sub>+ 0.03M (NH<sub>4</sub>)<sub>2</sub>S<sub>2</sub>O<sub>3</sub> and (b) 0.15M ZnSO<sub>4</sub>+ 0.30M (NH<sub>4</sub>)<sub>2</sub>S<sub>2</sub>O<sub>3</sub>; growth time, 30 minutes.

The results of XRD carried out on layers from electrolytes baths are presented in Figures 3(a) and 3(b). No strong peaks were observed from both as-deposited and annealed layers. Layers from low  $Zn^{+2}$  concentration bath shows a presence of a weak peak as identified by JCPDS reference file No: 00-036-1450, but the peaks had no improvement from annealing. The amorphous nature did not improve after annealing, and this is comparable to the previously reported results [12].

SEM micrographs showing the surface morphology of ZnS layers are shown in Figure 4(a) and 4(b). These figures show uniform distribution of grains (~30 nm) in layers from both electrolytes. However, it is evident that the grain sizes of ZnS layers from the lower  $Zn^{+2}$  bath were noticeably larger (~50 nm) than those of from the higher  $Zn^{+2}$  bath. Furthermore the thicknesses of layers from the respective baths are shown in Figure 5. The layer thicknesses are comparable (~700 nm) with slightly larger thickness is noticed in the ZnS layers grown from the lower  $Zn^{+2}$  bath. Qualitative analysis of EDX of layers from both electrolytes confirmed the presence of Zn and S on these electro-plated layers (Figure 6). The other elements are due to the glass/FTO substrate and contaminations.

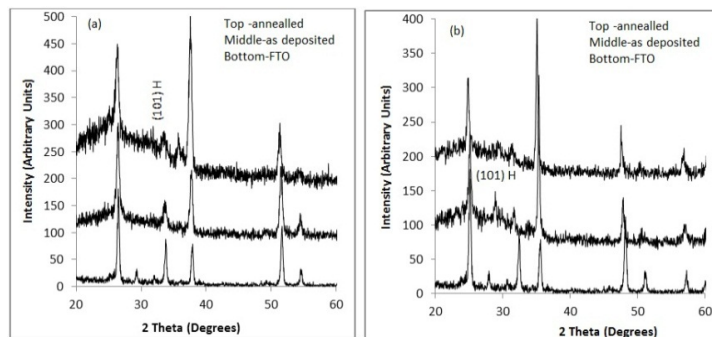


Figure 3: XRD plots of ZnS layers grown at: (a)  $V_g = 1545$  mV, from  $0.30M ZnSO_4 + 0.03M (NH_4)_2S_2O_3$  and (b)  $V_g = 1410$  mV, from  $0.15M ZnSO_4 + 0.30M (NH_4)_2S_2O_3$ .

Interestingly ZnS layers of both *n*-type and *p*-type electrical conduction properties were obtained from both electrolytes at different growth voltages, as illustrated in Figure 7(a) and (b). This observation is encouraging, indicating the possibility of growing *p*, *i* and *n*-type ZnS layers using electro-plating. The doping of layers due to composition is complex in this system because of S precipitation. These conditions need to be established on the future. This presents an opportunity to develop ZnS as window and buffer layers once the conditions of depositing *p*, *i* and *n*-type layers are established [13] as well as to be used in graded bandgap devices [14].

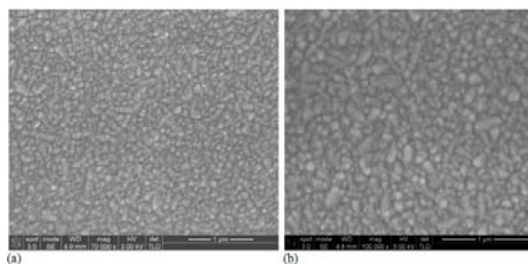


Figure 4: SEM images of ZnS layers from: (a)  $0.30M ZnSO_4 + 0.030M (NH_4)_2S_2O_3$  and (b)  $0.15M ZnSO_4 + 0.30M (NH_4)_2S_2O_3$ .

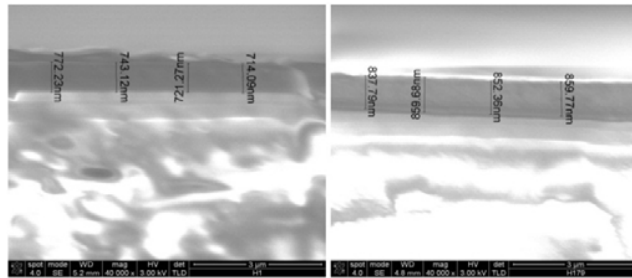


Figure 5: SEM images of cross section of ZnS layers: from: (a) 0.30M ZnSO<sub>4</sub> + 0.030M (NH<sub>4</sub>)<sub>2</sub>S<sub>2</sub>O<sub>3</sub> and (b) 0.15M ZnSO<sub>4</sub> + 0.30M (NH<sub>4</sub>)<sub>2</sub>S<sub>2</sub>O<sub>3</sub>.

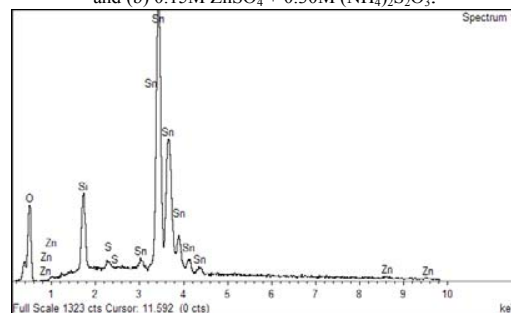


Figure 6: EDX spectrum of ZnS layers, qualitatively indicating the presence of Zn and S in the layers.

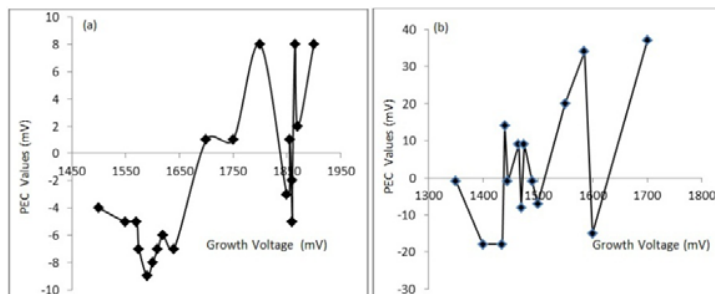


Figure 7: PEC signals of ZnS layers indicating the possibility of producing *p*, *i* and *n*-type ZnS layers: (a) 0.30M ZnSO<sub>4</sub> + 0.03M (NH<sub>4</sub>)<sub>2</sub>S<sub>2</sub>O<sub>3</sub> and (b) 0.15M ZnSO<sub>4</sub> + 0.30M (NH<sub>4</sub>)<sub>2</sub>S<sub>2</sub>O<sub>3</sub>, both deposited for 30 minutes.

The initial CdTe based solar cells fabricated using these electrodeposited ZnS as a window layer produced device parameters of  $V_{oc} \sim 510$  mV,  $J_{sc} \sim 12$  mAcm<sup>-2</sup> and FF  $\sim 0.40$ , with overall efficiency of  $\sim 2\%$ . These results indicate that these structures can be developed to achieve higher efficiencies by optimising material growth conditions.

#### 4. CONCLUSION

ZnS thin films were deposited by electrochemical method from an aqueous electrolyte using 2-electrode system. The electrodeposited layers have good adhesion to the glass/FTO substrates. Optical absorption studies show bandgap in the range (3.70 – 3.90)eV. Amorphous nature of the thin films was confirmed by the XRD results. SEM images show an average

(30-40) nm grain size and uniform layer thickness of ~ 700 nm from both electrolytes. The possibility of electrodepositing *p*, *i* and *n*-type ZnS layers is revealed by PEC studies. This opens the possibility of using electrodepositing ZnS in the graded bandgap solar cell structure with *p*-type window material and to develop various other devices based on nano-materials. High level of uniformity of the layers is obtained at lower temperatures of about ~30°C, hence a low use of electric power to produce electrodepositing ZnS.

## REFERENCES

1. FATHY, N., Kobayashi, R. and Ichimura, M. (2004). Preparation of ZnS thin films by the pulsed electrochemical deposition. *Materials science and engineering B*, **107** (3), 271-276.
2. HOSAKAWA, H. and Yamashita, T. (1990) ZnS micro-Fresnel lens and its uses, *Appl. Opt.*, **29**, 5106-5110 .
3. ZHANG, Y., Dang, X.Y., Jin, J., Yu, T., Li, B.Z., He, Q., Li, F.Y. and Sun, Y. et al. (2010). ZnS thin film deposited with chemical bath deposition process directed by different stirring speeds. *Applied surface science*, **256** (22), 6871-6875.
4. ROMERO, E., Vallejo, W. and Gordillo, G. (2008). Comparative study of ZnS thin films deposited by CBD and coevaporation. In: *Photovoltaic Specialists Conference, 2008. PVSC '08. 33rd IEEE*, 1-5.
5. YOSHIKAWA, A., Yamaga, S., Tanaka, K. and Kasai, H. (1985). Growth of low-resistivity high-quality ZnSe, ZnS films by low-pressure metalorganic chemical vapour deposition. *Journal of crystal growth*, **72** (1-2), 13-16.
6. GAYOU, V. L., Salazar-Hernandez, B., Constantino, M.E., Andrés, E., R., Díaz, T., Macuil, R. D., López, M. R., et al. (2010). Structural studies of ZnS thin films grown on GaAs by RF magnetron sputtering. *Vacuum*, **84** (10), 1191-1194.
7. MA, C., Moore, D., Li, J. and Wang, Z. (2003), Nanobelts, Nanocombs, and Nanowindmills of Wurtzite ZnS. *Advanced Materials*, **15**: 228–231
8. ICHIMURA, M., Ono, T. And Arai, E. (1999). Deposition of CdS and ZnS from aqueous solutions by a new photochemical technique. *Journal of crystal growth*, **198-199** (Part 1), 308-312.
9. LOSEY, M. W. and Kelly, J. J. (2008). Electrodeposition. In: Yogesh Gianchandani, Osamu Tabata and Hans Zappe (eds.). *Comprehensive microsystems*. Oxford, Elsevier, 271-292.
10. KASSIM, A., Nagalingam, s., Min, H. S. and Karrim, N. (2010). XRD and AFM studies of ZnS thin films produced by electrodepositing method. *Arabian journal of chemistry*, **3** (4), 243-249.
11. SZE, S. M. and Kwok Kwok, N. (2007). *Physics of semiconductor devices*. 3rd ed., Hoboken, N.J., Wiley-Interscience.
12. SANDERS, Brian W. and KITAI, Adrian H. (1990). The electrodepositing of thin film zinc sulphide from thiosulphate solution. *Journal of crystal growth*, **100** (3), 405-410.
13. NAKADA, T. and Mitutani, M. (2000). Improved efficiency of Cu(In,Ga)Se<sub>2</sub> thin film solar cells with chemically deposited ZnS buffer layers by air-annealing-formation of homojunction by solid phase diffusion. In: *Photovoltaic Specialists Conference, 2000. Conference Record of the Twenty-Eighth IEEE*, 529-534.
14. DHARMADASA, I. M., Roberts, J. S. and Hill, G. (2005). Third generation multi-layer graded band gap solar cells for achieving high conversion efficiencies—II: Experimental results. *Solar energy materials and solar cells*, **88** (4), 413-422.

**PHOTOLUMINESCENCE AND MAGNETIC PROPERTIES OF HEXAGONAL YMnO<sub>3</sub> NANOFIBERS PREPARED BY USING ELECTROSTATIC SPINNING**

HUIQING FAN

State Key Laboratory of Solidification Processing, School of Materials Science and Engineering,  
Northwestern Polytechnical University, Xi'an 710072, China

Corresponding Author, e-mail: hqfan@nwpu.edu.cn

**ABSTRACT**

Hexagonal YMnO<sub>3</sub> (h-YMnO<sub>3</sub>) nanofibers were fabricated by the post-annealing at 1100°C after an electrostatic spinning from manganese acetate and yttrium nitrate precursors. Photoluminescence spectrum was also measured to confirm the d orbit energy bands of the manganese ion split to 5T<sub>2</sub> and 5E bands. Furthermore, the h-YMnO<sub>3</sub> nanofibers showed paramagnetic, superparamagnetic and ferromagnetic phases at room temperature, 30 K and 5 K, respectively, which indicated the blocking temperature of superparamagnetism, T<sub>B</sub>, was above 5 K and below 30 K.

Keywords: Hexagonal YMnO<sub>3</sub>, Nanofibers, Electrostatic spinning, Magnetic properties.

**1. INTRODUCTION**

Multiferroic materials, in which magnetism and ferroelectricity coexist, have attracted great attention in recent years because of their fundamental as well as technical importance. The hexagonal yttrium manganese oxide YMnO<sub>3</sub> (abbreviated as h-YMnO<sub>3</sub>) is one of the best known multiferroics. The h-YMnO<sub>3</sub>, with a low dielectric constant of 20 and a remnant polarization (P<sub>r</sub>) of 5.5 μC/cm<sup>2</sup> in a single crystal form, is a new candidate for metal-ferroelectric-insulator-semiconductor field-effect transistors (MFIS-FET) [1-3]. These have been investigated as future nonvolatile memory devices with a nondestructive readable function. Besides, h-YMnO<sub>3</sub> may be an interesting candidate for an active laser medium because of the luminescence properties of Mn<sup>3+</sup> ion, as reported by Kück *et al.* [4]. So far, YMnO<sub>3</sub> has been investigated widely by many research groups [5-10]. X. Marti *et al.* prepared the orthorhombic YMnO<sub>3</sub> epitaxial thin films on Nb (0.5%-doped SrTiO<sub>3</sub> (001) substrates, and found that the dielectric peak amplitude was dependent on the unit cell distortion [5]. K. Asokan *et al.* studied the orthorhombic 3d-transition metal-doped yttrium manganites, and it was demonstrated that the positive effective charge of Mn ions were increased after the direct substitution of Me<sup>2+</sup> for Mn<sup>3+</sup> [8]. H.W. Zheng *et al.* fabricated hexagonal YMnO<sub>3</sub> nanoparticles by hydrothermal process, and found that the exchange-bias effect was attributed to an exchange coupling between an antiferromagnetic core and the spin-glassy-shell or ferromagnetic surface spins of the nanoparticles [10]. The combination of a high surface area, flexibility, and superior directionality makes one-dimensional materials the preferred structure for many applications. Therefore, in this work the magnetic properties as well as their photoluminescence property of one-dimensional h-YMnO<sub>3</sub> nanofibers prepared by the electrostatic spinning are studied in detail.

**2. EXPERIMENTAL PROCEDURES**

The h-YMnO<sub>3</sub> nanofibers were synthesized by sol-gel based on electrostatic spinning process using yttrium nitrate hexahydrate (Y(NO<sub>3</sub>)<sub>3</sub>·6H<sub>2</sub>O) (99.0%) and manganese acetate tetrahydrate (Mn(CH<sub>3</sub>COO)<sub>2</sub>·4H<sub>2</sub>O) (99.0%) as raw materials. Manganese acetate (Mn(CH<sub>3</sub>COO)<sub>2</sub>·4H<sub>2</sub>O) and yttrium nitrate (Y(NO<sub>3</sub>)<sub>3</sub>·6H<sub>2</sub>O) were dissolved in an aqueous solution

of citric acid ( $C_6H_8O_7$ ). The molar ratio of Y: Mn:  $C_6H_8O_7$  was kept to be 1: 1: 2. After setting aside for one day and heating at  $70\text{ }^\circ\text{C}$  for 5h, a polymer poly (vinyl pyrrolidone) (PVP) with a molecular weight of  $1.3 \times 10^6$  was then added to the solution directly and stirred continuously to form a 1 M polymer solution, with the concentration of PVP controlled at around 0.035 g/ml. The solution was then pumped into a plastic syringe with a 1 mm internal diameter stainless steel needle at constant flow rate of 0.5 ml/h. A high voltage of 25 KV was supplied at the stainless steel needle by a direct current power supply. A piece of grounded silicon wafer was placed 20 cm below the tip of the needle to collect the nanofibers [11]. The collected electrospun nanofibers were then dried at  $125\text{ }^\circ\text{C}$  for 6 h. The dried electrospun precursors were then annealed in a furnace at  $1100\text{ }^\circ\text{C}$  for 6 h in air.

Powder X-ray diffraction (XRD) was detected on an X'Pert MPD Philips diffractometer with  $CuK\alpha$  radiation. Scanning electron microscopy (SEM) was performed using a FE-SEM JEOL-6700F microscope. The photoluminescence (PL) spectrum was measured at room temperature by excitation with a He-Cd continuous wave laser emitted at 325 nm (20 mW). A superconducting quantum interference device (SQUID) magnetometer was employed to characterize the magnetization (M) as a function of temperature (T) and magnetic field (H).

### 3. RESULTS AND DISCUSSION

The corresponding morphology of the fibers heated at  $1100\text{ }^\circ\text{C}$  is shown in Fig. 1(a). It can be seen that the fibers with the diameter ranging from 200 nm to 800 nm are made up of ceramic particles with irregular geometry, which are stacked closely and continuously. All of the reflections in the XRD spectrum shown in Fig. 1(b) can be indexed that the pure h- $YMnO_3$  nanofibers is obtained after heating at  $1100\text{ }^\circ\text{C}$ . The reflections are sharp and well-defined, which indicates that samples are well-crystallized. The size of h- $YMnO_3$  crystals on the different crystal planes were also calculated on the basis of the Scherrer formula from XRD pattern [12], the average sizes of crystals were confirmed less than 100 nm.

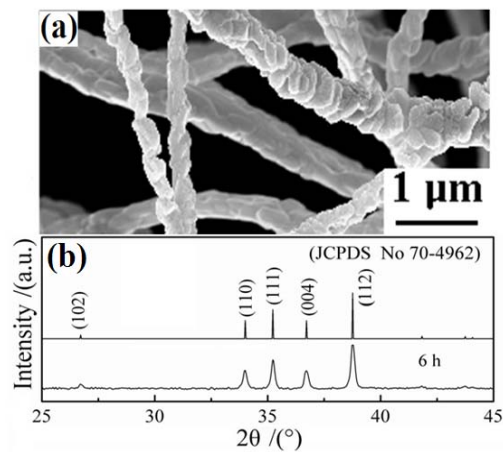


Fig. 1 (a) SEM image and (b) XRD pattern of the h- $YMnO_3$  nanofibers prepared by using electrostatic spinning.



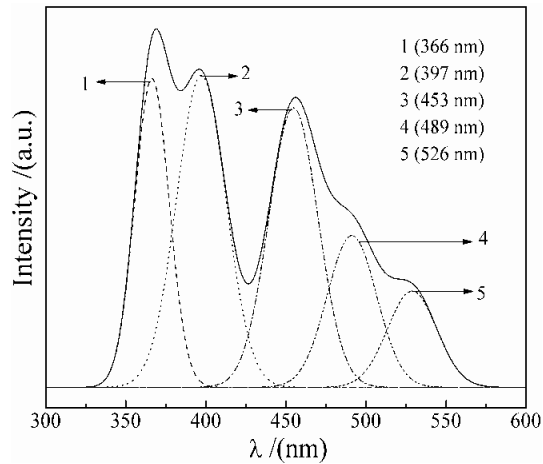


Fig. 2 Photoluminescence spectra of the h-YMnO<sub>3</sub> nanofibers prepared by using an electrostatic spinning.

A photoluminescence spectrum of h-YMnO<sub>3</sub> nanofibers is given in Fig. 2. There are five prominent peaks, located at the wavelengths of 366, 397, 453, 489 and 526 nm, respectively. Manganese ion has a  $d^4$  electron configuration. On the basis of the crystal field theory, the d orbit energy bands split to  $^5T_2$  and  $^5E$  bands because the electrons occupying the d orbit of manganese ion are influenced by the oxygen octahedron. The peaks should be due to the transition of the manganese ion from  $^5T_2$  to  $^5E$ .

The magnetic measurements on the h-YMnO<sub>3</sub> nanofibers are performed in order to investigate the magnetic ordering at different temperatures. It is necessary to point out that the h-YMnO<sub>3</sub> nanofibers for the measurements are random and the data represents the average of all orientations. Figure 3 shows the temperature dependence of the magnetization,  $M(T)$ , under zero-field-cooled (ZFC) and field-cooled (FC) conditions, applying a field of 1000 Oe. Irreversibility (i.e., splitting between the FC and ZFC curves) is observed below  $T \approx 30$  K. The ZFC magnetization curve presents one sharp peak at  $T \approx 25$  K. E. Winkler *et al.* [13] reported the 3 nm NiO nanoparticles had the similar magnetic behavior previously. They indicated, with decreasing temperature, the particle core moment freezing occurred, which led to the first peak in the  $M_{ZFC}$ . While the temperature continually decreased, the surface collective freezing occurred, as shown in Fig. 3 the second peak in the  $M_{ZFC}$  finally. But in our result, there is only one peak, located at the low temperature, it can be explained that no core moment freezing occurs in our sample. The peak of our sample at the low temperature is due to the particle surface moment is frozen, which implies the sample is possible to display the superparamagnetic property. F. Gao *et al.* [14] reported that, due to the significant size effect for nanoscale materials, the spin-glass-like surface layer contributed essentially to the sample's superparamagnetism, which would be in a frozen state at very low temperature. In fact, earlier reports on NiO [13] presented a similar superparamagnetic behavior at low temperature due to the nanoscale size effect. Under the field-cooling condition, the measured  $M$  increases with the decreasing of the temperature. At  $T \approx 50$  K, the measured  $M$  increases rapidly, then, it reaches a saturated value about 0.016 at  $T \approx 20$  K. Under the FC condition, the magnetic domains will be directionally ordered to some extent, resulting in the enhanced  $M$ .

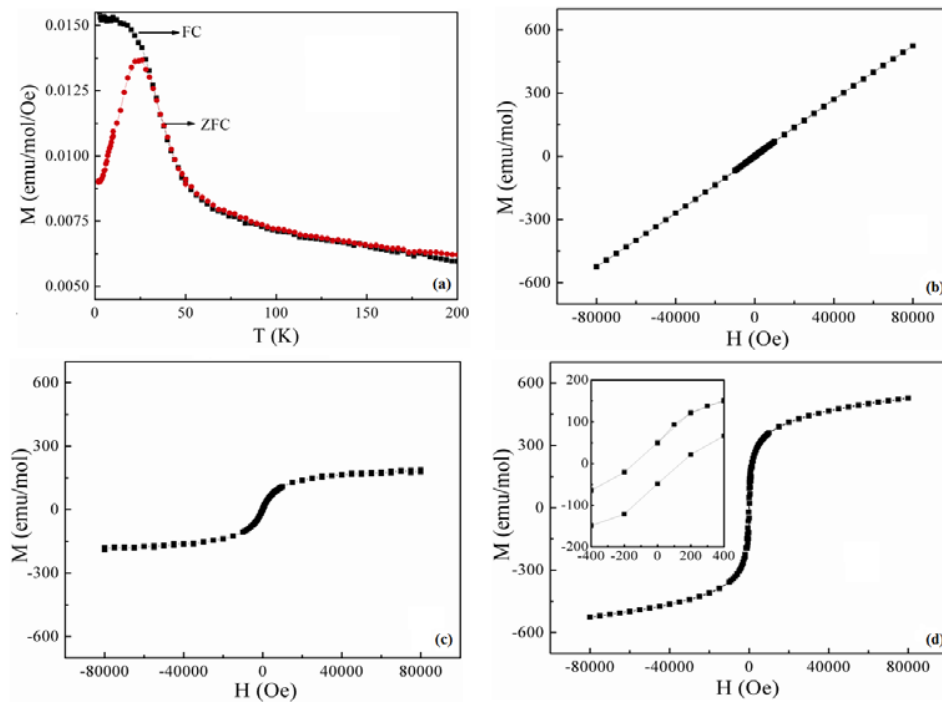


Fig. 3 Magnetic susceptibility for the h-YMnO<sub>3</sub> nanofibers in zero-field-cooled (ZFC) and field-cooled (FC) conditions (H=1000 Oe). Magnetic hysteresis loop of the YMnO<sub>3</sub> nanofibers measured at various temperatures under the 1000 Oe magnetic field, (b) 300K; (c) 30K; (d) 5K, the inserted figure shows magnetic hysteresis loop of low magnetic field at 5K.

M vs H measurements are performed up to 1000 Oe at different temperature. As shown in Fig. 3(a), h-YMnO<sub>3</sub> nanofibers display the linear  $M$ - $H$  relationship, and no hysteretic behavior is observed at the room temperature, which indicates that h-YMnO<sub>3</sub> nanofibers are paramagnetic. At  $T=30$  K, we observe the superparamagnetic of h-YMnO<sub>3</sub> nanofibers, the evidence is the reversible S-type curve in the Fig. 3(b). The  $M$ - $H$  relationship indicates h-YMnO<sub>3</sub> nanofibers are ferromagnetic in the Fig. 3(c). F. Gao *et al.* [14] reported that the cycloid structure of bulk BiFeO<sub>3</sub>, of which the wavelength was 62 nm, was partially destroyed in the BiFeO<sub>3</sub> nanowires which were about 50 nm in diameter, which contributed to the weak FM behaviors. Hence, the ferromagnetic property of our sample at 5 K derives from the presence of the particle which diameter is smaller than the critical dimension of the single domain. It also implied that the blocking temperature of superparamagnetism ( $T_B$ ) is above 5 K and below 30 K. Moreover, it is worth noticing that the hysteresis loops are symmetrical at 5 K as shown in Fig. 3(d), the demagnetizing and remagnetizing curves vary rapidly at low fields.

#### 4. SUMMARY

The h-YMnO<sub>3</sub> nanofibers in the diameter ranging from 200 nm to 800 nm were fabricated by using an electrostatic spinning. It is paramagnetic phase at room temperature. The ferromagnetism is confirmed by the existence of magnetic hysteresis loop at 5 K. At low temperature, significant superparamagnetic behaviors have been observed. It was also confirmed that the  $T_B$  is above 5 K and below 30 K.

## 5. ACKNOWLEDGEMENTS

This work was financially supported by the National Nature Science Foundation (50672075), the 111 Program (BO8040) of MOE, the Xi'an Science and Technology Foundation (XA-AM200905, XA-AM200906, XA-AM201003), the Fundamental Research Foundation (NPU-FFR-200703) of NPU, and the SKLSP Research Fund (40-QZ-2009) of China.

## REFERENCES

1. R. Ramesh and N.A. Spaldin, *Nature Mater.*, Vol. 16 (2007), p. 21.
2. Y. Aikawa, T. Katsufuji, T. Arima and K. Kato, *Phys. Rev. B*, Vol. 71 (2005), p. 184418.
3. X. Martí, F. Sánchez, D. Hrabovsky, J. Fontcuberta, V. Laukhin, V. Skumryev, M.V. Garcia-Cuenca, C. Ferrater, M. Varela, U. Lüders, J.F. Bobo, S.Estradé, J. Arbiol and F. Peiró, *J. Cryst. Growth*, Vol. 299 (2007), p. 288.
4. S. Lee, M.S. Kang, C. Lee, A. Hoshikawa, M. Yonemura, T. Kamiyama and J.G. Park, *Physica B*, Vol. 405 (2006), p. 385.
5. X. Martí, I. Fina, V. Skumryev, C. Ferrater, M. Varela, L. Fábrega, F. Sánchez and J. Fontcuberta, *Appl. Phys. Lett.*, Vol. 95 (2009), p. 142903.
6. X. Martí, F. Sánchez, D. Hrabovsky, L. Fábrega, A. Ruyter, J. Fontcuberta, V. Laukhin, V. Skumryev, M.V. Garcia-Cuenca, C. Ferrater, M. Varela, A. Vilà, U. Lüders and J.F. Bobo, *Appl. Phys. Lett.*, Vol. 89 (2006), p. 032510.
7. C.G. Zhong, Q. Jiang, H. Zhang and X.F. Jiang, *Appl. Phys. Lett.*, Vol. 94 (2009), p. 224107.
8. K. Asokan, Y.S. Chen, C.W. Pao, H.M. Tsai, C.W.O. Lee, C.H. Lin, H.C. Hsueh, D.C. Ling, W.F. Pong, J.W. Chiou, M.H. Tsai, O. Peña and C. Moure, *Appl. Phys. Lett.*, Vol. 95 (2009), p. 131901.
9. T. Jungk, Á. Hoffmann, M. Fiebig and E. Soergel, *Appl. Phys. Lett.*, Vol. 97 (2010), p. 012904.
10. H.W. Zheng, Y.F. Liu, W.Y. Zhang, S.J. Liu, H.R. Zhang and K.F. Wang, *J. Appl. Phys.*, Vol. 107 (2010), p. 053901.
11. Y.X. Ye, H.Q. Fan and J. Li, *Mater. Lett.*, Vol. 64 (2010), p. 419.
12. X.L. Chen, H.Q. Fan and L.J. Liu, *J. Crystal. Growth*, Vol. 284 (2005), p. 434.
13. E. Winkler, R.D. Zysler, M.Vasquez Mansilla and D. Fiorani, *Phys. Rev. B*, Vol. 72 (2005), p. 132409.
14. F. Gao, Y. Yuan, K.F. Wang, X.Y. Chen, F. Chen and J.M. Liu, *Appl. Phys. Lett.*, Vol. 89 (2008), p. 102506.

## **EFFECT OF APPLIED VOLTAGE ON ZnO NANORODS SYNTHESIZED USING CONTINUOUS SPRAY PYROLYSIS (CoSP) TECHNIQUE**

CHARU DWIVEDI\* and V. DUTTA

*Photovoltaic Laboratory, Centre for Energy Studies, Indian Institute of Technology Delhi,  
Hauz Khas, New Delhi-110016, India*

\*Corresponding Author, e-mail: [charudwi.iitd@gmail.com](mailto:charudwi.iitd@gmail.com)

### **ABSTRACT**

Well-aligned ZnO nanorods were fabricated on ITO coated glass substrate via self assembly of ZnO nanoparticles created using CoSP technique. The spray solution containing Zn precursor was atomized using gas pressure and also using electric pressure by applying a voltage (varied from 0 to 1 kV) across the spray nozzle and an annular ground electrode kept at a distance of ~ 2 mm. The droplet size decrease and the polarization of the created ZnO nanoparticles led to formation of different nanostructures on the substrates kept inside the furnace. SEM and AFM images of ZnO nanorods showed that the average diameter of nanorods/nanostructures increased from 500 nm to 7  $\mu$ m when the applied voltage was increased from 0 to 0.8 kV and decreased abruptly to 230 nm at 1 kV.

### **1. INTRODUCTION**

One-dimensional (1D) semiconductor nanostructures such as rods, wires, belts and tubes have in recent years attracted much attention due to their many unique properties and the possibility that they may be used as building blocks for future electronics and photonics [1–3], as well as for life-science applications [4]. Among them 1D ZnO nanostructures attract special attention due to the large excitonic binding energy of 60 meV, high electron mobility and high mechanical and thermal stabilities [5]. ZnO is being extensively investigated due to its applications in devices such as solar cells [6], UV photonics [7], transparent high-power electronics, varistors [8], surface acoustic wave devices, piezoelectric transducers [9] and gas sensing devices [10]. Recently, 1D nanostructures of ZnO, including nanowires, nanobelts, and nanotubes, have been fabricated by various methods [11–13]. In order to produce aligned ZnO nanorods, both vapor growth and solution-growth processes have been used. Compared to other solution growth techniques, spray pyrolysis offers the possibility of preparing nanoparticles at low cost and scaling up for large scale production. A spray pyrolysis system for fabrication of nanoparticles/nanostructure has been reported by us earlier and the process is termed Continuous Spray Pyrolysis, since the process can be continued as long as the solution flow is maintained. The properties can be easily controlled over a wide range by changing the spray parameters, thus eliminating major drawbacks of chemical methods. Hence, we can have the control over the product in terms of size, shape and stoichiometry by suitably controlling the physical and chemical parameters during the process. In addition, by inserting substrates in the spray system, one can obtain nanostructure due to self-assembly of the created nanoparticles.

In this work, the morphological changes in ZnO nanocrystalline films grown by a continuous spray pyrolysis reactor are investigated as a function of the applied voltage. The substrates were pre-treated by dip-coating with a solution comprising of zinc salt serving as a seed layer, and spray pyrolyzed ZnO nanoparticles self assembly on the pre-treated substrate leads to nanorod formation. The effect of applied voltage on the morphology of the nanorod formation is studied.

## 2. EXPERIMENTAL

Well-aligned ZnO nanorods were fabricated on ITO coated glass substrate via self assembly of ZnO nanoparticles created using CoSP technique. The details of the experimental setup is reported earlier.

The spray solution containing Zn precursor dissolved in distilled water is injected into the reactor, which leads to ZnO nanoparticle creation. Some of these nanoparticles will self assemble if a substrate coated with a seed layer is kept near the reactor outlet, allowing rest of the nanoparticles to be collected in the collection chamber. A round bottom flask connected to the outlet works as the collection chamber. Thus, the technique has the advantage of fabricating both the nanoparticles and the nanostructured films at the same time.

Zinc acetate dihydrate of 0.1 M,  $(\text{CH}_3\text{COO})_2\text{Zn}\cdot 2\text{H}_2\text{O}$  (Sigma- Aldrich 98% pure), was dissolved in 100 ml of distilled water and kept for stirring until it forms a clear transparent solution. The solution flow rate and gas pressure were kept constant at 2 ml/min and  $2 \text{ kgf/cm}^2$ .  $\text{N}_2$  was used as the carrier gas. The methodology for nanorod formation is reported elsewhere [14] in which pre-treated glass or ITO substrates were placed in the third zone of the furnace and the self-assembly of ZnO nanoparticles on the pre-treated substrates leads to the vertically aligned nanorod growth. Since atomization can be affected by applying electric field, a DC voltage (upto 1kV) was applied between the spray nozzle and a circular metal electrode (perforated sheet) placed 2mm from it for creating the electric pressure on the droplets during atomization. The morphological changes of ZnO nanostructures a function of applied voltage (0-1kV) were studied using ZEISS EVO-50 model scanning electron microscope (SEM). The absorbance of the films in the visible region was measured using ECIL double beam UV-VIS spectrophotometer. An atomic force microscope (AFM, Dimension 3100) was use to detect the morphology of ZnO nanorods.

## 3. RESULTS AND DISCUSSION

Fig. 1 shows the  $1.5 \mu\text{m} \times 1.5 \mu\text{m}$  AFM images of the samples grown at 0.4, 0.6, 0.8 and 1.0 kV. The average diameter of nanorods/nanostructures increases from 500 nm to 7  $\mu\text{m}$  (may be termed microrods) when the applied voltage is increased from 0 to 0.8 kV and decreases abruptly to 230 nm at 1 kV.

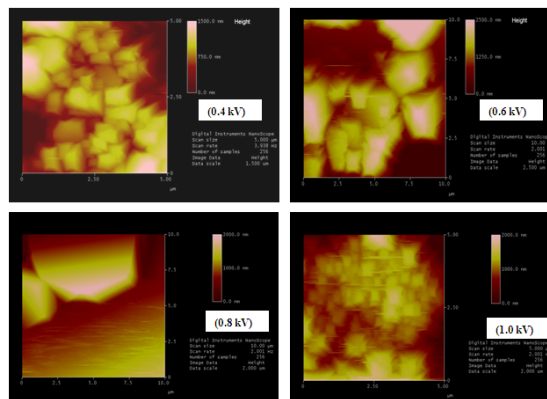


Fig. 1 AFM images of zno nanorods at different applied voltages.

Fig. 2 shows the SEM (Scanning Electron Microscopy) images of ZnO nanorods grown under applied voltage which further supports the AFM data. Roughness analysis shows that the surface roughness follows almost the same trend. For 0.4 kV applied voltage, roughness (rms) is 319 nm, for 0.6 kV, it is 687 nm and for 1.0 kV, it is 308 nm.

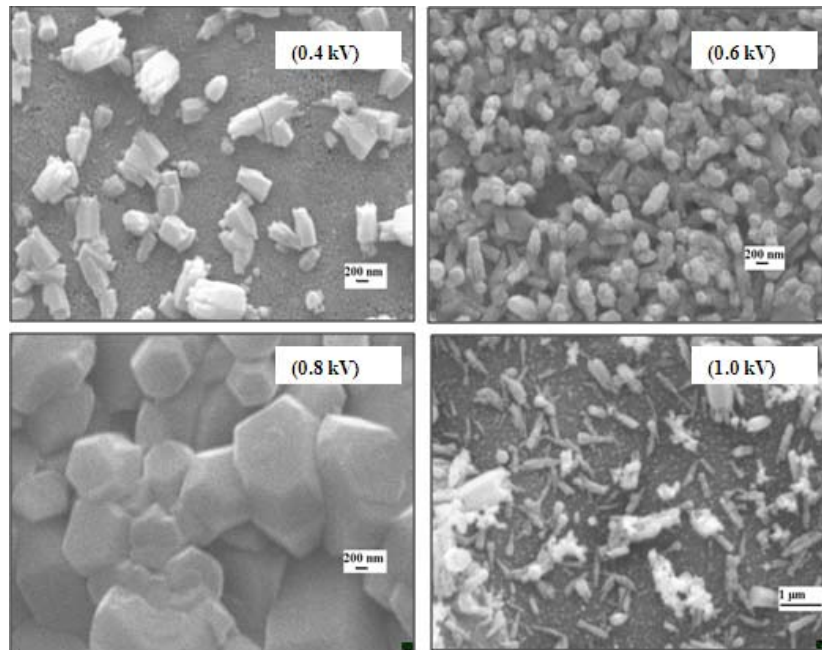


Fig. 2 SEM images of zno nanorods at different applied voltages.

As voltage is applied to the nozzle, more charge is created at the droplet surface exerting increased electrical forces. As a result, the size of the drop coming off of the nozzle decreases and the frequency of drops increases [15]. The pyrolytic action within the droplet creates the ZnO nanoparticals, which following the trend of droplet size decrease should ideally show size reduction with the increased voltage. Correspondingly the nanorod dimension should also be decreasing. The observed increase and then decrease of the nanorod diameter is suggestive of coalescence of the nanoparticles before the nanorod formation which may be dictated by the nanoparticle size. The increasing trend is reversed at 1 kV which is not commensurate with the above explanation. It can be surmised that when the droplet size is very small as expected at 1 kV, the effect of the large electric charge needed to support the electric field may be preventing the coalescence and the self assembly creates a smaller nanorod diameter. This may be a possible explanation for the decrease in the size of the nanorods beyond 800 V.

The x-ray diffraction (XRD) pattern (Fig. 3) confirms high-purity wurtzite hexagonal phase, and all the diffraction peaks match well with standard hexagonal ZnO ( $a = 3.249 \text{ \AA}$  and  $c = 5.206 \text{ \AA}$ , JCPDS 36-1451). The intensities of the reflections of the planes gradually increases for

the nanorods synthesized with voltage (0.4 - 0.8 kV) and decreases thereafter (at 1 kV) which further supports the SEM results.

Fig. 4 shows the optical absorption spectrum of the ZnO nanorods synthesized at different applied voltages (0.4 - 1.0 kV). The room temperature UV-visible spectrum exhibits a strong absorption with an onset around 376 nm which corresponds to a band gap of 3.29 eV.

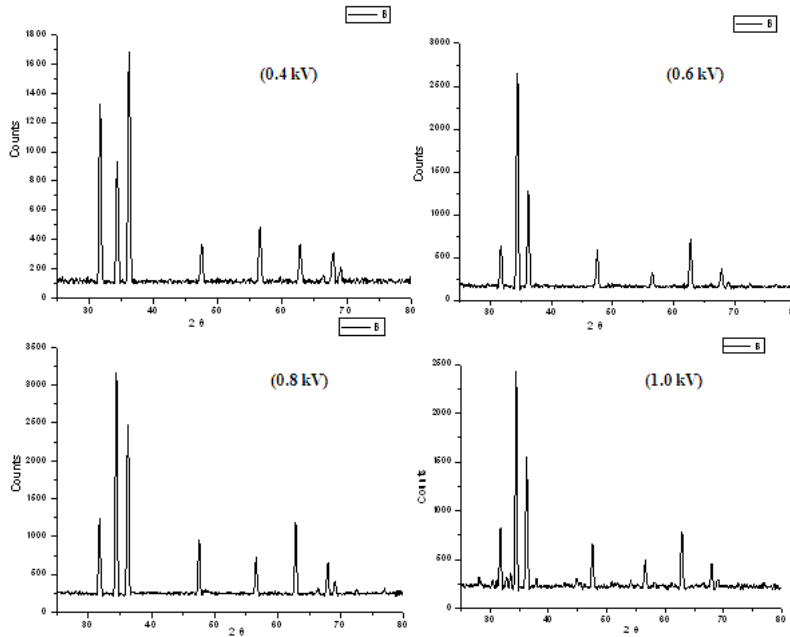


Fig. 3 XRD spectrum of zno nanorods at different applied voltages.

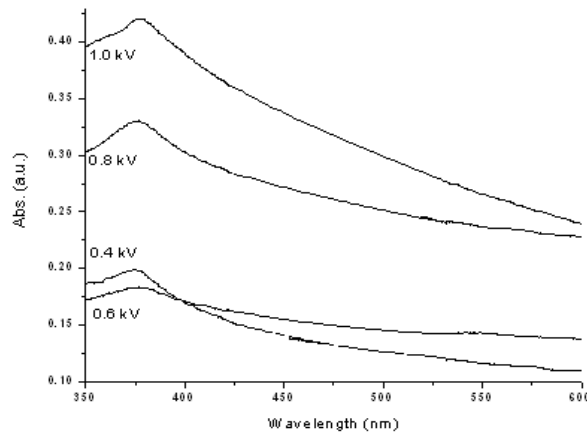


Fig. 4 Absorption spectra of zno nanorods at different applied voltages.

#### **4. CONCLUSION**

ZnO nanorods were successfully prepared by continuous spray pyrolysis reactor using aqueous zinc precursor solution. The effect of applied voltage on the synthesized nanorods is studied. The presence of a high DC voltage results in an increase in the dimension of rods from 500 nm to 7  $\mu$ m when the voltage is increased from 0.4 to 0.8 kV and then decreasing to 230 nm at 1.0 kV. AFM, SEM and XRD data all support this behaviour.

This process is well repeatable and can give a high yield of the products, which may make this simple strategy a potential method for the controllable syntheses of other oxide nanoparticles/nanostructures. The possibility of doing a continuous operation will have a great potential in developing nanoparticles for large area devices like Dye Sensitized Solar Cells and hybrid organic solar cells. In fact, since the nanorod dimensions can be easily manipulated by changing the applied voltage, one can create different nanorod structures and study the effect on DSSC characteristics in order to achieve high conversion efficiency by combining the high effective area for dye absorption and high charge extraction through nanorods.

#### **REFERENCES**

1. D. Appell, *Nature* **419** (2002) 553.
2. L. Samuelson, *Mater. Today* **6**, 22 (2003).
3. X.F. Duan, Y. Huang, Y. Cui, J.F. Wang and C.M. Lieber, *Nature* **409**, 66 (2001).
4. Y. Cui, Q. Wei, H. Park and C.M. Lieber, *Science* **293**, 1289. (2001)
6. M.H. Huang, S. Mao, H. Feick, J.Q. Yan, Y.Y. Wu, H. Kind, E. Weber, R. Russo, P.D. Yang, *Science* **292**, 1897(2001).
7. Z.W. Pan, Z.R. Dai, Z.L. Wang, *Science* **291**, 1947(2001).
8. J.J. Wu, S.C. Liu, C.T. Wu, K.H. Chen, C.L. Chen, *Appl. Phys. Lett.* **81**, 1312 (2002).
9. Z.S. Wang, C.H. Huang, Y.Y. Huang, Y.J. Hou, P.H. Xie, B.W. Zhang, H.M. Cheng, *Chem. Mater.* **13**, 678 (2001).
10. C.H. Chia, T. Makino, K. Tamura, Y. Segawa, M. Kawasaki, A. Ohtomo, H. Koinuma, *Appl. Phys. Lett.* **82**, 1848 (2003).
11. M. Singhal, V. Chhabra, P. Kang, D.O. Shah, *Mater. Res. Bull.* **32**, 239 (1997).
12. V.E. Wood, A.E. Austin, *Magnetoelectric Interaction Phenomena in Crystals*, Gordon and Breach, London, (1975).
13. C.J. Lee, T.J. Lee, S.C. Lyu, Y. Zhang, H. Ruh, H. Lee, *Appl. Phys. Lett.* **81**, 3648 (2002).
14. V. Dutta and C. Dwivedi, Method of producing ZnO nanorods by self assembly of spray pyrolyzed nanoparticles. (patent under process).
15. C. Berkland, D.W. Pack, K. Kim, *Biomaterials* **25**, 5649 (2004).



## EFFICIENT DYE SENSITIZED SOLAR CELLS BASED ON TiO<sub>2</sub> NANOTUBES AND NANOTUBE-NANOPARTICLE COMPOSITES

E.V.A. PREMALAL\*, R.M.G. RAJAPAKSE, K. MURAKAMI AND A. KONNO

Graduate School of Science and Technology, Shizuoka University, Hamamatsu, Japan

\*Corresponding Author, e-mail: vikum77@yahoo.com

### ABSTRACT

Vertically-aligned, reasonably dense, 500 nm long TiO<sub>2</sub> nanotubes (NTs) are prepared on transparent conducting tin oxide (CTO) surfaces by a wet chemical procedure involving three steps: (a) seeding the CTO surface with ZnO crystals, (b) depositing sacrificial ZnO nanorods (NRs) on seed crystals, and (c) Covering ZnO NRs with TiO<sub>2</sub> and simultaneously dissolving ZnO NRs and replacing them with TiO<sub>2</sub> NTs. The Dye-Sensitized Solar Cells (DSCs) fabricated using such active electrodes and N719 dye with usual I<sup>-</sup>/I<sub>3</sub><sup>-</sup> in acetonitrile liquid electrolyte system yield 2.46% solar-to-electricity conversion efficiency ( $\eta$ ) without the aqueous TiCl<sub>4</sub> treatment and 3.40% with aqueous TiCl<sub>4</sub> treatment at 1000 W m<sup>-2</sup> simulated AM 1.5 irradiation. These values are higher and impressive for shorter NT arrays of ~ 500 nm length. The successive introduction of TiO<sub>2</sub> NPs by deliberate spraying into the void spaces of NTs to form NT-NP composite films results in linear increase of dye coverage throughout the range of mass ratio of NT:NP studied (1:0 to 1:3.2). The variation of  $\eta$  as a result of NT-NP composite structure (with aqueous TiCl<sub>4</sub> treatment) shows a gradual increase up to 8.53% at 1:2.2 NT:NP mass ratio, beyond which it slowly decreases. At the highest NP mass used the  $\eta$  has shown 4.6 % decrease from its maximum value. The performance of the DSC with the composite NT and NP film is better than that with NP alone at the same total TiO<sub>2</sub> mass. The NTs in NT-NP composite films help by allowing faster 1-D electron transport which provides by-pass fast-track route as opposed to “random-walk” path available in the interconnected NP alone system. However, excessive increase in NP amount in the NT-NP composite system increases NP alone characteristics and hence gradually increases recombination thus decreasing the solar-to-electricity conversion efficiency.

### 1. INTRODUCTION

The Dye-sensitized Solar Cell (DSC) invented by O’Brion and Grätzel in 1991 [1] has now reached 11.5% photon-electricity conversion efficiency [2]. This DSC is composed of a highly porous, nanocrystalline, interconnected titania nanoparticles of typical thickness around 15  $\mu$ m deposited on F<sup>-</sup> doped SnO<sub>2</sub> (FTO) surface as the working electrode, lightly platinized FTO as the counter electrode with non-aqueous electrolyte comprising of I<sup>-</sup>/I<sub>3</sub><sup>-</sup> redox couple sandwiched between the two electrodes. The interconnected titania surfaces are fully covered with a dye (typically ruthenium bipyridyl dicarboxylate based dyes) for the light absorption. The excited dye molecules inject electrons to the CB of TiO<sub>2</sub> particles in femtosecond time scale. The electrons diffuse along the interconnected titania particles in a slow “random walk” path and thereby providing ample opportunities for recombination with triiodide ions in the solution and the dye cations attached to TiO<sub>2</sub> surfaces. The use of one-dimensional arrays of nanomaterials, attached perpendicular to the FTO surface, provides fast track along the material and the absence of grain boundaries reduces the possibility of recombination. In this presentation, we reveal the recent advancements in the DSC based on 1-D titania nanotubes. The first report of the formation of porous surface of titanium metal due to electrochemical oxidation in fluoride ion containing electrolyte is by Zwilling and co-workers in 1991 [3]. A decade later, Grimes *et al* [4] reported the formation of titania nanotube (NT) arrays due to the anodic oxidation of titanium metal in the above electrolyte. Since then, synthesis, optimization and use of titania NTs in DSCs have been extensively explored. There are several methods for the production of TiO<sub>2</sub> NTs, which include the following.

- Anodic oxidation of Ti in fluoride containing electrolytes
- Deposition into the pockets of nanoporous alumina templates
- Sol-gel approach using organic gelator templates
- Seeded growth
- Hydrothermal processes

Table 1 below shows some selected literature on the TiO<sub>2</sub> NT based DSCs prepared using N 719 dye and the usual liquid electrolyte containing I<sup>-</sup>/I<sub>3</sub><sup>-</sup> redox couple.

**Table 1:** Some selected literature on solar cell parameters of DSCs based on TiO<sub>2</sub> NTs

Reference	Method	Solar Cell Parameters under 1 sun
[4] Uchida <i>et al</i> , Electrochemistry <b>70</b> , 418 (2002)	Hydrothermal Synthesis	V <sub>OC</sub> = 0.70 V, I <sub>SC</sub> = 1.26 mA cm <sup>-2</sup> , FF = 0.66, η = 2.9%
[5] Macak <i>et al</i> , Electrochem. Commun. <b>7</b> , 1137 (2005)	Anodization in F <sup>-</sup> containing electrolyte	2.5 μm long tubes, IPCE <sub>max</sub> (at 540 nm) of 3.3% and 500 nm long tubes, IPCE <sub>max</sub> 1.6% (at 530 nm)
[6] Raja <i>et al</i> , J. Power Sources <b>159</b> , 1258 (2006)	Anodization in F <sup>-</sup> containing electrolyte	η = 4% in 1 M KOH
[17] Paulose <i>et al</i> , Nanotechnology <b>17</b> , 1446 (2006)	Potentiostatic anodization of Ti foil	Back-side illumination I <sub>SC</sub> = 8.79 mA cm <sup>-2</sup> , V <sub>OC</sub> = 841 mV FF = 0.57 η = 4.24%
[7] Wei <i>et al</i> , J. Electrochem. Soc. <b>153</b> , A1232 (2006)	Hydrothermal Synthesis	η = 7.5%
[8] Paulose <i>et al</i> , J. Phys. D-Appl. Phys. <b>39</b> , 2498 (2006)	Potentiostatic anodization of Ti film	Front-side illumination: I <sub>SC</sub> = 10.3 mA cm <sup>-2</sup> , V <sub>OC</sub> = 0.84V, FF = 0.54 and η = 4.7% Back-side illumination: I <sub>SC</sub> = 10.6 mA cm <sup>-2</sup> , V <sub>OC</sub> = 0.82 V, FF = 0.51 and η = 4.4%
[9] Stergiopoulos, Nanotechnology <b>19</b> , 7 (2008)	Anodization	η = 0.85% using a composite polymer redox electrolyte, η = 1.65% using a liquid electrolyte
[10] Shankar <i>et al</i> , Nano Letters <b>8</b> , 1654 (2008)	Anodization	14.4 μm long TiO <sub>2</sub> nanotubes Back-side illumination: η = 6.1%. 1 μm long tubes: Front side illumination: η = 4.1%
[11] Xie <i>et al</i> , Nanotechnology <b>19</b> , 6 (2008)	Anodization	η = 0.67%

[12] Yang <i>et al</i> , J. Am. Ceramic Soc. <b>91</b> , 3086 (2008)	Anodization	$\eta = 3.4\%$
[13] Li <i>et al</i> , Microelectronics Journal <b>40</b> , 108 (2009)	Hydrothermal Synthesis	Indolin Dye: $\eta = 9.8\%$
[14] Kang <i>et al</i> , Nano Letters <b>9</b> , 601 (2009)	Anodization	$\eta = 3.5\%$
[15] Qu <i>et al</i> , J. Phys. Chem. C <b>113</b> , 3359 (2009)	Hydrothermal Synthesis	$\eta = 7.71\%$
[16] Roy <i>et al</i> , Electrochem. Commun. <b>11</b> , 1001 (2009)	Hydrothermal Synthesis	TiCl <sub>4</sub> treatment has doubled $\eta$ from 1.9% to 3.8%
[17] Chen <i>et al</i> , J. Electrochem. Soc. <b>156</b> , C304 (2009)	Anodization	0.3 (0.5 vol % HF), 12 (0.5 wt % KF), and 18 mm (0.5 wt % NH <sub>4</sub> F) had $\eta = 0.13, 3.76, \text{ and } 6.18\%$ respectively.
[18] Varghese <i>et al</i> , Nature Nanotechnology <b>4</b> , 592 (2009)	Electrochemical approach to produce NTs on FTO	$\eta = 6.9\%$ .
[19] Charoensirithavorn <i>et al</i> , J. Electrochem. Soc. <b>156</b> , H803 (2009)	ZnO seeding method	4 $\mu\text{m}$ thickness $I_{\text{SC}} = 8.37 \text{ mA cm}^{-2}$ , an $V_{\text{OC}} = 0.80 \text{ V}$ , FF = 0.67, $\eta = 4.53\%$
[20] Lin <i>et al</i> J. Mater. Chem. <b>20</b> , 1073 (2010)	Anodization followed by flaking. Deposition on FTO with TiO <sub>2</sub> under layer	Closed end NTs $\eta = 5.3\%$ open end NTs $\eta = 9.1\%$ ,
[21] Chen <i>et al</i> , Current Appl. Phys., <b>10</b> , S176 (2010)	Arc ion plating of Ti on FTO for anodization	$\eta = 1.88\%$
[22] Li <i>et al</i> , Mat. Chem. Phys. <b>124</b> , 179 (2010)	90% NT + 10% NP	$\eta = 7.41\%$
[23] Xiao <i>et al</i> , Electrochim. Acta, <b>55</b> , 4573 (2010)	Hydrothermal	$\eta = 4.0\%$
[24] Park <i>et al</i> , Sol. Energy Mat. Sol. Cells, <b>95</b> , 184 (2011)	Anodization	15 $\mu\text{m}$ $\eta = 2.91\%$
[25] Lie <i>et al</i> , Renewable Energy, <b>36</b> , 1177 (2011)	ZnO seeding	$\eta = 2.1\%$

## 2. EXPERIMENTAL

In our study, we used the seeded growth technique as described in the literature [14]. By changing variables, we obtained 500 nm long, reasonably dense, TiO<sub>2</sub> NTs on FTO plates. The I-V characteristics of DSCs made from pristine NTs and those subjected to TiCl<sub>4</sub> treatment, and those containing varying amounts of TiO<sub>2</sub> NPs of 2-3 nm diameters were studied. Figure 1 below shows the I-V characteristics of such DSCs at 1 sun illumination. The N719 dye, the usual liquid electrolyte containing I<sup>-</sup>/I<sub>3</sub><sup>-</sup> redox couple and lightly platinized FTO counter electrode were used in the fabrication of DSCs in the usual manner.

### 3. RESULTS AND DISCUSSION

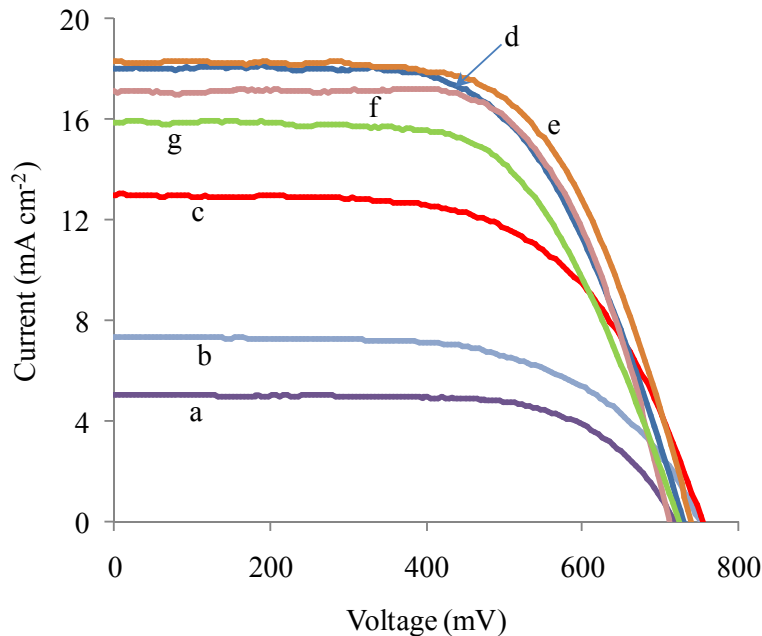


**Figure 1:** I-V curves for the DSCs made using pristine TiO<sub>2</sub> NTs without TiCl<sub>4</sub>-treatment (curve a), pristine TiO<sub>2</sub> NTs with TiCl<sub>4</sub>-treatment (curve b), composite films of nanotubes with increased amounts of TiO<sub>2</sub> nanoparticles with TiCl<sub>4</sub>-treatment (curves c – f) and using only nanoparticle with TiCl<sub>4</sub>-treatment (curve g).

The TiO<sub>2</sub> nanotubes (NTs) prepared by chemical bath, by the seeded growth of sacrificial ZnO nanorods, produces vertical NTs with approximately 500 nm length and 80 nm thickness and 45 nm pore diameter (Figure 2).

The void density was found to be 52.6%. The DSSC made using N719 dye gives 2.46% efficiency at AM 1.5 irradiation but upon TiOCl<sub>2</sub> treatment, the efficiency is increased to 3.48% due to 30% increase in the dye coverage. The gradual introduction of TiO<sub>2</sub> nanoparticles into the voids and calcinations at 500 °C to result in interconnected nanoporous matrix systematically increases the dye coverage and the collection efficiency and a maximum value of 8.53% could be obtained at NT:NP mass ratio of 0.5:1.1 mg cm<sup>-2</sup>. When the active electrode is made entirely of TiO<sub>2</sub> NPs with the same mass as the sum of masses of NPs and NTs the collection efficiency is lowered. The enhanced collection efficiency in the presence of NTs is due to the fast 1-D electron transport along defect-free NTs. The collection efficiencies reported herein are much higher than those reported for NTs with similar lengths. Table 2 provides the I-V data of the DSCs fabricated together with the dye coverage in the active electrodes.

Figure 2: SEM images of (a) TiO<sub>2</sub> nanotubes and (b) nanotube-nanoparticle composite materials.

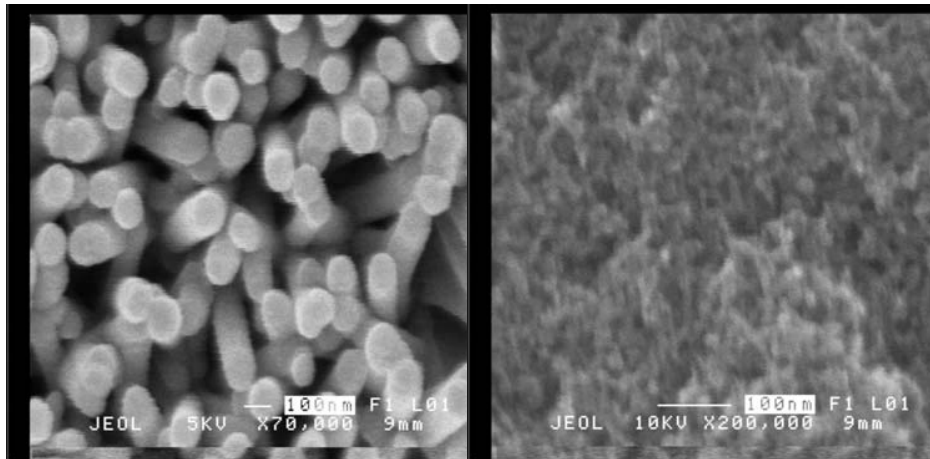


Table 2: Nanoparticle-loading and dye adsorption together with photovoltaic parameters of the cells (a) to (g) under the simulated sunlight irradiation (AM 1.5, 100 mW cm<sup>-2</sup>)

Cell	Mass of NT/ mg cm <sup>-2</sup>	Mass of NP/ mg cm <sup>-2</sup>	J <sub>sc</sub> /mA cm <sup>-2</sup>	V <sub>oc</sub> /mV	FF	η%	Dye adsorption/ Molecules cm <sup>-2</sup>
a	0.5	0	5.11	720	0.670	2.46	5.69x10 <sup>15</sup>
b	0.5	0	7.45	753	0.607	3.40	7.44x10 <sup>15</sup>
c	0.5	0.1	12.87	755	0.613	5.96	2.23x10 <sup>16</sup>
d	0.5	0.9	17.90	731	0.615	8.04	6.23x10 <sup>16</sup>
e	0.5	1.1	18.00	740	0.640	8.53	6.41x10 <sup>16</sup>
f	0.5	1.6	17.10	712	0.669	8.14	8.19x10 <sup>16</sup>
g	0	1.4	15.86	725	0.620	7.13	3.58x10 <sup>16</sup>

#### 4. CONCLUSIONS

TiO<sub>2</sub> nanotubes were prepared by a wet chemical procedure and used in DSC applications. An overall conversion efficiency of 2.46% was obtained. TiO<sub>2</sub> nanoparticles filled in the void spaces of NTs gave increasing efficiency as the amount is increased up to 1:2.2 mass ratio and a maximum efficiency of 8.53% was obtained. The efficiency then decreased due to the further introduction of NPs.

#### REFERENCES

1. B. O'Reagan, M. Grätzel, Nature **353**, 737(1991)
2. C.Y. Chen, M. Wang, J.Y. Li, N. Pootrakulchote, L. Alibabaei, C.H. Ngoc-le, J.D. Decoppet, J.H. Tsai, C. Grätzel, C.G. Wu, S.M. Zakeeruddin, M. Grätzel, ACSNANO, **3** 3103(2009)
3. V. Zwillling, M. Ancourtner, E. D. Ceretti, Electrochim. Acta, **45**, 9219(1991)
4. T. Rattanavoravipa, T. Sagawa, S. Yoshikawa, Solar Energy Mater. Solar Cells, **92**, 1445 (2008)

5. J. M. Macak, H. Tsuchiya, A. Ghicov, and P. Schmuki, *Electrochem. Commun.* **7**, 1133 (2005)
6. K. S. Raja, V. K. Mahajan, and M. Misra, *Journal of Power Sources* **159**, 1258 (2006)
7. D. Wei, Y. Konishi, H. S. Zhou, H. Sugihara, and H. Arakawa, *J. Electrochem. Soc.* **153**, A1232 (2006)
8. M. Paulose, K. Shankar, O. K. Varghese, G. K. Mor, B. Hardin, and C. A. Grimes, *Nanotechnology* **17**, 1446 (2006)
9. T. Stergiopoulos, A. Ghicov, V. Likodimos, D. S. Tsoukleris, J. Kunze, P. Schmuki and P. Falaras, *Nanotechnology* **19**, 235602 (2008)
10. K. Shankar, J. Bandara, M. Paulose, H. Wietasch, O. K. Varghese, G. K. Mor, T. J. LaTempa, M. Thelakkat, and C. A. Grimes, *Nano Letters* **8**, 1654 (2008)
11. Z. B. Xie, S. Adams, D. J. Blackwood, and J. Wang, *Nanotechnology* **19**, 6 (2008)
12. Y. Yang, X. H. Wang, and L. T. Li, *J. Am. Ceramic Soc.* **91**, 3086 (2008)
13. Q. Y. Li and G. X. Lu, *J. Power Sources* **185**, 577 (2008)
14. Tae-Sik Kang, Adam P. Smith, Barney E. Taylor and Michael F. Durstock. *Nano Letters*, **9**, 601 (2009)
15. J. Qu, X. P. Gao, G. R. Li, Q. W. Jiang, and T. Y. Yan, *J. Phys. Chem. C* **113**, 3359 (2009)
16. P. Roy, D. Kim, I. Paramasivam, and P. Schmuki, *Electrochem. Commun.* **11**, 1001 (2009)
17. C. C. Chen, W. D. Jehng, L. L. Li, and E. W. G. Diau, *J. Electrochem. Soc.* **156**, C304 (2009)
18. O. K. Varghese, M. Paulose, and C. A. Grimes, *Nature Nanotechnology* **4**, 592 (2009)
19. P. Charoensirithavorn, Y. Ogomi, T. Sagawa, S. Hayase, and S. Yoshikawa, *J. Electrochem. Soc.* **156**, H803 (2009)
20. C.J. Lin, W-Y Yu, S.H. Chien, *J. Mater. Chem.* **20**, 1073 (2010)
21. C-H Chen, K-C Cheng, J-L He, *Current Appl. Phys.*, **10**, S176 (2010)
22. X.D. Li, D.W. Zhang, S. chen, Z.A. Wang, Z. Sun, X.J. Yin, S.M. Huang, *Mat. Chem. Phys.*, **124**, 179 (2010)
23. X. Xiao, J. Wu, G. Yue, G. Xie, J-Lin, M. Huang, *Electrochim. Acta*, **55**, 4573 (2010)
24. H. Park, W-R Kim, H-Y Jeong, J-J Lee, H-G Kim, W-Y Choi, *Sol. Energy Mat. Sol. Cells*, **95**, 184 (2011)
25. Z. Lie, C. Liu, J. Ya, E. Lie, *Renewable Energy*, **36**, 1177 (2011)

## CHEMICALLY MODIFIED CUSCN FOR ALL SOLID-STATE, TiO<sub>2</sub>/N719/CUSCN, DYE-SENSITIZED SOLAR CELLS

E.V.A. PREMALAL<sup>1\*</sup>, N. DEMATAGE<sup>1</sup>, G.R.R.A. KUMARA<sup>2</sup>, R.M.G. RAJAPAKSE<sup>2</sup>, A. KONNO<sup>1</sup>

<sup>1</sup>Graduate School of Science and Technology, Shizuoka University, Hamamatsu, Japan

<sup>2</sup>Department of Chemistry, University of Peradeniya, Sri Lanka

\*Corresponding Author, e-mail: vikum77@yahoo.com

### ABSTRACT

A method was found to outstandingly improve the conductivity of CuSCN structure prepared by incorporating triethylamine coordinated Cu(i) sites in its structure. It was done by mixing triethylamine hydrothiocyanate with CuSCN in Propyl sulphide solution and allowed to stand still in the dark for few weeks in a closed sample tube. AC impedance studies clearly show the increase of conductivity of CuSCN upon reacting with triethylammonium ions in the presence of O<sub>2</sub> in propyl sulphide. The use of such conductivity-enhanced CuSCN for the formation of all-solid-state dye-sensitized solar cells (DSSCs) gives improved performances of I-V characteristics. As such the solar cell performance gradually increases to an optimum value beyond which it decreases. The best result obtained for conversion efficiency is 3.39% at AM 1.5 and is 41.8% enhancement from the best reported value in the literature. The best value obtained is 14 times higher than that obtained for the DSSC made with ordinary CuSCN.

### 1. INTRODUCTION

The dye-sensitized solid-state solar cell (DSSC) is an offshoot of more familiar dye sensitized liquid electrolyte based solar cell (DSC) invented by O'Reagon and Gratzel in 1991[1]. However, the presence of a liquid electrolyte in the DSC is naturally associated with typical drawbacks of liquids. These involve the improper sealing leading to liquid leakage, dye desorption, solvent evaporation, corrosive nature of I<sub>3</sub><sup>-</sup> present in the electrolyte, and so on. The all-solid-state solar cell is expected to be free of these obstacles. As such, Tennakone and coworkers have first introduced the FTO/TiO<sub>2</sub>/Dye/p-type CuI/Pt-FTO cell, in which p-type CuI was used to act as a hole conductor whose role is to accept and carry holes away from the oxidized dye molecules [2]. The working principle of this solar cell has been well documented in the literature [3-7]. After that that various attempt has been made to improve DSSC system using several hole conductors.

Out of many p-type semiconductors investigated for use as hole conductors, such as CuAlO<sub>2</sub> [8,9], NiO [10-12], CuI [2,13,14], CuSCN [15-17], the latter material CuSCN is of particular interest due to its unique chemical robustness due to its polymeric structure [19,20]. In spite of its stability and durability, the major problem associated with this system is its rather poor energy conversion efficiency ( $\eta$ ). The major drawback of CuSCN as p-type semiconductor in this solar cell is its very poor hole conductivity ( $10^{-4}$  S cm<sup>-1</sup>) [21]. In an attempt to increase p-type conductivity of CuSCN, Perera *et al* [7] have exposed solid CuSCN to halogen gases such as Cl<sub>2</sub> or to a solution of (SCN)<sub>2</sub> in CCl<sub>4</sub> and thereby doped the semiconductor with (SCN)<sub>2</sub> to create acceptor levels 2.6 eV below the band gap (3.6 eV) of CuSCN. This modification has enhanced the performance of the solar cell considerably with a 1.64% enhancement of  $\eta$  from 0.75% without SCN doping and 2.39% after SCN doping.

We have investigated a versatile procedure of improving the p-type conductivity of CuSCN. We reveal in this publication the method we adapted and characterization of the materials

and the solar cell performance of all-solid-state solar cells fabricated using such conductivity enhanced  $\beta$ -CuSCN materials.

## **2. EXPERIMENTAL**

### *Preparation of modified CuSCN*

All chemicals used were purchased from Kanto Chemicals Co., Japan. The structure-modified CuSCN was prepared as follows. CuSCN (0.5g) was mixed with sufficient amount of triethylamine hydrothiocyanate (THT) to obtain a paste which was then stirred with 10.0 ml of propyl sulphide (PS) and allowed to stand still in the dark in a closed sample tube. As time proceeds, white particles begin to become blackish though the solution part still remains colorless up to ~3 days of reaction time. Darkening of the solution phase also begins afterwards and eventually the whole solution becomes black in colour. Then this solution was spread on a heated glass substrate to prepare CuSCN films.

### *Characterization of Materials*

In order to characterize the materials formed in the reaction mixture, same volume of the solution phase were withdrawn using a glass dropper at designated time intervals (1, 3, 5, 10, 15, 20 and 30 days) and thin layers of films were deposited on pre-heated (~100 °C) platinized glass plates having a groove of 1 mm width in which platinum particles have been removed (in order for the either sides of the groove to act as the two electrodes, figure 1). Then these films were used to carry out AC impedance analysis using a Solartron SI 1260 Impedance/Gain-Phase Analyzer.

XRD measurements were carried out using the films deposited on the glass plates (or powder for pure CuSCN) from the solution mixture of particular aged reaction period (Rigaku Miniflex X-Ray Diffractometer). SEM Pictures of CuSCN deposited on dyed TiO<sub>2</sub> film were taken using a JSM-6320F Scanning Electron Microscope.

### *Fabrication of DSSCs*

Mesoporous TiO<sub>2</sub> films were prepared by the procedure described below. Titanium tetra-isopropoxide (8 ml) mixed with propan-2-ol (25 ml) and acetic acid (8.5 ml) was hydrolyzed by addition of water (8 ml) to the mixture and agitated mechanically after mixing with 0.7 g of P25 Degussa TiO<sub>2</sub> powder until the mixture become white viscous solution. A few drops of this solution were lightly spread on pre-heated (~230 °C) transparent conducting glass sheet (1 cm x 2 cm), fluorine-doped SnO<sub>2</sub> glass with a sheet resistance 10  $\Omega/\square$ ) and sintered at 450 °C for 3 minutes. After allowing the plate to cool, the loose crust on the surface was wiped off and then this process was repeated until a film of ~15  $\mu\text{m}$  was formed. Then N719 (*cis*-diisothiocyanato-bis (2,2'-bipyridyl-4,4'-dicarboxylato) ruthenium(II) bis (tetrabutylammonium) was adsorbed by dipping a TiO<sub>2</sub> film in N719 solution for 15 hours at room temperature ( $4 \times 10^{-4}$  M, in 1:1 volume ratio of Acetonitrile and t-Butanol). Above prepared CuSCN solution at a particular reaction time was spread on a pre-heated (100 °C) dye-coated TiO<sub>2</sub> film by dropwise allowing to evaporate the solvent. Thickness of the CuSCN film was ~3 $\mu\text{m}$  from the top of the TiO<sub>2</sub> surface. Then IV measurements were carried out by applying a thin layer of graphite film on top the CuSCN films and having gold sputtered FTO glass plate as a counter electrode (AM 1.5, 100 mW cm<sup>-2</sup> - JASCO, CEP-25BX).

## **3. RESULTS AND DISCUSSIONS**

### *Characterization of CuSCN products*

Figure 1 shows the XRD spectra of CuSCN film prepared by the reaction mixture containing CuSCN and triethylammonium thiocyanate in propyl sulphide at different reaction



times and pure CuSCN. All the pattern of the peaks of spectra 'b', CuSCN from one day reaction mixture, consist of only CuSCN characteristic peaks as shown in figure 4.3 (JSPDS 29-0581). But in spectra c, the film prepared from 20<sup>th</sup> day reaction mixture, an additional peak is appeared at  $2\theta = 24.6^\circ$ . This appearance of new peak suggests that the crystal structure of CuSCN has slightly changed after reacting CuSCN with triethylammonium thiocyanate in the propyl sulphide medium.

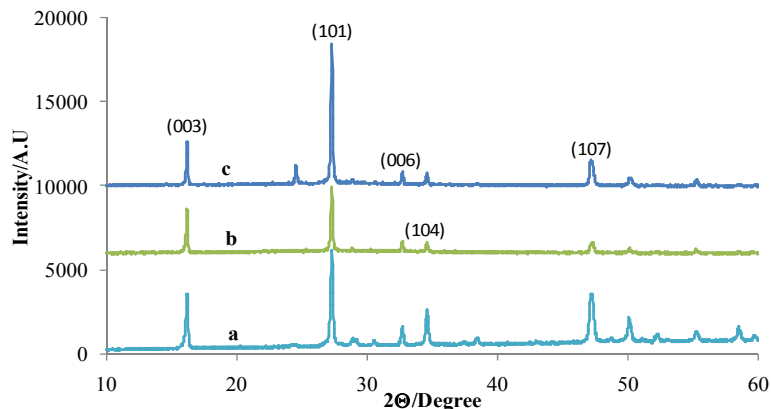


Figure 1. The XRD spectra of CuSCN film prepared by the reaction mixture containing CuSCN and triethylammonium thiocyanate in propyl sulphide allowed to react for (b) 1 day (c) 20 days and (a) pure CuSCN.

Further evidence for the change of structure is highlighted in the SEM images of the TiO<sub>2</sub>/dye/CuSCN electrodes shown in figure 2. The texture of CuSCN consists of plate-like discs of nearly 100 nm in diameter as can be seen in the image 2 (a). When treated with THT the crystalline structure of modified CuSCN is completely different to that of pure CuSCN and crystal size gradually increases as the material reacts with triethylammonium thiocyanate in the propyl sulphide medium. Also those clearly show the improved packing of CuSCN surface morphology and then suggest the enhanced pore filling by CuSCN in the interconnected TiO<sub>2</sub> particle matrix. This would lead to enhancement of the performance of the cell as well as in the recombination of electrons in the CB of TiO<sub>2</sub> with the holes in CuSCN.

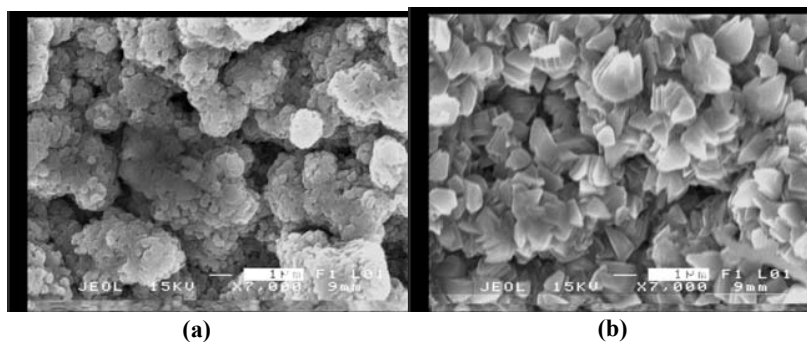


Figure 2. The top view of the SEM images of TiO<sub>2</sub>/Dye/CuSCN system prepared using (a) pure CuSCN dissolved in propyl sulphide (b) CuSCN and triethylammoniumthiocyanate in propyl sulphide allowed to react for 20 days.

Figure 3 shows the nyquist plot of CuSCN films prepared from the reaction mixture containing CuSCN and triethylammonium thiocyanate in propyl sulphide allowed to react for different time period. The impedance plot of pure CuSCN shows only a vertical pure capacitive line but with increased days of reaction time the Nyquist plots show semicircles of systematically decreased diameters (figure 3). Figure 4 shows the plot of conductivity values of the samples calculated from the Nyquist plot as a function of reaction time which clearly indicates significant and controllable enhancement of conductivity of the material. The maximum conductivity of  $1.10 \text{ S m}^{-1}$  was observed for the CuSCN film prepared from 30<sup>th</sup> day reaction mixture of CuSCN with triethylammonium thiocyanate in propyl sulphide as shown in figure 4.

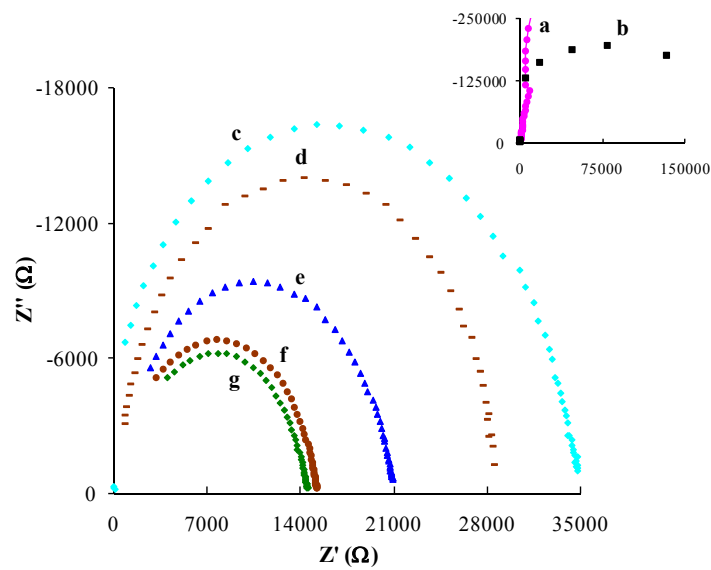


Figure 3. Nyquist plots for impedance measurements of the samples prepared from (a) pure CuSCN (b) 1 day (c) 5 days (d) 10 days (e) 15 days (f) 20 days and (g) 30 days of reacting CuSCN with triethyl ammonium thiocyanate in propyl sulphide

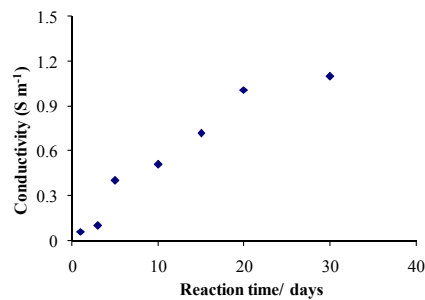


Figure 4. Conductivity variation of the CuSCN films prepared from the reaction mixture containing CuSCN and triethylammonium thiocyanate in propyl sulphide allowed to react for different time period.

Solar cell characteristics

We have used such conductivity enhanced CuSCN in fabricating solid-state dye-sensitized solar cells as described below. The TiO<sub>2</sub>/N719 Dye/CuSCN solar cells were fabricated using the usual procedure described in the experimental section using CuSCN from the reaction solution at different reaction times. The IV characteristics of these DSSCs are given in figure 5 and the corresponding data are extracted in Table 1.

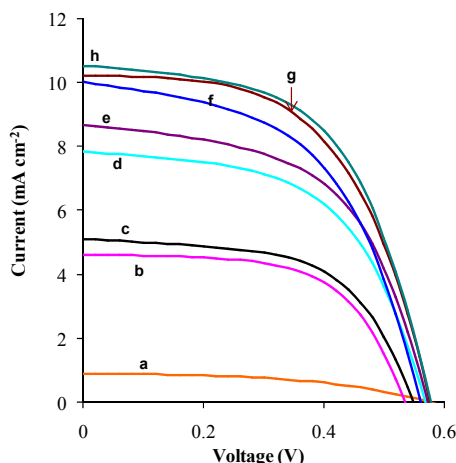


Figure 5. The I-V curves of the TiO<sub>2</sub>/N719/CuSCN cells prepared using (a) pure CuSCN (b) 1 day (c) 3 days (d) 5 days (e) 10 days (f) 30 days (g) 15 days and (h) 20 days of reacting CuSCN with triethyl ammonium thiocyanate in propyl sulphide.

Table 1. I-V parameters for the solar cell TiO<sub>2</sub>/N719/CuSCN prepared using CuSCN taken from the solution phase of the reaction mixture of CuSCN and triethylammonium thiocyanate in propyl sulphide at different reaction times.

Reaction Time/ Days	J <sub>sc</sub> (mA cm <sup>-2</sup> )	V <sub>oc</sub> (V)	FF	η%
0 (No THT)	0.90	0.576	0.477	0.25
1	4.59	0.535	0.609	1.50
3	5.11	0.549	0.580	1.63
5	7.83	0.569	0.554	2.47
10	8.67	0.573	0.548	2.73
15	10.22	0.576	0.553	3.26
20	10.52	0.578	0.556	3.39
30	10.00	0.561	0.522	2.93

As the reaction time is increased, the p-type conductivity of CuSCN enhances and consequently the open circuit voltage (V<sub>oc</sub>), short-circuit current density (J<sub>sc</sub>) and the overall conversion efficiency (η) show progressively increase up to 20 days of reaction time. The fill factor (FF) also increases initially and then slightly decreases eventually plateauing at around 0.55 up to 20 days of reaction time (Table 1). This is also in agreement with the progressive increase of the amount of holes in CuSCN as the reaction proceeds. Although the p-type conductivity of CuSCN is progressively increasing even up to 30 days of reaction time the solar cell performance of the DSSC made using CuSCN at 30 days of reaction time is inferior to that made using CuSCN at 20

days of reaction time. The enhancement of conductivity causes the decrease in FF. But efficient regeneration of dye thus efficient charge injection to TiO<sub>2</sub> will increase the Fermi level of TiO<sub>2</sub> slightly in turn improving V<sub>OC</sub>.

#### 4. CONCLUSIONS

A versatile procedure was developed to increase the p-type conductivity of CuSCN structure. It was done by allowing CuSCN to react with THT in propyl sulphide in the presence of oxygen. The conductivity of the materials prepared from the solution phase of the reaction mixture increases gradually with reaction time. This accompanies a change in CuSCN structure in such a way to possess hole-bearing Cu(II) ions in some sites, some of which accompanying coordinated triethylamine molecules. Such modified CuSCN structures give progressively improved DSSC performances in all-solid-state TiO<sub>2</sub>-N719-CuSCN solar cells. The best result obtained is very impressive for the conversion efficiency of such a solar cell and is 48.7% higher than the best value reported so far in the literature. The best result is 14 times higher than that obtained when unmodified CuSCN is used.

#### REFERENCES

1. B. O'Regan and M. Grätzel, *Nature* 353 (1991) 737.
2. K. Tennakone, G.R.R.A. Kumara, A.R. Kumarasinghe, K.G.U. Wijayantha, P.M. Sirimanne, *Semicond. Sci. Technol.* 10 (1995) 1689.
3. K. Tennakone, A. R. Kumarasinghe, P. M. Sirimanne, and G. R. R. A. Kumara, *Thin Solid Films* 261 (1995) 307-310.
4. G. R. R. A. Kumara, A. Konno, G. K. R. Senadeera, P. V. V. Jayaweera, D. B. R. A. De Silva, and K. Tennakone, *Sol. Energy Mater. Sol. Cells* 69 (2001) 195-199.
5. B. O'Regan, D. T. Schwartz, S. M. Zakeeruddin, and M. Gratzel, *Adv. Mater.* 12 (2000) 1263-1267.
6. B. O'Regan, S. Scully and A.C. Mayer, *J. Phys. Chem. B* 109 (2005) 4616-4623.
7. V.P.S. Perera, M.K.I. Senevirathna, P.K.D.D.P. Pitigala and K. Tennakone, *Sol. Energy Mater. Sol. Cells* 86 (2005) 443-450.
8. H. Kawazoe, M. Yasukawa, H. Hyodo, M. Kurita, H. Yanagi, and H. Hosono, *Nature* 389 (1997) 939.
9. J. J. He, H. Lindström, A. Hagfeldt, and S. E. Lindquist, *J. Phys. Chem. B* 103 (1999) 8940.
10. J. Bandara and H. Weerasinghe, *Sol. Energy Mater. Sol. Cells* 85 (2005) 385.
11. S. S. Kim, K.W. Park, J. H. Yum and Y. E. Sung, *Sol. Energy Mater. Sol. Cells* 90 (2006) 283.
12. Y. M. Lee and C. H. Lai, *Solid-State Electronics* 53 (2009) 1116.
13. K. Tennakone, V. P. S. Perera, I. R.M. Kottegoda, and G. R. R. A. Kumara, *J. Phys. D Appl. Phys.* 32 (1999) 374.
14. B. Li, L. D. Wang, B. Kang, P. Wang, Y. Qiu, *Sol. Energy Mater. Sol. Cells* 90 (2006) 549.
15. K. Tennakone, A. R. Kumarasinghe, P. M. Sirimanne, G. R. R. A. Kumara, *Thin Solid Films* 261 (1995) 307.
16. B. O'Regan, D. T. Schwartz, *Chem. Mater.* 10 (1998) 1501.
17. B. O'Regan, D. T. Schwartz, S. M. Zakeeruddin, M. Gratzel, *Adv. Mater.* 12 (2000) 1263.
18. R. Hehl, G. Thiele, *Z. Anorg. Allg. Chem.* 626 (2000) 2167.
19. D.L. Smith, V.I. Saunders, *Acta Cryst.* B37 (1981) 1807.
20. AIP ADVANCES 1, 022107 (2011)

## SUPPRESSION OF RECOMBINATION IN DYE SENSITIZED SOLAR CELLS BASED ON TiO<sub>2</sub> WITH BARRIER LAYER OF METAL OXIDES

L.R.G.WICKRAMASINGHE<sup>1\*</sup>, V.P.S.PERERA<sup>1</sup>, G.K.R.SENADEERA<sup>1,2</sup>

1. The Open University of Sri Lanka ,Nawala ,Nugegoda , Sri Lanka

2. Institute of Fundamental Studies, Hantane Road, Kandy, Sri Lanka

\*Corresponding Author, e-mail [ranjana5vck@yahoo.com](mailto:ranjana5vck@yahoo.com)

### ABSTRACT

Dye sensitized PECs were made from nanocrystalline films of TiO<sub>2</sub> treated with AlCl<sub>3</sub> (1×10<sup>-3</sup>M) & MgCl<sub>2</sub> (1×10<sup>-3</sup>M) in aqueous solutions & sensitized with Ruthenium N3 dye in dye sensitized solar cells and compared with equivalent cells made from untreated films. The surface concentration of Al<sub>2</sub>O<sub>3</sub> & MgO on the TiO<sub>2</sub> was optimized to cover the surface of the films at molecular level and dye was adsorbed on it. After the treatment photovoltage and photocurrent of the cells treated with Al<sub>2</sub>O<sub>3</sub> and MgO has greatly improved. Flat band potential of the semiconductor is a determinant factor of the photovoltage of the cell & formation of trap states moves the flat band potential to a lower energy level in the energy scale. In this study we have also measured the flat band potential of the films after treating TiO<sub>2</sub> films with Al<sub>2</sub>O<sub>3</sub> & MgO for 24 hrs with Mott-schottky measurements. The flat band potential of the TiO<sub>2</sub> film increased after the treatment with Al<sub>2</sub>O<sub>3</sub> and MgO. The increment in the flat band potential after the treatment is described as a result of passivation of surface states in the semiconductor film.

### 1. INTRODUCTION

The degradation of the photo voltage followed by the photo current is general scenario in dye sensitized solar cells (DSSCs) with prolong illumination where the efficiency decreases to a lower values as a consequence. The life time of dye sensitized solar cell may vary depending on the type of the dye and the semiconductor material used to fabricate DSSCs where semiconductor materials are polycrystalline metal oxides [1], so that the traps originated at the grain boundaries could led to recombination of charge carriers. Passivation of these trap states in polycrystalline metal oxide semiconductors with Al<sub>2</sub>O<sub>3</sub> and MgO reported to improve the efficiency and lifetime of DSSCs [2-3]. In this study we have measured the flat band potential of the TiO<sub>2</sub> films with Mott-schottky measurements after treating the films with Al<sub>2</sub>O<sub>3</sub> and MgO. The flat band potential of the TiO<sub>2</sub> film increased after the treatment with Al<sub>2</sub>O<sub>3</sub> and MgO. The increment in the flat band potential after the treatment is described as a result of passivation of surface states in the semiconductor film.

### 2. EXPERIMENTAL

TiO<sub>2</sub> films were deposited on CTO glass by doctor blade method using a past made grinding Degussa powder with acetic acid and ethanol. Then the films were sintered at 450 °C in a furnace for 30 minutes. They were separately immersed in AlCl<sub>3</sub> (1×10<sup>-3</sup> M) and MgCl<sub>2</sub> (1×10<sup>-3</sup> M) in ethanol for 24 hours. Then the films were sintered again in a furnace at 450 °C, for 45 minutes. The Al<sub>2</sub>O<sub>3</sub> and MgO treated films were coated with ruthenium bipyridyl dye by immersing the films in a 0.5 mM dye solution. The fabrication of the electrochemical cell is done by placing a Pt coated CTO glass on the dye coated surface of the film and filling the capillary space with an electrolyte containing I/I<sup>-3</sup> redox couple. Then the films were illuminated with white light with the intensity of 100mW/cm<sup>2</sup>. The flat band of (a) TiO<sub>2</sub> films as deposited on CTO glass, (b) Al<sub>2</sub>O<sub>3</sub> treated TiO<sub>2</sub> films (c) MgO treated TiO<sub>2</sub> films, (d) bare TiO<sub>2</sub> films coated with ruthenium bipyridyl dye (e) Al<sub>2</sub>O<sub>3</sub> treated TiO<sub>2</sub> films coated with ruthenium bipyridyl dye, (f) MgO treated TiO<sub>2</sub> films coated with ruthenium bipyridyl dye, (g) dye coated TiO<sub>2</sub> films after degradation of

the solar cell (h) dye coated Al<sub>2</sub>O<sub>3</sub> treated TiO<sub>2</sub> films after degradation of the solar cell and (i) dye coated MgO treated TiO<sub>2</sub> films after degradation of the solar cell were measured using Mott-shottky measurement. The capacitances of the films were measured using a HP LCZ meter coupled to a computer at the frequencies 1.5 kHz and 1.0 kHz. Electrolyte used in the Mott-shottky measurements was 0.5 M Na<sub>2</sub>SO<sub>4</sub> solution.

### 3. RESULTS AND DISCUSSION

Figure 1 shows the Mott-schottky plot of TiO<sub>2</sub> film deposited on CTO glass plate. The curves (a) and (b) refers to measurements taken at 1.5 kHz and 1.0 kHz respectively. The point at which the extrapolated lines meet the voltage axis gives the flat band potential with respect to the reference electrode. The reference electrode used was a standard calomel electrode (SCE) in this experiment. Therefore from these curves it can be seen that the flat band potential of TiO<sub>2</sub> film lies around -0.05 V with respect to the SCE.

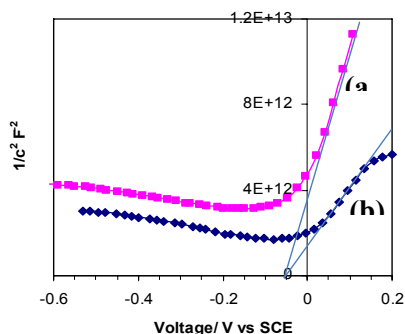


Fig. 1: Mott-schottky plots of TiO<sub>2</sub> film measured at (a) 1.5 kHz and (b) 1.0 kHz.

Figure 2 and 3 shows the Mott-schottky plots of Al<sub>2</sub>O<sub>3</sub> and MgO treated TiO<sub>2</sub> films deposited on CTO glass plates respectively. The flat band potential of TiO<sub>2</sub> shifted to higher energy levels of -0.35 V and -0.4 V after treating the films with Al<sub>2</sub>O<sub>3</sub> and MgO respectively.

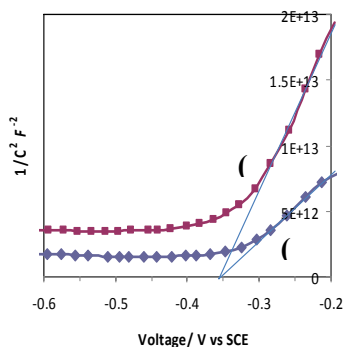


Fig. 2 Mott-schottky plot of Al<sub>2</sub>O<sub>3</sub> treated TiO<sub>2</sub> film measured at (a) 1.5 kHz and (b) 1.0 kHz.

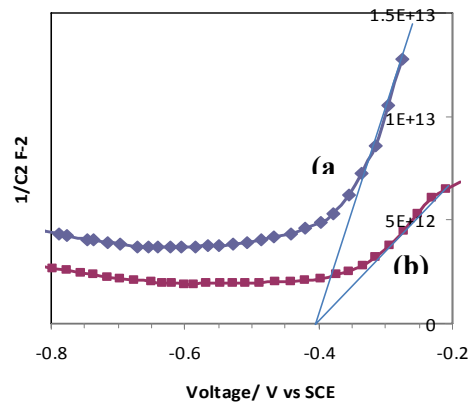


Fig 3. Mott-schottky plot of MgO treated TiO<sub>2</sub> film measured at (a) 1.5 kHz and (b) 1.0 kHz.

Table 1 Flat band potential of dye coated TiO<sub>2</sub> films.

Film	Flat band potential (V vs SCE)
TiO <sub>2</sub> +dye	-0.30
Al <sub>2</sub> O <sub>3</sub> treated TiO <sub>2</sub> +dye	-0.52
MgO treated TiO <sub>2</sub> +dye	-0.65
TiO <sub>2</sub> +dye(after degradation)	0.0
Al <sub>2</sub> O <sub>3</sub> treated TiO <sub>2</sub> +dye(after degradation)	-0.30
MgO treated TiO <sub>2</sub> +dye(after degradation)	-0.35

Table 1 depicts the flat band potential of TiO<sub>2</sub> films calculated from the Mott-schottky measurements after coating ruthenium bipyridyle dye. The flat band potential of all the films including bare TiO<sub>2</sub> film, Al<sub>2</sub>O<sub>3</sub> and MgO treated TiO<sub>2</sub> films shifted to higher energy levels of -0.30 V, -0.52 V and -0.65 V respectively vs SCE after coating the dye on the films.

Solar cells were fabricated using bare TiO<sub>2</sub> films, Al<sub>2</sub>O<sub>3</sub> and MgO treated films and they were illuminated with white light for several days. Initially, photovoltage and photocurrent of all those cells were above 650mV and 10mA/cm<sup>2</sup> respectively. The photovoltage and photocurrent remain the same for the first few days but after that the photovoltage started to decay followed by the photo current. But the photocurrent and photo voltage of the TiO<sub>2</sub> films coated with Al<sub>2</sub>O<sub>3</sub> and MgO was not rapid as bare TiO<sub>2</sub> films. The photovoltage decreased to 250mV and photocurrent decreased to 6mA/cm<sup>2</sup> in 6 days of consecutive illumination of the bare TiO<sub>2</sub> cell. At this stage the cells were dismantled and TiO<sub>2</sub> films coated with dye were taken for the Mott-schottky measurements after washing out the electrolyte. From the table 1, it is clear that the flat band potential of TiO<sub>2</sub> films coated with Al<sub>2</sub>O<sub>3</sub> and MgO still remains high but bare TiO<sub>2</sub> film has decreased to 0 V vs SCE.

According to the above results it can be seen that the flat band potential of TiO<sub>2</sub> films moves higher energy level by treating with Al<sub>2</sub>O<sub>3</sub> and MgO and also the flat band potential of Al<sub>2</sub>O<sub>3</sub> and MgO treated TiO<sub>2</sub> films moves further high in the energy scale by coating the dye on the surface. This is attributed due to the passivation of surface states of TiO<sub>2</sub> as well as Al<sub>2</sub>O<sub>3</sub> and

MgO by chelation of dye molecules on the surface [4]. But according to the table 1 it is very clear that photovoltage and photo current of the dye sensitized solar cells decreases because of the lowering of the flat band potential of TiO<sub>2</sub> electrodes. This can happen due to formation of trap states which could originate in two ways. One way is reopening of the passivated trap states on prolong illumination due to loosening or removal of dye chelated on the semiconductor films. The other possibility is formation of new surface states on the semiconductor due to exposure to high energy rays such as UV radiation. Anyway it can be concluded that trap states are formed on the surface of the semiconductor film with prolong illumination of the cells where Al<sub>2</sub>O<sub>3</sub> and MgO treatment retards that process which lead to lowering the efficiency of the dye sensitized solar cells.

#### **4. CONCLUSION**

The possible reasons for the gradual degradation of dye sensitized solar cells were investigated observing the variation of the flat band potential of TiO<sub>2</sub> films measuring with Mott-schottky measurements. It is evident that the flat band potential of the TiO<sub>2</sub> films is enhanced by treating the films with Al<sub>2</sub>O<sub>3</sub> and MgO which passivate surface states in the semi conductor and formation of trap states due to prolong illumination lowers the flat band potential of the semiconductor films decreasing the efficiency of the solar cells.

#### **REFERENCES**

1. C.J.Barbe, F.Arendse,P.Comte, M.Jirousek, F.Lenzmann,V.Shklover and M.Gratzel, "Nanocrystalline Titanium oxide Electrodes for Photovoltaic Applications", *J.Am. Ceram.Soc.* 80,1977, 3157-71.
2. G R R A Kumara, K Tennakone, V P S Perera, A Konno, S Kaneko and M Okuya, *J. Phys. D: Appl. Phys.* 34 (2001) 868–873.
3. K Tennakone, J Bandara, P K M Bandaranayake, G R A Kumara and A Konno, *Jpn. J. Appl. Phys.* 40 (2001) pp. L732-L734.
4. G.Ramakrishna,A.Das and H.N.Gosh," Effect of surface modification on Back Electron Transfer Dynamics of Dibromo Fluorescein sensitized TiO<sub>2</sub> nano particles", *Langmuir* 2003.



## **THE IMPROVED PERFORMANCE OF DYE SENSITIZED SOLAR CELL BY PYRROLIDINEDITHIOCARBAMATE MODIFIED TiO<sub>2</sub> SURFACE**

D.M.B.P. ARIYASINGHE<sup>1\*</sup>, H.M.N. BANDARA<sup>2</sup>, R.M.G. RAJAPAKSE<sup>2</sup>, M. SHIMOMURA<sup>1,3</sup>

<sup>1</sup> *Graduate School of Science and Technology, Shizuoka University, 432-8011 Hamamatsu, Japan*

<sup>2</sup> *Faculty of Science, University of Peradeniya, Peradeniya, Sri-lanka*

<sup>3</sup> *Research Institute of Electronics, Shizuoka University, 432-8011 Hamamatsu, Japan*

Corresponding Author, e-mail: [dmbuddhi@gmail.com](mailto:dmbuddhi@gmail.com)

### **ABSTRACT**

In this work, surface modification of TiO<sub>2</sub> electrode for dye-sensitized solar cell (DSSC) by pyrrolidinedithiocarbamate (PDTC) is studied. Results by X-ray photoelectron spectroscopy (XPS) indicates that two sulfur atoms of PDTC are in the same chemical environment and positively charged after adsorption on the TiO<sub>2</sub> surface. DSSC conversion efficiency with the PDTC-treated electrode was clearly improved because of increasing of the short circuit current.

### **1. INTRODUCTION**

Increasing the energy crisis and concern about the global warming the improvement of dye sensitized solar cells (DSSCs) have been attracted industrial and academic interests since their discovery in 1991[1]. This has been recognized as a hopeful research field for alternative energy sources due to low production cost and high efficiency [2]. After Grätzel and O'Regan reported DSSC photovoltaic efficiency of 11%with low cost, many investigators have made great efforts to enhance the performance of DSSCs by improving properties of the constituents to produce the high efficient solar cell [1]. These efforts can largely be categorize into four groups of development: anodic materials [3,4], sensitizers [5,6], electrolytes [7,8], and the modification of anodic materials. Although other semiconductors such as ZnO, SnO<sub>2</sub>, CdS have been used in DSSCs, none of them showed better performance than TiO<sub>2</sub> [3,9]. Thus, TiO<sub>2</sub> has been most commonly used as an anodic material in a DSSC due to its predominantly moderate charge transport capability and chemical stability [1]. Furthermore, back reaction of photo-generated electrons into electrolyte solution and carrier recombination of excited electrons and holes are serious problem that takes place at the TiO<sub>2</sub> surface. Investigations have been carried out to modify the TiO<sub>2</sub> layer to reduce the recombination. It was found that charge recombination reaction can be remarkably reduced by coating the TiO<sub>2</sub> either with an insulator [10,11] or with another semiconductor[12,13]. These modification materials build up to control the back electron transfer into the electrolyte or sensitizer [13].

Dipoles formed at a semiconductor surface play key roles in determining the energy barriers between a semiconductor and a sensitizer, depending on the modification process [14]. The electric dipole layer that exists at the TiO<sub>2</sub>/sensitizer interface results the permanent dipole moment of the molecule itself. One of most successful methods is forming a self-assemble monolayer (SAM) on the TiO<sub>2</sub> surface. Despite of diminishing the electron conductivity by SAM, overall conversion efficiency is improved due to the enhancement of the short circuit current density (J<sub>SC</sub>) [10,13,14]. While many researchers have intensively studied on generating energy barriers for the repression of electron recombination, little attention has been paid to this approach. Therefore, we tried to coat 1-pyrrolidinedithiocarbamate (PDTC) on TiO<sub>2</sub> layers via dip coating process in ammonium 1-pyrrolidinedithiocarbamate (APDTC) solution. We expected that PDTC to possibly induce the surface dipoles on the TiO<sub>2</sub> surface resulting in the increase of J<sub>SC</sub>. In this

study, adsorption structures of PDTC on the anatase TiO<sub>2</sub> particles are studied by X-ray photoelectron spectroscopy (XPS). The effect of the surface treatment by PDTC on the performance improvement of DSSCs was also investigated by comparing the cell performances.

## 2. EXPERIMENTAL

Fluorine-doped tin oxide (FTO) glass substrates were cleaned in a detergent solution in an ultrasonic bath for 15 min, and thoroughly rinsed with ethanol. TiO<sub>2</sub> thin layer with nano-particles was formed by spraying nano-particle sol (TKC-302; TAYCA) on the heated FTO glass substrate using spray pyrolysis deposition technique. Then, TiO<sub>2</sub> large particles (400-600nm) were additionally deposited on the TiO<sub>2</sub> film of the nano-particles as a light scattering layer. The TiO<sub>2</sub> coated substrates were subsequently sintered at 500 °C in air for 1 hour. One of the electrodes was soaked in the aqueous solutions (1mM) of APDTC for 10 minutes to deposit PDTCs onto the TiO<sub>2</sub> surface. Then, resulting electrodes were rinsed with ethanol, and dried at 50 °C for 2 min. The TiO<sub>2</sub>/FTO and PDTC-TiO<sub>2</sub>/FTO samples were separately immersed into a 0.5 mM of N719 dye solution (acetonitrile/tertbutyl alcohol, v/v= 1) for 24 hours. Anhydrous electrolyte containing I<sup>-</sup>/I<sub>3</sub><sup>-</sup> was sandwiched between the dye-adsorbed TiO<sub>2</sub> electrode and a platinum coated counter electrode to construct a dye-sensitized solar cell. I-V characteristics and photocurrent action spectra were recorded using a calibrated solar cell evaluation system (JASCO, CEP-25BX) at AM 1.5, 100 mW/cm<sup>2</sup> illumination. XPS analysis of S 2p peak was performed for the prepared PDTC-TiO<sub>2</sub>/FTO sample, N719 dye adsorbed PDTC-TiO<sub>2</sub>/FTO sample, and APDTC powder. XPS experiment was performed by using a hemispherical electron energy analyzer (ESCALAB-MkII, VG) and an Al K $\alpha$  X-ray tube (1486.6eV).

## 3. RESULTS AND DISCUSSION

Figure 1a shows the XPS spectrum of the Sulfur 2p core levels obtained from APDTC powder sample. The spectrum were fitted by two components corresponding to the C-S<sup>-1</sup> bond (164.0 eV) and C=S bond (166.0 eV). Figure 1b shows S 2p spectrum of the PDTC-TiO<sub>2</sub>/FTO electrode. Only one component was observed in Fig 1b. Therefore, two sulfur atoms of PDTC are in an identical chemical environment after adsorption on the TiO<sub>2</sub> surface. In addition, binding energy of S 2p at 169.2 eV, which is clearly higher than those of APDTC powder, indicates that electronic charge transfer from sulfur to the TiO<sub>2</sub> surface is induced after the adsorption. It should be also noted that PDTC related S 2p peak for the N719 dye adsorbed PDTC-TiO<sub>2</sub>/FTO sample was located at the same binding energy as that without dye. It means that sulfur bonding configuration of PDTC was not changed during the dye adsorption process. Thus, we confirmed that PDTC were successfully deposited onto TiO<sub>2</sub> surface with positively charged sulfur linkers. It was reported that formation of electric dipole layer at the TiO<sub>2</sub> surface results the permanent dipole moment of the PDTC itself [14]. This surface dipole may have an effect of the DSSC performance. It will be discussed later. Then we fabricated DSSCs with the PDTC-TiO<sub>2</sub>/FTO electrodes and measured their performance.

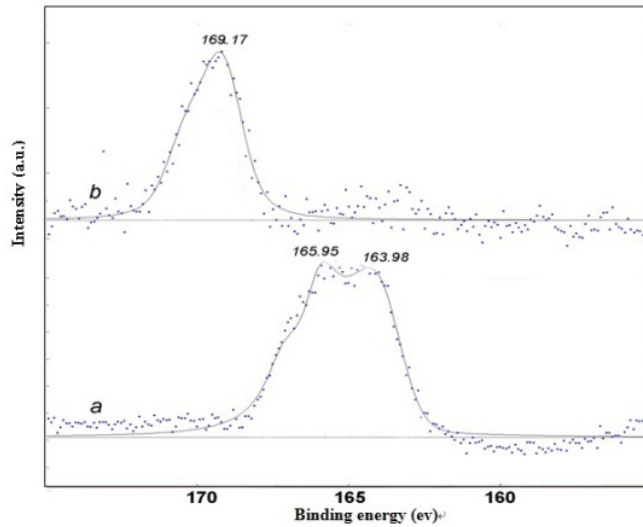


Figure 1. a. XPS spectrum of the Sulfur 2p peak in pyrrolidinedithiocarbamate (PDTC) powder. b. XPS spectrum of the sulfur 2p peak which are detected in PDTC - TiO<sub>2</sub>/FTO electrode.

Photocurrent–voltage curves of DSSC’s using the bare and PDTC-treated TiO<sub>2</sub> layers are compared in Figure 2. Photo-conversion efficiencies of the DSSCs are presented in Table 1 together with fill factor (FF), short circuit photocurrent (J<sub>SC</sub>), and open circuit voltage (V<sub>OC</sub>). Conversion efficiency with the bare TiO<sub>2</sub>/FTO was 5.38%, and with PDTC-TiO<sub>2</sub>/FTO photo-electrode it increases to 6.54%. Especially, it is remarkable that J<sub>SC</sub> for the PDTC-TiO<sub>2</sub>/FTO photo-electrode increased to 13.72 mA/cm<sup>2</sup> while the bare photoelectrode was 10.64 mA/cm<sup>2</sup>. Two reasons of increase of J<sub>SC</sub> are expected as follows. One possible reason is that PDTC preferentially adsorbs at defect sites of TiO<sub>2</sub> nano porous structure, therefore back donation of photoelectrons from TiO<sub>2</sub> to electrolyte and N719 dye would be decreased.

Table 1 Performance comparison of the DSSCs employing TiO<sub>2</sub>/FTO and PDTC- TiO<sub>2</sub>/FTO as photoanodes.

Applied electrodes	FF(%)	EFF (%)	J <sub>SC</sub> (mA/cm <sup>2</sup> )	V <sub>OC</sub> (V)
TiO <sub>2</sub> /FTO	0.68	5.38	10.64	0.74
PDTC- TiO <sub>2</sub> /FTO	0.67	6.54	13.72	0.71

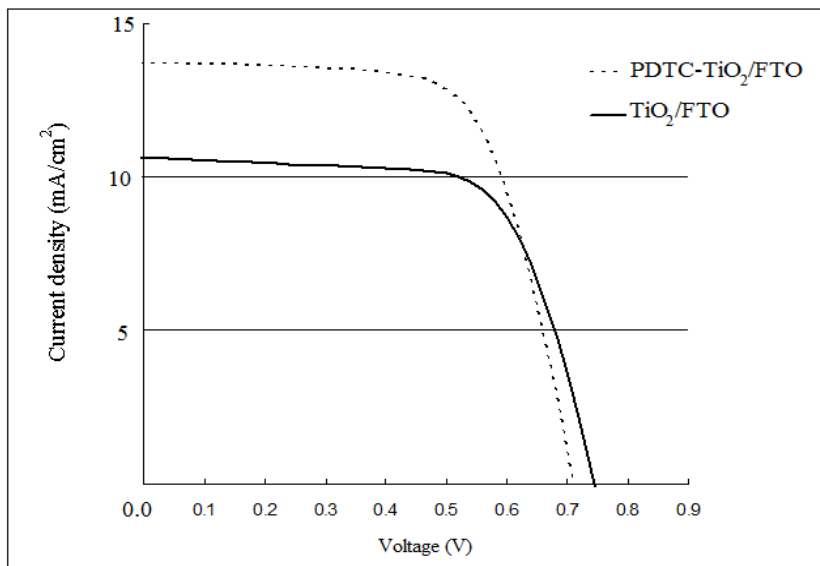


Fig. 2. Current-voltage characteristics of DSSCs with TiO<sub>2</sub> layer and PDTC-coated TiO<sub>2</sub> layer.

This indicates that the increase in  $J_{SC}$  by the PDTC-treatment resulted in the improvement in the energy conversion efficiency. Another possible reason is that surface dipole induced by the PDTC attachment would modify the redox potential.

Figure 3 illustrates how the dipole of PDTC modify the conduction band energy ( $E_{CB}$ ) of TiO<sub>2</sub> with respect to the redox potential ( $E_{redox}$ ) of the electrolyte in DSSC. Our XPS result revealed that sulfur atoms of PDTC are more positive like sulfate ions after adsorption on the TiO<sub>2</sub> surface. Thus, the surface dipoles at the TiO<sub>2</sub> /PDTC interface decrease the back donation of photoelectrons into the electrolyte. On the other hand, the surface dipole decline of  $V_{OC}$  would be expected as illustrated in Fig. 3. In reality,  $V_{OC}$  of PDTC-TiO<sub>2</sub>/FTO photo-electrode decreased from 0.74 V to 0.71 V as listed in table 1. As described above, the PDTC-TiO<sub>2</sub>/FTO photo-electrode has shown slight diminishing in  $V_{OC}$  due to the positive shift of TiO<sub>2</sub> conduction band edge, which could cause, at the same time, efficient electron injection from the excited sensitizer into the conduction band of modified TiO<sub>2</sub>.

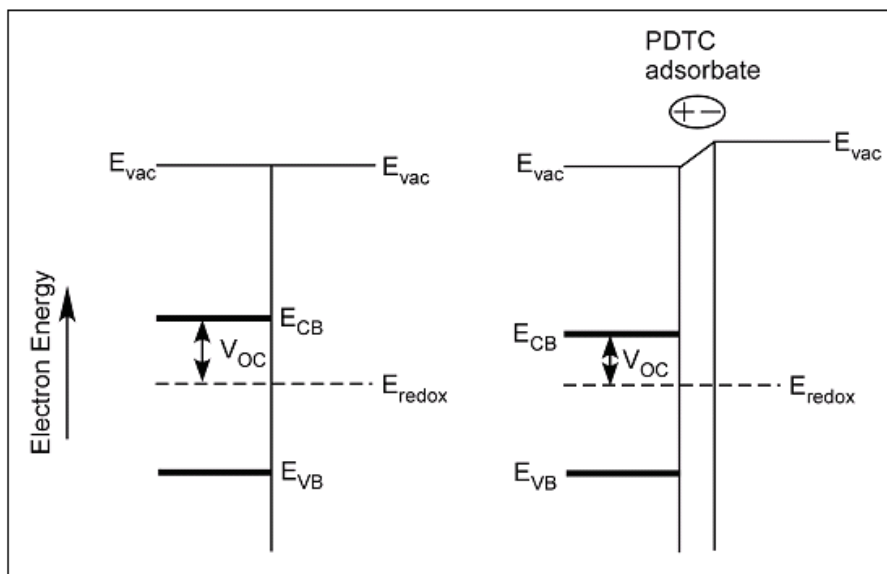


Figure 3. Modified energy of the  $\text{TiO}_2$  conduction band ( $E_{\text{CB}}$ ) with respect to redox potential ( $E_{\text{redox}}$ ) of the electrolyte [14].

#### 4. CONCLUSION

Effect of PDTC adsorption on the surface of  $\text{TiO}_2/\text{FTO}$  electrodes via dip-coating process was studied. XPS results indicate that PDTC successfully deposited on  $\text{TiO}_2$  surface with positively charged sulfur. We applied the resulting electrodes (PDTC- $\text{TiO}_2/\text{FTO}$ ) to the photoanode of a DSSC and observed their effect on the cell performance. When PDTC- $\text{TiO}_2/\text{FTO}$  was used as the photoanode of a DSSC, The PDTC treatment was found to reduction in  $V_{\text{OC}}$  due to the positive shift of  $\text{TiO}_2$  conduction band edge, which could cause efficient electron injection from the excited sensitizer into the conduction band of modified  $\text{TiO}_2$  and increasing of short circuit photocurrent of DSSC was observed. Also the presence of PDTC can diminish back electron transfer but overall conversion efficiency is improved due to short circuit current enhancement. Finally we obtained the improved conversion efficiency when having employed PDTC- $\text{TiO}_2/\text{FTO}$  as the photoanode rather than that without PDTC treatment.

#### REFERENCES

1. O'Regan B., Graetzel M., *Nature* 353(1991), 737.
2. Hagfeldt A., Grätzel M., *Chem. Res.*, 2000, 33 (5), 269–277.
3. Liao J.Y., Ho K.C., *Sol. Energ. Mat. Sol. Cell* 86 (2005), 229.
4. Chen Z., Tang Y., Zhang L., Lu L., *Electrochimica Acta*, 51 (2006), 5870–5875.
5. A. Zaban, S. Ferrere, Gregg B.A., *J. Phys. Chem. B.* 102 (1998), 452.
6. Choul C., Wu K., Chil Y., Yu S.J., Lee G.H., Lin C., Chou P., *Angewandte Chemie Int. Ed.*, Vol. 50(9), 2011, 2054–2058.
7. Gregg B.A., *Coordination Chemistry Reviews* 248 (2004), 1215–1224.
8. Kawano R., Matsui H., Matsuyama C., Sato A., Susan M.A.B.H., Tanabe N., Watanabe M., *Photochem J., J. Photochem. Photobiol. A-164* (2004), 87.

10. Sheng X., Zhao Y., Zhai J., Jiang I., Zhu D., Appl. Phys. A-87(2007), 715–719.
11. Frank A.J., Neale N.R., Kopidakis N. and Lagemaat J., Conference Paper, NREL/CP-590-38978, November 2005.
12. Balraju P., Kumar M., Roy M.S., Sharma G.D., Synthetic Metals 159 (2009), 1325–1331.
13. Subasri R., Deshpande S., Seal S., Shinohara T., The Electrochemical Society, Electrochemical and Solid-State Letters, 9 (1), B1-B4 (2006).
14. Subasri R., Shinohara T., Mori K., Science and Technology of Adv. Mat. 6 (2005), 501–507.
15. Wrochem F., Wessels J., Gao D., Ford W., Rosselli S., Wirtz R., Patent app. pub.,
16. US 2011/0031481 A1, 2011.
17. Keis K., Magnusson E., Lindstrom H., Lindquist S.E., Hagfeldt A., Sol. Energ. Mat. & Sol. Cell-73 (2002), 51.
18. O'Regan B.C., Scully S., Mayer A.C., Palomares E., Durrant J., J. Phys. Chem. B. 109 (2005), 4616.

## HIGHLY TRANSPARENT SnO<sub>2</sub>/CaCO<sub>3</sub> COMPOSITE FILMS FOR DYE-SENSITIZED SOLAR CELLS WITH SUPERIOR PERFORMANCE

S. G. ANURADHA, H.M.N. BANDARA\*, W.A.P.N. WICKRAMAARACHCHI,  
G.R.A. KUMARA AND R.M.G. RAJAPAKSE

*Department of Chemistry, University of Peradeniya, Peradeniya, Sri Lanka*

\*Corresponding Author, e-mail: *hmn@pdn.ac.lk*

### ABSTRACT

Fabrication of semi-transparent SnO<sub>2</sub>/CaCO<sub>3</sub> composite films on conductive glass plates for applications in Dye-Sensitized Solar Cells (DSCs) will be described. Here, the interconnected SnO<sub>2</sub> particles in the thin film on FTO are covered by a approximately 1 nm thick layer of CaCO<sub>3</sub> which effectively prevents the recombination of injected electrons in ZnO particles by the oxidized species of the redox couple or with the oxidized dye molecules formed due to electron injection. *I-V* characteristics of the DSCs can be conveniently controlled by varying the thickness of the CaCO<sub>3</sub> layer. A novel spray deposition technique called the Atomized Spray Pyrolysis (ASP) has been used to make a highly uniform composite film with about 60% transmittance in the red region of the visible spectrum. This is attributed to the absence of particle aggregation in the composite film. The system was optimized to produce a DSC that gives 4.5% power conversion efficiency. In spite of the high transparency, 83% of the conversion efficiency of the similar but non-transparent DSC, which has the advantage of light scattering, can be obtained for the transparent cell. The novel transparent cell has the advantage of producing on window panes for solar-to-electricity conversion while allowing some light to pass through it. The effect of CaCO<sub>3</sub> layer thickness upon the *I-V* performances will be revealed.

### 1. INTRODUCTION

The Dye-sensitized Solar Cell (DSC) employs a monolayer of dye adsorbed on an interconnected nanoparticles of TiO<sub>2</sub> layer deposited on a transparent conducting fluorine doped tin oxide coated glass (FTO) as an active electrode, together with lightly platinized FTO counter electrode, with a liquid electrolyte containing I<sup>-</sup>/I<sub>3</sub><sup>-</sup> sandwiched between the two electrodes. Since its first report in 1991 [1] innumerable modifications effected on this technologically most important invention now gives an overall light to electricity conversion efficiency,  $\eta$ , of 12% [2]. Electrons injected into the CB of TiO<sub>2</sub> from the excited dye molecules undergo a random walk through the semiconductor particulate network, which is a slow rate determining process. Electrons which are trapped in surface traps react with I<sub>3</sub><sup>-</sup> in the liquid electrolyte or the oxidized dye molecules which results in lower efficiencies. DSCs based on SnO<sub>2</sub> give low efficiencies typically less than 2% [3]. To improve the performance of DSCs extensive modifications have been done to the semiconductor layer by covering the exposed surfaces of the semiconductor matrix, such as TiO<sub>2</sub>, SnO<sub>2</sub> or ZnO, by a wide band-gap semiconductor or with an insulator such as Al<sub>2</sub>O<sub>3</sub>, CaCO<sub>3</sub> and MgO [4],[5],[6],[7]. We have used SnO<sub>2</sub> covered with CaCO<sub>3</sub> to produce a DSC with 5.4% efficiency [8]. We now report the preparation of transparent SnO<sub>2</sub>/CaCO<sub>3</sub> electrodes and their DSC applications. Transparent thin films are diverse in their importance and practical use. Doherty and Fitzmaurice [9] have used Langumire-Bloget technique to prepare mono-layers of TiO<sub>2</sub> *via* hydrolysis of titanium tetraisopropoxide. Jiu *et al* [10] have described the preparation of nanocrystalline TiO<sub>2</sub> particles with 3-10 nm diameters using a surfactant template method. Various other methods for preparing TiO<sub>2</sub> and other semiconductor films with high defined morphologies have been reported. But spray deposition systems are more attractive in producing thin films for DSC applications. The ASP technique [11] developed here gives highly uniform crack free films due to avoidance of agglomeration of particles that is happening in a normal spray method. This

method also helps to prepare large area active electrodes. Transparent films can be used in window panes, windscreens, glass materials etc. for harvesting solar energy. Transparent SnO<sub>2</sub>/CaCO<sub>3</sub> composite films with unique and highly uniform morphology can be conveniently made on conductive glass by the ASP technique. Therefore, transparency and high efficiency can be amalgamated in a single device. Several DSCs were fabricated by changing the SnO<sub>2</sub>/CaCO<sub>3</sub> molar ratio and DSCs were prepared using conventional counter electrode and the electrolyte solution. In this presentation, we reveal the effect of SnO<sub>2</sub>:CaCO<sub>3</sub> molar ratio for the optimizing the insulating layer thickness for best solar-to-electricity conversion efficiency.

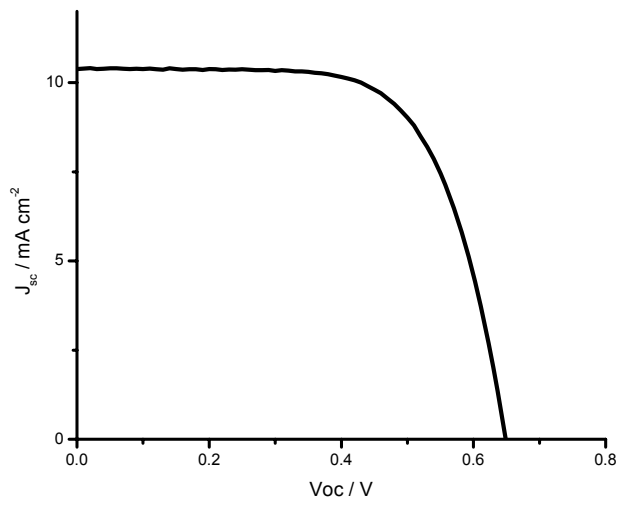
## **2. EXPERIMENTAL**

In a typical experiment, 3 ml of SnO<sub>2</sub> colloidal suspension in water( 15%, Alfa-Esar) was mixed with 6 ml of glacial acetic acid and 40 ml of 90% Ethanol. To this solution 0.05 g of CaCO<sub>3</sub>( Breckland scientific ) was added and ultra-sonicated for 10 min. FTO coated glasses were cleaned well and the above suspension was sprayed on to them at 130 °C for 30 min. ASP technique was used to prepare the thin composite layer on the FTO plates. The resulting thin film was sintered for 20 min at 500 °C. Upon sintering and bringing down the temperature to ca. 80 °C, glass plates with the composite layers were dipped in D358 dye for 12 hours. This composite film coated glasses were used to fabricate DSCs by sandwiching I<sup>-</sup>/I<sub>3</sub><sup>-</sup> containing liquid electrolyte in between the volume of the active electrode and the lightly platinized FTO counter electrode. The weight of CaCO<sub>3</sub> was varied and DSCs were prepared as described. I-V characteristics were measured using EKO Model MP-160 IV tracer with AM 1.5 filter (Fig.1). The optical transmittance was measured by Shimadzu UV-1800 spectrophotometer (Fig.2).The surface morphology was studied by SEM images taken by SEM-JOEL6320F (Fig.3). The thickness and composition of SnO<sub>2</sub> : CaCO<sub>3</sub> of the Composite layer were varied and the highest transparent and efficient DSC characteristics are reported.

## **3. RESULTS AND DISCUSSION**

The highest efficiency recorded was 4.5% for the transparent composite film (Fig.1).This conveys the idea that the efficiency has not been markedly reduced although the electrode was made transparent in the red region as the best efficiency recorded for non-transparent composite cell was 5.4%. CaCO<sub>3</sub> covered SnO<sub>2</sub> will give high number of scattering centers than SnO<sub>2</sub> alone. The fill factor (FF) and the open circuit photovoltage, V<sub>oc</sub>, have been remarkably increased upon increasing the amount of CaCO<sub>3</sub> (Table 1). This can be attributed to the prevention of recombination between excited electrons and the redox species in the liquid electrolyte as well as with oxidized dye molecules. Upon increasing the amount of CaCO<sub>3</sub>, the short-circuit current density, J<sub>sc</sub> has decreased due to the increasing thickness of insulating layer, prohibiting the electron injection from the excited dye molecules into the CB of SnO<sub>2</sub> particles (Table 1). The UV-visible transmittance data show that the composite cell has ~60% transmittance at around 670 nm and ~52% at around 460 nm. This emphasizes the non-agglomerated nature of the particles of the semiconductor film (Fig 2). SEM image gives a clear picture about the uniformity of the layer (compared to the normal hand spray method presented previously [8] ) where white areas are the CaCO<sub>3</sub> covered SnO<sub>2</sub> which have insulating properties. In conventional spray method, the same composite film has cracks and flocks of CaCO<sub>3</sub> covered SnO<sub>2</sub> which occur due to agglomeration of particles.





$V_{oc} = 0.64 \text{ V}$   $J_{sc} = 10.38 \text{ mA cm}^{-2}$   $FF = 0.67$   $\eta = 4.51\%$   
Fig 1: I-V characteristics of the transparent composite DSC for the highest efficiency recorded.

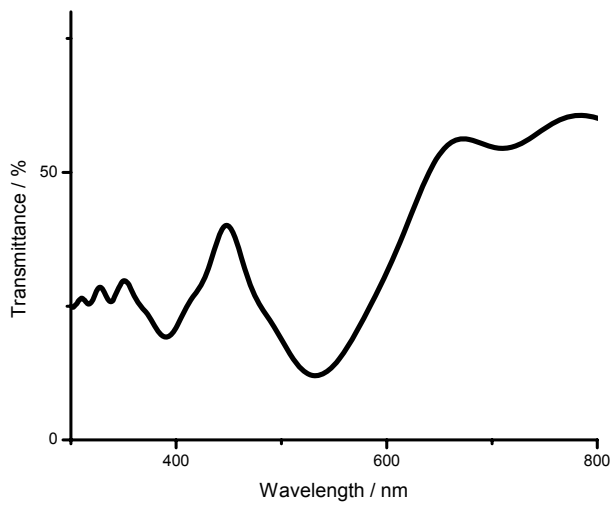


Fig. 2 UV-Visible transmittance spectrum of the highest efficient composite DSC.

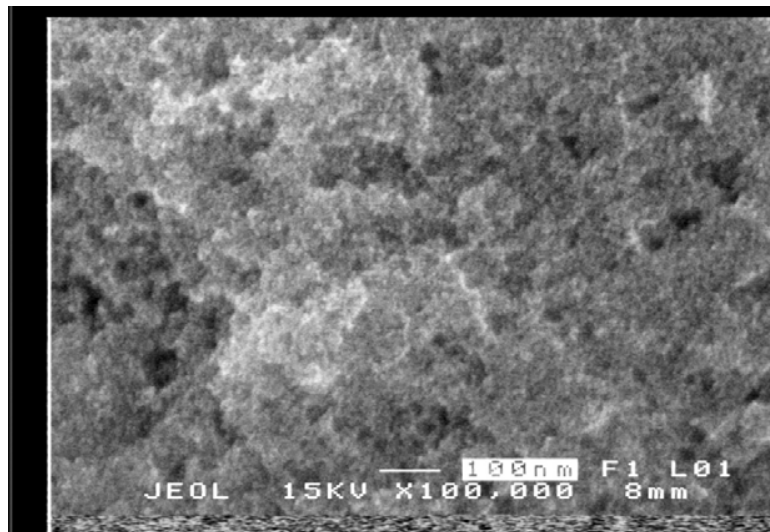


Fig 3: SEM image of the SnO<sub>2</sub> / CaCO<sub>3</sub> composite film on FTO coated conductive glass.

Table 1: I-V characteristics of the composite DSC upon variation of the amount of CaCO<sub>3</sub>.

SnO <sub>2</sub> :CaCO <sub>3</sub> molar ratio.	Jsc/ mA cm <sup>-2</sup>	Voc/ V	FF	η%
1 : 0.14	12.4	0.56	0.54	3.83
1 : 0.29	11.18	0.60	0.59	3.99
1 : 0.58	10.52	0.63	0.61	4.10
1 : 0.72	10.38	0.64	0.67	4.51
1 : 0.86	10.32	0.63	0.66	4.36
1 : 1.16	10.65	0.62	0.54	3.68
1 : 1.30	9.79	0.58	0.55	3.18

## REFERENCES

1. B. O'Regan, M. Gratzel, *Nature*, **1991**, 353, 737.
2. C.Y. Chen, M. Wang, J.Y. Li, N. Pootrakulchote, L. Alibabaei, C.H. Ngoc-le, J.D. Decoppet, .H. Tsai, C. Gratzel, C.G. Wu, S.M. Zakeeruddin and M. Gratzel, *ACS NANO*, **2009**, 3, 3103.
3. K. Tennakone, I. R. M. Kottegoda, L. A. A. De Silva and V. P. S Perera, *Semiconduct Sci,Tech*, **1999**, 14,975 S.
4. N. Tsuda, K. Nasu, A. Fujikori, K. Siratori in *Electronic Conduction in Oxides*, Second Edition, Springer, ISSN 0171-1873. 10.
5. K. Tennakone, P. K. M. Bandaranayake, P.V.V. Jayaweera, A Konno, G.R.R.A. Kumara, *Physica*, **2002**, E 14,190

6. Xin-tong Zhang, Irwan Sutanto, Taketo Taguchi, Kenichi Tokuhira, Qing-bo Meng, Tata N. Rao, Akira Fujishima, Hiroko Watanabe, Toshie Nakamori and Masayuki Uragam, *Solar Energy Materials and Solar Cells* **2003**, *80*, 315-326
7. K. Tennakone, J. Bandara, P. K. M Bandaranayake, G. R. A. Kumara and A. Konno, *J. appl. Phys.* **2001** *40*,L732.
8. H.M. N. Bandara, K.A.T. Amalka Perera, S. Gaveshana Anuradha, G.R. Asoka Kumara , M. Lal Paranawithana and R.M. Gamini Rajapakse, *Electrochimica Acta*, 2011, *56*,11,4135-4138
9. Doherty, D. Fitzmaurice, *J. Phys. Chem.*, 1996, **100**, 10732.
10. J. Jiu, S. Isoda, M. Adachi, H. Wang, *J. Mater. Sci: Mater. Electron.*, 2007, **18**, 593
11. Patent pending, H.M.N. Bandara, R.M. G. Rajapakse, G.R.R.A. Kumara, University of Peradeniya, Sri Lanka

**DYE SENSITIZED SOLAR CELLS WITH POLYMETHYLMETHACRYLATE (PMMA) BASED GEL POLYMER ELECTROLYTE AND TETRAPROPYLAMMONIUM IODIDE SALT ( $\text{Pr}_4\text{N}^+\text{I}^-$ )**

H. IQBAL<sup>1</sup>, K. PERERA<sup>1,3</sup>, V.A. SENEVIRATNE<sup>1</sup>, W.N.S. RUPASINGHE<sup>1,2</sup>, C.A. THOTAWATTHAGE<sup>2</sup>, G.K.R. SENADEERA<sup>1,4</sup> AND M.A.K.L. DISSANAYAKE<sup>1,2\*</sup>

<sup>1</sup>*Department of Physics, University of Peradeniya, Peradeniya, Sri Lanka*

<sup>2</sup>*Institute of Fundamental Studies, Kandy, Sri Lanka*

<sup>3</sup>*Department of Electronics, Wayamba University of Sri Lanka, Kuliyaipitiya, Sri Lanka*

<sup>4</sup>*Department of Physics, The Open University of Sri Lanka, Nawala, Nugegoda, Sri Lanka*

\*Corresponding Author, e-mail: makldis@yahoo.com

**ABSTRACT**

In order to obtain a highly viscous gel polymer electrolyte giving highest performances in dye sensitized solar cells, polymethylmethacrylate (PMMA) based polymeric electrolyte comprising ethylene carbonate (EC), propylene carbonate (PC), tetrapropylammonium iodide ( $\text{Pr}_4\text{N}^+\text{I}^-$ ) and iodine ( $\text{I}_2$ ) was prepared and characterized. In this process, initially, the weight ratio between solid phase (PMMA + EC+ Salt) and liquid phase (PC) of the electrolyte was optimized and the best composition was found to be with the ratio of 70 : 30. Finally, a composition having highest room temperature conductivity was achieved by varying the weight ratio between PMMA and  $\text{Pr}_4\text{N}^+\text{I}^-$ , while maintaining the weight ratio between PC and EC at 1:1.

The composition, PMMA: $\text{Pr}_4\text{N}^+\text{I}^-$ :EC:PC: $\text{I}_2$  having the weight ratios, 10:30:30:30:4 showed the highest room temperature conductivity value of  $3.26 \times 10^{-3} \text{ S cm}^{-1}$  while retaining the quasi solid state structure. Dye adsorbed nano porous  $\text{TiO}_2$  films were prepared by spreading a  $\text{TiO}_2$  paste by "doctor blade" method on an FTO glass and sintering it at  $450^\circ\text{C}$ . Sintered films were then immersed in a water free ethanolic Ruthenium (N179) dye solution for 18 hours for the dye molecules to be adsorbed into the  $\text{TiO}_2$  film.

Solar cells fabricated with cell configuration, Glass/FTO/ $\text{TiO}_2$ /Dye/Gel electrolyte,  $\text{I}_2$  /Pt / FTO/Glass exhibited the highest room temperature conductivity and delivered a short circuit current density of  $8.0 \text{ mA cm}^{-2}$  with an open circuit voltage of 668.4 mV under the irradiance of  $1000 \text{ W m}^{-2}$  (1.5 AM). The corresponding average fill factor and the efficiency were 62.7 % and 3.33% respectively.

**1. INTRODUCTION**

Dye sensitized solar cells (DSSCs) using liquid electrolytes have received considerable attention because of their relatively high solar energy conversion efficiencies of more than 10% and low production cost [1]. Unfortunately the practical viability of these DSSCs are not foreseen yet, because of the problems encountered with the use of a liquid electrolyte containing volatile solvents. Therefore, replacement of the liquid electrolyte by a solid state hole transport material circumvents the above problems and several attempts have been made to replace the liquid electrolyte by p-type semiconductors [2-4] or organic hole transport materials [5,6]. However the conversion efficiencies of these devices were relatively low particularly under high light irradiance.

An alternative approach to retain the good device properties of the liquid electrolytes while drastically reducing the above problems is the use of quasi solid electrolyte materials such as polymer gel electrolytes. Polymethylmethacrylate (PMMA), Polyacrylonitrile (PAN) and Poly(vinylidene fluoride) (PVDF) are some of the polymer host materials that have been widely used to produce these gel electrolytes. In this work, we report the performance of a dye sensitized solar cell fabricated using a PMMA based gel polymer electrolyte incorporating

tetrapropylammonium iodide ( $\text{Pr}_4\text{N}^+\text{I}^-$ ) as the iodide salt and a dye sensitized, nano porous  $\text{TiO}_2$  as the photoanode. Ruthenium (N179) dye was used as the dye sensitizer.

## **2. EXPERIMENTAL**

### *2.1 Preparation of the electrolyte*

Polymethylmethacrylate (PMMA) (Aldrich), propylene carbonate (PC) (Aldrich) and Iodine were used as received. Ethylene carbonate (EC) (Aldrich) was vacuum dried at room temperature and  $\text{Pr}_4\text{N}^+\text{I}^-$  was vacuum dried at  $80^\circ\text{C}$  prior to use. Several trials were made to obtain the optimum composition and the required heating and drying conditions to get a bubble free, homogeneous film having a good mechanical stability. At first, the ratio between the solid phase to liquid phase was selected to be 70: 30 (by weight% of PMMA+EC+Salt and PC) (7). PMMA was first dissolved in acetone and magnetically stirred for 1 hr at room temperature in a closed bottle. The appropriate amounts of EC, PC and salt were then added to the bottle and were again magnetically stirred for 15 min at room temperature. Then, the resultant mixture was heated at  $80^\circ\text{C}$  for 1 hr and after that appropriate amount of iodine was added. The hot gel electrolyte was pressed in between two clean glass plates and left in a vacuum desiccator for overnight. This way it was possible to get a homogeneous film free from pin holes. Ratio between solid phases to liquid phase was varied as 60: 40 and 80: 20 and films were prepared following the same method. After determining the solid to liquid phase ratio which corresponds to the optimum room temperature conductivity, as well as good mechanical stability, fine tuning of the composition was done by varying the polymer to salt ratio as 1 : 3, 2 : 2 and 3 : 1. The ratio between EC and PC was kept at 1: 1 and the amount of iodine was fixed at 4% by weight of PMMA, EC, PC and the salt.

### *2.2 Conductivity measurements*

A small disc shape sample of diameter about 11 mm was cut from the gel electrolyte film and sandwiched between two stainless steel electrodes in a home made cell holder. Impedance measurements were taken from room temperature upto  $55^\circ\text{C}$ . A Schlumberger SI1260 Impedance Analyser was used to take the measurements in the frequency range 1 Hz to 1 MHz.

### *2.3 Fabrication of the DSS cell*

Fluorine doped tin oxide (FTO) glass slides were cleaned well. The dimension of each glass slide was 2 cm x 0.5 cm.  $\text{TiO}_2$  (Degussa) powder of average particle size 25 nm was grounded well with Triton, acetic acid and ethanol. A thin film of the resultant mixture was deposited on FTO glass slides using the 'doctor blade method'. After leaving sometime for drying, only an area of 0.5 cm x 0.5 cm was left by scratching off the rest. Films were then sintered at  $450^\circ\text{C}$  for 45 min and cooled down to room temperature and immersed in a dye solution and slightly heated using a hair dryer and left for 18 hrs. Films were then removed and washed with water free ethanol and dried. DSSCs were then fabricated by sandwiching a gel electrolyte film in between the dye sensitized  $\text{TiO}_2$  electrode and a clean FTO glass plate coated with a thin Pt layer. The final assembled cells had the configuration, Glass/FTO/ $\text{TiO}_2$ /Dye/Gel electrolyte,  $\text{I}_2$  /Pt / FTO/Glass. The gel electrolyte, which exhibited the highest room conductivity was used for the fabrication of these solar cells.

### *2.4 Characterization of DSS cells*

The photocurrent-photovoltage characteristics of the cells were studied under the irradiance of  $1000 \text{ Wm}^{-2}$ , (AM 1.5) simulated sunlight using a homemade setup coupled with Keithly 2000 multimeter with potentiostat/galvonostat HA-301 via computer controlled software. To get the simulated sunlight with above intensity, Xenon 500 lamp was used with AM 1.5 filter.

### 3. RESULTS AND DISCUSSION

#### 3.1 Characterization of the electrolyte

Compositions of the electrolytes prepared by varying the solid phase to liquid phase ratios are shown in Table 1. As seen from this Table, out of the three compositions studied, the gel electrolyte with composition (a) had the highest conductivity, but it had a thick liquid like behavior. The gel electrolyte with composition (b) had the next highest conductivity and also a quasi-solid or gel like behavior. Sample with composition (c) had the behavior of a soft solid like rubber but was low in conductivity.

Table 1 : Compositions of the electrolytes prepared by varying the solid phase to liquid phase weight ratios.

Sample	PMMA/g	EC/g	Pr <sub>4</sub> N <sup>+</sup> T <sup>-</sup> /g	PC/g	Solid:liquid wt ratio	I <sub>2</sub> /g	$\sigma_{RT} \times 10^{-3} / S\ cm^{-1}$
a	0.1	0.4	0.1	0.4	60:40	0.04	4.52
<b>b</b>	<b>0.2</b>	<b>0.3</b>	<b>0.2</b>	<b>0.3</b>	<b>70:30</b>	<b>0.04</b>	<b>3.26</b>
c	0.2	0.2	0.4	0.2	80:20	0.04	2.15

Fig.1 shows the conductivity variation of the above electrolyte samples with temperature.

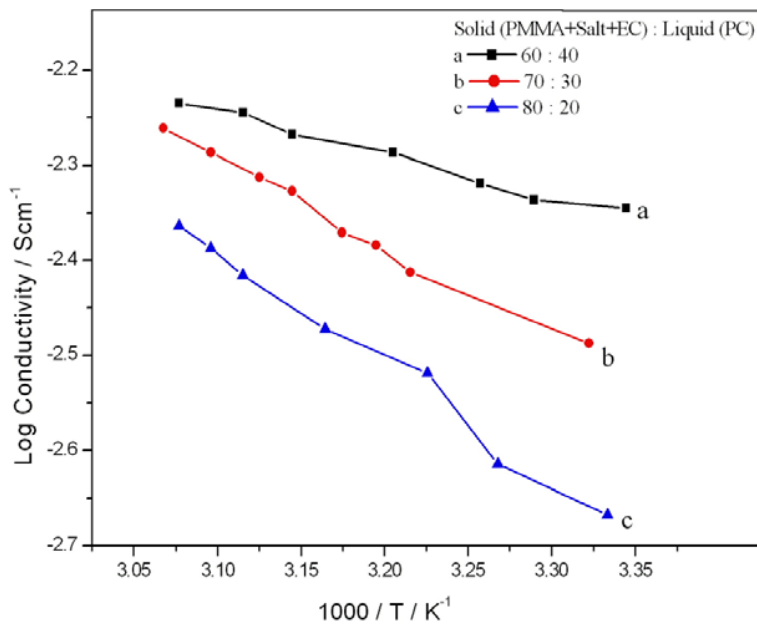


Fig.1. Variation of conductivity with inverse temperature for the gel electrolyte samples :  
 (a) 10%PMMA+10% Pr<sub>4</sub>N<sup>+</sup>T<sup>-</sup>+40%EC : 40%PC; (b) 20%PMMA+20% Pr<sub>4</sub>N<sup>+</sup>T<sup>-</sup>+30%EC :30%PC; and  
 (c) 20%PMMA+40% Pr<sub>4</sub>N<sup>+</sup>T<sup>-</sup>+20%EC : 20%PC

A typical PMMA based gel electrolyte essentially consists of an electrolyte solution of an iodide salt dissolved in an organic polar solvent like propylene carbonate (PC). The electrolyte solution is “trapped” in polymer cages formed by the PMMA matrix. Therefore, the conductivity of the gel electrolyte increases with increasing fraction of the liquid. The maximum conductivity was obtained with the sample having a higher amount of liquid phase (sample - a). Ionic conductivity is governed by several factors such as ion mobility, ion concentration, interactions with polymer network etc. In the liquid phase, ion mobility is high and therefore, conductivity is high. But, as far as the mechanical stability is considered, sample (a) with highest conductivity was more closer to liquid phase. Hence, the sample (b) which had the next highest conductivity and gel like behavior was selected for further studies. The composition of this electrolyte was further fine tuned by changing the ratio between the polymer and the salt. The corresponding compositions are given in Table 2.

Table 2 : Compositions of the electrolytes prepared by varying the polymer to salt ratio.

Sample	PMMA/g	Pr <sub>4</sub> N <sup>+</sup> I <sup>-</sup> /g	EC/g	PC/g	Polymer: salt wt ratio	I <sub>2</sub> /g	$\sigma_{RT} \times 10^{-3} / \text{Scm}^{-1}$
<b>d</b>	<b>0.1</b>	<b>0.3</b>	<b>0.3</b>	<b>0.3</b>	<b>1 : 3</b>	<b>0.04</b>	<b>3.26</b>
e	0.2	0.2	0.3	0.3	2 : 2	0.04	3.08
f	0.3	0.1	0.3	0.3	3 : 1	0.04	1.19

The conductivity variation of the fine-tuned electrolyte samples with temperature is shown in Fig. 2.

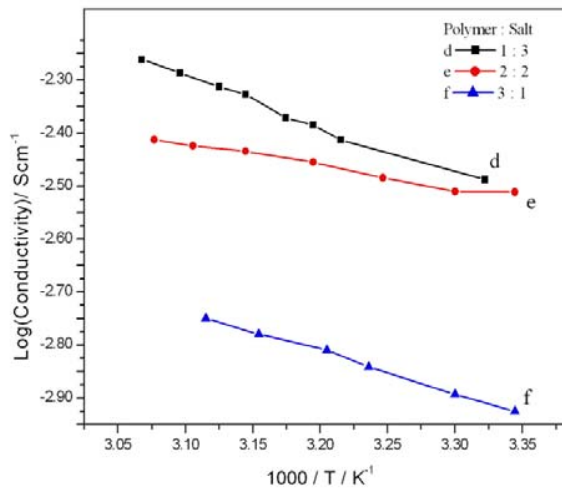


Fig.2. Variation of conductivity with inverse temperature of fine tuned samples:  
 (d) 10% PMMA+30% Pr<sub>4</sub>N<sup>+</sup>I<sup>-</sup>+30% EC : 30% PC:      (e) 20% PMMA+20% Pr<sub>4</sub>N<sup>+</sup>I<sup>-</sup>+30% EC :30% PC;  
 (f) 30% PMMA+10% Pr<sub>4</sub>N<sup>+</sup>I<sup>-</sup>+30% EC : 30% PC.

With increase in the weight ratio of polymer/salt, the room temperature conductivity decreases as expected. When the relative amount of polymer increases, the network structure becomes more dense and ionic motion is hindered due to the blocking effect. Also, when the salt concentration decreases, the ion concentration reduces and the conductivity drops [8]. Both these factors contribute to lowering of the conductivity. The highest room temperature conductivity of  $3.26 \times 10^{-3} \text{ S cm}^{-1}$  was obtained with polymer to salt ratio of 1: 3 (sample (d)) which retained the quasi-solid (gel) structure.

### 3.2 Characterization of the dye sensitized solar cells

Since  $\text{Pr}_4\text{N}^+$  ion is relatively a large cation, the major contribution to conductivity is expected from the iodide ions ( $\text{I}^-$ ) in the gel electrolyte. The photocurrent vs. voltage variation for the solar cell with the gel electrolyte having the maximum conductivity (sample “d”) is shown in Fig.3.

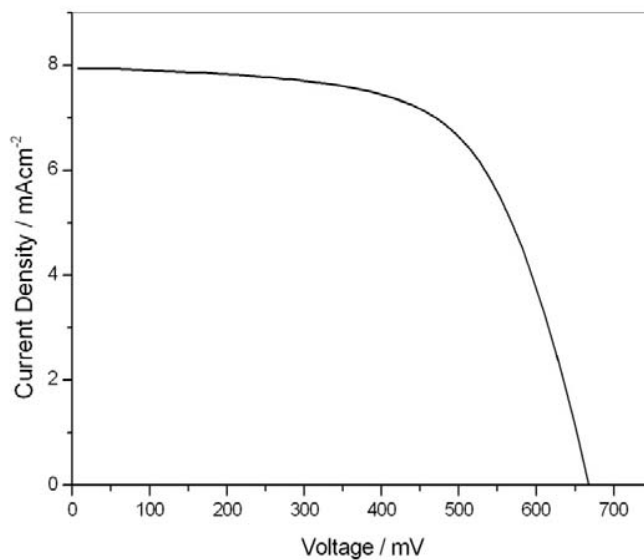


Fig.3. Photocurrent vs voltage variation of the solar cell with configuration, Glass/FTO/TiO<sub>2</sub>/Dye/Gel electrolyte, I<sub>2</sub>/Pt / FTO/Glass fabricated with the gel electrolyte (d).

For this solar cell, the average value of the short circuit current density was  $8.0 \text{ mA cm}^{-2}$  and the open circuit voltage was 668 mV. The average fill factor and the efficiency were 62.7% and 3.33% respectively. This efficiency is relatively high compared to most of the reported values for DSS cells based on other polymeric gel electrolytes using the same salt [6,9]. The work is in progress in order to improve the efficiency of these cells further by incorporating ionic liquids and nano fillers into the gel structure.



## REFERENCES

1. A.F. Nogueira, C. Longo, M.A. DE Paoli, *Coordination Chemistry Review*, 248 (2004) 1455.
2. S. Luzzati, M. Basso, M. CAtellani, C.J. Brabec, D. Gebeyehu, N.S. Sariciftci, *Thin Solid Films*, 403-404, (2002) 52.
3. P.R. Somani, C. Dionigi, M. Murgia, D. Palles, P. Nozar, G. Ruani, *Solar Energy Materials and Solar Cells*. 87, (2005) 513.
4. S. Luzzati, M. Basso, M. CAtellani, C.J. Brabec, D. Gebeyehu, N.S. Sariciftci, *Thin Solid Films*, 403-404, (2002) 52-56, P.R. Somani, C. Dionigi, M. Murgia, D. Palles, P. Nozar, G. Ruani, *Solar Energy Materials and Solar Cells*. 87, (2005) 513.
5. S. Spiekermann, G. Smestad, J. Kowalik, L.M. Tolbert, M.Gratzel, *Synthetic Metals*, 121 (2001) 1603.
6. O.A. Illeperuma, M.A.K.L. Dissanayake, S. Somasundaram, L.R.A.K. Bandara, *Solar Energy Materials and Solar Cells*, 84 (1-4) (2004) 117.
7. M.A.K.L. Dissanayake, L.R.A.K. Bandara, R.S.P. Bokalawela, P.A.R.D. Jayathilaka, O.A. Illeperuma, *Materials Research Bulletin*, 37, (2002) 867.
8. T.M.W.J. Bandara, P. Ekanayake, M.A.K.L. Dissanayake, I.Albinson, B.E. Mellander, *J. of Solid State Electrochemistry*, 13 (2009) 1825.
9. O.A. Illeperuma, M.A.K.L. Dissanayaka, S. Somasundaram, *Electrochimica Acta*, 47 (2002) 2801.

## HIGHLY EFFICIENT, OPTICALLY SEMI-TRANSPARENT, ZnO-BASED DYE-SENSITIZED SOLAR CELLS WITH INDOLINE D-358 AS THE DYE

K. PREMARATNE<sup>\*1</sup>, R.M.G. RAJAPAKSE<sup>2</sup>, G.R.A. KUMARA<sup>1</sup> AND M.L.KARUNARATHNE<sup>1</sup>

<sup>1</sup>*Department of Physics, <sup>2</sup>Department of Chemistry, University of Peradeniya, Peradeniya, Sri Lanka*

\*Corresponding Author, e-mail: *kprema@pdn.ac.lk*

### ABSTRACT

Highly compact, transparent, ZnO films have been prepared, on fluorine-doped tin(IV) oxide (FTO) glass plates, from 30 nm colloidal ZnO solution, with the help of novel atomized-spray pyrolysis deposition technique (ASP). These films were used to construct dye-sensitized solar cells (DSCs) with Indoline D-358 dye. The DSC shows an optical transmittance of approximately 40 % in the visible range. The cells show impressive parameters of 635 mV open circuit photovoltage ( $V_{oc}$ ), 15.0 mA cm<sup>-2</sup> of short-circuit current density ( $J_{sc}$ ) and 0.62 fill factor (FF), with an overall efficiency ( $\eta$ ) of 5.9 % under air mass (AM) 1.5 illumination.

### 1. INTRODUCTION

Dye-sensitized photovoltaic cells fabricated utilizing pigments for trapping sunlight continue to receive attention as promising systems for the conversion of solar energy into electricity due to their simplicity, low cost and reasonably good power conversion efficiency. Such artificial solar energy conversion devices were a mere curiosity until late nineteen eighties, because of their low energy conversion and low quantum efficiencies [1-6]. A major breakthrough that changed the situation was the observation that nanocrystalline and porous semiconductor films of large surface area produced higher efficiencies [7-9]. A typical DSC comprises of a dye-absorbing porous nanocrystalline semiconductor film prepared on a conducting glass plate, a lightly platinumized counter electrode, and an electrolyte containing I<sup>-</sup>/I<sub>3</sub><sup>-</sup> redox couple sandwiched between the electrodes. The dye sensitizer absorbs photons and the resulting excited state injects electrons to the conduction band of the semiconductor. The resultant oxidized dye is quickly reduced back to its original state by the reduced species in the electrolyte. The oxidized species of the redox couple is reduced back at the counter electrode. A crucial factor affecting the overall efficiency of the solar cell is the morphology of the semiconductor film. A high surface area is required to obtain a high light absorption from a single monolayer of the sensitizer dye which is adsorbed on the semiconductor surface. In order for the electrons injected to the conduction band of the semiconductor to move fast towards the back contact, the nature of the semiconductor film is crucial. Highly compact interconnected small nanoparticles in the film contribute not only to high electron conductivity but also to the increased surface area for dye absorption. The smaller particles (< 100 nm) in the film allow the light to pass through them, without significant scattering, resulting in a semi-transparent thin film. DSCs based on nanostructured TiO<sub>2</sub> are the most investigated systems to-date and are the most efficient ones. However, from a fundamental point of view, ZnO with its band gap energy of 3.2 eV, and having band positions similar to TiO<sub>2</sub> but with higher electron mobility, should give equal or better solar cell performance.

There have been a considerable number of attempts made to use ZnO in DSCs. The preparation techniques used, span a wide range of thin film deposition methods which involve electrodeposition [10], sol gel techniques [11] and screen printing [12]. The maximum efficiency reported so far is for the cell fabricated by sol-gel deposited ZnO is around 5% [13].

Electrodeposition of ZnO in the presence of various dyes have been explored by Yoshida *et al* who have reported 5.56 % efficiency for the ZnO-Indoline dye combination [14]. Out of these techniques, screen printing and spray technologies give crack-free and compact thin films. However, particle aggregation reduces the surface area due to the formation of larger particles and hence the films become translucent or opaque. To rectify these problems, we have designed and developed a novel spray pyrolysis technique called the “Atomized Spray Pyrolysis” where the colloidal solution aspirated impinges on a spherule and individual particles get deposited in the thin film.

Ruthenium complex dyes are not suitable for cost-effective environmentally-friendly photovoltaic systems, because ruthenium is a rare and expensive metal.

Recently, a metal-free indoline dye(D-358) (figure 1)having a high molar absorption coefficient of  $67000 \text{ mol}^{-1}\text{cm}^{-1}$  at 532 nm has been reported by Tsutsui *et al.*[15].

In this paper, we present the preparation of crack-free, semi-transparent thin films without particle aggregation and their DSC applications with metal-free indoline D-358 dye.

## **2. EXPERIMENTAL**

### *Preparation of semi-transparent ZnO film*

ZnO powder (30 nm, Wako, 0.6 g) acetic acid (10 drop) and ethanol (40 ml) were mixed and ultrasonically dispersed for 10 min. Then the solution mixture was sprayed onto heated (150°C) FTO glass substrate using the atomized SPD machine and subsequently sintered in air at 500°C for 30 min.

### *Dye Adsorption*

The semi-transparent ZnO electrode, pre-heated to 80 °C, was immersed in a mixture of acetonitrile/tert-butyl alcohol (volume 1:1) containing  $3 \times 10^{-4}$  M Indoline D-358 for 12 h. The plates were removed and rinsed with acetonitrile and allowed to dry in air. The amount of adsorbed dye was determined by spectroscopic measurement of dye desorbed from the film surface. This was done by treating with NaOH (0.1 M) in a mixture of water and ethanol (50 : 50 by volume).

### *Preparation of transparent Pt counter electrode*

A small quantity of Hexachloroplatinic acid ( $\text{H}_2\text{PtCl}_6$ , 5 mM in isopropanol) was sprayed on to pre-heated FTO glass plate (150 °C) and sintered at 400 °C for 15 min.

### *Construction of the DSC*

The dye-coated ZnO electrode was sandwiched with a transparent Pt counter electrode and the intervening space was filled with an electrolyte (0.1 M LiI, 0.05 M  $\text{I}_2$ , 0.6 M dimethylpropylimidazolium iodide in methoxyacetonitrile). The current-voltage (I-V) characteristics of the cells at AM 1.5 ( $100 \text{ mW cm}^{-2}$ ) simulated sunlight irradiation were recorded with a calibrated solar-cell evaluation system (PECCELL).

The particle size and surface morphology of the ZnO films were studied using Scanning Electron Microscopy (SEM, JOEL 6320 F). The transmittance and absorbance of the cell was measured using a JASCO V-570 spectrophotometer.

### 3. RESULTS AND DISCUSSION

SEM micrograph shows the surface morphology of semi-transparent ZnO film prepared by novel atomized-spray pyrolysis deposition technique (Figure 2). It is clearly seen that ~30 nm particles are deposited in a compact manner forming a highly porous film. Figure 3 shows the light absorption spectra of indoline D-358 dye in t-butyl alcohol-acetonitrile (50:50) solution and that of the dye-adsorbed ZnO film. The shape of the absorption spectrum of indoline D-358 adsorbed on the ZnO surface is almost the same as that of indoline D-358 dye and is remarkably broadened. This broadening is a good indication of anchoring of the dye on to ZnO which is essential for proper performance of the cell. The absorption peak occurs at a wavelength ( $\lambda_{max}$ ) of 532 nm. The molar absorption coefficient of D-358 has been observed to be  $67000 \text{ mol}^{-1} \text{ cm}^{-1}$ . This is much higher compared to  $13900 \text{ mol}^{-1} \text{ cm}^{-1}$  at 541 nm for N719 dye under the same conditions [16].

Figure 4 shows the visible transmittance spectrum of a D-358 dye-sensitized ZnO solar cell. The average transmittance is 40 % in the range of 500 to 900 nm.

The photovoltaic properties of the DSC were measured under Am 1.5 irradiation ( $100 \text{ mW cm}^{-2}$ ). Figure 5 shows the I-V characteristics of a DSC having the highest performance. The cells show impressive parameters of 635 mV open circuit photovoltage ( $V_{oc}$ ),  $15.0 \text{ mA cm}^{-2}$  of short-circuit current density ( $J_{sc}$ ) and 0.62 fill factor (FF, with an overall efficiency ( $\eta$ ) of 5.9 % under air mass (AM) 1.5 illumination.

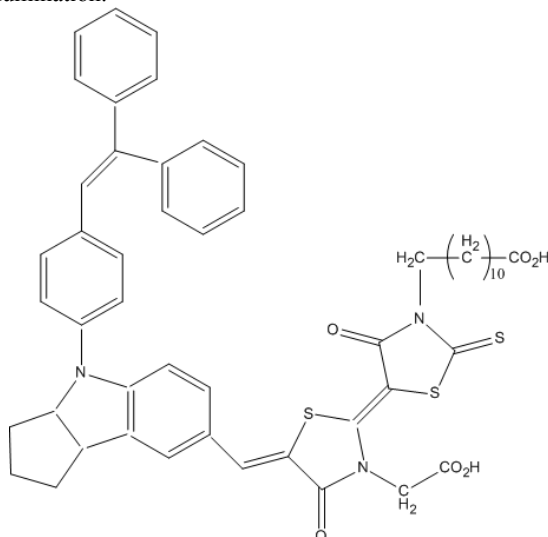


Fig 1. Molecular structure of Indoline D-358 dye

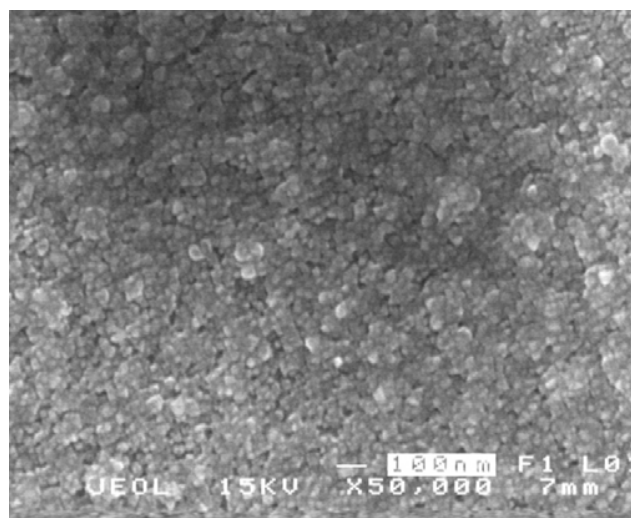


Fig. 2 SEM micrographs showing the surface morphology of semi-transparent ZnO film

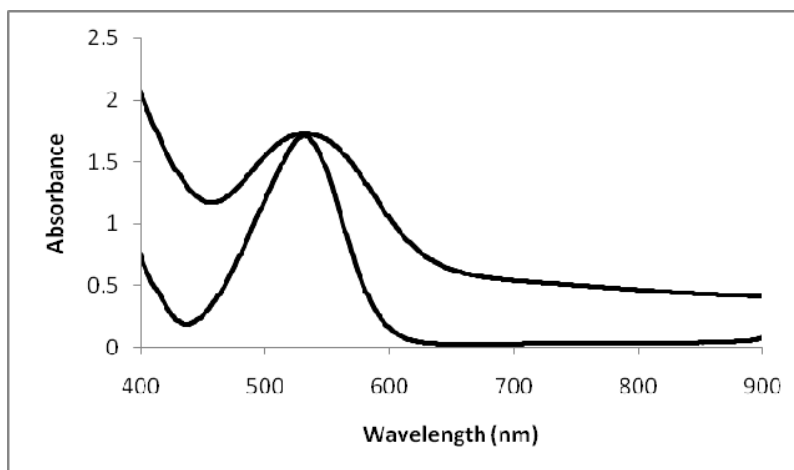


Fig. 3 Absorption spectra of Indoline D-358 dye in t-BuOH/CH<sub>3</sub>CN (dashed line) and that of the dye-adsorbed ZnO film (solid line)

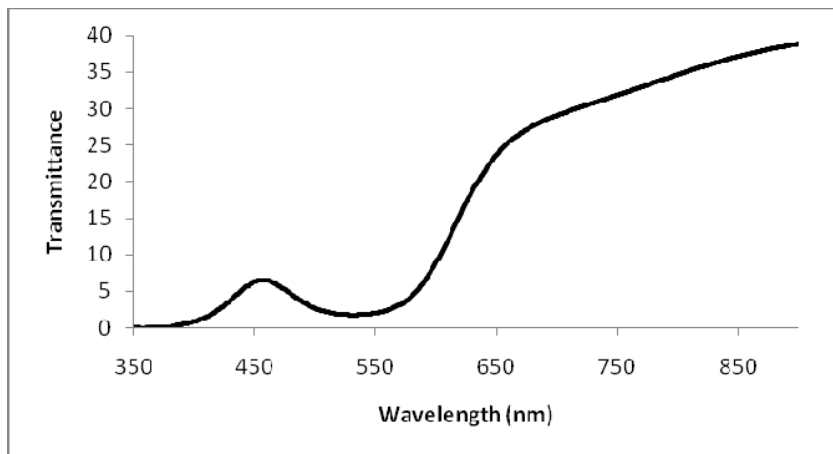


Fig.4 Transmittance spectrum of a D-358 dye-sensitized ZnO solar cell.

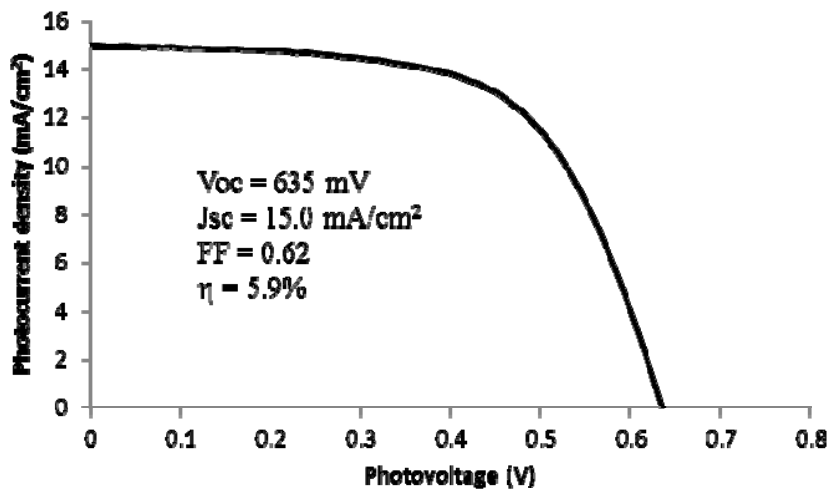


Fig. 5 I-V characteristics of the solar cell (cell area = 0.25 cm<sup>2</sup>) at AM 1.5 irradiation.

#### REFERENCES

1. H. Gerischer and H. Tributsch, B. Bunsenges: *Phys. Chem.* **72** (1968) 437.
2. R. Memming: *Photochem. Photobiol.* **16** (1972) 325.
3. J. Bourden: *J. Phys. Chem.* **69** (1965) 705.
4. M. Matsumura, Y. Nomura and H. Tsubomura: *Bull. Chem. Soc. Japan.* **82** (1979) 1559.
5. H. Tsubomura, M. Matsumura, Y. Nomura and T. Amamia: *Nature.* **261** (1979) 402.
6. M. Nako, K. Itoh and K. Honda: *J. Phys. Chem.* **88** (1984) 4906.
7. N. Vlachopoulos, p. Liska, J. Augstynski and M. Gratzel: *J. Am. Chem. Soc.* **110** (1988) 1216.
8. B.O. Regan and M. Gratzel: *Nature.* **353** (1991) 737.

9. M.K. Nazeeruddin, A. Kay, J. Rodicio, R. Humphry Baker, and M. Gratzel: *J. Am. Chem. Soc.* **115** (1993) 6382.
10. Kasuteru Nomomura, Tsukasa Yoshida, Derck Schlettwein, and Hideki Minoura: *Electrochimica Acta* **48** (2003) 3071 – 3078.
11. Kaidi Yuan, Xin Yin, Giangtian Li, Jianjun Wu, Yaoming Wang, and Fuqiang Huang: *Journal of Alloys and Compounds* **489**(2010) 694 – 699.
12. Kohjiro Hara, Takaro Horoguchi, Tohru Kinoshita, Kazuhiro Sayama, Hideki Sugihara and Hironori Arakawa: *Chemistry Letters* (2000) 316 – 317.
13. Karin Keis, Eva Magnusson, Henrik Lindström, Sten-Eric Lindquist and Anders Hagfeldt: *Solar Energy Materials and Solar Cells*, (2002) 51-58.
14. T. Yoshida, J. Zhang, D. Komatsu, S. Sawatani, H. Minoura, T. Pauporte, D. Lincot, T. Oekermann, D. Schlettwein, H.Tada, D. Wohrle, K. Funabiki, M. Matsui, H. Miura, and H. Yanagi *Adv. Funct. Mater.* **19** (2009) 17–43.
15. Tsutsui Yuko, Sanehira Yoshikawa, Uchida Satoshi, KUBO, Takaya, Segawa Hiroshi, Takata Masakazu, Sumioka Koichi, Kasai Takaaki: *The Chemical Society of Japan* (2010)
16. M. K. Nazeeruddin, S. M. Zakeeruddin, R. Humphry-Baker, M. Jirousek, P. Liska, N. Vlachopoulos, C. H. Fischer and M. Gratzel, *Inorg. Chem.*, (1999) **38**, 6298-6305.

## MIXED CATION EFFECT IN ENHANCING THE EFFICIENCY OF DYE SENSITIZED SOLAR CELLS BASED ON POLYACRYLONITRILE (PAN) AND NANO-POROUS TiO<sub>2</sub>

C.A. THOTAWATTHAGE<sup>1,\*</sup>, G.K.R. SENADEERA<sup>1,2</sup>, T.M.W.J. BANDARA<sup>3</sup>,  
M.A.K.L. DISSANAYAKE<sup>1</sup>

<sup>1</sup> Institute of Fundamental Studies, Hantana Road, Kandy, Sri Lanka

<sup>2</sup>Department of Physics, The Open University of Sri Lanka, Nawala, Nugegoda, Sri Lanka

<sup>3</sup>Department of Physics, University of Rajarata, Mihinthale, Sri Lanka.

\* Corresponding Author, email: thotawatthageca@yahoo.com

### ABSTRACT

In the past decade, dye-sensitized solar cells based on nano-porous TiO<sub>2</sub> and quasi-solid polymer (or gel) electrolytes have drawn the interest of many research groups. These cells have become potential, low cost alternatives to conventional inorganic photovoltaic devices. However, a major drawback of these solar cells with gel electrolytes is their relatively low power conversion efficiencies compared to their liquid electrolyte counterparts. Several attempts have been made to enhance the efficiencies of these cells. Using gel electrolytes with polymer hybrids, incorporating better plasticizers, optimizing the electrolyte compositions and incorporating ionic liquids are among some of these methods.

In this paper, we report the effect of using a mixed iodide salt system with two cations to enhance the power conversion efficiency of dye sensitized solar cells made with polyacrylonitrile (PAN) based gel electrolyte and nano-porous TiO<sub>2</sub> electrode. Instead of a single iodide salt, a mixture of two salts, namely MgI<sub>2</sub> and tetrapropylammonium iodide (Pr<sub>4</sub>NI) were used to provide iodide ion conductivity. Solar cells of configuration Glass/FTO/TiO<sub>2</sub>/Dye/electrolyte/Pt/FTO/glass were fabricated using nano-porous TiO<sub>2</sub> electrode sensitized with Ruthenium dye (N719). The composition of the gel electrolyte was: PAN(10.36 wt %), EC (41.43 wt%), PC (41.43 wt%), salt (6.21 wt%) and I<sub>2</sub>(0.57wt%).

With identical electrolyte compositions, the cell with MgI<sub>2</sub> alone gave an efficiency of 2.5 % and the cell with Pr<sub>4</sub>NI alone gave an efficiency of 3.3 %. The cell with the mixed iodide system, MgI<sub>2</sub>: Pr<sub>4</sub>NI = 36:64(molar ratio) however, showed an enhanced efficiency of 3.7 % with a short circuit current density (J<sub>sc</sub>) of 8.61 mA cm<sup>-2</sup>, open circuit voltage (V<sub>oc</sub>) of 743 mV and a fill factor of 58.2 %.

### 1. INTRODUCTION

Solar cells provide an alternative energy source which can produce energy from freely available solar radiation. Due to lower manufacturing cost compared to solid state photovoltaic solar cells, dye sensitized solar cells (DSSCs) are emerging as an alternative technology for solar energy conversion. After the first report by Regan and Gratzel in 1991, liquid electrolyte based DSSCs using nano-porous, dye sensitized TiO<sub>2</sub> photo anode at present can yield power conservation efficiencies close to 11%[1]. For these DSSCs, the electrolytes usually consist of I<sub>3</sub><sup>-</sup>/I<sup>-</sup> redox couple dissolved in an organic solvent. Optimum device efficiencies for DSSCs up to date have been obtained by using liquid electrolytes [1, 2]. However, cells using liquid electrolytes have many disadvantages such as, their lower long term stability, difficulty in robust sealing, evaporation and leakage of electrolyte in case of improper sealing or damage. To overcome these problems many efforts have been made to replace the liquid electrolyte by gel polymer electrolyte (or quasi – solid electrolyte) [3-10]. In these studies gel polymer electrolytes based on polyacrylonitrile (PAN) are being widely used and cells incorporating divalent salts like magnesium iodide (MgI<sub>2</sub>) have shown maximum efficiency ~ 2.5% [11] and those using tetrapropyl ammonium iodide (Pr<sub>4</sub>NI) have shown maximum efficiency ~ 2.99% [12]. In the present work we have studied the effect of using a mixture of two iodide salts, MgI<sub>2</sub> and Pr<sub>4</sub>N<sup>+</sup>I<sup>-</sup>, on the efficiency of PAN based DSSCs.



## **2. EXPERIMENTAL**

Polyacrylonitrile (PAN) and magnesium iodide ( $MgI_2$ ) of purity 98% were purchased from Aldrich and ethylene carbonate (EC), propylene carbonate (PC), iodine chips ( $I_2$ ) and Tetra propyl ammonium iodide ( $Pr_4N^+I^-$ ) with purity greater than 98% were purchased from Fluka. Ru dye was purchased from Solaronix SA. All the chemicals except  $MgI_2$ ,  $I_2$  and PC were vacuum dried for 24 hours in a vacuum oven prior to use.  $MgI_2$  was kept in a nitrogen ( $N_2$ ) environment with humidity less than 10%.

### *2.1 Electrolyte preparation*

For preparing the electrolyte samples, the weights of PAN(0.10 g), EC(0.40 g) and PC(0.40 g) were kept unchanged while the total weight of  $MgI_2$  and  $Pr_4N^+I^-$  was kept at 0.06 g. The weight of  $I_2$  was taken to be one tenth of the mole amount of the iodide salt. Appropriately weighed quantities were mixed in a glass bottle by magnetic stirring. Initially EC, PC and PAN were mixed by continuously stirring at 80 °C for about for 2 hours until the entire polymer has been dissolved. Then  $Pr_4N^+I^-$  was added and the mixture was stirred further keeping it at 80 °C for about 30 min. Finally  $MgI_2$  was added inside a  $N_2$  filled and humidity (<10%) controlled glove box and the mixture was stirred again at 80 °C for about 30 min until  $MgI_2$  was fully dissolved. The mixture was then allowed to cool down to room temperature and  $I_2$  chips were added. Then the mixture was again continuously magnetically stirred overnight (12 hours) to obtain a homogeneous gel electrolyte. This procedure was repeated for all the compositions shown in table 1.

### *2.2 $TiO_2$ electrode preparation*

$TiO_2$ paste was prepared by grinding 0.20g of  $TiO_2$  (Degussa P-25) with 12 drops of glacial acetic acid, one drop of triton X-100 and about 2 ml of ethanol. This paste was spread on a pre-cleaned, fluorine-doped conducting tin oxide (FTO) glass (Nippon sheet glass 10-12  $\Omega$ /sq). An active cell area of 0.25  $cm^2$  was obtained by spreading the paste using the doctor blade technique and sintering at 450 °C for 45 minutes. The resulting  $TiO_2$ nano-porus film was allowed to cool down to room temperature. The thickness of the film on FTO glasses was measured with the help of a homemade, calibrated profilometer and the average film thickness of the  $TiO_2$  film was found to be around 12  $\mu m$ . Dye absorbance was carried out by immersing the above film in ethanolic dye solution containing Ruthenium dye N719 [ $RuL_2(NCS)_2:2TBA$  where, L= 2,2'-bipyridyl-4,5'-dicarboxylic acid; TBA = tetrabutylammonium] for 24 hours.

### *2.3 Solar cell preparation*

Dye sensitized solar cells (DSSC) of configuration Glass/FTO/ $TiO_2$ /Dye/electrolyte/Pt/FTO/glass were fabricated by sandwiching the polymer electrolyte between the dye adsorbed  $TiO_2$  electrode and a platinum (Pt) coated FTO glass. The current-voltage (I-V) characteristics of the cells were measured under the illumination of 100mW  $cm^{-2}$  (AM 1.5) simulated sunlight using a homemade computer controlled setup coupled to a Keithley 2000 millimeter with potentiostat/galvonostat HA-301. A Xenon 500 lamp was used with AM 1.5 filter to obtain the simulated sunlight with above intensity.

## **3. RESULTS AND DISCUSSION**

Different compositions of  $MgI_2$  and  $Pr_4N^+I^-$  used in this study are shown in table 1.

Table 1: Electrolyte compositions, where the weights of PAN, EC and PC were kept at 0.10 g, 0.40 g and 0.40 g respectively.

Electrolyte	MgI <sub>2</sub> (g)	Pr <sub>4</sub> N <sup>+</sup> I <sup>-</sup> (g)	I <sub>2</sub> (g)	Mole ratio [MgI <sub>2</sub> ]:[Pr <sub>4</sub> N <sup>+</sup> I <sup>-</sup> ]
a	0.00	0.06	0.0055	0:100
b	0.01	0.05	0.0054	18.4:81.6
<b>c</b>	<b>0.02</b>	<b>0.04</b>	<b>0.0053</b>	<b>36.0:64.0</b>
d	0.03	0.03	0.0052	52.9:47.1
e	0.06	0.00	0.0049	100:0

Solar cell parameters such as the open circuit voltage ( $V_{oc}$ ) and the short circuit current density ( $J_{sc}$ ) were measured and the fill factor (FF %) was calculated using the formula,

$$FF = \frac{J_{opt} \cdot V_{opt}}{J_{sc} \cdot V_{oc}}$$

where  $J_{opt}$  is the current density at maximum power output and  $V_{opt}$  is the voltage at maximum power output. The power conversion efficiency ( $\eta$ %) was calculated from the following equation.

$$\eta = \frac{J_{sc} \cdot V_{oc} \cdot FF}{\text{Total incident power density}}$$

Fig. 1 shows the I-V characteristics of the solar cell containing the best electrolyte with 36 mole % MgI<sub>2</sub> and 64 mole % Pr<sub>4</sub>N<sup>+</sup>I<sup>-</sup> and the power density of the same solar cell.

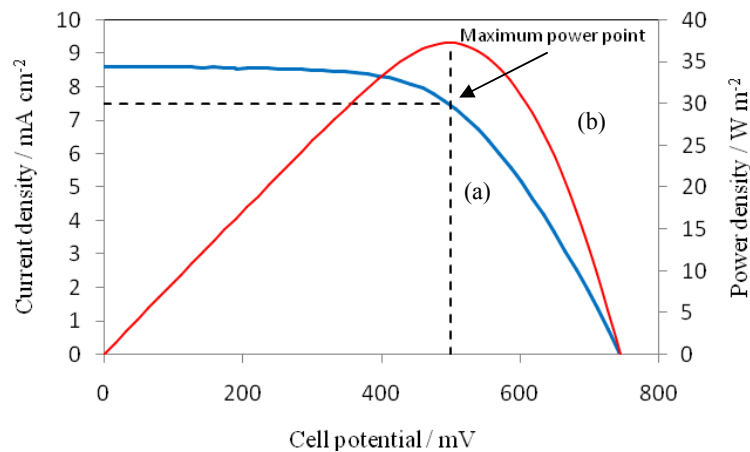


Fig. 1: curve (a) shows the I-V characteristics of the solar cell containing the best electrolyte with 36 mole % MgI<sub>2</sub> and 64 mole % Pr<sub>4</sub>N<sup>+</sup>I<sup>-</sup>. Curve (b) shows the power density of the same solar cell.

All important parameters of solar cells fabricated using electrolytes with different MgI<sub>2</sub>/ Pr<sub>4</sub>N<sup>+</sup>I<sup>-</sup> ratios shown in Table 1 are listed in Table 2.

Table 2: Parameters of solar cells with electrolytes of different  $MgI_2/Pr_4N^+I^-$  molar ratios.

Electrolyte	$J_{sc}$ mA $cm^{-2}$	$V_{oc}$ mV	FF %	$\eta$ %
a	8.99	649.5	56.76	3.32
b	8.53	729.2	58.65	3.65
<b>c</b>	<b>8.61</b>	<b>743.4</b>	<b>58.18</b>	<b>3.73</b>
d	8.83	718.9	54.66	3.47
e	6.38	684.5	55.16	2.41

Fig. 2 shows the variation of the efficiency of DSSCs with molar ratio  $[MgI_2]/[Pr_4N^+I^-]$ %. According to Fig. 2, it is clear that the efficiency reaches a maximum when the mole ratio  $[MgI_2]:[Pr_4N^+I^-] = 36:64$ .

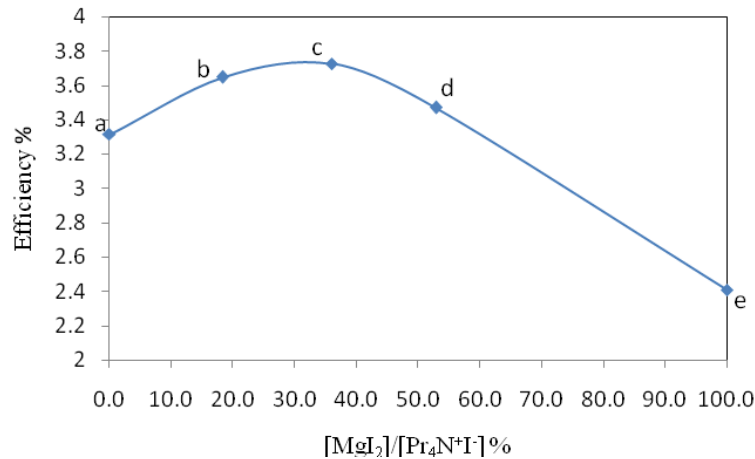


Fig. 2: The variation of the efficiency with molar ratio  $[MgI_2]/[Pr_4N^+I^-]$ % for the solar cells.

Out of the five solar cells studied, the cells fabricated using the electrolyte composition with  $MgI_2/Pr_4N^+I^-$  molar ratio of 36:64 exhibits the highest  $V_{oc}$  of 743.4 mV and the highest efficiency of 3.73 %. A PAN based gel electrolyte essentially consists of an electrolyte solution, formed by dissolving an ionic salt in an organic solvent such as propylene carbonate (PC), “trapped” in “cages” formed by the PAN matrix [13]. As far as we are aware, there are no reports which discuss specifically the effect of mixed cation electrolytes on the performance of dye sensitized solar cells. Cation-cation association in aqueous mixed electrolyte solutions has been studied using NMR [14]. Mixed anion effect in a PEO based polymer electrolyte has shown that  $Na^+$  cationic transference number reaches a maximum of 0.6 for the electrolytic composition with 35%  $NaI^+$  65%  $NaSCN$  [15]. The influence of cations of different sizes on electron transfer in the  $TiO_2$  electrode has also been reported [17].

In a dye sensitized solar cell employing a PAN based gel electrolyte, the cation-cation association can influence the electron injection dynamics at the electrolyte/ $TiO_2$  interface[16-17]. In the absence of an accepted explanation, we can only speculate about the effect of mixed cations on the performance of the solar cell. As discussed by Hoshikawa et al [17], cations at the electrolyte/ $TiO_2$  interface can form charge pairs with the injected electrons to keep the electrode surface neutral. Therefore, the transfer of the injected electrons from the dye can be efficient.

In the present system, the compositions with  $\text{MgI}_2$  alone would result a zero or weak  $\text{Mg}^{2+}$ ...  $\text{Mg}^{2+}$  attraction. Similarly the composition with  $\text{Pr}_4\text{N}^+\text{I}^-$  alone would result a zero or weak  $\text{Pr}_4\text{N}^+$ ... $\text{Pr}_4\text{N}^+$  attraction. However in the mixed composition, at the optimum  $\text{MgI}_2/\text{Pr}_4\text{N}^+\text{I}^-$  molar ratio of 36:64 the  $\text{Mg}^{2+}$ ... $\text{Pr}_4\text{N}^+$  cation-cation association possibly results the strongest attraction, thereby leads to the most efficient electron transfer at the  $\text{TiO}_2$  surface. This can increase the fill factor and the  $V_{oc}$  and enhance the over all cell efficiency to 3.7% .

#### 4. CONCLUSIONS

PAN based, gel type polymer electrolytes containing a mixture of  $\text{MgI}_2$  and  $\text{Pr}_4\text{N}^+\text{I}^-$  iodide salts have been prepared by incorporating the plasticizers EC and PC. With identical electrolyte compositions, the cell with  $\text{MgI}_2$  alone gave an efficiency of 2.5 % and the cell with  $\text{Pr}_4\text{NI}$  alone gave an efficiency of 3.3 %. The cell with the mixed iodide system,  $\text{MgI}_2:\text{Pr}_4\text{NI} = 36:64$  (molar ratio), however, showed an enhanced efficiency of 3.7 % with a short circuit current density ( $J_{sc}$ ) of  $8.61 \text{ mA cm}^{-2}$ , open circuit voltage ( $V_{oc}$ ) of 743 mV and a fill factor of 58.2 %. The enhancement of efficiency has been attributed to the strong ionic association between the two dissimilar cations influencing the electron dynamics at the gel electrolyte/ $\text{TiO}_2$  electrode.

#### REFERENCES

1. B.O. Regan and M. Gratzel, *Nature* **353**,737, (1991).
2. M. Gratzel, *J. Photochem. Photobiol. A* **164**, 3 (2004).
3. H. Yang, M. Huang, J. Wu, Z. Lan, S. Hao, *Mat. Chem.Phys.* **110**,38 (2008).
4. J. Xia, F. Li, C.H. Huang, *Sol. Energy Mater. Sol. Cells* **90**, 944 (2006).
5. W. Kubo, S. Kambe, S. Nakade, T. Kitamura, K. Hanabusa, S. Yanagida, *J.Phys. Chem. B* **107**, 4374 (2003).
6. Z. Lan, J.H. Wu, D.B. Wang, S.C.J.M. Lin, *Solar Energy* **80**, 1483 (2006).
7. K. Tennakone, G.K.R. Senadeera, V.P.S. Perera, *Chem.Mater.* **11**, 2474 (1999).
8. T.M.W.J. Bandara, M.A.K.L. Dissanayake, B.-E. Mellander, *ElectrochimicaActa***55**, 2044(2010).
9. O. A. Ileperuma, M. A. K. L. Dissanayake, S. Somasunderam, L. R. A. K. Bandara, *Sol. Energy Mater. Sol. Cells* **84**, 117 (2004).
10. O. A. Ileperuma, G.R. Asoka Kumara, Hong-Sheng Yang, Kenji Murakami, *J. Photochem and Photobio A: Chem***217**, 308 (2010)
11. T.M.W.J. Bandara, M.A.K.L. Dissanayake, I. Albinsson, B.-E. Mellander, *J. Power Sources* **195**, 3730(2010).
12. O.A. Ileperuma, M.A.K.L. Dissanayake, S. Somasunderam, *ElectrochimicaActa***47** 2801 (2002).
13. P.A.R.D. Jayathilaka, M.A.K.L. Dissanayake, I. Albinsson, B.-E. Mellander, *Solid State Ionics* **156**, 179 (2003).
14. M. Holz, K.J. Patil, *Berichte der Bunsengesellschaft für physikalischechemie*, **95**, 107 (1991).
15. A. Chandra and S.Chandra, *J.phys.D: Appl. Phys.* **27** (1994)2171.
16. S.E. Koops, B.C. O'Regan, P.R.F. Barnes, J.R. Durant, *J.Am.ch.soc*131(13) (2009) 4808.
17. T Hoshikawa, T Ikebe, R Kikuchi, K Eguchi, *Electrochimica Acta* 51 (2006) 5286.

## **EFFICIENT QUASI- SOLID POLY (ACRYLONITRILE) (PAN) BASED POLYMERIC ELECTROLYTE FOR DYE SENSITIZED SOLAR CELLS AND ITS CHARACTERISTICS**

P.D.N.GUNASEKARA<sup>1</sup>, Y.P.Y.P. ARIYASINGHE<sup>1</sup>, T.R.C.K. WIJAYARATHNA<sup>1</sup>, C.A. THOTAWATTHAGE<sup>1</sup>, M.A.K.L. DISSANAYAKE<sup>1</sup> AND G.K.R. SENADEERA<sup>1,2,\*</sup>

<sup>1</sup> *Institute of Fundamental Studies, Hantana Road, Kandy, Sri Lanka*

<sup>2</sup> *Department of Physics, The Open University of Sri Lanka, Nawala, Nugegoda, Sri Lanka.*

\* Corresponding Author, e-mail: [gkrsena@yahoo.com](mailto:gkrsena@yahoo.com)

### **ABSTRACT**

Dye-sensitized solar cells (DSSC) have generated a considerable research interest in the past decade because of their high energy conversion efficiency (~10%) and low production cost. However, the efficient DSSCs consist of liquid electrolytes having volatile solvents which cause some practical problems due to leakage, evaporation of solvent, high-temperature instability and flammability. Therefore the development of new solid electrolyte materials such as quasi solid state or gel type for DSSCs has become an important area of research at present.

In the present study, investigations were carried out on DSSCs comprising Ru bipyridyl dye sensitized TiO<sub>2</sub> photoelectrodes with poly (acrylonitrile) (PAN) based polymeric electrolytes having configuration FTO/TiO<sub>2</sub>-Dye/Polymer electrolyte/Pt-FTO. The best composition of the polymer electrolyte having PAN (9.98%) / EC (ethylene carbonate, 39.92%) / PC (Propylene carbonate, 39.92%) / LiI (9.98%) / I<sub>2</sub> (0.20%) (by weight) , showed an overall energy-conversion efficiency of about 4.53% under the irradiation of white light (100 mW cm<sup>-2</sup>) . The introduction of the nano sized ceramic filler TiO<sub>2</sub> into the electrolyte slightly enhanced the performance of the cell efficiency up to 4.80 % .The ionic conductivities estimated by AC impedance technique were 5.58 x 10<sup>-3</sup> and 3.3 x 10<sup>-3</sup> S cm<sup>-1</sup> for the electrolytes with and without the filler.

### **1. INTRODUCTION**

Harvesting energy directly from sunlight using photovoltaic technology is one of the ways to address growing global energy needs with renewable resources while minimizing the detrimental effects on the environment by reducing atmospheric emissions. In this context, nanostructured, dye – sensitized solar cells (DSSCs) combined with liquid electrolytes, show promise as a low cost alternative to conventional solid state solar cells [1]. However encapsulation of the liquid electrolyte in these cells leads, to some technical difficulties such as leakage and evaporation of the electrolyte with volatile solvents etc. Therefore, replacing the liquid electrolyte in these systems with a solid or gel material may give practical advantages. Thus, many efforts have been made to replace the liquid electrolyte either with gel electrolytes such as polymer gel electrolytes [2-4], organic hole-transport materials [5], and solid polymer electrolytes [6,7]. To date polyethylene oxide (PEO) has been the most widely studied [8] polymer host because it contains only unstrained CO, CC and CH bonds. Moreover, it is chemically and electrochemically stable. However, this material has not yet been employed in practical applications due to its high melting points of the crystalline phase and low ionic conductivity at room temperature [9]. Since the potential of polymeric materials have been realized for commercial exploitation, other polymers such as polyacrylonitrile (PAN) [10,11], poly(methyl methacrylate) (PMMA), poly(vinylchloride)(PVC) have been proposed as hosts in electrolyte system. To date, however, DSSCs employing polymer-based electrolytes have exhibited low cell efficiency. This is mainly attributed to the inferior mass-transfer rates of the redox couples (I<sup>-</sup>/I<sub>3</sub><sup>-</sup>) in the highly viscous medium and to high electron-transfer resistance at the electrolyte/electrode interfaces.

Hence, it is necessary to increase the ion mobility in the polymer medium to improve cell efficiency. An alternative to increase the ionic conductivity of a polymer electrolyte is the addition of plasticizers, which are low molecular weight organic liquids or oligomers, that increase the flexibility of the polymer chains (e.g. increase the free volume), enhancing the mobility of the ionic species [12]. However, plasticizers also cause losses in the mechanical properties of the system, leading to the formation of “gel-type” electrolyte, rather than a solid-state polymer electrolyte. In this context, the introduction of inorganic particles to polymer electrolytes has become an interesting alternative. The addition of such particles enhances the thermal and mechanical stability of such materials and in some cases increases the ionic conductivity[13]. Several groups including our group, working in this area have used this approach with the introduction of inorganic nanofillers, [14,15] and hybrid organic-inorganic electrolytes (*i.e.* ionic liquids together with nanoparticles) [16-18]. This has become a common route to employ polymer (or gel) electrolytes with improved ionic conductivity and mechanical properties. Therefore, keeping these in mind as a continuation of our investigations towards the achievement of highly efficient DSSC with solid or gel polymeric electrolyte, we report here a polymer-gel electrolyte system, fabricated to achieve relatively high energy-conversion efficiency in DSSCs.

## **2. EXPERIMENTAL**

### *2.1 Starting materials*

All chemicals employed were analytical grade or of the best available purity. Propylene Carbonate (PC) (99%, Fisher Scientific), Ethylene Carbonate (EC) (99%, Fisher Scientific), poly(Acrylonitrile) (PAN) (99%, Fisher Scientific), Tritrin-X (Aldrich), Lithium iodide (99%, Aldrich), iodine (99.985%, Aldrich), 2-propanol (99.5%, Fisher Scientific), absolute ethanol (99.9%, Fisher Scientific), sodium hydroxide (97%, Fisher Scientific) and acetic acid (99%, Fisher Scientific) were used as received. Conductive FTO glass plates (Fluorine doped SnO<sub>2</sub> over-layer, sheet resistance 12 Ohm /square) were used as a substrate for placing TiO<sub>2</sub> porous film. TiO<sub>2</sub> powder (P-25) was purchased from Degussa AG. Ruthenium dye (N719, Solaronix) was used as sensitizer.

### *2.2 Preparation of the polymer electrolyte*

#### *(a) PAN/EC/PC/LiI system*

PAN, EC, PC and LiI (Aldrich) were used as starting materials. Different composition ratios of polymer gel electrolyte systems comprising PAN, EC-PC, I<sub>2</sub> and LiI were initially optimized in order to get both quasi solid (or gel) structure but flexible film with high photo-responses in the dye solar cells. The optimized polymeric system was obtained as follows. PAN (9.98%) was dissolved in a mixture of EC and PC keeping the EC/PC ratio at 1:1 (by weight, 39.92%). The mixture was heated at 140 °C under stirring, until the mixture turned into a clear, homogeneous, viscous gel in about 8 hours. Then 9.98% of LiI was added with continuous stirring. The mixture was cooled down to room temperature and 0.20% of I<sub>2</sub> was then added, to avoid loss of I<sub>2</sub> due to evaporation. The molar ratio of [I<sub>2</sub>]:[I<sup>-</sup>] was 1:10.

#### *(b) TiO<sub>2</sub> additives with PAN/EC/PC/LiI System*

In order to see the effect of addition of filler to the polymer electrolyte on the solar cell performances, polymer electrolytes were prepared with different amounts of nano TiO<sub>2</sub> and finally ending up with the best composition prepared as follows. PAN (9.90%) was dissolved in a mixture of EC and PC keeping the EC/PC ratio at 1:1 (by weight, 39.60%) and 0.80% of TiO<sub>2</sub> was added to the PAN above mixture. The mixture was heated at 140 °C under stirring, until the mixture turned in to a clear, homogeneous, viscous gel (~ 8 hours). Then 9.90% of LiI was added

with continuous stirring. Finally, 0.20% of I<sub>2</sub> was added, after the mixture was cooled to room temperature to avoid loss due to evaporation. The molar ratio [I<sub>2</sub>]:[I<sup>-</sup>] is 1:10.

### 2.3 Preparation of photo electrode

200 mg of P-25 TiO<sub>2</sub> powder (Degussa) was mixed well with 10 drops acetic acid, one drop of Triton X-100 and 3 ml of Ethanol and, ground until it becomes a creamy paste. The pastes were applied on Fluorine doped conducting glass substrate (sheet resistance 15 ohm/square, 0.5 x 1.5 cm<sup>2</sup>, active area 0.25 cm<sup>2</sup>) by well known doctor blade method to obtain ~10 micrometer thick TiO<sub>2</sub> film. Films were then sintered at 550 °C for 30 min and cooled down to room temperature. TiO<sub>2</sub> films were then immersed in water free ethanolic dye solution for 12 hours at room temperature and then slightly warmed (50 °C) for better dye adsorption. Electrodes were removed, washed with water free ethanol and allowed to air-dry. DSSCs were then assembled by sandwiching platinum coated conducting tin oxide (CTO) glass plate with the dyed TiO<sub>2</sub> films by placing above polymer electrolyte between them.

### 2.4. Characterization

UV-visible absorption measurements of Ruthenium dye (N71, Solaronix) in ethanol was carried out with a Shimadzu dual wavelength/double beam spectrophotometer (model UV-3000). Current voltage (*I-V*) characteristics of the cells at 100 mW cm<sup>-2</sup> (Am 1.5) were measured using a home made *I-V* measuring setup coupled with Keithly 2000 multimeter in to HA-301 Potentiostat via computer controlled software. Xenon 500 W lamp was used with AM 1.5 filters to obtain the simulated sunlight with the intensity of 100 mW cm<sup>-2</sup>. Dark-*I-V* measurement was taken for each solar cell. The *I-V* curves were used to calculate the short-circuit photocurrent density (*J<sub>sc</sub>*), the open-circuit voltage (*V<sub>oc</sub>*), the fill factor (*FF*), and the energy conversion efficiency (*η*) of DSSC. The effectiveness of the cell to convert light of various wavelengths into electrical current was measured as the incident photon to current conversion efficiency (*IPCE*), defined as the number of electrons generated by light per number of photons incident on the cell, i.e.  $IPCE\% = 1240J_{sc}/\lambda W_i$ , where *J<sub>sc</sub>* is the short-circuit current density (A m<sup>-2</sup>), *λ* is the excitation wavelength (nm) and *W<sub>i</sub>* is the photon flux (W m<sup>2</sup>) using a Nikon monochromator auto-scanner ASC-1101 coupled to a Keithly multimeter via a computer. The ionic conductivities (*σ*) of the polymer electrolytes were estimated by AC impedance technique using a Schlumberger SI1260 Impedance Analyser in the frequency range 1 Hz to 1 MHz.

## 3. RESULTS AND DISCUSSION

Current-Voltage (*I-V*) characteristics of DSSCs comprising TiO<sub>2</sub>/Ruthenium N-719 electrode with optimized gel electrolyte with and without TiO<sub>2</sub> filler under illumination of 100 mW cm<sup>-2</sup>, are shown in figure 1. While curve (a) shows *I-V* characteristics of the system PAN/PC/EC/LiI/I<sub>2</sub>, curve (b) shows the same for the system with TiO<sub>2</sub> in the electrolyte, under the same illumination. Table 1 shows the calculated cell parameter. According to the figure and the table, the DSSC having polymer electrolyte with TiO<sub>2</sub> filler shows slightly higher solar cell parameters than the system without the TiO<sub>2</sub> filler. The efficiency of the cell was also slightly improved due to increased open circuit voltage and the short circuit current density caused by the TiO<sub>2</sub> in the electrolyte. One of the reasons for this slight enhancement could be due to the reduction in viscosity of the polymer electrolyte in the presence of TiO<sub>2</sub>, which eventually improves the mobility of I<sup>-</sup>/I<sub>3</sub> redox. However, it was not possible to see the viscosity change by the naked eye and both the electrolytes were quasi solid. The small size of the PAN monomer as well as its low viscosity allow an easy penetration into the pores of dye adsorbed Titanium dioxide electrode, giving reasonably high photo-responses of these dye solar cells. However further

addition of TiO<sub>2</sub> filler reduces the photo responses of these solar cells. The maximum efficiency of these solar cells was achieved when the amount of TiO<sub>2</sub> was at 0.80% (by weight).

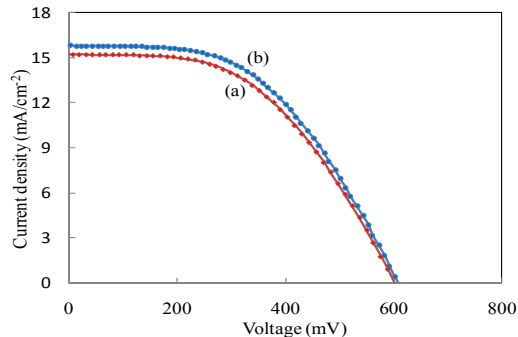


Figure 1. Current- voltage curves of DSSCs with polymer electrolyte containing (a) PAN/PC/EC/LiI/I<sub>2</sub> system (b) PAN/PC/EC/TiO<sub>2</sub>/LiI/I<sub>2</sub> system.

Table 1. Solar cell parameters ( $J_{sc}$  = short-circuit photocurrent density,  $V_{oc}$  = open-circuit voltage,  $\eta$  % efficiency and  $FF$  = fill-factor ) of DSSC with polymer electrolyte containing (a) PAN/PC/EC/LiI/I<sub>2</sub> system (b) PAN/PC/EC/TiO<sub>2</sub>/LiI/I<sub>2</sub> system.

Electrolyte	$J_{sc}$ (mA/cm <sup>2</sup> )	$V_{oc}$ (mV)	$FF$ (%)	$\eta$ (%)
(a)	15.23	603.8	49.35	4.53
(b)	15.89	615	49.40	4.80

The comparison of dark *IV* Characteristics DSSCs having polymer electrolyte with and without TiO<sub>2</sub> filler are shown in figure 2. DSSCs having polymer electrolyte with TiO<sub>2</sub> filler shows better rectification than the other system. The current onsets of DSSC systems having polymer electrolyte with and without TiO<sub>2</sub> filler under reversed bias were at 0.19 V and 0.24 V respectively. The better rectification indicated that, higher suppression of recombination in the system with the filler.

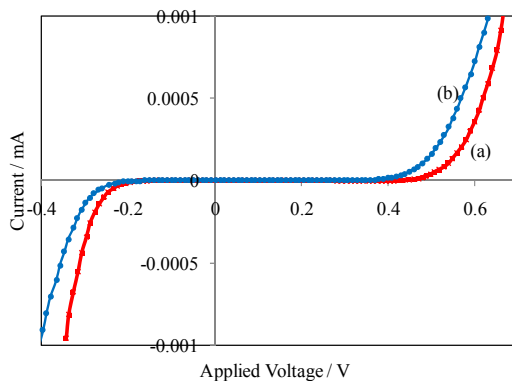


Figure 2. Dark I-V Characteristics DSSCs having polymer electrolyte (b) with and (a) without TiO<sub>2</sub> filler.



UV – Visible absorption spectrum of Ru N-719 and IPCE action spectra of DSSCs sensitized with Ru N-719 and polymer electrolyte containing (b) PAN/PC/EC/LiI/ I<sub>2</sub> system, (c) PAN/PC/EC/TiO<sub>2</sub>/LiI/ I<sub>2</sub> system are shown in figure 3. Two absorptions peaks which are around 520 nm and 367 nm were appeared for Ru N-719 dye as shown in figure 3 (a). On the right hand peak (367 nm) is the ultraviolet radiation part, which can be absorbed by a lot of dark color matters. The absorption peak around 520 nm in visible region is very important for sensitization process of dye Sensitized Solar cell when using Ru N-719 dye. Corresponding maximum IPCE values were 65% and 55% for DSSCs having polymer electrolyte with and without filler respectively. One of the reasons for these different IPCE values might be due to improvement of the conductivity of the electrolyte due to the addition of TiO<sub>2</sub> fillers to the electrolyte.

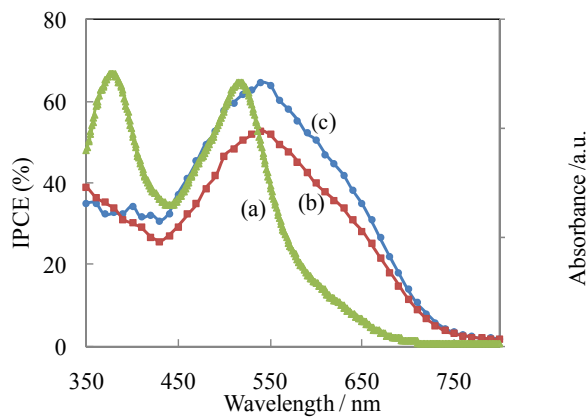


Figure 3 (a) UV – Visible absorption spectrum of Ru N-719 and IPCE action spectra of DSSC with polymer electrolyte containing (b) PAN/PC/EC/LiI/I<sub>2</sub> system (c) PAN/PC/EC/TiO<sub>2</sub>/LiI/ I<sub>2</sub> system.

Figure 4 shows the impedance plot (Nyquist Plot) for the Polymer electrolytes with and without the filler TiO<sub>2</sub>. The resistance values of both electrolytes were determined by using the plots of Z'' (real) Vs Z' (imaginary) and the line interpreted by computer software package as shown in the figure. The calculated conductivity values for the electrolytes with and without the TiO<sub>2</sub> were  $5.58 \times 10^{-3}$  and  $3.3 \times 10^{-3}$  S cm<sup>-1</sup> respectively.

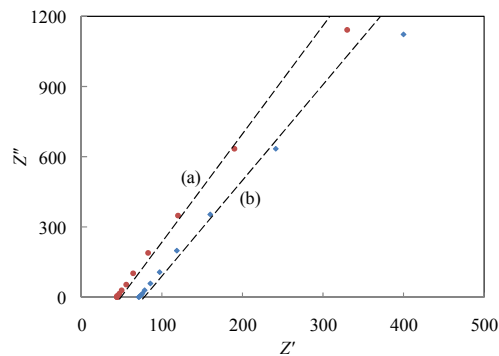


Figure 4. The impedance plot of polymer electrolyte containing (a) PAN/PC/EC/TiO<sub>2</sub>/LiI/ I<sub>2</sub> system (b) PAN/PC/EC/LiI/I<sub>2</sub> system

#### 4. CONCLUSION

We have fabricated DSSCs incorporating a novel quasi-solid electrolyte based on PAN with and without TiO<sub>2</sub> filler and a triiodide/iodide redox couple. Combination of these materials provides solar energy conversion efficiencies of over 4%. An especially noteworthy advantage is the laminating property of the PAN (“Super Glues”) that allows for a very easy production of mechanically stable large area solar cells. Solar cells assembled by combining the TiO<sub>2</sub> filler and the plasticized polymer electrolyte exhibited an overall efficiency of 4.8%. Long-term stability measurement of these DSSCs show promising results, which can be further improved by structural engineering of this cell. Even though the enhancement in conductivity due to TiO<sub>2</sub> is not so significant, this enhancement can be clearly observe in all our samples. We believe that, this enhancement could be due to the decrease in the viscosity of the electrolyte which eventually improves the ion mobility.

#### References

1. B.O Regan, M. Gratzel, *Nature* **353**, 737 (1991)
2. O.A. Ileperuma, M.A.K.L. Dissanayake, S. Somasundaram, *Electrochim. Acta* **47**, 2801 (2002)
3. K. Tennakone, G.K.R Senadeera, V.P.S. Perera, I.R.M Kottegoda, L.A.A. De Silva, *Chem. Mater.* **15**, 1825 (2003)
4. W. Kubo, S. Kambe, S. Nakade, T. Kitamura, K. Hanabusa, Y Wada, S. Yanagida, *J. Phys. Chem., B* **107**, 4374 (2003)
5. U. Bach, D. Lupo, P. Comte, J.E. Moser, F. Weissfrtel, J. Salbeck, H. Spreitzer, M. Grätzel, *Nature* **395**, 583 (1998)
6. A.F.Nogueira, J.R. Durrant, M.A. De Paoli, *Adv. Mater.*, **13**, 826. (2001)
7. T. Stergiopoulos, I.M. Arabatzis, G. Katsaros, P. Falaras, *Nano Lett.*, **2**, 1259 (2002)
8. Y.T. Kim and E.S. Smotkin, *Solid State Ionics*, **49**, 1-2, 29-37. (2002)
9. P.V. Wright, *Br. Polymer. J.*, **24**, 319-324. (1975)
10. B. Ito, J. de Freitas, M.A. De Paoli and A. F. Nogueira, *J. Braz. Chem. Soc.*, Vol. **19**, 4, 688-696, (2008)
11. Z. Jiang, B. Caroll and K.M.Abraham, *Electrochimica Acta.*, **42**(17), 2667-2677 (1997)
12. M. Kumar, S.S. Sekhon, *Eur. Polym. J.*, **38**, 1297 (2002)
13. F.Croce, G. Appetecchi, L. Persi, B. Scrosati, *Nature*, **394**, 456. (1998)
14. T. Stergiopoulos, I. M. Arabatzis, G. Katsaros, P. Falaras, *Nano Lett.*, **2**, 1259 (2002)
15. G. Katsaros, T. Stergiopoulos, I. M. Arabatzis, K. G. Papadokostaki, P. Falaras, *J. Photochem. Photobiol. A*, **149**,191 (2002)
16. H. Usui, H. Matsi, N. Tanabe, S. Yanagida, *J. Photochem.Photobiol. A*, **164**, 97. (2004)
17. T. Kato, T. Kado, S. Tanaka, A. Okazaki, S. Hayase, *J. Electrochem. Soc.*, **153**, A626, (2006)
18. T. Kato, S. Hayase, *J. Electrochem. Soc.*, **154**, B117 (2007)

**QUASI-SOLID STATE DYE SENSITIZED SOLAR CELLS WITH POLY(VINYLIDENE-FLUORIDE) (PVDF) BASED GEL POLYMER ELECTROLYTE AND NANO-POROUS TiO<sub>2</sub> ELECTRODE**

H. A. C. S. PERERA<sup>1</sup>, K. PERER<sup>1,3</sup>, K. VIDANAPATHIRANA<sup>1,3</sup>, V.A. SENEVIRATNE<sup>1</sup>,  
W.N.S. RUPASINGHE<sup>1,2</sup>, C.A. THOTAWATTHAGE<sup>2</sup>, G.K.R. SENADEERA<sup>2,4</sup> AND  
M.A.K.L. DISSANAYAKE<sup>1,2\*</sup>

<sup>1</sup>Department of Physics, University of Peradeniya, Peradeniya, Sri Lanka

<sup>2</sup>Institute of Fundamental Studies, Kandy, Sri Lanka

<sup>3</sup>Department of Electronics, Wayamba University of Sri Lanka, Kuliyaipitiya, Sri Lanka

<sup>4</sup>Department of Physics, The Open University of Sri Lanka, Nawala, Nugegoda, Sri Lanka

\*Corresponding Author, e-mail: makldis@yahoo.com

**ABSTRACT**

In the context of problems associated with long term stability and the encapsulation of dye sensitized solar cells (DSSCs), the usage of polymeric gel electrolytes in DSSCs have many advantages over the liquid electrolytes employed in them. Therefore, in order to develop gel polymer electrolytes suitable for DSSC's, Poly(vinylidene-fluoride) (PVdF) based polymer electrolyte systems, PVdF, EC: PC, Pr<sub>4</sub>N<sup>+</sup>T<sup>-</sup>: I<sub>2</sub> with different composition ratios were studied. The ionic conductivity of these gel polymer electrolytes were optimized by varying the polymer : salt ratio first and then the weight percentages of EC and PC. The maximum conductivity of  $4.49 \times 10^{-3} \text{ S cm}^{-1}$  at 31 °C was obtained for the composition with PVdF(10%): EC(40%): PC(40%): Pr<sub>4</sub>N<sup>+</sup>T<sup>-</sup>(10%) by weight and with I<sub>2</sub> (4% from the total weight). DSSCs with this electrolyte yielded maximum efficiency of 4.05 %. The short circuit current density (J<sub>sc</sub>) and the open circuit voltage (V<sub>oc</sub>) obtained under the incident light intensity of 1000 W m<sup>-2</sup> were 8.84 mA cm<sup>-2</sup> and 731 mV respectively.

**1. INTRODUCTION**

The use of alternative energy sources to generate electricity has drawn the attention of the scientists around the world. Solar energy is mainly focused because it is the most clean, freely and extensively available alternative energy source. Conversion of solar energy directly to electricity can be done by using a solar cell. After the discoveries of dye sensitized solar cells by Michel Grätzel and Brian O' Regan in 1990's, DSSCs are of current scientific and technological interest because they have relatively high power conversion efficiencies, and inexpensive fabrication procedures in contrast to amorphous silicon solar cells [1].

Generally, DSSCs are made up of an electrolyte which is a substance containing I<sup>-</sup>/I<sub>2</sub> redox couple as the conductive medium, sandwiched between a dye-absorbed nano-porous TiO<sub>2</sub> (or ZnO) photo-electrode and a platinum coated counter electrode. However, incorporation of the redox couple in a liquid electrolyte presents serious problems, including long term stability, solvent evaporation and difficulties in encapsulation of these devices [2-4]. An alternative approach is to replace the liquid electrolyte with a solid polymer or a gel polymer-based one. These include plasticized polymers, where small amounts of organic liquids are added to polymer/salt complexes, and gel electrolytes, where electrolyte solutions are incorporated into a polymer matrix. Both these classes of gel polymer electrolytes have been utilized in the fabrication of laboratory scale DSSCs. On the other hand, the mechanical properties of polymer electrolytes are also greatly beneficial as they ensure device durability and offer the possibility of fabrication on flexible substrates [5-7].

In this paper we report on gel electrolytes of relatively high conductivity formed with PVdF, ethylene carbonate(EC), propylene carbonate(PC) as the solvent and Tetra-propyl ammonium iodide ( $\text{Pr}_4\text{N}^+\text{I}^-$ ) as the iodide salt along with  $\text{I}_2$  making the  $\text{I}^-/\text{I}_2$  redox couple and their physiochemical characterization.

## 2. EXPERIMENTAL

PVdF (M.W. 534000 Da),  $\text{Pr}_4\text{N}^+\text{I}^-$ ,  $\text{I}_2$ , EC, PC, with purity greater than 98% (Aldrich) have been used as starting materials. Prior to use, PVdF was vacuum dried at 100 °C for nearly 5 hrs. Both Tetra-propyl ammonium iodide ( $\text{Pr}_4\text{N}^+\text{I}^-$ ) and EC were vacuum dried under 80 °C for 3 hrs and subsequently at room temperature for 6 more hrs.

### 2.1 Electrolyte preparation

*Systems prepared:* Initially, three systems of polymer electrolytes were prepared by varying the solid (PVdF+EC+  $\text{Pr}_4\text{N}^+\text{I}^-$ ) to liquid (PC) ratio, keeping the PC: EC ratio as 1:1 and 10% PVdF by weight. First system was prepared with (10%) PVdF: (20%) EC: (20%) PC: salt (50%) with  $\text{I}_2$  (4% from the total weight) giving a solid to liquid ratio of 80:20 (Sample A). The second system was prepared with PVdF (10%): EC (30%): PC (30%): salt(30%) with  $\text{I}_2$  (4% from the total weight) giving a solid to liquid ratio of 70:30 (Sample B). In the third system the solid to liquid ratio was kept as 60:40 (Sample C) with PVdF (10%): EC (40%): PC (40%): salt (10%) with  $\text{I}_2$  (4% from the total weight). Since the sample C, which had a pseudo-solid or gel structure, has shown the highest conductivity, it has been fine tuned further by varying the polymer:salt ratio as shown in Table 2.

*Film preparation:* First, 0.1000 g (10%wt) of PVdF was added to 0.4000 g (40%wt) of EC, 0.1000 g (10%wt) of  $\text{Pr}_4\text{N}^+\text{I}^-$ , 0.4000 g (40%wt) of PC and magnetic stirred at room temperature for about an hour. Then, the mixture was heated to 125 °C in a Büchi oven (TO-50) for about 30 min.. After that,  $\text{I}_2$  (0.0400 g - 4% from the total weight) was added to the sample controlling the heat to avoid iodine getting evaporated. The resulting viscous fluid was casted onto a glass plate and pressed by another glass plate and finally obtained a sandwiched thin film. The above procedure was repeated in preparing all three systems. After preparation, the salt rich samples (Sample A and B) were more solid like and the sample C was quasi-solid or gel like. Electrolyte samples with higher or lower polymer/salt ratio than 1:1 had conductivity values lower than the sample C. Therefore the sample C was used to fabricate the DSSCs.

### 2.2 Photo-electrode preparation

A  $\text{TiO}_2$  paste was prepared by mixing 0.2000 g of  $\text{TiO}_2$  (Degussa P-25), 12 drops of acetic acid, one drop of Triton X-100 and about 3 ml of ethanol. First,  $\text{TiO}_2$  were ground and 3 drops of acetic acid were added while grinding. Then, one drop of Triton X-100 and another 3 drops of acetic acid were added and ground well. After that, 6 drops of acetic acid were added and ground about 30min while adding ethanol. The prepared  $\text{TiO}_2$  paste was then applied on previously prepared, Fluorine doped tin oxide (FTO) glass substrates (Nippon sheet, 10-12  $\Omega\text{cm}^{-2}$ , active area 0.25  $\text{cm}^2$ ) using the “Doctor Blade” method. Then, these plates were sintered at 450 °C for 45 min and allowed to cool down to room temperature. These prepared FTO glass plates were then immersed in an ethanolic solution of *cis*-diisothiocyanato- $\text{N,N}''$ -bis(2,2'-bipyridyl-4,4'-dicarboxylicacid)-ruthenium(II) dihydrate [ $\text{RuL}_2(\text{NCS})_2 \cdot 2\text{H}_2\text{O}$ ] dye and was heated ~ 60 °C. The  $\text{TiO}_2$  coated electrodes were left for adsorption of dye in the dye solution for about 24 hrs before withdrawing. Finally they were washed thoroughly with ethanol to remove any un-adsorbed dye.

### 2.3 Characterization of electrolyte

The bulk electrical conductivities of the prepared polymer electrolytes were measured using a Schlumberger SI 1260 Impedance analyser (Solartron) in the frequency range from 1 Hz to 1 MHz and in the temperature range of 25 °C – 55 °C. For conductivity measurements, a disk shaped polymer electrolyte film (cut from a pressed film with a thickness less than 1 mm) sandwiched between two polished stainless steel (SS) dies with the configuration of SS/electrolyte/SS was used.

In order to study the contributions of electronic and ionic conductivities of the electrolytes, DC polarization test was carried out by sandwiching disk shape electrolytes with a configuration SS/electrolyte/SS under room temperature.

### 2.4 Characterizing solar cells

The dye sensitized solar cell structure was fabricated by sandwiching polymer electrolyte in between platinum (Pt) coated FTO and dye adsorbed TiO<sub>2</sub> electrodes with the configuration, glass/FTO/TiO<sub>2</sub>/Dye/Electrolyte/Pt/FTO/Glass. The current-voltage (I-V) characteristics of the cells were determined under the illumination of 1000 W m<sup>-2</sup>, (Xenon 500 lamp with AM 1.5 filters ) solar simulator coupled with Keithely 2000 multimeter into Potentiostat/Galvanostat HA-301 via computer controlled software.

## 3. RESULTS AND DISCUSSION

### 3.1 Conductivity measurements

In solid polymer electrolytes (SPE), such as those based on polyethylene oxide (PEO), ionic conductivity is increased as the salt content is increased from low values and achieves a maximum at moderate salt concentrations. Further increase of the salt generally results in decreasing the conductivity due to solubility problems and formation of polymer-salt crystalline compounds [8, 9]. In these SPEs, the polymer chains are facilitating the ion migration through segmental motions of the polymer chains. This means that the increase of crystalline nature hinders the ionic conductivity [10]. However, in the case of gel electrolytes formed by trapping a electrolyte solution in “cages” formed by a host polymer matrix, such as PAN, PMMA and PVDF, the polymer is not significantly influencing the ion migration, but essentially acts as a host net work holding the electrolyte solution. Previous studies have shown that as the polymer content is increased relative to the amount of the liquid electrolyte, the ionic conductivity is decreased due to the blocking of ions by the dense polymer network [11]. In these gel electrolytes, the dependence of ionic conductivity on salt content and solvent content is complex when considered together. If only the amount of salt is increased while keeping the amount of solvent constant, the conductivity first starts increasing and then starts decreasing due to solubility problems and formation of aggregate ions [11].

Figure 1 depicts the variation of conductivity with inverse temperatures for above three different electrolyte samples A, B and C. According to Figure 1, the sample C with the solid to liquid ratio of 60:40 has shown the highest conductivity at all temperatures. The highest temperature at which the conductivity was measured for these systems was 51°C.

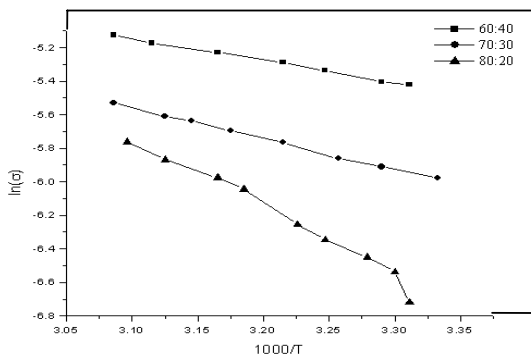


Figure 1. The ln(conductivity) versus 1000/T for three samples with different Solid to liquid ratios (Sample A, B and C).

The conductivities of the three samples A,B and C at 31 °C are given in Table 1. Table 1 also gives the weight ratio of polymer to salt (PVDF: Pr<sub>4</sub>N<sup>+</sup>T<sup>-</sup>) of each sample. According to these results, high liquid (or solvent) content is favourable for higher conductivity and it has decreased as the salt content is increased.

Table 1. The conductivity values of the three systems with different solid : liquid ratios at 31°C.

Solid (PVDF+Pr <sub>4</sub> N <sup>+</sup> T <sup>-</sup> +EC)% : Liquid (PC) %	Salt (Pr <sub>4</sub> N <sup>+</sup> T <sup>-</sup> ) %	Polymer(PVDF)% : Salt (Pr <sub>4</sub> N <sup>+</sup> T <sup>-</sup> )%	Conductivity (σ) (10 <sup>-3</sup> S cm <sup>-1</sup> )
80 : 20 (Sample A)	50	1:5	1.451
70 : 30 (Sample B)	30	1:3	2.711
60 : 40 (Sample C)	10	1:1	4.493

Figure 2 (i) shows the temperature dependence of ln σ with 1/T for conductivity (σ) measurements taken at different temperatures (T) for three different samples prepared by varying the polymer to salt weight ratio while keeping the amount of solvent constant (*i.e.* 40% PC). Figure 2 (ii) shows the conductivity variation at 31 °C of the Samples C, D and E as a function of the salt content.

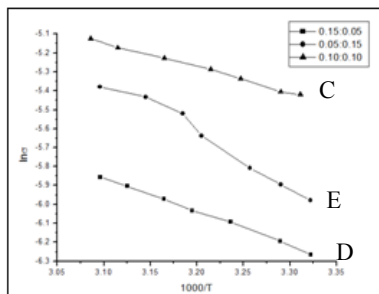


Figure 2\_(i)

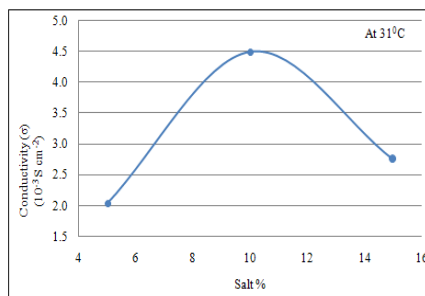


Figure 2\_(ii)

Figure 2\_(i) The lnσ versus 1000/T for three samples with the same liquid to solid ratio but with different polymer to salt ratios (Samples C, D and E). (ii) The conductivity variation at 31 °C of the Samples C, D and E as a function of the salt content.

Table 2 gives the conductivity values at 31 °C of the gel electrolytes prepared with the solid to liquid ratio of 60:40 and with different polymer to salt ratios. From our results it is evident that the sample with 60:40 liquid to solid ratio and 1:1 polymer to salt ratio (Sample C) has the highest ionic conductivity. The conductivity behavior of these gel electrolyte systems (C, D, E) agrees with the previous studies [10]. In this system, as the amount of salt is increased while keeping the solvent amount constant, the conductivity goes through a maximum when the polymer to salt ratio is 1:1.

**Table 2.** Conductivity values for systems with different Polymer: Salt ratios of the Sample C at 31°C

Solid (PVDF+Pr <sub>4</sub> N <sup>+</sup> T+EC)% : Liquid (PC) %	Salt (Pr <sub>4</sub> N <sup>+</sup> T) %	Polymer(PVDF)% : Salt (Pr <sub>4</sub> N <sup>+</sup> T)%	Conductivity (σ) (10 <sup>-3</sup> S cm <sup>-2</sup> )
60:40 (Sample D)	5	1:0.3	2.040
60:40 (Sample C)	10	1:1	4.493
60:40 (Sample E)	15	1:3	2.750

### 3.2 DC polarization test

Figure 3 shows the DC current vs. time measured during the polarization test. The saturated current is about 1% of the initial current, which means that the conductivity is predominantly due to ions.

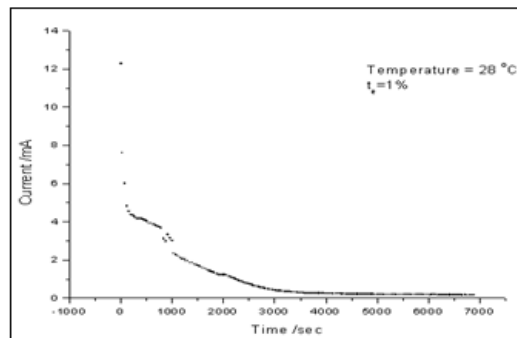


**Fig. 3.** Current versus time plot for the sample with solid to liquid ratio 60:40 and polymer to salt ratio of 1:1 taken from the DC polarization measurements at 28 °C.

### 3.3 Solar cell characterization

In this study, two sets of solar cells were fabricated using the electrolytes B and C. Solar cells fabricated with the electrolyte C where the solid to liquid ratio was kept at 60:40 has shown the best performance. In all these electrolytes the EC to PC ratio is 1:1, while in the electrolyte C, the polymer to salt ratio (PVDF:Pr<sub>4</sub>N<sup>+</sup>T) is also 1:1 and this composition exhibits the highest ionic conductivity out of all the electrolytes prepared.

Figure 4 shows the photocurrent-voltage (J-V) characteristics obtained for the solar cells assembled by sandwiching the gel polymer electrolytes under the illumination of 100 W m<sup>-2</sup>. While curve ( B) shows the J-V characteristics of the cells made with the polymer electrolytes having the solid to liquid ratio of 70:30 , the curve (C) shows the above characteristics of the cells containing the electrolyte with solid to liquid ration of 60:40.

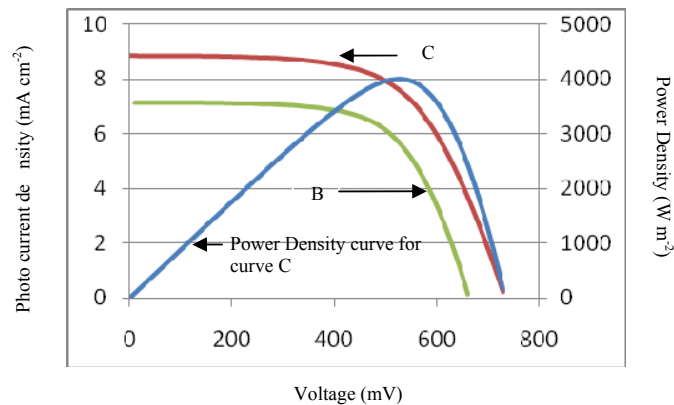


**Fig. 4.** Photocurrent – voltage curves for solar cells fabricated with different electrolytes with different solid : liquid ratios and the power density curve corresponding to the curve C.

The photovoltaic properties derived from Figure 4 are summarized in Table 3. The DSSCs assembled with the polymer electrolyte with the composition 70: 30 has a lower short circuit current density and an open circuit voltage than the cells fabricated with the polymer electrolyte with the solid to liquid ratio 60:40. The lower value of the  $J_{sc}$  in the DSSCs fabricated with the polymer electrolyte having solid to liquid ratio of 70:30 possibly originates from the lower conductivity of the electrolyte than the electrolyte with 60:40 weight ratio. A higher resistance to ion migration reduces the supply of  $I_3^-$  to the Pt counter electrode. This causes reduction of  $I_3^-$  and also retards the kinetics of dye regeneration and therefore, decreases the  $J_{sc}$ .

**Table 3.** Performance characteristics of solar cells with different electrolytes

Solid (PVDF+Pr <sub>4</sub> N <sup>+</sup> I <sup>-</sup> +EC)% : Liquid (PC) %	$J_{sc}$ (mA cm <sup>-2</sup> )	$V_{oc}$ (mV)	FF %	Efficiency %
60:40	8.84	731.3	61.92	4.01
70:30	7.13	661.2	65.17	3.07

Efficiency of DSSCs fabricated using gel polymer electrolytes based on PAN and tetrapropyl ammonium iodide are somewhat lower compared to the present system. This may suggest that the PVDF is a better host polymer for making polymer gel electrolytes for dye sensitized solar cells than PAN [12-15].

#### 4. SUMMARY

In this study we could confirm that the conductivity of gel polymer electrolytes decreases with the increase of salt content or decrease of amount of solvent. The maximum conductivity of  $4.49 \times 10^{-3} \text{ S cm}^{-1}$  at 31 °C was obtained for the PVdF(10%): EC(40%): PC(40%): Pr<sub>4</sub>N<sup>+</sup>I<sup>-</sup>(10%) electrolyte with I<sub>2</sub> (4% from the total weight) sample. The efficiency of DSSCs made with this electrolyte was 4.1 % . The short circuit current density ( $J_{sc}$ ) was 8.84 mA cm<sup>-2</sup> and the open circuit voltage ( $V_{oc}$ ) was 731.1 mV for an incident light intensity of 1000 W m<sup>-2</sup>.



## REFERENCES

1. Brian O'Ragen, Micheal Gratzel, *Nature* 353 (1991)(6346): 737-740.
2. T. Kato, M. Fujimoto, T. Kado, S. Sakaguchi, D. Kosugi, R. Shiratuchi, W. Takashima, K. Kaneto, s. Hayase, *J. Electrochem. Soc.* 152 (2005) A1105.
3. K. Tennakone, G. R. R. A. Kumara, I. R. M. Kottegoda, V. P. S. Perera, *Chem. Commun.* 1 (1999) 15.
4. Z. Jiang, B. Carrol, K. M. Abraham, *Electrochimica Acta*, Vol. 42, No. 17, pp. 2667, 1997.
5. J. Y. Saong, Y. Y. Wang, C. C. Wan, *J. of Power Sources* 77 (1999) 183.
6. J. P. Southall, H. V. St. A. Hubbard, S. F. Johnston, V. Rogers, G. R. Davies, J. E. McIntyre, I. M. Ward, *Solid State Ionics* 85 (1996) 51.
8. Gadjourova, Z., Andreev, Y. G., Tunstall, D. P. And Bruce, P. G. (2001a). "Ionic Conductivity in Crystalline Polymer Electrolytes." *Nature* **412**(2 August): 520.
9. Gadjourova, Z., Marero, D. M. Y., Anderson, K. H., Andreev, Y. G. And Bruce, P. G. (2001b)."Structures of the Polymer Electrolyte Complexes PEO<sub>6</sub>:LiXF<sub>6</sub> (X=P, Sb), determined from Neutron Powder Diffraction Data" *Chem. Mater.* **13** : 128.
10. Gray, F. M. (1991). *Solid Polymer Electrolytes Fundamentals and technological Applications*, VCH Publishers, Inc.
11. Sekhon, S. S., "Conductivity behaviour of polymer Gel Electrolytes: Role of Polymer ", *Bull. Mater. Sci.*, Vol. 26, No. 3, April 2003, pp. 321.
12. O.A. Illeperuma, M.A.K.L. Dissanayake, S. Somasundaram, L.R.A.K. Bandara, *Solar Energy Materials and Solar Cells*, 84 (1-4) (2004) 117.
13. M.A.K.L. Dissanayake, L.R.A.K. Bandara, R.S.P. Bokalawela, P.A.R.D. Jayathilaka, O.A. Illeperuma, *Materials Research Bulletin*, 37, (2002) 867.
14. T.M.W.J. Bandara, P. Ekanayake, M.A.K.L. Dissanayake, I. Albinson, B.E. Mellander, *J. of Solid State Electrochemistry*, 13 (2009) 1825.
15. O.A. Illeperuma, M.A.K.L. Dissanayaka, S. Somasundaram, *Electrochimica Acta*, 47 (2002) 2801.

## ESTIMATION OF ION TRANSPORT PARAMETERS BY MODELING SPACE CHARGE RELAXATION IN PEO BASED SOLID POLYMER ELECTROLYTE INTENDED FOR PHOTOELECTROCHEMICAL SOLAR CELLS

T.M.W.J. BANDARA,<sup>1,2,3\*</sup> M.A.K.L. DISSANAYAKE,<sup>1,4</sup> P.S.L. FERNANDO,<sup>2</sup>  
W.J.M.J.S.R. JAYASUNDARA,<sup>1</sup> AND B.-E. MELLANDER<sup>3</sup>

<sup>1</sup>Department of Physics and Postgraduate Institute of Science, University of Peradeniya, Peradeniya, Sri Lanka

<sup>2</sup>Department of Physical Sciences, Rajarata University of Sri Lanka, Mihintale, Sri Lanka

<sup>3</sup>Department of Applied Physics, Chalmers University of Technology, Göteborg, Sweden

<sup>4</sup>Institute of Fundamental studies, Kandy, Sri Lanka

\*Corresponding Author, e-mail: [awijendr@yahoo.com](mailto:awijendr@yahoo.com)

### ABSTRACT

Equations obtained for dielectric loss tangent is used to calculate the diffusion coefficient, the mobility and the density of charge carriers in an electrolyte by means of complex impedance data. In order to compute necessary parameters the measured data for dielectric loss tangent was fitted to the model equation. The equations were tested with a polymer electrolyte, PEO/EC/Hex<sub>4</sub>N<sup>+</sup>I<sup>-</sup>/I<sub>2</sub> and reliable values were obtained for the mobility and the density of charge carriers. The charge carrier densities of the samples are around 10<sup>24</sup> m<sup>-3</sup> and the ionic mobility are about 10<sup>-8</sup> m<sup>2</sup>V<sup>-1</sup>s<sup>-1</sup>. The mobility of charge carriers in the crystalline phase is higher than that in the amorphous phase. A conductivity maximum is shown for the electrolyte having 65% mass fraction of Hex<sub>4</sub>N<sup>+</sup>I<sup>-</sup> with respect to mass of PEO and this optimized electrolyte was used to fabricate solar cell. The short circuit current density, open circuit voltage and the energy conversion efficiency of the cell are 1.26 mA cm<sup>-2</sup>, 745 mV and 0.6%, respectively under irradiation of 1000 W m<sup>-2</sup> light.

### 1. INTRODUCTION

During the last few decades, ionic conductors or electrolytes have gone through a remarkable development due to comprehensive research stimulated by their potential to be employed in numerous energy conversion and storage devices such as secondary batteries, photo-electrochemical solar cells, fuels cells and super capacitors [1,2,3,4]. Intensive research in this field, has lead to the development of new electrolytes, including solid or gel polymer electrolytes, glass electrolytes and ionic liquids which have emerged as alternatives to traditional electrolytes by way of superior stability, durability, wide operating temperature range and higher efficiencies for device application [**Error! Bookmark not defined.**,**Error! Bookmark not defined.**,**Error! Bookmark not defined.**,5]. For instance, the development of novel electrolytes with enhanced ionic conductivity is necessary in order to optimize photo-electrochemical (PEC) solar cells.

For a single ion conducting electrolyte the conductivity,  $\sigma$ , is given by the equation;

$$\sigma = ne\mu \quad (1)$$

where,  $\mu$  is the ionic mobility and  $n$  is the charge carrier concentration. Therefore, it is very important to calculate the ionic mobility and charge carrier concentration in order to characterize and optimize electrolyte materials. For instant, electrolyte with high iodide ion conductivity, attained by increasing both the mobility and the concentration of iodide ions, is needed to develop PEC solar cells. However, the determination of  $n$  and  $\mu$  values of electrolytes is not an easy task,

although these parameters are vital to develop and characterize novel electrolyte materials to be used in the new generation of electrochemical power sources. In addition, the existing theories which can be used to estimate these parameters appear to be grossly inadequate, particularly in the case of newly emerging classes of electrolyte materials such as solid polymer electrolytes and ionic liquids.

Several approaches have been made to determine ion mobility in electrolytes under an applied electric field, including impedance spectroscopic methods. It is reported that transient ionic direct current measurements have been employed to determine the ion mobility [6,7]. In the method the current is measured as a function of time under an applied *dc* voltage in order to determine the mobility. Nuclear Magnetic Resonance, NMR, spectroscopy can be also employed to obtain these physical parameters. For instance, NMR has been applied for some ionic liquids and polymer electrolytes. However, there are limitations. For example, the NMR method cannot be employed for all types of ions [8]. However, despite a number of efforts, the mechanisms of ion conduction are still not well understood in many systems [9,10] and in particular there is still some controversy about the values of ion mobility in some solid-state electrolyte systems [**Error! Bookmark not defined.**]. Therefore, a reliable and convenient method to determine the mobility and density of charge carriers is required.

The analysis of impedance spectroscopy of an electrochemical system gives several advantages over other electrochemical techniques. Particularly, in impedance analysis a small sinusoidal potential is applied across the sample cell minimizing possible charge carrier concentration changes during the measurements. In addition, to minimum changes owing to very small voltage applied, the time average of the changes imposed to the electrolyte, due to the applied sinusoidal potential, is zero for impedance analysis. Literature reveals some committed approaches to determine the mobility and charge carrier concentration based on impedance spectroscopic methods [10,11]. The method used by Schütt *et al* [12] for ion conducting glasses is interesting. However, this method has some problems when it applied for other systems [13]. Another recently developed model by Runt *et al* uses the frequency dependence of complex dielectric loss,  $\epsilon''$ , and loss tangent,  $\tan(\phi)$ , data in order to extract both the mobility and the concentration charge carriers [**Error! Bookmark not defined.**]. This method is based on an analysis of electrode polarization at low frequency electric fields. However, the values obtained for the mobile charge carrier concentrations are very low, nearly four orders of magnitude lower than that of the total number of ions available in the salt. As a consequence of this, the analysis leads to very high mobility values for the selected solid-state electrolytes.

Recently, a reliable method has been developed by us to calculate both the density and mobility of charge carriers employing impedance analysis. In that approach real part of the dielectric constant is plotted against the frequency and the data were fitted to model equation in order to determine the relevant parameters. However, in this study the dielectric loss tangent is used for the calculations due to many advantages over the use of real part of the dielectric constant.

## 2. EXPERIMENTAL

Analytical grade Polyethyleneoxide (PEO: Mw.  $4 \times 10^6$ ), tetrahexylammonium iodide  $\text{Hex}_4\text{N}^+\text{I}^-$ , iodine ( $\text{I}_2$ ), and ethylene carbonate (EC), purchased from Aldrich, were used as starting materials. PEO and  $\text{Hex}_4\text{N}^+\text{I}^-$  were vacuum dried for 12 h in a vacuum oven at 50 °C prior to use. For preparing the electrolyte samples, the weights of PEO (0.5 g) and EC (0.5 g) were kept unchanged, and the weight of  $\text{Hex}_4\text{N}^+\text{I}^-$  was varied. The mass fraction of  $\text{Hex}_4\text{N}^+\text{I}^-$  salt ( $x\%$ ) refers

to an electrolyte composition of PEO : Hex4N<sup>+</sup>Γ = 100 : x. Iodine was incorporated to all the electrolyte samples maintaining the 10:1 fixed salt to iodine molar ratio.

For electrolyte sample preparation, the selected compositions of chemicals were dissolved in anhydrous acetonitrile solvent by magnetic stirring for 12 hours at room temperature. The resulting slurry was casted on to a Teflon plate and kept inside a fume box for 24 hours to evaporate the solvent gradually at room temperature. This procedure yielded visually homogeneous polymer electrolyte films which were vacuum dried for 12 h before used for measurements.

Disk-shaped electrolyte films of thickness 0.2–0.5 mm were sandwiched between two polished stainless steel blocking electrodes to measure complex impedance in order to compute the conductivity and complex dielectric data. Complex impedance measurements were performed using a HP 4291 ARF and HP 4292 ARF impedance analyzers in the temperature range of 20 to 80 °C. During the measurement a flow of nitrogen gas was purged over the sample to prevent contact with atmospheric moisture.

For the fabrication of PEC solar cells, nanoporous-TiO<sub>2</sub> thin films were prepared on fluorine-doped tin oxide (FTO) glass plates using the already published procedure [14]. The TiO<sub>2</sub>-coated electrode was immersed in ethanolic solution of the dye, cis-diisothiocyanato- N,N'-bis(2,2'-bipyridyl-4,4'-dicarboxylic acid)-ruthenium (II) dihydrate [RuL<sub>2</sub>(NCS)<sub>2</sub>.2H<sub>2</sub>O] while both were hot (~60 °C). After 24 h absorption, the electrode was withdrawn from the dye solution and subsequently washed thoroughly with acetone to remove unabsorbed dyes and loosely bound TiO<sub>2</sub> particles from the dye-coated electrode. Finally, PEC solar cells were fabricated with the configuration glass/FTO/TiO<sub>2</sub>/dye/electrolyte/Pt/FTO/glass. The cells were characterized by measuring *I-V* curves using an eDAQ potentiostat EA161 with the aid of eDAQ e-corder ED401 under the irradiation of 1000 W m<sup>-2</sup> (1.5 AM) solar simulator.

### 3. THEORY

The standard and commonly used method to determine the bulk ionic conductivity of an electrolyte is complex impedance analysis. The electrical behaviour under an applied electric signal of an electrolyte sandwiched between two blocking electrodes can be understood by the equivalent circuits. Therefore according to our previous work, if we assume Debye type relaxation for a electrolyte sandwiched between two blocking electrodes, the effective complex dielectric constant can be represented by equation [Error! Bookmark not defined.,15];

$$\tilde{\epsilon}^* = \epsilon'_{\infty} \left\{ \left( 1 + \frac{\delta}{1 + (\omega\tau)^2} \right) - i \left( \frac{\omega\tau\delta^{3/2}}{1 + (\omega\tau)^2} \right) \right\} \quad (2)$$

where,  $\epsilon'_{\infty}$  is the high frequency permittivity,  $\tilde{\epsilon}^*$  is the effective complex dielectric constant,  $\omega$ , is the angular frequency of the signal,  $\delta$  is a constant and  $\tau$  is the dielectric relaxation time corresponding to the maximum dielectric loss tangent. Therefore, the dielectric loss tangent,  $\tan \phi$ , can be obtained by equation;

$$\tan(\phi) = \frac{\omega\tau\sqrt{\delta}}{1 + \omega^2\tau^2} \quad (3)$$

The  $\delta$  is given by,

$$\delta = \frac{d}{(D\tau)^{1/2}} = \frac{d}{\lambda} \quad (4)$$

where  $2d$ , and  $\lambda$  are sample length and the Debye length. The Nernst-Einstein relation gives the relationship between the mobility and the diffusion coefficient;

$$\mu = \frac{eD}{k_B T} \quad (5)$$

where,  $k_B$  is the Boltzmann constant and  $T$  is the absolute temperature.

$$n = \frac{\sigma k_B T}{e^2 D} \quad (6)$$

#### 4. RESULTS AND DISCUSSION

The conductivity isotherms at 30, 40, 50, 60 and 70 °C for PEO/EC/ Hex<sub>4</sub>N<sup>+</sup>I<sup>-</sup>/I<sub>2</sub> electrolyte containing different Hex<sub>4</sub>N<sup>+</sup>I<sup>-</sup> mass fractions are shown in Fig. 1. These conductivities were extracted from complex impedance measurements by using a HP 4291 A RF impedance analyzer in the high frequency range of 1 MHz- 1GHz. A conductivity maximum is shown for the electrolyte having 65% mass fraction of Hex<sub>4</sub>N<sup>+</sup>I<sup>-</sup> with respect to mass of PEO. This optimum electrolyte shows a conductivity of  $4.7 \times 10^{-4}$  at 30 °C and this sample shows conductivities higher than  $10^{-3}$  S cm<sup>-1</sup> for temperatures above 45 °C. However, complex impedance data obtained in the high frequency region were not suitable to determine the diffusion coefficient ( $D$ ), the mobility ( $\mu$ ) and the density of charge carriers ( $n$ ) as the maximum in  $\tan \phi$  is not appeared inside the measuring window. Therefore, complex impedance was measured from 5 Hz to 10 MHz (low frequency region) employing HP 4292 A RF impedance analyzer.

Electrolyte samples containing 60 and 75% Hex<sub>4</sub>N<sup>+</sup>I<sup>-</sup> were selected to estimate the diffusion coefficient ( $D$ ), the mobility ( $\mu$ ) and the density of charge carriers ( $n$ ) employing this new method. Fig. 2 shows the dielectric loss tangent,  $\tan \phi$ , as a function of frequency for 75% Hex<sub>4</sub>N<sup>+</sup>I<sup>-</sup> containing sample at 20, 30, 40, 50, 60, 70 and 78 °C. The maximum of  $\tan \phi$  was appeared within the measured

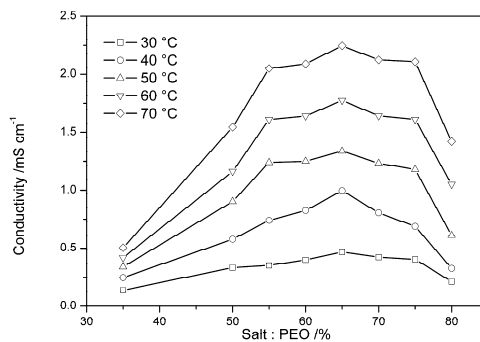


Fig. 1. The conductivity isotherms of PEO/EC:Hex<sub>4</sub>N<sup>+</sup>I<sup>-</sup>/I<sub>2</sub> electrolytes for different Hex<sub>4</sub>N<sup>+</sup>I<sup>-</sup> mass fractions ( $X\%$ ), where  $X = \text{salt/PEO}$ .

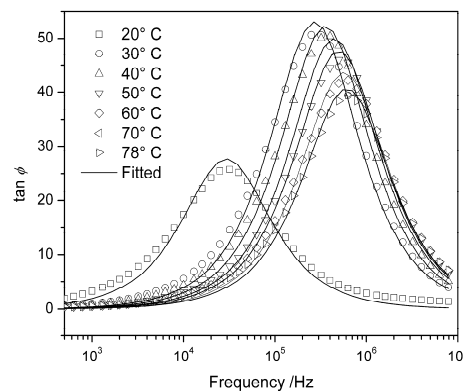


Fig. 2  $\tan \phi$  versus frequency isotherms for the 75% Hex<sub>4</sub>N<sup>+</sup>I<sup>-</sup> containing sample at 20, 30, 40, 50, 60, 70 and 78 °C. Fitted curves to the equation (3) also shown by using solid lines.

frequency range. Hence, the data in Fig. 2 were fitted to equation (3) in order to estimate values for  $\tau$  and  $\delta$ . Fitted curves to the equation (3) are also shown in Fig. 2 using solid lines and values obtained for  $\tau$  and  $\delta$  is given in the Table 1. The reliability of the model equations for this system is established by the excellent fitting of the measured data to the equation (3). The standard deviations of estimated  $\tau$  and  $\delta$  values were smaller than 5% of the values. In order to determine the  $D$ ,  $\mu$  and  $n$   $\delta$  and  $\tau$  values estimated by means of curve fitting was used in equations (4), (5) and (6). Table 1 gives the values obtained for  $D$ ,  $\mu$  and  $n$  for sample containing 75%  $\text{Hex}_4\text{N}^+\text{I}^-$ .

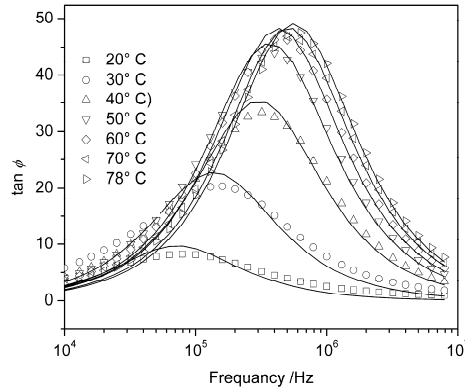


Fig. 3  $\tan \phi$  versus frequency isotherms for the 60%  $\text{Hex}_4\text{N}^+\text{I}^-$  containing sample at 20, 30, 40, 50, 60, 70 and 78 °C. Fitted curves to the equation (3) also shown by using line symbol.

Fig. 4 shows the dielectric loss tangent,  $\tan \phi$ , data as a function of frequency for the sample containing 60%  $\text{Hex}_4\text{N}^+\text{I}^-$  at 20, 30, 40, 50, 60, 70 and 78 °C and the fitted curves to equation (3).  $\tau$  and  $\delta$  estimated by curve fitting for this system is given in the Table 2. This data set also fitted well to the equation (3) confirming the reliability of the model equation.

The charge carrier densities estimated for the samples were  $\sim 10^{24} \text{ m}^{-3}$  and the ionic mobility values were  $\sim 10^{-8} \text{ m}^2\text{V}^{-1}\text{s}^{-1}$ . These values are reasonable compared to concentration of the salt in the electrolyte and the mobility of aqueous electrolytes. It can be inferred from the data given in Table 1 and 2 that the charge carriers have different transport mechanisms below and above the crystallite melting temperature of the PEO electrolyte samples ( $\sim 40$  °C) [Error! Bookmark not defined.]. At the temperatures bellow  $\sim 40$ °C, (crystalline phase) the free charge carriers have a high mobility compared to that at higher temperatures (amorphous phase). This may seems strange but is possibly related to the structural differences between the crystalline and amorphous forms of PEO/EC complex and the increase in ion-ion interactions with drastic increase of the number of change carriers. However, the mobility of ion shows a slight increase with increasing temperature after the crystallite melting. According to data in Table 1 and 2 the increase in conductivity of the low temperature phase appears to be largely due to the increase in the concentration of mobile charge carriers. It may be due to the limited number of available pathways for the mobile ions in the crystalline phase and lower flexibility of long polymer chains in crystalline phase.

Table 1. The diffusion coefficient ( $D$ ), carrier density ( $n$ ) and mobility ( $\mu$ ) for the polymer electrolyte, PEO/EC/ $\text{Hex}_4\text{N}^+\text{I}^-$  / $\text{I}_2$  containing 75% of  $\text{Hex}_4\text{N}^+\text{I}^-$ .

Temperature /°C	$\tau$ / s	$\delta$	$D$ / $\text{m}^2\text{s}^{-1}$	$\mu$ / $\text{m}^2\text{V}^{-1}\text{s}^{-1}$	$n$ / $\text{m}^{-3}$
30	$9.3 \times 10^{-8}$	11252.0	$3.1 \times 10^{-9}$	$1.9 \times 10^{-8}$	$4.8 \times 10^{24}$
35	$7.8 \times 10^{-8}$	11069.8	$3.8 \times 10^{-9}$	$2.3 \times 10^{-8}$	$5.0 \times 10^{24}$
40	$7.1 \times 10^{-8}$	10922.1	$4.3 \times 10^{-9}$	$2.5 \times 10^{-8}$	$5.0 \times 10^{24}$

43	$6.4 \times 10^{-8}$	10468.3	$5.1 \times 10^{-9}$	$3.0 \times 10^{-8}$	$4.9 \times 10^{24}$
50	$5.7 \times 10^{-8}$	9997.5	$6.3 \times 10^{-9}$	$3.6 \times 10^{-8}$	$4.8 \times 10^{24}$
55	$5.4 \times 10^{-8}$	9650.1	$7.1 \times 10^{-9}$	$4.0 \times 10^{-8}$	$4.6 \times 10^{24}$
60	$5.1 \times 10^{-8}$	9106.9	$8.6 \times 10^{-9}$	$4.7 \times 10^{-8}$	$4.4 \times 10^{24}$
64	$4.7 \times 10^{-8}$	8445.8	$1.0 \times 10^{-8}$	$5.8 \times 10^{-8}$	$4.0 \times 10^{24}$
70	$4.4 \times 10^{-8}$	7644.5	$1.4 \times 10^{-8}$	$7.5 \times 10^{-8}$	$3.6 \times 10^{24}$
78	$4.3 \times 10^{-8}$	7084.3	$1.6 \times 10^{-8}$	$9.0 \times 10^{-8}$	$3.3 \times 10^{24}$

**Table 2.** The diffusion coefficient ( $D$ ), carrier density ( $n$ ) and mobility ( $\mu$ ) for the polymer electrolyte, PEO/EC/Hex<sub>4</sub>N<sup>+</sup>I<sub>2</sub> containing 60% of Hex<sub>4</sub>N<sup>+</sup>.

Temperature /°C	$\tau$ / s	$\delta$	$D$ / m <sup>2</sup> s <sup>-1</sup>	$\mu$ / m <sup>2</sup> V <sup>-1</sup> s <sup>-1</sup>	$n$ / m <sup>-3</sup>
30	$1.8 \times 10^{-7}$	2071.6	$4.6 \times 10^{-8}$	$2.8 \times 10^{-7}$	$1.2 \times 10^{23}$
35	$1.3 \times 10^{-7}$	3419.5	$2.4 \times 10^{-8}$	$1.4 \times 10^{-7}$	$3.3 \times 10^{23}$
40	$8.3 \times 10^{-8}$	5023.4	$1.7 \times 10^{-8}$	$1.0 \times 10^{-7}$	$6.5 \times 10^{23}$
45	$6.9 \times 10^{-8}$	6920.8	$1.1 \times 10^{-8}$	$6.3 \times 10^{-8}$	$1.3 \times 10^{24}$
50	$6.9 \times 10^{-8}$	8349.5	$7.5 \times 10^{-9}$	$4.3 \times 10^{-8}$	$2.1 \times 10^{24}$
55	$6.4 \times 10^{-8}$	8987.7	$7.0 \times 10^{-9}$	$3.9 \times 10^{-8}$	$2.6 \times 10^{24}$
60	$5.9 \times 10^{-8}$	9315.8	$7.0 \times 10^{-9}$	$3.9 \times 10^{-8}$	$2.9 \times 10^{24}$
68	$5.2 \times 10^{-8}$	9389.8	$7.9 \times 10^{-9}$	$4.3 \times 10^{-8}$	$3.1 \times 10^{24}$
70	$5.0 \times 10^{-8}$	9373.8	$8.2 \times 10^{-9}$	$4.4 \times 10^{-8}$	$3.1 \times 10^{24}$
78	$4.5 \times 10^{-8}$	9629.0	$8.6 \times 10^{-9}$	$4.6 \times 10^{-8}$	$3.4 \times 10^{24}$

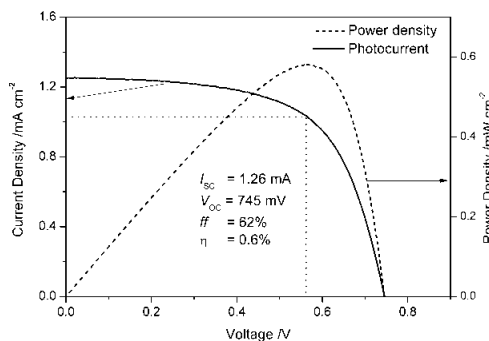


**Fig. 4.**  $I$ - $V$  characteristics of PEC solar cell prepared with PEO/EC/Hex<sub>4</sub>N<sup>+</sup>I<sub>2</sub> electrolyte containing 65% Hex<sub>4</sub>N<sup>+</sup> under irradiation of a 1,000-Wm<sup>-2</sup> Xenon lamp. The dashed line shows the output power density of the cell.

An all-solid state PEC solar cell was fabricated using the electrolyte with optimum composition (65% Hex<sub>4</sub>N<sup>+</sup>). Fig.4 shows the  $I$ - $V$  characteristics curve and power output performance of the cell. The Short circuit current density,  $I_{SC}$ , and open circuit voltage,  $V_{OC}$ , of the cell are 1.26 mA cm<sup>-2</sup> and 745 mV under irradiation of 1000 W m<sup>-2</sup> light. The energy conversion efficiency of the cell, 0.6%, is rather low compared to cells with gel or liquid polymer electrolytes due to poor ionic conductivity in the solid polymer electrolyte. However, an all-

solid state configuration has a number of advantages regarding mechanical and chemical stability.

## 5. CONCLUSIONS

Equations were obtained to calculate the diffusion coefficient, the mobility and the density of charge carriers in an electrolyte using complex impedance data. In order to calculate the

necessary parameters the measured data for dielectric loss tangent is fitted to the model equation,  $\tan(\phi) = \omega\tau\sqrt{\delta}/(1 + \omega^2\tau^2)$  where,  $\omega$ ,  $\tau$  are angular frequency, dielectric relaxation time. The equations were tested with a polymer electrolyte, PEO/EC/Hex<sub>4</sub>N<sup>+</sup>I<sub>2</sub> and reliable values were obtained for the mobility and the density of charge carriers. The charge carrier densities of the samples are around  $\sim 10^{24} \text{ m}^{-3}$  and the ionic mobility values were  $\sim 10^{-8} \text{ m}^2\text{V}^{-1}\text{s}^{-1}$ . A conductivity maximum is shown for the electrolyte having 65% mass fraction of Hex<sub>4</sub>N<sup>+</sup>I<sub>2</sub> with respect to mass of PEO. This optimized electrolyte was used to fabricate an all-solid state solar cell. The short circuit current density, open circuit voltage and the energy conversion efficiency of the cell are 1.26 mA cm<sup>-2</sup>, 745 mV and 0.6% respectively under irradiation of 1000 Wm<sup>-2</sup> light.

## 6. ACKNOWLEDGEMENT

*Research support provided by IPPS Uppsala, the Swedish Research Council and NSF Sri Lanka is gratefully acknowledged.*

## REFERENCES

1. A.S. Arico, P. Bruce, B. Scrosati, J.-M. Tarascon, W. van Schalkwijk, *Nature Materials* 4 (5) (2005) 366-377
2. A.M. Christie, S.J. Lilley, E. Staunton, Y.G. Andreev, P.G. Bruce, *Nature*, 433 (2005) 50-53.
3. P. Simon, Y. Gogotsi, *Nature Materials*, 7 (11) (2008) 845-854.
4. M. Grätzel, *Nature*, 414 (6861) (2001) 338-344.
5. P. Wang, S.M. Zakeeruddin, J.E. Moser, M.K. Nazeeruddin, T. Sekiguchi, M. Grätzel, *Nature Materials*, 2 (6) (2003) 402-407.
6. M. Watanabe, S. Nagano, K. Sanui, and N. Ogata, *Solid State Ionics*, 911 (1988) 28.
7. M. Watanabe, S. Nagano, K. Sanui, and N. Ogata, *Solid State Ionics*, 338 (1986) 18-19.
8. K. Hayamizu, E. Akiba, T. Bando, Y. Aihara, *J. Chem. Phys.* 117-12, (2002) 5929-5939
9. R.C. Agrawal, R. Kumar. R. K. Gupta, *Materials Science and Engineering*, B57 (1998) 46-51.
10. R.J. Klein, S. Zhang, S. Dou, B. H. Jones, R. H. Colby, J. Runt, *J. Chemical Physics* 124 (2006) 144903-8.
11. G.A. Niklasson, A. K. Jonsson, M. Stromme, Impedance Response of Electrochromic Materials and Devices. In *Impedance Spectroscopy*, 2nd ed.; Y. Barsoukov, J. R., Macdonald, Wiley: New York, (2005) 302-326.
12. H.J Schütt, *Solid State Ionics*, 505 (1994) 70-71.
13. T.M.W.J Bandara, M.A.K.L. Dissanayake, B.-E. Mellander, I. Albinsson, *Solid State Ionics*, 189 (2011) 63-68
14. T.M.W.J. Bandara, P. Ekanayake, M.A.K.L. Dissanayake, I. Albinsson. B.-E. Mellander, *J. Solid. State. Electrochem.* 14 (2010) 1221-1226
15. T.M.W.J Bandara, B.-E. Mellander, Evaluation of Mobility, Diffusion Coefficient and Density of Charge Carriers in Ionic Liquids and Novel Electrolytes. In *Ionic Liquids: Theory, Properties, New Approaches* Ed. Alexander Kokorin, InTech, Rijeka, Croatia, (2011), 383-406



## CHITOSAN-BASED POLYMER ELECTROLYTE FOR DYE-SENSITIZED SOLAR CELL

M.H. BURAIDAH<sup>1</sup>, L.P. TEO<sup>1</sup>, S.N.F. YUSUF<sup>1</sup>, M.M. NOOR<sup>1,2</sup>, M.A. CAREEM<sup>3</sup>, S.R. MAJID<sup>1</sup>,  
A.K. AROF<sup>1\*</sup>

<sup>1</sup>Centre for Ionics University Malaya, Department of Physics, Faculty of Science,  
University of Malaya, 50603 Kuala Lumpur, Malaysia

<sup>2</sup>Centre for Foundation Studies, International Islamic University Malaysia,  
Jalan Universiti, 46350 Petaling Jaya, Selangor, Malaysia

<sup>3</sup>Department of Physics, University of Peradeniya, Peradeniya, Sri Lanka

\*Corresponding Author, e-mail: akarof@um.edu.my

### ABSTRACT

Anthocyanin dye extracted in ethanol from blueberry (*Vaccinium myrtillus*) has been used as sensitizer in dye-sensitized TiO<sub>2</sub> solar cell. Absorption spectrum of the extract exhibits a peak at 541 nm. The absorbance peak shifted to 555 nm for the anthocyanin-TiO<sub>2</sub> complex. Three types of polymer electrolytes i.e. (chitosan-PEO)-NH<sub>4</sub>I, (chitosan-PVA)-NH<sub>4</sub>I and chitosan-NH<sub>4</sub>I-IL have been prepared by the solution cast technique. Ionic liquid (IL) used is 1-butyl-3-methylimidazolium iodide (BMII) is used. Some iodine (I<sub>2</sub>) crystals were added into the polymer electrolytes to provide the I<sup>-</sup>/I<sub>3</sub><sup>-</sup> redox couple. Dye-sensitized solar cells were fabricated by sandwiching the chitosan-based polymer electrolytes between TiO<sub>2</sub>/dye photoelectrode and Pt counter electrode, respectively. The cell sensitized with blueberry anthocyanin exhibits short circuit current density,  $J_{sc}$  of 1.705 mA cm<sup>-2</sup>, open circuit voltage,  $V_{oc}$  of 385 mV, fill factor of 0.39 and efficiency,  $\eta$  of 0.3 %.

Keywords: blueberry, anthocyanin, chitosan, ionic liquid

### 1. INTRODUCTION

Photoelectrochemical application based on dye-sensitized nanostructured TiO<sub>2</sub> solar cell has attracted much attention as a low cost alternative to conventional silicon solar cells [1]. In 1991, dye-sensitized solar cell (DSSC) based on liquid electrolyte with efficiency about 11 % was first reported by O' Regan and Graetzel [2]. Guo *et al.* [3] reported that the dye-sensitized solar cell with electrolyte containing 0.1 mol L<sup>-1</sup> LiI, 0.35 mol L<sup>-1</sup> I<sub>2</sub> and 0.5 mol L<sup>-1</sup> *N*-methylbenzimidazole (NMBI) in pure *S*-propyltetrahydrothiophenium iodide (T<sub>3</sub>I) exhibits short-circuit photocurrent density ( $J_{sc}$ ) of 11.22 mA cm<sup>-2</sup> and open circuit voltage ( $V_{oc}$ ) of 0.61 V. TiO<sub>2</sub>/CdSe(6)/0.5M Na<sub>2</sub>S-0.1M S-0.2M KCl/gold solar cell has been reported by Chong *et al.* [4]. Short-circuit photocurrent density ( $J_{sc}$ ) of 7.43 mA cm<sup>-2</sup> and open circuit voltage ( $V_{oc}$ ) of 0.37 V was obtained. Due to problems with liquid electrolytes, polymer electrolytes are actively used in solar cell research [5-7].

Extensive studies on polymer electrolytes have been done by researchers in order to solve the problems that exist in liquid electrolytes specifically leakage and solvent evaporation. The use of polymer electrolytes in solar cell application provide advantages such as compatibility, easy to prepare in different forms, no leakage, electrochemically stable and easy to process [8-9]. Many types of polymers have been used in the search of good polymer electrolyte. These polymers are chosen due to their properties. However, to date there is no polymer which could meet all requirements of an excellent polymer electrolyte. Chitosan is one of the polymers that have been tested. It is biodegradable, biocompatible, odorless and has high mechanical strength [10,11]. It is non-toxic and thus environmental friendly [12]. Singh and co-authors [13] have reported an open-

circuit voltage of 0.53 V and short-circuit current density of 2.62 mA cm<sup>-2</sup> from dye-sensitized solar cell employing polymer electrolyte based on chitosan with sodium iodide (NaI), iodine crystals and ionic liquid. Ionic liquid (IL) are also known as room temperature molten salts and are non-volatile, non-flammable and high solvating capability [14].

Unlike chitosan, polyethylene oxide (PEO) is a synthetic polymer that is electrochemically stable [15]. PEO is the most widely used polymer electrolyte in solar cell applications [16-18]. PEO is one of the outstanding polymers due to its ability to solvate in high concentrations a wide variety of salts [19]. Kalaiganan *et al.* [20] studied dye-sensitized solar cell using PEO-KI-I<sub>2</sub> electrolyte and Ru(4,4'-dicarboxylicacid-2,2' bipyridine)<sub>2</sub> (thiocyanate) as a dye. The highest  $J_{sc}$  of 6.12 mA cm<sup>-2</sup>, lowest  $V_{oc}$  of 0.59 V and fill factor of 0.56 obtained for DSSC utilizing electrolyte with the composition of 12 PEO: 1 KI: 0.105 I<sub>2</sub>. Similar to PEO, PVA is also a synthetic polymer that exhibits properties such as biocompatibility, simple to prepare and has good mechanical strength [21,22]. Till date, no report on PVA-based polymer electrolyte in solar cell applications is found in the literature.

In this work, the fabricated DSSC comprises anthocyanin pigment from blueberry to sensitize titanium dioxide (TiO<sub>2</sub>) photoelectrode and polymer electrolyte containing chitosan blended with PEO and PVA, respectively incorporated with ammonium iodide (NH<sub>4</sub>I) salt and iodine crystals (I<sub>2</sub>). The effect of ionic liquid 1-butyl-3-methylimidazolium iodide (BMII) on chitosan-NH<sub>4</sub>I(+I<sub>2</sub>) electrolyte for DSSC application has also been investigated in this work. BMII in this work is self-prepared. To the best of our knowledge, no previous report has been published on DSSC employing blueberry as sensitizer with polymer electrolyte. Blueberry (*Vaccinium myrtillus*) is chosen because they are rich in anthocyanin content [23] and there are only few reports available in the literature on DSSC utilizing blueberry as photosensitizer but with liquid electrolyte [24,25].

## **2. EXPERIMENTAL**

### *2.1 Materials*

Highly viscous chitosan was purchased from Fluka and PEO from Aldrich. Both iodine (I<sub>2</sub>) and ammonium iodide (NH<sub>4</sub>I) were procured from Ajax chemicals and glacial acetic acid from Ajax Finechem. Titanium dioxide (TiO<sub>2</sub>) paste was purchased from JGC Catalysts & Chemicals Ltd. The indium tin-oxide conducting glass (ITO) used in this work has sheet resistance of 5 Ω cm<sup>-2</sup>. Ti(IV) bis(ethyl acetoacetato)-diisopropoxide which serves as blocking layer was purchased from Aldrich. Anthocyanin dye solution was extracted from blueberry. Ethanol and 1 % acetic acid were used as solvents.

### *2.1 Electrolyte preparation*

Chitosan-NH<sub>4</sub>I-IL, (Chitosan-PEO)-NH<sub>4</sub>I and (Chitosan-PVA)-NH<sub>4</sub>I electrolytes were prepared by the solution cast technique. Chitosan, PEO and NH<sub>4</sub>I were stirred in 50 ml dilute acetic acid (1 %). The solutions were then cast in different Petri dishes and allowed to evaporate slowly at ambient temperature to form films. Impedance of the films was measured by the complex impedance technique using the HIOKI 3531-01 LCR Hi-Tester in the frequency range from 50 Hz to 1 MHz.

### *2.2 Device assembly*

Ti(IV) bis(ethyl acetoacetato)-diisopropoxide (0.38 M) was coated on indium tin-oxide (ITO) glass as a blocking layer and heated at 723 K for 30 minutes. The ITO glass was previously cleaned with acetone and distilled water. After that, TiO<sub>2</sub> paste was coated on the blocking layer using the doctor-blade method and the thickness of the layer was controlled using adhesive tape of

thickness 100  $\mu\text{m}$ . The  $\text{TiO}_2$  layer was then heated at 773 K for 1 hour. The resistance of  $\text{TiO}_2$  was found to increase from 5  $\Omega \text{ cm}^{-2}$  to 11  $\Omega \text{ cm}^{-2}$  after heating. After cooling to 373 K, the  $\text{TiO}_2$  electrode was soaked into the anthocyanin solution which has been extracted from blueberry for 24 hours. The  $J$ - $V$  characteristics of the dye-sensitized solar cells were obtained under white light illumination (100  $\text{mW cm}^{-2}$ ) using Keithley 2400 electrometer.

### 3. RESULTS AND DISCUSSION

Fig. 1 shows the absorption spectra of anthocyanin extracted from blueberry in solution and  $\text{TiO}_2$  soaked anthocyanin. It can be observed that the spectrum of anthocyanin shows a broad absorption band in the visible region ascribed to charge transfer transitions from highest occupied molecular orbital (HOMO) to lowest unoccupied molecular orbital (LUMO) [26,27]. The absorption peak of anthocyanin in solution is observed at  $\lambda_{\text{max}} = 541 \text{ nm}$  while  $\text{TiO}_2$  soaked anthocyanin electrode showed maximum absorption at  $\lambda_{\text{max}} = 555 \text{ nm}$ . The shift to lower energy is due to the reaction between the anthocyanin and the  $\text{TiO}_2$  surface. Chemical adsorption of this anthocyanin is the result of condensation of alcoholic-bound protons with the hydroxyl groups on the surface of nanostructured  $\text{TiO}_2$ . Adsorption of anthocyanin to the  $\text{TiO}_2$  surface stabilizes the excited state of the HOMO and LUMO of the anthocyanin pigments, thus affect the energy gap resulting in the shift towards lower energy of the absorption spectrum [28,29].

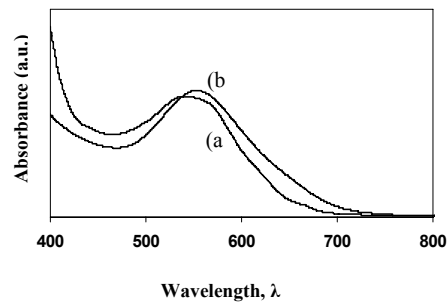


Fig. 1. The absorption spectra of anthocyanin from blueberry (a) in solution and (b) adsorbed onto  $\text{TiO}_2$  electrode

The visible absorption band is pH and solvent sensitive, showing the dye to appear red flavylium form in acidic solution and purple quinonoidal form as pH increases [27-28,30]. Fig. 2 shows the absorption spectra of anthocyanin solution at different pH. From the figure, it can be observed that anthocyanin solution at pH 1 gives the highest absorption intensity compared to pH 2, 3, 4 and 5. The higher intensity indicates that the anthocyanin dyes can absorb more light at pH 1 condition. Due to high absorption, pH 1 was chosen for fabrication of dye-sensitized solar cells.

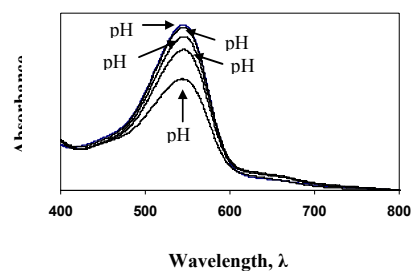


Fig.2. The absorption spectra of anthocyanin solutions at pH 5 to pH 1 extracted from blueberry

Dye-sensitized solar cells were fabricated by sandwiching electrolytes with TiO<sub>2</sub>/dye photoelectrode and platinum (Pt) counter electrode. For solar cell application, 0.04 g iodine was added to the electrolytes to produce the redox couple (I/I<sub>3</sub><sup>-</sup>). Redox couple in the electrolytes is very important in order to complete the circuit for charge flow in the electrolyte. The performance of dye-sensitized solar cells was evaluated in terms of short circuit current density  $J_{sc}$ , open circuit voltage  $V_{oc}$ , fill factor  $FF$  and efficiency  $\eta$  % which are tabulated in Table 1. The cell using dye extracted from blueberry as sensitizer with the electrolyte composition of 27.5 wt. % chitosan-22.5 wt. % NH<sub>4</sub>I-80 wt. % BMII exhibits the highest  $J_{sc}$  of 0.31 mA cm<sup>-2</sup> compared to other electrolytes composition. This shows that the highest conducting electrolyte gives the highest  $J_{sc}$ . The same trend has been reported by Ileperuma *et al.* [31]. The fill factor and efficiency were calculated from the following equations:

$$FF = \frac{P_{max}}{V_{oc} \times J_{sc}} \quad (6)$$

$$\eta \% = \frac{V_{oc} \times J_{sc} \times FF}{P_{in}} \times 100 \quad (7)$$

Here,  $P_{max}$  is maximum power output ( $P_{max} = V_{max} \times J_{max}$ ) and  $P_{in}$  is input power. Most of the efficiency of the natural dye-sensitized solar cells is less than 1%. In the work of Wongcharee *et al.* [32], TiO<sub>2</sub> DSSC employing dye extracted from blue pea as sensitizer, liquid electrolyte and Pt counter electrode exhibits  $J_{sc}$  of 0.37 mA cm<sup>-2</sup>,  $V_{oc}$  of 0.37 V, FF of 0.33 and  $\eta$  of 0.05 %, respectively.

Table 1: Electrolyte composition and photoelectrochemical parameters of DSSCs

Composition	Conductivity, $\sigma$ (S cm <sup>-1</sup> )	$J_{sc}$ (mA cm <sup>-2</sup> )	$V_{oc}$ (V)	$FF$	$\eta$ %
27.5 wt. % chitosan-27.5wt.% PVA-45 wt. % NH <sub>4</sub> I	$1.77 \times 10^{-6}$	0.19	0.30	0.43	0.02
16.5 wt. % chitosan-38.5wt.% PEO-45 wt. % NH <sub>4</sub> I	$3.66 \times 10^{-6}$	0.27	0.34	0.40	0.04
27.5 wt. % chitosan-22.5 wt. % NH <sub>4</sub> I-80 wt. % BMII	$1.76 \times 10^{-4}$	0.31	0.35	0.47	0.05

$J$ - $V$  characteristics of the dye-sensitized solar cell for 27.5 wt. % chitosan-22.5 wt. % NH<sub>4</sub>I-80 wt. % BMII electrolyte using blueberry extracts as dye is illustrated in Fig. 3. Power density against voltage is also shown in Fig. 3. The maximum power output is 0.051 mW cm<sup>-2</sup>. Patrocínio *et al.* [24] reported  $J_{sc}$  of 1.0 mA cm<sup>-2</sup> and  $V_{oc}$  of 0.59 V for TiO<sub>2</sub> DSSC utilizing blueberry as sensitizer, liquid electrolyte and Pt counter electrode. Higher  $J_{sc}$  and  $V_{oc}$  of their DSSC are due to higher ionic conductivity of liquid electrolyte compared to solid electrolyte used in the present work. Other than that, the contact between liquid electrolyte and TiO<sub>2</sub> is better compared to electrolyte in film form. In liquid form, electrolyte can enter the nanostructure TiO<sub>2</sub> and make better electrode-electrolyte contact and large surface area compared to the electrolyte in film form which the contact occurs only on the surface.

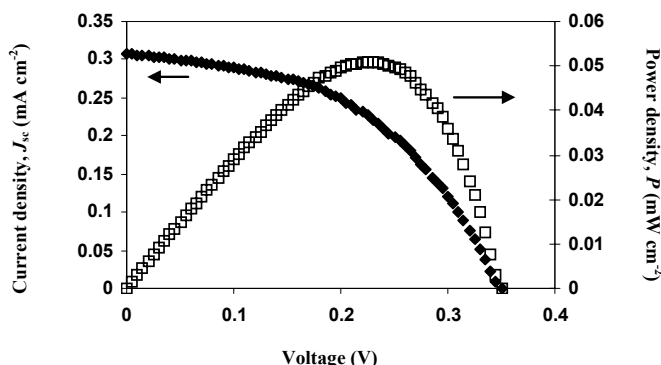


Fig. 3.  $J$ - $V$  characteristics for dye-sensitized solar cell for 27.5 wt. % chitosan-22.5 wt. %  $\text{NH}_4\text{I}$ -80 wt. % BMII electrolyte

Fig. 4 shows  $J$ - $V$  characteristic of dye-sensitized solar cell using 27.5 wt. % chitosan-22.5 wt. %  $\text{NH}_4\text{I}$ -80 wt. % BMII electrolyte in gel form. As expected, the performance of dye-sensitized solar cell is improved by using gel electrolyte. The cell exhibits short circuit current density,  $J_{sc}$  of  $1.705 \text{ mA cm}^{-2}$ , open circuit voltage,  $V_{oc}$  of 385 mV, fill factor of 0.39, maximum power output of  $0.26 \text{ mW cm}^{-2}$  and efficiency,  $\eta$  of 0.3 %.

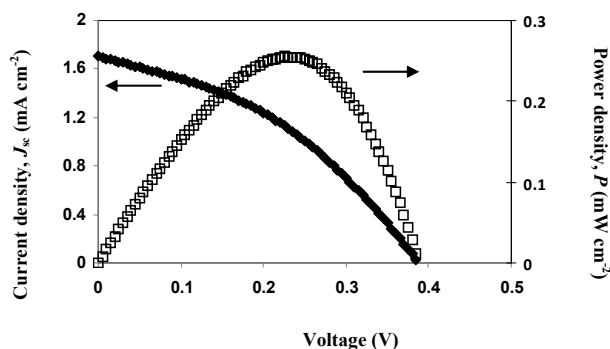


Fig. 4.  $J$ - $V$  characteristics for dye-sensitized solar cell for 27.5 wt. % chitosan-22.5 wt. %  $\text{NH}_4\text{I}$ -80 wt. % BMII electrolyte (gel form)

#### 4. CONCLUSIONS

Chitosan based polymer electrolytes have been prepared. Highest ionic conductivity of  $1.76 \times 10^{-4} \text{ S cm}^{-1}$  was obtained with incorporation of IL. A natural dye of anthocyanin solution was used in fabricating dye-sensitized solar cells. The cell using electrolyte with composition 27.5 wt. % chitosan-22.5 wt. %  $\text{NH}_4\text{I}$ -80 wt. % BMII in gel form exhibited better performance compared to other electrolytes.

## REFERENCES

1. M.K. Nazeeruddin, A. Kay, I. Rodicio, M. Grätzel, *J. Am. Chem. Soc.* 115 (1993) 6382-6390.
2. B. O' Regan, M. Grätzel, *Nature* 353 (1991) 737-740.
3. L. Guo, X. Pan, C. Zhang, W. Liu, M. Wang, X. Fang, S. Dai, *Sol. Energy* 84 (2010) 373-378.
4. L.-W Chong, H.-T. Chien, Y.-L. Lee, *J. Power Sources* 195 (2010) 5109-5113
5. A.F. Nogueira, J.R. Durrant, M.A. De Paoli, *Adv. Mater.* 13 (2001) 826-830.
6. J.H. Kim, M.-S. Kang, Y.J. Kim, J. Won, N.-G. Park, Y.S. Kang, *Chem. Commun.* 14 (2004) 1662-1663.
7. J.H. Kim, M. -S. Kang, Y.J. Kim, J. Won, Y.S. Kang, *Solid State Ionics* 176 (2005) 579-584.
8. F. Wu, T. Feng, Y. Bai, C. Wu, L. Ye, Z. Feng, *Solid State Ionics* 180 (2009) 677-680.
9. S.A. Mohamad, R. Yahya, Z.A. Ibrahim, A.K. Arof, *Sol. Energy Mater. Sol. Cells* 91 (2007) 1194-1198.
10. Z. Zong, Y. Kimura, M. Takahashi, H. Yamane, *Polymer*, 41 (2000) 899-906.
11. R.A.A. Muzzarelli, 1973, in "Natural Chelating Polymers: Alginic Acid, Chitin and Chitosan", New York: Pergamon Press, Oxford.
12. M. Jumaa, and B.W. Muller, 1999, *Int J. Pharmaceutics*, 183, 175
13. P.K. Singh, B. Bhattacharya, R.K. Nagarale, K.-W. Kim, H.-W. Rhee, *Synth. Met.* 160 (2010) 139-142.
14. T. Ueki and M. Watanabe, *Macromolecules* 41 (2008) 3739-3749
15. H.(H.) Zhang, P. Maitra, S.L. Wunder, *Solid State Ionics* 178 (2008) 1975-1983.
16. Y. Ren, Z. Zhang, S. Fang, M. Yang, S. Cai, *Sol. Energy Mater. Sol. Cells* 71 (2002) 253-259.
17. M. Shaheer Akhtar, K.K. Cheralathan, Ji-M. Chun, O.-B. Yang, *Electrochim. Acta* 53 (2008) 6623-6628.
18. M. Wang, X. Xiao, X. Zhou, X. Li, Y. Lin, *Sol. Energy Mater. Sol. Cells* 91 (2007) 785-790.
19. T. Kuila, H. Acharya, S.K. Srivastava, B.K. Samantaray, S. Kureti *Mater. Sci. Eng., B* 137 (2007) 217-224.
20. G. P. Kalaiganan , M.-S. Kang, Y. S. kang, *Solid State Ionics* 177 (2006) 1091-1097.
21. Y.-T. Jia, J. Gong, X.-H. Gu, H.-Y. Kim, J. Dong, X.-Y. Shen, *Carbohydr. Polym.* 67 (2007) 403-409.
22. C.-C. Yang and G.M. Wu, *Mater. Chem. Phys.* 114 (2009) 948-955.
23. R.C. Khanal, L.R. Howard, R.L. Prior, *Food Research International* 43 (2010) 1464-1469
24. A.O.T. Patrocínio, S.K. Mizoguchi, L.G. Paterno, C.G. Garcia, N.Y.M. Iha, *Synthetic Metals* 159 (2009) 2342-2344
25. A.O.T. Patrocínio, and N.Y.M. Iha, *Quimica Nova* 33 (2010) 574-578
26. A.S. Polo and N.Y. Murakami Iha, *Sol. Energy Mater. Sol Cells* 90 (2006) 1936-1944
27. N.J. Cherepy, G.P. Smestad, M. Gratzel, J.Z. Zhang, *J. Phys. Chem. B* 101 (1997) 9342-9351
28. G. Calogero and G. Di Marco, *Sol. Energy Mater. Sol Cells* 92 (2008) 1341-1346
29. A.S. Polo, M.K. Itokazu, N.Y. Murakami Iha, *Coord. Chem. Rev.* 248 (2004) 1343-1361
30. Q. Dai and J. Rabani, *N. J. Chem.* 26 (2002) 421-426
31. O. A. Ileperuma, M. A. K. L. Dissanayake, S. Somasunderam, L. R. A. K. Bandara, *Sol. Energy Mater. Sol. Cells* 84 (2004) 117-124.
32. K. Wongcharee, V. Meeyooa, S. Chavadej, *Sol. Energy Mater. Sol. Cells* 91 (2007) 566-571.

## DYE-SENSITIZED SOLAR CELL WITH CHLOROPHYLL AND PLASTICIZED PVDF-HFP BASED ELECTROLYTES

M.M. NOOR<sup>1,2</sup>, M.H. BURAIHAH<sup>2</sup>, S.N.F. YUSUF<sup>2</sup>, M.A. CAREEM<sup>3</sup>, S.R. MAJID<sup>2</sup>, A.K. AROF<sup>2,\*</sup>

<sup>1</sup>Centre for Foundation Studies, International Islamic University Malaysia, Jalan Universiti, 46350 Petaling Jaya, Selangor, Malaysia

<sup>2</sup>Centre for Ionics University Malaya, Department of Physics, University of Malaya, 50603 Kuala Lumpur, Malaysia

<sup>3</sup>Department of Physics, University of Peradeniya, Peradeniya, Sri Lanka

\*Corresponding Author, e-mail: akarof@um.edu.my

### ABSTRACT

In this study chlorophyll extracted from leaves of fragrant screwpine (*Pandanus amaryllifolius*) or locally known as *pandan* leaves has been used as natural dye sensitizer to fabricate dye-sensitized solar cells (DSSCs). The electrolyte used was poly(vinylidene fluoride-co-hexafluoropropylene) (PVDF-HFP) based electrolyte comprising a binary mixture of plasticizer (ethylene carbonate and propylene carbonate) (EC/PC=1:1) and sodium salt which have been prepared using solvent evaporation method. The best conducting electrolyte composition is 19 wt. % PVDF-HFP - 31 wt. % Na<sub>2</sub>S<sub>9</sub>H<sub>2</sub>O - 50 wt. % EC/PC (w/w =1) with the conductivity value of  $8.40 \times 10^{-4}$  S cm<sup>-1</sup>. Different amounts of sulphur (1 wt. % to 9 wt. % of Na<sub>2</sub>S) were added to this electrolyte to produce active redox couple (S<sup>2-</sup>/S<sub>x</sub><sup>2-</sup>). Observation shows that 5% sulphur gives better performance. The pH of the dye solution was varied with tartaric acid and the solution with pH= 1 gives better overall absorption. The DSSC fabricated with dye deposited with pH 1 dye solution and the electrolyte containing 5% sulphur shows the best overall performance with short-circuit current density of 1.07 mA/cm<sup>2</sup>, open-circuit voltage of 0.43 V, fill factor of 0.33 and efficiency of 0.2 % under illumination 100 mW cm<sup>-2</sup> white light .

Keywords: Dye-sensitized solar cell, natural dye, chlorophyll, PVDF-HFP

### 1. INTRODUCTION

DSSCs have stimulated much attention due to their high-energy conversion efficiency and low production cost as compared to silicon solar cells [1]. The DSSC consists of a TiO<sub>2</sub> photoelectrode coated on conducting glass, dye sensitizer, an electrolyte containing redox couple such and a counter electrode. Since the dye plays an important role in harvesting light and solar energy conversion to electricity, much effort has been focused on dye materials. The commercial synthetic ruthenium (II) polypyridyl complexes such as N719 and N3 are widely used in the DSSC since they have satisfactory photoelectric conversion efficiency up to 10% [2-4]. However, these dyes use metal compounds, which are expensive and produce environmental pollution [5]. Another interesting approach is the use of natural dyes, which is more environmentally friendly, non-toxic, biodegradable and cheaper compared to the synthetic dyes [6]. Natural sensitizer dyes used are usually anthocyanins [7-9]. In this study, DSSCs prepared use chlorophyll extracted from a fragrant screwpine (*Pandanus amaryllifolius*) leaves as dye. The leaves are green in colour, easily obtainable in Malaysia, cheap and are rich in chlorophyll. Chlorophylls, which act as an effective photosensitizer in photosynthesis of green plant, has absorption maximum at 670 nm thus, it is an attractive potential compound as a photosensitizer in visible region [10-11].

### 2. EXPERIMENTAL

#### 2.1. Materials

Poly(vinylidene fluoride-hexafluoropropylene), P(VdF-HFP) of MW 400,000, tetrahydrofuran (THF), ethylene carbonate (EC) and propylene carbonate (PC) were purchased from Sigma Aldrich and hydrated sodium sulphide ( $\text{Na}_2\text{S}\cdot x\text{H}_2\text{O}$ ) (Ajax) were used as received. *Diisopropoxytitanium bis(acetylacetonate)* solution and a *chloroplatinic acid* both purchased from Sigma Aldrich were diluted to 0.38 M in ethanol and 0.005 M in 2-propanol respectively prior to uses.  $\text{TiO}_2$  paste used was PST-18NR procured from JGC Catalyst and Chemicals Ltd. Japan.

### 2.2. Preparation of Polymer electrolytes

Electrolytes were prepared by solvent casting method. A fixed amount of P(VdF-HFP) was added to tetrahydrofuran (THF) and stirred continuously for about 2 hours at 40 °C until the polymer is fully dissolved. Different amounts of  $\text{Na}_2\text{S}\cdot x\text{H}_2\text{O}$  salt from 0 to 45 wt. % were added into the polymer solution and vigorously stirred until the solution becomes homogenous. The polymer-salt solution was then cast onto separate clean glass plates to allow the solvent to evaporate slowly until the polymer-salt films are formed. A mixture of propylene carbonate (PC) and ethylene carbonate (EC) at 1:1 weight ratio added as plasticizer to the highest conducting sample of polymer-salt to enhance the conductivity. The plasticizer amount from 20 to 70 wt. % were added to the highest conducting polymer-salt electrolyte before casting onto separate clean glass plates to produce the best conducting plasticized polymer-salt films. A small amount of sulphur was added to the highest conducting composition to make the electrolyte redox active. The sulphur content were varied from 1 until 9 % of  $\text{Na}_2\text{S}$  to get a compatible active redox couple since the sulphur/sulphide electrolyte were not commonly used as redox mediator in DSSC compared to iodide/tri-iodide redox couple which has been reported as a common mediator for DSSCs [1-11]. The use of sulphur/sulphide as redox couple was because the electrolyte system prepared contained sulphide salt. Furthermore, no report on DSSC using natural dye and electrolyte with this redox couple was found in the literature.

### 2.3. Preparation of natural dye sensitizers

Fresh *pandan* leaves were cleaned with distilled water and dried before rinsing with ethanol. 20 g *pandan* leaves were cut into small pieces were soaked into 200 ml ethanol solution and kept for 24 hours in the dark place. Residues were separated from the solution by filtration.

### 2.4. Preparation of electrodes

Two types of electrodes were prepared to fabricate the DSSC. The electrodes are working electrode which consists of  $\text{TiO}_2$  layer and the other is the counter electrode which consists of a platinum layer. Indium tin oxide (ITO) glass is used as transparent conducting oxide (TCO) substrate for both electrodes. To prepare the working electrode or photoanode,  $\text{TiO}_2$  paste was spread on the ITO surface using doctor blade technique [12-14]. The ITO glass has been coated with *diisopropoxytitanium bis(acetylacetonate)* by spin-coating at 3000 rpm for 10 seconds to improve adhesion of  $\text{TiO}_2$  on the ITO glass and provide a larger  $\text{TiO}_2$ / ITO contact area. This procedure also minimizes contact between the redox electrolyte and the conductive ITO surface which can reduce electron recombination in the DSSC hence preventing in efficiency reduction [15]. The layers were sintered at 450 °C for 30 minutes after each process. The prepared  $\text{TiO}_2$  electrode was immersed in the dye solution and left to react for 24 hours in the dark place in to allow the dye to attach to the dye to the  $\text{TiO}_2$ . The electrode should be stained green color and washed in ethanol and dried before it is assemble in the DSSC. While the  $\text{TiO}_2$  electrode is being immersed in the chlorophyll solution, the counter electrode can be made using another cleaned ITO glass. A thin layer of platinum (Pt) solution was spin-coated on the conducting surface of the ITO glass and sintered at 450 °C for 30 minutes [16].

### 2.5. Preparation of DSSCs



The DSSCs were fabricated by sandwiching the highest conducting plasticized electrolyte containing redox couple between the ITO/TiO<sub>2</sub>/dye photoelectrode and Pt-coated ITO counter electrode. The effective area of photoelectrode is 0.16 cm<sup>2</sup>.

### 2.6. Characterization and measurement

For the polymer electrolytes, electrochemical impedance spectroscopy (EIS) technique was used to determine the highest conducting composition. The impedance of the samples was measured using the HIOKI 3531-01 LCR Hi-Tester interfaced to a computer with frequency ranging from 50 Hz to 1MHz at room temperature. Each sample was sandwiched between two stainless steel electrodes of diameter 2.0 cm before performing the measurement. To the composition giving the highest conductivity, equal amounts by weight of EC and PC were added to enhance the conductivity. The conductivity was calculated using equation:

$$\sigma = \frac{l}{R_B A}$$

Here  $R_B$  is the bulk resistance taken at the intersection of the plot with the real impedance axis,  $l$  is the film thickness and  $A$  is the surface area of the electrode/electrolyte contact. The absorption spectrum of the chlorophyll dye at various pH was taken with a UV-vis spectrometer. The photocurrent-voltage (I-V) characteristics of the DSSCs were measured under an illumination at one sun (AM1.5, 100 mW cm<sup>-2</sup>) white light. The fill factor (FF) was calculated using the equation

$$FF = \frac{I_{max} V_{max}}{I_{sc} V_{oc}}$$

where  $I_{max}$  and  $V_{max}$  are the maximum output value of current and voltage respectively, and  $I_{sc}$  and  $V_{oc}$  are the short-circuit current and open-circuit voltage respectively. The total energy conversion efficiency was calculated using the equation:

$$\eta = \frac{I_{sc} V_{oc} \times FF}{P_m}$$

where  $P_m$  is the power of incident light.

## 3. RESULTS AND DISCUSSION

### 3.1. Conductivity of polymer electrolytes

Conductivity variations for various salt and plasticizer compositions are illustrated in Figure 1(a) and (b) respectively. Figure 1(a) shows that in the P(VDF-HFP)/Na<sub>2</sub>S electrolyte of composition, ionic conductivity increases with the salt content and reaches a maximum value of  $1.34 \times 10^{-4}$  S cm<sup>-1</sup> (at 30 °C) at the content of (65:35) wt. % ratio. Addition of 50 wt. % of EC/PC as plasticizer enhanced the conductivity to a maximum value of  $8.40 \times 10^{-4}$  S cm<sup>-1</sup> as shown in Figure 1(b).

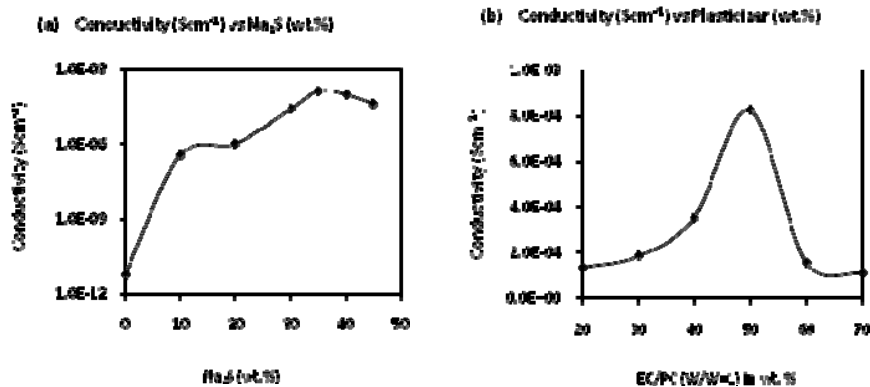


Figure 1: Conductivity versus wt. % of (a) Na<sub>2</sub>S salt and (b) Plasticizer (EC: PC = 1:1 w/w)

### 3.2. Characterizations of natural dye sensitizers

Figure 2 shows the UV/Vis absorption spectrum of chlorophyll extracts in ethanol solution at different pH. The pH value was varied by adding tartaric acid. The characteristic absorption peak of chlorophyll dye can be found in the wavelength ranges from 400 to 500 nm and from 600 to 750 nm [17]. From the figure, both of characteristic absorption peaks are observed in all chlorophyll extract samples. The intensity of absorption peak in the range of 400 to 450 nm is higher compared to the absorption peak in 650 to 700 nm indicating that absorbability of chlorophyll dye is better in the range of 400 to 450 nm. The intensity of absorption peak at 665 nm is almost the same for the solution at pH 1, 3 and 6. However the solution at pH 1 shows the highest absorption intensity at 413 nm therefore, this solution was chosen as sensitizer for DSSC fabrication.

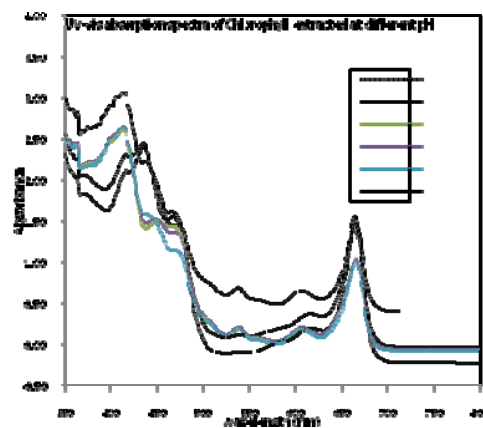


Figure 2: Absorption spectra for Chlorophyll

### 3.3. Characterizations of DSSCs

The photocurrent density–voltage graph for a DSSC at different sulphur content is shown in **Fig. 3(a)**. The values of the open-circuit voltage ( $V_{OC}$ ), short-circuit current density ( $J_{SC}$ ), fill factor ( $FF$ ) and conversion efficiency ( $\eta$ ) obtained from the graph are summarized in **Table 1** and the variation of the DSSC conversion efficiency with sulphur content is shown in **Fig. 3(b)**. Sulphur content is strongly affecting the short circuit current of the studied DSSC, but the trend of their changes is different. This behaviour is as per the known behaviour of active redox couple. According to S.Y. Cha et. al. (2010), the short-circuit current ( $J_{SC}$ ) of the solar cell is strongly influenced by the mobility of redox couple. As can be seen from **Figure 3(b)** and **Table 1**, the lowest short circuit current is  $0.83 \text{ mA cm}^{-2}$  obtained when 1 wt. % sulphur is added into the plasticized PVDF based electrolyte. Therefore the lowest value of  $J_{SC}$  in this sample can be attributed to the low mobility of active redox couple. When the sulphur content in the plasticized PVDF-based electrolyte sample is increased i.e. 3, 5 and 7 wt. % of sulphur, the obtained short-circuit current ( $J_{SC}$ ) value is 1.19, 1.07 and  $1.12 \text{ mA cm}^{-2}$  respectively which are higher compared to the sample with 1 wt. % sulphur. Further addition of sulphur content (9 wt. % S) caused a decreased in short-circuit current value to  $0.95 \text{ mA cm}^{-2}$  which can be assigned to difficulty of active redox couple to be transported in the sample. In addition, DSSC with the plasticized PVDF-based electrolytes containing 3 and 5 wt. % sulphur gave the efficiency of 0.14 and 0.15 % under the illumination of  $100 \text{ mW cm}^{-2}$  white light. This observation suggests that the higher interaction between TiO<sub>2</sub> particles, chlorophyll and active redox couple has occurred and contribute to better

charge-transfer performance which improves the efficiency of the studied cell. The highest open circuit voltage ( $V_{OC}$ ) was obtained when the sulphur content is 5%.

Table 1: The performance of the DSSCs at different content of sulphur (wt. %) in the polymer electrolyte

Sulphur (%)	9	7	5	3	1
Voc (V)	0.38	0.33	0.43	0.38	0.38
Jsc(mA cm <sup>-2</sup> )	0.95	1.12	1.07	1.19	0.83
FF	0.33	0.27	0.33	0.32	0.24
Efficiency (%)	0.1	0.1	0.2	0.1	0.1

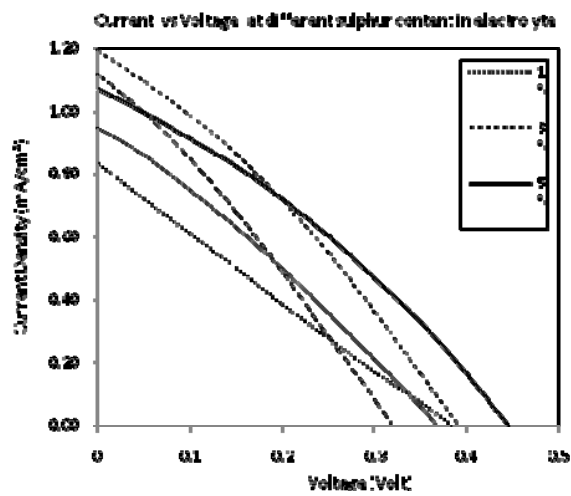


Figure 3(a):  $J$ - $V$  curves for DSSCs at different content of sulphur in the polymer electrolyte

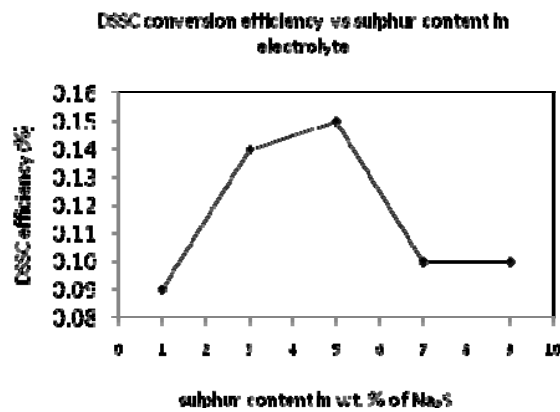


Figure 3(b): DSSC efficiency at different content of sulphur in the polymer electrolyte

#### 4. CONCLUSION

A DSSC was successfully fabricated with chlorophyll-sensitized TiO<sub>2</sub> photoelectrode, platinized counterelectrode, plasticized PVDF-HFP based polymer electrolyte and with sulphur/sulphide redox mediator. The studied DSSC with deposited chlorophyll dye solution at pH 1 and the electrolyte containing 5 wt. % sulphur exhibits the best overall performance with the short-circuit current density of 1.07 mA cm<sup>-2</sup>, open-circuit voltage of 0.43 V, fill factor of 0.33 and efficiency of 0.15% under the illumination of 100 mW cm<sup>-2</sup> white light .

#### 5. ACKNOWLEDGEMENT

The authors would like to thank University of Malaya for the financial support (IPPP/UPGP/(RU/PPP)PS325/2009C) grant to carry out this research work. M.M. Noor wishes to thank the International Islamic University Malaysia (IIUM) for the study leave awarded.

#### REFERENCES

1. M.K. Nazeeruddin, E. Baranoff, M. Graetzel; Dye-sensitized solar cells: A brief overview; *Solar Energy* 85 (2011) 1172–1178
2. A.F. Nogueira, C. Longo, M.A. De Paoli; Polymers in dye sensitized solar cells: overview and perspectives; *Coordination Chemistry Reviews* 248 (2004) 1455–1468
3. D.W. Kima, Y.B. Jeong, S. H. Kim, D.Y. Lee, J.S. Song; Photovoltaic performance of dye-sensitized solar cell assembled with gel polymer electrolyte; *Journal of Power Sources* 149 (2005) 112–116
4. T. Asano, T. Kubo, Y. Nishikitani; Electrochemical properties of dye-sensitized solar cells fabricated with PVDF-type polymeric solid electrolytes; *Journal of Photochemistry and Photobiology A: Chemistry* 164 (2004) 111–115
5. H. Changa, H.M. Wu, T.L. Chen, K.D. Huang, C.S. Jwo, Y.J. Lo; Dye-sensitized solar cell using natural dyes extracted from spinach and ipomoea; *Journal of Alloys and Compounds* 495 (2010) 606–610
6. A.O.T. Patrocinio, S.K. Mizoguchi, L.G. Paterno, C.G. Garcia, N.Y. Murakami Iha; Efficient and low cost devices for solar energy conversion: Efficiency and stability of some natural-dye-sensitized solar cells; *Synthetic Metals* 159 (2009) 2342–2344
7. K. Wongcharee, V.Meeyoo, S. Chavadej; Dye-sensitized solar cell using natural dyes extracted from rosella and blue pea flowers; *Solar Energy Materials & Solar Cells* 91 (2007) 566–571
8. S. Furukawa, H. Iino, T. Iwamoto, K. Kukita, S. Yamauchi; Characteristics of dye-sensitized solar cells using natural dye; *Thin Solid Films* 518 (2009) 526–529
9. S. Hao, J. Wu, Y. Huang, J. Lin; Natural dyes as photosensitizers for dye-sensitized solar cell; *Solar Energy* 80 (2006) 209–214
10. Y. Amao, Y. Yamada, K. Aoki; Preparation and properties of dye-sensitized solar cell using chlorophyll derivative immobilized TiO<sub>2</sub> film electrode; *Journal of Photochemistry and Photobiology A: Chemistry* 164 (2004) 47–51
11. H. Zhou, L. Wu, Y. Gao, T. Ma; Dye-sensitized solar cells using 20 natural dyes as sensitizers; *Journal of Photochemistry and Photobiology A: Chemistry* 219 (2011) 188–194
12. C. Sima, C. Grigoriu, S. Antohe; Comparison of the dye-sensitized solar cells performances based on transparent conductive ITO and FTO; *Thin Solid Films* 519 (2010) 595–597

13. D. Saikia, C.C. Han, Y.W. Chen-Yang; Influence of polymer concentration and dyes on photovoltaic performance of dye-sensitized solar cell with P(VdF-HFP)-based gel polymer electrolyte; *Journal of Power Sources* 185 (2008) 570–576
14. Y. Ren, Z. Zhang, S. Fang, M. Yang, S. Cai; Application of PEO based gel network polymer electrolytes in dye-sensitized photoelectrochemical cells; *Solar Energy Materials & Solar Cells* 71 (2002) 253–259
15. H. Yu, S. Zhang, H. Zhao, G. Will, P. Liu; An efficient and low-cost TiO<sub>2</sub> compact layer for performance improvement of dye-sensitized solar cells; *Electrochimica Acta* 54 (2009) 1319–1324
16. Y.L. Lee, C.L. Chen, L.W. Chong, C. H. Chen, Y. F. Liu, C.F. Chi; A platinum counter electrode with high electrochemical activity and high transparency for dye-sensitized solar cells; *Electrochemistry Communications* 12 (2010) 1662–1665
17. H. Chang, Y. J. Lo; Pomegranate leaves and mulberry fruit as natural sensitizers for dye-sensitized solar cells; *Solar Energy* 84 (2010) 1833–1837.
18. S.Y. Cha, Y.G. Lee, M.S. Kang, Y.S. Kang; Correlation between ionic conductivity and cell performance in solid-state dye-sensitized solar cells employing polymer electrolyte; *Journal of Photochemistry and Photobiology A: Chemistry* 211 (2010) 193–196

## SYNTHESIS AND CHARACTERIZATION OF N-PHTHALOYLCHITOSAN BASED POLYMER ELECTROLYTES FOR DYE-SENSITIZED SOLAR CELL

S. N. F. YUSUF<sup>1</sup>, M.M. NOOR<sup>1,2</sup>, M.H. BURAI DAH<sup>1</sup>, M.A. CAREEM<sup>3</sup>, R. YAHYA<sup>1</sup>,  
S. R. MAJID<sup>1</sup>, A.K. AROF<sup>1\*</sup>

<sup>1</sup>Centre for Ionics University Malaya, Department of Physics, Faculty of Science, University of Malaya,  
50603 Kuala Lumpur, Malaysia

<sup>2</sup>Centre for Foundation Studies, International Islamic University Malaysia, Jalan Universiti, 46350 Petaling  
Jaya, Selangor, Malaysia

<sup>3</sup>Department of Physics, University of Peradeniya, Peradeniya, Sri Lanka

\*Corresponding Author, e-mail: akarof@um.edu.my

### ABSTRACT

Phthaloylation is applied to modify chitosan so as to improve its solubility in organic solvents. The structure of N-Phthaloylchitosan (PhCh) has been confirmed using FTIR and <sup>1</sup>H NMR spectroscopy. From FTIR spectroscopy, characteristic peaks of phthalimido and aromatic group from PhCh are observed at 1772, 1708, and 721 cm<sup>-1</sup> respectively. <sup>1</sup>H NMR spectrum shows two sets of peaks centered at 3.0 and 7.5 ppm verifying that chitosan has been phthaloylated. Polymer electrolytes have been prepared by varying lithium iodide from 5 wt.% to 50 wt.%. PhCh film with 50 wt.% of LiI shows the highest conductivity among all the films in the system with the value of 1.88 x 10<sup>-4</sup> S cm<sup>-1</sup> at room temperature. On addition of 2.5 wt.% ionic liquid (IL) into the highest conducting composition, the conductivity was further increased to 6.94 x 10<sup>-4</sup> S cm<sup>-1</sup>. The highest conductivity of polymer electrolyte 48.75 wt.% PhCh-48.75 wt.% LiI-2.5 wt.% ionic liquid is used to fabricate dye-sensitized solar cells (DSSCs) using anthocyanin extracted from two natural sources, black rice and red cabbage. 1 wt.% iodine crystal has been added to the 48.75 wt.% PhCh-48.75 wt.% LiI-2.5 wt.% IL composition. The solar energy conversion efficiency,  $\eta = 0.21$  is obtained from black rice sensitized solar cell that exhibits  $J_{sc}$  up to 2.31 mA/cm<sup>2</sup>,  $V_{oc}$  of 0.34 V and fill factor of 0.30. In the case of red cabbage extract, the value of  $J_{sc}$  is 2.20 mA/cm<sup>2</sup>,  $V_{oc}$  of 0.35 V, fill factor of 0.26 and  $\eta$  is 0.20.

Keywords: N-phthaloylation, Chitosan, Dye-sensitized solar cell, FTIR, <sup>1</sup>H NMR

### 1. INTRODUCTION

Chitosan containing repeating units of  $\beta$ -(1-4) linked 2-amino-2-deoxy-D-glucopyranose has been studied as a polymer host to prepare polymer electrolytes [1-4]. It is non-toxic, odorless, non-immunogenic, biocompatible and enzymatically biodegradable [5-11]. Chitosan has been used in the development of high conductivity polymeric systems because it demonstrates polyelectrolyte behavior due to the protonated amino group in the polymeric backbone. However, the formation of intra and/or inter hydrogen bonding between the amino group at C-2 and hydroxyl groups at C-3 and C-6 leads to poor solubility of chitosan in organic solvents [12-14].

One of the potential methods to improve the solubility of chitosan in organic solvents is N-phthaloylation. In this method, the phthaloyl group in phthalic anhydride replaces the hydrogen atom in the amino group at the second carbon of the monomer. Solubility is increased as the bulky phthaloyl groups destroy the formation of specific hydrogen bond interactions. PhCh is soluble in DMF, DMSO, DMAc and also pyridine [6,11,15]. The wider range of non-aqueous solvents enable PhCh to solvate a variety of salts to form the desired ion conducting polymer electrolyte. This will enable solid polymer electrolytes to be prepared from PhCh and replace the use of liquid electrolytes. The major drawbacks of liquid electrolytes are leakage, solvent evaporation, corrosion

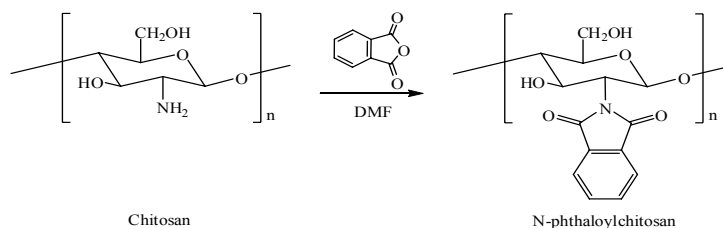
and instability of liquid electrolyte at high temperatures [16-20]. Thus can be overcome using solid polymer electrolyte.

In this work, we investigate the effectiveness of N-phthaloylchitosan as a solid polymer electrolyte and its feasibility as an electrolyte in a dye-sensitized solar cell (DSSC). DSSCs consist of three main components; (1) an active mesoporous nanocrystalline semiconductor photo-electrode which has been soaked in a dye solution, (2) an electrolyte that contains  $I^-/I_3^-$  redox couple to ensure internal electrical contact between the two electrodes, and (3) a platinum counter electrode coated onto the conductive glass substrates. The natural dye solvent-extracted from black rice and red cabbage consists of anthocyanin, which is the most important pigment in vascular plants. This pigment is responsible for the orange, pink, red, violet, and blue colors in flowers and fruits [21]. Due to the hydroxyl groups present in anthocyanin molecules, it can be bound with the surface of a porous semiconducting  $TiO_2$  film enhancing photoelectric conversion effect [22].

## 2. EXPERIMENTAL

### 2.1 Phthaloylation of chitosan

The synthesis procedure is similar to that of Kurita et al. [23]. Chitosan (Aldrich) and phthalic anhydride (DC Chemical Co. Ltd.) were refluxed at  $100^\circ\text{C}$  to  $120^\circ\text{C}$  under nitrogen atmosphere for 6 h in dimethylformamide (DMF). DMF was purchased from R & M Chemicals. The temperature was then reduced to  $60^\circ\text{C}$ , and the mixture was left overnight. The product of reaction between chitosan and phthalic anhydride dissolved in DMF to form a yellowish solution. This solution was poured into ice water to precipitate the product, N-phthaloylchitosan. The precipitate was collected and washed with ethanol in a Soxhlet extractor for 8 h. Ethanol was obtained from J. T. Baker and was distilled prior to use. The product was dried in vacuum. N-phthaloylchitosan (PhCh) was produced according to the equation shown in Scheme 1.



Scheme 1: Reaction of N-phthaloylation [23].

### 2.2 Preparation of N-phthaloylchitosan based polymer electrolyte

PhCh-based electrolytes were prepared by the solvent casting technique using DMF as the solvent. 0.5 g of synthesized PhCh was completely dissolved in 10 mL DMF. 5 wt.% to 50 wt.% of lithium iodide (LiI) was added to the PhCh solutions. The mixture was further stirred before casting into a petri dish. The solutions were then heated in an oven at  $60^\circ\text{C}$ . The films obtained were stored in a vacuum desiccator prior to characterization and analysis.

### 2.3 Characterization

#### 2.3.1 Fourier Transform Infra-Red (FTIR)

The Fourier transform infra-red (FTIR) spectra were recorded on Spotlight 400 Perkin-Elmer spectrometer at a resolution of  $1\text{ cm}^{-1}$  with 32 scanning numbers using attenuated total reflectance (ATR) method. The spectrum was recorded from wavenumber  $650$  to  $4000\text{ cm}^{-1}$  at room temperature.

### 2.3.2 Proton Nuclear Magnetic Resonance ( $^1\text{H}$ NMR)

Proton nuclear magnetic resonance was taken at 399.65 MHz with JNM-GSX270 spectrometer. The sample was dissolved completely in DMSO- $d_6$  with sample concentration of about 20% (w/v).

### 2.3.3 Electrical Impedance Spectroscopy (EIS)

A HIOKI 3531 Z Hi tester was used to measure the impedance of the films in the frequency range from 50 Hz to 1 MHz. The films were sandwiched between two stainless steel discs. The impedance data were presented in a complex impedance plot where the imaginary part,  $Z_i$  of impedance was plotted against its real part  $Z_r$ . The ionic conductivity of the samples can be calculated by using the following equation,

$$\sigma = \frac{d}{R_b \times A} \quad (1)$$

where  $d$  is the thickness of the film,  $R_b$  is bulk impedance taken at the intersection of the plot with the real impedance axis and  $A$  is the film-electrode contact area.

### 2.3.4 Fabrication of solar cell

Black rice and red cabbage were extracted in ethanol for 24 h at room temperature. Solutions were filtered to remove the entire residue. pH of dye was adjusted in acidic condition, pH 1 with 0.02 mol  $\text{dm}^{-3}$  hydrochloric acid (HCl). Original pH of both black rice and red cabbage is pH 5. Transparent tin-doped indium oxide or indium tin oxide (ITO) conductive glass was used for both the photoactive and counter electrodes. ITO glasses were rinsed with distilled water and ethanol successively before use. Photoactive electrodes were prepared by spin-coating a compact layer, diisopropoxytitaniumbis(acetylacetonate) solution at 3000 rpm for 30 s onto ITO glass, followed by heating at 450 °C for 30 min. Commercialized nanocrystalline  $\text{TiO}_2$  paste (STI 18NR-T) was applied onto the compact layer on the glass by the doctor blade technique. An adhesive tape (Scotch 3M) was fixed on the four sides of the glass substrate to restrict the thickness of the  $\text{TiO}_2$  porous layer to about 0.11 mm. This was followed by sintering at 450 °C for 30 min. The ITO glass with  $\text{TiO}_2$  layer was then immersed in the prepared dye solution at room temperature for 24 h. The dye-sensitized  $\text{TiO}_2$  film was rinsed with distilled water and acetone. Counter electrodes were prepared by spin coating a solution of 0.01M  $\text{PtCl}_2$  in isopropyl alcohol at 3000 rpm for 30 s onto ITO glass. The transparent Pt-coated glass was sintered at 500 °C for 40 min. The polymer electrolyte (50 wt.% PhCh-50 wt.% of LiI+0.05g of  $\text{I}_2$ ) was sandwiched between working and counter electrodes and the two electrodes were clipped together for photovoltaic measurements. The photocurrent performance of DSSCs was carried out using the Keithley 2400 electrometer. From the I-V characteristic curves, the short circuit current ( $I_{\text{SC}}$ ), open circuit voltage ( $V_{\text{OC}}$ ), fill factor (FF) and energy conversion efficiency ( $\eta$ ) can be calculated from the following equations:

$$FF = \frac{I_{\text{max}} \times V_{\text{max}}}{I_{\text{SC}} \times V_{\text{OC}}} \quad (2)$$

$$\eta = \frac{P_{\text{out}}}{P_{\text{in}}} \times 100 = \frac{I_{\text{SC}} \times V_{\text{OC}} \times FF}{P_{\text{in}}} \times 100 \quad (3)$$

## 3. RESULTS AND DISCUSSION

### 3.1 Synthesis of N-phthaloylchitosan

The FTIR spectra of pure chitosan have been compared with the spectra of phthaloylation product (PhCh) in Figure 1. The  $\text{NH}_2$  band appearing around 1601  $\text{cm}^{-1}$  in the pure chitosan spectrum 1(a) has disappeared indicating that substitution has occurred onto the N atom of chitosan. The spectrum of pure phthaloylchitosan (Figure 1(b)) exhibits peaks corresponding to the carbonyl



anhydride at 1772 and 1708  $\text{cm}^{-1}$ . There is also an absorption peak at 721  $\text{cm}^{-1}$  indicating the presence of an aromatic ring. These results verified the synthesis of N-phthaloylchitosan. Previous works have reported three main peaks appearing after phthaloylation took place onto the amino group of chitosan [3,5,7,11,18]. Two peaks that belong to phthalimido group can be observed between 1711 and 1715  $\text{cm}^{-1}$  and between 1772 and 1777  $\text{cm}^{-1}$ . The third band is dedicated to aromatic group which appear at 721  $\text{cm}^{-1}$  wavenumber. Treatment of chitosan with phthalic anhydride generally results in partial O-phthaloylation in addition to the N-substitution [24]. From the FTIR spectra, some O-phthaloylation has also occurred in addition to N-phthaloylation as the peaks around 1240-1300  $\text{cm}^{-1}$  were also observed. Previous work by Kurita et. al [25], showed similar indication of O-Phthaloylation. From Figure 2, two sets of peaks appear on the  $^1\text{H}$  NMR spectrum of PhCh. Kurita et. al [18] have also obtained similar sets of peaks whereby the first set centered at 3.0 ppm corresponding to the hydrogen from chitosan backbone. The other set of peaks centered at 7.5 ppm is attributed to the hydrogen from the phthaloyl aromatic ring. Thus, both FTIR and  $^1\text{H}$  NMR spectra verified that phthaloylation of chitosan has occurred.

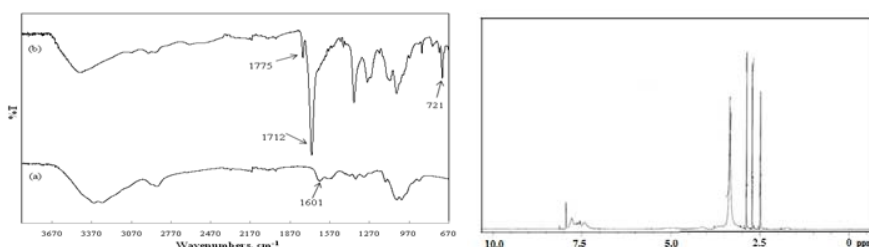


**Figure 1:** FT-IR spectra of (a) pure chitosan and (b) synthesized N-phthaloylchitosan. **Figure 2:**  $^1\text{H}$  NMR spectra of the phthaloylated chitosan.

### 3.2 Impedance spectroscopy

The plot of conductivity values of PhCh based polymer electrolyte as a function of LiI salt concentration at room temperature is shown in Figure 3. After 10 wt.% of LiI is added, the conductivity increases to  $4.07 \times 10^{-8} \text{ S cm}^{-1}$  compared to the conductivity value of pure PhCh film which is  $1.80 \times 10^{-10} \text{ S cm}^{-1}$ . The conductivity is observed to increase gradually with LiI concentration. The highest conductivity exhibited is  $1.88 \times 10^{-4} \text{ S cm}^{-1}$  for PhCh - 50 wt.%LiI. The increment in conductivity is due to the increase in number of free mobile ions [26]. Mishra et. al[27], studied PEO-PVA using the same salt and found that conductivity increased by four to five orders of magnitude when LiI concentration is doubled from 10 to 20 mole %. On addition of more than 50 wt.%LiI, a free standing film cannot be formed. Thus, in this work, preparation of polymer electrolyte was stopped until 50 wt.% of LiI which exhibited the highest conductivity. In order to improve the efficiency of the DSSCs, various percentages of ionic liquid, 1-butyl-3-methylimidazolium, has been added into the most conducting polymer electrolyte, 50 wt.%PhCh with 50 wt.% of LiI. Although ionic liquid possess some drawbacks such as evaporation, volatility, and corrosion which are known critical factors that limit the long-term stability of the DSSC [28], the best way to use it as solid electrolyte in DSSC is to dope the ionic liquid into the polymeric matrix and develop free standing polymer electrolyte film [29]. Figure 4 shows the ionic conductivity of 50 wt.%PhCh - 50 wt.% of LiI doped with various concentrations of ionic liquid at room temperature. After 2.5 wt.% of ionic liquid has been doped into the solid polymer electrolyte, the ionic conductivity value increases to  $6.94 \times 10^{-4} \text{ S cm}^{-1}$  compared to the free ionic liquid film,  $1.88 \times 10^{-4} \text{ S cm}^{-1}$ . This enhancement in conductivity is attributed to the enhanced concentration of free ions from ionic liquid doping [29]. After more than 2.5 wt.% of ionic liquid was introduced, the conductivity value decreased to  $4.08 \times 10^{-5} \text{ S cm}^{-1}$ .

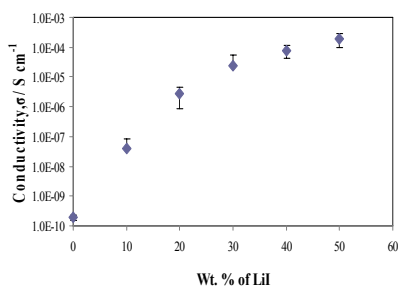


**Figure 3:** Effect of LiI concentration on the conductivity of PhCh-LiI at room temperature

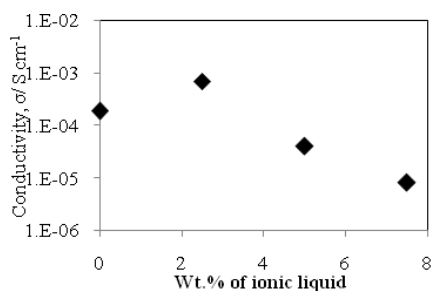


**Figure 4:** Variation of ionic conductivity with wt.% of ionic liquid in PhCh-LiI solid polymer electrolyte system at room temperature.

### 3.5 Solar cell

The electrolyte composition that gives the highest conductivity, 48.75 wt. % PhCh – 48.75 wt. % LiI – 2.5 wt.% IL was prepared with iodine crystal (1 wt.% the mass of LiI) added to the solution. The film was then used for the fabrication of a DSSC. In this work, natural dye was used instead of the synthetic sensitizer, ruthenium polypyridyl complexes, which is harmful to the environment, complicated to synthesize and is also costly. The natural dye in this work has been extracted from black rice and red cabbage. The current-voltage characteristics of the cells at pH 1 are shown in *Figure 5*. pH of the dye was set to 1 following the works of Buraidah et. al [30]. Extracted dye from black rice gave a wider area curve compared to the extracted dye from red cabbage. The comparison of DSSC parameters such as short circuit photocurrent ( $I_{SC}$ ), open-circuit voltage ( $V_{OC}$ ), fill factor (FF) and efficiency ( $\eta$ ) are shown in *Table 1*. From *Figure 5* and *Table 1*, it can be seen that both solar cells have the same efficiency in converting sunlight to electricity.

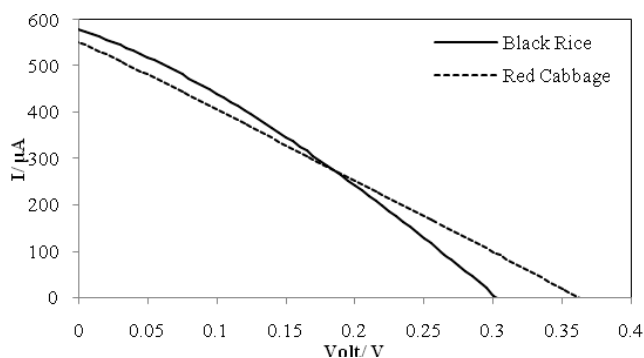


**Figure 5:** Current-voltage curves of DSSC using extracted dye from black rice and red cabbage

**Table 2:** Performance of DSSCs using natural dyes at pH 1

Dyes	$V_{oc}/V$	$I_{sc}/mA$	$J_{sc}/mA\ cm^{-2}$	FF	$\eta$
Black Rice	0.30	0.58	2.31	0.30	0.21
Red Cabbage	0.35	0.55	2.20	0.26	0.20

Figure 6 shows the absorption spectra of the acid-treated dyes extracted from black rice and red cabbage. The maximum absorption peak value of black rice is at the wavelength of 532 nm. However, the absorption spectrum of the red cabbage shows maximum absorption value at 526 nm. In acidic solution it will show red flavylium form ( $TiA^+H$ ) and purple deprotonated quinonoidal form ( $TiA$ ) as pH increases [23]. According to Bakowska et. al [23,31], at pH below 2, anthocyanin exists as flavylium ions, the stable form of anthocyanin and increasing the pH will hydrate this ion to quinonoidal bases. These compounds are labile and can be transformed into colorless carbinolpseudobase and chalcone.

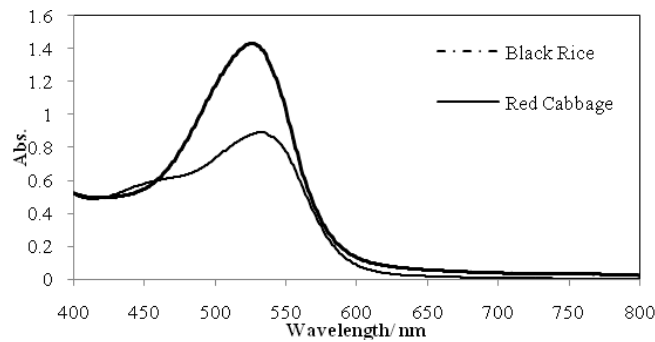


**Figure 6:** UV spectra of dye extracted from black rice and red cabbage

The difference in the absorption characteristic is due to the different types of anthocyanins and colors of the extracts [32]. The difference in colors of the dye has been observed as the color of the dye extracted from black rice is purplish-red and from red cabbage is reddish-maroon. Figure 7 (a) exhibited the chemical structure of anthocyanin mainly present in red cabbage. However, anthocyanin extracted from black rice was identified as containing cyanidin-3-glucoside and peonidin-3-glucoside [33] and the chemical structures are shown in Figure 7(b). It can be seen that structure of anthocyanin in red cabbage extract has longer group attached at the middle heterocyclic ring, compared to that of cyanidin-3-glucose and peonidin-3-glucose complexes in black rice extract. This results in a stronger steric hindrance for anthocyanin to form bond with the oxide surface and prevents the anthocyanin molecules from arraying on the  $TiO_2$  layer effectively [22]. These lead to a deficiency of electron transfer from dye molecule to conducting band of  $TiO_2$ .

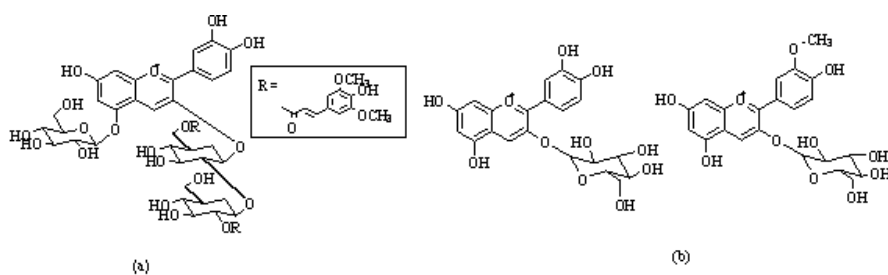


Figure 7: Chemical structure of dye mainly present in (a) red cabbage [36] and (b) black rice

#### 4. CONCLUSIONS

N-phthaloylchitosan was successfully synthesized and its structure has been verified by FTIR and <sup>1</sup>H NMR spectra. The highest conductivity  $1.88 \times 10^{-4} \text{ S cm}^{-1}$  was exhibited by the 50 wt.% PhCh - 50 wt.% LiI. The 50 wt.% PhCh-50 wt.% LiI polymer electrolyte was applied in a DSSC. A natural dye (anthocyanin) was obtained from two sources, black rice and red cabbage. The pH value of the dye was adjusted to 1. The fill factor is 0.30 and 0.26 for DSSC with dye extracted from black rice and red cabbage, respectively. The DSSC utilizing anthocyanin from the two sources exhibit the same efficiency.

#### 5. ACKNOWLEDGEMENTS

The author thanks the University of Malaya for the travel assistance to attend Solar Asia 2011.

#### REFERENCES

1. M.H. Buraidah, L.P. Teo, S.R. Majid, A.K. Arof. *Physica B* 404 (2009) 1373–1379
2. M.H. Buraidah, L.P. Teo, S.R. Majid, A.K. Arof. *Optical Mater.* 32 (2010) 723–728
3. S.B. Aziz, Z.H.Z. Abidin, A.K. Arof. *Physica B* 405 (2010) 4429–4433
4. S.A. Mohamad, R. Yahya, Z.A. Ibrahim, A.K. Arof. *Sol. Energy Mater. Sol. Cells* 91 (2007) 1194–1198
5. X.L. Wang, Y. Huang, J. Zhu, Y.B. Pan, R. He, Y. Zhong Wang, *Carbohydr. Res.* 344 (2009) 801
6. U. Janciauskaite, R. Makuska, *Chemija* 2 (2008) 35
7. L. Liu, Y. Li, Y. Li, Y.E. Fang, *Carbohydr. Polym.* 57 (2004) 97
8. M.A. Garcia, A. Pinoth, M. Martino, N. Zaritzky, *Food Hydrocolloids* 23 (2009) 722
9. R. Yoksan, M. Akashi, S. Biramontri, S. Chirachanchai, *Biomacromolecules* 2(2001) 1038
10. V. Tangpasuthadol, N. Pongchaisirikul, V. P. Hoven, *Carbohydr. Res.* 338 (2003) 937
11. D.K. Rout, S.K. Pulapura, R.A. Gross, *Biomolecules* 26 (1993) 5999
12. J.M. Zohuriaan, *Iranian Polymer Journal* 14 (2005) 253
13. V.K. Mourya, N.N. Inamdar, *React. Funct. Polym.* 68 (2008) 1013
14. K.V. Harish Prashanth, R.N. Tharanathan, *Trends Food Sci. Technol.* 18 (2007) 117
15. F. Bian, L. Jia, W. Yu, M. Li, *Carbohydr. Polym.* 76 (2009) 454
16. S.A. Mohamad, M. H. Ali, R. Yahya, Z. A. Ibrahim, A. K. Arof, *Ionics* 13 (2007) 235

17. J.N. Freitas, C. Longo, A.F.Nogueira, M. A. Paoli, Sol. Energy Mater. Sol. Cells 92 (2008) 1110
18. E.Chatzivasiloglou, T.Stergiopoulos, A.G. Kontos, N. Alexis, M.Prodromidis, P.Falaras, J. Photochem. Photobiol. A 192 (2007) 49
19. D. Saikia, C.C.Han, Y.W.Chen-Yang. J. Power Sources 185 (2008) 570
20. O.A.Iperuma, M.A.K.L. Dissanayake, S.Somasunderam. L.R.A.K. Bandara, Sol. Energy Mater. Sol. Cells 84 (2004) 117
21. A.C. Ovando, M.L.P. Hernandez, M.E.P. Hernandez, J.A. Rodriguez. C.A.G. Vidal, Food Chem. 113 (2009) 859
22. S. Hao, J. Wu, Y. Huang, J. Lin. Sol. Energy 80 (2006) 209
23. K. Kurita, H. Ikeda, M. Shimojoh, J. Yang, Polym. J. 39 (2007) 945
24. V.L. Finkenstadt, Appl. Microbiol. Biotechnol. 67 (2005) 735
25. G. Calogero, G. D. Marco, Sol. Energy Mater. Sol. Cells 92 (2008) 1341
26. M.Z.A. Yahya, A.K. Arof, Eur. Polym. J. 38 (2002) 1191
27. R. Mishra, N. Baskaran, P.A. Ramakrishnan, K.J. Rao. Solid state Ionics 112 (1998) 261
28. P.K. Singh, N.A. Jadhav, S.K. Mishra, U.P. Singh, B. Bhattacharya. Ionics 16 (2010) 645–648
29. P.K. Singh, B. Bhattacharya, R.K. Nagarale, S.P. Pandey, K.W. Kim, H.W. Rhee. Synthetic Metals 160 (2010) 950–954
30. M.H. Buraidah, L.P. Teo. S.R. Majid, R. Yahya, R.M. Taha, A.K. Arof, Int. J. Photoenergy (2010) 1
31. A.M. Baruah, A. Karmakar, J. B. Barua, Polyhedron 26 (2007) 4479
32. K. Wongchareea, V. Meeyooa, S. Chavadej. Sol. Energy Mater. Sol. Cells 91 (2007) 566
33. X. Xia, W. Ling, J. Ma, M. Xia, M. Hou, Q. Wang, H. Zhu, Z. Tang. American Society for Nutrition J. Nutr. 136 (2006) 2220-2225

**QUASI SOLID-STATE SOLAR CELLS CONTAINING NOVEL GEL POLYMER  
ELECTROLYTE BASED ON POLYACRYLONITRILE AND  
TETRAHEXYLAMMONIUM IODIDE SALT**

T. SVENSSON<sup>1</sup>, T.M.W.J. BANDARA\*<sup>1,2,3</sup>, E. LUNDELL<sup>1</sup>, I. SVENSSON<sup>1</sup>, M. FURLANI<sup>1</sup>,  
I. ALBINSSON<sup>3</sup>, B.-E. MELLANDER<sup>1</sup>

<sup>1</sup>Department of Applied Physics, Chalmers University of Technology, Gothenburg, Sweden

<sup>2</sup>Department of Physical Sciences, Rajarata University of Sri Lanka

<sup>3</sup>Department of Physics, University of Gothenburg, Gothenburg, Sweden

\*Corresponding Author, e-mail: [awijendr@yahoo.com](mailto:awijendr@yahoo.com)

**ABSTRACT**

Solar cells provide a convenient method to convert solar energy directly into electricity. The iodide ion conduction in gel polymer electrolytes and performance of dye sensitized solar cells containing such an electrolyte can be enhanced by incorporating an iodide having a bulky cation into the electrolyte. Gel polymer electrolytes, based on PAN host polymer were prepared by incorporating the salt, Hex<sub>4</sub>N<sup>+</sup>I<sup>-</sup>, and plasticizers ethylene carbonate (EC) and propylene carbonate (PC). The electrolyte containing 120% salt with respect to PAN weight showed the highest conductivity. This optimum electrolyte showed a glass transition at -102.3 °C and a conductivity of 2.0×10<sup>-3</sup> S cm<sup>-1</sup> at 25 °C. The predominant ionic behaviour of the conduction in the electrolyte was inferred from the *dc* polarization data. In addition, cationic transport is negligible and hence the dominant iodide ion transport makes sure the potential for using this PAN/EC/PC:Hex<sub>4</sub>N<sup>+</sup>I<sup>-</sup> polymer electrolyte in DSSCs. Four different cells were fabricated employing different preparation methods. The best cell showed 1.48% energy conversion efficiency and 4.56 mA cm<sup>-2</sup> of short circuit current density.

**1. INTRODUCTION**

The mostly used energy resources today are fossil fuels and nuclear energy. The excessive consumption of fossil fuels during the last few decades and uneven distribution of fossil fuels in the world have arouse serious environmental problems, mainly due to the emission of green house gases and many other pollutants while nuclear power is troubled with safety issues in addition to problems associated with radioactive waste [1]. To overcome these problems, development of renewable, clean energy sources are essential. In this regard, utilization of solar energy is a good alternative. Solar cell has been considered as an easy and potentially economical method to convert solar energy directly to electricity. However, the high cost of the Si based solar cell is an obstacle to utilize it universally. Hence, the low cost dye sensitized solar cell (DSSC) is an attractive alternative to fulfilling future energy needs [2]. The efficiency of such cells needs to be improved to make commercially credible dye sensitized solar cells. This study is focused on preparing a gel polymer electrolyte for DSSCs due to many favorable characteristics of gel polymer electrolytes for photo-electrochemical (PEC) solar cells [3,4].

Gel polymer electrolytes intended for PEC solar cells have been investigated using various host polymers and plasticizers incorporating different iodides [4,5,6]. The reports on incorporation of different alkaline metal iodides MI (M = Li, Na, K, Cs) in PAN based [7] and PEO based [8] polymer electrolytes for PEC solar cells are interesting. Studies on electrolytes based on PAN have reported that the short circuit photocurrent density ( $J_{SC}$ ) enhances with increasing size of the cation (M<sup>+</sup>) for Li, Na, K and Cs. This can be understood, because the mobility of the anion (I<sup>-</sup> ion) depends on the interaction between the M<sup>+</sup> ion and the polymer [9]. The larger the size of the cation the stronger is the interaction with the polymer due to viscous forces [7]. In addition, the cations in the electrolyte coordinate with hetero-atoms in the polymer (nitrogen for PAN) and larger cations have higher coordination numbers. The study on PEO based gel polymer electrolyte

with different alkyl metal iodides reports a conductivity enhancement with cation size for all alkali iodides but CsI. The application of these electrolytes in DSSCs reveals a clear improvement of the open circuit voltage with size of the cation. Thus, it is evident that in general conductivity of iodide ion conducting gel polymer electrolytes and performance of DSSCs containing such an electrolyte can be enhanced by incorporating an iodide salt containing a bulky cation in the electrolyte.

Consequently, quaternary-ammonium iodides are attractive material to be used in electrolytes intended for PEC solar cells possibly owing to the larger size of the cation. For instance, tetrapropylammonium iodide ( $\text{Pr}_4\text{N}^+\text{I}^-$ ) has been used with PEO and with PAN host polymers and reasonably good cell performance have been reported, reaching about 3% overall cell efficiency, for PAN based electrolytes [10]. DSSCs containing PAN and tetrabutylammoniumiodide ( $\text{Bu}_4\text{N}^+\text{I}^-$ ) salt have also been reported to show very good cell performance reaching 5.3% cell efficiency [6,7]. The ionic radii of  $\text{Pr}_4\text{N}^+$  and  $\text{Bu}_4\text{N}^+$  ions are 4.6 and 5.0 Å respectively and thus significantly larger in the size than the alkali-metal ions [11,12]. When the size of the cation increases it enhances the salt solvation and anion transference number leading to high iodide ion conductivity which is important to improve the performance of the solar cell. In an earlier work by us, the use of  $\text{Hex}_4\text{N}^+\text{I}^-$  with PEO host polymer for the electrolytes for all-solid solar cells was reported [13]. For the present work,  $\text{Hex}_4\text{N}^+\text{I}^-$  salt was selected to be used with PAN host polymer to fabricate a gel polymer electrolyte for PEC solar cells expecting higher  $\text{I}^-$  ion conductivity and PEC solar cell performance owing to the larger size of the cation. In general, gel polymer electrolytes can have better conductivities than solid-state electrolytes, hence quasi solid-state DSSCs having such gel electrolytes has reported higher efficiencies than all solid-state DSSCs [2,4,5,13,14]. In this study, gel polymer electrolytes were fabricated using  $\text{Hex}_4\text{N}^+\text{I}^-$  salt, PAN host polymer and the plasticizers ethylene carbonate (EC) and propylene carbonate (PC) and they were characterized by using thermal and electrical measurements. Finally, quasi solid-state solar cells were fabricated using an optimized electrolyte for the conductivity and the cells were characterized by using  $V$ - $I$  curves.

## 2. EXPERIMENTAL

PAN,  $\text{Hex}_4\text{N}^+\text{I}^-$ , iodine chips ( $\text{I}_2$ ), and EC and PC all with purity greater than 98%, purchased from Aldrich, were used as starting materials. PAN and  $\text{Hex}_4\text{N}^+\text{I}^-$  were vacuum dried for 24 hours in a vacuum oven at 50 °C prior to use. For preparing the electrolyte samples the weights of PAN (0.1 g), EC (0.4 g) and PC (0.4 g) were kept unchanged and the weight of  $\text{Hex}_4\text{N}^+\text{I}^-$  was varied to determine the composition giving optimum conductivity. The weight of iodine in the electrolyte was maintained so that the molar ratio  $\text{Hex}_4\text{N}^+\text{I}^- : \text{I}_2$  is 10:1. The samples were prepared using the hot press method. The selected compositions of chemicals were heated to about 80 °C and magnetically stirred for few minutes until a homogeneous viscous solution was obtained. The resulting slurry was cast on to a glass plate and pressed by another glass plate in order to obtain polymer electrolyte film for measurements. The complex impedance measurements were performed using a HP 4292 ARF impedance analyzer in the frequency range of 10 Hz – 10 MHz and in the temperature range of 20 °C to 80 °C. Disc shaped electrolyte films of diameter ~10.5 mm and thickness 0.1-0.4 mm, sandwiched between two polished stainless steel blocking electrodes, were used for impedance measurements. The DC polarization test was carried out at room temperature by sandwiching a disc shaped electrolyte sample between two stainless steel blocking electrodes. The thermal properties of the samples were analyzed using a Mettler Toledo DSC 30 differential scanning calorimeter between -140 °C to 100 °C in consequent heating and cooling cycles, with a rate of 10 °C  $\text{min}^{-1}$ .

A TiO<sub>2</sub> compact-layer was coated on fluorine-doped tin oxide (FTO) glass ( purchased from Solaronix SA) using a solution containing 5 ml titanium isopropoxide, 30 ml methanol, 5 ml acetic acid and 4 drops of concentrated nitric acid. The resultant transparent solution was then spin-coated onto well cleaned FTO conducting glass plate at 3000 rpm for 60 s followed by annealing in air at 450 °C for 30 minutes. This procedure was repeated twice to get the desired compact layer thickness. A TiO<sub>2</sub> nano-porous layer was coated on a FTO glass or on a compact TiO<sub>2</sub> layer using Degussa P25 powder. For porous layer preparation, 0.5 g of Degussa powder (TiO<sub>2</sub>) was ground well for ~30 minutes with ~2 ml of HNO<sub>3</sub> (pH = 1) in an agate motor. The resulting colloidal suspension was diluted to get a 5% (W/V) solution and subsequently, it was stirred overnight at 60 °C. Then ~0.1 g of carbowax and a few drops of Triton X 100 (surfactant) were added and mixed well. This colloidal suspension was used to prepare a porous TiO<sub>2</sub> film with a thickness of 5-10 µm using doctor blade method. The coated TiO<sub>2</sub> were sintered at 450 °C for 30 min.

Quasi solid-state PEC solar cells were fabricated by sandwiching polymer electrolyte films of thickness from 0.1 to 0.4 mm between the dye-coated TiO<sub>2</sub> electrode and a previously prepared platinized FTO electrode in the configuration Glass/FTO/TiO<sub>2</sub>/Dye/Electrolyte/Pt/FTO/Glass. Four different cells were fabricated with different cell preparation methods. Cell-1 was fabricated using a photo-electrode having a porous TiO<sub>2</sub> layer only. Cell-2 was fabricated using a photo-electrode having a porous TiO<sub>2</sub> layer on the spin coated TiO<sub>2</sub> layer. Cell-3 was fabricated in the same way as Cell-1, however the cell was annealed to 50 °C enabling the electrolyte to go into the pores in the TiO<sub>2</sub> electrode. In Cell-4 the Pt counter electrode, was painted directly on the electrolyte as well as on the FTO glass. All the fabricated solar cells were characterized by measuring *V-I* curves using a computer controlled eDAQ Potentiostat and e-Coder under ~1000 W m<sup>-2</sup> irradiation (1.5 AM) with a LOT-Oriel GmbH solar simulator.

### 3. RESULTS AND DISCUSSION

Fig. 1 shows the conductivity Arrhenius plots for PAN/EC/PC: Hex<sub>4</sub>N<sup>+</sup>I<sup>-</sup> electrolyte samples for different PAN: Hex<sub>4</sub>N<sup>+</sup>I<sup>-</sup> = 100: *x* mass fractions up to 120% mass fraction. Out of these samples, the highest conductivity is shown for the electrolyte sample containing 120 wt% Hex<sub>4</sub>N<sup>+</sup>I<sup>-</sup> for all the measured temperatures. Subsequent conductivity Arrhenius plots for salt mass fractions from 120 to 200% is shown in Fig. 2. All the samples shown in Fig. 2, which represent high salt concentration, have reasonably good conductivities. However, 120% and 140% salt containing electrolytes seems to have slightly higher conductivities especially at low temperatures. The trend is not very significant in Fig. 2. The sample with 120% Hex<sub>4</sub>N<sup>+</sup>I<sup>-</sup> has an ionic conductivity of 2.0 × 10<sup>-3</sup> S cm<sup>-1</sup> at 25 °C and 2.9 × 10<sup>-3</sup> S cm<sup>-1</sup> at 50 °C. The conductivity variation with inverse temperature shows more or less Arrhenius behaviour within the measured temperature range. Hence, the activation energy, *E<sub>a</sub>*, was calculated fitting the data to the Arrhenius equation.

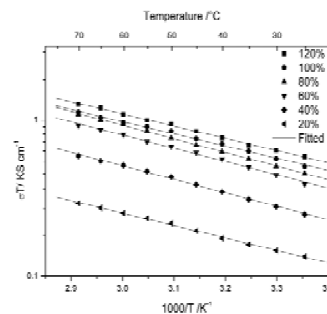


Fig. 1.  $\sigma T$  versus  $1000/T$  for PAN/EC/PC electrolytes containing *x* wt % of Hex<sub>4</sub>N<sup>+</sup>I<sup>-</sup> with respect to PAN mass fraction. The fitted lines to the Arrhenius equation are also shown.



$$\sigma T = B \exp\left(-\frac{E_a}{k_B T}\right) \quad (1)$$

where,  $B$  is a pre-exponential factor,  $E_a$  the activation energy,  $k_B$  the Boltzmann constant, and  $T$  the absolute temperature. The fitted curves are also shown in Figures 1 and 2 and  $E_a$  values calculated are given in Table 1. Highly conducting samples have shown lower activation energies as expected.

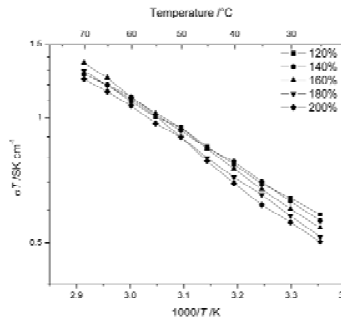


Fig. 2.  $\sigma T$  versus  $1000/T$  for PAN/EC/PC electrolytes containing  $x$  wt % of  $\text{Hex}_4\text{N}^+\text{I}^-$  with respect to weight of PAN.

Fig. 3 shows the variation of ionic conductivity as a function of the mass fraction of the salt ( $x$  %) with respect to PAN at temperatures 30, 40, 50, 60, and 70 °C. A conductivity increase is shown for the low salt compositions more or less up to 120% salt composition. However, the conductivity increase is more significant for the salt compositions up to 60%. This conductivity increase with added salt can be attributed basically to increase of both the number of charge carriers and their mobility with the increasing amount of  $\text{Hex}_4\text{N}^+\text{I}^-$ . The mobility increase in this region may be due to the disorder imposed by added ions. The low conductivity increase shown for salt mass fractions from 60% to 120% may be the result of a decline of the increase of mobile ions due to increase of ion association with the increasing number of ions in the electrolyte. 120% salt containing electrolyte with respect to PAN weight shows the highest conductivity at least at low temperatures and this sample gave the minimum activation energy according to values given in Table 1. Hence, further addition of salt may not significantly contribute to the conductivity increase owing to very little increase of the number of dissociated ions at these concentrations and the decline of mobility possibly due to increase of ion-ion interactions. In this concentration region non-dissociated salt in the electrolyte may also impose a blocking effect to ion mobility. The effect of this none dissociated salt is not clearly visible in the conductivity plots shown in Fig. 3. However, graphs of equivalent conductivity (molar conductivity) versus square root of salt concentration of the electrolyte as described in detail for other polymer systems is interesting [15,16]. According to graphs (not shown) of equivalent conductivity (molar conductivity) versus square root of the salt concentration of this system, the equivalent conductivity shows a maximum at the 60% salt containing sample. The conductivity variation with salt composition cannot be described by carrier concentration alone as there can be mobility contributions which can to some extent be understood by thermal studies. Even though maximum conductivity is shown for the sample with 120 % salt mass fraction at 30 °C, this maximum has deviated towards high salt composition for high temperatures which can be attributed to the increase of salt solvation with increasing temperature (or increase of dissociation constant). However, this trend is not very significantly apparent in Fig. 3.

Table 1. The activation energy,  $E_a$ ,  $T_g$ , for samples containing different mass fractions of,  $x$  wt%, of Hex<sub>4</sub>N<sup>+</sup>I<sup>-</sup>.

$x$ wt%	20	40	60	80	100	120	140	160	180	200
$E_a$ /eV	0.16	0.17	0.17	0.17	0.16	0.15	0.16	0.18	0.18	0.18
$T_g$ /°C	-101.68	-101.75	-101.77	-101.9	-101.94	-102.3	-102.19	-102.04	-101.95	-101.9

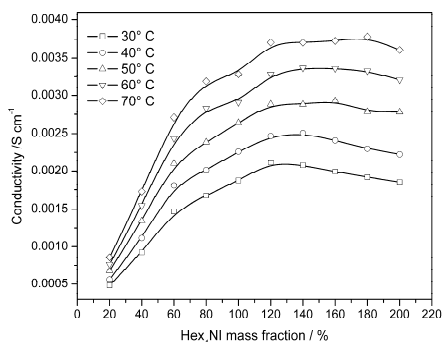


Fig. 3. Conductivity as a function of salt mass fraction with respect to PAN in PAN/EC/PC electrolyte for different temperatures.

crystallization peaks in the DSC cycles for samples containing more than 120% salt can be attributed to the effects imposed by the phase containing non-dissociated salt which possibly hinders the conductivity increase as shown in Fig. 3. It seems that the samples are undercooled during the cooling and thus the crystallization appears during the heating. A clear glass transition can be observed for all samples. The glass transition temperatures,  $T_g$ , obtained in this work using 2<sup>nd</sup> heating cycle is shown in Table 1 and the obtained  $T_g$  values appear around -100 °C as reported in literature for PAN/EC/PC electrolytes for other salt systems [17].

Since  $T_g$  is related to the segmental flexibility of the host polymer and the disordered structure [18,19], the  $T_g$  result can be related to a change in the segmental flexibility of polymeric chains of the electrolyte. Hence finally,  $T_g$  can be related to the mobility of charge carriers [20]. The minimum value  $T_g$ , -102.3 °C was observed for the electrolyte containing 120 wt% Hex<sub>4</sub>N<sup>+</sup>I<sup>-</sup> with respect to weight of PAN and as expected this salt concentration gives the maximum conductivity. For salt concentrations less than 120%, the  $T_g$  is higher and with increase of salt concentration the  $T_g$  decreases probably due to structural disorder caused by bulky Hex<sub>4</sub>N<sup>+</sup> and I<sup>-</sup> ionic species added. This shows the contribution to the ionic conductivity enhancement due to structural modifications caused by the salt added. Hence, the conductivity increase shown in Fig. 3 is in part contributed by the increase of mobility due to the increase of segmental flexibility made

Fig. 4 shows the differential scanning calorimetric (DSC) thermograms of gel polymer electrolyte samples with different Hex<sub>4</sub>N<sup>+</sup>I<sup>-</sup> mass fractions ( $x$  %) for the 2<sup>nd</sup> heating run. There were minor dissimilarities between DSC thermograms obtained during the 1<sup>st</sup> and the 2<sup>nd</sup> heating runs. The measurements of samples obtained during the 2<sup>nd</sup> cycle were selected for this study in order to eliminate the negative impact of thermal history. In the DSC thermograms shown in Fig. 4, a 1<sup>st</sup> order phase transition is observed in particular for the samples with high Hex<sub>4</sub>N<sup>+</sup>I<sup>-</sup> concentrations (more than 120%). The existence of very significant melting and

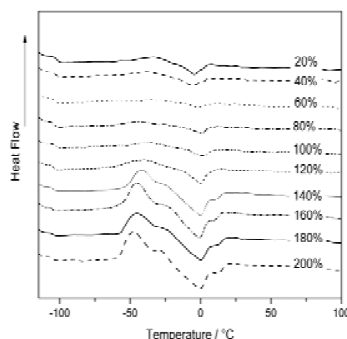


Fig. 4. DSC thermograms of PAN/EC/PC polymer electrolytes containing  $x$  wt % of Hex<sub>4</sub>N<sup>+</sup>I<sup>-</sup> with respect to PAN weight.

evident by the decrease of the  $T_g$  and an increasing amount of ionic species. When the salt concentration is increased further (more than 120%), the  $T_g$  shows an increase. This could possibly be due to the “geometrical constrictions” imposed by non-dissociated  $\text{Hex}_4\text{N}^+\text{I}^-$  grains, making the long PAN chains “immobilized”. The subsequent decline of conductivity increase shown for higher salt concentration (more than 120%) in Fig. 3 is explained by these geometrical constrictions.

DC Polarization measurements [21] using 1.0 V *dc* bias voltage and stainless steel (SS) blocking electrodes in the SS/Electrolyte/SS configuration showed the predominantly ionic nature (more than 90%) of the electrolyte. Polarization measurements in the SS/I<sub>2</sub>/Electrolyte/I<sub>2</sub>/SS symmetrical configuration showed no appreciable current drop during a time period of a few hours, ensuring that the electrolyte is predominantly an iodide ion conductor. Therefore, in this system the transference number of the  $\text{Hex}_4\text{N}^+$  ion is very small possibly owing to the large size of the ion. Hence, this electrolyte can be suitable for PEC solar cells.

The *V-I* characteristic curves for the cells fabricated using PAN based gel-typed electrolyte containing 120 wt%  $\text{Hex}_4\text{N}^+\text{I}^-$  at room temperature are shown in Fig. 5. Four different cells were fabricated employing different preparation methods. The short-circuit photocurrent density ( $J_{\text{SC}}$ ) and open-circuit voltage ( $V_{\text{OC}}$ ) for a solar light intensity of  $1000\text{ W m}^{-2}$  for all the cells are shown in Table 2. The fill factor, *ff*, was calculated using;

$$ff = \frac{J_{\text{opt}} V_{\text{opt}}}{J_{\text{SC}} V_{\text{OC}}} \quad (2)$$

where,  $J_{\text{opt}}$  is the current density at maximum power output,  $V_{\text{opt}}$  the voltage at maximum power output. The fill factor and the energy conversion efficiency,  $\eta$ , of the cells are also included in table 2 for all cells.  $\eta$  is calculated using;

$$\eta = \frac{J_{\text{SC}} V_{\text{OC}} ff}{\text{Total incident power density}} \quad (3)$$

All cells exhibited energy efficiencies of more than 1.25%. The energy conversion efficiencies of these DSSCs are anyhow low compared with solar cells containing other gel polymer electrolytes with comparable ionic conductivity. The comparison of performance of solar cells fabricated in different laboratories is difficult since the cell performance is dependent on many parameters. However, the experimental results reveal that the photocurrent and cell efficiency increases slightly when the compact layer is introduced. This can be understood, since the compact  $\text{TiO}_2$  layer acts as a barrier for internal short-circuiting favouring the cell performance development while it reduces the dye absorption. The porous layer, on the other hand, contributes to dye adsorption. Cell- 3 showed a significant performance enhancement compared to Cell-1 as a result of the improvement of the electrolyte filling into the pores in the  $\text{TiO}_2$  electrode due to the heating and pressing procedure. As the measurements were done at room temperature this  $J_{\text{SC}}$  and efficiency enhancement of cell-3 is thus due to the improvement of the interfacial contact between  $\text{TiO}_2$  electrode and the electrolyte. In addition, an improved cell preparation method employed to enhance the interfacial contact between Pt electrode and electrolyte has worked well since the highest  $J_{\text{SC}}$ , and efficiency were

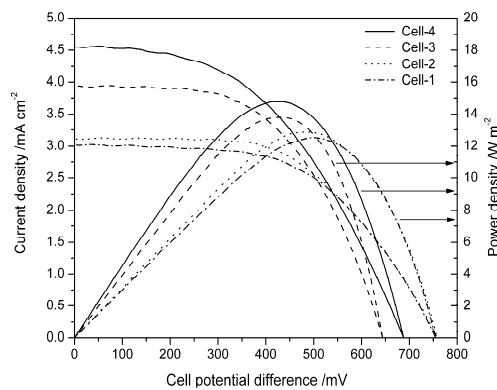


Fig. 5. Photocurrent versus cell potential difference curves for the four different DSSCs fabricated using PAN/EC/PC electrolyte containing 120 wt%  $\text{Hex}_4\text{N}^+\text{I}^-$  under irradiation of a  $1000\text{ W m}^{-2}$  Xenon lamp.

recorded for Cell-4. Since the major objective of this work was to fabricate a polymer electrolyte with a high iodide ion conductivity using a bulky *quaternary ammonium iodide* salt for PEC solar cells further studies of solar cells using this electrolyte would be interesting.

**Table 2.** The performance of Cell-1 , Cell-2, Cell-3 and Cell-4

cell	$J_{sc}$ /mA	$V_{oc}$ /mV	$J_{opt}$ /mA	$V_{opt}$ /mV	$ff$ /%	Power/ W cm <sup>-2</sup>	Efficiency /%
1	3.02	754	2.51	500	55.01	12.5	1.25
2	3.11	756	2.65	486	54.72	12.9	1.29
3	3.95	644	3.18	434	54.29	13.8	1.38
4	4.56	688	3.46	428	47.15	14.8	1.48

#### 4. CONCLUSIONS

A gel polymer electrolyte, based on PAN host polymer was prepared by incorporating the salt, Hex<sub>4</sub>N<sup>+</sup>I<sup>-</sup>, and plasticizers EC and PC. The electrolyte containing 120% salt with respect to PAN weight showed the maximum conductivity out of samples measured. This optimum conductivity electrolyte membrane showed  $2.0 \times 10^{-3}$  S cm<sup>-1</sup> conductivity at 25 °C and it has a low  $T_g$  value of -102.3 °C. The predominantly ionic behaviour of the conductivity in the electrolyte can be inferred from the *dc* polarization data. In addition, cationic transport is negligible and hence the dominant iodide ion transport makes sure the potential for using this PAN/EC/PC:Hex<sub>4</sub>N<sup>+</sup>I<sup>-</sup> polymer electrolyte in TiO<sub>2</sub> DSSCs. Four different DSSCs were fabricated using this optimized electrolyte. Cell-3 and Cell-4 exhibited better performance owing to the improved interfacial contact between electrodes and electrolyte. The best cell out of four cells, Cell-4, showed 1.48% energy conversion efficiency and 4.56 mA cm<sup>-2</sup> of short circuit current density. It should be possible to further improve the efficiency by optimizing the cathode using advanced fabrication methods and the research is in progress to investigate possible ways to enhance the energy conversion efficiency in such DSSCs.

#### 5. ACKNOWLEDGEMENTS

Research support from IRQUE project Faculty of Applied Sciences, Rajarata University of Sri Lanka and IPPS as well as from the Swedish Research Council are gratefully acknowledged.

#### REFERENCES

1. D. Abbott, *Proceedings of the IEEE*, Vol. 98- 1 (2010) 42.
2. B. Li, L. Wang, B. Kang, P. Wang, Y. Qiu, *Sol Energy Mater Sol Cells*, **90** (5) 549-573 (2006).
3. J. Wu, Z. Lan, D. Wang, S. Hao, J. Lin, Y. Huang, S. Yin, T. Sato, *Electrochim. Acta*, **51**, 4243 (2006).
4. T.M.W.J. Bandara, M.A.K.L. Dissanayake, I. Albinsson, B.-E. Mellander, *J Power Sources* **195**, (2010) 3730
5. O.A. Ileperuma, M.A.K.L. Dissanayake, S. Somasunderam, L.R.A.K. Bandara, *J Sol Energy Mater Sol Cells*, **84** (2004) 117.
6. O.A. Ileperuma, G.R.A. Kumara, K. Murakami, *Chemistry Letters*, **37**(1) (2008) 36-37.
7. K. Tennakone, G.K.R. Senadeera, V.P.S. Perera, I.R.M. Kottegoda, L.A.A.D. Silva *J Chem Mater* **11** (1999) 2474.

8. X. Shen, W. Xu, J.Xu, G. Liang, H. Yang, M. Yao, *Solid State Ionics* 179 (2008) 2027–2030.
9. P.G. Bruce, P.M. Gray, *Polymer Electrolytes II: Physical principle*, in: Bruce, PG (ed), *Solid State Electrochemistry*, Cambridge Press, Cambridge, (1995) 119-160.
10. M.A.K.L. Dissanayake, L.R.A.K. Bandara, R.S.P. Bokalawala, P.A.R.D. Jayathilaka, O.A. Ileperuma, S. Somasunderam, *Mater Res Bull*, 37 (2002) 867.
11. D.S. Gill *Electrochim Acta*, 24 (1979) 701-703.
12. A. Shimizu, Y. Taniguchi *Bull Chem Soc Jpn*, 63 (1990) 3255-3259.
13. T.M.W.J. Bandara, P. Ekanayake, M.A.K.L. Dissanayake, I. Albinsson, B.-E. Mellander, *J. Solid State Electrochem.* DOI 10.1007/s10008-009-0951-x
14. T.M.W.J. Bandara, M.A.K.L. Dissanayake, O.A. Ileperuma, K. Varapathan, K. Vignarooban, B-E. Mellander, *J. Solid State Electrochem*, 12 (2007) 913.
15. I. Albinsson, B.-E. Mellander, J.R. Stevens, *Solid State Ionics*, 60 (1993 ) 63.
16. I. Albinsson, B.-E. Mellander, J. R. Stevens, *Solid State Ionics*, 72 (1994),177
17. T.M.W.J. Bandara,, M.A.K.L. Dissanayake, I. Albinsson, B.-E. Mellander *Electrochim Acta*, 55 (2010) 2044.
18. Y. Tominaga, S. Asai, M. Sumita, S. Panero, B. Scrosati, *J. Power Sources*, 146 (2005) 402.
19. Y.-J. Wang, Y. Pan, L. Wang, M.-J. Pang, L. Chen, *Materials Letters*, 59 (2005) 3021.
20. S. Zhang, S. Dou, R.H. Colby, J. Runt, *J. Non-Crystalline Solids*, 351 (2005) 2825.
21. M. Watanabe, S. Nagano, K. Sanui, N. Ogata, *Solid State Ionics* 28-30 (1988) 911.

## NANOCRYSTALLINE TiO<sub>2</sub> PHOTO-SENSITIZED WITH NATURAL DYES

P. ABEYGUNAWARDHANA<sup>1</sup>, S. PALAMAKUBURA<sup>2</sup>, C.A. THOTAWATTAGE<sup>2</sup>,  
M.A.K.L. DISSANAYAKE<sup>2</sup> AND G.K.R. SENADEERA<sup>1,2\*</sup>

<sup>1</sup> Department of Physics, The Open University of Sri Lanka, Nawala, Nugegoda, Sri Lanka.

<sup>2</sup> Institute of Fundamental Studies, Hantana Road, Kandy, Sri Lanka

\* Corresponding Author, e-mail: gkrsena@yahoo.com

### ABSTRACT

Dye sensitized solar cells (DSSCs) are one of the most promising and fast developing photovoltaic technology, specially due to its low cost comparing with the other photovoltaic technologies. Generally DSSCs consist of ruthenium (II) polypyridine complexes as sensitizers of wide band gap semiconductors like TiO<sub>2</sub>. However the cost in synthesis of these dyes with rare metal complexes is still an expensive process. Therefore, many of the researchers including us have been investigating the possibilities to replace these expensive dyes with various materials like conducting polymers, natural dyes, etc. Therefore, in this work we extended our investigations employing natural dyes extracted from plants widely spread over the Sri Lankan territory.

Among the 65 studied natural dyes, *Hibiscus sabdariffa*, Fire fern (*Oxalis hedysaroides*), Begonia (Black velvet), and *Ficus salicifolia* sensitized solar cell showed comparatively higher photo responses. The short circuit current densities ( $J_{sc}$ ) were ranging from 2.4 to 0.9 mA cm<sup>-2</sup>, while the open circuit voltages varied from 565 mV to 425 mV. The highest efficiency obtained from *Hibiscus sabdariffa*, was  $\approx 0.5\%$ . However, dramatic enhancement in efficiency in these cells were obtained from the acid treated dye extracts with con HCl. The DSSCs fabricated with acid treated dye solution obtained from fire fern leaves showed  $\approx 1\%$  efficiency showing its promising usage in low cost DSSCs for novel disposable bio sensor applications at room temperature under low light conditions.

### 1. INTRODUCTION

Dye sensitized photoelectrochemical solar cells (DSSCs) are devices for the conversion of visible light into electricity based on sensitization of wide band gap semiconductors like TiO<sub>2</sub>. DSSC is assembled with a cathode of mesoporous nanocrystalline TiO<sub>2</sub> film on a conductive glass substrate anchored a monolayer of dyes, an anode of conductive glass coated with platinum and an electrolyte of certain organic solvents containing a redox couple such as iodide/triiodide. The adsorbed dye absorbs visible light and injects electrons into the conduction band of TiO<sub>2</sub>. Since dye plays an important role in absorbing visible light and transferring photon energy into electricity, much attention has been paid to survey the effective sensitizer dyes. No doubtedly, one of the most efficient sensitizers are synthetic dyes, such as ruthenium(ii) polpyridyl complexes with carboxylic ligands, since these compounds present intense and wide range absorption of visible light as well as suitable ground and excited state energy levels with respect to the band positions of TiO<sub>2</sub> and the redox potential of electron donor I<sup>-</sup>. (1). Apart from that many organic and inorganic dyes including natural dyes have employed in these devices but the performances of them in DSSCs were poor due to the weak binding nature to the semiconductor TiO<sub>2</sub> (2-6). However, in nature, fruits, flowers and leaves of plants show various colours from red to purple and contain various natural dyes. Because of the simple preparation techniques, widely source and low cost, natural dye as an alternative sensitizer for DSSCs is promising, specially for some practical applications such as usage of DSSCs in portable, disposable bio sensors (7-9). Therefore, the present work extends our investigations involving natural dyes as semiconductor sensitizers and reports some of the dyes which can be used successfully in DSSCs as sensitizers aiming to use them in fabrication of low cost bio sensors.

## **2. EXPERIMENTAL**

### *2.1 Extraction of pigments*

Petals of flowers and barks of trees chosen were cut into small pieces and extracted into ethanol (Fluka, 96%(v/v)), by keeping for overnight. Then residual parts were removed by filtration and the filtrate was washed with hexane several times to remove any oil or chlorophyll present. The ethanol fraction was separated and divided into two solutions and one fraction was used as it was (without any further treatments) and the other fraction was treated with few drops of conc. HCl acid so that the solution color becomes more dark ( $\text{pH} < 1$ ). These solutions were directly used as the dye solutions for preparation of photovoltaic devices.

### *2.1 Preparation of $\text{TiO}_2$ electrodes*

Fluorine doped tin oxide (FTO) glass slides were cleaned well. The dimension of each glass slide was 2 cm x 0.5 cm.  $\text{TiO}_2$  (Degussa) powder of average particle size 25 nm was grounded well with Triton, acetic acid and ethanol. A thin film of the resultant mixture was deposited on FTO glass slides using the 'doctor blade method'. After leaving sometime for drying, only an area of 0.5 cm x 0.5 cm was left by scratching off the rest. Films were then sintered at 450°C for 45 minutes and cooled down to room temperature.

### *2.3 Fabrication of photo-electrochemical cells (PECs)*

Above  $\text{TiO}_2$  electrodes were dipped in each dye solutions for 12 hours. Dyed electrodes were then removed and rinsed with ethanol and dried using an airflow. DSSCs were constructed by introducing the redox electrolyte containing tetrabutylammonium iodide (TBAI)(0.5M) /  $\text{I}_2$  (0.05M), in a mixture of acetonitrile and ethylene carbonate (6:4, v/v) between the dyed  $\text{TiO}_2$  electrode and Platinum counter electrode.

### *2.4 Characterization*

UV-visible absorption measurements of dyes in ethanol were carried out with a Shimadzu dual wavelength/double beam spectrophotometer (model UV-3000). Current voltage ( $I$ - $V$ ) characteristics of the cells at  $100 \text{ mW cm}^{-2}$  (Am 1.5) were measured using a home made  $I$ - $V$  measuring setup coupled with Keithly 2000 multimeter in to HA-301 Potentiostat via computer controlled software. Xenon 500 W lamp was used with AM 1.5 filters to obtain the simulated sunlight with the intensity of  $100 \text{ mW cm}^{-2}$ . The  $I$ - $V$  curves were used to calculate the short-circuit photocurrent density ( $J_{sc}$ ), the open-circuit voltage ( $V_{oc}$ ), the fill factor ( $FF$ ), and the energy conversion efficiency ( $\eta$ ) of DSSC.

## **3. RESULTS AND DISCUSSIONS**

Figure 1 (A) shows the UV-visible absorption spectra of different dye extracts in ethanol. Since the purpose of this study is to use the dye extracts without any pigmental isolation, elucidation of exact structures were not carried out in this stage. However, according to the literature (10,11 ) the red extracts obtained from fire fern, begonia black velvet and hibiscus sabdariffa, which have the main absorption wave bands at 500 to 580 nm, it would be possible to presume that all these dyes contain cyanidin, peonidin, pelargonidin, malvidin, delphinidin, quercetin and flavonol co-pigments. Further, since the red-coloured varieties would contain lower content of delphinidin derived pigments, but a more variable amount of flavonolglycosides, the extracts obtained from above species should contain higher concentrations of above pigments.

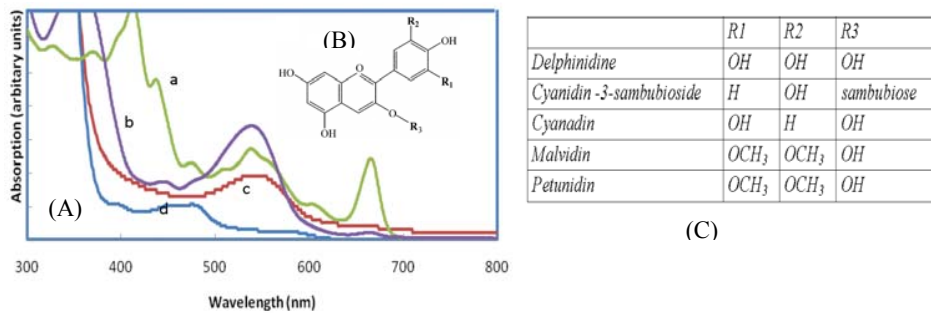


Figure 1. (A) UV-visible absorption curves of (a) Fire fern (b) Begonia black velvet (c) Hibiscus sabdariffa, (d) Ficus salicifolia (B) and (C) Basic chemical structures of the most abundant anthocyanidins .

The other species employed in this study, orange-red coloured Ficus salicifolia , which mainly absorb in the region below 475 nm , would contain a large amount of cyanidin 3,5-O-diglucoside and relatively lesser amount of flavonol-glycosides (7,10,11 ). However, in general, can be seen from the figure, they all absorb in the visible part of the spectrum. In the case of extracts from fire fern the absorption is border than that of the others and it absorbs light from 400-700 nm with an absorption in higher wavelengths.

While figure 2 shows the current –voltage (I-V) curves of the DSSCs employed with different pigments as indicated, table 1 presents the performances of DSSCs in term of short-circuit photocurrent densities ( $J_{sc}$ ), open circuit voltage ( $V_{oc}$ ), fill factor (FF) and the power conversion efficiencies ( $\eta$ ). The efficiency of cell sensitized by the fire firm was significantly higher than DSSCs sensitized by the other pigments. This is in good agreement with the broader range of the light absorption of fire firm on TiO<sub>2</sub>, and higher interaction between TiO<sub>2</sub> and anthocyanin as depicted in the figure 4. The DSSCs employed with Ficus salicifolia dye has the lowest photoelectric conversion, which again agrees with the weaker absorption spectrum of the dye.

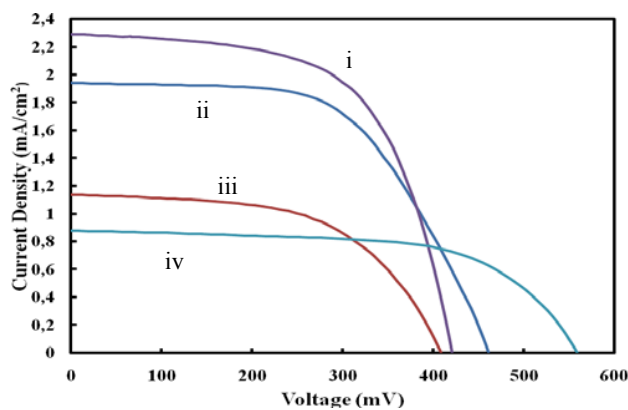






Figure 2. Current –voltage (I-V) characteristics of, (i) Fire fern (ii) Hibiscus sabdariffa (iii) Begonia black velvet (iv) Ficus salicifolia



**Table 1.** photovoltaic performances of DSSCs employed with extracted flower pigments

Name	$J_{sc}$ (mA $cm^{-2}$ )	$V_{oc}$ (mV)	FF	$\eta\%$	Flower/leave/bark
(a) Fire fern	2.354	422	49	0.49	
(b) Hibiscus sabdariffa	1.968	457	50	0.45	
(c) Begonia black velvet	1.140	408	56	0.26	
(d) Ficus salicifolia	0.864	565	52	0.25	

The effect of pH of these dye solutions were also investigated. The original pH of these extracted were found to be in the range from 3.00 to 4.5. However, in this preliminary studies pH of these extracts were changed to the values lower than 1 ( $pH < 1$ ) by adding trace amounts of conc HCl. Figure 3 (A) shows the chelation mechanism of anthocyanidins with  $TiO_2$  while figure 3(B) presents the possible reaction of the pigments with HCl as proposed by Hao *et al* (7). According to the literature, in an acidic solution, the oxonium ion results in an extended conjugation of double bonds through three rings of the aglycone moiety, which helps in the absorption of photons in the visible spectra. Addition of a base disrupts the conjugation of double bonds between the second and third rings and results in absorption of photons in the UV range, rather than in the visible range (7,10,11). Therefore, the change in pH on increasing the number of conjugated double bonds in the molecule, lowers the energy level of the electronic transition between the ground state and the excited states and in turn results in the absorption of photons at greater wavelength (Figure not shown).

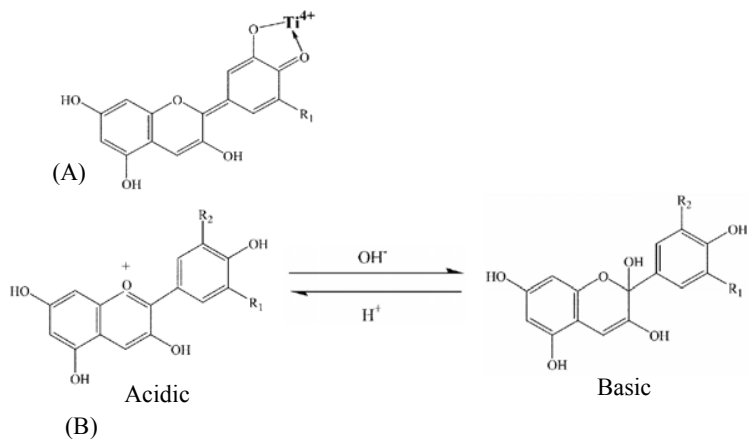


Figure 3 (A) Chelation mechanism of anthocyanidins with  $TiO_2$ , (B) Two chemical structures of anthocyanidins in acidic and basic media.

Figure 4 presents the  $I-V$  characteristics of the DSSCs employed with acidified pigment extracts. The photoelectric parameters of DSSCs sensitized with acidified extracts under the irradiance of  $100\text{ mW cm}^{-2}$  were summarized in table 2. As can be seen from the table, the acidity of dye solution is found to affect the resulting photocurrent values. Again, it can be seen from the data presented in the table 2, fire fern exhibits the best photoelectrochemical performances among the others. The photoelectric power conversion efficiency ( $\eta$ ) of DSSCs sensitized with acidified fire fern is two times higher than that of the non acidified dye.

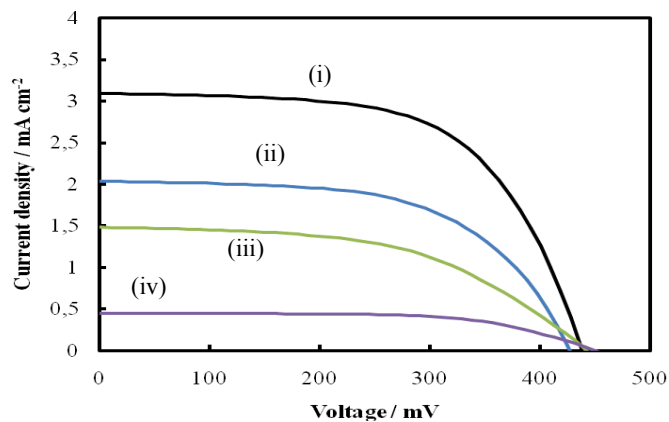


Figure 4. Current –voltage characteristics of pigments after acidification (i) Fire fern (ii) Begonia black velvet (iii) Ficus salicifolia (iv) Hibiscus sabdariffa

**Table 2.** photoelectrochemical parameters of the DSSCs sensitized by acidified pigment extracts

	$J_{sc}$ (mA cm <sup>-2</sup> )	$V_{oc}$ (mV)	FF	$\eta\%$
(i) Fire fern	3.09	438	61	0.82
(ii) Begonia black velvet	2.03	426	59	0.506
(iii) Ficus salificifolia	1.48	442	52	0.339
(iv) Hibiscus sabdariffa	1.12	443	56	0.298

The Highest Occupied Molecular Orbital (HOMO) level and the Lowest Unoccupied Molecular Orbital level (LUMO) of three extracts were calculated using cyclic voltammograms and the UV-visible absorption spectra, according to the method described elsewhere (12) and tabulated in the table 3.

**Table 3.** Estimated physical parameters of the dye extracts obtained from cyclic voltammetry and UV-visible absorption spectroscopic techniques.

Name of the dye solution	Band Gap (eV)	HOMO (eV)	LUMO (eV)
Fire Fern	2.13	-5.01	-2.88
Begonia(Black velvet)	3.10	-4.90	-1.80
Hibiscus sabdariffa	3.43	-4.99	-1.57

As it is evident from the , table 3, the excited state energy levels for the extracts are higher than the energy level of TiO<sub>2</sub> conduction band edge (-4.40 eV) (1,2,19) showing that the electron injection should be possible energetically. Therefore, upon illumination of the cell, dye extracts absorb light and get excited from the HOMO level to the LUMO level and eject electrons to the conduction band of TiO<sub>2</sub>, which transports these electrons to the transparent bottom electrode (FTO) and then to the other end of the cell via external load and being received by the redox mediator ( $I_3^- / I^-$ ) in the electrolyte. Finally the electrolyte ( $I_3^- / I^-$ ) regenerates the dyes to their ground state, completing the cell reaction

#### 4. CONCLUSION

Under the present preparation and irradiation conditions, it was found that the DSSCs fabricated with fire fern extracts possesses the best photosensitized effect in the extracts studied in this study. Therefore, fire fern extracts should be an alternative anthocyanin source for DSSCs fabrication in geographical regions that fire fern is widely available. Moreover, the DSSCs fabricated with acidified fire fern extracts having  $\approx 1\%$  efficiencies, could easily employed in low cost , disposable DSSCs which can be employed in DNA bio- sensors specially under room temperature low light intensity conditions. Therefore, the use of a natural dye for the semiconductor sensitizer with a straight forward preparation would provide alternative to commonly used synthetic dyes in many environmentally friendly applications.

## REFERENCES

1. Regan, B.O and Gratzel, M.. *Nature* **353**, 737 (1991)
2. Campbell, W. M., Burrell, A. K., Officer, D. L. and Jolley, K. W., *Coord. Chem. Rev.*, **248**, 1363 (2004)
3. Senadeera, G. K. R., Jayaweera, P. V. V., Perera, V. P. S. and Tennakone, K., *Sol. Energy Mater. Sol. Cells*, **73**, 103 (2002)
4. Senadeera, G. K. R., Nakamura, K., Kitamura, T., Wada, Y. and Yanagida, S., *Appl. Phys. Lett.*, **83**, 5470 (2003)
5. Tennakone, K., Kumarasinghe, A. R., Kumara, G. R. R. A., Wijayantha, K. G. U. and Sirimanne, P. M., *J. Photochem. Photobiol. A: Chem.*, **108**, 193 (1997)
6. Yamazaki, E., Murayama, M., Nishikawa, N., Hashimoto, N., Shoyama, M. and Kurita, O. *Sol. Energy*, **81**, 512 (2007)
7. Hao, S., Wu, J. H., Huang, Y. and Lin, J., *Sol. Energy*, **80**, 209 (2006)
8. Dai, Q. and Rabani, J., *Chem. Commun.*, **20**, 2142 (2001)
9. Bernacka-Wojcik, I., Senadeera, R., Wojcik, P.W., Silva, L.B., Doria, G., Baptista, P., Aguas, H., Fortunato, E., Martins, R., *Biosensors and Bioelectronics* **25** 1229 (2010)
10. Nielsen, A. H., Olsen, C. E. and Møller, B. L., *Phytochemistry*, **66**, 2829 (2005)
11. <http://www.answers.com/anthocyanin>
12. Smestad, G. P. *et al.*, *Sol. Energy Mater. Sol. Cells*, **76**, 85 (2003)

## **UTILIZATION OF NATURAL PIGMENT EXTRACTED FROM HENNA LEAF IN COMBINATION WITH GELATINE AS A SENSITIZER IN PHOTOELECTROCHEMICAL SOLAR CELLS**

C. N. NUPEARACHCHI <sup>a\*</sup>, T. R. C. K. WIJAYARATHNA <sup>b</sup> and V. P. S. PERERA <sup>a</sup>

<sup>a</sup> *Department of Physics, The Open University of Sri Lanka, Nawala, Nugegoda, Sri Lanka*

<sup>b</sup> *Institute of Fundamental Studies, Hantana, Kandy, Sri Lanka*

\*Corresponding Author, e-mail: [chathunilnupe@gmail.com](mailto:chathunilnupe@gmail.com)

### **ABSTRACT**

Due to the high efficiency, low cost and simple assemble technology, dye-sensitized solar cells (DSSC) are a technically and economically credible alternative to the present day photovoltaic devices. It consist of a photoelectrode made of nanocrystalline semiconductor film coated with a dye deposited on a transparent conducting tin oxide (CTO) glass plate, a counter electrode of Pt sputtered CTO glass plate and an electrolyte in between the two plates. Typically, the semiconductor film is titanium dioxide and the electrolyte is an organic solvent containing I<sub>3</sub><sup>-</sup>/I<sup>-</sup> redox couple.

Dyes in these cells serve as the absorber of solar energy whose properties determine the light harvesting efficiency. In search for an efficient dye, our interest inevitably was drawn towards the natural pigments because dye sensitization mimics the natural photosynthesis. The leaves of henna plant (*Lawsonia inermis*) which contains a natural red-orange organic pigment, naphthaquinone was used as the sensitizer in this study. Gelatine which is a protein produced by partial hydrolysis of collagen was used to enhance the performance of henna. The strong chelation of gelatine with henna was justified by the increased photovoltaic parameters of the cells compared to the cells made from henna alone.

These cells exhibited a photovoltage of 465 mV and photocurrent of 120  $\mu$ A which is higher than the cells sensitized only with henna. Although these results are not significant for a practically viable solar cell, several challenging problems remain to be resolved as this area is open for further investigation of efficient dye sensitizers. Reason for low photocurrent even after chelating henna with gelatine may be due to poor light absorption of gelatine in the visible region. However, combination of gelatine could serve as a model for the synthesis of more efficient other suitable pigments, which will motivate further research in this field.

### **1. INTRODUCTION**

Solar energy is the most abundant renewable energy source which can be converted to electricity by solar cells. Dye Sensitized Solar Cell (DSSC), which was developed by Michael Grätzel at EPFL in 1990s acts as an alternative to expensive Silicon solar cells (O'Regan and Gratzel, 1991). DSSCs are a combination of materials, consisting of a transparent mesoporous film of nanocrystalline TiO<sub>2</sub> electrode coated with a dye, an electrolyte containing a suitable redox couple and a Pt sputtered counter electrode (Longo and Paoli, 2003).

The use of sensitizers which has a broad absorption band in conjunction with oxide films of nanocrystalline morphology permits to harvest a fraction of sunlight. The illumination leads the dye to its excited state which is quenched by the electron transfer to the conduction band (CB) of the semiconductor, leaving the dye in an oxidized state. The oxidized dye is reduced by the electron donor which is present in the electrolyte. The collected electrons in the CB flow through the external circuit to the counter electrode where they cause the reverse reaction of the redox mediator. The voltage generated under illumination corresponds to the difference between the

quasi Fermi level of the electron in the semi conductor electrode and the redox potential of the electrolyte.

The ideal sensitizer should be firmly grafted to the semiconductor oxide surface and inject electrons to the CB. Its redox potential should be sufficiently high that it can be regenerated rapidly via electron donation from the electrolyte.

Dye in this cell serves as the absorber of solar energy whose properties have much effect on the light harvesting efficiency. Since dye sensitization is a similar process to natural photosynthesis, concern for using natural pigments in DSSCs has created an interest.

Several natural pigments from flowers, fruits, leaves etc. have been used as sensitizers of DSSCs because of their ability to inject electrons from excited pigments to the semi conductor electrode. The leaves of henna plant (*Lawsonia inermis*) have a red-orange dye molecule, a naphthaquinone. Normally, it has been used as a hair dye over the years.

A DSSC was fabricated using extracts of henna leaves in combination with gelatine which is a protein produced by partial hydrolysis of collagen extracted from the boiled bones, connective tissues, organs and some intestines of animals. The efficiency of the solar cell was compared with a cell made from henna alone as a dye sensitizer.

## **2. METHODOLOGY**

TiO<sub>2</sub> films (1 cm × 1 cm) of thickness 10 μm were prepared using doctor blade method on conducting tin oxide (CTO) glass plates (15 Ωcm<sup>-2</sup>) which was made grinding Degussa powder with acetic acid and ethyl alcohol. These films were sintered at 450 °C in a furnace for 30 minutes.

First, 1.5 g of 200 bloom gelatine was dissolved in 50 ml water in 80 °C. Bloom is a measure of gel strength of gelatine. Same amount of dried plant powder of henna was added to the solution and stirred while the constant temperature was maintained for one hour. Simultaneously, a separate henna solution was made by dissolving 1.5 g in 50 ml of water in 80 °C.

Then both solutions containing henna alone and (henna + gelatine) were filtered. TiO<sub>2</sub> films were immersed in the filtrates for 12 hours. Dye sensitized solar cells were fabricated by attaching a Pt sputtered CTO glass plate on the top of the dye coated electrode as the counter electrode. The capillary space in between was filled with an electrolyte containing KI + I<sub>2</sub> (KI = 0.5 mol dm<sup>-3</sup>, I<sub>2</sub> = 0.05 mol dm<sup>-3</sup>) which was dissolved in ethylene carbonate and acetonitrile in 4:1 ratio.

Cells were characterized by illuminating with tungsten filament light (100 mW cm<sup>-2</sup>) and a source meter coupled to a computer. Illumination was carried out through the TiO<sub>2</sub> layer of the cell. Absorption spectra were obtained with the Shimadzu UV-3000 spectrometer.

## **3. RESULTS AND DISCUSSION**

The pigment extracted from henna leaves mainly contains hennatannic acid (pH ~ 5) or 2-hydroxy -1, 4 - naphthaquinone which is red-orange in colour. The hydroxyl group of the hennatannic acid reacts with the Ti<sup>4+</sup> ions on the surface of TiO<sub>2</sub> film. Thus, the pigment can readily chelate with the surface Ti<sup>4+</sup> ions by eliminating a water molecule as shown in Figure 1.

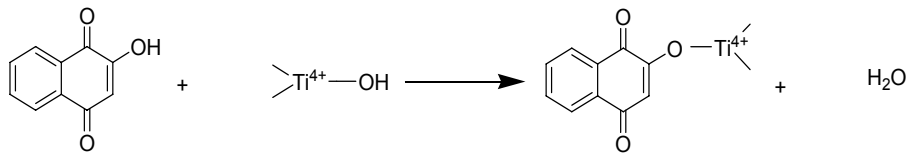


Figure 1. Mechanism of chelation of hennatannic acid with TiO<sub>2</sub>

Gelatine (pH ~ 6) mainly consists of two amino acids namely Glycine (21.4 %) and Proline (12.4 %). When triple helices in gelatine are heated in water, they open up and some hydrolyzed ends fray out to tangle with other bonds. Water is trapped in the strands and the result is a gel, semi solid mass. Glycine and Proline react with henna according to Micheal addition as shown in Figure 2.

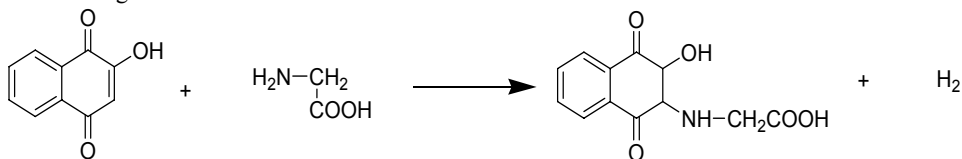


Figure 2. Micheal addition of Glycine and henna

The resultant structure (pH ~3) will have a COOH group which can react with the surface Ti<sup>4+</sup> ions by eliminating a proton as in Figure 3.

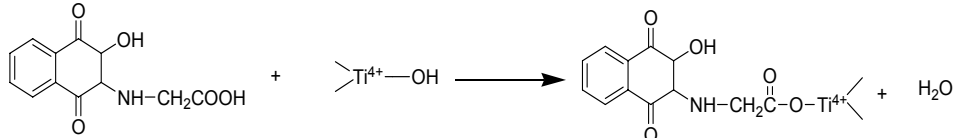


Figure 3. Mechanism of chelating with TiO<sub>2</sub> by (henna+gelatine)

In the conjugated chromophores, the electrons jump between energy levels that are extended  $\pi$  orbitals, created by a series of alternating single and double bonds, in aromatic systems. The metal complex chromophores arise from the splitting of d-orbitals by binding of a transition metal to ligands. Examples of such chromophores can be seen in biochemical reactions such as chlorophyll in plants uses for photosynthesis, hemoglobin, hemocyanin and in colorful minerals such as malachite and amethyst as well.

Absorption spectra for henna and gelatine coated TiO<sub>2</sub> film is shown in Figure 4. It has exhibited an intense absorption band in UV region around 280 nm.

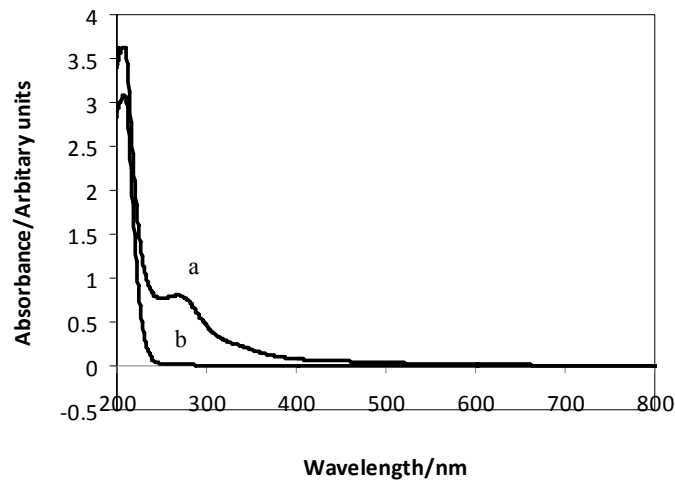


Figure 4. Absorption spectra of a) henna and b) gelatine

The open circuit voltage of  $\sim 465$  mV and short circuit current of  $\sim 120$   $\mu$ A could be measured for cells sensitized with (henna + gelatine) while it was  $\sim 365$  mV and  $\sim 100$   $\mu$ A respectively for the cells sensitized only with pigments extracted from henna leaves. I-V characteristics shows (henna + gelatine) sensitized film with greater photocurrent and photovoltage (Figure 5). The increased photovoltage and photocurrent was due to the increased binding energy of COOH group.

The observed photocurrent is minute as the light absorption occurs in the UV region. But when the chromophore of hennatannic acid bonds to amino acids like Glycine and Proline, its colour become darken and shows increased photo electric properties due to its structural change. Therefore experiments are underway to use this pigment as efficient sensitizer in DSSCs after structural modifications.

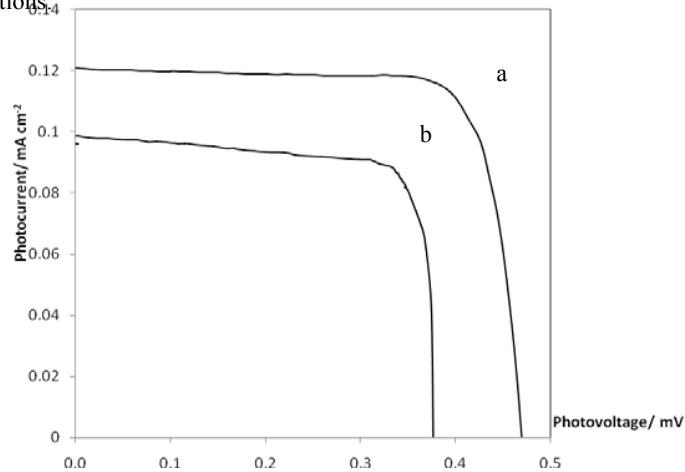


Figure 5. I-V characteristics of a) (henna+gelatine) and b) henna sensitized cells



#### **4. CONCLUSION**

A natural pigment of henna was used with gelatine as a sensitizer. These cells exhibited a higher photovoltage and photocurrent than the cells sensitized with henna. Several challenging problems remain to be resolved as this area is open for further modifications of effective dye sensitizers in solar cells. However, combination mechanism of gelatine could serve as a model for the synthesis of suitable pigments to extend the absorption of hennatannic acid towards visible region which motivates further research in DSSCs.

#### **5. ACKNOWLEDGEMENT**

This work was financially supported by National Science Foundation of Sri Lanka.  
(Grant: RG/2007/W & E/ 03)

#### **REFERENCES**

1. Longo, C. and De Paoli, M. (2003), *Journal of Brazilian Chemical Society*, **14**, 889-901.
2. O'Regan, B. and Gratzel, M. (1991), *Nature*, **353**, 737.

## COMPARISON OF NATURAL PIGMENTS IN BLACK TEA AND GREEN TEA WITH DSSCs

C.N. NUPEARACHCHI <sup>a\*</sup>, C.A. THOTAWATTHAGE <sup>b</sup>, G.K.R. SENADEERA <sup>a, b</sup> and V.P.S. PERERA <sup>a</sup>

<sup>a</sup> Department of Physics, The Open University of Sri Lanka, Nawala, Nugegoda, Sri Lanka

<sup>b</sup> Institute of Fundamental Studies, Hantana, Kandy, Sri Lanka

\*Corresponding Author, e-mail: [chathunilnupe@gmail.com](mailto:chathunilnupe@gmail.com)

### ABSTRACT

An increasing interest has been developed during the past few years about the potential health promotion properties of tea (*Camellia sinensis*). These beneficial effects of tea have been attributed to the antioxidant and other properties of some of the polyphenolic components, particularly the catechin (flavan-3-ol) derivatives.

Three types of tea are produced from the leaves of *Camellia sinensis*. Namely, they are green tea (non-fermented), oolong tea (semi-fermented) and black tea (fermented). The fermentation of tea leaves induces enzymatic oxidation of flavan-3-ols and leads to the formation of two major pigments in black tea, theaflavins (TFs) and thearubigins (TRs). The catechins in green tea are epicatechin (EC), epicatechin 3-gallate (ECG), epigallocatechin (EGC) and epigallocatechin 3-gallate (EGCG).

Natural pigments from flowers, fruits, leaves etc. have been used as sensitizers in DSSCs because of their ability to inject electrons from excited pigments to the semiconductor electrode. Extracts from black tea has been used as a sensitizer in DSSC in the past, but no one has compared the effect of pigments of black tea and green tea so far as a sensitizer of DSSCs. Since the pigments of black tea and green tea contain hydroxyl groups, they can easily get attached with TiO<sub>2</sub> films of DSSCs.

In this study, DSSCs were fabricated using the extracts of black and green tea leaves as sensitizers. There were no specific differences between the photocurrent and photovoltage of those cells. Even the UV visible spectra of the two extracts did not show a significant difference. But when these pigments coated TiO<sub>2</sub> films were analyzed with impedance spectroscopy, there was a remarkable difference between the films coated with extracts of green and black tea. After coating green tea extract, the impedance of TiO<sub>2</sub> film of 10 μm thickness which was about 315 kΩ has increased to 14 MΩ while impedance of black tea coated TiO<sub>2</sub> film was only increased to 1 MΩ. Therefore, impedance analysis of TiO<sub>2</sub> films coated with extracts of green tea and black tea is a simple approach to identify the major pigments of green tea and black tea which are, ECGC and TF respectively. When compared to chemical techniques such as chromatography or electrophoresis, impedance measurement technique seems to be an easy way of identifying active pigments in green and black tea qualitatively and quantitatively. The change in the impedance of the TiO<sub>2</sub> film of those pigments after adsorption can be explained considering the surface coverage.

### 1. INTRODUCTION

For many centuries, tea (*Camellia sinensis*) has been used as health promoting drink where its benefits to the human body are not studied descriptively. Numerous epidemiological studies link the drinking of tea to a reduction of the risk in cardiovascular diseases and cancers in humans but the results are not consistent. The health benefits of tea have been attributed to the antioxidant and other properties of some of the polyphenolic components, particularly the catechin (flavan-3-ol) derivatives (Menet et al., 2004).

Mainly there are three types of tea that humans around the world consume as a drink. They are green tea (non-fermented), oolong tea (semi-fermented) and black tea (fermented). The fermentation of tea leaves induces enzymatic oxidation of flavan-3-ols and leads to the formation

of two major pigments in black tea, theaflavins (TFs) and thearubigins (TRs). Theaflavins contribute a yellowish orange colour. Typically a finer black tea has more theaflavins content and thus gives a more orange tone.

The catechins in green tea are epicatechin (EC), epicatechin 3-gallate (ECG), epigallocatechin (EGC) and epigallocatechin 3-gallate (EGCG). Of all the catechins, EGCG has the most scientific attention, being singled out among them as a key contributive element to the possible health effects of tea and has been found in highest concentration in green tea.

With the development of material science and engineering, various devices have been fabricated to replace the expensive silicon based solar cells. Among them, one of the promising device is the low cost and high efficient dye sensitized solar cell (DSSC) with simple assemble technology which was developed by Micheal Grätzel at EPFL in 1990s (O'Regan and Gratzel, 1991).

The use of sensitizers which has a broad absorption band in conjunction with oxide semiconductor films of nanocrystalline morphology permits to harvest a fraction of sunlight. The illumination leads the dye to its excited state which is quenched by the electron transfer to the conduction band (CB) of the semiconductor, leaving the dye in an oxidized state. The oxidized dye is reduced by the electron donor, which is present in the electrolyte. The collected electrons in the CB flow through the external circuit to the counter electrode where they cause the reverse reaction of the redox mediator. Attention has drawn for the use of natural pigments in DSSCs as the dye sensitization is a process similar to the natural photosynthesis. Several natural pigments from flowers, fruits, leaves etc. have been used as sensitizers of DSSCs because of their ability to inject electrons from excited pigments to the semiconductor electrode. In this study, DSSCs were fabricated using the extracts of black and green tea leaves as sensitizers.

## **2. METHODOLOGY**

TiO<sub>2</sub> films (1 cm × 1 cm) of thickness 10 μm were prepared using doctor blade method on conducting tin oxide (CTO) glass plates (15 Ωcm<sup>-2</sup>) which was made grinding Degussa powder with acetic acid and ethyl alcohol. These films were sintered at 450 °C in a furnace for 30 minutes.

First, 3.0 g of both green tea and black tea were heated separately in 50 ml of water at 100 °C and stirred while maintaining the constant temperature for 15 minutes.

Then the solutions containing green tea and black tea were filtered. TiO<sub>2</sub> films were immersed in the filtrates for 12 hours. Dye sensitized solar cells were fabricated by attaching a Pt sputtered CTO glass plate on the top of the dye coated electrode as the counter electrode. The capillary space in between was filled with an electrolyte containing KI + I<sub>2</sub> (KI = 0.5 mol dm<sup>-3</sup>, I<sub>2</sub> = 0.05 mol dm<sup>-3</sup>) which was dissolved in ethylene carbonate and acetonitrile in 4:1 ratio. Cells were characterized by illuminating with tungsten filament light (100 mW cm<sup>-2</sup>) and a source meter coupled to a computer. Illumination was carried out through the TiO<sub>2</sub> layer of the cells. Absorption spectra were obtained with the Shimadzu UV-3000 spectrometer. Also, the complex plane impedance spectra of these films and a separate TiO<sub>2</sub> film were analyzed by Solartron 1260 frequency response analyser using SMART software provided with the instrument. A sweep was carried out for these films coated on CTO glass with Pt as the counter electrode by setting AC level at 500 mV in the frequency range from 1 MHz to 1 Hz while measuring the impedance in 1.0 s integration.

### 3. RESULTS AND DISCUSSION

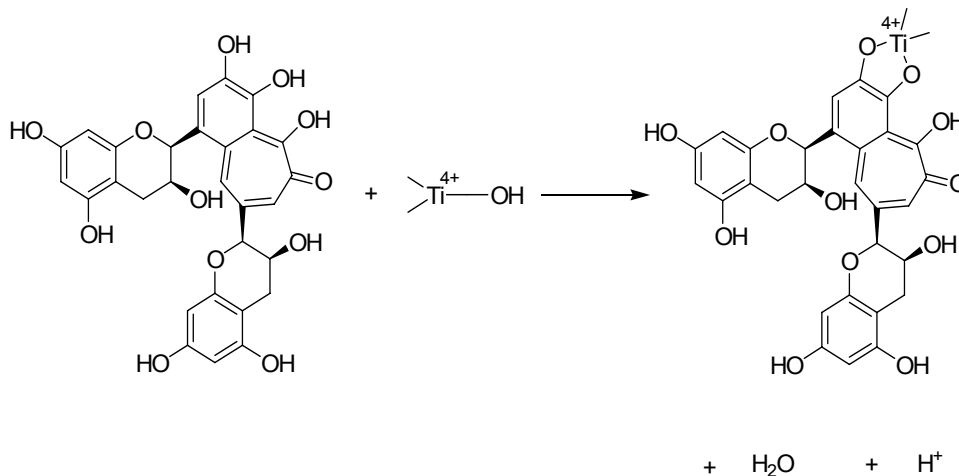


Figure 1. Mechanism of chelation of TF with  $\text{TiO}_2$

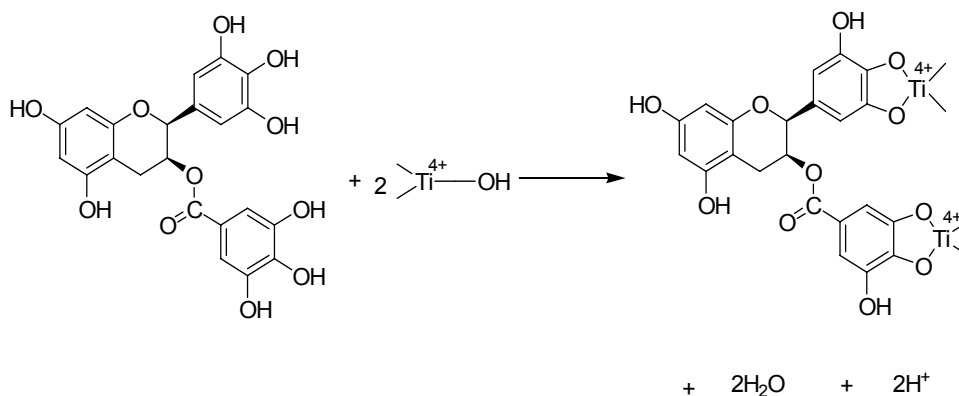


Figure 2. Mechanism of chelation of EGCG with  $\text{TiO}_2$

The pigment extracted from black tea leaves mainly contains theaflavins (TFs) which is the major contributor to its yellowish orange colour. The hydroxyl group of TF reacts with the  $\text{Ti}^{4+}$  ions on the surface of  $\text{TiO}_2$  film. Thus, the pigment can readily chelate with the surface  $\text{Ti}^{4+}$  ions by eliminating a water molecule as shown in Figure 1. Comparatively green tea leaves have epigallocatechin 3-gallate (EGCG) reacts with two  $\text{Ti}^{4+}$  ions on the surface of  $\text{TiO}_2$  film. Thus, this pigment can readily chelate much more surface  $\text{Ti}^{4+}$  ions by eliminating two water molecules as shown in Figure 2.

Comparatively, black tea TF makes a stable five ring chromophore structure where as green tea EGCG makes two less conjugated structures.

There were no specific differences between the photocurrent and photovoltage of those cells. Even the UV visible spectra of the two extracts did not show a significant difference.

But when these pigments coated TiO<sub>2</sub> films were analyzed with impedance spectroscopy, there was a remarkable difference between the films coated with extracts of green and black tea. After coating green tea extract, the impedance of TiO<sub>2</sub> film of 10 μm thickness which was about 315 kΩ has increased to 14 MΩ while impedance of black tea coated TiO<sub>2</sub> film was only increased to 1 MΩ. (Figure 3)

This observation supports that adsorption occurs with hydroxyl groups attached to phenyl group which withdraws more electrons from the film increasing the impedance. But when the adsorption occurs with the hydroxyl group in the black tea complex, it may not deplete electron concentration in TiO<sub>2</sub> film as the green tea. The molecular arrangement of EGCG on the film surface also facilitates to pack more molecules on TiO<sub>2</sub> than TF without voids.

But the main disadvantage of both films made from black tea and green tea is that, it does not absorb any visible light. Therefore, experiments are underway to use different chemicals in acidic and basic media which absorb visible light that will increase the efficiency of the DSSCs after chelating with tea.

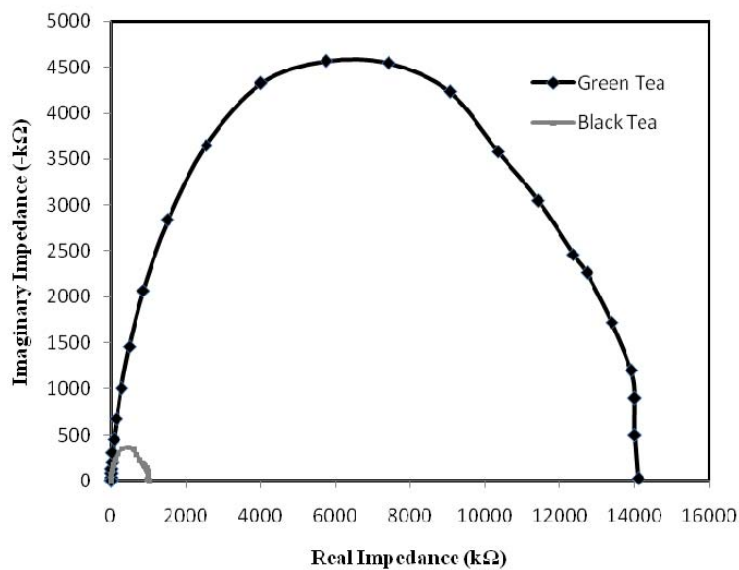


Figure 3. Nyquist plot of one of the samples made from black tea and green tea

#### **4. CONCLUSIONS**

In this study, we have succeeded to fabricate a DSSC with green tea and black tea. The impedance spectroscopic measurements supported that the EGCG chelates strongly than the TF in black tea with TiO<sub>2</sub> which occurs via the hydroxyl groups in the pigments. Several challenging problems remain to be resolved as this area is open for further studies of effective dye sensitizers for solar cells. However, this study would help to synthesis suitable pigments for DSSCs which motivates further research.

#### **REFERENCES**

1. Menet, M.C., Sang, S., Yang, C. S., Ho, C. T. and Rosen, R. T. (2004), *J. Agric. Food Chem.*, **52**, 2455- 2461.
2. O'Regan, B. and Gratzel, M. (1991), *Nature*, **353**, 737.

**EVALUATION OF DYES FROM *MELASTROMA MALABATHRICUM*: A NATIVE PLANT OF BORNEO, AS POTENTIAL NATURAL COLOUR FOR DYE-SENSITIZED SOLAR CELLS**

PIYASIRI EKANAYAKE<sup>1\*</sup>, RINA ZAIN<sup>1</sup>, MOHAMED ISKANDAR<sup>1</sup>, KUSHAN TENNAKOON<sup>2</sup>, SUSUMU YOSHIKAWA<sup>3</sup> AND ROHAN SENADEERA<sup>4</sup>

<sup>1</sup>Applied Physics Program, Faculty of Science, University of Brunei Darussalam, Jalan Tungku Link, BE1410, Negara Brunei Darussalam, <sup>2</sup>Biology Program, Faculty of Science, University of Brunei Darussalam, Jalan Tungku Link, BE1410 Negara Brunei Darussalam, <sup>3</sup>Institute of Advanced Technology, Uji, Kyoto, 611-0011, Japan, <sup>4</sup>Institute of Fundamental Studies, Hantana Road, Kandy and Department of Physics, The Open University of Sri Lanka, Nawala, Nugegoda, Sri Lanka

\*Corresponding Author, e-mail: piyasiri.ekanayake@ubd.edu.bn

**ABSTRACT**

Dye sensitized solar cells (DSSCs) were assembled and tested by using natural dyes extracted from *Melastoma malabathricum* L.(Melastomaceae), a native Bornean plant species adapted to thrive under intense tropical sunlight. Pigments from both the leaves and flower petals were tested and the results were compared. The photosynthetic pigments chlorophyll (chlorophyll *a* and *b*) and carotenoids (carotene and lutein) were extracted and separated from the leaves of *Melastoma malabathricum*, while sap pigment anthocyanin (flavanoid class) was extracted from the flowers. Mesoporous nanocrystalline,  $\approx 10\mu\text{m}$  thick (determined by SEM) thin films of  $\text{TiO}_2$  layers coated by *Doctor Blade* method on pre-cleaned fluorine-doped conducting tin oxide (FTO) glasses were dipped in above dye solutions and used as photoelectrodes. Devices were assembled with Pt coated counterelectrodes and redox electrolyte containing  $\text{I}_3^-/\text{I}^-$ , and cell performances were tested under the irradiance of  $750 \text{ W/m}^2$ . The best device performances were obtained from the flower extracts (anthocyanin). The DSSC with this dye has shown an open circuit voltage of 469 mV, a short circuit current density of  $1.696 \text{ mA cm}^{-2}$ , and a fill factor of 0.55 resulting an overall efficiency of 0.62%. While the DSSCs sensitized with chlorophyll *a*, chlorophyll *b* and carotenoid pigments showed relatively low efficiency. Highest occupied molecular orbital (HOMO) and lowest unoccupied molecular orbital (LUMO) levels of the flower extract were calculated to be 2.50 eV and 4.56 eV with respect to the vacuum level.

**1. INTRODUCTION**

Most energy resources used by human are based on the stored energy from fossil fuels such as coal, oil and natural gas; and nuclear fuel for instance, Uranium isotope -U235 [1]. Both fossil and nuclear fuels are limited reserves [2]. Moreover, the combustion of fossil fuel increase the concentration of carbon dioxide in the atmosphere which ultimately effecting in enhancing the greenhouse effect, global warming and the acidification of the global water cycle [3]. Thus alternative renewable resources play a major role in the power generation for the future demand. Among the renewable power sources, solar energy is one of the best and abundant resources which could supply the energy requirements in the future through the devices called solar cells which converts the radiation from the sun directly into the electricity [2].

Conventional solar cells that consist of solid-state p-n junctions are usually made of silicon and have been dominated the semiconductor industry. However, a new generation of solar cells known as dye-sensitized solar cells (DSSCs) that are based on nanotechnology has emerged [4]. The device was invented by Michael Grätzel and Brian O' Regan in 1991 and it consists of a nanocrystalline  $\text{TiO}_2$  thin-film electrode, ruthenium complex dye, and an iodide-triiodide redox electrolyte. The efficiencies of these DSSCs are now exceeding 10% and much of the work are being carried out in outdoor testing and usage [5]. The main principle use in these DSSCs is the

dye sensitization of wide band gap semiconductors such as TiO<sub>2</sub>, ZnO, SnO<sub>2</sub>, etc. by suitable regenerative dyes which ultimately converts solar irradiation to electricity [4,7].

To date, the most efficient DSSCs consist of expensive transition metal compounds such as ruthenium and osmium polypyridyl complexes; as the effective sensitizers. This is due to their intense absorption in the whole visible range, long excited lifetime, and highly efficient metal-to-ligand charge transfer [5-8]. However, ruthenium polypyridyl complexes contain a heavy metal which is environmentally undesirable [9] and the preparation involve a complicated procedures which made them expensive [6,7,9,10]. Alternatively, the use of non-toxic natural pigments as sensitizers have been actively studied as they are environmentally friendly, easily available; and very cheap to extract with minimal chemical procedures [7,9,10]. These natural dyes can be easily extracted from fruits, vegetables, leaves, flowers and algae that varies from different colors in the visible spectra (red to violet) [7,10] can be employed in DSSCs and have been extensively investigated as sensitizers [9-14].

The aim of this study was to extract natural dyes of different molecular groups namely chlorophyll 'a' and 'b', carotenoids (carotene & lutein)- all are considered as plastid pigments; and anthocyanin (sap pigments) to test them in dye-sensitized solar cells. DSSCs were assembled using the extracted dyes as their sensitizers and their full characteristics were explored. The natural dyes used in this study were extracted from an evergreen native pioneer plant *Kuduk-Kuduk* (*Melastoma malabathricum* L. ; family Melastomaceae), grown in clearings, along roads, waste ground and disturbed sites of Brunei Darussalam. It has dark purple to pinkish flowers comprising five simple petals and narrow leaves with 3 prominent longitudinal veins. The plastid pigments were extracted from leaves while the sap pigments were extracted from flowers.

## 2. EXPERIMENTAL

The sap pigment anthocyanin was extracted from the petals of the *Melastoma malabathricum* flowers by crushing in a narrow specimen tube with a minimum amount of ethanol (Fluka 95% v/v) and leaving overnight. The residual parts were filtered on a Buchner funnel. Unwanted non-polar pigments absorbed into a petroleum ether layer were removed from the filtrate and it was subsequently measured for absorbance at 530nm using Varian Cary 5E UV-Vis-NIR double beam spectrophotometer, to confirm the presence of anthocyanin.

The chlorophyll and carotenoid pigments of *Melastoma malabathricum* were extracted from freshly harvested fully mature leaves exposed to full sunlight in the field. Immediately after harvesting, the leaf tissues were ground in a blender with excess acetone (Fluka 90% v/v) until all the color is released from the tissue [15,16]. To confirm the presence of Chlorophyll a & b pigments, the absorbance was measured at 663 nm and 645 nm respectively. Similarly to confirm the presence of carotenoids, the absorbance was measured between 400- 450nm. The plastid pigment extract mixture was further separated into two groups of pigments viz. *Chlorophyll 'a'* and *carotene*, and *Chlorophyll b* and *lutein* depending on their relative polarities using the solubility properties of these pigments in the solvents of pet ether, acetone and methyl alcohol [16].

TiO<sub>2</sub> paste purchased from Solaronix (nanoxide-T, colloidal anatase particles size: ~13 nm, ~120 m<sup>2</sup>/g (BET), Switzerland) was coated by Doctor Blade method on precleaned fluorine-doped conducting tin oxide (FTO) glasses (Nippon sheet glass 10<sup>-12</sup> Ω sq<sup>-1</sup>). The electrodes were preheated (~50°C) using a hair-drier and then sintered at 450°C for 40 min, and then allowed to cool to room temperature. The thickness of the TiO<sub>2</sub> electrodes was found to be ~4-5 μm (Dektak profilometer; Veeco, Dektack 3).



The TiO<sub>2</sub> electrodes were dipped in each dye solution for 12 h. The electrodes were then removed and rinsed with ethanol and dried using an airflow. DSSCs were constructed by introducing the redox electrolyte containing tetrabutylammonium iodide (TBAI; 0.5 M)/I<sub>2</sub> (0.05 M), in a mixture of acetonitrile and ethylene carbonate (6:4, v/v) between the dyed TiO<sub>2</sub> electrode and platinum counterelectrode. UV-visible absorption measurements of extracted pigments were carried out with a Varian Cary 5E UV-Vis-NIR double beam spectrophotometer.

For estimation of oxidation potential of pigments, cyclic voltammetry (CV) experiments were carried out in a three-electrode cell consisting of a glassy carbon working electrode, a platinum counter electrode and a Ag/AgCl reference electrode using a scan rate of 50 mV/s (Solartron 1286). Few drops of the dye solution on the top of the glassy carbon electrode were allowed to dry in air. The supporting electrolyte was 0.1 M KNO<sub>3</sub> in distilled water.

### 3. RESULTS AND DISCUSSION

Figure 1(a) shows the absorption spectrum of *chlorophyll 'a'* and *carotene* pigment mixture extracted from *Melastoma malabathricum*. An intense absorption was observed in the region 330-460 nm due to the combined contributions of the *chlorophyll 'a'* and *carotene* (410 nm). Additionally, the *carotene* had minor peaks on either side of its maxima peak (i.e 376 nm and 432 nm).

*Lutein*, being a member of the carotenoid pigment group showed a similar absorption curve to carotene with numerous peaks but at different wavelength positions as illustrated in Figure 1(b). Intense absorptions between 350-500 nm was seen at which the maximum peak was observed at 423 nm with minor peaks on either sides at 404, 445 and 471 nm. The peak at 661 nm was due to *chlorophyll 'b'* absorption that was red shifted from 645 nm.

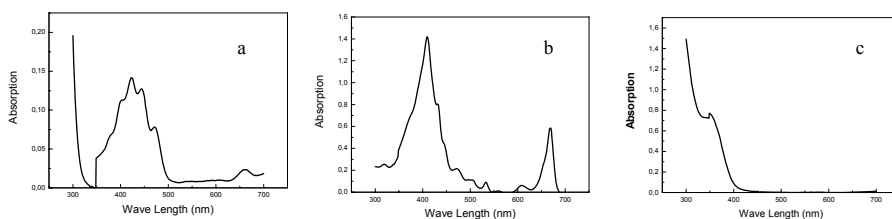


Figure 1. UV-Vis absorption spectra of: (a) chlorophyll 'a' and carotene, (b) chlorophyll 'b' and lutein, (c) anthocyanin.

*Anthocyanin* extraction showed an intense absorption towards lower wave lengths (see Figure 1(c)) however a careful examination revealed a low intense but wider absorption peak centered around 550 nm.

A few drops of 1% HCl could be added to the anthocyanin pigment extraction to intensify this peak [15]. However, for this study HCl was not incorporated to the filtrate to enhance the absorbance intensity. Hence the results reported here should be considered as interpretations originated from un-modified natural anthocyanin pigments present under natural conditions.

Figure 4 and Figure 5 illustrate the J-V (current density-voltage) characteristics and P-V (power-voltage) curve of the prepared DSSCs using petals extracts of *Kuduk-Kuduk* plant as the natural dye, respectively. The power conversion efficiency ( $\eta$ ) was calculated according to the

following equation:  $\eta = FF \times J_{sc} \times V_{oc}/I$ , where  $J_{sc}$  is the short-circuit photocurrent density ( $A\ cm^{-2}$ ),  $V_{oc}$  the open-circuit voltage (V),  $I$  the intensity of the incident light ( $W\ cm^{-2}$ ) and FF the fill factor defined as  $FF = J_m V_m / J_{sc} V_{oc}$ , where  $J_m$  and  $V_m$  are the optimum photocurrent and voltage that can be extracted from the maximum power point of the  $I-V$  characteristics.

The characteristics of the DSSCs with all the extracted dyes are summarized in Table 1.

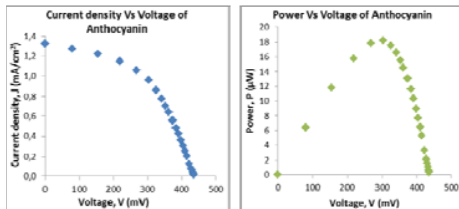


Figure 4. J-V characteristics of DSSC's of anthocyanin.

Figure 5. P-V curve of anthocyanin.

Sample Name	$I_{sc}(mA)$	$V_{oc}(V)$	FF	$\eta\%$
Chl 'b' + lutein	0.102	0.292	0.47	0.322
Anthocyanin	0.106	0.469	0.55	0.619
Chl 'a' + carotene	0.020	0.169	0.14	0.011

Table 1: Characteristic of dye-sensitized solar cell with melastomamalabathricum extract.

The best performance was obtained from DSSC prepared by using the *anthocyanin* extract in which the conversion efficiency ( $\eta$ ) was 0.619 %, with open circuit voltage ( $V_{oc}$ ) of 469 mV and short circuit current density ( $J_{sc}$ ) of 1.696 mA/cm<sup>2</sup>, and fill factor (FF) of 0.55, under the irradiance of 750 W m<sup>-2</sup>. The lowest conversion efficiency obtained was from mixture of *chlorophyll 'a'* and *carotene* extract. Interestingly, the mixture produced poor performance despite being the most absorbent dye amongst all and had extended spectral absorption at lower energies. This suggests *chlorophyll 'a'* and *carotene* extract did not absorb efficiently onto TiO<sub>2</sub> from most polar organic solvents due to the fact that ester ketone and carbonyl groups have weak interaction with the oxide surface [7]. On the other hand, DSSCs using the mixture of *chlorophyll 'b'* and *lutein* extract produced better photocurrent when considering its poor light harvesting properties compared to *chlorophyll 'a'* and *carotene* mixture.

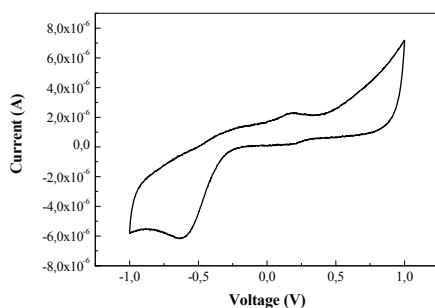


Figure 6. Cyclic Voltammogram of Anthocyanin extracted from melastoma malabathricum.

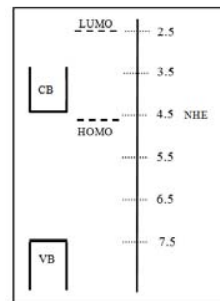


Figure 7. Schematic diagram showing the calculated positions of HOMO and LUMO levels of anthocyanin with respect to vacuum level. Edges of the conduction and valence bands of TiO<sub>2</sub> are also shown. All the values are in electron volts (eV).

Cyclic voltammetry was used to study the electrochemical behavior of the dyes. Figure 6 shows a cyclic voltammogram for the *anthocyanin* extracted from *melastoma malabathricum* which showed the best cell performance. Oxidation potential was calculated from the oxidation peak of CV curve to be 0.182 V. This result together with absorption edge determined from the

UV-Vis absorption spectra are used to calculate HOMO and LUMO levels according to a method described elsewhere [15,17] and the values are 2.500 eV and 4.562 eV, respectively, with respect to the vacuum level. Figure 7 illustrates a schematic diagram depicting the calculated positions of HOMO and LUMO levels of *anthocyanin* with respect to vacuum level. Edges of the conduction and valence bands of TiO<sub>2</sub> are also shown.

#### 4. CONCLUSIONS

In this investigation DSSCs were fabricated using natural dyes obtained from leaves and flower petals as photosensitizers and the performance of each DSSC are reported.

*Chlorophyll 'a'* and *carotene* pigment mixture had excellent light harvesting but produced a poor performance in DSSCs. A better cell performance was exhibited by the *Chlorophyll 'b'* and *Lutein* pigment mixture. According to our experimental results, the best overall energy conversion efficiency of 0.62% was obtained from the sap pigment *anthocyanin* extracted from the flower petals of *Melastoma malabathricum* with V<sub>OC</sub> of 469 mV, J<sub>SC</sub> of 1.7 mA/cm<sup>2</sup>, FF of 0.55; and P<sub>max</sub> 434 μW/cm<sup>2</sup>. Highest occupied molecular orbital (HOMO) and lowest unoccupied molecular orbital (LUMO) levels of the flower extract were calculated to be 2.500 eV and 4.562 eV with respect to the vacuum level.

#### 5. ACKNOWLEDGMENTS

Financial support for this study was provided by the University of Brunei Research grant UBD/PNC2/2/RG/1(176). We thank Dr. J. Santos for the assistance extended for CV experiments.

#### REFERENCES

1. Würfel, P. (2005) *Physics of Solar Cells: From Principles to New Concepts*. Weinheim: Wiley-Vch Verlag GmbH & Co.
2. Overstraeten, R.J.V. and Mertens, R.P. (1986) *Physics, Technology and Use of Photovoltaics*. Bristol: Adam Hilger Ltd.
3. Markvart, T. (2000) *Solar Electricity*. 2nd ed. West Sussex: John Wiley & Sons.
4. Gratzel, M. Dye-sensitized solar cells. *Journal of Photochemistry and Photobiology C: Photochemistry Reviews* 4, 2003, 145-153.
5. Hara, K. and Arakawa, H. Dye-sensitized Solar Cells. In Luque, A. and Hegedus, S., Ed. *Handbook of Photovoltaic Science and Engineering*. West Sussex: John Wiley & Sons Ltd, 2003, Chapter 15, pp. 663-700.
6. Junghänel, M. Novel aqueous electrolyte films for hole conduction in dye sensitized solar cells and development of an electron transport model. Doctoral thesis. Freie Universität Berlin, 2007.
7. Calogero, G., et al. Natural dye sensitizers for photochemical cells. *Energy and Environmental Science*, 2, 2009, 1162-1172.
8. Ryan, M. progress in Ruthenium Complexes for DSSCs. *Platinum Metal Review*, 53(4), 2009, pp 216-218.
9. Wongcharee, K., et al. DSSC using natural dyes extracted from rosella and blue pea flowers. 2006.
10. Chang, H., and Lo, Y. Pomegranate leaves and mulberry fruit as natural sensitizers for DSSCs. *Solar Energy*, 84, 2010, pp 1833-1837.
11. Polo, A.S., and Iha, N.Y.M. Blue sensitizers for solar cells: Natural dyes from Calafate and Jabotica. *Solar energy materials & solar cells*, 90, 2006, pp 1936-1944.

12. Hao, S., et al. Natural dyes as photosensitizers for DSSC. *Solar energy*, 80, 2006, pp 209-214.
13. Calogero, G., et al. Efficient DSSCs using red turnip and purple wild Sicilian prickly pear fruits. *International Journal of Molecular Sciences*, 11, 2010, pp 254-267.
14. Zhang, D., et al. Betalain pigments for DSSCs, *Journal of photochemistry and photobiology A: Chemistry*, 195, 2008, pp 72-80.
15. J.M.R.C. Fernando and G.K.R. Senadeera, Natural anthocyanins as photosensitizers for dye-sensitized solar devices, *Current Science*, 95, 5, 2008, pp 663 -666.
16. Harbone J.B. 1973. *Phytochemical methods*. London, UK: Chapman & Hall Ltd. pp 204-21
17. Smestad G.P., et. Al. A technique to compare polythiophene solid-state dye sensitized TiO<sub>2</sub> solar cells to liquid junction devices, *Solar Energy Materials & Solar Cells*, 76, 2003, pp 85-105

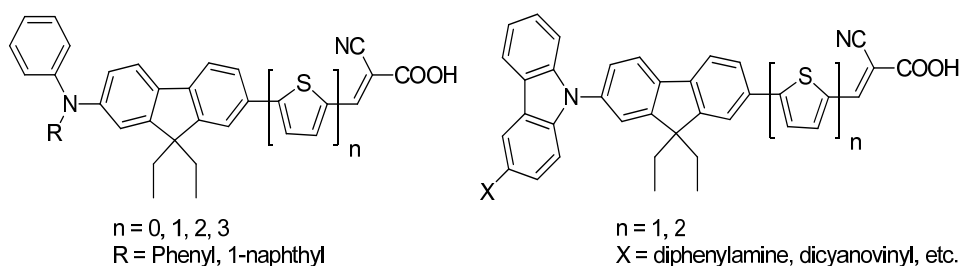
## FLUORENE-BASED ORGANIC DYES FOR DYE-SENSITIZED SOLAR CELLS

K. R. JUSTIN THOMAS

Department of Chemistry, Indian Institute of Technology Roorkee, Roorkee – 247 667, India

Corresponding Author, e-mail: [krjt8fey@iitr.ernet.in](mailto:krjt8fey@iitr.ernet.in)

### ABSTRACT



We have synthesized a series of fluorene-based organic dyes featuring donor-acceptor architecture and characterized by optical and electrochemical measurements. The effect of thiophene incorporation in the conjugation pathway and the role of auxiliary donor chromophores on the electro-optical properties were investigated by synthesizing suitably designed organic dyes. The absorption properties of the dyes were dependent on the nature of the  $\pi$ -bridge as well as the donor strength of the auxiliary chromophores. Incorporation of additional thiophene units in the conjugation pathway enhanced the donor-acceptor interactions due to the reduced aromaticity of thiophene and led to red-shifted absorption profile. Additionally the thiophene being electron-rich enhanced the donor strength of the  $\pi$ -bridge and facilitated the oxidation potential of the dyes. Auxiliary donors and acceptors played their corresponding roles in the electro-optical properties. Particularly the dicyanovinyl substituent due to the conjugation extension bathochromically shifted the absorption peak and positively shifted the oxidation potential originating due to the removal of electron from the triarylamine unit. The differences observed in the electro-optical properties were rationalized by the TDDFT electronic structure calculations using various theoretical models (B3LYP, CAM-B3LYP and M06). The nanocrystalline  $\text{TiO}_2$ -based dye-sensitized solar cells were fabricated using these organic dyes as sensitizers and found to exhibit excellent overall conversion efficiencies ( $\sim 7\%$ ).

Baheti, P. Tyagi, K. R. Justin Thomas, Y.-C. Hsu, and J. T. Lin, *J. Phys. Chem. C* **2009**, *113*, 8541-8547.

## VISIBLE LIGHT RESPONSIVE NANOCRYSTALLINE TITANIUM DIOXIDE FOR DYE SENSITIZED SOLAR CELLS

B. KAJITHA,<sup>a</sup> S. SARATHCHANDRAN,<sup>b</sup> M. SENTHILNANTHANAN<sup>a</sup> AND P. RAVIRAJAN<sup>b\*</sup>

<sup>a</sup>Department of Chemistry, University of Jaffna, Sri Lanka

<sup>b</sup>Department of Physics, University of Jaffna, Sri Lanka

\*Corresponding Author, e-mail: pravirajan@gmail.com

### ABSTRACT

Dye sensitized solar cells (DSSC) have been extensively studied in the past decade due to their potential as cost-efficient solar cells. In these solar cells, sensitizer molecules which are firmly anchored on the surface of nanocrystalline metal oxide film absorb visible light and inject electron into the conduction band of the semiconducting metal oxide.  $I^-/I_3^-$  redox couple is used to regenerate the photo-oxidized sensitizer and thus serves as hole transporter while semiconducting metal oxide serves to transport the electron. Strong interaction with the sensitizer is a preferable quality expected in the semiconductors in view of enhancing the performance.

This study focuses on fabricating DSSC employing a visible light responsive  $TiO_2$  (VLR- $TiO_2$ ) prepared in a mixture of equal volumes of methanol and ethyl acetate. Dye extracted from grape fruit coat, which had already been reported as a promising natural sensitizer, was used to sensitize the VLR- $TiO_2$ . The devices were made by spin-coating the VLR- $TiO_2$  on Fluorene doped tin oxide (FTO) coated glass substrates. Pt coated FTO was used as the top contact. To compare the performance with VLR- $TiO_2$ , control devices were also fabricated using commercially available nanocrystalline  $TiO_2$ . Devices were characterized in dark and under solar simulator with AM 1.5 spectral filter at  $60 \text{ mWcm}^{-2}$  intensity. The spin-coated VLR-  $TiO_2$  showed improvements in the short circuit current density, open-circuit voltage and the fill factor, which improved the power conversion efficiency by a factor of eight compared to the control device.

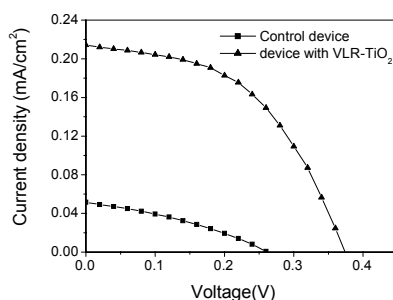


Figure 1: Comparison of current density-voltage characteristics of solar cells having VLR- $TiO_2$  and  $TiO_2$ .

## 1. INTRODUCTION

Dye-sensitized solar cells (DSSC) are one of the third-generation solar cell technologies with the potential to render solar energy as an economically attractive sustainable energy source. Power conversion efficiencies as high as 11% have been reported with these class of solar cells.<sup>1-3</sup> In DSSC, the monolayer of dye sensitizer anchored onto the surface of the wide-bandgap semiconductor films such as titanium dioxide ( $TiO_2$ ) / Zinc oxide( $ZnO$ ) harvests the sun light. The semiconductor film acts as an electron transporting material. The liquid DSSC incorporates

iodide/triiodide redox couple ( $I^-/I_3^-$ ) as hole transporter. Light absorbed in the sensitizer causes the injection of electrons into the conduction band and holes into the hole transporter. Electron and hole transporters are separately connected through selective contacts to the terminals of the device.

The  $TiO_2$  semiconductor being the most popular semiconducting material for its excellent optical and electronic properties, low cost, non toxicity, thermal stability. Out of the three different phases of  $TiO_2$  namely anatase (tetragonal), rutile (tetragonal) and brookite (orthorhombic) the anatase phase which has the highest band gap (3.2 eV) has been extensively used in solar cell applications. Moreover the Rutile is known to be the most stable phase of  $TiO_2$ . The mixture of rutile and anatase such as P-25 serves as the semiconductors in DSSCs. It has been further reported that the performance of these mixtures usually limited by recombinations of photo-generated electron/hole pairs and inefficient visible light utilization. Hence the quality of the  $TiO_2$  might play a leading role in enhancing the performance of DSSC's. <sup>4,6</sup> This illustrates the importance of a new search for the n-type semi conducting material having enhanced properties. This study focuses visible light responsive  $TiO_2$  as alternative acceptors to  $TiO_2$  nanocrystalline electrodes. The recent interest in anatase was motivated by its key role in the injection process in a photo chemical solar cell with high conversion efficiency. The VLR- $TiO_2$  powder used in this study was yellow in colour and the particle size and the mean pore diameter are specified as 53 nm and 8.2 nm respectively.<sup>5</sup>

## **2. MATERIALS AND METHODS**

Fluorine doped Tin oxide (FTO) coated glass substrates ( $25 \Omega/cm^2$ ) were cleaned using acetone and isopropyl alcohol and then annealed to remove any organic residue. To prepare the solution to deposit the porous nanocrystalline VLR- $TiO_2$ , the VLR-  $TiO_2$  powder was dissolved in a 1:1 v/v mixture of methanol and ethyl acetate and sonicated in Ultrasons-H model ultrasonicator for 10 hours.

Commercial  $TiO_2$  paste was dissolved in tetrahydrofuran to make the solution to deposit the porous nanocrystalline  $TiO_2$ . The solutions of VLR- $TiO_2$  and the commercial  $TiO_2$  were spin coated onto the cleaned FTO substrates.

The spin coated VLR- $TiO_2$  and commercial  $TiO_2$  films were sintered at 450 °C for 30 minutes and allowed to cool to room temperature and then dipped in the natural dye solutions extracted from grapes fruit coat, prepared as described in the Ref.[7] for 24 hour. To prepare the top contact Plastisol (Transparent Platinum catalyst paint) was brushed on a cleaned FTO glass plate and sintered at 400 °C for 10 minutes to be used as the top contact.

The dye adsorbed  $TiO_2$  and the Pt top electrode were pressed firmly together to make the solar cell. The liquid hole transporting material  $I^-/I_3^-$  redox couple was prepared as described in the Ref.[8] and introduced between the electrodes using a syringe.

The Current -voltage characterization of the solar cells were carried out in dark and under solar stimulator (SCIENCETECH) with AM 1.5 spectral filter at  $60 mWcm^{-2}$  intensity using a computer controlled Source-Measure unit (Keithley-2400).

## **3. RESULTS AND DISCUSSION**

Figure 2 shows the absorption spectra of the grape fruit dye solutions in water solvent. The absorption spectra of bare  $TiO_2$  and the dye adsorbed  $TiO_2$  are represented in the figure 3 for both the commercial  $TiO_2$  and for the VLR- $TiO_2$  films. The dye from grape fruit showed promising

performance even comparable to that of the commercial dyes such as Z907 [*cis*-bis(isothiocyanato)(2,2'-bipyridyl-4,4'-dicarboxylato)(2,2'-bipyridyl-4,4'-dinonyl) ruthenium (II)]. This is the reason for selecting this dye in this study comparing the performance of commercial TiO<sub>2</sub> and the VLR-TiO<sub>2</sub>. The grape fruit dye shows a fairly broader visible range absorption peaking around 530 nm.

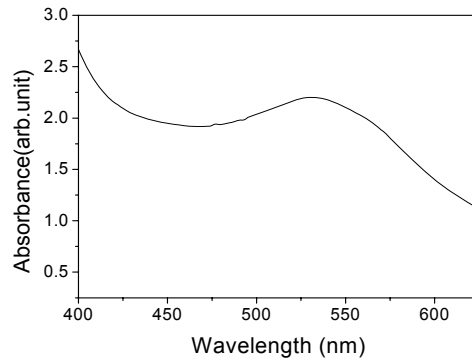


Figure 2: Optical absorption of Grape fruit coat dye solution prepared in water solvent

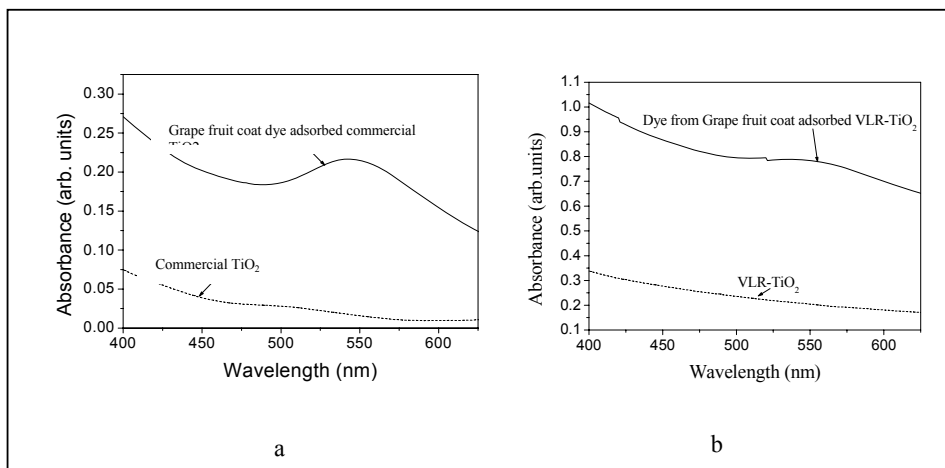


Figure3: Absorption features of (a) commercial TiO<sub>2</sub> and grape fruit dye adsorbed TiO<sub>2</sub> (b) VLR-TiO<sub>2</sub> and grape fruit dye adsorbed VLR-TiO<sub>2</sub>

The enhanced optical absorption observed with the VLR-TiO<sub>2</sub> most probably due to the content of the anatase phase as well as its open structure. Another possible reason will be the favorable anchoring that could occur in case of the VLR-TiO<sub>2</sub>. The firmly attachable anchoring groups such as the carboxylic acid groups might have the capability of enhancing the adsorption on VLR-TiO<sub>2</sub> film. Comparatively wider range absorbance is another striking and encouraging



feature observed with the dye adsorbed VLR-TiO<sub>2</sub> film. The surface area of the TiO<sub>2</sub> nanoparticle is another important aspect to be taken into account as far as the dye adsorption is concerned.

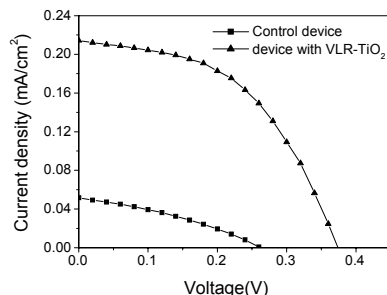


Figure 4: Comparison of current density-voltage characteristics of solar cells having VLR-TiO<sub>2</sub> and TiO<sub>2</sub>.

The Figure 4 illustrates the current density-voltage characteristics of the solar cells utilizing VLR-TiO<sub>2</sub> and commercial TiO<sub>2</sub> both of these employing grape fruit coat dye. More than a factor of three increase observed in the short-circuit current density whereas the open-circuit voltage shown an increase of about 42 % in the solar cells utilizing VLR-TiO<sub>2</sub>. Highly anatase content in VLR-TiO<sub>2</sub> could explain for the enhanced photovoltaic performance. It has been reported that the high anatase TiO<sub>2</sub> could facilitate the electron transport.<sup>9</sup>

#### 4. CONCLUSIONS

This study identified the VLR-TiO<sub>2</sub> as a promising n-type semiconductor for the DSSC applications. The Photovoltaic performance of the VLR-TiO<sub>2</sub> was compared with that of the commercial TiO<sub>2</sub>. VLR-TiO<sub>2</sub> shows significant optical absorption features compared to the commercial TiO<sub>2</sub>. The power conversion efficiency of the VLR-TiO<sub>2</sub> incorporates device is shown to increase by more than 75% compared to the control device due to more than three fold increase in the short-circuit current density and about 42% increase in the open-circuit voltage. VLR-TiO<sub>2</sub> probably attributed to the high anatase content in VLR-TiO<sub>2</sub> which could enhance the dye adsorption and charge transport that lead to enhanced photovoltaic performance.

#### REFERENCES

1. Y. Chiba, A. Islam, Y. Watanabe, R. Komiya, N. Koide, L. Han, *Jpn. J. Appl. Phys.*, 45, L638, (2006).
2. M. Grätzel, *J. Photochem. Photobiol*, 3, 164, (2004)
3. Novel Cyclometallated Ruthenium dye sensitizer for nanocrystalline TiO<sub>2</sub> based Solar cells, M.Senthilnathanan, S.Sarathchandran, John.M.Brown, S.Sivaraya and P.Ravirajan, Proceedings of the International conference on “Advances in Continuum mechanics, Nanoscience and Nanotechnology: Dedicated to Professor Munidasa P.Ranaweera”, University of Peradeniya, Sri Lanka, September 26-27, 2008
4. H. Shon, S. Phuntsho, Y. Okour, D.L. Cho, K. S. Kim, H. J. Li, S. Na, J. B. Kim and J. H. Kim, *J.Korean Ind.Eng.Chem*, 1-16, 19 (2008)
5. M.Senthilnathanan, D.P.Ho,S.Vigneswaran, H.H.Ngo, H.K. Shon, *Separation and purification technology*, 75 (2010)

6. H. Tang, K. Prasad, R. Sanjinbs, P. E. Schmid, and F. Levy, *J. Appl. Phys.* 75, 2042-2047 (1994)
7. Utilisation of Plant pigments in Dye-Sensitized Nanoporous TiO<sub>2</sub> Solar Cells  
T.Jaseetharan, S.Sarathchandran, K.Jeyakanthan, M.Senthilnathanan, S.Sivaraya and P.Ravirajan, *National Conference on Advanced Materials for Emerging Technologies (NCAMET 2007)* Peradeniya ,21-22 July 2007
8. G.P.Smestad and M.Gratzel,*J.Chem.Ed.*,75, 752 (1998)
9. Y. Chang Liu, Y. F. Lu, Y. Z. Zeng, C. H. Liao, J. C. Chung, T. Y. Wei, *Nanostructured Mesoporous Titanium Dioxide Thin Film Prepared by Sol-Gel Method for Dye Sensitized Solar Cell.*

**ENHANCING THE PERFORMANCE OF HYBRID TiO<sub>2</sub>/POLYMER MULTILAYER SOLAR CELLS BY MODIFYING THE TiO<sub>2</sub>/POLYMER INTERFACE BY SINGLE WALL CARBON NANOTUBE**

K. BALASHANGAR, T. JASEETHARAN, S. SARATHCHANDRAN AND P. RAVIRAJAN\*

*Department of Physics, University of Jaffna, Sri Lanka*

\*Corresponding Author, e-mail: *pravirajan@gmail.com*

**ABSTRACT**

The hybrid titanium dioxide/polymer solar cells in which the nanocrystalline titanium dioxide serves as electron acceptor have several merits compared to the all-organic solar cells. Although the chemical and mechanical stability of the hybrid titanium dioxide/polymer solar cells is better than those of polymer solar cells, the power conversion efficiency is still lower than the organic counterparts mainly due to poor rate of photocurrent generation attributed to the lower interfacial area available for exciton dissociation. Improved performance has been reported with the introduction of suitable TiO<sub>2</sub>/polymer interface modifiers and/or by increasing the effective area for exciton dissociation by controlling the device structure.

This study focuses on improving the performance of hybrid TiO<sub>2</sub>/polymer solar cells through incorporating n - type Single Wall carbon Nanotube (SWNT) in order to enhance the quality of the nanoporous TiO<sub>2</sub>/polymer interface. The TiO<sub>2</sub> substrates coated on to the Indium Tin oxide (ITO) coated glass substrates were dipped in the SWNT solution prepared in Tetrahydrofuran, before dipped into the polymer solution. Optical and electrical characterizations were carried for the SWNT incorporated solar cells as well as its control.

The overall power conversion efficiency of SWNT incorporated solar cell was significantly enhanced compared to the control cell most possibly due to the improved charge carrier generation, enhanced path for electron transport and reduced recombination aided with SWNT.

**Key words:** Solar cell, single wall carbon nanotube, TiO<sub>2</sub>, hybrid, polymer, photovoltaic

**1. INTRODUCTION**

The organic polymers and nanocrystalline inorganic metal oxides have concerned great interest due to their potential application in developing low-cost, large-area, mechanically flexible solar cells with increased stability.<sup>1-4</sup> Organic semiconductors are promising materials for photovoltaic cells and other optoelectronic applications. Multilayer structures have been developed to optimise photogeneration of charges and transport. Although the presently reported power conversion efficiency of these hybrid solar cells is much lower than that of the all organic solar cells, there are several rooms for development as promised by the control of the morphology and fabrication techniques offered by the nanocrystalline metal oxides. The lower interfacial area available for exciton dissociation is one of the main limiting factors identified in these hybrid metal oxide/polymer solar cells.<sup>5</sup>

Among the hybrid metal oxide/polymer solar cells that having porous TiO<sub>2</sub> templates infiltrated by the polymer has been the most studied system as it could allow efficient exciton dissociation and reasonable charge transportation. Improving the charge transport with reduced recombination is a viable route to enhance the performance of these solar cells. With this perception, some of the nanomaterials possessing favourable electrical and mechanical properties have been attempted to incorporate with these solar cells. Carbon nanotubes is one of that materials which has also been used in some recent photovoltaic researches with different

structured solar cells mainly for its unique electrical properties, high aspect ratio and low density.<sup>6-8</sup> In these studies carbon nanotubes played wide range of roles, for instance serving as transparent flexible electrode,<sup>8,9</sup> modified electrode,<sup>10</sup> buffer layer<sup>11</sup> and active component blended with polymer.<sup>11</sup> It has also been shown that the TiO<sub>2</sub> nanoparticles dispersed on n- type single wall carbon nanotubes (SWNT) films improved photoinduced charge separation and transport of carriers to the collecting electrode.<sup>10</sup>

The incorporation of an organic n-type material like SWNT has an added advantage compared to the n-type inorganic materials. The organic – organic miscibility attains in SWNT and the polymer could provide improved charge separation. With this background this work focuses the inclusion of n- type SWNT in nanoporous hybrid TiO<sub>2</sub>/polymer solar cells in which the porous TiO<sub>2</sub> templates are dipped in SWNT solution. This SWNT dipping step precedes the dipping in polymer. Here the electron transporting function carried out by TiO<sub>2</sub> is expected to be facilitated by SWNT. One of the crucial requisite about the dimension of the SWNT is that it should not exceed the thickness of the active layer comprising TiO<sub>2</sub>, SWNT and the polymer in order to avoid the direct contacts between the top and bottom electrodes.

## 2. EXPERIMENTAL DETAILS

All samples were prepared on Indium Tin Oxide (ITO) coated glass substrates which were first cleaned thoroughly in acetone and then in isopropanol several times. After blown with nitrogen the substrates were annealed for the purpose of removing organic residual. A dense layer of TiO<sub>2</sub> was then spray-coated onto these cleaned substrates as described in the Ref. [12] and subsequently sintered at 450 °C for 30 min. The TiO<sub>2</sub> obtained from Dyesol Australia Pvt. Ltd. was dissolved in tetrahydrofuran. The TiO<sub>2</sub> solutions were then spin-coated onto the dense TiO<sub>2</sub> and these substrates were again sintered at 450 °C for 30 min, allowed to cool and then dipped in the solution of SWNT, filtered through 0.22 micron sized filter. These substrates were then baked in order to remove any solvent and were dipped in poly(3-hexylthiophene) (P3HT) polymer(Merck Chemicals Ltd.) in chlorobenzene. After blown with nitrogen gas they were soft baked at 50 °C for 5 min. and the P3HT solution was spin-coated onto these substrates.

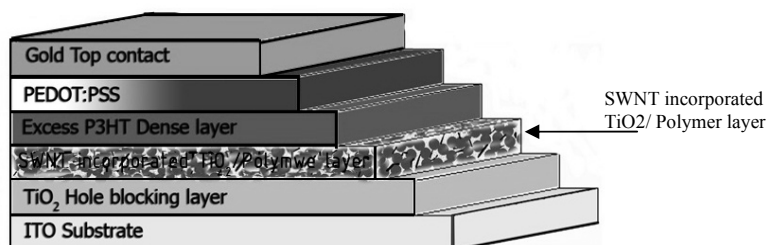


Fig. 1. Schematic diagram of the hybrid SWNT incorporated nanocrystalline TiO<sub>2</sub>/ polymer solar cell.

The aqueous solution of Polystyrene sulfonate doped poly (ethylene dioxythiophene) (PEDOT: PSS) (BAYTRON) which was first filtered through 0.45 micron filter and then heated at 90 °C for 5 min was spin-coated on the P3HT layer. These were baked at 100 °C for 5 min in a nitrogen filled home-built annealing box. On top of the PEDOT: PSS layer Au electrode was fabricated by thermal evaporation under vacuum better than 10<sup>-5</sup> torr. The schematic diagram of hybrid SWNT incorporated TiO<sub>2</sub>/ Polymer solar cell is shown in Fig. 1. The electrical characterization of the solar cells were carried out using source measure unit (Keithley 2400) in dark and illumination under solar simulator (SCIENCETECH) with AM 1.5 G filter. The optical

characterization was made for samples without top contact using UV-VIS-IR spectrometer (JASCO).

### 3. RESULTS AND DISCUSSION

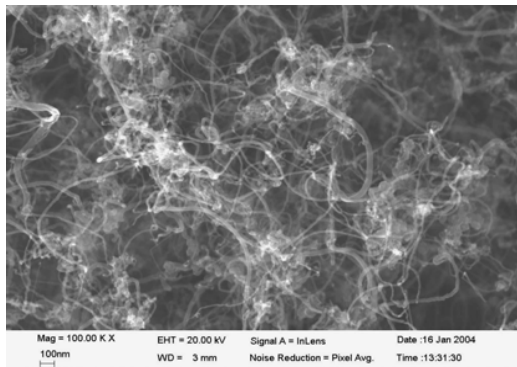


Fig 2. SEM image of bundles of SWNTs

The fig 2 depicts that the SWNT exist in bundles of carbon nanotubes with the size approximately in the range of 10 – 20 nm. Since this order is compatible with that of typical TiO<sub>2</sub> pore diameter, there is a high possibility for these bundles to penetrate into the pores.

It is also an important requisite that the incorporation of the SWNT in these solar cells should not vulnerable the polymer intake and optical screening. The most similar visible range absorption spectra depicted in Fig 3 ensured that this condition has not been violated in our design incorporating SWNT.

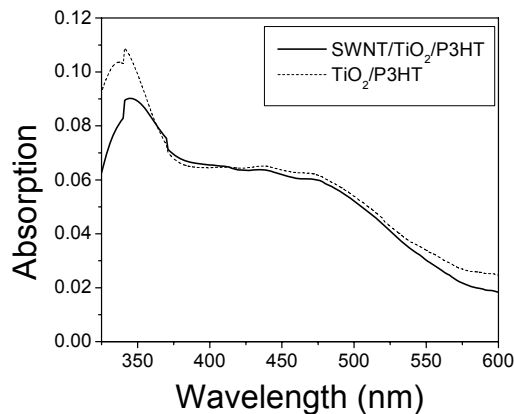


Fig 3 Optical absorbance of SWNT incorporated TiO<sub>2</sub>/ Polymer and control TiO<sub>2</sub>/ Polymer layers

The exciton dissociation efficiency, exciton quenching and charge transport efficiency are the expected qualities that need to be improved. The aim of this study is not to optimize the performance of the hybrid TiO<sub>2</sub>/polymer solar cells in the absolute terms but to explore the

feasibility of enhancing them by incorporating SWNT. As such some of the other performance enhancing fabrication steps like dipping in sensitizers prior to the dipping in the polymer and the post annealing treatment have been skipped to simplify the analysis.

The variation of the current density ( $J_{SC}$ ) with the applied voltage is shown in the Fig.4 for the control and the experimental solar cells both in dark and under the AM 1.5 G illumination with  $60 \text{ mWcm}^{-2}$  intensity.

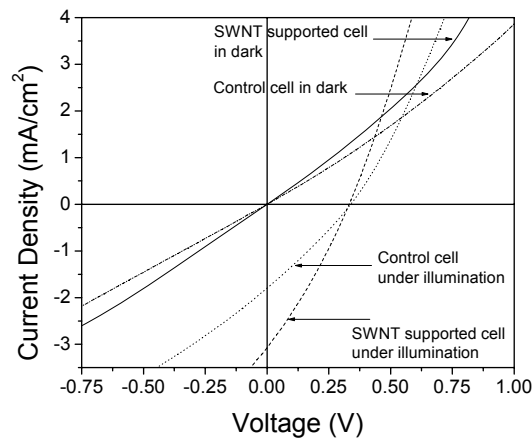


Fig. 4 JV characteristics of control hybrid  $\text{TiO}_2$  /P3HT and SWNT incorporated solar cells in dark and under AM 1.5G illumination from a solar simulator with  $70 \text{ mW/cm}^2$  intensity.

The short-circuit current density of the SWNT incorporated solar cells has shown an increase as high as 50% compared to the control cells. The incorporation of the SWNT slightly diminished the open-circuit voltage might be originated from the shift in energy levels. The significant increase in the short-circuit current density improved the overall power conversion efficiency by a factor of two compared to the control cell, most probably attributed to the efficient transport of electrons, reduction in the trap charge carriers, reduced resistive and recombination losses.

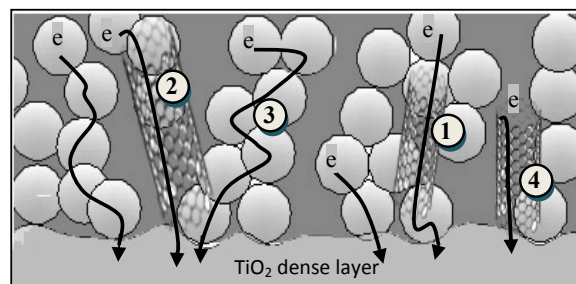


Fig. 5. Possible electron transport after the exciton dissociation occurred at  $\text{TiO}_2$ /Polymer interface (1) by Scaffolding and (2) by freeing from dead zones, supported by SWNT, (3) through nanoporous  $\text{TiO}_2$ . (4) The electron transport through SWNT, if there is a possibility for exciton dissociating at SWNT/Polymer interface.

Scaffolding and minimizing dead zones in the TiO<sub>2</sub> phase are the major ways in which the SWNT may facilitate electron transport in the hybrid TiO<sub>2</sub>/polymer solar cells as illustrated by numbers 1 and 2 in the Fig. 5. The electron mobility in n-SWNT has been reported as  $(2-6) \times 10^4 \text{ cm}^2/(\text{Vs})^{13}$  while that in porous TiO<sub>2</sub> is in the order of  $10^{-6} - 10^{-7} \text{ cm}^2/(\text{Vs})$ .<sup>6</sup> Hence the electron mobility in SWNT is effectively  $10^9$  times higher than that in porous TiO<sub>2</sub> and therefore it will be advantageous for the electron to travel through SWNT than the unsupported path provided by porous TiO<sub>2</sub> with 50 % porosity denoted by 3. Intra TiO<sub>2</sub> charge trapping, which could be another possible limiting factor of the electron collection in the TiO<sub>2</sub> based solar cells, could also be reduced by the assistance of SWNT. Enhanced transport of electrons on the other hand reduces the possibility of back electron transfer and hence minimizing the charge carrier recombination which is a common performance limiting factor that usually originates in poorly formed interfaces and conduction pathways. The SWNT supported percolation routes effectively reduce the series as well as shunt resistive losses. The study reported in the Ref. 11. confirmed and reinforced the result of the reduced series resistance of TiO<sub>2</sub> when supported with the CNT. The introduction of SWNT not only has the potential of improving the charge transport efficiency but also could boost the photocurrent generation rate by providing additional exciton dissociation sites available at SWNT/Polymer interface provided the work functions supports the dissociation.

#### 4. CONCLUSION

We found that the introduction of the n type SWNT in the hybrid TiO<sub>2</sub> / polymer solar cells improved the short-circuits current density by 50 % and leading to an overall increase in the power conversion efficiency of the SWNT incorporated solar cells by about 75% compared to the unsupported SWNT solar cell. This may be attributed to the enhanced charge transport associated with reduction in the series resistance, reduced shunt pathways, reduced recombination and back direction electron transport, reduced exciton quenching increased charge separation efficiencies, SWNT scaffolding, reduction in dead ends and incomplete pathways.

#### REFERENCES

1. T. Ishwara, D. D. C. Bradley, J. Nelson, P. Ravirajan, I. Vanseveren, T. Cleij, D. Vanderzande, L. Lutsen, S. Tierney, M. Heeney, and I. McCulloch, *Appl. Phys. Lett.* 92, 053308 (2008)
2. P. Ravirajan, D. D. C. Bradley, J. Nelson, S. A. Haque, J. R. Durrant, H. J. P. Smit and J. M. Kroon, *Appl. Phys. Lett.* 86, 143101 (2005)
3. Y. Kim, S. A. Choulis, J. Nelson, D. D. C. Bradley, S. Cook, and J. R. Durrant, *Appl. Phys. Lett.* 86, 063502 (2005)
4. P. Ravirajan, A. M. Peiro', M. K. Nazeeruddin, M. Graetzel, D. D. C. Bradley, J. R. Durrant, and J. Nelson, *J. Phys. Chem. B*, 110, 7635 (2006)
5. S. Sarathchandran, K. Haridas, Y. Kim, and P. Ravirajan, *J. Nanoelectron. Optoelectron.* 5, 243 (2010)
6. P. Ravirajan, S. A. Haque, J. R. Durrant, D. D. C. Bradley and J. Nelson, *Adv. Funct. Matter.* 15, 609 (2005)
7. J. Boucle, P. Ravirajan and J. Nelson, *J. Mater. Chem.*, 17, 3141 (2007)
8. Michael W. Rowell, Mark A. Topinka Michael D. McGehee, Hans-Jürgen Prall, Gilles Dennler, Niyazi Serdar Sariciftci, Liangbing Hu and George Gruner, *Appl. Phys. Lett.* 88, 233506 (2006)
9. Aurelien Du Pasquier, Husnu Emrah Unalan, Alokik Kanwal, Steve Miller, and Manish Chhowalla, *Appl. Phys. Lett.* 87, 203511 (2005)
10. Anusorn Kongkanand, Rebeca Marti'nez Domi'nguez, and Prashant V. Kamat, *Nano Lett.* 7, 676-680, (2007)

11. E. Kymakis and G. A. J. Amaratunga, *Appl. Phys. Lett.* 80, 112 (2002)
12. L. Kavan and M. Gratzel, *Electrochim. Acta* 40, 643 (1995)
13. R. Tameev, L. L. Jimenez, L. Y. Pereshivko, R. W. Rychwalski and A. V. Vannikov, *J. Phys: Conf. Ser.* 61, 1152 (2007)



**CONVERSION OF SOLAR ENERGY TO ELECTRICITY BY NATURAL  
DYE-SENSITIZATION**

C.I.F. ATTANAYAKE <sup>1\*</sup>, B.A.J.K. PREMACHANDRA <sup>1</sup>, A.A.P. DE ALWIS <sup>1</sup> and  
G.K.R. SENADEERA <sup>2,3</sup>

<sup>1</sup> *Department of Chemical and Process Engineering, University of Moratuwa, Moratuwa, Sri Lanka*

<sup>2</sup> *Institute of Fundamental Studies, Hantana Road, Kandy, Sri Lanka*

<sup>3</sup> *Department of Physics, The Open University of Sri Lanka, Nawala, Nugegoda, Sri Lanka.*

\*Corresponding Author, e-mail: [ivancamilus2011@gmail.com](mailto:ivancamilus2011@gmail.com)

**ABSTRACT**

Preliminary investigations on the identification of natural pigments in the dye-sensitization of nanocrystalline n-type TiO<sub>2</sub> were carried out. Fresh extracts of Mangoostein, Rambutan, Mango, Tomato, Carrot, Kingcoconut, Pumpkin, Red Banana, Beetroot, Turmeric, Venivel, Orange, Grape, Spinach, Wattakka, Ginger etc were employed as sensitization in thin layer sandwich type photoelectrochemical dye – sensitized solar cells (DSSC's).

After electrical and electronic analysis, it was observed that many useful dyes which could be extracted from natural products by simple procedure could be used as photo sensitizers for DSSC's. It was also observed that dye extracts of Turmeric and Mangoostein yielded better results.

The current-voltage curves obtained with solar cells employing the photoanode with TiO<sub>2</sub> sensitized by different dyes were observed. The values of short circuit current density (J<sub>sc</sub>), open circuit voltage (V<sub>oc</sub>), fill factor (ff), and efficiency (η) obtained for solar cells employing photoanodes with TiO<sub>2</sub> sensitized with different fruit / vegetable extracts were noted . The dye extracts of Turmeric root and Mangoostein fruit were found to be superior to those obtained from other dyes , and were J<sub>sc</sub> = 0.54 mAcm<sup>-2</sup> and 0.44 mAcm<sup>-2</sup>, V<sub>oc</sub> = 599.1 mV and 565.2 mV, ff = 69.03 % and 65.66 % , η = 0.22 % and 0.17 % respectively.

This work done incorporates the foundation on which research could be done to develop low-cost, high efficiency solar energy to electricity conversion units for use in countries like Sri Lanka.

## **EFFECT OF THIN ZINC OXIDE TRANSPARENT LAYERS ON CRYSTALLINE SILICON SOLAR CELLS**

G.D.K. MAHANAMA<sup>1\*</sup> and H.S. REEHAL<sup>2</sup>

<sup>1</sup>*Department of Physics, University of Ruhuna, Matara, Sri Lanka*

<sup>2</sup>*Department of Engineering and Design, London South Bank University, 103 Borough Road, London SE1 0AA, UK*

\*Corresponding Author, e-mail: [mahanama@phy.ruh.ac.lk](mailto:mahanama@phy.ruh.ac.lk)

### **ABSTRACT**

Low temperature (200-325°C) ECR (electron cyclotron resonance) plasma enhanced CVD has been used to deposit microcrystalline and epitaxial emitter layers in simple crystalline Si solar cell structures. Zinc Oxide (ZnO) transparent layers have been used on these silicon solar cells as anti-reflecting coatings (ARC). The RF magnetron sputtering technique was used for depositing these ZnO layers on silicon solar cells. The dependence of electrical and optical properties of the films as a function of substrate temperature and deposition pressure have been investigated. Films deposited at room temperature were highly resistive. A low resistivity value of  $4.7 \times 10^{-4} \Omega\text{cm}$  could be achieved with increasing the deposition temperature up to  $\sim 350^\circ\text{C}$ . A thickness of 70-80 nm is optimum for use of the films as anti-reflection coatings. After ZnO ARC application, the cell efficiency could be improved up to 13.1% for an epitaxial emitter cell from the original value of 10.8%.

Keywords: c-Si, Micro Crystalline Si, Epitaxial emitter, ZnO anti-reflective coatings

## **1. INTRODUCTION**

Thin film silicon/crystalline silicon (c-Si) heterojunction solar cells are attracting considerable attention. These have been investigated as an alternative to conventional c-Si cells which use diffused p-n junctions and require high temperature processing. Much of the work on Si heterojunction cells has focused on the use of amorphous Si (a-Si:H) layers with n-type monocrystalline Si substrates and these devices are in commercial production [1]. In this work we report on the properties of heterojunction Si solar cells with micro crystalline silicon ( $\mu\text{c-Si}$ ) and epitaxial silicon emitters on p-type monocrystalline substrates. Improvement of cell performance has been studied with the inclusion of zinc oxide anti-reflective coatings. This shows a significant improvement of cell short-circuit current and, hence, the efficiency.

## **2. EXPERIMENTAL**

### *2.1 Film growth*

ECR PECVD has been used to deposit the n-type silicon emitter films. A description of the growth system has been given in reference [2]. It was of stainless steel construction with a base pressure of  $\sim 10^{-7}$  Torr provided by a 1000 l/s turbomolecular pump. The ECR source is operated at the standard microwave frequency and magnetic field of 2.45 GHz and 875 G, respectively. For this work, a 2% phosphine in hydrogen source has been used as the doping gas. Micro crystalline Si and epitaxial Si films were grown at temperatures  $\leq 325^\circ\text{C}$  and  $440^\circ\text{C}$ , respectively on p-type (1-10  $\Omega\text{cm}$  resistivity) wafers using a high hydrogen dilution. The hydrogen and silane flow rates were fixed at 30 sccm and 1 sccm, respectively. The wafers were cleaned by the standard RCA method, given a dilute HF dip and dried with dry  $\text{N}_2$  before insertion into the load-lock chamber of the ECR system. Microwave power used was 400 W and the growth pressure was controlled between (4-5) mTorr.

Structural properties of the deposited films were measured by X-Ray diffraction using a Philips X'Pert system and Raman spectroscopy using a Renishaw Ramascope 2000 system with 488 nm Ar ion excitation. Film sheet resistance was determined using the four-point probe method. DEKTAK profilometry was used to measure film thickness.

## 2.2 Solar cell preparation

The layer thickness of these emitters was  $\sim 150$  nm. Mesa structures of  $1 \text{ cm}^2$  were formed using photolithography. Top and bottom contacts were made using thermally evaporated aluminium, after mesa formation. The bottom contacts were evaporated first and annealed at  $500^\circ\text{C}$  for 30 minutes in a  $\text{H}_2/\text{N}_2$  ambient. Then top contacts were deposited through a shadow mask to complete the cell structure. In this study, we have not used high efficiency features such as texturization step. The active area of the cells was  $\sim 0.80 \text{ cm}^2$ .

## 2.3 Anti-reflective coating deposition

For this process, 70-80 nm thick ZnO layers were deposited as anti-reflective coatings on top of the cells with  $\mu\text{-Si}$  and epitaxial emitters. This was done using RF sputtering at a substrate temperature of  $250\text{-}300^\circ\text{C}$ . Deposition pressure, RF power and Ar flow rates used were 3 mTorr, 200 W and 20 sccm, respectively. For these sputter depositions, a 3-inch diameter disk type ZnO (99.999% purity) target doped with  $\text{Al}_2\text{O}_3$  (2 wt%) was used. Cell I-V and spectral response data were measured before and after anti-reflective coating deposition.

## 2.4 Solar cell characterization

Current-voltage (I-V) characteristics have been measured by a Hewlet Packard 4145 semiconductor parameter analyzer controlled by VEE software. The light intensity of the solar simulator was calibrated to  $100 \text{ mW/cm}^2$  by using a reference cell from BP Solar. A peltier heat pump was used to control the sample base temperature at  $25^\circ\text{C}$  throughout the measurement. The spectral response measurements were carried out over the wavelength range 400-1200 nm.

# 3. RESULTS AND DISCUSSION

## 3.1 ZnO:Al Films

Initially, the ZnO:Al films were prepared at different temperatures in order to obtain low resistivity films. Films deposited at room temperature were highly resistive. The resistivity variation with deposition temperature is shown in Figure 1 where the strong dependence on the deposition temperature can be seen. We could achieve a low resistivity value of  $4.71 \times 10^{-4} \Omega\text{cm}$  with increasing the deposition temperature up to  $\sim 350^\circ\text{C}$ . These depositions were done under a pressure of 3 mTorr. J.Yoo et al [3]. have reported similar results in their study of ZnO:Al films deposited by RF sputtering. They obtained values down to  $\sim 2 \times 10^{-4} \Omega\text{cm}$  at a deposition temperature of  $300^\circ\text{C}$  and a low deposition pressure of 2.05 mTorr (0.27 Pa).

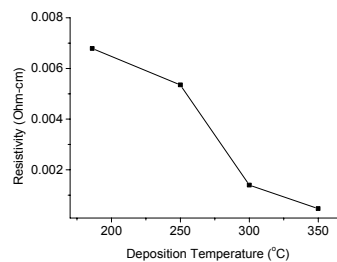


Figure 1: Resistivity variation with deposition temperature

In order to investigate the optical properties of these films, transmittance and reflectance measurements were done using a Cary 500 UV-Vis-NIR spectrophotometer. Transmittance spectra for films grown at different temperatures are shown in Figure 2. Transmission values are always  $\geq 80\%$  for these films. This shows that the ZnO:Al films have a good transmission and are suitable for use as TCO (transparent conductive oxide) layers on heterojunction solar cells. The structure in the data in Figure 2 is due to interference effects. The temperature indicated next to each curve is the substrate temperature. This was measured with a thermocouple attached to a sample during a calibration run.

The transmittance with ZnO:Al layer thickness is shown in Figure 3. This Figure shows that the interference fringes increase with increasing film thickness as expected. These films were deposited at a temperature of  $186^\circ\text{C}$  and pressure of 5 mTorr. D.Song et al [4]. have reported that the interference fringes of the spectra indicate the smoothness of the surface of the films. In the case of reflectance, the film with the lowest thickness (80 nm) gives the lowest reflectance (not shown). A thickness of 70-80 nm is optimum for use of the films as anti-reflection coatings.

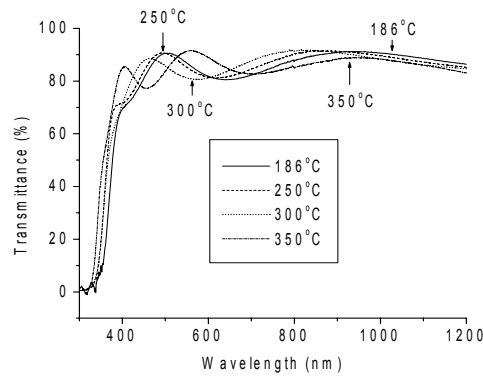


Figure 2: Transmittance variation of ZnO:Al films with deposition temperature.

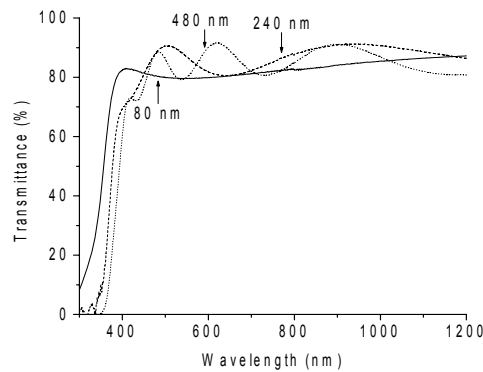


Figure 3: Transmittance variation with ZnO:Al film thickness.

The other most important parameter for ZnO:Al film deposition was the background pressure. We have deposited ZnO:Al films in the pressure range of 3-20 mTorr in order to

investigate the effect on the electrical and optical properties. These depositions were done at ~ 350°C and 30 minutes of deposition time was used. The resistivity variation with deposition pressure is shown in Figure 4.

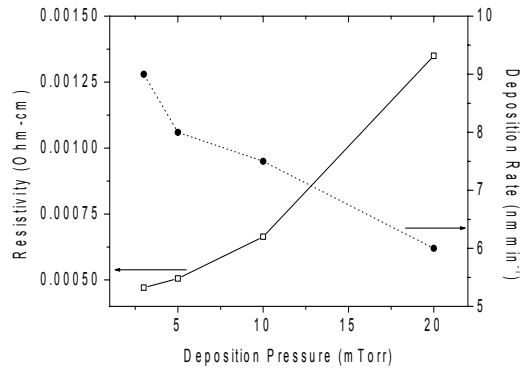


Figure 4: Resistivity and deposition rate variation with ZnO:Al deposition pressure

It can be seen that the film resistivity has a strong dependence on the deposition pressure. We could lower the resistivity down to  $4.71 \times 10^{-4} \Omega \text{ cm}$  by using a low pressure of 3 mTorr. J.Yoo et al.<sup>3</sup> have also reported a similar behaviour for resistivity variation with the deposition pressure. The resistivity,  $\rho$  is proportional to the reciprocal of product of doping concentration (N) and the Hall mobility ( $\mu$ ) [5]. Therefore, the change in resistivity with argon gas pressure might be due to the change in N or  $\mu$  or both. We have not separately measured these parameters but it is possible that the reduction with pressure of the deposition rate alters the film structure and hence the mobility of the carriers. The decrease of deposition rate with increasing pressure is also shown in Figure 4. J.Yoo et al.<sup>3</sup> have reported similar behavior.

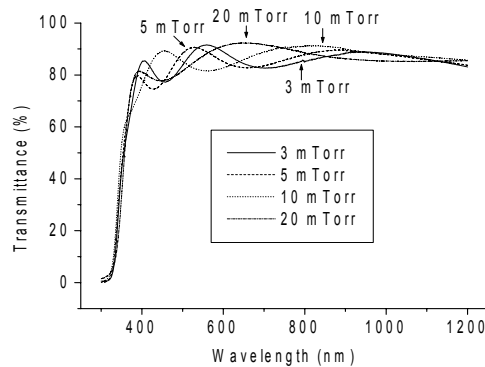


Figure 5: Transmission spectra with ZnO:Al deposition pressure

Transmission spectra with deposition pressure are shown in Figure 5. The data is broadly similar showing the film transmission does not depend strongly on pressure. The interference structure reflects the change in film thickness with pressure. The optimised layers had very good transparency (transmission > 80% in the spectral range of 300-1200 nm) and a very low resistivity of  $4.7 \times 10^{-4} \Omega \text{ cm}$ .

### 3.2 Solar Cell Behaviour

Solar cell performance data before and after antireflective coating application for both epitaxial and microcrystalline cells is shown in Figure 6 (a) and (b), respectively. The initial efficiency of both cells is similar, with similar open circuit voltages ( $V_{oc}$ ). After application of the ZnO:Al layers the short circuit current density ( $J_{sc}$ ) shows a significant increase for both cells due to the AR effect of the coatings. The  $V_{oc}$  also increases by a similar amount for both cases. The fill factor (FF), however, degrades for both cells, the fall being larger for the microcrystalline emitter cell which has a lower starting FF.

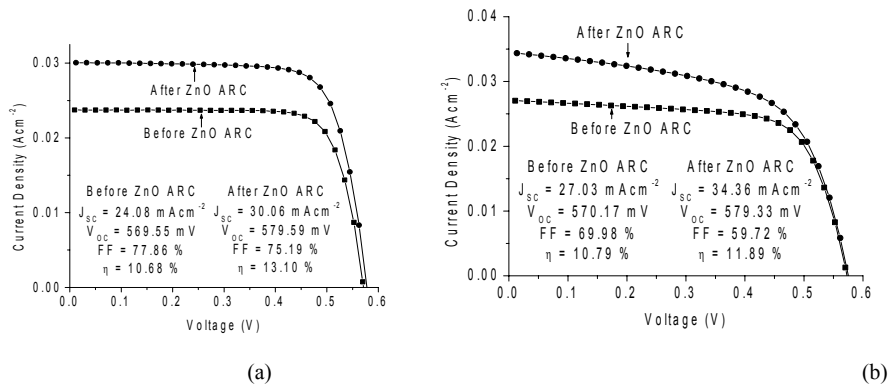


Figure 6: J-V curves for (a) epitaxial and (b) microcrystalline emitter cells before and after ZnO AR coating application

Detailed analysis of the I-V data of the cells shows that the initially lower FF of the microcrystalline emitter cell is due to a significantly lower shunt resistance. The shunt resistance decreases even further after ZnO application to reduce the FF even more. Further work is required to account for these observations.

The improvement of the short-circuit current density due to the ZnO AR coatings can be seen and is reflected in the spectral response data. Spectral response curves for the epitaxial and microcrystalline emitter cells before and after anti-reflective coating application are shown in Figure 7 (a) and (b), respectively. Interestingly, the improvement in the spectral response occurs not only in the visible region but also in the IR region. This improvement is larger for the microcrystalline emitter cell confirming the bigger improvement of the short-circuit current.

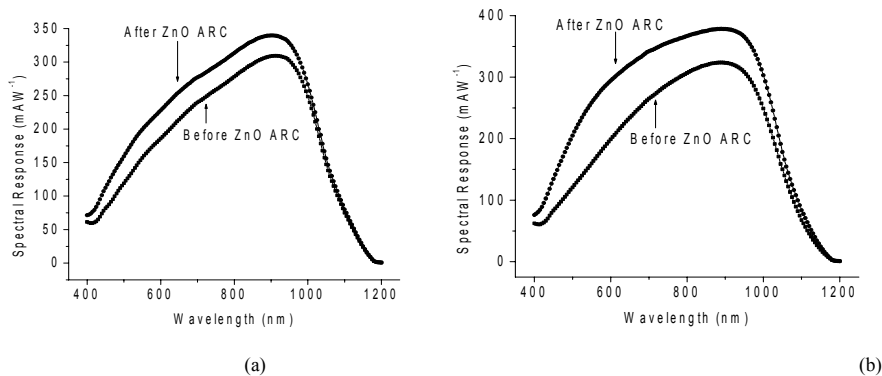


Figure 7: Spectral response curves for (a) epitaxial emitter cell and (b) microcrystalline emitter cell before and after ZnO:Al ARC application

#### 4. CONCLUSIONS

Simple heterojunction cell performance has been studied as a function of zinc oxide layer thickness and deposition parameters. This study shows that the resistivity of ZnO layers decreases with annealing temperature. The resistivity of the films also depends strongly on the sputtering pressure and deposition temperature. ZnO:Al thin films with very good transmittance and low resistivity can be obtained at a growth temperature of  $\sim 350^{\circ}\text{C}$  and a pressure of 3 mTorr by RF sputtering. The application of these ZnO ARCs to solar cells shows a significant improvement in cell performance due, especially, to an increase in the short-circuit current.

#### 5. ACKNOWLEDGEMENTS

We would like to thank Mr. T. Quinn for help with the sputter deposition.

#### REFERENCES

1. T. Mishima, M. Taguchi, H. Sakata, E. Maruyama, *Solar Energy Materials & Solar Cells*, 95 (2011) 18-21.
2. S. Summers, H.S. Reehal, G.H. Shirkoobi, *J. Phys. D: Appl. Phys.* 34 (2001) 2782.
3. J. Yoo, J. Lee, S. Kim, K. Yoon, I. J. Park, S. K. Dhungel, B. Karunakaran, D. Magalaraj, J. Yi, *Thin Solid Films*, 480-481, (2005) 213-127.
4. D. Song, A. G. Aberle, J. Xia, *Appl. Surf. Sci.*, 195, (2002) 291-296.
5. Y. Igasaki, H. Kanma, *Appl. Surf. Sci.*, 169-170, (2001) 508-511.

## **GROWTH OF ZINC OXIDE NANOSTRUCTURES ON (100) SILICON SURFACE FOR CRYSTALLINE SOLAR CELL**

HRISHIKESH DHASMANA\*, CHARU DWIVEDI and VIRESH DUTTA

*Photovoltaic Laboratory, Centre for Energy studies,  
Indian Institute of Technology Delhi, Hauz Khas, New Delhi-110016, India*

\*Corresponding Author, e-mail: [h\\_dhasmana@rediffmail.com](mailto:h_dhasmana@rediffmail.com)

### **ABSTRACT**

Nanostructured layers of ZnO having different morphologies (like nanorods and flower like nanosheet) have been deposited on polished (100) Si surface by continuous spray pyrolysis (CoSP). The layer formation requires a seed layer of ZnCl<sub>2</sub> which plays a major role in nanostructure formation. The effect of anisotropic Si surface etching in ZnO nanorod growth has been examined by XRD and SEM. The vertical aligned growth of ZnO has been found to be dependent on amount of etched Si surface and accordingly nanorod density, nanorod diameter variation has been observed. The techniques is shown to give nanostructured layers of ZnO on differently treated Si surface which can help in reducing the reflection for better light coupling in solar cells. The possibility of incorporating the process for large scale production Si solar cell production is also discussed.

Keywords: ZnO, Si (100), etching, nanostructures, spray pyrolysis, reflection loss.

### **I. INTRODUCTION**

Crystalline silicon (Si) solar cell technology is the dominant technology for Photovoltaic (PV) power generation. But the cost of Si solar cells leads to a high solar electricity cost and has limited the growth of PV applications. Even if this is true, the advantages offered by the PV technology continue to help in the growth and developments in all aspects – from device technologies to diversity of applications. The three generations of solar cells encompass a variety of materials (from single element to multi components) and solar cell architectures. The underlying effort is directed to improve the light harvesting and conversion of photons into mobile charge carriers for delivering power to the load. The improved efficiency without much addition to the cost will help PV Technology to penetrate the electricity generation market and be competitive to other electricity generating technologies, without adding to the global warming. The maturity in the Si solar cell fabrication technology has led to cell efficiency ~17% under large scale production (in 100 MW range). Apart from proper junction and contact formations, surface texturization, and antireflection coating (silicon nitride coating by plasma CVD ,e.g.) help increase the efficiency by the way of reduced reflection loss [1]. The process steps and equipments required for the surface treatment add to the fabrication cost. A simpler inline process to create similar improvements can possibly lead to increased efficiency without any significant cost enhancement. Nanostructures can be created on Si surface which can help achieve the required reduction in reflection from the surface by having the required surface morphology to achieve light trapping. The material used should have a matching refractive index and low absorptivity to create the desired improvement. Moreover, the deposition technique should be easily integrated with the existing production technology in order to offer the cost advantage as well. Nanostructure parameters such as size and shape, should also be tunable to effect proper control over the surface characteristics.

In recent years, Zinc Oxide(ZnO) nanostructures growth on Si-based substrates have been receiving increased interest due to the advantages , viz. a good transparency in visible wavelength region, appropriate refractive index (nearly 2), ability to form textured coating via anisotropic



growth etc. Various types of Zinc Oxide (ZnO) nanostructures on Si surface, such as nanorods, porous particles are being suggested for minimizing reflection loss on Si (silicon) surface to enhance photocurrent in silicon solar cell [2,3]. Fabrication of ZnO nanostructures on silicon (Si) wafer have been reported by several research groups based on gas phase synthesis [4,5,6]. But these techniques are costly and require sophisticated equipment with rigorous experimental conditions. Therefore, in spite of various methods existing for preparation of ZnO layers having nanostructures, there is still a need for developing a method that can produce the layers with high repeatability and low cost. Solution based synthesis such as chemical spray pyrolysis technique can offer several advantages of being inexpensive, easy to use, relatively fast, vacuum less and scaling up for large-area deposition in an inline mode [7]. There are few reports on ZnO growth over Si surface by ultrasonic spray pyrolysis (USP) [8,9]. Continuous spray pyrolysis (CoSP) has been established in the lab for fabricating nanoparticles as well as nanostructure layers on glass [10]. The process for making similar layers on Si substrate has now been successfully developed and the results are being reported in this paper.

Various research groups have attempted to grow ZnO on (100) Si surface and other material substrate surfaces such as alumina ( $\text{Al}_2\text{O}_3$ ), gallium nitride (GaN), aluminum nitride (AlN) etc. They compared the growth of nanostructures and reported that the lattice matching between ZnO and substrate plays an important role in the alignment of ZnO nanostructures. The large lattice mismatch between (100) Si surface and wurtzite ZnO nanostructures suggests difficulties in the growth of ZnO nanostructures on bare Si surface. So specific treatment of (100) Si surface such as seed layer growth for suitable ZnO nanorods growth are suggested in various deposition techniques [11,12]. Moreover, the effect of Potassium Hydroxide (KOH) etching on Si polished wafers is also studied for ZnO growth over Si surface. The KOH etching of (100) Si surface is performed at room temperature, which results into V shaped etch pits in (111) direction [13]. The substrates (etched, seed layer coated) are placed in the third zone of a three-zone furnace for spray deposition. This paper reports on various ZnO nanostructures created using CoSP on (100) Si surface and discusses the possible growth mechanism.

## **2. EXPERIMENTAL**

The ZnO nanostructured layer cannot be deposited on an unprepared polished Si substrate may be because of large lattice mismatch. Therefore, prior surface treatment such as seed layer growth and KOH etching is required for the growth of ZnO nanostructure on (100) Si surface by CoSP. The Si surface was treated in KOH etching solution for (a) 4 minutes and (b) 8 minutes at room temperature.  $\text{ZnCl}_2$  seed layer over polished, etched and oxidized Si surfaces is deposited by dipping the various substrate surface for nearly 10 minutes in 0.1 M  $\text{ZnCl}_2$  solution and then the substrate is heated at 100-125°C. The Si substrates having the  $\text{ZnCl}_2$  seed layer grown on polished, etched and oxidized surface are placed in the third zone of CoSP furnace for deposition at 850°C. 0.1 M Zinc acetate ( $\text{CH}_3\text{COO}$ )<sub>2</sub>Zn.2H<sub>2</sub>O (Sigma- Aldrich 98% pure), was dissolved in 100 ml distilled water and kept for stirring until transparent solution is observed. The solution flow rate and gas pressure were kept constant at 2 ml/min and 2 kgf/cm<sup>2</sup> for 5-20 minutes deposition time in CoSP. Oxygen gas was used as the carrier gas. The ZnO nanoparticles are created due to the pyrolysis of the spray droplets containing Zn precursor in the second zone which self-assemble to create nanostructure layer in third zone. The crystal structure and surface morphology of ZnO over (100) Si surface were investigated by Philips XPERD PRO(PW3040) X-Ray Diffractometer (XRD) and ZEISS EVO-50 model Scanning Electron Microscopy (SEM). All Si surfaces, apart

Table 1. Sample details of ZnO nanostructures over ZnO seed layer deposited Si surfaces.

S.No	Type of Si surface	Sample name	Deposition time
1.	Polished	SP	5
2.	4 minutes etched polished	SP4	10
3.	8 minutes etched polished	SP8	20
4.	Oxidized and textured	SO	10

from oxidized Si surface, are chosen with native oxide layers. Various research groups have suggested that the ZnO growth on seed layer is dependent on the seed grain size, seed layer thickness, surface characteristics and deposition time, which may result into the lateral growth of film [14,15]. The various surface profiles of ZnO seed layer is provided to the incoming ZnO self assemble nanoparticles in CoSP for further growth of ZnO nanostructure, which may be dependent on deposition time also. Sample details for ZnO nanostructures are given in the Table 1.

### 3. RESULTS AND DISCUSSION

The possible effect of seed layer on nanostructure formation by self assembly of nanoparticles has been dealt in 5 minute deposition on polished Si surface. While, the effect of various depth of etch pits in Si surface for ZnO growth have been dealt in 10 minute and 20 minute depositions. The index matched XRD

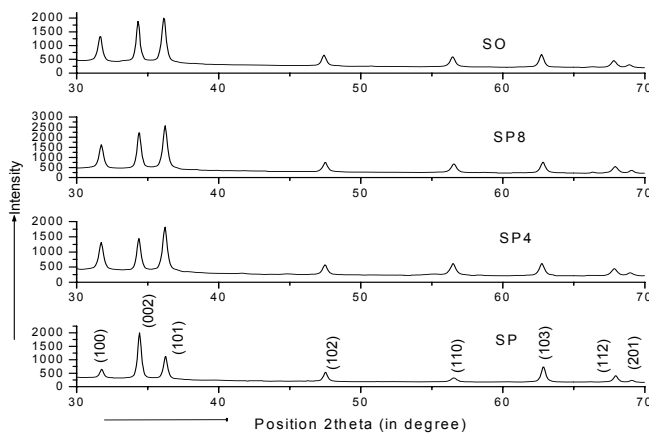


Figure 1. XRD pattern for (a) SP (b) SP 4 (c) SP 8 (d) SO

pattern for ZnO nanostructure layer on polished, etched and oxidized Si surface is shown in the Figure1 with the diffraction peaks indexed to hexagonal wurtzite ZnO (JCPDS Card No. 36-1451) giving lattice constants  $a = b = 3.249 \text{ \AA}$  and  $c = 5.206 \text{ \AA}$ . Since no major diffraction peaks from any other impurity has been detected, it indicates that the deposited thin films are pure ZnO with impurity level below the detectable limit. Compared with the standard spectrum, the (0 0 2) peak is much stronger than (1 0 0) and (1 0 1) peaks ( Fig.1 (a)), which indicates ZnO nanostructures preferentially grow along the [0 0 1] direction to the seed layer [001] plane

direction . The (103) relative intensity peak for SP has dominated over (100) plane. The XRD patterns for SP4 and SP8 have dominant peak corresponding to (101) plane. The (002) ZnO preferred orientation growth is regularly increasing in SP4, SP8 and SO with relative intensity values 71.75, 86.42 and 91.99 with respect to (101) plane as shown in Figure 1(b) , 1(c) and 1(d). The XRD pattern for SO sample further confirms that the growth of ZnO on oxidized surface is highly site specific because of the texturization of the Si surface.

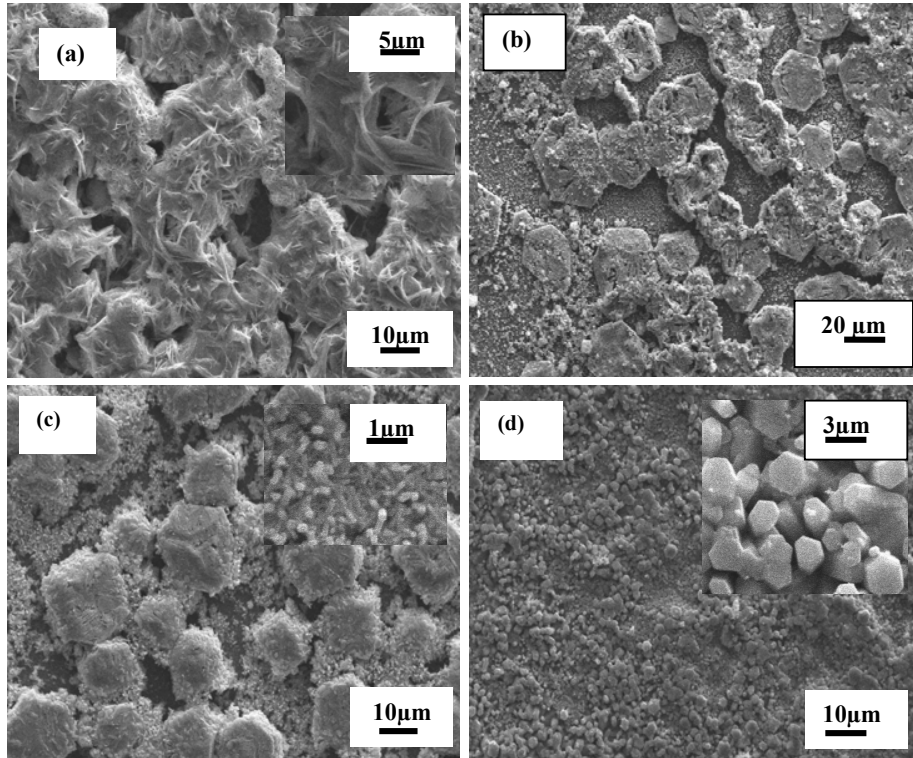


Figure2. SEM of ZnO on (100) Si surface (a) SP (b) SP4 (c) SP8 (d) SO

Figure 2 show the surface morphology of ZnO growth over various surface treated p-type Si wafers. Figure 2(a) depicts the surface morphology of ZnO for sample SP. In this figure, flower like nanosheet network of ZnO is observed. This nanosheet network films with high magnification is shown in inset image of Figure 2(a). The interconnected ZnO nanosheet results into hexagonal shape, which is clearly visible in high magnification image in inset Figure 2(a). The wall thickness of these nanosheets is in the range of  $\sim 500\text{nm}$  and the width of hexagonal flower like network sheet is  $5\ \mu\text{m}$ . The higher deposition time with respect to SP and 4 minute etching has led to the ZnO nanorods of diameter  $\sim 20\ \mu\text{m}$  as seen in the Figure 2(b). Some of the broken hexagonal rods are observed and couldn't result into well aligned (002) oriented ZnO growth due to the lower number of energetically favored nucleation site for ZnO growth as compared to SP8. Higher growth of ZnO nanorods is observed in SP8 with the increase in nanorod density as shown in Figure 2(c). In this case, the effect of KOH etching in the growth of ZnO film over Si surface has been dominated over seed layer effect. In between the ZnO hexagonal rods of diameter  $\sim 10\ \mu\text{m}$ , there are large numbers of randomly aligned nanorods of approximately  $400\text{nm}$  diameter as shown

in corresponding inset image, which suggests existing seed layer effect. The ZnO growth by CSP is also carried out on oxidized, textured Si wafer for SO as shown in Figure 2(d). The high depth (~10  $\mu\text{m}$ ) oxidized pyramids provide the additional mobility and higher growth as compared to SP8 to the Zinc (Zn) and Oxygen(O) ions for (002) ZnO oriented growth, which is clearly visible in the corresponding inset image with highly dense well aligned hexagonal rods of diameter 3 $\mu\text{m}$ .

### 3.1 Growth mechanism

In the case of SP, the deposition time is only 5 minutes and there are no etch pits in Si surface for seed layer. Reported work in the literature suggests that this seed layer induces the particular shape in the resulting film which may result into lateral growth also. Ahmad Umar et al reported ZnO nanosheet and nanodisc growth on Si surface [16] and suggested that two dimensional growth in [100] and [001] direction plays an important role in the formation of nanosheet. Here interestingly (103) peaks has dominated over (100) peak, which may be due to higher growth velocity of the plane, two dimensional growth supported by seed layer and also due to the higher grain area as compared to (100). This paper first time reports the growth of nanosheet network on Si (100) surface by CoSP, where the seed layer prior to the deposition support such flower like nanostructure formation on Si surface.

Growth mechanism for vertical alignment of ZnO crystal on Si surface has been discussed by Premkumar *et al* [17]. The reported ZnO crystal growth relation [18] is  $[0001] \rightarrow [01\bar{1}\bar{1}] \rightarrow [10\bar{1}0] \rightarrow [01\bar{1}\bar{1}]$ . For ZnO crystal growth over Si surface, relative velocity amongst crystal plane, deposition time and KOH etching time are the determining factors for the shape and size of ZnO nanostructures in the case of SP4, SP8 and SO. In the case of ZnO crystal growth, the [0001] plane has highest velocity and very unstable plane. After sometime, during the growth (002) plane disappears and (101) plane starts to dominate in the crystal growth because of least energy configuration, therefore (101) dominant peak is observed. For larger ZnO crystal growth, the ZnO nanorod grow along c axis and the incoming Zinc (Zn) and Oxygen (O) ions contribute to the radial growth in  $[10\bar{1}0]$  direction. This radial growth leads to coalescence of neighboring nanorod with each other and after coalescence large crystallite is resulted as shown in corresponding SEM images of sample. Verma *et al.* reported diameter increase of ZnO nanorods due to coalescence of nanocolumns and attributed it to the decrease in lattice mismatching between films and substrate [19]. In the case of SP4, the (002) preferred orientation in film has started to rise by increase in relative intensity for (002) plane with respect to the case of bulk ZnO crystal, which is confirmed in Figure 1(b) and Figure 2(b). The amount of depth of KOH etch pits is nearly 100nm. With low deposition time 10 minutes, the ZnO hexagonal rods growth seems to be due to the coalescence in radial direction [100] of ZnO crystal. This results into larger diameter of hexagonal rods and some broken hexagonal pieces as shown in Figure 1(b) and Figure 2(b). In the case of SP8, the etch pits depth is increased from 100 nm to 200 nm and deposition time is increased from 10 minutes to 20 minutes as compared to SP4. The additional energetically favored nucleation site and relative velocity amongst the crystal plane increases the hexagonal rod density, so decrease in the size of hexagonal rods from 20  $\mu\text{m}$  to 10 $\mu\text{m}$  is observed as shown in Figure 1(c) and 2(c). In the case of SO, oxidized surface of textured Si and high deposition time decreases the lattice mismatch effect between substrate and film therefore radial coalescence has been found to be decreased and the nanorod density is increased. The high depth pyramid upto ~10 $\mu\text{m}$  formed due to texturization offer additional mobility and higher ZnO growth rate in (002) direction. The (002) oriented ZnO growth is significantly increased in the case of SO with same deposition time of SP4 as shown in Figure 2(d). The diameter of hexagonal rods is also found to be decreased from 20  $\mu\text{m}$  to 3 $\mu\text{m}$  due to the higher number of nucleation sites and fast ZnO growth. The shoot up in relative intensity of (002) preferred orientation upto 91.99 % with respect to (101) is clear visible from Figure 1(d).

This site specific growth has resulted into well aligned vertical hexagonal rods of diameter upto 3 $\mu$ m.

#### 4. CONCLUSION

Significant effect of anisotropic KOH etching of (100) Si surface on ZnO surface morphology has been observed, which leads to the formation of vertically aligned nanorods with increase in (002) peak intensity in the X-ray diffractogram. The growth of ZnO nanosheet network due to the presence of seed layer on Si surface has been observed. These types of nanostructures are explained with the help of XRD and SEM measurements. This work suggests possible growth mechanism for nanorod array and nanosheet network of ZnO on Si surface by spray pyrolysis. This study also showed the growth of hexagonally shaped nanorods is site specific and etch pit characteristic has dominated in deciding the surface morphology over the effect of seed layer. These nanostructure layers can help in light trapping on Si surface and also can cause surface passivation to improve the device performance. The simplicity and cost effectiveness of this technique for ZnO nanostructure growth on Si surface can also be an important factor for incorporating the technique as an in-line deposition system in Si solar cell fabrication.

#### REFERENCE

1. M.A. Green, *Silicon Solar Cells: Advanced Principles and Practice*, Bridge Printer, Sydney (1995).
2. Y J Lee, Douglas S. Ruby, David W. Peters, Bonnie B. McKenzie, and Julia W. P. Hsu, *Nanoletters* 8(5) 1501-1505 (2008).
3. Viresh Dutta, Hrishikesh Dhasmana and Charu Dwivedi, XV International workshop on physics of semiconductor devices 947-950 (2009).
4. M. Kawakami, A. B. Hartington, Y. N. T. Okada, *Jpn. J. Appl. Phys.* 42 L33-L35(2003).
5. H. Verma, D. Mukherjee, S. Witanachchi, P. Mukherjee and M. Batzill, *J. Cryst. Growth* 312 2012-2018 (2010).
6. Kwang-Sik Kim, Hyoun Woo Kim, *Phys. B* 328 368-371(2003).
7. K.L. Chopra, S. Major, D.K. Panday, *Thin Solid Films* 102 1 (1983).
8. J. L. Zhao, X. M. Li, Sam Zhang, Chang Yang, X. D. Gao and W. D. Yu, Wei Dong, *J. Mater. Res.*, 21: 2185-2190 (2006).
9. V. V. Kireev, L. N. Dem'yanets, L. E. Li, and V. V. Artemov, *Inorganic Materials* 46 2 154-162 (2010).
10. V. Dutta and Charu Dwivedi, Method of producing ZnO nanorods by self assembly of spray pyrolyzed nanoparticles. (patent application filed).
11. Y.S. Bae, D.C. Kim, C.H. Ahn, J.H. Kim, H.K. Choa, *Surf. Interface. Anal.* 42 978-982(2010).
12. Ghayour H, Rezaie HR, Mirdamadi S, Nourbakhsh AA., *Vacuum*, doi 0.1016 /j.vacuum. 2011.
13. W. Kern and J. Vossen, *Thin Film Processes*, Academic Press: New York, 1978, Ch V.
14. J. Liu, J. She, S. Deng, J. Chen and N. Xu, *J. Phys. Chem. C*, 112, 11685-11690 (2008).
15. Y. T. Yin, W. X. Que, C. H. Kam, *J Sol-Gel Sci Technol* 53, 605-612, (2010).
16. Ahmad Umar, Y B Hahn, *Nanotechnology* 17 2174-2180 (2006).
17. T. Premkumar, Y. S. Zhou, Y. F. Lu and K. Baskar, *Appl. Mater. Inter.* 2 10 2863-2869 (2010).
18. Li, W. J.; Shi, E. W.; Zhong, W. Z.; Yin, Z. W. *J. Cryst. Growth*, 203, 186(1999).
19. Verma, H.; Mukherjee, D.; Witanachchi, S.; Mukherjee, P.; Batzill, M. *J. Cryst. Growth*, 312, 2012(2010).

## **SIMULATION AND CHARACTERIZATION OF SHUNTS IN SILICON SOLAR CELLS BY PSpICE AND LOCK-IN INFRARED THERMOGRAPHY**

P.SOMASUNDARAN, D.K.NANDI, R.GUPTA \*

*Department of Energy Science and Engineering,  
Indian Institute of Technology Bombay, Powai, Mumbai 400076, India*

\*Corresponding Author, e-mail: [rajeshgupta@iitb.ac.in](mailto:rajeshgupta@iitb.ac.in)

### **ABSTRACT**

Silicon solar cells often suffer from shunts, which are internal short circuits causing degradation in cell performance and overall efficiency. In this paper, simulations for multi-crystalline (m-c) Si solar cells have been performed using the distributed diode model of solar cell by PSpice to investigate the effects of shunts on the cells performance. Effect of spatial positioning of shunts has also been covered in the simulation. Lock-in infrared thermography (LIT) technique has been used for the location of shunt for simulation. LIT provides useful information for the possible causes of shunts and simulation of these shunts give information about the degradation in cell parameters. This type of simulation approach is useful to understand cell performance with varying parameters of shunts and can be used to classify shunts in different categories based on the level of tolerance and priority to solve the severity of shunting problems during production.

Keywords: Shunts, Lock-in thermography, PSpice, Simulation, Modeling.

### **1. INTRODUCTION**

Shunting is one of the major problems in solar cell which reduced the cell performance. Shunts can broadly be classified in two categories based on the origin: process induced shunts and material related shunts. Process induced shunts are formed during the production due to problems associated with fabrication machines. These types of shunts can be minimized by better process control, monitoring tool, and handling. Some typical process related shunt formation happens due to cracks in wafer, scratches, improper metallization contact, Aluminium particles, etc. Whereas, material related shunts are strongly recombinative crystal defects, macroscopic  $\text{Si}_3\text{N}_4$  inclusions, SiC particles and SiC filament-type precipitates [1]. These can be minimized by using better quality of material which will increase cost of cell.

Lock-in infrared thermography is a relatively recent technique for investigation of shunts in solar cells [2]. In this technique, sample is periodically biased with a programmable power supply in order to localize the generated heat near to the shunted region. Infrared camera, which was synchronized with power supply takes sequence of images and apply lock-in algorithm over the images in order to detect, even very small temperature change over the shunted region.

Electrical equivalent circuit of solar cell, consisting of single diode in parallel with current source and shunt resistance, with a series resistance has been exploited to study the effect of shunting on the cell performance.

### **2. METHODOLOGY**

The basic outline of the methodology for modeling and simulation is described in the flow chart shown in Fig.1. In this work, to know the effect of shunts on the solar cell, the cell was divided into 10,000 (100 x 100) elementary areas. Each elementary area was modeled by solar cell equivalent circuits consisting of a diode, a shunt resistance and a current source in parallel as

shown in Fig. 2. Resistances were connected between neighboring elementary areas corresponding to sheet and bulk resistance of the cell. The reverse saturation current ( $I_0$ ) and the ideality factor ( $n$ ) were calculated from the experimental dark I-V graph of the samples. Diodes were characterized with these respective  $I_0$  and  $n$ . For simulating the effect of shunts, obtained by thermography, two illuminated I-V curves for each sample, one with shunt and other without shunt were obtained and compared. Based on this simulation approach different types and severity of shunts located at different parts of solar cells have been simulated and studied their effects on cell performance.

Simulations have been performed using the distributed diode model of solar cell by PSpice [3] to investigate the effects of shunts on the cells performance [4,5]. From experimental dark I-V of the sample these two parameters are determined by plotting  $\ln(I) - V$  graph. The forward dark I-V characteristic of a diode can be written in the form of

$$\ln(I) = \ln(I_0) + qV/nkT. \quad (1)$$

The reverse saturation current ( $I_0$ ) and the ideality factor ( $n$ ) were calculated from the above equation. Diodes were characterized with these respective  $I_0$  and  $n$ .

Fig. 3(a) shows the image of the cell. The dimension of the solar cell is 4 cm x 4cm. So every elementary area has a dimension of 0.4mm x0.4 mm. Fig. 3(b) shows schematically how this elementary block has been formed for simulation. Every cell has one bus-bar and 15 fingers perpendicular to it. For obtaining the I-V characteristics, varying voltage was applied across the p and n side. In case of illuminated I-V curve, current source corresponding to the short circuit current of elementary diode was applied.

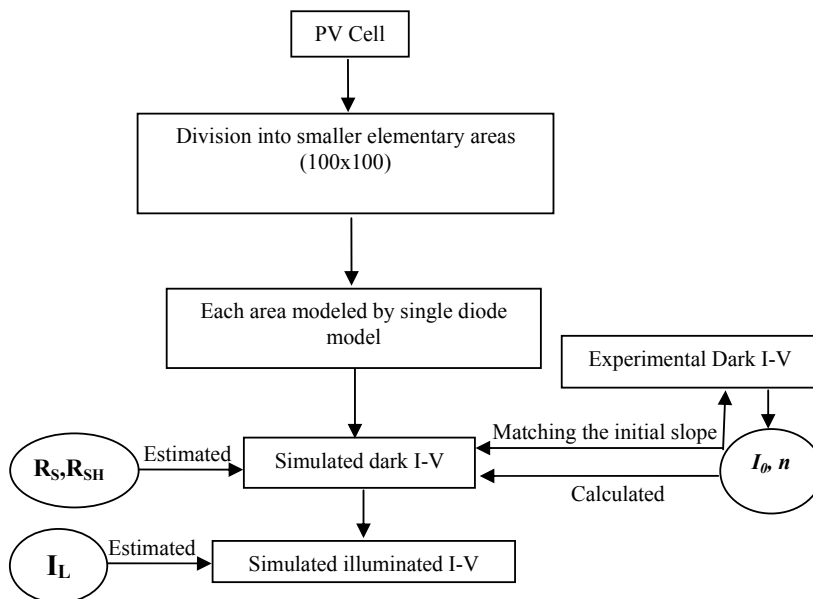


Fig.1 Flow chart showing the methodology used for modeling and simulation

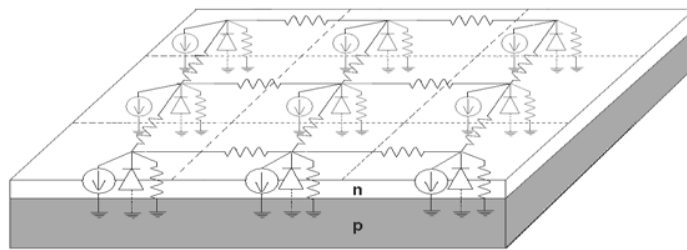


Fig.2 Distributed diode model approach of solar cell

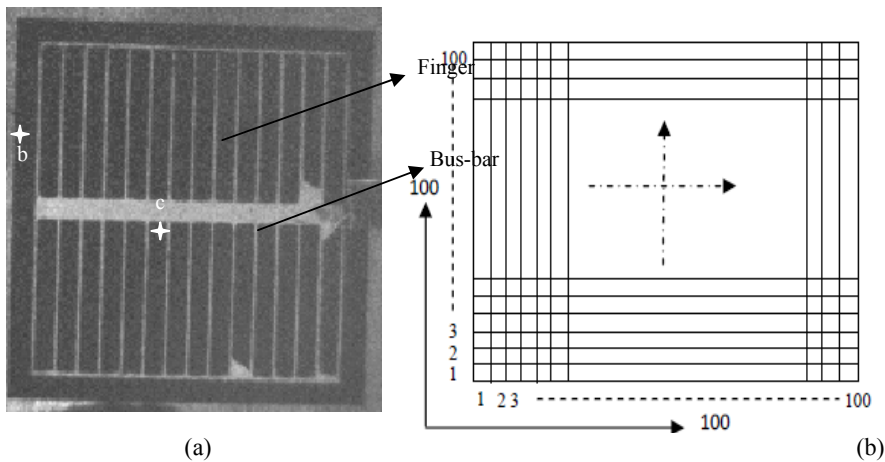


Fig.3 (a) Image of the cell (b) Meshing over the cell

### 3. EXPERIMENT

Based on the excitation sources to the cell, there are mainly two different types of lock-in thermography methods: Dark-LIT (DLIT) and Illuminated-LIT (ILIT). In DLIT, cell is periodically excited by external power supply whereas in case of ILIT cell is periodically excited by light source. Each of these methods has its own advantages and limitations. In this work, we are mainly concentrating on DLIT which has an advantage to classify the ohmic and non-ohmic shunts apart from its simplicity in realization compared to ILIT. In DLIT, only dark current will flow through the cell. At shunt sites, an increased current causes heating of the solar cell which can be detected by lock-in thermography technique [6]. To determine whether the shunt is ohmic or non-ohmic, DLIT images are to be taken under both positive and negative bias. If the DLIT signals at shunts position have same strength in both images, the shunts are ohmic. If the signals differ significantly, those shunts are non-ohmic. In reverse bias conditions, no current flows through the sample except the leakage current which is negligible therefore it will be easy to detect ohmic shunts in reverse bias.

The schematic diagram of lock-in thermography setup is shown in Fig. 1 which was used to perform DLIT tests on mono-crystalline Si samples. The system is equipped with an Indium Antimonide (InSb) detector with focal plane array; Stirling cooled camera head with a pixel



resolution of 320 x 256 pixels. The detector is sensitive in 3-5  $\mu\text{m}$  wavelength and works at maximum frame rate of 162 Hz in full window. One programmable DC power supply acts as an excitation source for DLIT tests. Controller synchronizes the power supply excitation with the frames of camera to implement lock-in algorithm over the captured images.

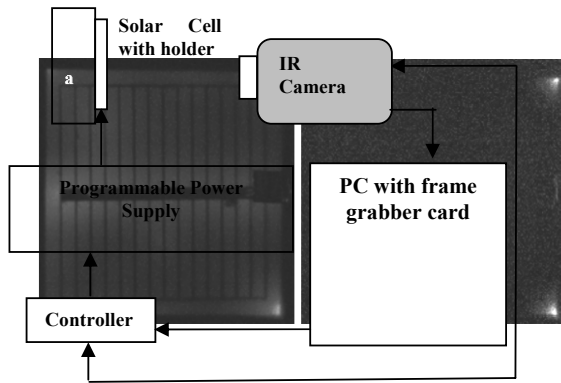


Fig.4 Block diagram of the experimental set-up

Fig.5 LIT images of sampleA measured under (a) forward and (b) reverse bias

Solar cell samples were investigated both in forward and reverse bias in order to understand the characteristics of shunts. In this study, three m-c Si cells (A, B, C) have been used, which had different shunt resistances. LIT has been performed on these samples. Different types of shunts were observed on samples. Fig. 5 shows a lock-in thermography image of sample A. It shows shunts at the corners, which may be due to edge isolation process (to isolate the n-layer from the back side of cell). Sometime edge isolation process creates such type of shunts at the corners. Generally laser has been used for the process. Sometimes laser generates enough heat to melt the surroundings n-layer and it get in direct contact of with the base of the cell creating a shunt at that point. Fig. 6 shows that sample (B) had a shunted region exactly on the fingers which is ohmic in nature. It may be due to metallization related process problem. In sample A and B, lock-in signal in forward and reverse bias is same, which shows that these shunts are ohmic in nature; therefore it can be modeled by a simple resistance. However in case of sample C (Fig. 7), some shunts are only visible in forward bias, which shows non-ohmic nature of shunts. These shunts are more challenging to model accurately. In this we are concentrated only on the linear type of shunts.

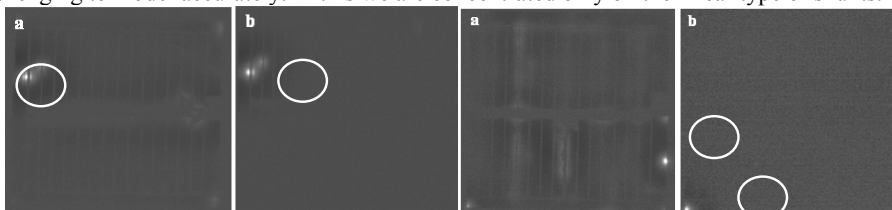


Fig. 6 LIT images of sampleB under (a) forward and (b) reverse bias Fig. 7 LIT images of sampleC under (a) forward and (b) reverse bias

Lock-in thermography helps to determine the location of the shunts accurately and its nature in a cell. Sometimes it also helps to know the probable reason for appearing of these shunts. By simulating these cells with the help of its electrical equivalent circuit, the effects of the shunts on these corresponding cells can be determined.

#### 4. SIMULATION

Results obtained from Lock-in thermography gives information about the location of the shunts and its nature. This information has been used in simulations to understand the impact of these shunts on cells performance. In this work, simulation and modeling was performed only for linear or ohmic shunts.

At very low voltages under forward biased condition, current does not flow through the diodes and it is predominantly controlled by shunt resistance ( $R_{SH}$ ) of the cell.  $R_{SH}$  value of sound region of cell was obtained experimentally and used in the simulation for the each elementary area. Latter this value was corrected at shunt location. The relative shunt strength has been obtained by relative value of LIT signal. By lowering the resistance at the shunt positions in same proportion as of LIT signal, initial slope of simulated dark I-V curve was fitted with the initial slope of experimental dark I-V curve at around zero voltage. Only  $R_{SH}$  value at the shunt positions have been changed to match with the total cell  $R_{SH}$ . After obtaining the shunt resistance value at different location of cells, total dark I-V curve of the cell have been obtained by fitting the average sheet resistance values, which was also measured experimentally. This resistance was kept same everywhere in the network. For obtaining the illuminated I-V curves, current source parallel to each diode have been connected in the network to model uniform incident radiation close to short circuit current under standard condition.

#### 5. RESULTS

Based on the above mentioned methodology and simulation approach, dark I-V curves were plotted for sample A and Bin Fig. 8 (a) and 9 (a) respectively. Two simulated illuminated I-V curves were also plotted in Fig. 8(b), 9(b) for each sample, one in presence of shunt and the other in absence of shunt, after obtaining all parameters required for plotting.

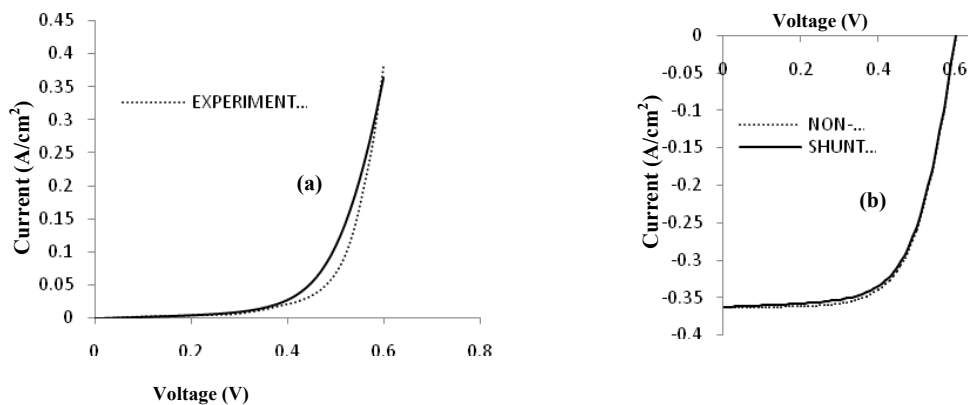


Fig.8 I-V curves of sample A: (a) Dark I-V (b) Simulated Illuminated I-V

From the illuminated I-V curves, the power reduction from each sample has been calculated to understand the impact of shunts. In case for sample A, the maximum power reduction was around 2.5 % and in case of sample B, it was around 15 %. It was observed that if the shunt is located inside finger pattern rather than on the edges (sample B case), it has more significant effect on the cell performance. It is due to the reason that these shunts are in proximity of several fingers which causes more sinking of current.

Emphasis in this work is on the approach rather than percentage reduction number, which can be more or less depending on the type of shunt. Area of cell will also play an important role because chances of shunting will be higher for large area cells.

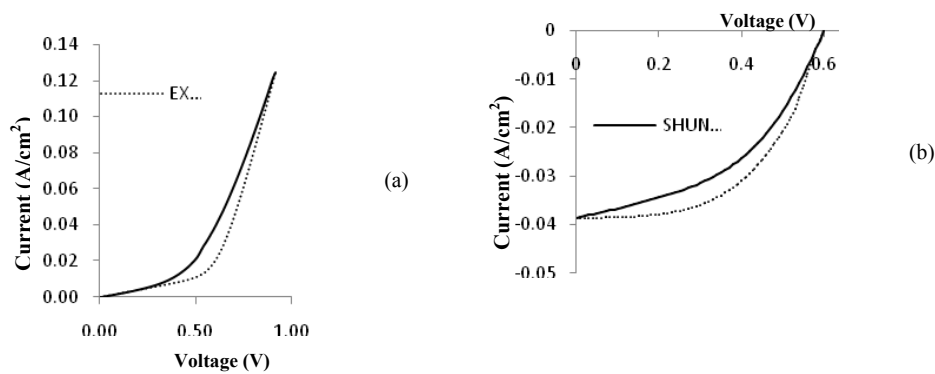


Fig.9 I-V curves of sample B: (a) Dark I-V (b) Simulated Illuminated I-V

#### Spatial dependence of shunts

Effect of spatial positioning of shunts was investigated by modeling the shunts of same magnitude at different locations: a) at the edge, b) between the fingers of the cell and c) under the bus bar as shown in Fig. 3(a). In all cases, the magnitude of  $R_{SH}$  at shunt location was kept same. Under small forward bias condition ( $\sim 0-50$  mV), diode current is mainly dominated by shunt resistance and shows a linear relationship between current and voltage [7]. Based on the slope of I-V curve shunt resistances of the complete cell was calculated for three different locations of shunts as mentioned earlier. It was found out that percentage degradation of overall shunt resistance of the cell was highest for the case where shunt was located under the bus bar (c). This was expected because the bus bar provides good conductive path for the current to flow and provide an easy channel for current to sink. In comparison to this, the shunt at the edge (a) had the least effect, because it was farthest from the finger, whereas the percentage degradation for the shunt located in between fingers (b) was in between the two cases. Percentage degradation of cell  $R_{SH}$  was calculated around 4 % for the shunt which was between the fingers and 5.5 % for the shunt which was under the bus bar compared to shunt located at the edge. These values will strongly be affected by the sheet resistance of cell and therefore it will vary from cell to cell and depend on cell design and technology. However, in each case this approach can be performed to estimate the effect of shunt at different location of cell.

The simulation approach presented here was applied to the laboratory solar cells of small area. However, this particular approach can be extended to the industrial solar cells as well to study the effects of shunts on their performance.

## **6. SUMMARY AND SCOPE FOR FUTURE WORK**

Presented simulation approach is useful to study severity of shunts located at different parts of solar cells to estimate the effect of shunts on cell performance. Spatial dependence of shunt has been studied and estimated the variation of cell  $R_{SH}$  at different locations of shunt. This type of simulation based on some experimental data is useful to estimate cell performance with varying parameters of shunts. It is also useful to classify shunts in different categories based on the level of tolerance in order to tackle shunts related problem during production.

This simulation approach have further some scope of refinement by taking into account nonuniformity of series resistance, finite resistance of metallization, bulk resistance and precisemodeling of non-linear shunts. However, contribution of these parameters will not be very significant.

## **7. ACKNOWLEDGMENT**

This work is funded by Department of Science and Technology of India under a joint Indo-UK project on Stability and Performance of Photovoltaics.

## **REFERENCES**

1. O. Breitenstein, J. P. Rakotoniaina, M. H. Al Rifai and M. Werner, "Shunt Types in Crystalline Silicon Solar Cells, *Progress in Photovoltaics: Research and Applications*, Vol. 12, 529–538, 2004
2. O. Breitenstein, M. Langenkamp: *Lock-in thermography: basics and use for functional diagnostics of electronic components* (Springer – Verlag, Berlin, 2003)
3. OrCAD PSPICE release 16.2, Cadence Design System Inc., (2009).
4. R. Gupta, O. Breitenstein and J. Schneider, "Characterization of Crystalline Silicon on Glass (CSG) modules by Surface Potential Mapping", 22<sup>nd</sup> European Photovoltaic Solar Energy Conference, Milan, Italy, (2007)
5. S.E. Foss, B. R. Olaisen, E. S. Marstein and A. Holt, "A New 2.5D distributed SPICE model of solar cells", *Proceedings of the 21st Europeans Photovoltaic Solar Energy Conference*, 4-8 September, 2006.
6. R. Gupta and O. Breitenstein, "Unsteady-state lock-in thermography – application to shunts in solar cells", *Quantitative Infra Red Thermography Journal*. 4(1), pp. 85-105, 2007
7. J. Salinger, "Measurement of Solar Cell Parameters with Dark Forward I-V Characteristics", *Acta Polytechnica*, 46, 25-27, 2006.

## **SOLAR PV BASED MICRO-GRID SYSTEM FOR EMERGENCY SITUATIONS**

WONG TECK SION<sup>1</sup>, LIYANAGE C DE SILVA<sup>1,2\*</sup>, M ISKANDAR PETRA<sup>1</sup>

<sup>1</sup> *Faculty of Science, University of Brunei Darussalam, Brunei Darussalam*

<sup>2</sup> *School of Engineering and Advanced Technology (SEAT), Massey University, Palmerston North, New Zealand*

\*Corresponding Author, e-mail: [liyanagecd@yahoo.co.nz](mailto:liyanagecd@yahoo.co.nz)

### **ABSTRACT**

In this paper we present a prototype implementation of a micro-grid system that we have designed and built to run on solar energy with the aim of power supply during emergency situations. This system is equipped with multiple sensors for monitoring the solar energy production and its usage. A control system is also introduced to switch between the grid power and solar supply. In order to monitor and observe the behavior of the micro-grid system at any time, a Graphical User Interface (GUI) is also incorporated. Data from the sensors are converted from analogue to digital using a microcontroller and displayed on the GUI for monitoring and control. The components in the micro-grid system are PV (Photovoltaic) array, charge controller which controls the current flow to the battery and load, inverter, battery storage. The test loads consists of energy saving fluorescent bulbs, siren and a portable radio (which is a must to have during an emergency situation).

In order to show the capability of the PV array to charge the battery, the amount of current for 24 hours period is monitored to calculate the average current from the PV array. The characteristics of the charge controller are also observed to understand the behavior of the controller on different scenarios of the day and night. The voltage and current from the battery is also observed to calculate the time taken for the battery to be fully discharged and therefore more importantly to measure its sustainability during an emergency situation. In this paper we present the details of our analysis based on our preliminary study which is required for future expansion of the idea to a much broader and larger solar-PV based grid installation to support a smaller isolated communities during emergency situations.

### **1. INTRODUCTION**

In this era where oil and gas resources are depleting, it is important to harness alternative sources of energy such as solar and wind. Solar power based renewable energy is simple to harness as it requires a simple technology like a solar cell to capture energy and moreover the energy is from the natural environment which are free. Most of the countries have been advancing in the renewable energy to reduce the usage of fossil fuels and furthermore pollution. It also can reduce the dependency on the national main grid and generator for isolated areas.

Eran Tal et. al. [12] proposed a system for providing environmentally friendly, sustainable power called SuPer (Sustainable Power for Electrical Resources). In this project, a prototype of 400Wh/day, 12V solar system is built to develop a low-cost, sustainable and renewable source of electrical power for the 20 billion people with no electricity over a 20 year life cycle under a total cost of \$500. The results they showed are that their system is able to produce electrical power of about 0.7kWh/day, yielding a cost of energy = US 29cents/kWh. Another approach is presented by De Silva et. al. [3] for smart homes where the energy consumption is being monitored and controlled to improve the efficiency by reducing the wastage

Since renewable energy is limited as it depends on the weather condition, energy management is very crucial. Energy management involves controlling and monitoring the energy generation and usage. This enables us to keep track of the amount of energy available for use and also prevent any energy waste. Therefore a power system with a Graphical User Interface is needed to collect data, calculate and display important information such as battery operating time

left. By combining renewable energy sources with power technology such as inverter and charge controller and a monitoring and control system, a small energy distribution system or a micro-grid is produced. This micro-grid concept can be an alternatives solution for black-out problems and energy crisis.

The aim of this paper is to design and build a prototype solar micro-grid system which can control and monitor the electrical energy generation and its usage. And also able to measure its sustainability of the micro-grid on solar power which can be used as a backup energy sources when there is no electricity from the grid.

Therefore by using a solar power charging system, the battery can be charged during the day and the energy can be used during night without much difficulty. Together with a Graphical User Interface (GUI) which provides information on the amount of electricity left, it can help the user to be aware of the energy usage. Hence in short what is unique about this project is how we implemented a fully functional micro-grid system and its analysis and recommendations for future research. The Figure 1 shows the schematic diagram of our prototype implementation.

## 2. OVERVIEW OF THE MICRO-GRID SYSTEM

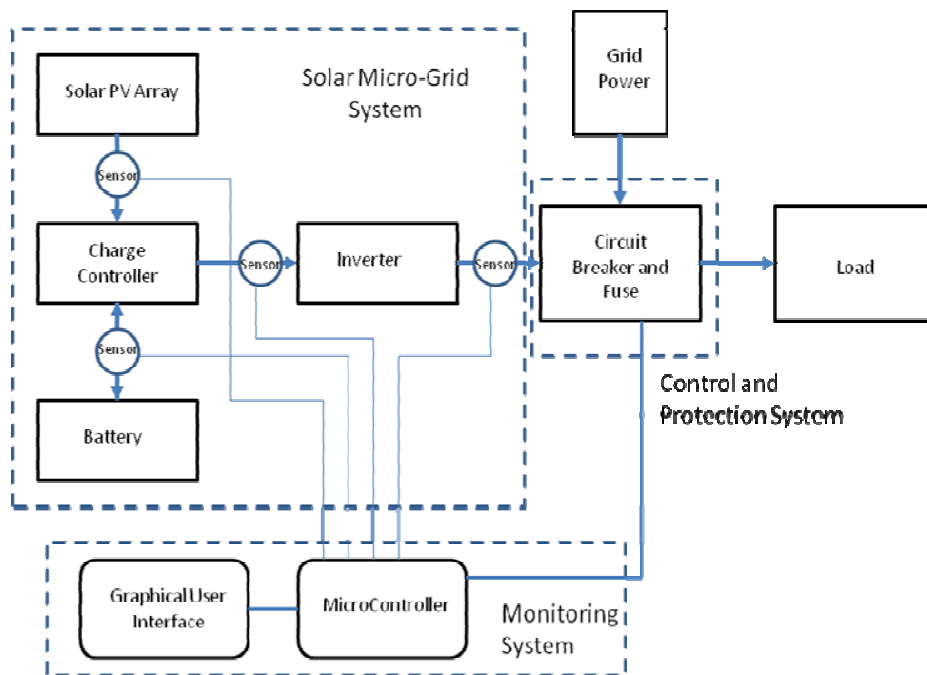


Figure 1: Schematic Diagram of Prototype Micro-grid System

The prototype micro-grid system we have implemented is made up of 4 main components: a solar PV array for harnessing the solar energy, a charge controller for regulating the amount of electrical energy into the battery, a battery storage for storing the electrical energy to use in night time and a inverter for converting DC to AC Figure 2. The micro-grid system is equipped with monitoring system and control and protection system. The monitoring system uses a BASIC STAMP microcontroller to measure and read the signal from the current and voltage sensor. The

analog signal is processed into digital information and display on the GUI using a computer. The microcontroller also connected to the circuit contactor to control the switching between solar power and grid power. The micro-grid protection system consists of fuse and miniature circuit breaker which protects the system from overloading and short circuit. The micro-grid will be easy to install as it does not require any extra wirings and directly connect to a house's central fuse box.



**Figure 2** The main components of our prototype implementation

### 3. OBSERVATIONS AND ANALYSIS

In this section, we present the observation and results of our micro-grid system. First we have obtained the I-V and P-V characteristics of our solar panel as shown in Figure 3. The graphs shows the I-V and P-V characteristics of the polycrystalline solar cell used in this prototype system at afternoon. From these graphs, the maximum power can be determined for the purpose of calculating the efficiency of the solar cell.

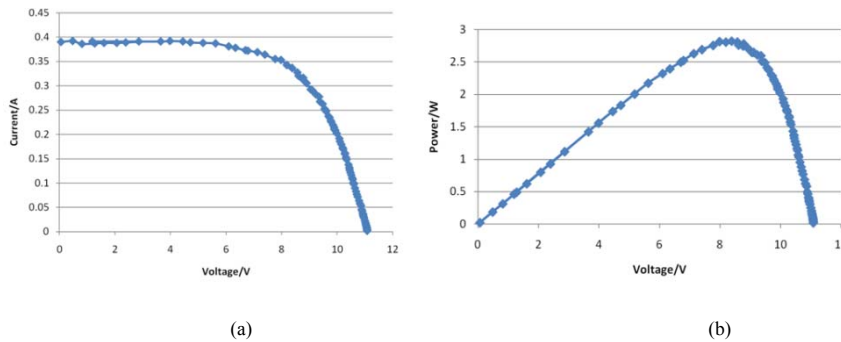


Figure 3 (a) I-V characteristics (b) P-V characteristics of the solar panel

Then the insolation of the sun is measured using a pyranometer. It is capable of producing a maximum irradiance of  $2000\text{W/m}^2$  and has a sensitivity ranging of  $10$  to  $35\mu\text{V}$  per  $\text{W/m}^2$ . The output signal ranges from  $0$  to  $500\text{mV}$ . Under theoretical conditions, its sensitivity is  $15\mu\text{V}$  per  $\text{W/m}^2$ . Therefore  $1\text{mV}$  produces  $66.667\text{W/m}^2$ . The average output voltage from the insolation is  $4.536\text{mV}$ . This gives a  $302.402\text{W/m}^2$  of irradiance. Using this value and the power output from the I-V characteristics graph of the solar cell, the efficiency can be determined.

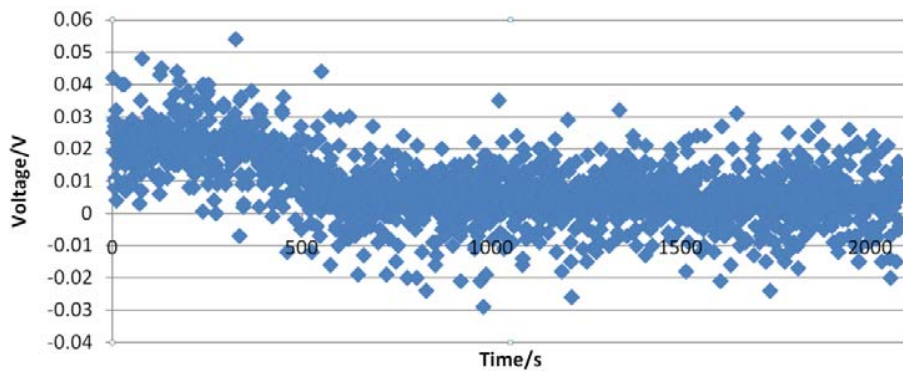


Figure 4: Sun's Insolation measured using our prototype system

#### 4. SUSTAINABILITY OF THE SYSTEM

In our preliminary studies of the micro-grid system, a car battery storage instead of a deep-cycle battery is used as it is easily available and cheap. The sustainability of the micro-grid system is tested by allowing the load to run on the battery until it falls below the minimum voltage. From the testing, it is found that charging the battery for two days straight will only be able to operate the load of 5 bulbs and a fan for two hours as given in the Table 1 below. The sustainability of the system is very weak due to the limitation of the battery. The battery used in this prototype is a car battery which is used mainly to withstand power surge and provide large current for a short amount of time. In theory, if the battery is fully discharge, it provide  $46\text{Ah}$  which can support the load for a long period of time and because it only can discharge  $20\%$  of its total, the mount of current available is very limited.



**Table 1:** Sustainability of the system

<i>Load</i>	<i>Charging</i>	<i>Discharging</i>
1 Bulb of 8W	2 days	6 hours +
1 Fan of 26W	2 days	6 hours +
2 Bulbs of 46W	2 days	3 hours 50mins
4 Bulbs of 74W	2 days	2 hours 30 mins
5 Bulbs of 82W + 1 Fan of 26W	2 days	2 hours

## 5. EFFICIENCY OF THE INVERTER

Efficiency is the ratio of power out to power in, expressed as a percentage (Table 2). If the efficiency is 90 percent, 10 percent of the power is lost in the inverter. The efficiency of an inverter varies with the load. The current drawn by the inverter is 0.156A in our set up and therefore power loss is calculated to be 1.903W.

**Table 2:** Efficiency of the Inverter

<i>Load</i>	<i>Input Power</i>	<i>Output Power</i>	<i>Efficiency</i>
1 Bulb	$11.64V \times 2.3A = 26.772W$	23W	85.9%
1 Fan	$11.64V \times 2.61A = 30.3804W$	26W	85.6%
1 Bulb + 1 Fan	$11.28V \times 5.08A = 44.304W$	49W	85.8%
2 Bulb	$11.42V \times 4.71A = 53.788W$	46W	85.5%
2 Bulb + 1 Fan	$11.07V \times 7.62A = 84.35W$	72W	85.4%
5 bulb + 1 Fan	$11.20V \times 11.30A = 126.56W$	108W	85.3%

## 6. CHARACTERISTICS OF THE CHARGE CONTROLLER

The function of charge controller is to adjust the charging current and change the way of charging the battery according to voltage of the battery. It ensures that the battery is always fully charge and prevents the battery from over-charging and over-discharging. At addition it also prevents the battery from supplying power to solar panels during nights which can damaged the solar panels.

**Table 3** Charge Controller Characteristics

Maximum Voltage	12V	Voltage of stop power supply	10.8V
Maximum Charging Current	10A	Voltage of resume power supply	11.8V
Maximum Load Current	10A	Voltage of stop charging	14V

**MONITORING AND GRAPHICAL USER INTERFACE(GUI)**

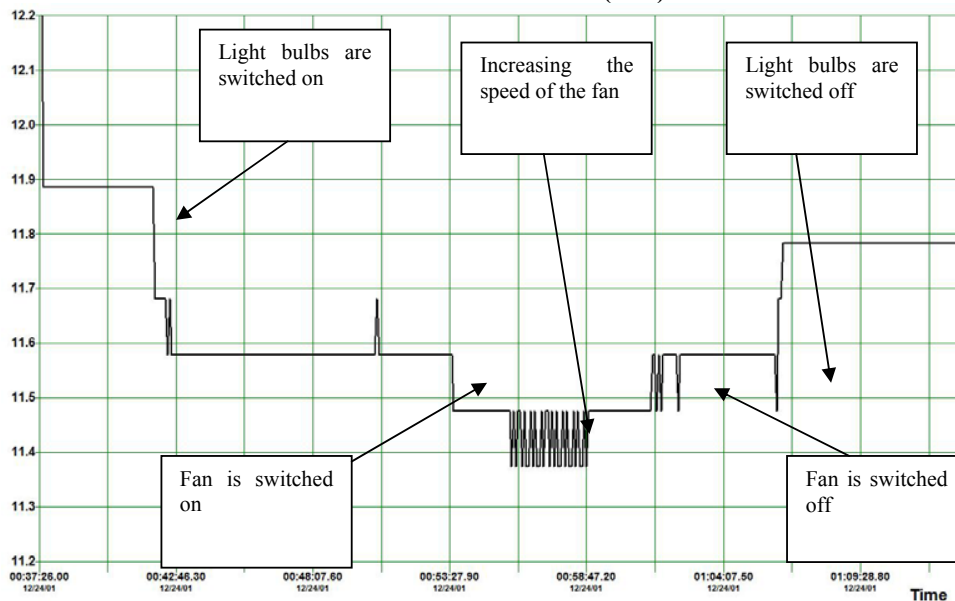


**Figure 5:** Status of the battery voltage during operation

From the graph in Figure 5, it is found how the status of the battery changes when operating on a load. When the light bulbs are switched on, the voltage drops indicating discharging. But when the speed of the fan is increased, the voltage is not stable as it is fluctuating. This is due to the motor load of the fan. Figure 6 shows the Graphical User Interface we are currently developing for the monitoring and control of the grid power system that we have developed.

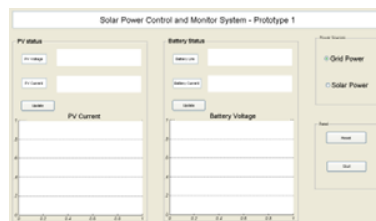


**Figure 6:** GUI (Graphical User Interface)

**7. CONCLUSIONS**

For Brunei Darussalam, which is located in the equatorial region has an abundant amount of sunlight 4. This free energy can be made use to reduce our country's dependent on natural resources in energy production. Brunei Darussalam has started to use solar energy by building Tenaga Suria Brunei at Seria, the largest solar power demonstration plant in Southeast Asia 5. However building a large scale solar power station requires large area of land which involves cutting down trees making it not a totally environmentally friendly solution in an area with very high vegetation index.

However applying a distributed micro-grid system that we are proposing, the amount of space required is reduced drastically because each house will have their own system depends on their amount of usage. Using solar, micro-grid will not only reduce the electricity bills but also can provide a sustainable supply of electrical energy. This is very important during emergency situations such as blackouts or any disaster which cut off the grid power. A solar micro-grid will be able to provide us lighting for few weeks and with free energy from the sun, it is a long lasting solution. For load and energy optimization, energy management is one of the solutions. By creating a GUI which can provide information on the micro-grid system, user can manage their energy wisely. This is crucial during emergency situations where energy is limited. Overall we can conclude that a solar micro-grid system can not only provide a reliable, sustainable free renewable energy source of electrical power but also a security for energy in an emergency situation.

## **REFERENCES**

1. Tal Eran. "SuPER System Prototype Design and Implementation". Master's thesis, California Polytechnic State University 2006.
2. Tyler Sheffield and Eran Tal, Cal Poly Sustainable Power For Electrical Resources Project, California Polytechnic State University 2006.
3. Liyanage C De Silva and Sathyajith Mathew, "Energy Efficient Smart Homes", in the proceedings of the 1st International Conference of Institution of Engineering and Technology Brunei Darussalam Network. (IETBIC2008) held in The Rizqun International Hotel, Brunei Darussalam, 26-28 May 2008.
4. Measurement of Global Solar radiation over Brunei Darussalam, A. Q. Malik and Ak Abd Raub Bin Pg Hj Ghani, Department of Physics, University of Brunei Darussalam, Jalan Tungku Link, Gadong BE1410, Brunei, Science and Technology Vision.
5. HM inaugurates Tenaga Suria Brunei-Brunei Times (URL: <http://www.bt.com.bn/news-national/2011/05/27/hm-inaugurates-tenaga-suria-brunei>) Accessed on 11 June 2011.

## **WIND POWER DEVELOPMENT: AN INNOVATIVE MEANS OF REDUCING GLOBAL WARMING EMISSIONS**

O.I. OLUSOLA\* AND S.S. OLUYAMO

*Department of Physics, Federal University of Technology, P. M. B. 704, Akure*

\*Corresponding Author, e-mail: *olajideibk@yahoo.com*

### **ABSTRACT**

Wind energy as one of the active solar technologies involved in energy generation has historically been used to propel sailing ships or converted into mechanical energy for pumping water or grinding grain; the principal application of wind power today is the generation of electricity. Wind energy as power source is favoured by many environmentalist as an alternative to fossil fuels, as it is plentiful, renewable, widely distributed, clean, and does not produce greenhouse gas emissions which is one of the major contributors to global warming. This paper describes the anatomy of a wind power turbine system, a set of statistics from the American Wind Energy Association (AWEA) to quantify the comparative emissions of both air pollutants and greenhouse gases of wind and other fuels.

Keywords: wind power, environment, greenhouse gases, global warming, emissions

### **1. INTRODUCTION**

Energy is vital for all living – beings on earth; modern life-style has further increased its importance. Some of the resources available for generating electrical energy are: thermal, hydroelectric, wind power, fuel cells, photovoltaic cells and so on. Solar radiation, along with secondary solar-powered resources such as wind and wave power, hydroelectricity and biomass, account for most of the available renewable energy on earth. However, all renewable energies, other than geothermal and tidal, derive their energy from the sun (Olson, 2010).

In Nigeria for example, the main sources of electrical energy generation are the thermal power station and the hydroelectric power station. The country generates less than 20% of its daily needs; today, non availability and non reliability of electricity has become a way of life. Nigeria with a population of about 150 million people generates about 4,000 megawatt of power. Thailand with a population of about 70million people generates close to 40,000mW of power (Flowers, 2010). South Africa with a population of 45 million generates 46,000mW of power; Ghana with a population close to 21 million generates 1,900mW. United Kingdom and United States of America generates 77,000mW and 300,000mW of electricity power respectively (Sinclair, 2008).

From research, it was discovered that countries which generate higher megawatt of power make use of different sources such as thermal, hydroelectric, wind power, photovoltaic cells to generate their electrical energy (Lema et al., 2007). For example, as at the end of the year 2007, Germany was able to generate 22,247mW of electricity from wind power, United States was able to generate 16,818 mW of electricity from wind power, Spain was able to generate 15,145 mW of electricity from wind power, India generated 8,000 mW of electricity from wind power, while United Kingdom was able to generate 2,389 mW of power from wind (Wald, 2011). Germany generates a total of 370,783mW of power out of which 22,247mW is attributed to wind energy generation.

## 2. METHODOLOGY

The design and development of a wind turbine system involve the use of electronic, electrical and mechanical materials. A wind turbine is a rotating machine which enables the conversion of kinetic energy in wind into mechanical energy (Mukund, 2006). If the mechanical energy is used directly by machinery, such as a pump or grinding stones, the machine is usually called a windmill, if the mechanical energy is then converted to electricity, the machine is called a wind generator, wind turbine, wind power unit (WPU) or wind energy converter (WEC). Small wind generation systems with capacities of 10kW or less are usually used to power homes, farms and small businesses (Zavadil et al., 2005). Wind turbines have been used for household electricity generation in conjunction with battery storage in remote areas (Demeo et al., 2005). Since the wind speed increases with height, a tower of 10m length is suitable for mounting the turbine.

The wind generator was designed to charge sets of 12 – Volt batteries connected in both series and parallel. A digital power electronic control circuit also known as inverter was incorporated on the output side of the turbine system to convert the direct current energy into an alternating current of energy to enable the general populace have access to it; the reason being that most of the equipment being used by the general populace make use of alternating source of energy. Figure 1 shows the anatomy of a wind turbine system and the functions of the various components that make up a wind turbine system (Hannele, 2006).

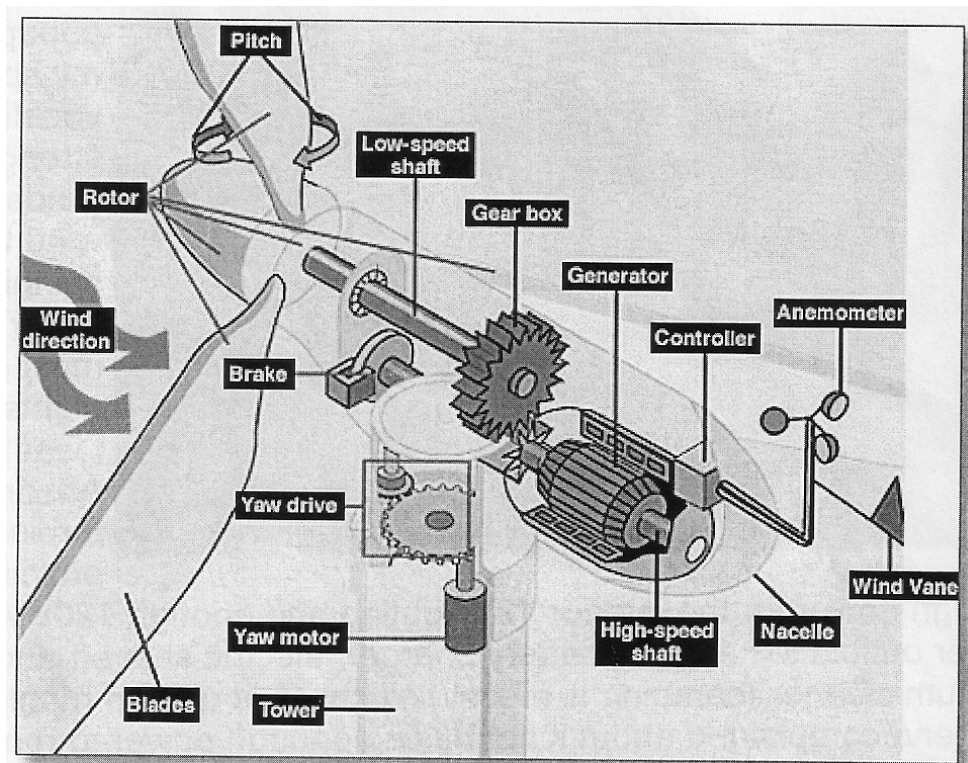


Figure 1: Anatomy of a Wind Generator

Anemometer: Measures the wind speed and transmits wind speed data to the controller.

Blades: Most turbines have either two to four. Wind blowing over the blades causes the blades to “lift” and rotate.

Brake: This is needed for stopping the turbine for repairs, in an emergency, for routine maintenance, or when the energy is not needed. Many turbines have “dynamic braking”, which simply shorts out the three electrical phases and acts as a disconnect. Others have mechanical braking, either via a disc or drum brake, activated by a small winch at the base of the tower. Mechanical braking is usually more effective and reliable than dynamic braking.

Controller: The controller starts up the machine at wind speeds of about 8 to 16 miles per hour (mph) and shuts off the machine at about 55 mph. Turbines do not operate at wind speeds that is above or about 55 mph because they might be damaged by the high winds.

Gear Box: Gears connect the low-speed shaft to the high-speed shaft and increase the rotational speed from about 30 to 60 rotations per minute (rpm) to about 1000 to 1800 rpm, the rotational speed required by most generators to produce electricity. The gear box is a costly and heavy part of the wind turbine and engineers are exploring “direct-drive” generators that operate at lower rotational speeds and don’t need gear boxes.

Generator: The wind generator is what actually generates electricity in the system. Most modern wind generators are upwind designs. Three-bladed wind generators are most common, providing a good compromise between efficiency and rotor balance.

High-speed shaft: Drives the generator.

Low-speed shaft: The rotor turns the low-speed shaft at about 30 to 60 rotations per minute.

Nacelle: The nacelle sits atop the tower and contains the gear box, low-speed and high-speed shafts, generator, controller, and brake.

Pitch: Blades are turned, or pitched, out of the wind to control the rotor speed and keep the rotor from turning in winds that are too high or too low to produce electricity.

Rotor: The blades and the hub together are called the rotor.

Tower: Towers are made from tubular steel, concrete, or steel lattice. Because wind speed increases with height, taller towers enable turbines to capture more energy and generate more electricity.

Wind direction: This is an “upwind” turbine, so-called because it operates facing into the wind. Other turbines are designed to run “downwind” facing away from the wind.

Wind vane: Measures wind direction and communicates with the yaw drive to orient the turbine properly with respect to the wind.

Yaw drive: Upwind turbines face into the wind; the yaw drive is used to keep the rotor facing into the wind as the wind direction changes. Downwind turbines don’t require a yaw drive; the wind blows the rotor downwind.

Yaw motor: powers the yaw drive.

### 3. COMPARATIVE AIR EMISSIONS OF WIND AND OTHER FUELS

Wind energy as a power source is favoured by many environmentalists as an alternative to fossil fuels, as it is plentiful, renewable, widely distributed, clean, and does not produce greenhouse gas emissions which contribute to global warming thus causing changes in the climate (Sovacool, 2009). Wind power as a renewable form of energy produces no carbon dioxide during operation. While some emissions of these gases can take place during the design, manufacture, transport and erection of wind turbines, enough electricity is generated from a wind farm within a few months to totally compensate for these emissions. The installation of several wind turbines in a site make up what is known as wind farm. When wind farms are dismantled (usually after 20-25 years of operation), they leave no legacy of pollution for future generation.

Carbon dioxide (CO<sub>2</sub>) is a global warming pollutant; its buildup in the atmosphere contributes to global warming by trapping the sun's rays on the earth as in a greenhouse. The U.S., with 5% of the world's population, emits 23% of the world's CO<sub>2</sub>. The build-up of global warming pollution is not only causing a gradual rise in average temperatures, but also seems to be increasing fluctuations in weather patterns and causing more frequent and severe droughts and floods (Hall, 2006) .The World Meteorological Organization (WMO) warned in July, 2003, that extreme weather events appear to be increasing in number due to climate change. Carbon dioxide (CO<sub>2</sub>) is the most important of the global warming pollutants which are changing our climate. According to experts, to avoid dangerous levels of warming, level of CO<sub>2</sub> emissions must be cut by 80-90 per cent by 2050. That means switching to forms of energy generation that do not produce CO<sub>2</sub>. Given the scale of the CO<sub>2</sub> cuts needed, wind power as a developed renewable energy technology is one of the best energy renewable technology to deliver carbon emissions reductions on a large scale, quickly (Kempton et al., 2007).

Wind energy's most important environmental benefit is its lack of emissions of both air pollutants and greenhouse gases when compared with alternative methods of generating electricity. The American Wind Energy Association (AWEA) developed a set of statistics to quantify the comparative emissions of wind and other fuels, based on data gathered by the U.S. Department of Energy's Information Administration (EIA), which collects information on the U.S. utility industry. This, and similar fact sheets, can be found online at <http://www.awea.org/pubs/factsheets.html>. For carbon dioxide (CO<sub>2</sub>), the leading greenhouse gas associated with global warming, comparative emissions during electricity generation are shown in table 1.

Table1: Comparative Emissions of CO<sub>2</sub> during Electricity Generation

Fuel	CO <sub>2</sub> Emitted Per Kilowatt-hour (kWh) Generated (in pounds)	KWh Generated, 1997 (billions)	CO <sub>2</sub> Emitted, Total Generation (billion pounds)
Coal	2.13	1,788	3,807
Natural Gas	1.03	283.6	291
Oil	1.56	77.8	122
U.S. Average Fuel Mix [2]	1.52	3,494	5,313
Wind	0	3.4	0

For sulfur dioxide (SO<sub>2</sub>), the leading precursor of acid rain, comparative emissions during electricity generation are shown in table 2.

Table2: Comparative Emissions of SO<sub>2</sub> during Electricity Generation

Fuel	SO <sub>2</sub> Emitted Per Kilowatt-hour (kWh) Generated (in pounds)	KWh Generated, 1997 (billions)	SO <sub>2</sub> Emitted, Total Generation (billion pounds)
Coal	0.0134	1,788	24,028
Natural Gas	0.000007	283.6	2
Oil	0.0112	77.8	870
U.S. Average Fuel Mix [2]	0.0080	3,494	27,914
Wind	0	3.4	0

For nitrogen oxides (NO<sub>x</sub>), another acid rain precursor and the leading component of smog, comparative emissions during electricity generation are shown in table 3.

Table3: Comparative Emissions of NO<sub>x</sub> during Electricity Generation

Fuel	NO <sub>x</sub> Emitted Per Kilowatt-hour (kWh) Generated (in pounds)	KWh Generated, 1997 (billions)	NO <sub>x</sub> Emitted, Total Generation (million pounds)
Coal	0.0076	1,788	13,668
Natural Gas	0.0018	283.6	504
Oil	0.0021	77.8	162
U.S. Average Fuel Mix [2]	0.0049	3,494	17,112
Wind	0	3.4	0

A single 750-kilowatt wind turbine, operated for one year at a site with Class 4 wind speeds (winds averaging 12.5-13.4 mph at 10 meters), can be expected to displace a total of 2,697,175 pounds of carbon dioxide, 14,172 pounds of sulphur dioxide, and 8,688 pounds of nitrogen oxides, based on the U.S. average utility generation fuel mix.

#### 4. CONCLUSION AND RECOMMENDATION

The research work on secondary solar-powered resources such as wind energy generation using a turbine system is just a means to an end and since wind energy is plentiful and renewable, a large scale wind farm can be constructed to accommodate 50 to 100 wind generators to boost the output capacity (Archer et al., 2007). In addition to this, a hybrid system comprising of Photo-Voltaic modules and wind turbine system can also be used together to boost overall generated output power; this generated power can then be connected to the power grid lines. With grid-tied



systems, excess electricity can be sent to the transmission grid. Because of the metering of energy received by the local grid, the surplus power produced by domestic hybrid generators can, in some jurisdictions, be fed into the network and sold to the utility company, producing a retail credit for the hybrid generators owners to offset their energy costs and the investor can get a good return through payment from the grid authorities.

## REFERENCES

1. Archer C. L. and Jacobson M. Z. (2007). Supplying Baseload Power and Reducing Transmission Requirements by Interconnecting Wind Farms. *Journal of Applied Meteorology and Climatology (American Meteorological Society)* **46** (11): 1701–1717.
2. Demeo E.A., Grant W., Milligan M.R. and Schuerger M.J. (2005). Wind plant integration. *Power and Energy Magazine, IEEE* **3** (6): 38–46. [http://ieeexplore.ieee.org/xpls/abs\\_all.jsp?arnumber=1524619](http://ieeexplore.ieee.org/xpls/abs_all.jsp?arnumber=1524619)
3. Flowers L. (2010). Wind Energy Update. *Wind Engineering*: 191–200. [http://www.windpoweringamerica.gov/filter\\_detail.asp?itemid=746](http://www.windpoweringamerica.gov/filter_detail.asp?itemid=746).
4. Garvine R. and Kempton W. (2008). Assessing the wind field over the continental shelf as a resource for electric power. *Journal of Marine Research*, **66** (6): 751-773.
5. Hall M.J. (2006). A guide to calculating the carbon dioxide debt and payback time for wind farms. [http://www.viewsofscotland.org/snp\\_conference/PeatAudit-Guide.pdf](http://www.viewsofscotland.org/snp_conference/PeatAudit-Guide.pdf).
6. Hannele Holttinen, *et al.* (2006). Paper. Global Wind Power Conference, Australia. [http://www.ieawind.org/AnnexXXV/Meetings/Oklahoma/IEA%20SysOp%20GWPC2006%20paper\\_final.pdf](http://www.ieawind.org/AnnexXXV/Meetings/Oklahoma/IEA%20SysOp%20GWPC2006%20paper_final.pdf).
7. Kempton W., *et al.*, (2007). *Large CO<sub>2</sub> reductions via offshore wind power matched to inherent storage in energy end-uses*. Geophysical Research Letters. <http://www.agu.org/pubs/crossref/2007/2006GL028016.shtml>.
8. Lema A. and Ruby, K. (2007). "Between fragmented authoritarianism and policy coordination: Creating a Chinese market for wind energy", *Energy Policy* **35** (7): 3879–3890, <http://linkinghub.elsevier.com/retrieve/pii/S0301421507000365>
9. Mukund R. Patel (2006). *Wind and Solar Power Systems — Design, Analysis and Operation*. 2nd ed., pp. 303-310.
10. Olson, W. (2010). An Urban Experiment in Renewable Energy. <http://www.greenbeanchicago.com/urban-experiment-renewable-energy/>.
11. Sinclair M. (2008). *Growth Scenarios for UK Renewable Generation and Implications for Future Developments and Operation of Electricity Networks*. BERR Publication, 08 (1021)
12. Sovacool B. K. (2009). Contextualizing avian mortality: A preliminary appraisal of bird and bat fatalities from wind, fossil-fuel, and nuclear electricity. *Energy Policy* **37**: 2241–2248.
13. Wald M.L. (2011). "China's Galloping Wind Market". *The New York Times*. <http://green.blogs.nytimes.com/2011/01/11/chinas-galloping-wind-market/?partner=rss&emc=rss>.
14. Zavadil R., Miller N., Ellis A. and Muljadi E. (2005). "Making connections". *Power and Energy Magazine, IEEE* **3** (6): 26–37. [http://ieeexplore.ieee.org/xpls/abs\\_all.jsp?arnumber=1524618](http://ieeexplore.ieee.org/xpls/abs_all.jsp?arnumber=1524618).

## **DEVELOPMENT OF A 2.5kVA PULSE WIDTH MODULATED CONTROLLED AUTOMATIC INVERTER SYSTEM**

O.I. OLUSOLA\* and S.S. OLUYAMO

*Department of Physics, Federal University of Technology, P. M. B. 704, Akure*

\*Corresponding Author, e-mail: *olajideibk@yahoo.com*

### **ABSTRACT**

In this work, a 2.5kVA automatic inverter system capable of converting a 24V DC to 220V AC 50Hz with an optocoupler circuit designed to provide feedback and hence stability of the output voltage have been designed and implemented. The major modules of the inverter system consist of an oscillator section, a Pulse Width Modulation (PWM) controller IC, MOSFETs driver section, a quad 2-input NAND gate that serve as an interface circuit between the oscillator output section and MOSFETs driver section, inverter output section, a comparator for low voltage battery indication and overload detection. A change over circuit that comprise of electromechanical relay was made use of to provide automatic fast switching capabilities both in presence or absence of public power supply without voltage fluctuations supplied to loads during the power switching process. The system also has the ability to shut itself down whenever it senses a low battery voltage and load higher than the inverter capacity.

Keywords: Automatic Inverter System, Pulse Width Modulation (PWM), MOSFETs, Oscillator, Solar Energy Storage System (Battery).

### **1. INTRODUCTION**

The epileptic supply of power in Nigeria today causes a lot of disruptions in almost all sectors of the economy most especially in the academic and research institutions. Most of the researches carried out in our University Laboratories have not been able to reach their conclusive end due to this epileptic nature of our power supply. A forwarded research on DC to AC inverter will provide a partial or lasting solution to this end if properly harnessed. Moreover, the developed automatic inverter system will provide an alternative power source to research students and scientists in remote locations where electricity is not accessible.

An inverter is a device for converting direct current (DC) into conventional alternating current (AC) power. This power can be used to run almost any AC appliance absolutely anywhere (Gottles, 1985). They can work with items such as mobile phone chargers, lights, electrical appliances, power tools, television sets, and microwave ovens and so on. AC is the type of electrical power supplied by power companies. For example, in Nigeria, the mains electricity supplied by the Power Holding Company of Nigeria (PHCN) plc is 220V AC, 50 HZ. DC on the other hand, is the type of electricity stored in batteries and generated by alternative energy devices like wind generators and photo-voltaic (PV) arrays. Varieties of inverters design have been reported (Chan and Bowler, 1974). The predecessor of the modern solid-state converter was the vibrator power supply and the thyatron inverters but had efficiencies in vicinity of 40 percent (Gottles, 1985). Other types of inverter ranges from transistor inverters, FET driven inverters to IGBT driven inverters (Theraja, 2005).

The first commercial electrical systems set up by Thomas Edison were direct current based. However, it is very economical to distribute AC power over large distances, and this is why it is the most popular type of electricity in use today. Almost all electrical appliances today use AC electricity to power them. Most of these early inverters output change as the load on the output of

the inverter socket changes; this has been a major setback in the inverter design. With the introduction of a PULSE WIDTH MODULATION (PWM) technology, the problem experienced by the earlier inverter system becomes solved (Manahar, 2004). The quest for a PWM automatic inverter to supplement erratic power during laboratory experiments and/or research is the rationale behind this automatic inverter system design, development and construction. This paper presents a step-by-step guideline for designing an automatic inverter system for domestic purpose based on the pulse-width modulation techniques.

## **2. CIRCUIT DESCRIPTION**

The 2500VA/24V inverter is based on the PWM technology and comprises of various sections.

## **3. THE PWM SECTION**

The main ICs of this section are optocoupler IC 4N35 (IC1) and IC SG3524 (IC2). The IC SG3524 contains both oscillator and PWM controller; this is shown in figure 1. The IC SG3524 includes an on-chip regulator, error amplifier, programmable oscillator, pulse-steering flip-flop, two uncommitted pass transistors, current limiting amplifier and shutdown circuitry (Manahar, 2004).

### *How the PWM section stabilizes the output voltage*

Generally, the output of an inverter system change with the variation in the load at the output socket. One of the ways to generate an inverter with stable output voltage is to design the inverter transformer and switching circuits so that it is capable of generating the wanted output voltage at the full load. At lower load, this kind of circuit will usually give much higher voltage, but this can be solved with feedback electronics which monitors the output voltage either through a measuring transformer or opto-coupler circuit (Chan and Bowler, 1974). If it gets higher than needed, it reduces the power applied to the transformer. This kind of feedback when properly implemented will stabilize the output voltage. In this design, a pulse width modulation (PWM) technique is used to keep the output supply of inverter constant even at varying loads. The PWM technology controls the width of the oscillation (switching frequency) produced for the inverter output. The value of the alternating current (AC) supply at the inverter output depends on the width of the switching frequency from the oscillator section. In a PWM based inverter system, a small part of the output AC supply is given as a reference voltage to the PWM controller integrated circuit (IC). Based on this reference voltage, the PWM controller IC changes the width of the frequency produced by its oscillator section. This makes sure that the output stays constant even when the value of the load at the output changes.

In the battery mode, some part of the AC supply received by the inverter mains transformer TR1 is given to the bridge rectifier (D1, D2, D3 and D4), through R1. Bridge rectifier converts the AC supply into DC supply. The positive DC supply is given to pin-1 of IC1 and negative DC supply is given to pin-2 of IC1. IC1 is an opto-coupler IC. In this IC, a LED is connected between pin-1 and 2 and a phototransistor is connected at pin-4, 5, and 6. Collector of photo-transistor inside the IC1 is connected to the pin-5; this pin is given a regulated positive 12V supply. Photo-transistor emitter is connected to pin-4 of IC1. Pin-3 and 6 of IC1 are not used in this circuit. In the battery mode when the DC supply from bridge rectifier reaches pin-1 and 2 of IC1, the LED inside the IC starts to glow. Light from light emitting diode (LED) reach the base of photo-transistor inside the IC1 and the photo-transistor switch on. This will make the supply at the collector reach the emitter, which is pin-4 of IC1. This voltage at pin-4 is used as error voltage sample and given

to the pin-1 of IC2, through R4. Pin-1, 2 and 9 of IC2 are part of an operational-amplifier (Op-Amp), which is known as error amplifier.

5V regulated supply at pin-16 of IC2 is given to the pin-2 of IC2, through R6, as a reference voltage. As the load at the output of inverter changes, the output AC supply value also changes. Change in the output supply will change the value of error voltage at pin-4 of IC1. As the error voltage at pin-4 of IC1 changes, the voltage at pin-1 of IC2 also changes; this in turn changes the output of error amplifier accordingly. The error voltage produced by the error amplifier section reach the oscillator/duty cycle control section and changes the width of 50Hz pulse to keep the output constant. This duty cycle control section controls the width of 50Hz signal generated by the oscillator. As the width of 50Hz signal is controlled by the error amplifier output, the inverter output socket will always give a stable output, whatever the load value. If the PWM error voltage amplifier section stops working, the AC supply at the inverter output will vary according to the load connected to the output (Manahar, 2004). PWM adjustment preset VRI connected to pin-4 of IC1 can be used to manually change the error voltage given to pin-4 of this IC; this will adjust the UPS output supply voltage.

#### 4. OSCILLATOR SECTION

This section generates the 50Hz frequency required for the inverter output using timing resistors  $R_T$  and one timing capacitor C1. The resistors  $R_T$  consist of a fixed resistor R2 and a variable resistor VR2. The VR2 is used to set inverter output frequency to 50Hz. Based on the value of resistors and capacitor connected to the pin-6 and 7 of IC2 respectively, the internal oscillator of IC2 generates a fixed frequency signal according to equation 1.

$$F = \frac{0.67}{R_T C_T} \quad (1)$$

With a fixed timing capacitor C1 of value 0.22 $\mu$ F and  $R_T$  set to 61k $\Omega$ , a frequency of 50Hz is generated. Internally, this signal goes to the flip-flop section inside the integrated circuit (IC). From the flip-flop, this signal gets converted into two signals with changing polarity. Changing polarity means when the first signal is positive, the second signal will be negative and vice-versa (Malcolm, 1990). These changing polarity signals are output from output pins 11 and 14 of IC2. These signals at pin 11 and 14 are known as MOS (Metallic Oxide Semiconductor) drive signal. These MOS drive signals are between 4V and 6V. According to Hall (1989), the outputs on both pins should be of the same value but with opposite polarity, otherwise the MOSFETs at the output section could get damaged. MOS drive signal at pin 11 and 14 of IC2 is fed to the pin 2 and 6 of IC3 via limiting resistors R13 and R14 respectively. IC3 (CD4011) is a quad-2 input NAND gate. Each of the NAND gates inside this IC package has two inputs pins and one output pin. As a rule, when all the inputs of NAND gate are high, the output will be low; otherwise the output will be high. Pin 1 and 5 of IC3 receive regulated positive supply voltage through R21 and D7

The IC3 NAND gate is externally wired as an AND gate; this is illustrated in figure 2. The IC3A output is connected to the input pins of IC3D that is wired as an inverter. Since the two inputs of IC3D are joined together, it forms an inverter (Horowitz and Hill, 1997). The presence of high logic (logic 1) signal at pin 5 and 6 of IC3A gives a low logic (logic 0) signal at pin4 (output) of IC3A and pin 12 and 13 of IC3D. The IC3D now wired as an inverter converts the low logic signal at its input to high logic signal at its output (pin 11). A low logic at pin 3 of IC3B when fed to the input pins 8 and 9 of IC3C output a high logic signal at pin 10 of IC3C. Table 1 shows that if there is no MOS drive signal from pin 14 of IC2, there will be a low logic signal at pin 6 and this will finally result to a low output at pin 11.

Table1: Logic signals at the input pins of IC3

Input Pin 5 of IC3A	Input Pin 6 of IC3A	Output Pin 4 of IC3A / Input Pins of IC3D	Output Pin 11 of IC3D
0	0	1	0
0	1	1	0
1	0	1	0
1	1	0	1

*Function of IC3 (CD4011)*

The NAND gate IC3 is used in this circuit as an electronic switch between the MOS drive voltage at pin-11 and 14 of oscillator IC2, and MOS drive transistors T1 and T2 (figure 2). Using this switch, the MOS drive signals can be sent to or stopped from going to the MOS drive transistors. This facility is used to shut down the inverter output during the overload and low-battery conditions. This IC3 also protects the power MOSFETs from getting damaged. MOSFETs can easily get damaged if the gate of a particular MOSFET channel receive MOS drive signal while the other gate does not. With the presence of IC3, the MOS drive signals are either present on the gate of both MOSFET channels or not at all. If they are present, the MOSFETs conduct and if otherwise, the MOSFETs does not conduct. If only one of the MOSFETs channels conduct at a time, it will damage the other MOSFETs channel.

**5. MOS DRIVER SECTION**

The MOS drive signal at the output pin-10 and 11 of IC3 are not powerful enough to drive the output MOSFETs. These signals are sent to the driver transistors T1 and T2 to amplify them to a level that they will be able to drive the MOSFETs (Malcolm, 1990). The transistors T1 and T2 as shown in figure2 are connected in a Darlington pair configuration. MOS drive signal amplified by T1 and output at its emitter reach the gate of MOSFETs U, through D8 and R22-R27 while MOS drive signal amplified by T2 and output at its emitter reach the gate of MOSFETs V, through D9 and R28-R33. Value of the components used in both channels of MOS drive signals must be the same, so that the voltage level of both channels remain same, otherwise the MOSFETs could get damaged.

**6. LOW – BATTERY SHUTDOWN**

When the inverter is operating in battery mode, the inverter should stop using the battery once the battery is discharged to a limit; otherwise the battery will go into deep discharge state, which will reduce the battery life considerably. To protect the battery from this condition, a low-battery shutdown section is used in the inverter. This section, when the battery is low, will switch on the low-battery indicator D17 for some time and then automatically shutdown the inverter. This section uses Op-Amp, using Pin-5, 6 and 7 of IC4. An operational amplifier (Op-Amp) has 2 inputs namely inverting and non-inverting input with one output (Coughlin et.al, 1989).

Pin-5 (non-inverting) receives a +5V from Pin-16 of IC2 and Pin-6 (inverting input) receives regulated battery voltage through a potential divider network R49 and R50. When the battery has enough voltage, Pin-6 of IC4 will receive higher voltage than Pin-5. As the battery gets discharged, the voltage at Pin-6 will reduce. When the battery voltage reach around 9V, then voltage at Pin-6 of IC4 will become lower than the voltage at Pin-5. This will result in high voltage output from output Pin-7. This high output will turn on the low-battery indicator LED. A high voltage at Pin-7 of IC4 will start increasing slowly the voltage at Pin-10 (non-inverting input) of IC4. Pin-9 (inverting input) of IC4 is given a reference voltage of +5v from Pin-16 of IC2. When the voltage at Pin-10 becomes equal to voltage at Pin-9, the output Pin-8 will output a high voltage (about 10V).

High voltage at Pin-8 of IC4 will reach the base of T4 and switch the T4 on. When the T4 switches on, it switches on T3 and the voltage at collector of T3 becomes 0V. 0V at the collector of T3 reach Pin-1 and 5 of IC3, as a result of which Pin-10 and 11 of IC3 (CD 4011) will stop producing MOS drive signal. This will stop the operation of output MOSFETs and the supply at inverter output socket will also stop. The high voltage at Pin-8 of IC4 will also switch on an LED D16 to indicate a total shutdown of the system.

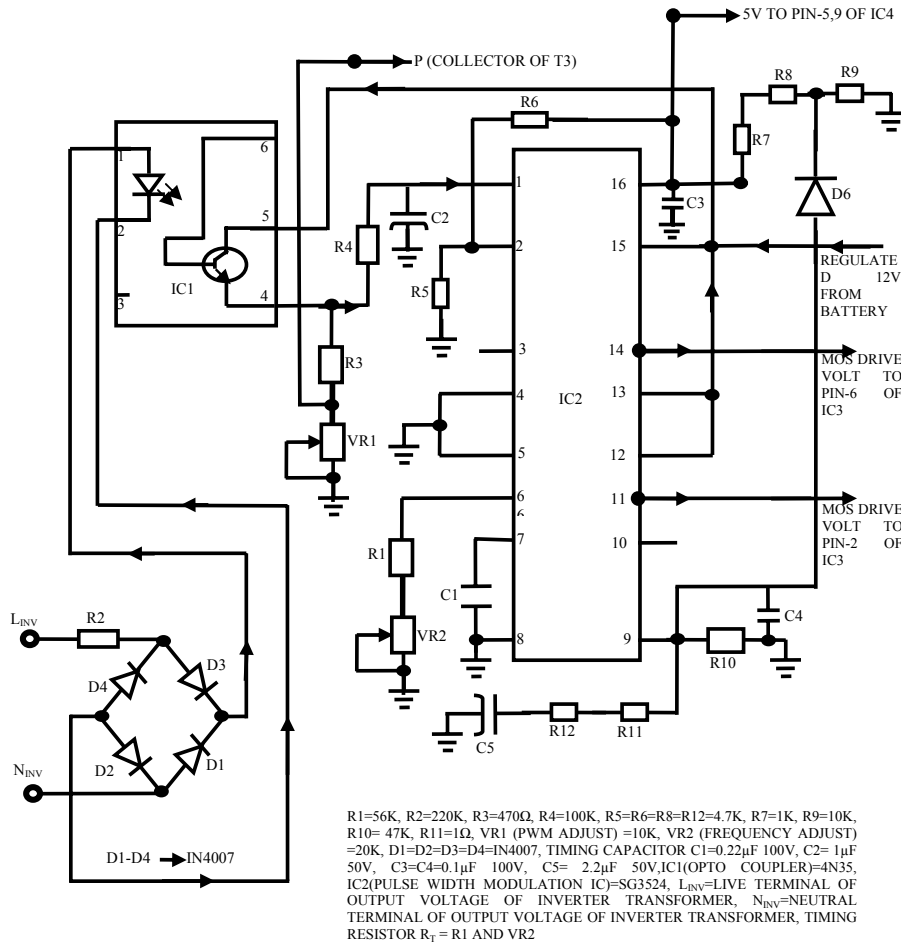


Figure1: Oscillator and PWM Section

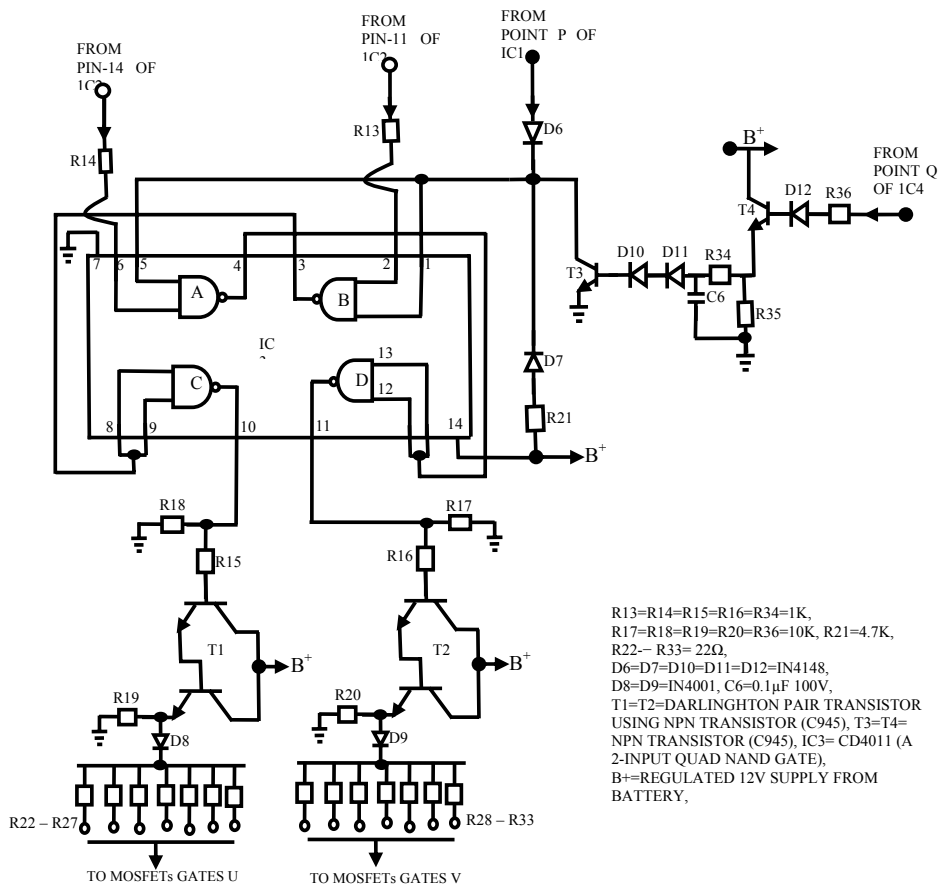
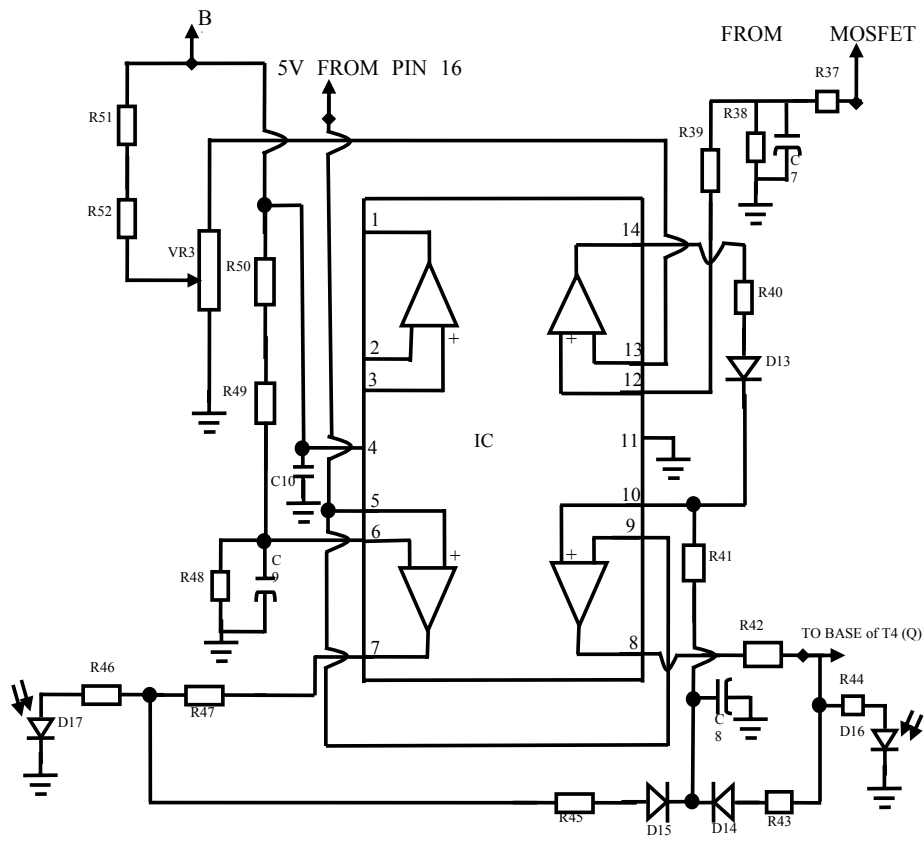


Figure 2: Nand Gate/MOS Driver section

## 7. OVERLOAD SHUTDOWN SECTION

If a load of higher value than the load for which the inverter is designed is connected to it, then the output MOSFETs and the mains transformer of the inverter could get damaged (Mottershead, 1981). To protect the system, an overload shutdown section is used. This section shuts down the inverter and protects the MOSFETs and mains transformer. Overload shutdown section uses Op-Amp using Pin-12, 13 and 14 of IC4. Pin-13 of IC4 receives a constant reference voltage, through R51, R52 and overload adjustment preset VR3 while Pin-12 is given supply from MOSFETs source. When loads of higher value are connected to the inverter, the MOSFETs source voltage increases; this results in the voltage at Pin-12 of IC4 getting higher than the voltage at the Pin-13 of IC4. A higher voltage at Pin-12 will output high voltage from the output Pin-14 of IC4. This high output will turn on the overload indicator D16. A high voltage at Pin-14 of IC4 will start increasing the voltage at Pin-10 of IC4. This will repeat the whole process which was explained in the low-battery shutdown section and the inverter will shutdown. The circuitry of the low battery and overload shutdown section is shown in figure 3.



R37=R40=R44=R46=R50=2.2K, R38=100K,  
 R39=R42=R47=1Ω, R43=R48=R51=47K, R45=330K,  
 R49=33K, R52=22K, D13=D14=D15=IN4148,  
 D16=OVERLOAD/SHUTDOWN LIGHT EMITTING  
 DIODE (LED) INDICATOR, D17=LOW BATTERY  
 LED INDICATOR, C7=100μF 50V, C8=47μF 50V,  
 C9=10μF 50V, C10=0.1μF 100V, IC4=LM324  
 (QUAD OPERATIONAL AMPLIFIER), VR3  
 (OVERLOAD ADJUSTMENT PRESET)=4.7K

Figure 3: Low Battery and Overload Circuitry



## **8. OUTPUT SECTION**

In the driver section, the MOS drive signals reach the gates of MOSFETs through  $22\Omega$  resistors. MOSFETs U make the first channel and V make the second channel of the output section. Drains of MOSFETs U are joined together and connected to one end of bifilar winding of mains transformer TRI. Drains of MOSFETs V are joined together and connected to other end of bifilar winding of mains transformer TRI. The sources of MOSFETs U and V are joined together and grounded through a shunt. The centre taping of the bifilar winding is connected to the positive supply of the 24V battery while the 12V regulated supply takes its source from the 24V unregulated battery supply through a 12V fixed Voltage regulator.

MOS drive signals of different polarity reach the gate of each MOSFET channels. As the polarity of signals is different, when first channel is on, the second channel will be off and when the second channel is on, the first channel will be off. Each channel will be on/off alternatively. This on/off process takes place 50 times per second. As these MOSFETs are connected to the primary of the mains transformer, continuous on/off will produce an alternating current (AC) in the primary winding of TRI. Alternating Current in the primary of TRI will induce an AC voltage in the secondary of TRI. This AC voltage is sent to the inverter output socket through an on/off switch.

### *Paralleling of MOSFETs*

Due to the step-up nature of the inverter transformer, the current at the primary and drain current of the MOSFET is very large (Theraja, 2005). Often times, a single MOSFET chip may not be able to cope with such current and there is then the need to parallel two or more MOSFETs. When MOSFETs are connected in parallel, the operating voltage is not affected but the maximum continuous drain current is doubled. Consequently, the power of the two MOSFETs is twice that of a single one. A ferrite bead or small resistors of equal value must be connected in series with each of the gates separately, so as to prevent imbalance load sharing due to possible variation in the MOSFETs characteristics. It must also be noted that equal number of FETs must be connected in parallel on both sides.

### *Automatic Change over Switch*

The inverter also makes use of electromechanical relays for automatic switching of the load either to the inverter power output channel or to public power supply when available, as well as charging the back-up batteries during the availability of public power supply. In situation where load of higher amperage is to be used, contactors of high current rating are preferred to electromagnetic relays.

## **9. CURRENT RATING/CAPACITY OF THE LEAD ACID BATTERY (AH- AMPERE HOUR)**

The lead-acid batteries are generally rated in terms of how much current the battery can supply for a fixed period of time. Battery capacity is rated in ampere-hour (Ah). Generally Ah value is based on 8 hours discharge time. A 200Ah battery can provide the load current of 25 amperes ( $\frac{200}{8} = 25$ ), for 8 hours. The battery can supply less current for longer time or more current for shorter time (Ronald, 1991). A 100Ah battery can provide 12.5 amperes current for 8 hours; if a high current is taken from the same battery, then the duration for which it can provide the required supply will reduce. If 20 Amperes current is consumed, the battery will be able to provide the current only for 5 hours. Table 2 shows how many hours one can use a fully charged 120Ah battery, when different amount of current is consumed.

Table 2: Table showing the variation of battery current consumption with time

Time (Hours)	120	60	40	30	24	12	6	4	3	2.4	2	1.5	1.2	1
Current (A)	1	2	3	4	5	10	20	30	40	50	60	80	100	120

From the Current-Time graph plotted in figure 4, an empirical relation shown in equation 2 was obtained between the current measured in Amperes and Time measured in hours. This equation thus shows the relationship between Current I and Time T.

$$Y = 120X^{-1}$$

(2)

From equation 2, the constant value is 120 while the variables are Y and X. The constant value 120 is the maximum current of the battery measured in Amperes Hour. The Pearson product moment correlation coefficient r between the variables plotted on the Current axis and Time axis is 1. Since Current I is plotted on the primary vertical (Y) axis against Time T on the horizontal (X) axis, equation 2 can thus be written as

$$I_{\text{var}} = I_{\text{max}} T^{-1}$$

(3)

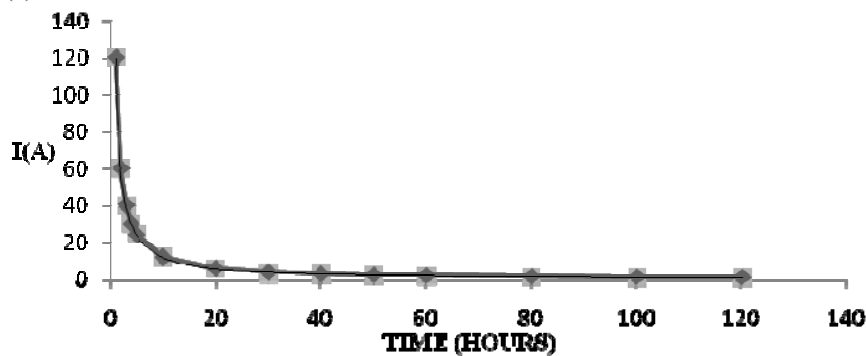


Figure 4: Variation of battery current consumption with time

The two batteries used in this design are rated 12V 120Ah each but their measured values were 13.5V respectively when fully charged. The desired frequency is 50Hz single phase and the cooling device for the inverter is an alternating current 220V 500mA suction fan. If two batteries rated 12V, 120Ah each connected in series are used with 2500w inverter, the peak current will be

$$I_P = \frac{V_S I_S}{V_P} = \frac{P_S}{V_P} = \frac{2500}{24} \cong 104.2A(\text{maximum})$$

(4)

This must be balanced with sufficient number of FETs in each phase/channel of the inverter such that the total current of the FETs in each phase when connected in parallel must be far greater than the peak current of an inverter. For example, if 20A IRF 540 MOSFET is to be used with 2500w 24V inverter, then a minimum of seven quantities of IRF 540 are required to be used in each phase thus giving a total MOSFETs current of 140As. Since the MOSFETs current is more

than the peak current of the inverter, the FETs are protected from damage that results from excessive heat generated from the coils of the inverter transformer. If four –12V batteries connected in series are used with 2500w inverter, the peak current will be

$$\frac{2500}{48} \cong 52.1A(\text{maximum})$$

(5)

Thus the number of FETs used in each phase can be reduced to four. With four 20A IRF 540, a total of 80A current is generated by the MOSFETs. Since the MOSFETs total current is greater than the inverter peak current, the FETs are protected from damage that can arise from heat generated from transformer. If the inverter peak current is more than the total MOSFETs current in each phase, the FETs will be damaged by the excess current; this is illustrated in table 3.

Table 3: Relationship between FETs total current and Inverter peak current

Capacity of Inverter	Peak Current of Inverter	No of MOSFETs in each phase	Normal Current of each FETs	Total Current of MOSFETs in each phase
200W/12V	17A	1	26A, IRF 150	26A
600W/24V	25A	2	20A, IRF 540	40A
1000W/24V	42A	3	20A, IRF 540	60A
2500W/24V	104A	7	20A, IRF 540	140A
2500W/36V	69A	5	20A, IRF 540	100A
2500W/48V	52A	4	20A, IRF 540	80A

## 10. CONCLUSION

The present design of a PWM automatic inverter system is an improvement over earlier constructed inverter system as it incorporates some safety control circuitry that can ensure the longevity of the inverter system. Some of these control circuitries as described in this paper are the low battery and overload shutdown circuit section. In addition to the above, there is also an external provision made to connect the inverter system to a DC energy output from a solar photovoltaic (PV) panel. The DC energy from the solar PV module can then be used to charge solar energy storage system such as batteries in the absence of public power supply from the utility company.

## REFERENCES

1. Chan, T. and Bowler, P. 1974. International Conference on Power Electronics, Power Semiconductors and their Applications. Oct. 7-9, pp.241-251.
2. Coughlin, R.F. and Driscoll, F.F. 1989. Operational Amplifiers and Linear Integrated Circuits. Prentice-Hall, New Delhi, India, pp.215-226.
3. Gottles, M.I. 1985. Power Supplies Switching Regulators Inverters and Converter Circuit. B.P.B Publication, New Delhi, India, pp. 28-41.
4. Hall, D.V. 1989. Digital Circuits and Systems. McGraw-Hill Inc., Singapore, pp.245- 272.
5. Horowitz, P. and Hill, W. 1997. The Arts of Electronics. Cambridge University Press, London, pp. 44-52, 125-130, 141-169.
6. Malcolm, P. 1990. Basic Electronics. Hodder and Stoughton Ltd., Britain, pp. 42-55C, 12-23D.
7. Manahar, L. 2004. Modern Uninterrupted Power Supply – Introduction, Servicing and Troubleshooting. B.P.B publication, New Delhi, India. pp. 23-48.

8. Mottershead, A. 1981. *Electronic Devices and Circuits*. Prentice-Hall, New Delhi, India, pp. 50-56.
9. Ronald, A.R. 1991. *Digital Electronics through Project Analysis*. Macmillan Publishing Company, New York, USA, pp. 25-28.
10. Theraja, B.L. and Theraja, A.K. 2005. *A textbook of Electrical Technology*. S. Chand and Company Ltd., New Delhi, India, pp.2365-22370.

## **STATE OF THE ART SOLAR AIR HEATER FOR COMMERCIAL APPLICATIONS**

A. CLARA DHANEMOZHI

*J. A. College for Women, Periyakulam, Theni District – 625 531,  
Tamilnadu, India*

Corresponding Author, e-mail: [jdhanemozhi@gmail.com](mailto:jdhanemozhi@gmail.com)

### **ABSTRACT**

The Sun is the source of all energy. The energy obtained from the sun is the most promising renewable energy sources since it is clean, safe and free. Applications of solar energy are commercially available and are used by millions of people in various parts of the world. One of the promising areas of the applications of solar energy is solar air heater. Solar air heaters are used for drying and space heating.

The rural mass in Periyakulam in Tamilnadu and its adjoining areas are mainly involved in agriculture. Grapes, Tea, Cardamom, Pepper, and Coffee are mainly cultivated. Drying the products in a hygienic manner is one of the important processes in agriculture. We have designed a **novel solar air heater** and studied the **thermal efficiency** for drying the products, which requires hot air at low temperature ranges from 40<sup>0</sup> C – 100<sup>0</sup>C.

Solar air heater fabricated consists of i) Glass cover ii) Absorber plate (Aluminium sheet) iii) Baffles iv) Drying unit. Sunlight passes through the glass and strikes the absorber plate, which is black coated. Baffles are fixed on the absorber plate through which air is circulated by mechanical fans. The heat absorbed by the plate heats the air that flows through the baffles, which increases the thermal efficiency. The hot air passes through the products in the drying chamber immediately after it leaves the baffles. No insulation material is needed in this type, which reduces the cost.

This type of air heater can be utilised for various applications such as dehydration and drying. This would be beneficial not only in conserving the fossil fuels, but also in protecting the environment by the emissions of harmful pollutants and green house gases.

**Key words:** Solar energy, dehydration, thermal efficiency.

### **1. INTRODUCTION**

The Sun is the source of all energy. The energy obtained from the sun is the most promising renewable energy sources since it is clean, safe and free. Applications of solar energy are commercially available and are used by millions of people in various parts of the world. One of the promising areas of the applications of solar energy is solar air heater. Solar air heaters are used for drying and space heating.

The rural mass in Periyakulam in Tamilnadu and its adjoining areas are mainly involved in agriculture. Grapes, Tea, Cardamom, Pepper, and Coffee are mainly cultivated. Drying the products in a hygienic manner is one of the important processes in agriculture. We have decided to design a **novel solar air heater** and study the **thermal efficiency** for drying the products, which requires hot air at low temperature ranges from 40<sup>0</sup> C – 100<sup>0</sup>C [1]. This type of air heater can be utilised for various applications such as dehydration and drying [2]. This would be beneficial not only in conserving the fossil fuels, but also in protecting the environment by the emissions of harmful pollutants and green house gases.

## 2. DESIGN AND FABRICATION OF SOLAR AIR HEATER

Solar air heater fabricated consists of i) Glass cover ii) Absorber plate (Aluminium sheet) iii) Baffles iv) Drying unit. No insulation material is needed in this type, which reduces the cost. Sunlight passes through the glass and strikes the absorber plate, which is black coated. Baffles are fixed on the absorber plate through which air is circulated by mechanical fans. The heat absorbed by the plate heats the air that flows through the baffles, which increases the thermal efficiency. The hot air passes through the products in the drying chamber immediately after it leaves the baffles as shown in fig. 1.

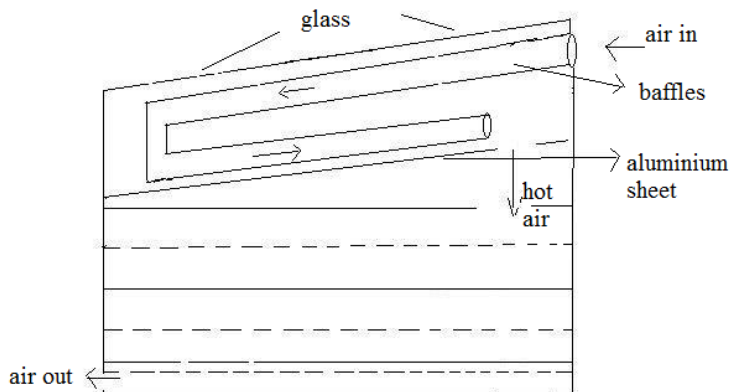


Fig. 1 Two pass Air heater with drying chamber

## 3. TEST CONDITION

The collector mounting frame angle, orientation and location influence the results of thermal performance tests. So, the appropriate considerations were taken into account in respect of the collector mounting frame, orientation and tilting angle and choice of location in the present investigation. The solar air heater was mounted such that their lower edges were higher than 3.5cm above the local ground surface. It was mounted at an angle of  $20^{\circ}$  from horizontal so as to have a normal incidence of solar radiation. It was also located in such a way that shadows would not fall on the air heater at any time and no reflection taking place on it by surrounding building or surfaces.

## 4. RESULTS AND DISCUSSION

Solar air heater was constructed with Aluminium sheet of thickness 0.40 mm and area of 1m x 0.5m. It was mounted outdoors at an angle of  $20^{\circ}$  from horizontal so as to have normal incidence of solar radiation and 3.5 cm above the ground level. All experiments were conducted during sunny days, from August to February, and from 11.00 am to 4.00 pm. It was found that the efficiencies were maximum during 11.00 am to 1.00 pm, which recorded a maximum value of solar radiation. ( $610 \text{ w/m}^2$ ). The maximum temperature difference between the inlet and outlet temperature was  $29^{\circ}\text{C}$ . This shows that the temperature difference is one of the major factors that determine the thermal efficiency of SAH [3]. Efficiency was calculated using the formula

$$\eta = \frac{W \times L}{I \times A_c}$$

W - Mass of moisture evaporated

L - Latent heat of evaporation of water at the dryer temperature

I - Solar radiation

A<sub>c</sub> – Area of the collector.

The commercial products such as Grapes, Cardamom, Pepper, Potato slices, Pappads were dried using it [3, 4]. The products were spread on the trays and on the perforated trays. The hot air directly falls on the products. The crop is heated and the moisture is removed. The samples were collected periodically and weighed for finding out the moisture content of the samples. The readings are tabulated as shown in table(i) and table(ii) for cardamom and pepper.

TABLE (i) CARDAMOM Inlet Temp: 35°C

TIME	INTENSITY (W/m <sup>2</sup> )	TEMP (°C) OUTLET	MASS OF MOISTURE EVAPORATED (gm)	EFFICIENCY
11.30-1.30	390	60	4	31.66
12.45-1.45	480	55	4	25.72
1.45-2-45	410	50	3	22.58

TABLE (ii) Inlet Temp: 37°C PEPPER

TIME	INTENSITY (W/m <sup>2</sup> )	TEMP (°C) OUTLET	MASS OF MOISTURE EVAPORATED (gm)	EFFICIENCY
10.30-11.00	595	65	5	25.94
11.30-12.00	555	55	4	22.24
1.30-2.00	500	60	3	18.52
2.15-2.45	445	55	2	13.87

It was found that the moisture content is completely removed from potato slices and pappads within 30 minutes. 15% of moisture content was removed from cardamom within 3 hrs and for pepper within 2 hrs. Drying of tea leaves, cereals can also be tried.

## **5. CONCLUSION**

With these results, it is found that this drying technology can be utilised in the small scale industries and cottage industries. The main advantage is that no insulation material is needed (which reduces the cost) as air passes directly into the dryer. It is compact and can be installed at any places.

Based on the experimental data and calculations, it is concluded that this type of solar air heater can be used for dehydration and drying applications of commercial products mainly in the domestic, commercial, industrial and agricultural sectors.

## **REFERENCES**

1. Tiwari G. N. (2008), Applications of Solar Energy, P-218, Fourth edition, Narosa Publishing Pvt. Limited, New Delhi.
2. Rai G. D. (2000), Solar Energy utilisation, Fifth Edition, Khanna Publishers, New Delhi.
3. Jeba Raja Sekhar R. V. (1997), Comparison of thermal performance of two types of solar air heaters in fruit dehydration unit, M.Phil., Dissertation, School of Energy Sciences, Madurai Kamaraj University, Madurai, India.
4. Palaniappan P., Kolar A. K. and Haridassan T. M. (1997), Renewable Energy applications to Industries, Narosa publishing House, New Delhi.



**ENHANCED HEAT TRANSFER IN SOLAR WATER HEATER (WITH PARABOLIC COLLECTOR) USING PARTIALLY REFLECTIVE GLASS**

T. CHANDRASEGARAN

*Cognizant Technology Solution, Chennai (India)*

Corresponding Author, e-mail: *chand.candid@gmail.com*

**ABSTRACT**

Solar energy collectors are special kind of heat exchangers that convert the solar irradiation into internal energy of the flowing fluid. It is the major component of any solar system. There are basically two types of solar collectors: non-concentrating (or stationary) and concentrating. The concentrating type collectors require tracking mechanism for better performance. Solar water heaters with parabolic collectors are very common type. Line focusing type of collection of radiation energy is adopted in parabolic trough collectors. In this paper an attempt is made to incorporate partially reflective glass with the parabolic collector. Partially reflective glass will allow 50% of the radiation to pass through and the remaining 50% of radiation will be reflected back. This reflected radiation along with incoming radiation is from the source is collimated to form highly intense radiation. This high energy radiation, if allowed to focus on the flowing fluid will result in high temperature output.

**1. INTRODUCTION**

Nowadays, most(80%) of worlds energy demand is met from fossil fuels, massive exploitation of fossil fuels leads to a real threat to the environment, through global warming and acidification of the water cycle. The distribution of fossil fuels around the world is equally uneven. Middle East possesses more than half of the known oil reserves. This fact leads to economical instability around the world, which affects the whole geopolitical system. The present system as it is cannot be maintained for more than two generations. The impact it has on the environment as well to the humans cannot be disputed. So it is mandatory to switch to renewable resources.

Renewable energy technology produces marketable energy by converting natural phenomena into useful form of energy these technologies use the sun's energy and its direct and indirect effects on the earth (solar radiation, wind falling water and various plants, i.e. biomass), gravitational forces (tides), and the heat of the earth's core (geothermal) as the recourses from which energy is produced . These resources have massive energy potential, however, they are generally diffused and not fully accessible, most of them are intermittent, and have distinct regional variability's. These characteristics give rise to difficult, but solvable, technical and economical challenges.

Nowadays, improving the efficiency of collection and conversion, lowering the initial and maintenance cost, and increasing the reliability of and applicability make significant progress. Energy conversion system that is based on renewable energy technologies appeared to be cost effective compared to the projected high cost of oil. Furthermore, renewable energy system can have a beneficial impact on the environmental, economic and political issues of the world.

At the end of 2001 the total installed capacity of renewable energy system was equivalent to 9% of the total electricity generation. By applying a renewable energy intensive scenario the global consumption of renewable sources by 2050 would reach 318 joules.

## **2. SOLAR COLLECTORS**

Solar energy collectors are special kinds of heat exchangers that transform solar radiation energy to internal energy of the transport medium. The major component of any solar system is the solar collector. This is a device that absorbs the incoming solar radiation, converts it into heat, and transfers the heat to a fluid (usually air, water, or oil) flowing through the collector. The solar energy Collected is carried from the circulating fluid either directly to the hot water or space conditioning equipment or to a thermal energy storage tank, from which it can be drawn for use at night or on cloudy days.

There are basically two types of solar collectors: non-concentrating or stationary and concentrating. A non-concentrating collector has the same for intercepting and absorbing solar radiation, whereas a sun-tracking concentrating solar collector usually has concave reflecting surfaces to intercept and focus the sun's beam radiation to a smaller receiving area, thereby increasing the radiation flux. Concentrating collectors are suitable for high-temperature applications. Solar collectors can also be distinguished by the type of heat transfer liquid used (water, non-freezing liquid, air, or heat transfer oil) and whether they are covered or uncovered. When solar radiation passes through a transparent cover and impinges on the blackened absorber surface of high absorptive, a large portion of this energy is absorbed by the plate and transferred to the transport medium in the fluid tubes, to be carried away for storage or use. The underside of the absorber plate and the two sides are well insulated to reduce the conduction loss the liquid tubes can be welded the absorbing plate or they can be an integral part of the plate. The liquid tubes are connected in both the ends by large-diameter header tubes.

### *2.1. Using reflective surfaces*

In this type the collector consist of mirror in order to get a good reflection. Schematic diagram shows the collector with reflecting surfaces. Here an attempt is made to impart the partially reflecting mirror in between the collector and receiver, the purpose of partially reflecting mirror is to split the light into two halves. The detailed explanation is given below.

## **3. PHYSICS BEHIND PARTIALLY REFLECTIVE GLASS**

In this paper an attempt is made to impart the partially reflecting glass to improve the efficiency of the System. A partially reflected glass is also known as semi silvered glass which allows the light partially into the target and remaining into the source. It is used in lasers in order to achieve the high coherent and intense source of light. Initially small quantity of photon is generated by optical pumping and the photons lies in between the partially and fully reflected mirror, and then the generated photon is allowed to strike the partially reflective mirror. 50% of photons passed to the required target, and the remaining 50% enters into the source. By multiple reflections the intensity of the beam gets increased. In this solar heater, a partially reflected glass is placed in between the collector and receiver, when the incident sunlight fall on the collector it is passed to the partially reflective mirror. it send 50% of radiation to the receiver remaining 50% return back to the collector, but the collector receiving the radiation continuously, thus the intensity of the radiation get increased, thus very huge amount of heat is generated.

## **4. PRINCIPLE OF SUPER POSITION**

When two waves travel in a medium simultaneously in such a way that each wave represents its separate motion, then the resultant displacement at any point at any time is equal to the vector sum of the individual. It may be either constructive interference or destructive

interference, it is shown in the below figure (a&b). As per the above consideration the incident light is allowed to enter into the partially reflecting glass ,only 50% of radiation is allowed to strike the copper tube remaining 50% of radiation is return back to the collector, in the collector the incident radiation also strikes it imposes with each other resulting in either rise or fall in amplitude of the wave, when there is a rise in amplitude there is a rise in energy level, because energy is proportional to the square of amplitude, if it results in destructive interference the destructive energy is converted into heat however our ultimate aim is to increase the heat by both way we can increase the efficiency of the system.

## 5. TABLES, FIGURES, EQUATIONS AND LISTS

### 5.1. Tables

Tab. 1: Average reading for one week (during march 2010) without partially reflecting glass

Time	Amb tem	Inlet Temp	Outlet Temp	Temp Rise
9.00	33	31	31	0
10.00	33	30	32	2
11.00	33	30	34	4
12.00	34	32	38.5	6.5
13.00	34	33	41	8
14.00	34	33	41	8
15.00	34	33	40	7
16.00	34	34	40	6
17.00	28	33	37	4

Tab. 2: Average reading for one week (during march 2010) with partially reflecting glass

Time	Amb Tem	Inlet Temp	Outlet Temp	Temp Rise
10.00	33	30	31	1
10.03	33	30	34	4
11.00	33	30	40	10
12.00	26.5	29	43	14
13.00	25	29	44	15
14.00	26	30	50.5	20.5
15.00	26	32	43	11
16.00	26	32	41	9
17.00	25	32	40	8

5.2. Figures

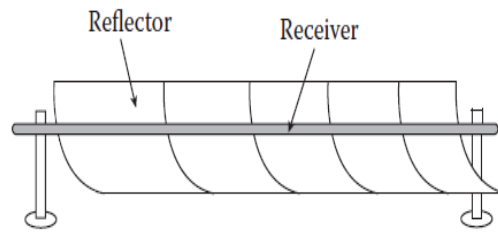


Fig. 1: Parabolic collector with reflective mirror

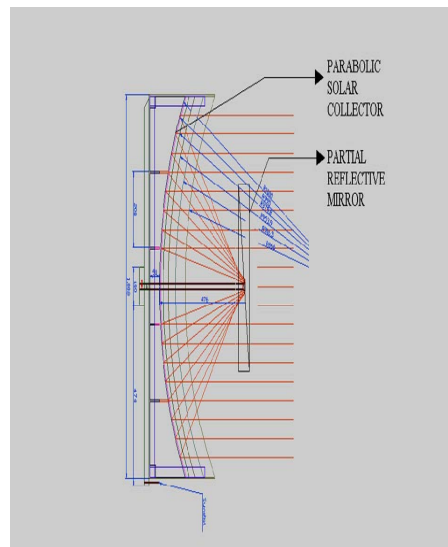


Fig. 2: Schematic diagram of collector along with partially reflecting mirror

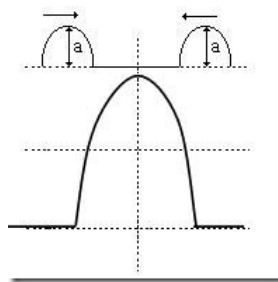


Fig. 3: Constructive & Destructive interference

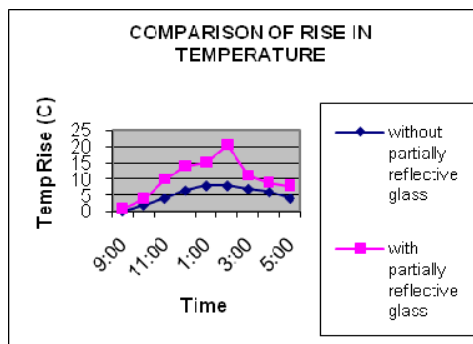
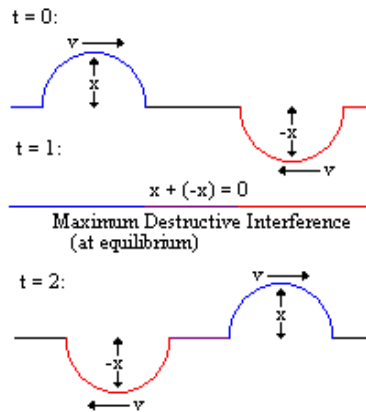


Fig. 4: Comparison of rise in temperature

## 6. CONCLUSION

In this paper an attempt is made to introduce the concept of laser (coherent beam) for the application in solar water heater. The experiments conducted shows there is scope to incorporate partially reflective glass in the path of the solar radiation and this also results in the increased outlet water temperature.

## REFERENCES

1. Alastair I.M.Rae-quantum physics illusion or reality, Cambridge University Press.
2. Barry L.Butler, golden, colo- light weight diaphragm mirror module system for solar collectors, US PATENT, 1985.
3. David K. Fork, Palo Alto, Calif-laser beam conditioner using partially reflective mirrors, US PATENT, Jan, 1999.
4. G.D Rai- non conventional energy sources-khanna publication-2007.
5. P.L.knight & A. miller- measuring the quantum state of light, Cambridge studies in modern optics.
6. Stu campell-build your own solar water heater, garden way publishing charlotte, Vermont 05445

## STRUCTURAL EVOLUTION OF INDIUM PHOSPHIDE FILMS PREPARED BY CO-EVAPORATION TECHNIQUE

R. N. GAYEN<sup>1</sup>, S. HUSSAIN<sup>2</sup>, R. BHAR<sup>1</sup> AND A. K. PAL<sup>1\*</sup>

<sup>1</sup>Department of Instrumentation Science, USIC Building, Jadavpur University, Calcutta-700 032, India

<sup>2</sup>UGC-DAE CSR, Kalpakkam Node, Kalpakkam, 603102, India

\*Corresponding Author, e-mail: [msakp2002@yahoo.com](mailto:msakp2002@yahoo.com)

### ABSTRACT

Indium phosphide films were deposited with three different In:P ratios to obtain three sets of phosphorous rich, stoichiometric and phosphorous poor InP films. The structural properties such as crystallinity, strain, and degree of disorder were studied by a combination of X-ray diffraction (XRD) and Raman spectroscopy. Microstructural and compositional studies indicated films to be polycrystalline in nature with grain size and shape varying with In:P ratio in the films. X-ray diffraction pattern indicated reflections from (111), (220) and (311) planes of InP only. The surface roughness of the films was estimated to be 30 nm. The PL spectrum measured at 300 K was dominated by a strong peak located ~1.41 eV. The intensity of this peak increased significantly when recorded at lower (10 K) temperatures and shifted towards higher energy (~1.54 eV). XPS studies indicated two peaks ~444.5 eV and ~451.9 eV, corresponding to peaks of 3d<sub>5/2</sub> and 3d<sub>3/2</sub> of In 3d core while the P 2p peak at ~129 eV was assigned to only P in InP. Characteristics Raman peaks for InP at ~303 cm<sup>-1</sup> (TO) and ~342 cm<sup>-1</sup> (LO) were observed.

Keywords: InP films; III-V semiconductor, Optical properties

### 1. INTRODUCTION

High radiation resistance and potentiality for achieving high efficiency made indium phosphide a very promising photovoltaic (PV) material for space solar cell applications [1-5]. Also, the electro-optical properties of InP along with the carrier recombination mechanism indicate that InP and related compound are the best candidate for optoelectronic and microwave devices. But large scale deployment of this material in PV industry is being deterred by the dearth of process technology for obtaining the material in thin film form by low-cost and scalable method.

Among the different techniques, reported so far for the deposition of InP films, liquid phase epitaxy [8], sputtering [9], electrodeposition [10], spray pyrolysis [11], flash evaporation [12] and organic chemical vapour deposition [13] are worth mentioning. InP films were also deposited by three temperatures method by Rusu [14] while InP grown in different nanocrystalline forms (nanoparticles, nano wires etc) have been reported by others [15-20]. But none of the above methods could effectively ensure large area deposition of InP films and the need of a reliable, low-cost and scalable process technology for synthesis of InP in polycrystalline form is the need of the day to expand the use of this material in different device technologies.

In the present paper, deposition of InP films with controlled composition on glass and silicon substrates has been demonstrated. The structural properties such as crystallinity, strain, and degree of disorder were studied by a combination of X-ray diffraction (XRD) and Raman spectroscopy. Raman spectroscopy gives useful information about the solid on a scale of the order of a few lattice constants, and can therefore be used to study the microscopic nature of structural disorder. X-ray photoelectron spectroscopy (XPS) analysis indicated the formation of an oxygen deficient film.

## 2. EXPERIMENTAL

InP films were deposited on glass and Si substrates at 423K by co-evaporating In and P (both 99.99% purity) from two independent alumina crucibles, heated indirectly by heavy duty tungsten basket heaters. The system pressure during deposition was better than  $10^{-6}$  Torr. We found the optimum substrate temperature to be  $\sim 423$  K. The following discussions are based on the InP films deposited at 423 K.

Compositional information was obtained by EDAX (Oxford Instruments' INCA Energy 250 Microanalysis System), which indicated that the films were nearly stoichiometric. The surface morphology of the films was studied by Field Emission Scanning Electron Microscope (FESEM) (Carl Zeiss SUPRA® 55 with GEMINI® Technology with resolution  $\sim 0.8$  nm @ 15 kV). AFM pictures were recorded by using a Nanosurf Easy Scan 2 in contact mode while X-Ray Diffraction (XRD) studies were carried out by Rigaku MiniFlex using Cu  $K\alpha$  line (0.154 nm). Photoelectron Spectroscopy (XPS) measurements were carried out using a M/s SPECS (Germany) make spectrometer. Al  $K\alpha$  line was used as the X-ray source at 1486.74 eV. The anode was operated at a voltage of 13kV and source power level was set to 300 W. An Ar ion source was also provided for sputter-etch cleaning of specimens. It was operated at 5kV and 50  $\mu$ A. The system sputter rate was approximately 10 nm per minute. This value varied depending on the sample. Spectra were collected using the PHOIBOS 150 MCD-9 analyzer with a resolution of 0.6 eV for 656 keps at pass energy of 12 eV. Photoluminescence (PL) measurements were recorded at 300 K and 10 K by using a 300 W xenon arc lamp as the emission source. A Hamamatsu photo multiplier along with a 1/4 m monochromator was used as the detecting system.

## 3. RESULTS AND DISCUSSION

### 3.1. Microstructural studies

Figures 1(a-c) show the SEM picture of three representative InP films deposited with three different In:P ratios such that three sets of phosphorous rich, stoichiometric and phosphorous poor InP films could be obtained. The films were deposited under identical experimental conditions discussed in the previous section and only variant was indium flux arriving the substrates. It may be noted here that all the films appear compact in nature and the size and shape of the grains depended on the composition of the films. Phosphorous rich films (Fig.1c) had nearly spherical grains with narrower size distribution while phosphorous poor films (Fig.1a) consisted of different sizes of grains with very broad size distribution. The morphology of the InP films with near stoichiometric composition (Fig.1(b)) had a bit oblong grains. All the films had rough surface as has been depicted in the AFM studies.

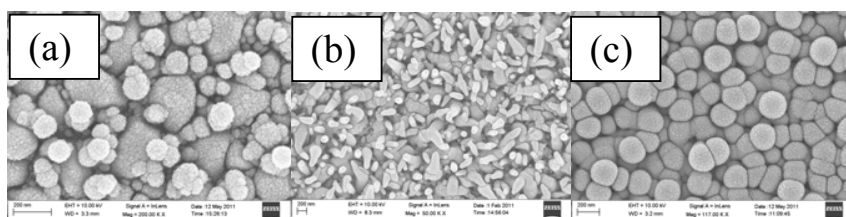


Fig-1 : SEM pictures of three representative InP films: (a) InP-8, (b) InP-01 and (c) InP-4

Z-scan picture of a representative InP-01 film is shown in Fig.2a. One may observe uniform distribution of In and P in the film. Composition of the films was obtained by EDAX measurements and the compositions of different films deposited here are shown in Table-1.

Table-1 : Compositions of different films deposited by this technique

P- poor			Stoichiometric			P – rich		
Sample	In at%	P at%	Sample	In at%	P at%	Sample	In at%	P at%
InP-3	55	45	InP-01	49	51	InP-1	45.5	54.5
InP-8	56	44	InP-6	51	49	InP-2	43	57
InP-9	62	38	InP-7	48	52	InP-4	45	55

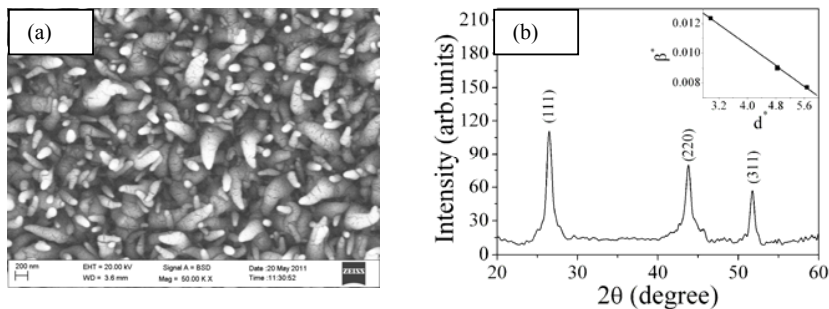


Fig-2: (a) Z-scan picture of a representative InP film and (b) XRD pattern of a representative InP films(InP-01). Inset shows the plot of  $\beta^*$  versus  $d^*$

The X-ray diffraction pattern for a representative InP films (InP-01) is shown in Fig.2(b). The film deposited with stoichiometric composition indicated peaks at  $2\theta=26.5^\circ$ ,  $43.8^\circ$  and  $51.7^\circ$  for reflections from (111), (220) and (311) planes of InP [21], respectively. The lattice constant (0.58 nm), calculated from the XRD pattern, was in good agreement with that reported earlier for InP bulk (0.5869 nm) with zinc blende structure [22]. Line profile analysis (LPA) was adapted to characterize the above films to assess the size–strain relationship and correlate them with physical properties of the resulting materials. We have utilized the Scherrer relation [23] to extract the size of the coherent diffracting domains from diffraction peak. The “apparent” domain size, a volume-weighted quantity, is given by:

$$t = (K\lambda/\text{FWHM}) \cos\theta \quad (1)$$

where K is a constant close to unity, FWHM corresponds to the full width at half maximum of the peak and  $\theta$  the Bragg angle of the [h k l] reflection. Another volume-weighted quantity was defined by Wilson [24] as an “integral breadth apparent size” and is given by:

$$(D)v = (K\lambda/\beta) \cos\theta \quad (2)$$

where, the integral breadth  $\beta = A/I_0$ , A being the peak area and  $I_0$  the height of the observed line profile. In both the relations, the peak broadening was attributed to the effect of the diffracting coherent domain size. When the broadening is solely due to the strain effect, the following Stokes and Wilson relation [25] may be applied:

$$\eta = \beta \cot\theta \quad (3)$$

$$e = \eta/4 = (\beta/4) \tan\theta \quad (4)$$

where  $\eta$  is the “apparent” strain and e, the maximum strain. In all practical cases, line broadening occurs due to simultaneous size and lattice distortion effects. To such cases, Williamson–Hall plot [26] may conveniently be utilized to separate these two effects. In this technique, plot of  $\beta$  for all

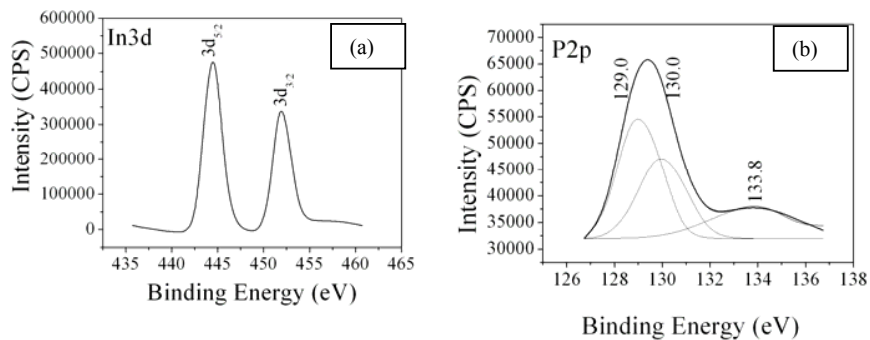


the reflections of the sample are expressed in terms of reciprocal unit ( $\beta^* = \beta \cos(\theta)/\lambda$ ) and as a function of  $d^*$  ( $d^* = 2 \sin(\theta)/\lambda$ ).

It is apparent that the plots of  $\beta^*$  versus  $d^*$  would be a straight line and the intercept would give the particle size ( $K/(D)v$ ) while the slope would give the strain ( $2\eta$ ). Inset of Fig.2b shows such a plot for the representative InP film deposited here. The particle size and the strain values obtained from the above were 58.8 nm and  $1.74 \times 10^{-3}$ , respectively. It may be observed that the crystallite size determined from the above calculations is lower than that obtained from the SEM studies. This is basically due to conglomeration of such crystallites forming polycrystallites which are apparently visible in the SEM micrograph. The strain value obtained from the above calculations indicated that residual strain (compressive) in the film was quite low. The indium rich films are more strained than the In-poor films while the stoichiometric films had the lowest strain. Thus peeling off the films with subsequent annealing required for heterojunction formation would be minimal.

### 3.2 XPS studies

X-ray photoelectron spectroscopy studies were carried out by using an Al  $K\alpha$  radiation (1486.71 eV). The XPS spectrum indicated that the film mainly consisted of In, P, and O, where oxygen might be adsorbed (physisorbed) onto the sample surface due to exposure of the sample to the ambient atmosphere. XPS scans of In 3d cores for a representative InP film (InP-01) surface is shown in Fig.3(a). The peak for In 3d core could be seen to consist of two peaks of In



for  $3d_{5/2}$  and  $3d_{3/2}$  located at  $\sim 444.5$  eV and 451.9 eV, respectively. The In  $3d_{5/2}$  peak at  $\sim 444.5$  eV was assigned to InP. Fig.3(b) shows the P 2p spectra for InP surface. The P 2p core-level spectrum was fitted with three peaks at  $\sim 129$  eV, 130 eV and 133.8 eV. The P 2p peak at 129 eV could be assigned to only P as in InP while the lower intensity peak located at  $\sim 130$  eV could be assigned to metallic phosphorous.

### 3.3. Optical studies

The absorption coefficients ( $\alpha$ ) of the InP films were determined by measuring transmittance (Tr) and reflectance (R) in these films [30,31]. The nature of the fall of the transmittance and absorption spectra (not shown here) near the band gap energy was not very sharp reflecting typical behaviour of a polycrystalline film. The absorption coefficient ( $\alpha$ ) as a function of the incident photon energy ( $h\nu$ ) may be written as:

$$\alpha = (A/h\nu)\{h\nu - E_g\}^m \quad (5)$$

where, A is a constant which is different for different transitions indicated by different values of m and  $E_g$  is the corresponding band gap. This eqn. (5) may be rewritten as:

$$[d(\ln\alpha hv)/d(hv)] = m/(hv - E_g) \quad (6)$$

Eqn.6 indicates that a plot of  $d[\ln(\alpha hv)]/d[hv]$  versus  $hv$  would show a divergence at  $hv = E_g$ , from which a rough estimate of  $E_g$  may be obtained and as such by using Eqn.5, the value of m can easily be evaluated from the slope of the plot of  $\ln(\alpha hv)$  versus  $\ln(hv - E_g)$ . Fig. 4 (inset) shows the plot of  $\ln(\alpha hv)$  versus  $\ln(hv - E_g)$  for a representative film and the value of m obtained from the slope was  $\sim 0.496$ , indicating allowed direct transition to be present in the films deposited here. The band gap,  $E_g$ , was determined by extrapolating the linear portion of the plot of  $(\alpha hv)^2$  versus  $hv$  (Fig.4) and was found to be  $\sim 1.42$  eV. This value matches well with the bulk value indicating superior quality of the InP films deposited here.

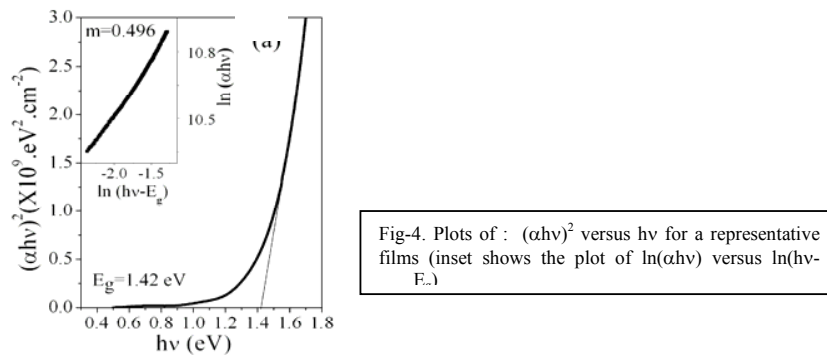


Fig-4. Plots of :  $(\alpha hv)^2$  versus  $hv$  for a representative films (inset shows the plot of  $\ln(\alpha hv)$  versus  $\ln(hv - E_g)$ .)

### 3.4. Photoluminescence studies

PL spectra recorded at 300 K and 10 K for a representative InP film at an excitation of 1.653 eV are shown in Fig.5(a) and 5(b), respectively. The PL spectrum measured at 300 K was dominated by a strong peak located  $\sim 1.41$  eV. The intensity of this peak increased significantly

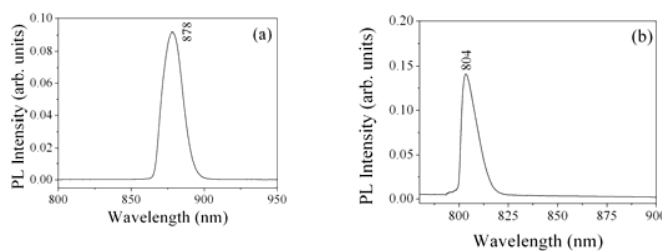


Fig.5. PL of a representative InP film recorded at (a) 300 K and (b) 10 K.

when recorded at lower (10 K) temperatures and the peak position shifted toward higher energy  $\sim 1.54$  eV. The energy of the room temperature PL peak located at  $\sim 1.41$  eV was lower than the

band gap energy ( $\sim 1.42$  eV) and this transition may thus be bound excitonic in nature. It may be noted here that no peaks for transitions due to native defects has been observed. This would reduce the possibility of minority carrier trapping in the PV devices formed with these InP films. The temperature coefficient of band gap energy obtained from this shift is  $\sim 4.48 \times 10^{-4}$  eV/K which tallied extremely well with that of bulk value [22].

### 3.5. Raman studies

Raman spectrum for a representative InP film is shown in Fig 6. One may observe two characteristic Raman peaks for InP located at  $\sim 304$   $\text{cm}^{-1}$  and  $342$   $\text{cm}^{-1}$ . The peak at  $\sim 304$   $\text{cm}^{-1}$  was identified as arising due to TO phonon scattering, which was symmetry forbidden for the  $([001] \parallel [001])$  configuration of InP only.

According to the selection rules for the backscattering geometry of crystals with zincblende structure, the incident light is expected to be scattered by LO phonons if the crystal surface is (100) and/or (111) oriented and by TO phonons if it is (110) and/or (111) oriented. Therefore, in the Raman spectra of a polycrystalline film, with crystallites oriented in different directions, both LO and TO phonon peaks should be present. In fact, the narrow Raman lines at about  $304$  and  $342$   $\text{cm}^{-1}$  attributed to TO and LO phonon scattering, respectively, are clearly visible (Fig.5) in each sample. The phonon energy is in good agreement with the phonon modes found in the literature for InP single crystals ( $303.7 \pm 0.3$  and  $345.0 \pm 0.3$   $\text{cm}^{-1}$  for TO and LO peaks, respectively [22]). It may be noted here that these values tallied extremely well with the values obtained by Mooradian and Wright [38] for single crystalline InP. Raman lines at  $304$   $\text{cm}^{-1}$  and  $345$   $\text{cm}^{-1}$  obtained by Perna *et al.*[7] for polycrystalline InP films are also close to the values obtained by us.

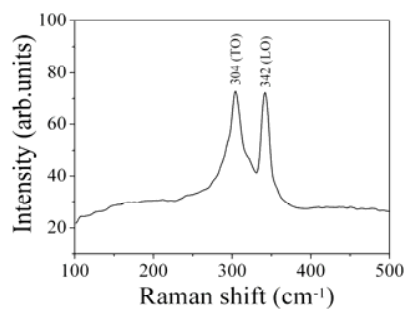


Fig-6. Raman spectra of a representative InP film.

## 4. CONCLUSIONS

It may be concluded that the use of the co-evaporation technique described in this paper would permit one to synthesize high quality polycrystalline InP films for device applications. The grain size was found to be  $\sim 78$  nm and the residual strain was quite low. Band gap of the films was  $\sim 1.42$  eV. PL studies indicated a peak  $\sim 1.41$  eV which was ascribed to be bound excitonic in nature. XRD patterns indicated peaks at  $2\theta \sim 26.5^\circ$ ,  $43.8^\circ$  and  $51.7^\circ$  for reflections from (111), (220) and (311) planes, respectively for zinc blende structure. XPS scans of In 3d cores and P 2p core-level spectra for InP film indicated that both the peaks can be fitted with two peak. The In 3d core consisted of two peaks for 3d<sub>5/2</sub> and 3d<sub>3/2</sub> while the P 2p could be deconvoluted at 129 eV and 130 eV. The peak at 444.5 eV was due to bonding between In and P while that for P 2p at 129

eV was due to InP. Two characteristic Raman peaks for InP located at  $\sim 304 \text{ cm}^{-1}$  and  $342 \text{ cm}^{-1}$  could be identified as arising due to TO phonon and LO phonon scattering, respectively.

## 5. ACKNOWLEDGEMENT

The authors wish to thank the Department of Science and Technology, Government of India for the financial assistance for executing this programme. One of us (RNG) wishes to thank Coal S&T, Government of India, for granting him fellowship. The authors would also like to thank Dr. G. Amarendra, Scientist-in-charge, UGC-DAE CSR, Kalpakkam Node, Kalpakkam for his kind support.

## REFERENCES

1. Weinberg I, Sol Cells 1990; 29: 225.
2. Schimper H. -J, Kollonitsch Z, Möller K, Seidel U, et al. J Cryst Growth 2006; 287: 642.
3. Yamaguchi M, Sol Energy Mater Sol Cells 2001; 68: 31.
4. Wanlass M W, Gessert T A, Emery K A, Coutts T J, Proc. 20th IEEE Photovoltaic Specialists' Conference, Las Vegas, 1988: 660.
5. Li X, Wanlass M W, Gessert T, Emery K A, Coutts T J, Appl Phys Lett 1989; 54: 2674.
6. Razeghi M, in: Willardson R K, Beer A C (Eds.) Indium Phosphide Crystal Growth and Characterization, Academic Press, New York, 1990: 243.
7. Perna G, Capozzi V, Augelli V et al. Semicond Sci Technol 2001; 16: 377.
8. Choi K Y, Shen C C, Miller B I, Proc. 19th IEEE Photovoltaic Specialists' Conference, IEEE, New York, 1987: 225.
9. Mitra P, Gupta P, Chaudhuri S, Pal A K, Mater Chem Phys 1994; 38: 81.
10. Sahu S N, Bourdillon A, phys stat solidi (a) 1989 ; III K : 179.
11. Öztas M, Bedir M, Kayah R, Aksoy F, J Mater Sci: Mater In Electronics 2006; 17: 841.
12. Gayen R N, Das S N, Dalui S, Paul R, Bhar R, Pal A K, Thin Solid Films 2010; 518: 3595.
13. Shahid N, Naureen S, Li M Y, Swillo M, Anand S, J Vac Sci Technol B 2011; 29: 031202-1.
14. Rusu G I, phys stat solidi (a) 1971; 4: 755.
15. Mattila M, Hakkarainen T, Jiang H, Kauppinen E I, Lipsanen H, Nanotechnology 2007; 18: 155301.
16. Duan X, Huang Y, Cui Y, Wang J, Lieber C M, Nature 2001; 409: 66.
17. Jasinskia J, Leppert V J, Lam Si-Ty, Gibson G A et al. Solid State Commun 2007; 141: 624.
18. Jun K W, Khanna P K, Hong K B et al. Mater Chem Phys 2006; 96 : 494.
19. Adam S, Talapina D V, Borchert H, et al. J Chem Phys 2005; 123: 084706.
20. Guo J, Huang H, Ren X, Yan X et al. J Vac Sci Technol B 2011; 29: 3.
21. Joint Committee on Powder Diffraction-International Centre for Diffraction Data (JCPDS-ICDD) 1997 Card No. 32-0452.
22. Bornstein L, Numerical Data and Functional Relationships in Science and Technology New Series Group III 17a , Springer Verlag, Berlin, 1982: 281.
23. Scherrer P, Nachr Ges Wiss Göttingen 1918; 26: 98
24. Wilson A C J, Mathematical Theory of X-ray Powder Diffractometry, Eindhoven, Philips, 1963.
25. Stokes A R, Wilson A C J, Proc Phys Soc London 1944; 56: 174
26. Manificier J C, Gasiot J, Fillard J P, J Phys E 1976; 9: 1002.
27. Bhattacharya D, Chaudhuri S, Pal A K, Bhattacharya S K, Vacuum 1992; 43: 313.

## **EFFICIENT WAY OF USING SOLAR SYSTEM TO THE HOUSEHOLDS' NORMAL APPLICATIONS**

J. AMALENDRAN and A. ATPUTHARAJAH\*

*Department of Electrical and Electronic Engineering, Faculty of Engineering, University of Peradeniya, Peradeniya, Sri Lanka*

\*Corresponding Author, e-mail: *atpu@ee.pdn.ac.lk*

### **ABSTRACT**

This paper discusses about how a solar cell can be used efficiently and effectively for normal home usages such as: pumping water to the over head tank and other home electrical goods. Efficient and effective usage of solar energy is analyzed by focusing on (i) minimizing the losses in the complete process of converting the solar energy into electrical energy, (ii) maximizing the power extraction from the solar cell by implementing the Maximum Power Point Traction (MPPT) controller and (iii) end terminal usage is also controlled based on the status of available energy. As a result it was found that the implemented system is the best for electrifying the households using the solar system.

This research paper will be organized with the following study information: (i) literature review on existing solar application systems, (ii) MPPT controller to extract maximum power out of the available power from the solar cells, (iii) study on battery charging controller applied in solar power systems, (iv) application study of a solar system to pump water to the over head tank, (v) efficient use of pump load to based on status of the energy in the battery storage system.

The simulation study is carried out using PSCAD/EMTDC simulation package. Here a MPPT control is implemented to study the improvement on the solar system's performance. A DC-DC converter (0 - 36 varying voltage at open circuited solar terminals to 12 fixed voltage at battery terminals) is modeled to match the solar output and battery bank and a DC-AC inverter is used to provide 230 V AC supply to the home circuits. A supervisory control is developed in this paper to detect the over head tank water level to operate the water pump with pre defined operational strategies. Further a facility is also added as a supervisory control to indicate level of energy available in the system in percentage. This will help for smart operations of the house holders to effectively use the energy with pre-plan.

Finally a practically implemented solar system at a house hold application is studied. Here one of the houses, which were already using the solar system, is taken for study. The proposed supervisory control system is embedded with normal operation of the implemented solar system in the house. The performance of the solar system with proposed modifications has proven the effective and efficient operation of the house hold solar system.

In conclusion in this research; literature review, studies in simulation and practically implemented system is discussed. A control including supervisory observation on stage of the energy is presented. It is confirmed that the solar system can be made effectively and efficiently through supervisory controls implemented embedded to the existing solar technologies. This also allows smart operations if the house owners required.

Every year, it can be observed that the cost of the solar system is decreasing. This also increases the usage of solar system. Therefore the proposed supervisory control will help the households' appliance to increase the economical viability on using solar systems.

### **1. INTRODUCTION**

Today the electricity generation from solar power plants is motivated with the help of Government of many countries. It is true that the cost of the solar power production cannot be competitive with the traditional power generation technologies such as hydro and coal. However, the cost of the solar system is decreasing rapidly year by year and it will become as one of the solution to meet future energy demand. Therefore it is important to open up an extensive research

and development on, one of the renewable energy technology such as solar to keep the world resources to the future generation while having good health to the present generation with clean environment.

## **2. LITERATURE REVIEW**

Sine the Stone Age, the solar power is being used by human for their livelihood support in several ways [1]. Especially heat energy is being utilized for drying fish, clothes, heating water etc.. It has been very well reported that the earth is receiving 174 PW ( $10^{15}$ ) of energy at the top atmosphere. Out of this solar radiation nearly 30% is being reflected back to space while the rest is absorbed by lands, Clouds, Ocean. This confirmed that there is a tremendous energy available in the solar radiation.

It has been very well address in [2] on planning a large scale solar power plant, where it has been indicated already more than 100 GW of solar power plant is already implemented globally in 2009. The German experience in 2007 on 3.8 GW solar power plants are clearly explain in [3] with hybrid operation of wind, biomass and hydro power technologies. Stand alone hybrid operation of wind and solar is explained in [4]. The Japan experience on grid connected solar power plants of 4.8 GW in 2007 is reported in [5]. Further several ways of energy balancing are also discussed in detail. Challenges on operating solar power plant by the utilities, growth of solar power industries and their business is discussed [6] in overall. The basic of solar power technology and their development with different technological advancements are explained in [7]. Solar mapping and availability of solar power is discussed with other challenges on solar power technology in [8].

As a result these studies' on existing solar power plants and their challenges summaries the importance given to the solar power plants in different part of the world. All has proven that they started with small technological development, which is mostly electrifying a single light, street lamp, small house hold equipment such as torches and lanterns, table lamps, calling bells, small fans, etc.

However, no paper discussed how we can improve the house hold electrification with good quality. Further making the solar power set with (i) easy to handle, (ii) less operational cost, (iii) automatic renew of power every day, (iv) noise free and (v) flexibility of solution will be more attractive to the users. Therefore this paper address on effective and efficient electrification of household equipment with solar cell in detail. Especially this has addressed the one example on pumping water to the over head tank and other home electrical goods through based on the smartness of the house hold owner.

## **3. MAXIMUM POWER POINT TRACKING CONTROLLER**

Maximum Power Point Tracking (MPPT) is a good controller to be accommodated with solar power systems. It maximizes the output power from the solar cell by changing its dc-like voltage. Basically it helps to extracts maximum power out from the solar cell for the specific solar radiation point. Or in other words it increases the solar cell efficiency. As a result of the MPPT, the payback of the total solar system will be reduced considerable. However, the MPP varies with illumination, temperature, radiation dose and other ageing effects as shown in Figures 1 and 2.

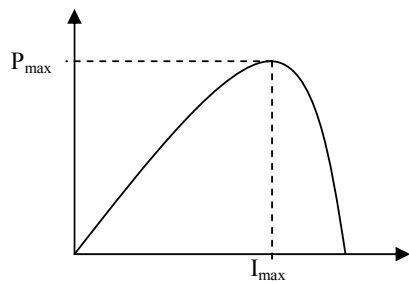


Fig. 1: Average output power vs average output current of a solar cell

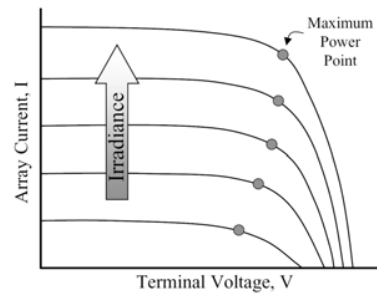


Fig. 2: Average output current vs average output voltage of a solar array

#### 4. PROPOSED SOLAR POWER SYSTEMS

The battery was having almost a fixed 12 V DC supply, which varies slightly (about  $\pm 2$  Volt based on its state of charge). The solar MPPT control varies the solar output from 36 Volt to 12 Volt based on the available power at the solar terminals. A DC-DC converter is used to couple the battery terminal with solar panel output terminals as shown in Figure 3. As a result the solar panel with the DC-DC converter has the flexibility on charging the batter while giving supply to the loads, which are connected to the battery terminals. Here the water pump made of a 12 V DC motor is used. Further if required (if full household equipment need to be covered then) a DC-AC converter can also be used to supply the house appliances. A light indicating system is developed to show up the level of charge in the battery. This gives a signal to the house owner to work smartly to utilize the energy manually or automatically such as watering to the garden. Mostly in dry day, where watering is needed to the garden, will have enough solar power.

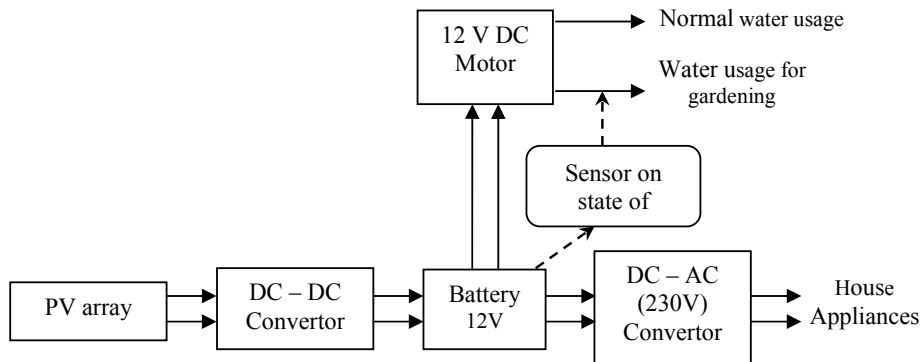


Fig. 3: Complete control block diagram of the solar power systems

#### 5. SIMULATION STUDY ON THE SOLAR POWER SYSTEMS

The complete control was implemented in the simulation using PSCAD/EMTDC software package. The battery model, which varies its output voltage based on the state of charge is shown in Figure 4. Here the initial charge in the battery can also be changed in the simulation, which helps to observe the performance of the system from any point of start. The battery characteristic graph, which is the variation of battery terminal voltage with its available energy, is shown in Figure 5.

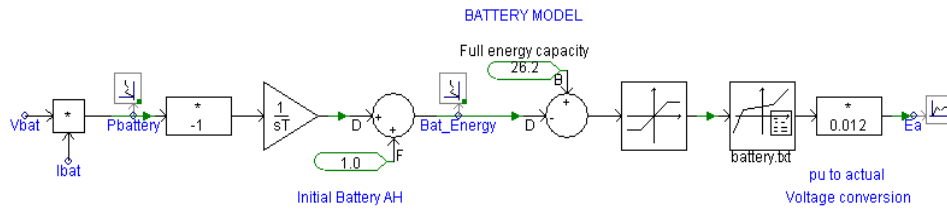


Fig. 4: Battery model used in this simulation study

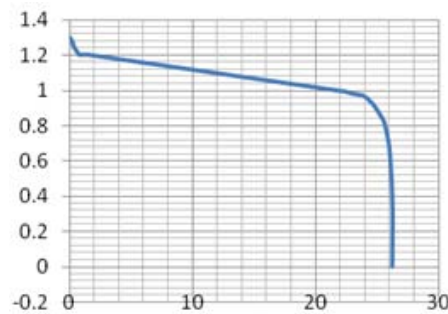


Fig. 5: Battery terminal voltage (in pu) vs Battery energy (in AH)

A simplified solar power systems with proposed control operations was modeled in PSCAD/EMTDC and shown in Figure 6. Here the solar cell is represented by a simple DC battery model with variable DC output voltage. A DC-DC converter is modeled using a single IGBT, which is switched on and off based on the MPPT controller. A free wheel diode is used together with a coupling inductor to smooth the current in the load side during the switching operation of the IGBT switch. Then the actual battery model, which was explained in Figure 4, is connected and finally the load is connected through a circuit breaker.

The variation in solar power radiation is applied through the variable input of the solar cell model. Connecting the load and disconnecting the load is achieved by the circuit breaker, which operates based on the water level in the tank and battery terminal voltage ( $V_{bat}$ ). This is an automated operation. However, there are instances where the tank will be full and the battery also charged fully. This is notified by checking the status of the battery energy and then activates the watering to the garden.



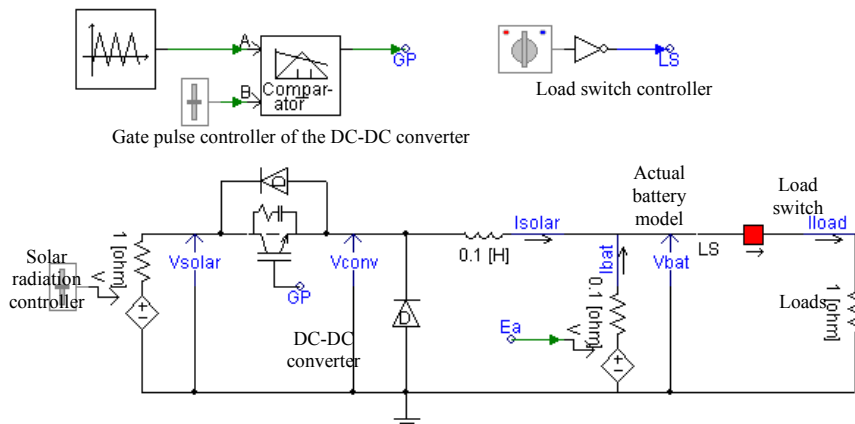


Fig. 6: Simulation model of the solar power system

## 6. SIMULATION RESULTS OF THE SOLAR POWER SYSTEMS

The complete operation of the solar system was studied in simulation. Some of the important simulation results are shown in Figure 7.

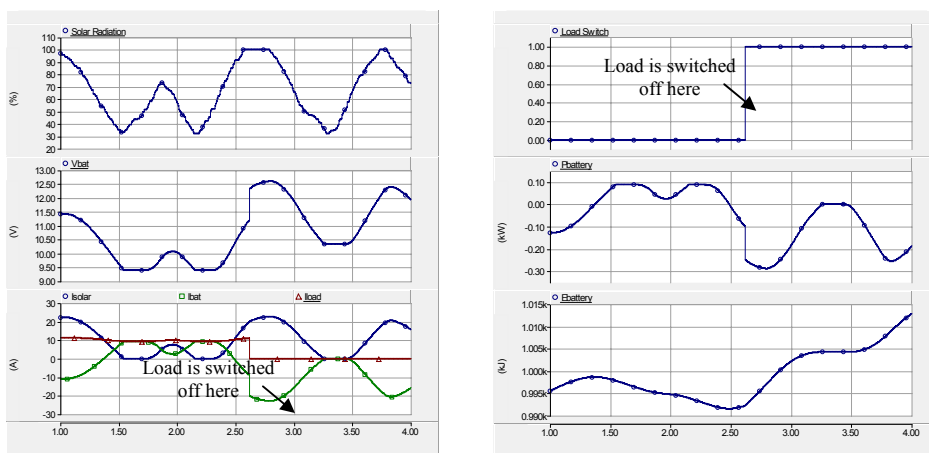


Fig. 7: Simulation results of the solar power system

Solar radiation is varied randomly as shown in the top graph. Variation of battery terminal voltage, current supplied by the solar cell, battery and load currents are shown in other graphs listed in the left side. It has clearly indicated that the load was switched off at about 2.6 seconds in the simulation and from there onwards the battery stored energy was increased as shown in the bottom right graph. This shows the autonomous operation of the solar power system with proposed control operations, where the excess energy is stored in the battery while when ever it is required supplied from the available sources.

## 7. EXPERIMENTAL IMPLEMENTATION OF THE SOLAR POWER SYSTEMS

### a. Automated water pumping system

This describes how the water pump is operated automatically based on the water level. Two sensors (low water level detection and full tank water level detection) were used to indicate the water level of the water tank. If the tank's water level is low and battery energy level is at satisfactory level then the DC motor is switched on to pump the water. When it is filled, which is identified by the second sensor, the DC motor is switched off. Here two relays with simple circuit are used to eliminate the malfunction of the motor operations closer to the threshold levels of the sensors.

### b. Complete experimental set up of the solar power system

Figure 8 shows the complete experimental set up of the solar power system. Here two MPPT controllers are used. One was the original MPPT controller, which was given by the supplier. The other was developed in the laboratory of the University of Peradeniya. The advantage of the developed one is simultaneous operation of water pump is possible while battery is get charged. Also it is very cost effective. Performance of both MPPT controllers are under testing process.

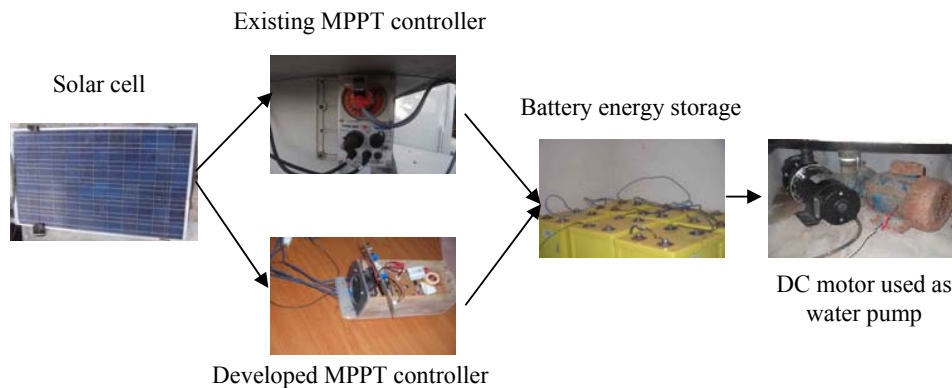


Fig. 8: Complete experimental set up of the solar power system

## 8. CONCLUSIONS

Initial study of this research has listed several literature on solar power systems. It has summarised several large scale to small scale systems, their operations and challenges. Finally a complete solar power system for household application was explained in details. The proposed system was modelled in simulation. It has been proven that the proposed maximum power point tracking control together with the supervisory control on indicating the state of charge of the battery energy storage, has made the system operation effectively and efficiently. Further the hardware implementation of the proposed system is completed and the operations are under monitored at a household for water pump application.

Recently it has been very well noticed that the rapid development is activated on developing the solar power systems. As a result of this many research and development with dedicated

conferences on solar power technologies are being conducted. This research is one of the contribution to enhance the knowledge on effective and efficient use of existing solar power system for house hold applications. It has been proven in simulation as well as implemented in hardware that the proposed added supervisory control technique added the value on the solar power systems.

## **9. ACKNOWLEDGMENT**

*The Authors acknowledge the National Research Council for their support to get the simulation package for this research. We thanks the Ceylon Electricity Board for supporting to Eng J Amalendran (Engineer, Office of the DGM(N), CEB) to do the MScEng study program at the University of Peradeniya.*

## **REFERENCES**

1. Alison Doig, "Off-grid electricity for developing countries", IEE Review, Volume 45, Issue 1, January 1999, Pages 25 – 28.
2. Jovan Bebic, Reigh Walling, Kathleen O'Brien, Benjamin Kroposki, "The Sun Also Rises – Planning for Large-Scale Solar Power", IEEE Power and Energy Magazine, May-June 2009, Pages 46 – 54.
3. Martin Braun, Gunter Arnold, Hermann Laukamp, "Plugging into the Zeitgeist – Experiences of Photovoltaic Network Integration in Germany", IEEE Power and Energy Magazine, May-June 2009, Pages 63 – 76.
4. Soysal O.A, Soysal H.S., "A residential example of hybrid wind-solar energy system: WISE", IEEE Power and Energy Society General Meeting, 20-24 July 2008, 5 pages.
5. Ryoichi Hara, Hiroyuki Kita, Takayuki Tanabe, Hiroyuki Sugihara, Akira Kuwayama, Shuya Miwa, "Testing the Technologies – Demonstration Grid-Connected Photovoltaic Projects in Japan", IEEE Power and Energy Magazine, May-June 2009, Pages 77 – 85.
6. Thomas Key, "Finding a Bright Spot – Utility Experience, Challenges and Opportunity in Photovoltaic Power", IEEE Power and Energy Magazine, May-June 2009, Pages 34 – 44.
7. Benjamin Kroposki, Robert Margolis, Dan Ton, "Harnessing the Sun – An overview of Solar Technologies", IEEE Power and Energy Magazine, May-June 2009, Pages 22 – 33.
8. Mark Mehos, Dan Kabel, Phil Smithers, "Planting the Seed – Greening the Grid with Concentrating Solar Power", IEEE Power and Energy Magazine, May-June 2009, Pages 55 – 62.

## **SYNTHESIS OF II–VI SEMICONDUCTOR NANOPARTICLES BY CONTINUOUS SPRAY PYROLYSIS (CoSP) FOR ORGANIC SOLAR CELL APPLICATIONS**

NEETESH KUMAR\* and V. DUTTA

*Photovoltaic Laboratory, Centre for Energy Studies, Indian Institute of Technology Delhi  
Hauz Khas, New Delhi-110016, India*

\*Corresponding Author, e-mail: [neetesh16@gmail.com](mailto:neetesh16@gmail.com)

### **ABSTRACT**

Continuous spray pyrolysis reactor has been used for synthesizing large quantity of high purity II–VI nanoparticles. The nanoparticles were synthesized using different precursors having 5mM concentrations of salt solutions. For CdS nanoparticles the spray solution contained  $\text{Cd}(\text{CH}_3\text{CO}_2)_2$  and  $\text{SC}(\text{NH}_2)_2$ , whereas for CdTe nanoparticles  $\text{CdCl}_2$ ,  $\text{TeO}_2$  were used as the starting materials, DI water and DI water-ammonia mixture were used as solvents, respectively. X-ray diffraction (XRD) pattern show that the products are hexagonal (CdS) and cubic structure (CdTe), with average crystallite size of 30 nm. Typically 100 mg of the nanoparticles can be created for ~ 100 ml of the spray solution.

### **1. INTRODUCTION**

Semiconductor nanoparticles have attracted widespread attention because of their special optical and electronic properties arising from the quantum confinement of electrons and large surface area [1–2]. Nanocrystals of II–VI semiconductors have been extensively studied due to their potential application organic solar cell fabrication. A variety of synthetic routes for II–VI nanocrystals have been reported in the literature, Bawendi and coworkers [2] have reported the preparation of various sizes of monodisperse CdE (E= S, Se, Te) starting from the corresponding organometallic precursors.

Nanocrystalline CdS is an II–VI semiconductor which shows the size dependent properties. Bulk CdS has 2.42 eV band gap and 1600 °C melting point, while 2 nm size nanoparticles have 3.57 eV band gap [2] and 2.5 nm CdS crystallites melt at a low temp of 400 °C [3]. However, very few studies have been reported for utilization of CdS as an important II–IV semiconductor in nanocrystals-conjugated polymer composite photovoltaic devices, probably due to the relatively large band gap (2.42 eV) that absorbs light between 300 and 512 nm, which mismatches with the solar terrestrial radiation (300–1500 nm) [4-7]. While, CdTe nanocrystals were selected in organic photovoltaic devices because they have a small band gap (1.49 eV), the smaller band gap allows for improved absorption of the solar spectrum in visible wavelength region [8-9].

CdS has three types of crystal structures namely hexagonal wurtzite, cubic zinc blend and high pressure rock-salt phase. Among these the hexagonal wurtzite has been intensively investigated because it is the most stable of the three phases and can be easily synthesized. Hexagonal phase has been observed in both the bulk and nanocrystalline CdS while cubic and rock-salt phases are observed only in nanocrystalline CdS [2]. CdS nanoparticles have been prepared using chemical precipitation method [10], solvothermal method [11], laser ablation method [12], hydrothermal method [13], photochemical method [14], one pot synthesis method [15], mesoporous copolymer Template method [16], Chemical Aerosol Flow Synthesis [17] etc. The CdTe nanoparticles have been prepared by chemical aerosol flow synthesis [17], laser ablation [18] etc.

Continuous Spray Pyrolysis technique has been used in the lab for fabrication of oxide nanoparticles/ nanostructures (Charu Dwivedi and Hrishikesh Dhamsana in this conference). Since one can create a large amount of nanoparticles continuously by spraying the required solution inside the three zone furnace, to meet such requirements for making devices like bulk heterojunction organic solar cells, the technique was developed further for making II-VI semiconductor nanoparticles. Since the materials involved toxic components, the collection chamber was enclosed so as to prevent any nanoparticle etc. from escaping. In this paper we have discussed the continuous spray pyrolysis (CoSP) for the synthesis of CdS and CdTe nanoparticles in details.

## 2. EXPERIMENTAL DETAILS

The details of the CoSP experimental setup has been described elsewhere<sup>[19]</sup>. The specially designed particles collection chamber was attached to reaction tube to *prevent environmental contamination from the volatile byproducts of the experiment*. The particles trapping bubbler was fitted inside the collection chamber as shown in fig.1.

In the present work, temperature profiles varied around 500 °C to 750 °C for the synthesis of CdS and CdTe nanoparticles. The generated droplets were carried to the reaction chamber by N<sub>2</sub> gas with the flow rate of 2 kgf/cm<sup>2</sup> and solution flow rate of 2.0ml/min. The particles generated from the furnace exit were collected in a bubbler inside the collection chamber. The collected nanoparticles washed with DI water and dried at 80°C in an oven.

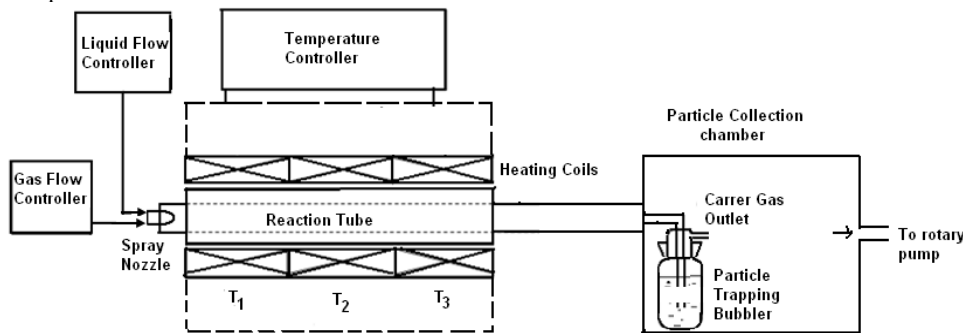
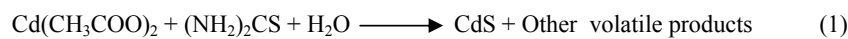


Fig.1. Schematic of continuous spray pyrolysis reactor with collection chamber

### 2.1 Synthesis of CdS nanoparticles

For synthesizing CdS nanoparticles the precursor solution of 0.005M concentration was prepared by dissolving high purity cadmium acetate (Cd(CH<sub>3</sub>COO)<sub>2</sub>) and thiourea (NH<sub>2</sub>CSNH<sub>2</sub>) in DI water. When the solution is sprayed, the following reaction takes place in reaction tube-



### 2.2 Synthesis of CdTe nanoparticles

For synthesizing CdTe nanoparticles the solvent is prepared from a mixture of DI water and ammonia in the ratio of 4:1. Cadmium and tellurium are added to this solvent in the form of cadmium chloride (CdCl<sub>2</sub>) and tellurium oxide (TeO<sub>2</sub>).The solution concentration was 0.005M. For 100 ml spray solution 2 – 3 ml of hydrazine hydride was used as a reducing agent to reduce Te<sup>4+</sup> ions into Te<sup>2-</sup> ions for reaction with Cd<sup>2+</sup> ions, pH value of the solution is adjusted to nearly 11.0 by adding hydrochloric acid<sup>[20]</sup>. When the solution is sprayed, the following reaction takes place in reaction tube-



The powder X-ray diffraction (XRD) analysis was made on a Philips XPERT PRO (PW3040) Glancing angle X-ray diffractometer using  $\text{CuK}\alpha$  radiation ( $\lambda = 0.15406 \text{ nm}$ ). Surface morphology was studied using ZEISS EVO-50 model scanning electron microscope (SEM). The absorbance of the films in the visible region was measured using ECIL double beam UV-VIS spectrophotometer. The particle size calculated using Debye-Scherrer's formula:

$$D = 0.94\lambda/\beta \cos(\theta) \quad (3)$$

where, D is the particle diameter,  $\lambda$  is the wavelength of X-ray used,  $\beta$  is the full-width at half-maximum and  $\theta$  is the scattering angle).

### 3. RESULTS AND DISCUSSION

Fig.2a shows the XRD pattern of the as-synthesized CdS products. All the diffraction peaks in Fig.2 (a) can be indexed to pure hexagonal structure CdS and no other byproduct peaks were found. Compared with the standard card (JCPDS No. 89-2944), the diffraction peaks of (100) and (101) are relatively strong, while the peak of (002) is weak. Which can be attributed to two factors as follows: the CdS particles may have a preferential orientation growth along the (101) direction. The average particle size from the XRD peaks is calculated to be 30 nm.

#### *CdTe particle preparation*

The XRD spectrum for CdTe nanoparticles as prepared is shown in Figure 2b. Six peaks are observed which correspond to the (111), (220), (311), (400), (331) and (422) planes of cubic CdTe (JCPDS No. 89-3053). The average particle size of CdTe nanoparticles is 27.0 nm, calculated by applying the Scherrer equ. (3) to the (111), (220) and (311) reflections. Absence of any other peak shows pure cubic phase of CdTe nanoparticles is being created in the process.

Fig. 3(a) & (b) presents the SEM images of the as-synthesized CdS and CdTe powders respectively. The shape of nanoparticle is spherical with some elongated structure and agglomerated clusters.

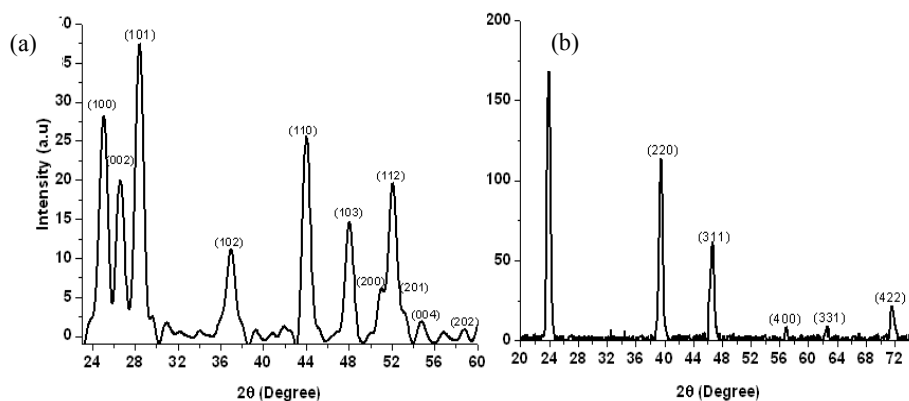


Fig.2. X-ray diffraction (XRD) patterns of the prepared CdS (a) and CdTe powders (b)

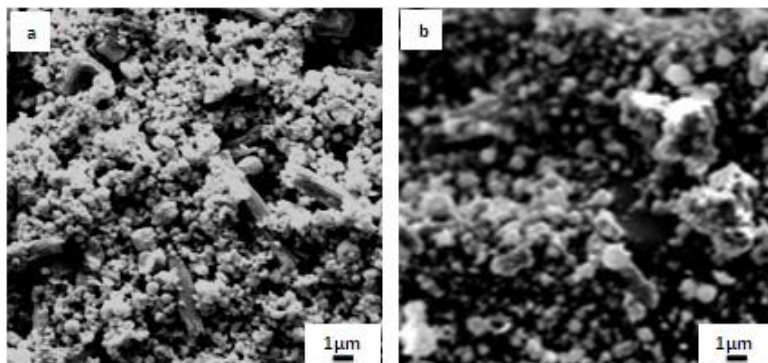


Fig.3. SEM images of CdS (a) and CdTe (b) nanoparticles

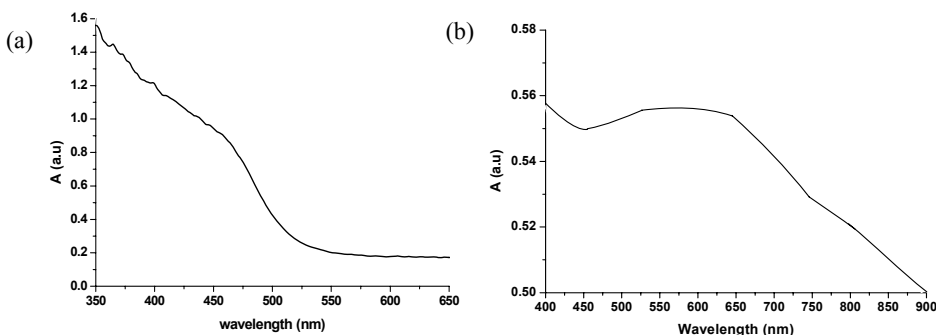


Fig.4. Absorption spectra of CdS (a) and CdTe (b) nanoparticles

The optical absorption of the II–IV semiconductor is well known to be closely related with their shape and size. The optical absorption spectra are shown in fig.4. The band gap of CdS and CdTe are 2.8 eV and 1.75 eV respectively which is higher than bulk values (2.4 eV and 1.45 eV).

#### 4. SUMMARY

In summary, we have synthesized the II–IV semiconductor nanoparticles by continuous spray pyrolysis technique with hexagonal and cubic structure. It was observed that both CdS and CdTe particles were spherical, but some amount of aggregated particles. The continuous spray pyrolysis is safe, cheap and convenient for large scale production, and yields nanocrystals of relatively narrow size distribution.

#### 5. ACKNOWLEDGMENTS

This research work was performed under the project sponsored by the Ministry of New and Renewable Energy (MNRE) of India.

## REFERENCES

1. P. Alivisatos, *Science, New Series*, **271**, 1996, 933-937.
2. C. B. Murray, D. J. Noms, and M. G. Bawendi, *J. Am. Chem. Soc.* **115**, 1993, 8706-8715.
3. A.N.Goldstein, C.M. Echer, A.P. Alivisatos, , *Science* , **256**, 1992, 1425-1427.
4. L. Wang, Y. S.Liu, Xi Jiang, D. H. Qin, and Y. Cao, *J. Phys. Chem. C* 2007, **111**, 9538-9542.
5. S. Dowland, T. Lutz, A. Ward, S. P. King, A. Ludlow, M. S. Hill, K. C. Molloy, and S.A. Haque, *Adv. Mater.* 2011, **XX**, 1-6
6. Y. Kang, D. Kim, *Solar Energy Materials & Solar Cells* **90**, 2006, 166-174.
7. H.C. Liao, S.Y.n Chen, and D.M. Liu, *Macromolecules* **42**, 2009, 6558-6563.
8. Y. Kang, N.G. Park, and D. Kim, *Applied Physice Letters* **86**, 2005, 113101.
9. T. Shiga, K. Takechi, T. Motohiro, *solar Energy Materials & Solar Cells* **90**, 2006 1849-1858.
10. V. Singh, P. Chauhan, *Journal of Physics and Chemistry of Solids* **70**, 2009, 1074-1079.
11. K. Ujjal. Gautam, R. Seshadri, C.N.R. Rao, *Chemical Physics Letters* **375**, 2003 560-564.
12. A. A. Lalayan, *Applied Surface Science* **248**, 2005, 209-212.
13. Z. Jinxin, Z. Gaoling and H. Gaorong, *Front Chem Chin* **2**, 2007, 98-101.
14. M. Marandi, N. Taghavinia, A. Irajizad and S. M. Mahdavi, *Nanotechnology* **16**, 2005, 334-338.
15. H.Tong and Y.J. Zhu, *Nanotechnology* **17**, 2006, 845-851.
16. A. F. G. Montea, N. O. Dantas, P. C. Morais, and D. Rabelo, *Brazilian Journal of Physics*, **36**, 2006, no. 2A.
17. Y.T. Didenko and K. S. Suslick, *J. AM. Chem. Soc.* **2005**, 127, 12196-12197
18. N. G. Semaltianos, Logothetidis, S. Perrie, W. Romani, S. Potter, R. J. Sharp, M. Dearden, G. Watkins, *Applied Physics Letters*, **95**, 2009.
19. V. Dutta and V. Phanikiran B., "Design of Externally Controlled Spray Pyrolytic Nanoparticles Fabrication System". (Patent application filed).
20. K. V. Krishna and V. Dutta, *journal of Applied Physics*, **96**, 2004, 3963-3971.



## **LOW-COST THERMOELECTRIC POWER GENERATION USING SOLAR ENERGY**

N.D. SUBASINGHE\*, N.B. SURIYAARACHCHI, T.B. NIMALSIRI

*Institute of Fundamental Studies, Hantana Road, Kandy, Sri Lanka*

\*Corresponding Author, email: *deepal@ifs.ac.lk*

### **ABSTRACT**

Thermal energy from sun can be converted to electricity using thermovoltaic (TV) devices or Thermoelectric generators (TEGs) as they are commonly known. They work on the principle of *Seebeck effect*. Currently there are commercial TEGs, most of which are semiconductor based and relatively expensive for domestic use. We investigate the possibility of producing low-cost TV devices for domestic use, utilising low-cost material such as metallic wires and sheets.

The performance and efficiency of a thermoelectric generator for a given temperature regime depend mainly on the materials used in the module construction and, the design/arrangement of thermoelectrical elements within the module. Essentially, any TE generator should have a set of "hot" junctions and a set of "cold" junctions, sometimes called "thermocouples". When the distance between cold and hot junctions is decreased, internal resistance drops and, as a result, the effective current should increase. Unfortunately this action will also increase the heat propagation thus reducing the temperature gradient between two sets of junctions. On the other hand, keeping hot and cold junctions far apart will facilitate maintaining higher temperature difference, hence a higher TE voltage output, but it may be partially compromised by increased resistance due to increased wire lengths between junctions. We investigate the effect of the variation of certain physical parameters such as length and diameter of the wires used in junctions, number of serial connections per module, temperature range, active and passive cooling and so on. Optimum values for certain parameters were determined.

Key words: Thermo Electric Generator, Seebeck effect, Thermoelectric power, solar energy conversion.

## **1. INTRODUCTION**

In the wake of using renewable energy in place of fossil fuel, solar energy is the first and foremost source that comes to our mind. When it comes to generate electricity, most of us concentrate only on the photovoltaic effect, forgetting the large amount of heat that comes with it. This research work investigates the use of thermoelectric (TE) devices to generate electricity from solar energy and waste heat from other sources. One of the major advantages of the TV modules over PV modules is that TV modules can generate electricity using any available heat source, not only the solar energy. The source of heat could be solar energy, waste heat from an industry, an automobile engine or a domestic cooker. Other applications of TV modules include battery-less electronic implants in patients, energy harvesting from thermal power plants and co-generation of electricity [1].

Photovoltaic cells essentially work on a single frequency or a limited range of frequencies, where as thermovoltaic cells, at least theoretically, has no such discrimination. A thermoelectric device is an energy conversion system that converts thermal energy directly into electrical energy. A device of this type is commonly referred to as a thermoelectric generator (TEG). It has been known that when a conductor is subjected to a temperature gradient, there is a flow of electrons along the conductor. In order to get these electrons as a useful current through an external circuit, it is necessary to make two junctions with dissimilar material and maintain a temperature difference between the junctions. The phenomenon that generates electricity this way is called *Seebeck effect*.

Seebeck effect is in fact a bulk effect, caused by the following processes:

- Temperature difference generates a difference in Fermi level
- Bandgap distance changes with temperature
- Diffusion coefficient is a function of temperature
- Charge carriers move from the heated side to cold side - thermodiffusion
- Electric field will be generated due to the transport of charge carriers

While many researchers in the field of thermoelectric research are engaged in improving material properties to increase the Seebeck coefficient, and hence the efficiency of the TE module, we attempt to introduce low-cost TEGs that produce electricity using solar heat or waste energy. Since such TEGs co-generate electricity by scavenging 'free' energy from any available heat source, efficiency is not an important issue. Our TEGs may be used in a way similar to that of the photovoltaic cells to generate electricity from the solar energy, but without the high initial cost. It is expected that low-cost TEGs can be produced by using scrap metal and without high-tech equipment.

Basic theory behind the thermoelectric generation and the module geometry are discussed here in brief, for the sake of completion. Seebeck coefficient  $S$  is defined as:

$$S = \frac{dV}{dT} \text{ where } V \text{ is voltage and } T \text{ is the temperature.}$$

A good thermoelectric material should have large Seebeck coefficient, low electrical resistivity and low thermal conductivity, in order to generate higher voltage.

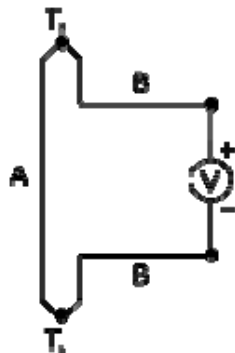


Fig. 1. A simple thermoelectric module.

$$V = \int_{T_1}^{T_2} (S_B(T) - S_A(T)) dT.$$

$S_A$  and  $S_B$  are the *Seebeck coefficients* of the metals A and B, and  $T_1$  and  $T_2$  are the temperatures of the two junctions. The Seebeck coefficients are non-linear as a function of temperature, and depend on the conductors' absolute temperature, material, and molecular structure. If the Seebeck coefficients are effectively constant for the measured temperature range, the above formula can be approximated as:

$$V = (S_B - S_A) \cdot (T_2 - T_1).$$

Four basic physical phenomena are associated with the thermoelectric generators (TEG). They are Seebeck effect, Peltier effect, Thomson effect and Joule effect. Seebeck effect describes the amount of electricity generated in a TEG module and others describe the negative effect on it. Thermal conduction and Joule heating are two irreversible processes that lower the thermoelectric effect to below the thermodynamic limit. Considering all physical phenomena, energy flow through a unit volume can be expressed in the following equations [2].

Neglecting Thomson effect as small, heat flow at hot junction can be expressed as:

$$Q_H = K_{TEG} (T_H - T_C) + S_{TEG} T_H I - \frac{1}{2} I^2 R_{TEG} \quad (1)$$

Similarly, for cold junction:

$$Q_C = K_{TEG} (T_H - T_C) + S_{TEG} T_H I + \frac{1}{2} I^2 R_{TEG} \quad (2)$$

Difference between  $Q_H$  and  $Q_C$  equals to the net power ( $P_{TEG}$ ) produced by the TEG module.

$$P_{TEG} = Q_H - Q_C = S_{TEG} (T_H - T_C) I - I^2 R_{TEG} \\ = [ S_{TEG} (T_H - T_C) - I R_{TEG} ] I \quad (3)$$

And the voltage output of the module ( $V_{TEG}$ ),  
 $V_{TEG} = S_{TEG} (T_H - T_C) - I R_{TEG} \quad (4)$

$$K_{TEG} = N(K_1 + K_2)G \quad (5)$$

$$S_{TEG} = N(S_1 + S_2) \quad (6)$$

$$R_{TEG} = N(\rho_1 + \rho) / G \quad (7)$$

$$G = \text{area/length} \quad (8)$$

Objective of this paper is to discuss the effect of selected physical parameters on the thermoelectric output. In this work, we test the effect of following factors on the final output:

- Active cooling vs. passive cooling
- Separation of the hot and cold sets of junctions

## 2. MATERIALS AND METHOD (Experimental)

Copper (0.38mm- $\Phi$ ) wires and Iron (0.44mm-  $\Phi$ ) wires were used to construct thermoelectric modules. Each module was constructed with 11 thermocouples and 2 parallel paths..

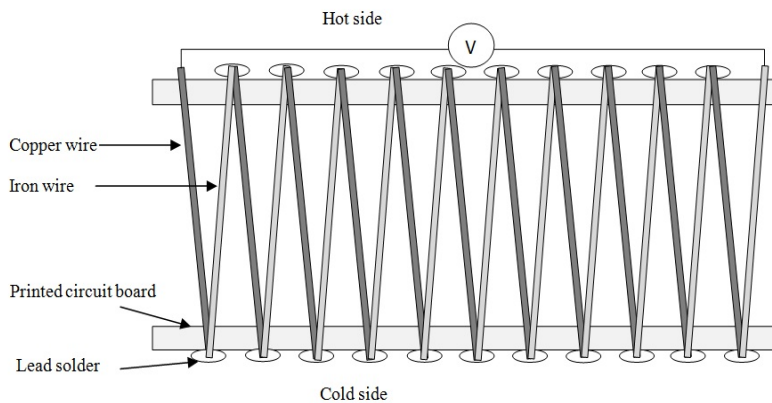


Fig. 2. Schematic diagram of the array of elements in thermoelectric modules

T = temperature
J = electrical current density
$\tau$ =Thomson coefficient
$\rho$ = electrical resistivity
$K_{TEG}$ = Thermal conductivity
$S_{TEG}$ = total Seebeck effect
$R_{TEG}$ = total resistance
G = geometry factor
$Q_H$ = heat flow at hot side
$Q_C$ = heat flow at cold side
$T_H$ = temperature of hot junction
$T_C$ = temperature of cold junction
I = current
$P_{TEG}$ = Net power of TEG
N= number of junctions in the module
$K_1$ = Thermal conductivity in material 1
$K_2$ =Thermal conductivity in material 2
$S_1$ = Seebeck coefficient in material 1
$S_2$ =Seebeck coefficient in material 2

This design gives a sufficiently large voltage and current so that the errors are minimised. Thermoelectric modules were assembled on printed circuit board (PCB) and lead solder was used to ensure contact of two metals. Figs. 2 show the design of the module.

Some of the important physical properties of the material used for TEG modules are given below.

Table. 1 Physical properties of materials used and to be used in TEG module

Material	Thermal Expansion $\times 10^{-6}/K$	Thermal conductivity W/mK	Specific Heat capacity J/kgK	Electrical conductivity $\times 10^6 \Omega m$	Seebeck coefficient $\mu V/K$
Iron	12	80	465	11.5	19
Copper	16.7	400	385	58	6.5
Aluminium	22.5	237	900	36	3.5
Lead	29.3	33	130	5.2	4.0

Experiments were conducted in four different ways.

01. Using two oil baths to maintain temperatures of hot and cold sides.
02. Using sand bath to heat up hot side and a fan to cool down the cold side.
03. Using sand bath to heat up the hot side with no active cooling at cold side.
04. Using melting ice at  $0^{\circ}C$  as reference in cold junction, while increasing the hot side temperature.

Different temperature gradients were maintained between hot and cold junctions. Corresponding voltages and current values were recorded for each experiment. Then voltage per thermocouple was calculated for each value obtained.

### 3. RESULTS AND DISCUSSION

Fig. 3 shows the output voltage per thermocouple for four different modules. Results clearly indicate that the output increases with the separation of hot and cold sides.

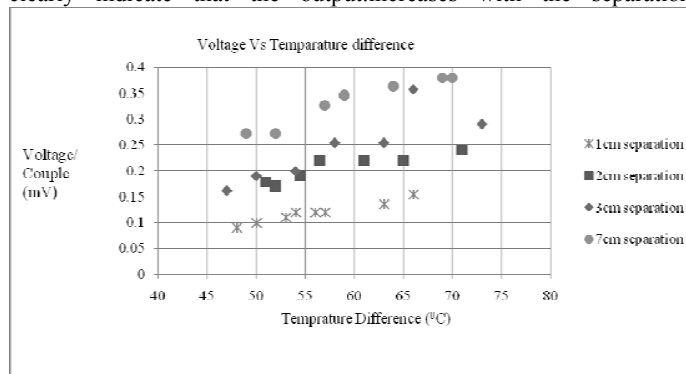
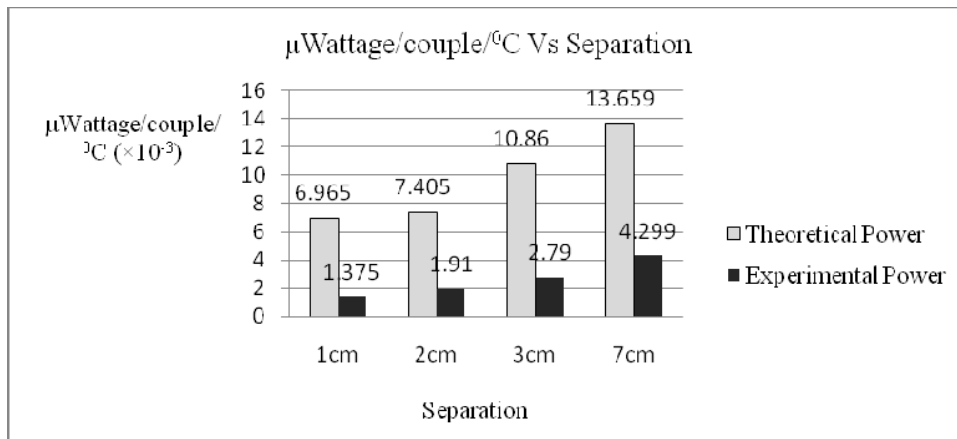


Fig. 3. Variation of output voltage with temperature difference for four modules produced.

Possible theoretical power output for the modules produced were calculated using aforementioned equations and material data published [3]. As shown in Fig. 5, experimental values fall far below the theoretical values. Highest experimental value is from the module with 7 cm separation and it is about 30% of the theoretical value. Reasons for these differences are discussed later.

As indicated in Tables 2 & 3, active cooling improves the thermoelectric output by a significant factor. However, when the total energy budget is considered, energy consumed in the cooling process vastly reduces the overall efficiency of the TEG. If the cold and hot junctions are sufficiently far apart and the hot junction temperature is maintained significantly higher than the ambient temperature, TEG may still have a good output without employing any active cooling. Since it is easier to maintain a higher temperature gradient at higher temperatures, concentrating solar energy onto the module may be useful.



**Fig. 4.** Power output per couple per degree Vs junction separation ( $0^{\circ}\text{C}$  reference). This also compares the experimental values with the possible theoretical values.

During this experiment, iron and copper were used in the construction of the TEG modules, since they are easier to obtain in required gauges and are easier to manipulate. However, in an industrial module, aluminium will be used in place of copper. Aluminium has several advantages over copper: 1. Cheaper, 2. Lighter, 3. Corrosion to iron will be reduced, since aluminium is higher in the electrochemical series, and, 4. Lower Seebeck constant means higher the difference; higher TE voltage per couple when combined with iron.

TEG modules used in this study generate few millivolts and few milliamperes of current. Probably more than thousand thermocouples will be required to generate few volts. Connecting thousands of thermocouples in series can cause contact problems and increase the internal resistance of the module. TEG modules can usually produce relatively higher currents, which will increase the ohmic loss. Therefore, we propose voltage clamping electronic circuits to enhance the generated voltage, while several parallelly connected modules help increasing the power output. If the modules are used at high-temperature, thermal expansion of the material used should also be considered, in order to sustain mechanical durability of the unit [4].

Power output values obtained in this experiment are lower than the theoretically calculated values (Fig. 4). Possible reasons for lower output: 1. contact resistance. 2. resistance of the elements may be higher than the expected. 3. impurities in material used (use of commercial grade metals). 4. not including the heat flow in the soldering material and parasitic heat losses in calculations. 5. Oxidation effects, especially the corrosion of iron while in contact with copper.

Table 02. Results from 7cm separation TEG module without active cooling.

Hot junction Temp. ( $^{\circ}\text{C}$ )	Voltage (mV)	mV/couple (mV)
27	1.02	0.0463
35	2.8	0.127
40	3.67	0.166
45	4.85	0.220
50	5.36	0.243
55	6.22	0.282
63	7.66	0.348
65	7.85	0.356
70	8.4	0.381
75	8.94	0.406
80	9.04	0.410
85	9.99	0.454
90	10.31	0.468
95	10.55	0.479
100	10.14	0.461
105	10.02	0.455
125	9.87	0.448
135	9.98	0.453
140	10.56	0.480
147	11.85	0.538
150	11.98	0.544

Table 03. Results from 7cm separation TEG module with The use of cooling fan (active cooling )

Temperature / $^{\circ}\text{C}$	Temp-Difference / $^{\circ}\text{C}$	Voltage /mV	mV/ couple
29	2	1.71	0.0909
30	3	4.3	0.1363
35	8	7.86	0.3636
40	13	11.15	0.5909
45	18	12.52	0.8181
50	23	14.69	1.0454
55	28	16.13	1.2727
60	33	18.2	1.5
65	38	20.92	1.7272
70	43	21.97	1.9545
77	50	25.27	2.2727
80	53	26.51	2.4090
85	58	31.58	2.6363

#### 4. CONCLUSION

Geometry and physical parameters of a TEG seriously affects its power output. It is important to find the optimum distance between hot and cold junctions. If the distance is too short sufficient temperature difference between hot and cold junctions cannot be maintained, although the internal resistance will be lower due to reduced wire length. Temperature of the cold sink is the most important factor in controlling the output of a given module. Increasing the distance will help to maintain a sufficient temperature difference, thus increasing the thermovoltaic output. However, this action increases the internal resistance and the cost of material. Although active cooling increases the output significantly, this has to be weighted against the amount of power consumed. Overall, it was found that increasing the separating distance between hot and cold sides works favourably.

#### REFERENCES

1. J. M. Damaschke, IEEE transactions on industry applications, 33(5)1203-1207 (2002).
2. P.G. Lau and R.J. Buist, Thermoelectrics, Proceedings ICT '97. XVI International Conference, Dresden, Germany (1997).
3. K.T. Zorbas, E. Hatzikraniotis, and K.M. Paraskevopoulos, 6<sup>th</sup> European Conference on Thermoelectrics, July 2 - 4, Paris, France (2008).
4. G. J. Snyder and T. S. Ursell, 22<sup>nd</sup> International Conference on Thermoelectrics - ICT, Montpellier, France. P.443-446 (2003).

## Author Index

- Abeygunawardhana P.W. 229  
Abuel-Rub K. 102  
Akilavasan J. 91  
Albinsson I. 221  
Amalendran J. 324  
Anuradha S. G. 158  
Ariyasinghe D.M.B.P. 152  
Ariyasinghe Y.P.Y.P. 180  
Arof A.K. 200, 206, 213  
Atputharajah A. 324  
Attanayake C.I.F. 264  
Aybek A.S. 103
- Balashangar K. 258  
Bandara H.M.N. 152, 158  
Bandara J. 91  
Bandara T.M.W.J. 96, 175, 193, 221  
Bhar R. 317  
Bhattacharjee A. 82  
Buraidah M.H. 200, 206, 213
- Careem M.A. 96, 200, 206, 213  
Chandrasegaran T. 312  
Clara Dhanemozhi A. 308
- De Alwis A.A.P. 264  
De Silva L.C. 284  
Dematage N. 142  
Dharmadasa I.M. 1, 16, 120  
Dhasmana H. 271  
Dhere R. 27  
Diso D.G. 120  
Dissanayake M.A.K.L. 102, 163, 175,  
180, 186, 193,  
229
- Dutta V. 131, 271, 331  
Dwivedi C. 131, 271
- Echendu O.K. 120  
Ekanayake P. 246
- Fan H. 126  
Fernando P.S.L. 193  
Furlani M. 221  
Garland J. 10  
Gayen R.N. 317  
Ghosh H.N. 70  
Grein C.H. 10  
Gunaratne L. 1  
Gunasekara P.D.N. 180  
Gupta R. 277
- Hahn S-R. 102  
Hidaka M. 105  
Hussain S. 317
- Illeperuma O.A. 51  
Iqbal H. 163  
Iskandar P.M. 246, 284
- Jaseetharan T. 258  
Jayanetti J.K.D.S. 112  
Jayasundara W.J.M.J.S.R. 193  
Jayathilaka K.M.D.C. 112  
Joshi S.S. 28  
Justin Thomas K.R. 252
- Kajitha B. 253  
Karunaratne M.L. 169  
Konno A. 44, 136, 142  
Kul M. 103  
Kumar N. 331  
Kumara G.R.R.A. 142, 158, 169  
Kumaraarachchi K. 96
- Lokhande C.D. 28  
Lundell E. 221
- Mahanama G.D.K. 265  
Majid S.R. 200, 206, 213  
Mellander B.-E. 60, 96, 193, 221

Murakami K. 136  
 Nandi D.K. 277  
 Nimalsiri T.B. 336  
 Noor M.M. 200, 206, 213  
 Nupearachchi C.N. 236, 241  
  
 Olusola O.I. 291, 297  
 Oluyamo S.S. 291, 297  
  
 Pal A.K. 61, 317  
 Palamakubura S. 229  
 Perera H.A.C.S. 186  
 Perera K. 163, 186  
 Perera V.P.S. 148, 236, 241  
 Premachandra B.A.J.K. 264  
 Premalal E.V.A. 44, 136, 142  
 Premaratne K. 169  
  
 Rajapakse R.M.G. 136, 142, 152, 158,  
 169  
 Ravirajan P. 253, 258  
 Reehal H.S. 71, 265  
 Rupasinghe W.N.S. 163, 186  
  
 Sarathchandran S. 253, 258  
 Senadeera G.K.R. 96, 148, 163, 175,  
 180, 186, 229, 241,  
 246, 264  
 Seneviratne V.A. 163, 186  
 Senthilnathanan M. 253  
 Shimomura M. 152  
 Sion W.T. 284  
 Siripala W. 36, 112  
 Sivananthan S. 10, 27  
 Somasundaran P. 277  
 Subasinghe N.D. 336  
 Suriyaarachchi N.B. 336  
 Svensson I. 221  
 Svensson T. 221  
  
 Tari S. 102  
 Taskopru T. 103  
  
 Tennakoon K. 246  
 Teo L.P. 200  
 Tewari S. 82  
 Thotawatthage C.A. 163, 175, 180, 186,  
 229, 241  
 Turan E. 103  
  
 Vidanapathirana K. 186  
  
 Weerasinghe A.R. 120  
 Wickramaarachchi W.A.P.N. 158  
 Wickramasinghe L.R.G. 148  
 Wijayarathna T.R.C.K. 180, 236  
 Wijesundera R.P. 105  
 Wijewarnasuriya P. 35  
  
 Yahya R. 213  
 Yoshikawa S. 246  
 Yusuf S.N.F. 200, 206, 213  
  
 Zain R. 246  
 Zor M. 103